

Masaryk University

Faculty of Science

Mapping galactic nuclei:
From the Galactic center to distant quasars
and back

HABILITATION THESIS



presented by

Michal Zajaček
from Malacky, Slovakia

Brno, 2024



Abstract

In this *Habilitation Thesis*, I first recall how we have mapped the gas and the stellar content in the central parsec of our Galaxy, which is the closest galactic nucleus to us, about 100 times closer than galaxies in the Local Group and approximately 1000 times closer than the nearest galaxy cluster. Around the compact radio source Sgr A* associated with the supermassive black hole (SMBH), there are fast-moving B-type stars and dust-enshrouded stellar objects that must have formed recently during the last hundred thousand to a few million years. This indicates a recent period of star formation preceded by an infall of a large amount of cold and dense gas. The amount of gas consumed by star formation is linked to the amount of gas available for accretion. Hence, our Galactic center was likely much more active and luminous a few million years ago, at the level of an active Seyfert galaxy. There are over a million active galaxies, but in their case a similar spatial resolution is unavailable. Therefore, mapping of the distribution of gas in active galactic nuclei (AGN) has traditionally been performed in the time domain to replace the lack of a sufficient angular resolution to resolve the inner regions. This so-called reverberation mapping employs reprocessing of the variable X-ray/UV continuum emission by more distant broad-line region clouds. In my work, I focused on the comparison of the radius of $H\beta$ -emitting clouds with the distance of MgII-emitting material as well as the radius corresponding to the FeII pseudocontinuum. In contrast with the radius-luminosity relations for $H\beta$ and the UV and optical FeII emission, the MgII radius-luminosity relation is flatter, although it still exhibits a significant correlation. These correlations open a way to measure supermassive black hole masses in distant quasars using just one-epoch spectroscopy. One can also employ the MgII radius-luminosity relation to standardize quasars and use them as alternative probes in cosmology. Finally, it is beneficial to combine the processes taking place in AGN with the visibly rich and dense stellar content in the Galactic center to see how an intermittently increased nuclear activity could have been impacting stars and vice versa. In particular, we studied the interaction of red giants with the activate jet and found that a large number of repetitive jet-star encounters can effectively ablate the envelopes of red giants. This can partially address the lack of large red giants in the innermost 0.5 pc of the Galactic center. *In summary, the spatial details accessible for the Galactic center complement the temporal studies of mostly unresolved AGN. On the other hand, the study of a sample of AGN with various accretion rates teaches us about the past and the potential future of the Milky Way.*

Keywords: Galactic center – Sgr A* – Central molecular zone – quasars – active galactic nuclei (AGN) – supermassive black holes – accretion flows – reverberation mapping – broad-line region – AGN feeding and feedback – cosmology



Contents

Abstract	iii
Contents	v
1 Introduction	1
1.1 Mapping the Galactic center	10
1.1.1 Stellar populations in the central parsec	13
1.1.2 Distribution of gas and accretion-flow structure	22
1.2 Mapping distant quasars	36
1.2.1 Reverberation mapping of accretion discs	44
1.2.2 Resolving spheres of influence of extragalactic nuclei	56
1.2.3 Signs of stellar-mass bodies close to extragalactic SMBHs	60
1.3 Synergies between the Galactic center and active galactic nuclei	64
1.4 Galactic nuclei as standardizable candles	67
1.5 This Thesis	70
2 Paper 1: Radio-Optical Properties of Active Galaxies	75
3 Paper 2: Reverberation-Mapping of HE 0413-4031	95
4 Paper 3: Red-Giant Depletion in the Galactic Center	125
5 Paper 4: Reverberation-Mapping of HE 0435-4312	145
6 Paper 5: Enhanced Doppler Beaming	171
7 Paper 6: Effect of Extinction on Quasar Distances	179
8 Paper 7: UV FeII Emission Model and BLR Time Delays	199
9 Discussion and Conclusions	219
Bibliography	227

Curriculum Vitae	243
Significant Research Results	245
First-author refereed publications	245
Publications in <i>Nature</i> , <i>Science</i> , and <i>Letter</i> format	247
Acknowledgements	249
Photogallery	252

Introduction

“Young people, especially young women, often ask me for advice. Here it is, valeat quantum. Do not undertake a scientific career in quest of fame or money. There are easier and better ways to reach them. Undertake it only if nothing else will satisfy you; for nothing else is probably what you will receive. Your reward will be the widening of the horizon as you climb. And if you achieve that reward you will ask no other.”

— Cecilia Payne-Gaposchkin
(1900-1979)

Foreword

Understanding the structure of a galactic nucleus is closely linked to the understanding of the structure of a galaxy, especially our own Milky Way. Since antiquity till the Middle Ages, the center of the Universe or practically the Galactic Center was associated with the Earth orbited by planets with a rather complex system of deferents and epicycles. “Non-changing” stars were attached to the distant celestial sphere. The Milky Way or the apparent brighter belt on the sky, essentially the largest object in terms of the apparent angular size observed by a naked eye, was not always associated with distant stars. Aristotle and his followers mostly interpreted it as an atmospheric phenomenon within the sub-lunar sphere created by the interactions of celestial spheres with the terrestrial sphere as they revolved around the Earth. However, there were alternative explanations during the “naked-eye” era as well, in particular during the Middle Ages, especially proposed by Arabic medieval scholars ([Eckart & Idriz 2023](#)).

The geocentric system developed by Appolonius of Perga towards the end of the 3rd century BC, Hipparchus in the 2nd century BC, and mastered by Claudius Ptolemy in *Almagest* in the 2nd century AD could address mainly the apparent retrograde motion of planets, yet the system became progressively more complex and impractical with too many auxiliary circles (bigger ones called deferents and smaller ones called epicycles) with an additional correction provided by an offset circle center or *equant* to account for the changing angular speed of planets at the perigee and the apogee.

With the (re)introduction of the heliocentric model by Nicolaus Copernicus (1474-1543), the center of the Universe, and thus also the Galaxy, was associated with the Sun (publication *De revolutionibus orbium coelestium* published in 1543, shortly before Copernicus's death). This *paradigm shift*, standing on the shoulders of the ancient astronomer Aristarchus of Samos, did not, however, provide much practical simplification of the calculations of planetary orbits. On the contrary, the system became even more complicated than the Ptolemaian geocentric model, with more and more epicycles needed to account for offsets between the predicted and the observed positions of planets. A "compromise" geoheliocentric model introduced by Tycho Brahe in the late 16th century associated the center with the Earth again, which was supposed to be too heavy to move fast as based on the Aristotelian vision of the heavy and light elements. The Moon, the Sun, and distant stars orbited around the Earth, while the five known planets at the time (Mercury, Venus, Mars, Jupiter, and Saturn) orbited around the Sun.

A real *paradigm shift* from the ideal regular circular motion was introduced by Johannes Kepler (1571-1630) in Prague, while he had a chance to study the precise positions of the planet Mars obtained previously by Tycho Brahe. He noticed that the orbital description can significantly be simplified when the closed trajectory is described by an ellipse, one of the four conic sections, with the Sun being at one of the foci. This analysis resulted into the publication of the first two Keplerian laws in 1609 in Prague (*Astronomia Nova*) and the third law (the ratio of the cube of the semi-major axis to the square of the orbital period, $a^3/P^2 = \text{const}$, remains constant) was published in 1619 (*Harmonice Mundi*) in Linz. The importance of Kepler's contribution lies in the applied scientific method, that is the application of a mathematical model (ellipse) to the orbital data. This way the perfect *Aristotelian* regular circular motion was abandoned and the Earth was finally shifted from the center of the Universe and its motion, as for the other planets, was generally not uniform around the center. An elliptical trajectory as a general orbit for a two-body problem whose special case is the motion of an object in the central potential dominated by one body was finally derived Sir Isaac Newton (1642-1726/1727) in his theory of universal gravitation published alongside the laws of motion in *Philosophiae Naturalis Principia Mathematica* (Mathematical Principles of Natural Philosophy) or shortly *Principia* in 1687.

In the subsequent centuries, the trend of confirming *Copernican* principle, i.e. that no location in the Universe is privileged, continued along with the significant developments of celestial mechanics in the 18th and the 19th century, where the conic sections in the two-body problem also evolve with time due to the perturbations from other bodies. The ability to mathematically handle the external gravitational influence led to the prediction of the position of the outermost planet Neptune by Urbain Le Verrier in 1845-1846 (independently from John Couch Adams) as based on the observed deviations of the Uranus motion from the nominal Keplerian orbit. Based on Le Verrier's calculations, Neptune was then officially discovered by Johann Gottfried Galle at the Berlin observatory on September 23rd, 1846. The Neptune position was within one degree from the predicted position, which was a remarkable accomplishment of the celestial mechanics. Subsequently, the general relativistic description

of spacetime introduced by Albert Einstein (1879-1955), in which the spacetime curvature determines the motion of bodies that, on the other hand, influence the curvature, added post-Newtonian effects, such as the prograde periaapse (Schwarzschild) precession of the orbit or the nodal precession due to the Lense-Thirring effect. The general relativistic effects were successfully applied to explain the remnant prograde precession of the Mercury orbit ($\sim 43''$ per century after subtracting the effect of other perturbing bodies) and were verified by the detection of the stellar light deflection by the Sun during the Solar eclipse on May 29, 1919 (Principe-Sobral expedition led by Arthur S. Eddington, [Dyson et al. 1920](#)). Let us now return back to the beginning of the 17th century, when another important milestone of technical nature was achieved.

The further study of the Milky Way was bolstered by the invention of a telescope by Hans Lippershey in or around 1608. Galileo Galilei (1564-1642) constructed his own refractive telescope and he was able to resolve, among other things, individual stars of the Galaxy, which once and for all discarded the theory of the Milky Way as an atmospheric phenomenon. The qualitatively correct interpretation of the brighter belt, or the Milky Way, seen on the sky was given by Thomas Wright in the mid-18th century. He put forward the model of a thin disc of stars held together by gravitational forces. In this simple model, the Earth is located at the geometric center of the disc and thus the edge-on view from within the disc creates the projected belt on the celestial sphere. This model also inspired philosopher Immanuel Kant, who in *Universal Natural History and Theory of the Heavens* (1755) also advocated that observed nebulae are distant galaxies like the Milky Way or separate “island universes”, which was objected by most of Kant’s peers at the time. Towards the end of 18th century, William Herschel constructed a more detailed distribution of stars within the Milky Way with the Sun at the Galactic center ([Herschel 1785](#)), which was possible thanks to the detailed observations with his own telescope. Herchel’s observations were assisted by his sister Caroline. In the same way as Tycho Brahe is considered one of the best observational astronomers before the invention of the telescope, Herschel can be considered one of the best astronomers capable of observations with their own, home-built telescopes (in his case – Newtonian reflectors). It was the time of enlightenment and technological progress, which resulted in the Industrial revolution. At this time, astronomy and technological progress had become more intertwined and it was quite common to discuss new discoveries and ideas within informal scientific circles, such as the Lunar Society based in Birmingham. Its members were also involved in the public outreach of the astronomical knowledge of that era. For instance, James Ferguson invented an *orrery*, a mechanical apparatus for demonstrating the motion of celestial bodies according to the Copernican heliocentric view. Typically, it involved the motion of the Moon around the Earth, the planets around the Sun, even including the motion of the moons of Jupiter and Saturn known at the time, see Fig. 1.1.

More than hundred years later, based on more sensitive observations by larger telescopes, Jacobus C. Kapteyn discovered that stars do not move randomly but their proper motions belong to two opposite streams. This was essentially the first proof of the Galactic rotation. In 1922, Kapteyn presented a lens-shaped Galactic model with the diameter of only about $\sim 40\,000$ light years with the Sun still close to the center (within 2 000 light years).

By the 1930s, there were several key measurements that led to the major revision of the Galactic center location, especially the shift from nearly the Solar position to much larger distances from the Solar system. This was achieved thanks to the observations by Harlow Shapley, who performed the measurements of the distances of 69 globular clusters surrounding the Milky Way. He used the period-luminosity relation of Cepheid variables, which was



Figure 1.1: Painting “*A philosopher lecturing on the orrery*” by Joseph Wright of Derby completed in 1766. The central figure may represent James Ferguson, one of the members of the informal circle referred to as the Lunar Society. Ferguson demonstrated the orrery, a simplified mechanical model of the movement of celestial bodies respecting the Copernican heliocentric view, in Birmingham in 1761.

discovered earlier by Henrietta Swan Leavitt by observing Cepheid variables in the Magellanic Clouds (Leavitt 1908; Leavitt & Pickering 1912), to determine their distances. He realized that globular clusters are not distributed uniformly around the Sun but rather concentrated towards the constellation of Sagittarius (Shapley 1918). This led to the paradigm shift from heliocentrism to galactocentrism and a significant enlargement of the Milky Way to several 10 000 light years. Older measurements did not consider the extinction (absorption and scattering) of stellar light by the interstellar gas and dust within the Galactic plane. This effect was discovered by Robert Julius Trumpler while he studied open clusters. More specifically, he noticed that more distant open clusters appear fainter than they should be (Trumpler 1930). When the interstellar extinction was taken into account, the position of the Sun with respect to the Galactic center became even larger. Nowadays, the Galactic extinction at different wavebands can be determined quite precisely. It is customary to express the extinction using the colour index $E_{B-V} = A_B - A_V$, where $A_B = B_{\text{obs}} - B_{\text{int}}$ and $A_V = V_{\text{obs}} - V_{\text{int}}$ are the extinction coefficients in optical B and V bands, respectively. In Fig. 1.2, the colour index value of E_{B-V} based on the full-sky $100 \mu\text{m}$ emission of dust (COBE/DIRBE and IRAS/ISSA data; Schlegel et al. 1998) is clearly correlated with the Galactic structure, being the largest close to the plane and the smallest around the Galactic poles.

In the first half of the 20th century, the question of whether the Milky Way constitutes the whole visible Universe or is just one of many galaxies was also finally resolved. Symbolically, the Great Debate between Harlow Shapley and Heber Curtis took place in Washington,

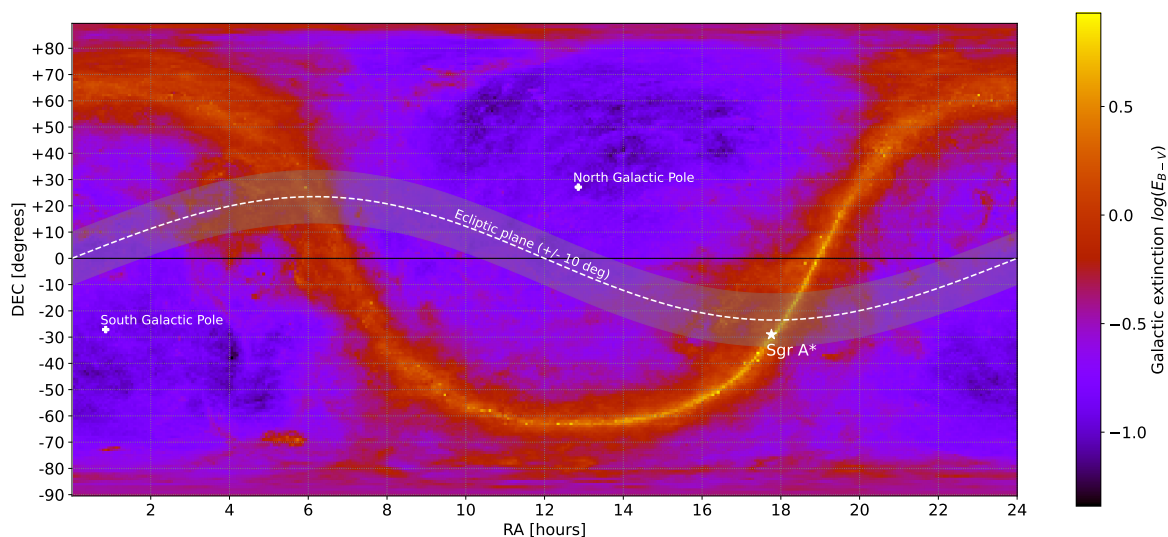


Figure 1.2: Dust extinction map of E_{B-V} (see the colour bar on the right) based on $100\ \mu\text{m}$ emission map of dust (Schlegel et al. 1998). Along the x -axis we show right ascension (RA) in hours, while along the y -axis we depict declination (DEC) in degrees. The Galactic center (Sgr A*) is represented by the star symbol and the North and the South Galactic poles are shown with the plus signs.

D.C., in 1920. Shapley was advocating for a large Galaxy and observed spiral nebulae were supposed to be located within it. In contrast, Curtis favoured a smaller Galaxy and spiral nebulae were considered to be separate galaxies in his view. At the time of the Debate, both astronomers lacked sufficiently precise observational data to support their different claims. The problem of spiral nebulae was resolved by Edwin Hubble, who discovered Cepheid variables in the nearby spiral nebulae (Andromeda, Triangulum) using the freshly completed 2.5-meter Hooker Telescope at Mt. Wilson. Using Leavitt’s period-luminosity relation, the derived distance clearly indicated that spiral nebulae are indeed other galaxies that are similar to the Milky Way galaxy. Apart from the Great Debate in 1920, there had been a few earlier “great debates” concerning the nature of the Milky Way, mainly along the line of its either atmospheric or stellar nature. Eckart & Idriz (2023) mainly stress the work of *Ibn al-Haytham* (Alhazen) (965-1040) who argued that since the Milky Way band does not have a measurable parallax it must be further than the Moon, whose parallax could be detected. This was in tension with the prevailing view at the time that the Milky Way is an atmospheric phenomenon in the sub-lunar sphere, first put forward by Aristotle as mentioned at the beginning.

The direction towards the center of the Milky Way was first broadly indicated by the measurement of the distribution of globular clusters by Harlow Shapley, which showed that globular clusters are concentrated towards the Sagittarius constellation. Subsequently, Karl G. Jansky identified a strong radio source towards the Sagittarius constellation at 20.5 MHz (14.6 meters) (Jansky 1933) with a rather low resolution of $24^\circ \times 35^\circ$. Grote Reber continued with the radio observations of the persistent emission from the Sagittarius region between 1938 and 1948 at a higher frequency of 160 MHz (1.9 meters) with his nine-meter radio dish. In 1951, Jack Piddington and Harry Minnett identified a discrete radio source denoted as the Sagittarius-Scorpius source at 1.21 GHz and 3 GHz using the Potts Hill radio telescope near Sydney (Piddington & Minnett 1951). The spectrum of the source appeared peculiarly flat. McGee & Bolton (1954) performed additional radio observations at 0.4 GHz of the Sagittarius-

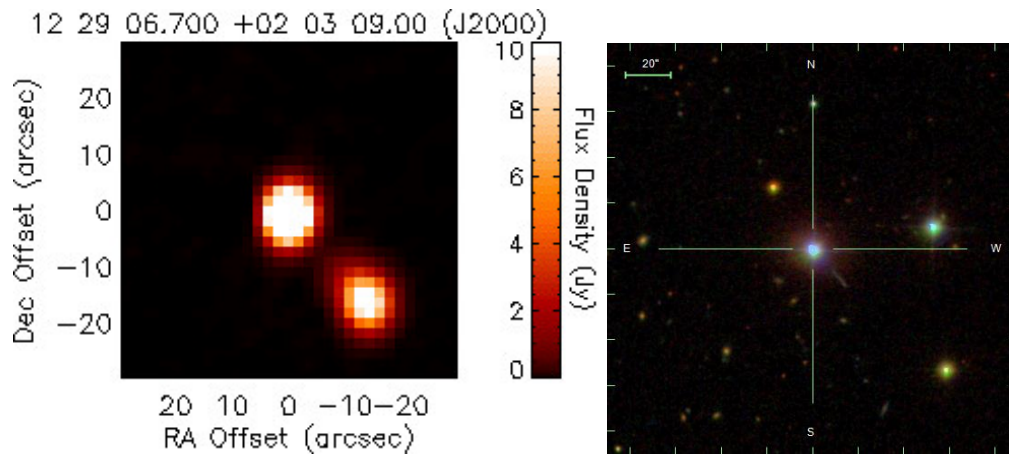


Figure 1.3: Radio and optical images of the brightest quasi-stellar object 3C 273 located in the constellation of Virgo. *Left panel:* Radio image at 1.4 GHz obtained by the *FIRST* survey (Becker et al. 1995). *Right panel:* Optical image adopted from the *SDSS* survey (Stoughton et al. 2002).

Scorpius source (known also as Sagittarius A) with the 24-meter "hole-in-the-ground" dish at Dover Heights in Australia and identified it with the position expected for the Galactic center. The discovery and the identification of Sagittarius A contributed to the redefinition of the Galactic coordinate system, which was based primarily on the HI observations of the Galactic rotation (Blaauw et al. 1960). The precisely determined position of Sgr A agreed well with the center inferred from the rotation motion of HI clouds. Within the extended radio emission of Sgr A, Balick & Brown (1974) identified a compact radio source unresolved at $< 0.1''$ with the brightness temperature larger than 10^7 K indicating a non-thermal nature. The identification of the compact source was possible thanks to a newly commissioned 35-kilometer interferometer Green Bank - Huntersville consisting of three 26-meter dishes and one 14-meter dish in Huntersville. The source was located within a few arcseconds from the near-infrared excess peak along the Galactic plane (Becklin & Neugebauer 1968). The subsequent monitoring revealed that the point source is multi-wavelength and variable. Because of its compact variable emission, it was denoted as Sagittarius A* (or Sgr A* for short; Brown 1982) to distinguish it from the extended Sgr A complex. This nomenclature was adopted later for other compact radio sources in galactic nuclei, such as M87* (Event Horizon Telescope Collaboration et al. 2019) or M81* (von Fellenberg et al. 2023).

In the meantime, as the radio emission of the Galactic center associated with Sgr A and Sgr A* had been pinpointed, broad emission lines with line widths equivalent to several 1000 km/s had been identified in the optical spectra of some galactic nuclei, indicating a high concentrated mass (type I; Seyfert 1943; Woltjer 1959; Schmidt 1963). Following the development of radar technologies during WWII, sources of strong radio emission were discovered. Some of them had prominent bipolar radio lobes with the total magnetic and kinetic (particle) energy of $\sim 10^5 - 10^7 M_{\odot} c^2 \sim 10^{59} - 10^{61}$ erg s^{-1} , assuming a synchrotron mechanism for the radio emission (Burbidge 1958). Such a large power output was inconsistent with any known long-lasting chemical, nuclear, or matter-antimatter annihilation process. The radio astronomy group at the University of Cambridge utilized a 4-element radio interferometer to make a systematic survey of the radio sky at 159 MHz. The identified sources were denoted as 3C (Third Cambridge catalogue), followed by the entry number (increasing numbers stood for

a larger right ascension; see [Edge et al. 1959](#)). Using the 5.1-meter Hale telescope on the Mt. Palomar, Thomas A. Matthews and Allan R. Sandage identified the first optical counterparts to the radio 3C sources – 3C 48, 3C 196, and 3C 286, which were point-like like stars and exhibited unusual optical spectra with very broad emission lines ([Matthews & Sandage 1963](#)). Because of the star-like appearance, these objects were called quasi-stellar objects (QSOs) or quasars. For the brightest QSO 3C 273 ($m_V \sim 12.9$), [Hazard et al. \(1963\)](#) determined the precise position of its two components (the core and the jet) using the method of lunar occultations. By observing the optical counterpart of 3C 273 and obtaining the spectrum using the Palomar telescope, Maarten Schmidt ([Schmidt 1963](#)) identified a series of hydrogen Balmer lines in the spectrum. For the comparison, in Fig. 1.3 we show radio and optical images of 3C273 in the left and right panels, respectively, where the radio emission clearly consists of two components. He noticed that the lines are redshifted to $z = 0.158$, which corresponds to the luminosity distance of ~ 760 Mpc. This definitely proved that QSOs are not only extragalactic but also that they are located at cosmological distances and have a huge bolometric energy output of $L_{\text{QSO}} \sim 10^{46} \text{ erg s}^{-1} \sim 10^{13} L_{\odot}$ or about two orders of magnitude more than the total luminosity generated by the stars in the host galaxy. The short variability within one month implied a compact source size of $c\delta t \leq 10^{17} \text{ cm} \sim 0.03 \text{ pc} \sim 7000 \text{ AU}$ for the generation of such a large luminosity.

Hence, this extraordinary evidence for the large QSO luminosity generated in a small volume comparable to the Solar System led to proposing extraordinary hypotheses and theories that were also discussed at the First Texas Symposium in Relativistic Physics in Dallas in 1963 ([Schucking 1989](#)). Among several detours, accretion onto compact objects, during which gravitational potential energy of matter is released in the form of intense radiation that is observed, turned out to be the most feasible ([Salpeter 1964](#); [Zel'dovich & Novikov 1965](#)). In parallel to new optical and radio observations of QSOs, and actually even before them, there had been several key theoretical developments that had shown that highly compact mass concentrations surrounded by the space-time boundary or the event horizon, from which even light cannot escape, can form in nature. The first such an idea was proposed by John Michell, and independently by Pierre-Simon Laplace, in the 18th century and it was based on the Newtonian corpuscular theory of light ([Schaffer 1979](#)), where the critical radius can be obtained by setting the escape velocity to the speed of light, i.e. $\sqrt{2GM/R} = c$, which leads to $R_S = 2GM/c^2$. The solid foundation stone to those models was laid though the General Theory of Relativity presented by Albert Einstein in 1915, and mainly the spherical symmetric solutions to the vacuum Einstein's field equations found by [Schwarzschild \(1916\)](#) for a non-rotating and an uncharged mass and by [Reissner \(1916\)](#) and [Nordström \(1918\)](#) for a non-rotating and charged point source and mass, respectively. However, the true singularity at the center of the coordinate system surrounded by the event horizon was rather difficult to grasp since no information, for instance even light waves, could travel out of it. Therefore, many physicists including Albert Einstein himself were sceptical of the formation of these “frozen stars” in nature ([Einstein 1939](#)). In contrast, for an idealized spherical collapse of a star, J. Robert Oppenheimer and Hartland Snyder showed that if the final mass of the star exceeds a certain limit (*Tolman-Oppenheimer-Volkoff or TOV limit* of about $\sim 1.5 - 3 M_{\odot}$), there is nothing, not even the pressure of degenerate matter, that can prevent the collapse of the object into singularity ([Oppenheimer & Snyder 1939](#)), hence the gravitational collapse will continue. Despite Oppenheimer's & Snyder's paper on the continuing gravitational collapse, most of the community remained sceptical about the formation of singularities in nature and considered them as pure mathematical curiosities. As Einstein, they rather tried to invoke mechanisms

that would decrease the mass below the TOV limit, such as strong stellar winds or rotation. The discovery of QSOs with large bolometric luminosities of $10^{45} - 10^{47} \text{ erg s}^{-1}$ generated within a small volume opened space for extraordinary hypotheses, including the accretion of matter onto highly compact objects that have collapsed into singularities surrounded by an event horizon. Moreover, considering the steady spherical accretion, the upper limit on the luminosity generated by accretion is given by the *Eddington luminosity*¹,

$$\begin{aligned} L_{\text{Edd}} &= \frac{4\pi GM_{\bullet} m_{\text{p}} c}{\sigma_{\text{T}}} \\ &= 1.26 \times 10^{38} \left(\frac{M_{\bullet}}{1 M_{\odot}} \right) \text{ erg s}^{-1}, \end{aligned} \quad (1.1)$$

which implies the mass of at least $\sim 10^7 - 10^9 M_{\odot}$ to generate the luminosity of QSOs. Such a large mass in a small volume with the radius of $\lesssim 0.03 \text{ pc}$ cannot be due to a cluster of Solar-mass stars since such a configuration would be unstable. Also, a main-sequence star of such a large mass would be highly unstable and short-lived. Essentially, any single object of this mass will inevitably collapse into a singularity. The central singular object in QSOs, if accreting close to the maximum possible (Eddington) rate, needs to consume

$$\begin{aligned} \dot{M}_{\text{Edd}} &= \frac{4\pi GM_{\bullet} m_{\text{p}}}{\eta_{\text{rad}} \sigma_{\text{T}} c} \\ &= 2.2 \left(\frac{M_{\bullet}}{10^8 M_{\odot}} \right) M_{\odot} \text{ yr}^{-1}, \end{aligned} \quad (1.2)$$

for $\eta_{\text{rad}} = 0.1$, which represents the radiative efficiency that compares the energy of the gas element at infinity with the one at the innermost stable circular orbit (ISCO). Hence, the consumption rate is equivalent to a few stars like the Sun per year. The accretion of matter onto collapsed highly massive or supermassive objects turned to be the most plausible among extraordinary models.

Around the time of the First Texas Symposium, the exact axisymmetric solution for a rotating mass was presented (Kerr 1963), and shortly afterwards, the most general stationary solution of Einstein field equations was found (Newman et al. 1965), which concerns masses possessing both the spin and the electric charge. Hence, it took about 45 years to find exact solutions for a rotating mass with axisymmetric spacetime. For convenience, we summarize the exact solutions of Einstein field equations with the basic parameters of mass M_{\bullet} , angular momentum J , and the electric charge Q in Table 1.1, including the authors of these solutions and the years when they were found.

Table 1.1: Overview of exact stationary solutions of Einstein field equations.

Charge/Angular Momentum	$J = 0$	$J \neq 0$
$Q = 0$	Schwarzschild	Kerr
References	Schwarzschild (1916)	Kerr (1963)
$Q \neq 0$	Reissner-Nordström	Kerr-Newman
References	Reissner (1916), Nordström (1918)	Newman et al. (1965)

¹The Eddington luminosity is, apart from the mass of the compact object M_{\bullet} , a function of just fundamental constants: gravitational constant G , speed of light c , and the Thomson cross-section σ_{T} .

SCIENCE NEWS LETTER for January 18, 1964

ASTRONOMY

"Black Holes" in Space

The heavy densely packed dying stars that speckle space may help determine how matter behaves when enclosed in its own gravitational field—By Ann Ewing

Figure 1.4: Origin of the word *black hole*. A newspaper snippet of the first published article on *black holes* published by Ann Ewing on January 18, 1964 in *Science News Letter* (Ewing 1964).

The formation of spacetime singularities in nature turned out to be feasible after Roger Penrose showed based on his analysis of the topological properties of spacetime (conformal structure; Penrose 1963) that the gravitational collapse into singularity is a general property of imploding stars when they reach a certain point, at which the formation of singularity becomes inevitable regardless of the initial geometry or the rotation of the collapsing star. In other words, a so-called *trapped surface* needs to form (Penrose 1965). It is also at this time when the term *black hole* first appeared. In the written form, the term appeared in the popular *Science News Letter* "*Black Holes*" in *Space* written by Ann Ewing (Ewing 1964), which was published on January 18th, 1964, see also Fig. 1.4. The article reported on degenerate compact objects discussed at the annual meeting of the American Association for the Advancement of Science (AAAS) in Cleveland, Ohio. The term was likely used directly at the meeting, potentially by the session chair Dr. Hong-ye Chiu, who might have adopted it from Robert Dicke. Three years later John A. Wheeler used the term *black hole* again at the annual meeting of the AAAS and after his keynote lecture was published in 1968 (Wheeler 1968), it started to be widely used in both popular and academic literature. Given the large masses of the order of $\sim 10^8 - 10^9 M_{\odot}$ to explain the large luminosities of quasars, the term *supermassive black holes* (hereafter SMBH) was adopted to distinguish them from the remnants of massive stars, i.e. stellar black holes. Electromagnetic emission of stellar black holes in binary systems started to be detected in the 1960s and 1970s thanks to the sounding rockets and the *Uhuru* satellite carrying the first X-ray detectors (Giacconi et al. 1972). Since 2015 merging stellar black hole binaries have also been detected via gravitational-wave emission (Abbott et al. 2016). Between stellar and supermassive black holes, there is a category of intermediate-mass black holes (IMBHs) with the masses in the range of $\sim 10^2 - 10^5 M_{\odot}$ with the firm detections only at the lowest and the highest values of this range (Greene et al. 2020).

At the time when SMBHs started to be associated with the large luminosity of QSOs, so was the compact radio source Sgr A* considered to be located at the very center of the Milky Way. The question was if there is a link between Sgr A* and those luminous SMBHs in QSOs. Or perhaps the Milky Way does not host an SMBH? Or could it be that Sgr A* is currently accreting much less than the SMBHs in the monitored QSOs that are at cosmological distances, and thus younger than the Milky Way? In 1969, Donald Lynden-Bell made the connection between the nuclear emission in nearby galaxies and distant quasars, and denoted the lower-luminosity nuclei as "collapsed old quasars", suggesting an evolutionary link (Lynden-Bell 1969). Two years later, in 1971, Donald Lynden-Bell and Martin Rees

suggested the existence of an SMBH in the Galactic center (Lynden-Bell & Rees 1971). They also outlined its basic properties and suggested to use broad emission lines, very long baseline interferometry, and infrared emission (and its variability) to detect the SMBH. As already mentioned, in 1974, Sgr A* was detected using the long-baseline radio interferometry (Balick & Brown 1974), and shortly afterwards, Sgr A* started to be associated with the SMBH.

The rest of the introduction to this *Habilitation Thesis* deals with the mapping of both the Galactic center and distant quasars and how these are related. Some answers have been found in previous studies, including my papers, yet many remain to be tackled in the future. In Section 1.1, we will look more closely at the SMBH in the Galactic center and its immediate surroundings within its sphere of gravitational influence of ~ 2 pc. In Subsection 1.1.2, we will consider the distribution of gas of different phases, while in Subsection 1.1.1, we will focus on stars and different stellar populations. The most active galaxies – or quasars – are then the topic of Section 1.2. There are several differences and contrasts between the Galactic center and quasars but also some similarities – in both cases, the main dynamical “engine” is the SMBH. Most importantly, there is an evolutionary connection. The current state of the Galactic center is common at low redshifts and represents the end product of the quasar state – the Galactic center could be described as the old or almost dead quasar or the “cinder” of the once very active SMBH (Lynden-Bell 1969). However, the last increased activity of the Galactic center did not necessarily take place billions of years ago. Some traces of the significant increase in the nuclear activity can be dated back to only a few millions years ago. We will discuss these evolutionary connections as well as more generally the feeding and the feedback of galactic nuclei in Section 1.3. Finally, in Section 1.4 we will discuss the possibility of using galactic nuclei as standardizable sources for cosmology. As we discussed, galactic nuclei are characterized by a large range of accretion rates and therefore also luminosities, hence they may not seem as ideal probes to constrain cosmological parameters. In addition, galactic nuclei are variable on the timescales of weeks to months, which also makes their standardization more difficult. However, there are two (and potentially more) non-linear power-law relations between quasar quantities that can be used to determine luminosity distances to them and therefore use them as standardizable candles. First, it is the relation between the radius of the broad-line region and the driving monochromatic luminosity, or the $R - L$ relation. Second, there is a correlation between the UV monochromatic luminosity L_{UV} typically measured at 250 nm and the X-ray monochromatic luminosity L_X determined at 2 keV, or the $L_X - L_{UV}$ relation. We will discuss the achieved constraints so far and the main systematic effects that seem to influence these relations.

1.1 Mapping the Galactic center

To understand the evolution of galaxies across the cosmic history, in particular how the activity of galactic nuclei evolves, it is essential to map their kinematic and geometrical structure. In this regard, it is practical to start with the extreme cases. On one hand, there are SMBHs that are very difficult to detect at the centers of galaxies because of their low luminosity due to a low level of accretion, i.e. significantly below the maximum stable spherical accretion, so-called the Eddington limit, see Eq. (1.2). Our Galactic center hosts such an “underfed” SMBH associated with the compact variable source Sgr A*. On the other hand, there are SMBHs that can accrete the equivalent of several Suns per year or actually they can reach or even exceed the Eddington limit. Such SMBHs are in the nuclei of quasars, the most active

galaxies, and they outshine the total stellar radiation of their host galaxies by several orders of magnitude.

The center of the Milky Way with the distance of ~ 8.1 kpc determined using different methods (Genzel et al. 2010) is the closest galactic nucleus to us, about ~ 93 -times closer than the closest nucleus hosting a low-accreting SMBH in M31 in the Local Group (~ 752 kpc; Riess et al. 2012) and ~ 531 -times closer than the closest active galactic nucleus (AGN) in NGC 4395 (~ 4.3 Mpc; Thim et al. 2004). With the diffraction-limited near-infrared observations, it is possible to resolve structures as small as $\sim (\lambda/D)d_{\text{SgrA}^*} = (\lambda/2.2 \mu\text{m})(D/8 \text{ m})^{-1}(d_{\text{SgrA}^*}/8 \text{ kpc}) \sim 454 \text{ AU}$. Since the mean distance between stars is typically larger, the Galactic center (GC) is the only galactic nucleus where one can observe individual stars as well as study the properties of the dense Nuclear Star Cluster (NSC) as a whole. Since the NSC represents one of the densest stellar environments in the Galaxy, the GC can be utilized as a unique test-bed for stellar dynamics in the dense cluster environment (Schödel et al. 2014b).

Furthermore, the multi-wavelength observations of the Galactic center reveal a multiphase gaseous-dusty environment, including denser molecular and neutral material outside the inner parsec and ionized warmer gas and hot X-ray emitting plasma within the inner parsec. The kinematic structure of the gaseous medium is quite complex. There are clear signs of the Keplerian motion of the gas on one hand, but most of the gas is actually outflowing, with a small fraction going inwards towards the extremely low-luminous SMBH (Morris & Serabyn 1996). The reasons behind low accretion onto Sgr A*, despite a large accumulation of gas within the Central Molecular Zone ($\lesssim 200$ pc from Sgr A*; CMZ), are likely the combination of star formation (matter is converted into stars, Henshaw et al. 2023) and the loss via thermally driven outflows, partially collimated by the large-scale magnetic field. The latter is partially caused by gas heating driven by shocks due to numerous supernovae and by the X-ray radiation field provided by numerous X-ray binaries (Morris 1993; Hailey et al. 2018).

In fact, the matter needs to lose angular momentum substantially in order to inspiral from Galactic scales towards the bound orbit around the SMBH. The specific angular momentum of gas (per unit mass) at the scale of ~ 500 pc and considering the speed of $\sim 250 \text{ km s}^{-1}$ is $l_{\text{gal}} \sim rv \sim 3.9 \times 10^{28} \text{ cm}^2 \text{ s}^{-1}$. If the matter orbits close to the innermost stable circular orbit or the ISCO around the SMBH, for instance at $r = 6$ gravitational radii (r_g) for a non-rotating (Schwarzschild) black hole, its angular momentum is $l_{\bullet} \sim rv \sim r_g c (r/r_g)^{1/2} \sim 4.3 \times 10^{22} \text{ cm}^2 \text{ s}^{-1}$. Hence, the difference is six orders of magnitude in terms of the specific angular momentum. The gas needs to bridge the length-scales between ~ 500 pc or the CMZ scales to the scales of the event horizon of the SMBH, which can be scaled by the gravitational radius r_g ,

$$r_g = \frac{GM_{\bullet}}{c^2} \sim 5.9 \times 10^{11} \left(\frac{M_{\bullet}}{4 \times 10^6 M_{\odot}} \right) \text{ cm}. \quad (1.3)$$

One gravitational radius corresponds to about 0.039 AU or about one tenth of the mean distance of Mercury from the Sun. The overall difference in the length-scale between the CMZ and the event horizon corresponds to the factor of $\sim 2.6 \times 10^9$.

The CMZ contains about ~ 5 to 10% of molecular gas of the Milky Way, which gives rise to the densest concentration of massive stars and star clusters in the Galaxy, including the most massive star-formation complexes – Sgr A and Sgr B2 (Morris & Serabyn 1996; Ferrière et al. 2007). The total mass of the dense gas ($\bar{n}_{\text{H}_2} \gtrsim 10^4 \text{ cm}^{-3}$) is $\sim 3 - 7 \times 10^7 M_{\odot}$ (Bally et al. 1987, 1988; Morris & Serabyn 1996; Ferrière et al. 2007). The inflow of gas towards

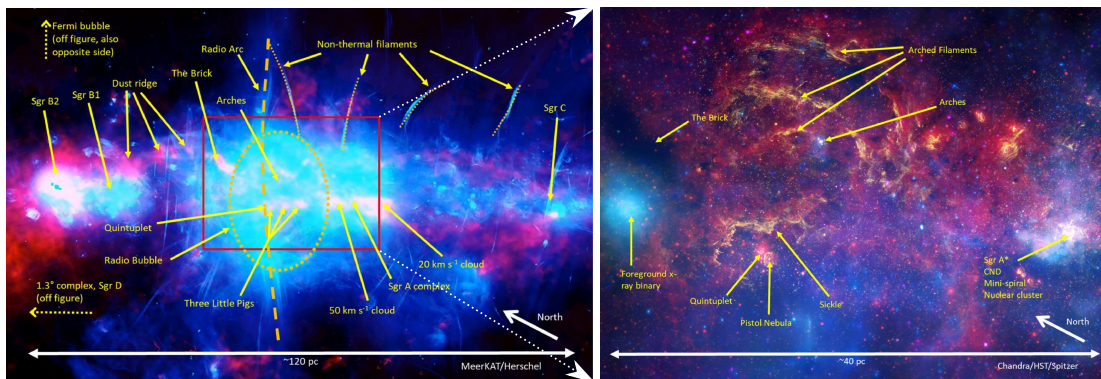


Figure 1.5: Multi-wavelength images of the Central Molecular Zone on the scale of 120 pc. *Left panel:* The inner 120 pc of the CMZ as observed by MeerKAT (0.9-1.6 GHz, blue; SARAO) and Herchel PACS HI+H₂ column density (red; inferred from dust continuum emission; see also [Molinari et al., 2011](#)), which traces the 100-pc Ring of molecular material presumably along the stable x_2 orbit. Composite image produced by John Bally. Arrows denote different structures including molecular complexes the Brick, Sgr B2, Sgr B1, 50 km/s, 20 km/s clouds, Sgr A complex, and Sgr C. The dashed yellow oval-shaped region denotes the Galactic center bubble between the Sgr A complex and the Brick. The red rectangle represents the 40-pc region shown in the right panel. *Right panel:* The 40-pc region of the CMZ. The composite image was created by the combination of the 1-8 keV image (blue, Chandra; [Wang et al., 2002](#)), the optical image (yellow, HST; NASA/ESA/STScI/Q.D.Wang), and the NIR-MIR image (3.6 – 24 μm , red, Spitzer; [Churchwell et al., 2009](#)). Images adopted from [Bryant & Krabbe \(2021\)](#).

the CMZ is governed by the gravitational potential of the Galactic stellar bar that extends on the scale of ~ 3 kpc from the Galactic center ([Morris & Serabyn 1996](#)). It is revealed by the radial-velocity profiles of CO and HI gas as a function of the Galactic longitude. From this analysis, it has been inferred that the Galactic bar is oriented $\sim 20 - 45^\circ$ with respect to our line of sight. In comparison with the Galactic disc, which is dominated by the rotational motion in the Galactic plane, the bar potential allows for a larger-amplitude vertical motion. This is also apparent in the maps of the surface density of the interstellar gas that exhibit a peak in the density at $\sim 3 - 4$ kpc and a drop inside 3 kpc, where the bar potential starts to dominate. In principal, the bar is triaxial and its potential allows for different families of gas-star orbits. The most prominent ones are x_1 orbits along the major bar axis and x_2 orbits that are perpendicular to x_1 and follow the minor bar axis ([Contopoulos & Mertzaniides 1977](#)).

The combination of x_1 and x_2 orbits along with the bar orientation and the sense of cloud motion can address the observed distribution of major molecular complexes, the clumpiness as well as the asymmetrical distribution of the CMZ. In Fig. 1.5, we show the multi-wavelength images of the inner 120 pc (radio+far IR; left image) and the inner 40 pc (X-ray+optical+NIR-MIR; right panel). In these composite images, one can notice the major molecular complexes that exhibit a star-formation activity, in particular Sgr A complex, Sgr B1, Sgr B2, and Sgr C. It is quite visible that in the positive Galactic longitudes (east of Sgr A*) there is a higher column density of molecular material in comparison with negative Galactic longitudes (west of Sgr A*). The western part is characterized by the occurrence of discrete 24 μm sources. One interpretation is that the star-formation activity within the central 100-pc Ring, along which molecular complexes are distributed, is not synchronized. We can rather see

star-formation process at different stages. In this picture, the region to the west could have already experienced a major starburst that led to the ejection of the cold molecular material via winds of massive young stars and supernova wind bubbles (see e.g. [Bally & Hi-GAL Team 2014](#), and references therein).

Most of the star formation within the CMZ takes place in the inner 100 pc, more specifically in the molecular complexes along the 100-pc Ring ([Molinari et al. 2011](#)), where one can localize the densest stellar clusters – the Arches, the Quintuplet, and the NSC. Because of the intense star-formation activity, winds of massive stars interact with the denser neutral and molecular material and push it away, creating the Galactic center bubble, see the yellow oval-shaped region in Fig. 1.5. The manifestation of this are the Arched filaments to the north. The molecular clouds along the 100-pc Ring are one to two orders of magnitude denser than in the Galactic plane and exhibit an order of magnitude larger line widths, indicating extra velocity shear and turbulence. Despite increased star formation in comparison with the Solar neighbourhood ($\sim 0.02 - 0.1 M_{\odot} \text{ yr}^{-1}$; [Morris & Serabyn 1996](#); [Yusef-Zadeh et al. 2009b](#); [Longmore et al. 2013](#)), the star-formation rate per unit mass of high-density gas is actually lower than in the Galactic plane. This decreased efficiency could be due to several mechanisms typical for the Galactic center region, especially increased turbulence, tidal stresses and shocks, stronger magnetic field, shocks due to cloud-cloud collisions, and their combination ([Kruijssen et al. 2014](#)).

To understand the overall dynamics of the gas inflow through the Galactic 3-kpc bar, CMZ with the 100-pc Ring, and all the way to the innermost parsec is one of the major challenges of the current Galactic dynamics. A partial understanding has been reached by applying the theory of x_1 - x_2 orbits within the bar on the distribution of molecular clouds and dense stellar clusters within the CMZ. In Fig. 1.6 (left panel), we illustrate the motion of the molecular material along the innermost stable x_1 orbit, while most of the star-forming clouds move along the inner x_2 orbits that are perpendicular to x_1 orbits. This can address the projected distribution of prominent molecular clouds with dense star-forming clusters along the 100-pc Ring, see Fig. 1.6 (right panels). The stable $x_1 - x_2$ orbits provide a way to transport the denser material from kiloparsec scales to 100-pc scales, where other mechanisms, such as cloud-cloud collisions, can yield a lower angular-momentum material that falls in towards parsec scales from the SMBH.

Overall, the CMZ with the Sgr A complex including Sgr A*, has played a major role in understanding star formation in the extreme conditions, the impact of the stellar feedback on the surrounding dense gas, and the overall gas transport from larger Galactic scales towards the SMBH. In fact, the Galactic center seems to be an example of a galactic nucleus where the SMBH is currently not the main feedback provider. Numerous massive stars control the SMBH growth and in fact keep it to a minimum via their stellar wind outflows and supernova feedback.

1.1.1 Stellar populations in the central parsec

The Galactic center Nuclear Star Cluster (NSC) has the size comparable to globular clusters but it is many times more massive. In fact, the stellar density is one of the largest among stellar environments in the Galaxy. For this reason, the NSC is a unique dynamical testbed for the stellar cluster whose inner part is dominated by the potential of the SMBH ([Schödel et al. 2014b](#)). Based on the monitoring of fast-moving B-type stars, it has been possible to determine the exact value of the mass of the compact radio source Sgr A*, $M_{\bullet} \simeq 4 \times 10^6 M_{\odot}$

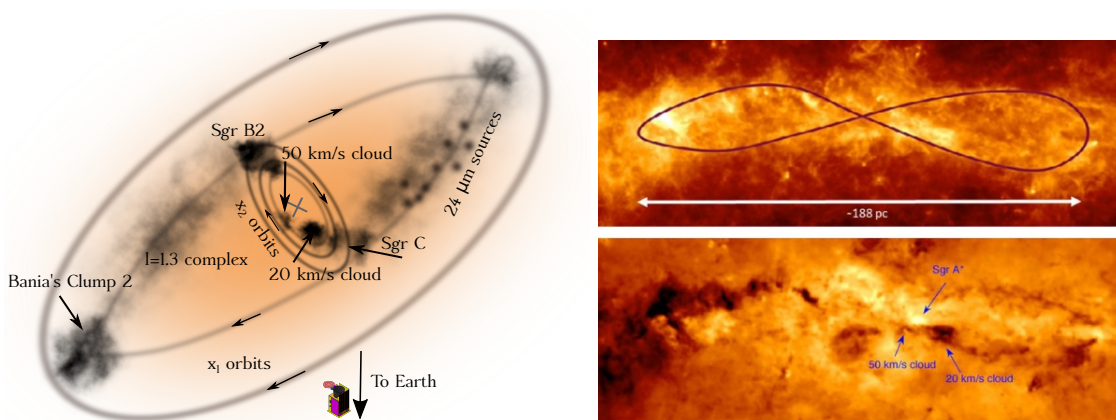


Figure 1.6: Motion of dense molecular material towards the Galactic center. *Left panel:* Illustration of the top-view of the Central Molecular Zone (CMZ; the inner 500 pc). The orange-shaded oval depicts the orientation of the Galactic bar with respect to the line of sight (the angle of $\sim 20 - 45^\circ$). Stars and gas move in the bar potential on stable x_1 orbits along the bar major axis. The lower angular-momentum x_1 orbits become self-intersecting - this is where the denser molecular complex Bania's Clump 2 may be located on the front side of the CMZ. Most of the CMZ molecular emission is associated with the x_2 orbits, which are perpendicular to x_1 orbits and are represented by three ellipses. Densest molecular clouds, in particular Sgr B2, 50 km/s cloud, 20 km/s cloud, and Sgr C move in the bar potential on these orbits and form the prominent 100-pc Ring (see the right panel). The illustration was inspired by [Bally & Hi-GAL Team \(2014\)](#). *Right panel:* The far-infrared image of the inner 94 pc obtained by the *Herschel* SPIRE at $250 \mu\text{m}$ (top panel). The black solid line shows the x_2 orbit that mimics the infinity sign, but in 3D it exhibits a closed-loop-like shape. The densest molecular clouds seem to follow this inner x_2 orbit in the bar potential as is apparent from the dust temperature map (bottom) obtained from the dust continuum emission between 70 and $500 \mu\text{m}$ ([Molinari et al. 2011](#)). This geometrical configuration of molecular clouds along with dense star-forming regions represents the 100-pc Ring. Adopted from [Bryant & Krabbe \(2021\)](#).

([Genzel 2022](#)), which is associated with the SMBH at the center of the Milky Way. This was possible based on the detection of stellar proper motions within one arcsecond of Sgr A* ([Eckart & Genzel 1996, 1997](#); [Ghez et al. 1998](#)) and later by also detecting accelerations along the orbit ([Ghez et al. 2000](#)). This eventually led to the determination of elliptical orbits of several tens of stars orbiting the SMBH ([Eckart et al. 2002](#); [Schödel et al. 2002](#); [Gillessen et al. 2009, 2017](#)).

In comparison with other galaxies, the NSC can be studied on sub-parsec and even milliparsec scales and it can be resolved into millions of stars whose spectral type and proper motion can be investigated. From these analyses it was found that the NSC is predominantly composed of late-type stars with the spectral types M, K, and G (>1 Gyr; [Pfuhl et al. 2011](#)). The distribution of stellar velocities is approximately isotropic, with the slow, solid-like rotation parallel to the rotation of the Galaxy (bar). The NSC is elliptical in shape and flattened along the Galactic plane with the symmetry ratio of $q = 0.71 \pm 0.02$. It is also point-symmetric with respect to Sgr A* and has a half-light radius of $r_{\text{hl}} = 4.2 \pm 0.4$ pc. Based on the mid-infrared images corrected for extinction, it was possible to constrain the luminosity of the NSC, $L_{4.5\mu\text{m}} = (4.1 \pm 0.4) \times 10^7 L_\odot$ and the total mass of $M_{\text{NSC}} = (2.5 \pm 0.4) \times 10^7 M_\odot$

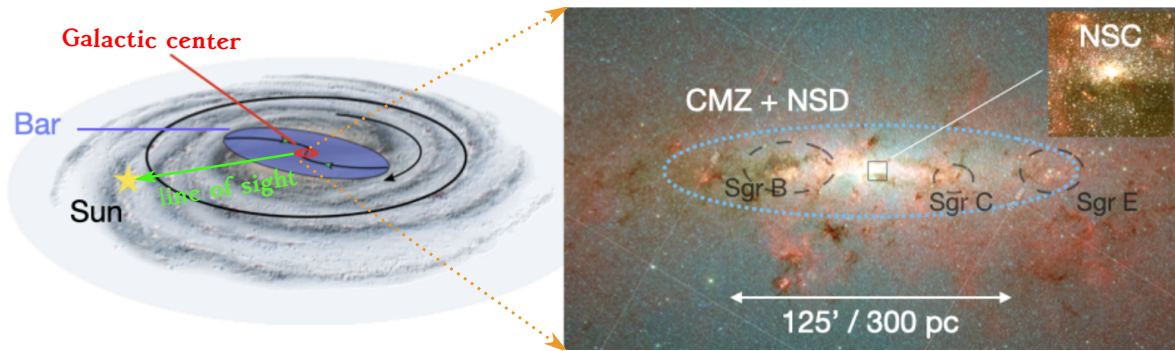


Figure 1.7: Localization of the Nuclear Star Cluster, Nuclear Stellar Disc, and the Central Molecular Zone within the Galaxy. *Left panel:* Illustration of the location of the Galactic center, including the Nuclear Stellar Disc and the Central Molecular Zone, in the Galaxy. *Right panel:* Composite infrared image ($3.6+4.5+8\ \mu\text{m}$) obtained from the Spitzer images where the Central Molecular Zone is depicted as a blue dashed oval, i.e. the region with the largest concentration of molecular gas. In this region, the large molecular complex/star-forming region Sgr B is shown as well as the HII regions Sgr C and Sgr E. The Nuclear Stellar Disc is an elongated bright structure, which is located within the CMZ and partially overlaps with it. At the very center, a nearly spherical Nuclear Star Cluster is located, which has a half-light radius of ~ 4.2 pc. Both figures were adopted with some modifications from [Schoedel et al. \(2024\)](#).

([Schödel et al. 2014a](#)), which gives an average mass-to-light ratio of $(M/L)_{4.5\mu\text{m}} \sim 0.6$, though it is clearly radius-dependent as there are numerous young massive OB/Wolf-Rayet stars within the inner 0.5 pc (see the discussion below).

The NSC is embedded within the larger, elongated Nuclear Stellar Disc (NSD), which has the total mass of $\sim 10^9 M_\odot$ and the length-scale of ~ 120 pc ([Launhardt et al. 2002](#)). It thus overlaps substantially with the CMZ, or the 100-pc Ring, see also Fig. 1.7 for the schematic illustration (left panel) and the composite infrared image showing the main structures within 300 pc (right panel). It is elongated along the Galactic plane, which implies the supply of material for the NSD build-up along the main axis of the bar. The star formation and the gas feeding was, however, not continuous as previously expected ([Nogueras-Lara et al. 2020](#)). The bulk of the NSD mass formed 8 Gyr ago or more, while there was another intense starburst ~ 1 Gyr ago, forming $\sim 5\%$ of the NSD mass. A few percent of stars formed within 500 Myr, with the continuation until 30 Myr ago. This suggests that in the Galactic center region, star formation is quite episodic with long periods (\sim several Gyr) of quiescence. The NSD is kinematically cool with the coherent rotation pattern with the velocity of $\sim 120\ \text{km s}^{-1}$ parallel to the Galactic plane. Its vertical extent is only ~ 50 pc, hence it is significantly flatter than the NSC with $q \sim 0.2 - 0.4$ ([Schönrich et al. 2015](#)).

In Fig. 1.8, we illustrate the different stellar structures – Nuclear Stellar Disc on 100-pc scales, Nuclear Star Cluster on the 10-pc scale, the region of fast-moving “S stars” ([Eckart & Genzel 1996, 1997; Ghez et al. 1998](#)) in the central parsec. In the further discussion, we focus on this region, which is well inside the sphere of gravitational influence of the SMBH. By the sphere of influence we mean the region with the radius where the circular velocity around Sgr A* equals the velocity dispersion σ_\star of the stars in the NSC, hence we have,

$$r_{\text{SI}} = \frac{GM_\bullet}{\sigma_\star^2} \sim 2.1 \left(\frac{M_\bullet}{4 \times 10^6 M_\odot} \right) \left(\frac{\sigma_\star}{90\ \text{km s}^{-1}} \right)^{-2} \text{ pc}, \quad (1.4)$$

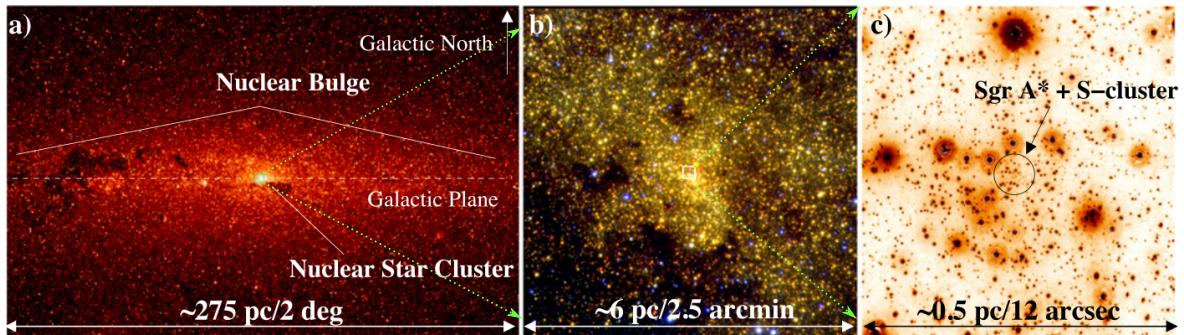


Figure 1.8: Towards the population of fast-moving “S stars” orbiting around Sgr A*. *Panel (a):* Spitzer/IRAC $4.5 \mu\text{m}$ depicting the elongated Nuclear Stellar Disc on the scale of 275 pc (based on [Schödel et al. 2014a](#)). *Panel (b):* The ISAAC composite image ($1.19+1.71+2.25 \mu\text{m}$) of the Nuclear Star Cluster on the scale of 6 pc, which corresponds to the cyan box in panel (a). Based on the data analyzed in [Nishiyama & Schödel \(2013\)](#). *Panel (c):* The NACO/VLT holographic image of the central half-parsec ([Schödel et al. 2013](#)), which corresponds to the white box in panel (b). The S cluster surrounding Sgr A*, which is at the center of all the images but typically very faint unless it is flaring, is depicted by a black circle. All of the three images were adopted from [Schödel et al. \(2014b\)](#).

where $\sigma_\star \sim 90 \text{ km s}^{-1}$ is estimated from the $M_\bullet - \sigma_\star$ relation ([Gültekin et al. 2009](#)). For the spherical cluster around the SMBH, this would correspond to the radius where the total stellar mass $M_\star(r < r_{\text{SI}}) = 2M_\bullet \sim 8 \times 10^6 M_\odot$ ([Merritt 2013](#)).

Inside r_{SI} stars undergo two-body relaxation by exchanging energy and angular momentum in the dominant potential of the SMBH. The characteristic non-resonant relaxation timescale is,

$$\begin{aligned} \tau_r &= \frac{0.34\sigma_\star^3}{G^2\rho_\star \langle m_\star \rangle \ln \Lambda} \\ &\simeq 4.2 \left(\frac{\sigma_\star}{90 \text{ km s}^{-1}} \right)^3 \left(\frac{\rho_\star}{2.1 \times 10^5 M_\odot \text{pc}^{-3}} \right)^{-1} \left(\frac{\langle m_\star \rangle}{1 M_\odot} \right)^{-1} \left(\frac{\ln \Lambda}{15} \right)^{-1} \text{ Gyr}, \end{aligned} \quad (1.5)$$

where ρ_\star is the stellar mass density estimated as the total stellar mass density within the sphere of influence, $\rho_\star \approx 6M_\bullet/(4\pi r_{\text{SI}}^3)$, $\langle m_\star \rangle$ is the mean stellar mass, which we set to $1 M_\odot$, and $\ln \Lambda$ is the Coulomb logarithm, which can be estimated as $\ln \Lambda \sim \ln(M_\bullet/m_\star) \sim 15$ in the potential of the SMBH ([Merritt 2013](#)). After τ_r , hence about half billion years for the Galactic center, the stellar system is expected to be dynamically relaxed – i.e. the orbital energy and angular momentum are exchanged to such an extent that the system does not possess any fingerprint of the initial orbital distribution. The relaxed system dominated gravitationally by the SMBH is expected to have an increasing density profile towards the SMBH, which can be utilized to reveal especially quiescent SMBHs in the nearby Universe ([Peebles 1972](#)). More precisely, the stellar density in such a cluster exhibits a power-law distribution as a function of the distance from the SMBH. This is a so-called *Bahcall-Wolf cusp* and the theoretical dependencies are $\rho_\star(r) \propto r^{-7/4}$ for stars with the same mass ([Bahcall & Wolf 1976](#)) and $\rho_\star(r) \propto r^{-3/2}$ for a two-mass stellar distribution ([Bahcall & Wolf 1977](#)).

Concerning the late-type stellar population in the inner parsec, it is old, specifically $\sim 80\%$ of the stellar mass formed 10 Gyr ago or more ([Schödel et al. 2020](#)). The velocity distribution is isotropic and the spatial distribution is slightly flattened along the Galactic plane as already

mentioned. Given its large age, the late-type population should be approaching a relaxed state, which should be demonstrated by a cusp-like distribution. Previous studies, however, found a core-like distribution for late-type stars within 0.5 pc (Sellgren et al. 1990; Buchholz et al. 2009). This hinted at a certain mechanism that led to the depletion of older red giants in the inner region, such as stellar collisions (Genzel et al. 1996) or their repetitive interaction with a massive starburst/accretion disc (Amaro-Seoane & Chen 2014) and/or a jet (Zajaček et al. 2020).

In contrast, subsequent more sensitive studies revealed that faint late-type stars do exhibit a cusp-like distribution (Habibi et al. 2019; Schödel et al. 2020), bringing non-resonant two-body relaxation into play. The same study by Schödel et al. (2020) showed that just brighter, bigger red giants (with K-band magnitudes of $m_K \lesssim 14.5$) exhibit a flat, core-like distribution, which hints at a depletion mechanism that is size-selective, affecting mostly larger giants with loose envelopes. Furthermore, there are indications from the overabundant population of low-mass X-ray binaries in the central parsec (Muno et al. 2005; Hailey et al. 2018) that stellar-mass black holes also exhibit a cusp-like distribution, which indicates that these populations (late-type stars and compact objects) are likely in a steady-state, dynamically relaxed state.

The apparent overabundance of young massive stars in the central ~ 0.5 pc has remained puzzling since massive OB/Wolf-Rayet stars as well as B-type stars in the central 0.5'' – so-called S stars – were spectrally identified. This was dubbed as the “paradox of youth” (Ghez et al. 2003). It has been considered a paradox since the tidal field of Sgr A*, intense radiation, large gas turbulence, strong magnetic field, and shock waves should significantly inhibit *in situ* star formation in the Galactic center (Morris 1993). An alternative to the *in situ* star-formation processes are successive inspirals of star clusters from the CMZ. This scenario has two basic problems: (i) a characteristic inspiral timescale of the cluster from the CMZ is typically much longer than the inferred age of massive OB stars (~ 5 million years); (ii) the cluster would be prone to tidal disruption before reaching the central parsec unless its core is very dense. An intermediate-mass black hole (IMBH) could stabilize the cluster core so that the stars are stabilized till they reach the central parsec. However, the IMBH would have to have the mass of $\sim 10\%$ of the initial cluster mass, which has been considered unrealistic for typical star-forming cluster masses (Kim et al. 2004).

A fraction of OB stars are a part of the coherent kinematic disc-like structure known as the Clockwise Disc (CWD; Levin & Beloborodov 2003) within the inner 0.5 pc. This stellar disc has a mean inclination of $\sim 122^\circ \pm 7^\circ$, a mean angle of the line of nodes $\sim 99^\circ \pm 3^\circ$, and an opening angle of 10° (see Genzel et al. 2010, and references therein). The disc-like structure of stars suggested, in combination with the fact that OB stars cannot be relaxed, that stars formed in a massive gaseous disc that underwent gravitational instability, which resulted in the formation of massive stars (Levin & Beloborodov 2003).

Several analytical and numerical models have been proposed to reproduce star formation close to the SMBH. Two star-forming channels emerged (Mapelli & Gualandris 2016):

- disc mode, where an infalling cloud forms a disc that is preceded by a cloud-cloud collision (Hobbs & Nayakshin 2009) or the collision of the cloud streamer with itself (Wardle & Yusef-Zadeh 2008). The formed disc around the SMBH becomes gravitationally unstable (Levin & Beloborodov 2003) when the Toomre’s criterion for instability is met: $Q = c_s \Omega_K / (\pi G \Sigma) < 1$, where c_s is the gas sound speed, Ω_K is the Keplerian angular velocity, and Σ is the surface density of the disc;

- infalling cloud mode, in which a cloud with a low angular momentum, potentially preceded by a cloud-cloud collision within the CMZ, falls towards the SMBH where it is tidally compressed at the periape in the direction perpendicular to its motion, which triggers gravitational collapse, fragmentation, a subsequent formation of a stellar association (Jalali et al. 2014).

Since massive young stars in the Galactic center are too young to be dynamically relaxed, their orbital distribution should bear signs of the formation mechanism. This can be used to test the proposed star-formation channels. von Fellenberg et al. (2022) spectroscopically identified 195 young OB stars within ~ 1.2 pc that exhibit Bry absorption line in their spectra. They found that the angular momentum distribution of these stars deviates significantly from an isotropic distribution, which is characteristic for the surrounding population of late-type stars (see e.g. Schödel et al. 2014b). More specifically, $\sim 75\%$ of young stars belong to coherent dynamical structures resembling discs, i.e. only a minority appears to be randomly distributed. von Fellenberg et al. (2022) identified five clusters of angular momenta on the inclination/ascending-node length plane. Two clusters stand for the warped clockwise disc (CWD), whose inner part has the mean semi-major axis of ~ 0.084 pc and the outer part of ~ 0.28 pc. Another feature represents the counter-clockwise disc (CCWD) on larger scales, which has the mean semi-major axis of ~ 0.3 pc. There are two more, previously non-identified features denoted as F2 and F3 with mean semi-major axes of ~ 0.2 pc and 0.4 pc. All of these features are consistent with *in-situ* star formation. In particular, the simulation runs of cloud-cloud collisions close to the Galactic center (Hobbs & Nayakshin 2009) typically result in the gas settling close to the SMBH in the form of a star-forming disc. In addition, there are typically a few remnant gaseous streamers, in which star formation also takes place. These additional streamers could then explain the presence of CCWD, F2, and F3 features in the analysis of von Fellenberg et al. (2022).

The innermost cluster of fainter, B-type stars or so-called S stars (Eckart & Genzel 1996, 1997) was originally considered to be nearly isotropic (Gillessen et al. 2009; Genzel et al. 2010). This was also confirmed by Gillessen et al. (2017), who determined orbits for 40 stars, 32 of which are distributed isotropically with the thermal distribution of eccentricities, i.e. the one that follows $n(e)de = 2ede$ (Jeans 1919). Such a distribution is expected for old, relaxed cluster. In contrast, S stars were found to be at least an order of magnitude younger than the two-body relaxation timescale, see Eq. (1.5), with the age comparable to the CWD and CCWD disc stars (< 15 Myr and $6.6^{+3.4}_{-4.7}$ Myr for the S2 star; Habibi et al. 2017). This implies that CWD stars and S stars formed simultaneously or potentially they have a common origin. One proposed mechanism to link the formation of OB/WR stars within the CWD and B-type S stars is the disc-formation mechanism (Chen & Amaro-Seoane 2014). It is plausible that the initial gaseous disc extended closer to the SMBH, producing both more massive O-type stars and less massive B-type stars in the inner arcsecond. Due to the Kozai-Lidov-like resonance and the oscillations of the eccentricity and the inclination induced by the outer part of the massive disc, more massive O-type stars were driven onto high-eccentric orbits, on which they got tidally disrupted. Lighter B-type stars increased their orbital eccentricities more slowly and they also acquired larger inclinations, which can address their nearly isotropic, thermalized distribution. The rapidly evolving region or RER suggested by Chen & Amaro-Seoane (2014) can thus elegantly connect the origin of the disc-like distribution of OB stars and the inner cluster of B-type S stars. Furthermore, based on the analysis of 112 S stars, 39 of which had orbital solutions, Ali et al. (2020) found a

significant deviation of their inclination and proper-motion distributions from the isotropic (uniform) distribution. The S cluster rather seems to consist of two nearly edge-on stellar discs that are oriented $\pm 45^\circ$ from the Galactic plane. The pole of the structure is inclined by $\sim 25^\circ$ from the line of sight. Moreover, each disc hosts stars of both angular-momentum directions. Such a two-disc structure could be a fingerprint of the formation mechanism of the S cluster a few million years ago – such as the RER mechanism due to the outer gaseous disc. Alternatively, it could be caused by the gravitational torques induced by a more distant perturber, such as an IMBH that could hypothetically be hosted by one of the denser stellar associations in the central parsec (IRS13; [Peißker et al. 2024a](#)). The systems of stars dominated by the SMBH potential typically undergoes a fast vector resonant relaxation, which causes the orbital inclinations to be randomized. Such a stellar system behaves similarly to liquid crystals ([Roupas et al. 2017](#)) in a way that it can undergo first- and second-order phase transitions between ordered-nematic and disordered-isotropic states. In the ordered phase, it can actually consist of two discs inclined by $\sim 90^\circ$ as found by [Ali et al. \(2020\)](#) and such a state is metastable.

Within the S-cluster region, a mysterious population of G-objects has been identified, whose members are characterized by a prominent infrared excess due to the spectral energy distribution dominated by dust emission with the effective temperature of $\sim 500 - 600$ K ([Ciurlo et al. 2020](#); [Peißker et al. 2020b](#)). In Fig. 1.9, we show their projected distribution around Sgr A* within the central parsec. The semi-major axes of G objects mostly coincide with the inner S cluster of B-type stars, i.e. $a_\star \lesssim 0.02$ pc. These objects also exhibit rather broad hydrogen and helium emission lines with FWHMs of $\sim 100 - 200$ km s $^{-1}$, which is indicative of an ionized gaseous-dusty envelope. The most representative G-object G2, which was intensively monitored between 2012-2016, was originally considered to be a tidally dissolving gaseous-dusty cloud with a head-tail structure ([Gillessen et al. 2012, 2013](#)). After its pericenter passage in the first half of 2014, it did not disintegrate and continued orbiting Sgr A* on the Keplerian trajectory ([Witzel et al. 2014](#); [Valencia-S. et al. 2015](#)). The emission maps revealed its compact structure along the whole orbit up until at least 2019 ([Peißker et al. 2021b](#)), including both *K*- and *L*-band continuum emission as well as Br γ -line emission. This has contributed to favouring the model scenarios that considered G2 and potentially all G-objects to be dust-enshrouded stars ([Eckart et al. 2013](#); [Scoville & Burkert 2013](#); [Zajaček et al. 2014](#)) rather than core-less gas and dust clumps, see also Fig. 1.10 for the illustration of this enigmatic population of dust-enshrouded stars. In the meantime, several other models have been proposed, some of which pertain to planet formation in the Galactic center; see [Zajaček et al. \(2024d\)](#) for a comprehensive overview. The origin of G objects within the S cluster remains puzzling. They could plausibly be young stellar objects of class I ([Zajaček et al. 2017](#)) or potentially binary-merger products ([Stephan et al. 2016](#)).

Regardless of the G-object origin (in situ or migration scenarios), they appear to be associated with the young stellar population of S stars and CWD stars as revealed by their kinematic structure that deviates from an isotropic orbital configuration ([Peißker et al. 2024b](#)). Given their dusty envelopes revealed by infrared excess, they could in principle be even younger than S stars ($\sim 0.1 - 1.0$ Myr). Based on the spectral energy distribution fits, the bolometric luminosity is lower than for typical S stars – for the G2 object, it is $L_{G2} \sim 10 L_\odot$. Therefore, G objects represent a lower-mass population within the S cluster that could have formed with a certain delay with respect to high-mass star formation (e.g. from the remnant gas that was compressed by stellar winds) or these objects could be evolving more slowly in comparison with higher-mass B-type stars.

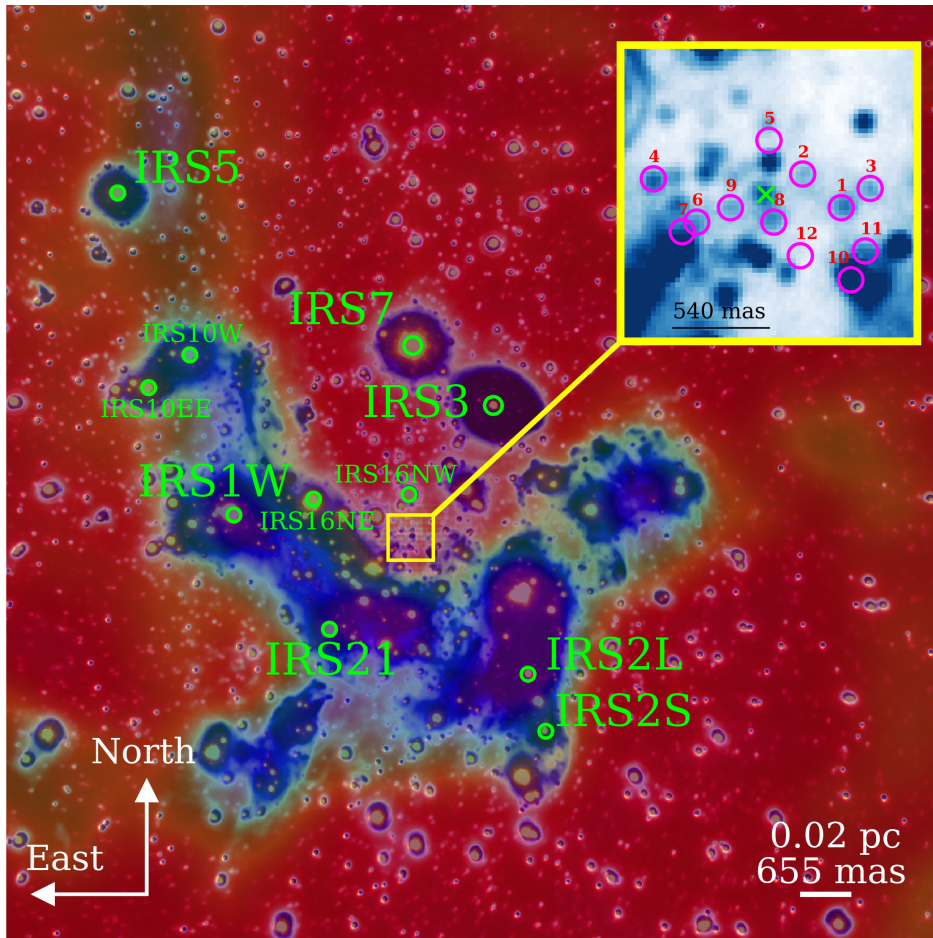


Figure 1.9: Projected distribution of G objects around Sgr A* and with respect to the Minispiral and prominent stars of the inner parsec. This multiwavelength image spanning across ~ 0.8 pc is the combination of K -band (red) and L -band (blue) images taken by NACO at the European Southern Observatory. The green colour depicts the ALMA 100 GHz continuum image reduced by Moser et al. (2017). The figure inset stands for a zoom-in of the yellow region at the very center. It depicts 11 G objects identified in the L -band emission that are in orbit around Sgr A*. The image was adopted from Peißker et al. (2024b).

To understand kinematical structure of stellar populations in the central parsec, it is instructive to compare estimated ages of early-type and late-type stars with the typical timescales of dynamical processes relevant for the NSC. These processes include two-body, non-resonant relaxation, see Eq. (1.5), as well as resonant relaxation processes (scalar and vector) that are relevant for stars bound to the SMBH (Hopman & Alexander 2006; Alexander 2017). When we imagine a star on an elliptical orbit around the SMBH, we can imagine it as a wire with a certain linear mass density when averaged over the orbital orbit. Such elliptical wires then induce torques on each other. The total torque for N stars within the distance r from the SMBH is $\sqrt{N(< r)}Gm_*/r$ and this is responsible for the process of resonant relaxation over many orbits. Another process relevant single stars and binaries is the von Zeipel-Lidov-Kozai (vZLK) resonance that takes place in the hierarchical three-body problem. This could be either a binary-SMBH system or the SMBH-star perturbed by an outer massive body (a stellar/gaseous disc or an IMBH). On the vZLK timescale, the orbital eccentricity and the



Figure 1.10: Illustration of the mysterious population of G objects close to the Galactic center. Currently, about 10 objects with a prominent near-infrared excess have been identified within the inner arcsecond (Ciurlo et al. 2020; Peißker et al. 2020b). The figure depicts prominent gaseous-dusty envelopes that embed stars. Such a model can address the observed infrared excess as well as broad hydrogen and helium recombination lines. The G objects orbit the central SMBH associated with Sgr A* (dark object at the center of the image surrounded by a whitish hot accretion flow) on Keplerian elliptical orbits to a good approximation. Image credit: Jack Ciurlo

inclination are interchanged for the inner binary (a stellar binary or the SMBH-star system) due to the conservation of the z -component of the orbital angular momentum. Consequently, during a high-eccentricity phase, the vZLK mechanism can trigger binary mergers or tidal disruptions of binary stars or single stars by the SMBH.

In Fig. 1.11, we compare dynamical timescales with the estimated age of known stellar populations in the Galactic center. In this figure, if the timescale of a given dynamical process is smaller than the age of a stellar population, it is expected to have affected the angular momentum distribution of those stars. For this plot, we assumed the isotropic background (old) cluster with the mass density distribution $\rho_{\star}(r) = 1.35 \times 10^5 (r/2 \text{ pc})^{-1.4} M_{\odot} \text{ pc}^{-3}$, which yields $M_{\star}(< 2 \text{ pc}) \approx 2M_{\bullet}$. We see that vector resonant relaxation could in principle be affecting the inner portions of the S cluster + CW/CCW discs (depending on the mean stellar mass). This can lead to orbital plane randomization. Late-type stars should have already been affected by vector resonant relaxation and the inner portion also by scalar resonant relaxation. This should have driven older stars on loss-cone orbits where they got tidally disrupted. G objects are likely too young to be affected by any resonant relaxation process. However, if a significant fraction of them originated as binary systems, these systems are expected to be undergoing a merger process due to the vZLK mechanism. In fact, as suggested by Stephan et al. (2019), they could be the manifestation of the merger process in the S cluster since a stellar merger is typically accompanied by the formation of a circumstellar gaseous-dusty envelope that gives rise to infrared excess.

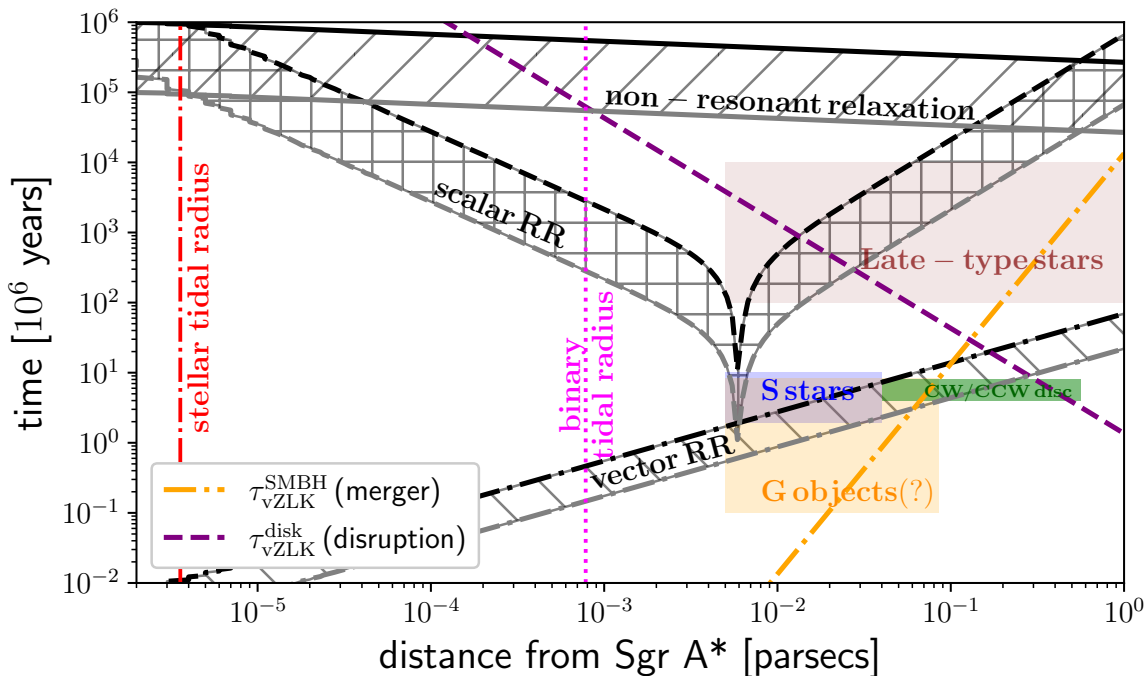


Figure 1.11: Comparison of characteristic dynamical timescales with the age of early-type and late-type stellar populations. We depict radial dependencies for the vector and scalar resonant relaxation, non-resonant relaxation, and the von Zeipel-Lidov-Kozai (vZLK) resonance induced by the SMBH on the binary system (merger) or the vZLK oscillations of the SMBH-star system perturbed by a distant massive stellar disc of $10^4 M_{\odot}$ with the mean radius of 0.23 pc (disruption). For the calculations, we adopted the stellar mass density $\rho_{\star}(r) = 1.35 \times 10^5 (r/2 \text{ pc})^{-1.4} M_{\odot} \text{ pc}^{-3}$ and two mean stellar masses, $1 M_{\odot}$ and $10 M_{\odot}$, depicted by black and gray colours, respectively. The vertical dotted magenta line stands for the tidal disruption radius of a binary system with the component separation of 1.59 AU and the total mass of $3.86 M_{\odot}$. The vertical dash-dotted red line represents the tidal disruption radius of a Solar-type star.

1.1.2 Distribution of gas and accretion-flow structure

The dense NSC surrounding Sgr A* coexists with multiphase gas and dust in the circumnuclear medium. A fraction of the gas originates in the CMZ, while the rest is supplied by the winds of massive young stars. In Fig. 1.12, we show the most characteristic gaseous-dusty structures along with the stars in the NSC. The ionized gas is shown in blue (continuum observations at 250 GHz and the H39 α line emission, ALMA observations, 0.75'' beam size), the molecular gas is depicted in green (CS(5-4) line map, ALMA observations, 0.75'' beam size). The dense molecular/neutral gas is represented as the white region, which is an inverted image and the region thus represents depression in the X-ray emission due to gas/dust extinction. The stellar population is shown in red and yellow colours (3.8 μm with the ESO VLT and narrow-band filters 1.19, 1.71, and 2.25 μm with ISAAC).

Within or close to the sphere of influence of Sgr A*, $r_{\text{SI}} \sim 2 \text{ pc}$, a distinct loop-like feature consisting of neutral and molecular gas is the clumpy Circum-Nuclear Disc (CND) with the number density range of $\sim 10^3 - 10^8 \text{ cm}^{-3}$, the mean temperature of $T \sim 100 \text{ K}$, the total gas mass of $\sim 10^6 M_{\odot}$, and the mean rotational velocity of $\sim 110 \text{ km s}^{-1}$ (Genzel et al. 1985;

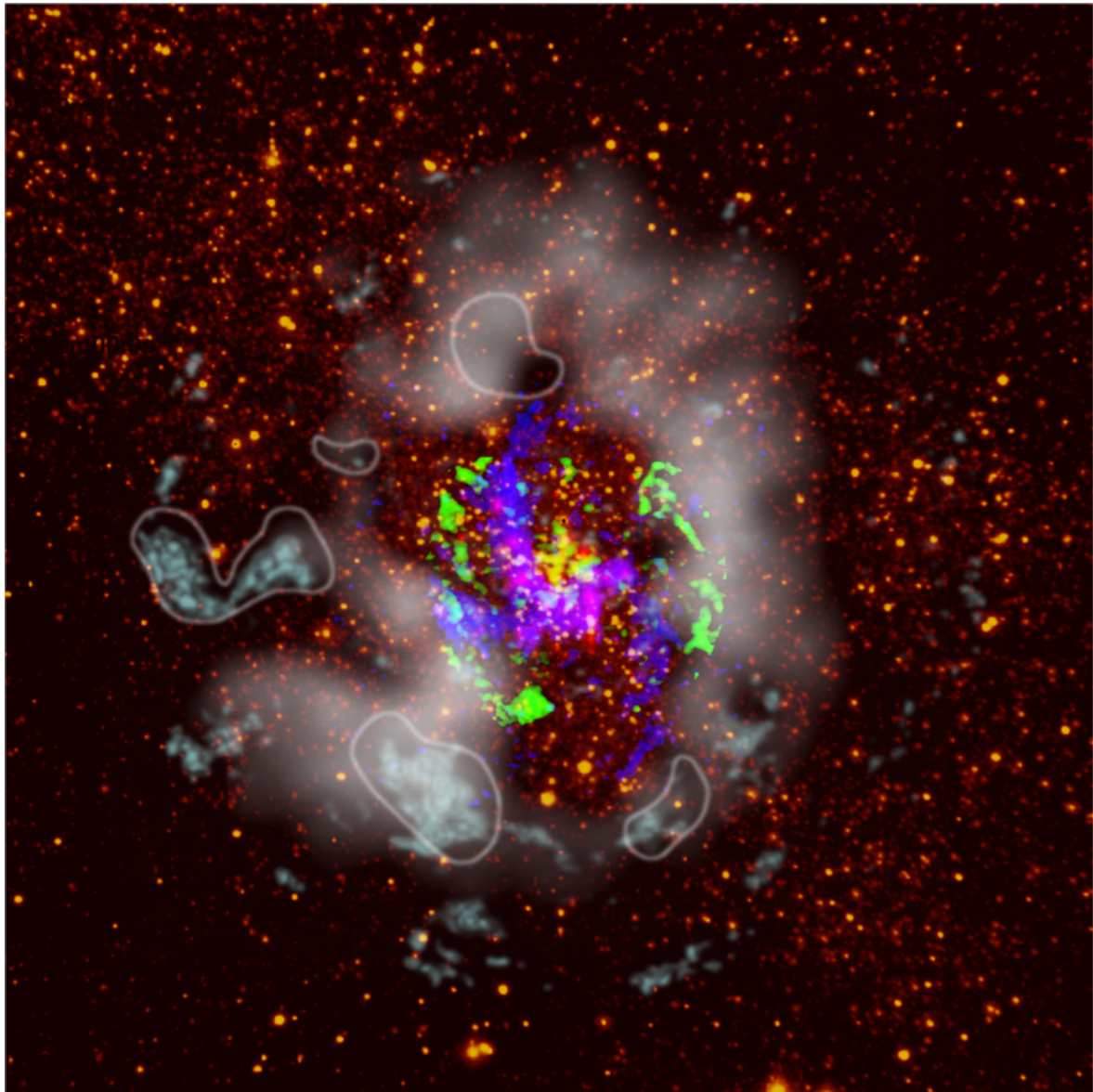


Figure 1.12: Composite multi-wavelength image depicting the coexistence of a dense Nuclear Star Cluster with the gaseous-dusty structures close to the Galactic Center (region 5.6×5.6 pc). The blue colour indicates an ionized gas concentrated mostly along the three arms of the Minispiral (250 GHz continuum + $H39\alpha$ data; ALMA, $0.75''$ beam size; Moser et al. 2017). The green patches correspond to CS(5-4) emission produced by the molecular material along the inner rim of the Circumnuclear disc (ALMA, $0.75''$ beam size; Moser et al. 2017). The white loop-like region is an inverted image of the X-ray emission towards the Galactic center – it represents the depression in the X-ray surface brightness caused mainly by the denser neutral/molecular gas in the Circumnuclear disc (Mossoux & Eckart 2018). The cyan regions pertain to the $N_2H^+(1-0)$ emission (Moser et al. 2017), which in several cases corresponds to the regions of severe extinction in the near-infrared domain (encircled regions). Warm dust and stars in the inner parsec are depicted by a red colour (L' band– $3.8 \mu\text{m}$, NACO at VLT@ESO; Sabha et al. 2012). Stars within the dense Nuclear Star Cluster are represented by a yellow colour (ISAAC@VLT composite image: $1.19+1.71+2.25 \mu\text{m}$ narrow near-infrared bands; Nishiyama & Schödel 2013). Image adopted from Eckart et al. (2019).

Guesten et al. 1987; Mezger et al. 1989; Christopher et al. 2005; Requena-Torres et al. 2012; Mills et al. 2017; Hsieh et al. 2021). The rotational motion of the CND dominates its motion. The peak of the molecular emission is close to ~ 1.6 pc with the extension to 4 – 7 pc from Sgr A* in projection. The density drops quite sharply at ~ 1.5 pc. This central region is rather dilute and filled with ionized gas, therefore it is often denoted as the *central cavity*. It is refilled with a rarefied ionized gas from the inner rim of the CND due to the interaction with the outflow of the NSC driven mostly by massive OB stars (Blank et al. 2016). The CND has high-density clumps with the mean length-scale of $\sim 0.05 - 0.2$ pc. Hsieh et al. (2021) identified of the order of 1000 CND clumps of this size using CS line maps. These can be categorized into warm ones with the temperature of $\sim 50 - 500$ K and number densities of $\sim 10^3 - 10^5 \text{ cm}^{-3}$ and colder ones with the temperature of $\lesssim 50$ K and the number density in the range of $10^6 - 10^8 \text{ cm}^{-3}$. Using the unmagnetized virial theorem with the inclusion of the tidal force, Hsieh et al. (2021) found that most of the CND clump mass ($\sim 84\%$) is tidally stable, yet the clumps do not collapse into stars due to a turbulent motion that increases the critical density. However, it is plausible that occasionally, because of the velocity dispersion among the clumps, two of them collide, which can help cross the density threshold and induce star formation. At the same time, cloud-cloud collision removes angular momentum via dissipation and afterwards the cloud starts inspiraling towards Sgr A*. This way young stellar associations can be found relatively close to the SMBH (Jalali et al. 2014) where in principle stars should not form due to high critical densities in excess of $\sim 10^8 \text{ cm}^{-3}$.

The central cavity is not isotropic – there are denser ionized regions concentrated along the three arms of the *minispiral*. The Northern arm and Western arc seem to originate from the inner rim of the CND (Christopher et al. 2005). Under the assumption that the gas motion is dominated by the potential of Sgr A*, all of the three arms can be fitted with the three bundles of Keplerian orbits – ellipses with Sgr A* at the focus of each ellipse (Zhao et al. 2009, 2010). The Northern and Eastern arms are relatively highly elliptical ($e \sim 0.8$) while the Western arc is only mildly elliptical ($e \sim 0.2$). The gas along the three arms does not orbit in the same plane – the Eastern arm is nearly perpendicular to the Northern arm and the Western arc, which share the common plane. This hints at the origin of these two components at the inner rim of the CND. The three arms consist of mostly ionized gas with the number density in the range of $\sim (3 - 21) \times 10^4 \text{ cm}^{-3}$ and the temperature of 5 000 – 13 000 K. The mass of the ionized gas within the minispiral is estimated to be $\sim 350 M_{\odot}$ (Zhao et al. 2010), hence 3 – 4 orders of magnitude smaller than the mass of the CND. Under the assumption that the minispiral gas is kept ionized due to external photoionization, the required Lyman continuum photon flux of $3 \times 10^{50} \text{ s}^{-1}$ implies that there should be ~ 250 O9-type main-sequence stars within the central parsec. Within the uncertainties, this is comparable to the number of identified 195 OB/Wolf-Rayet stars within the CWD/CCWD/F2/F3 structures (von Fellenberg et al. 2022).

Concerning the stability of the CND and the minispiral against tidal disruption in the potential of Sgr A* and the NSC, we can compare the characteristic densities of gas clumps in these regions with the critical number density given by the Roche limit. At the influence radius of ~ 2 pc, the total mass of the SMBH + NSC is $M_{\text{tot}} \sim 12 \times 10^6 M_{\odot}$, hence we obtain

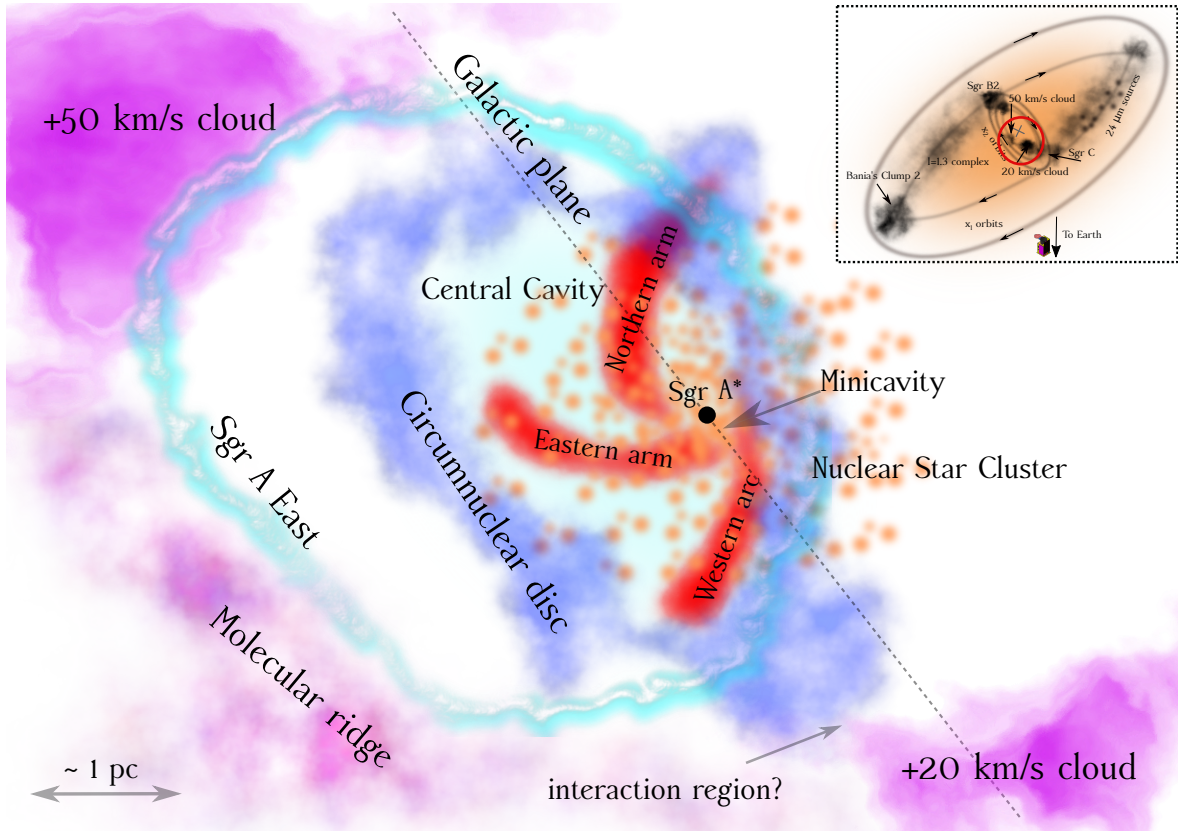


Figure 1.13: Illustration of different structures and gas phases of the circumnuclear medium close to the Galactic center. On larger scales, $\sim 3 - 15$ parsecs, there are two molecular clouds, $+20$ km/s and $+50$ km/s (magenta colour). In the gravitational sphere of influence of Sgr A*, the density of the Circumnuclear disc (CND; molecular and neutral gas; blue colour) drops by several orders of magnitude (central cavity – light blue). At the inner rim of CND, the ionized streamers of the minispiral (red) partially originate. CND and the minispiral coexist with the dense Nuclear Star Cluster (orange stars). The Minispiral dominates the thermal emission of the Sgr A West region while the supernova remnant Sgr A East is responsible for its non-thermal emission. The figure inset in the right upper corner shows the location of the whole region (red circle) within the central bar potential.

the critical CND density for tidal stability as follows,

$$n_{\text{Roche}}^{\text{CND}} > \frac{3M_{\text{tot}}}{2\pi m_{\text{H}} r_{\text{CND}}^3} \\ 2.9 \times 10^7 \left(\frac{M_{\text{tot}}}{12 \times 10^6 M_{\odot}} \right) \left(\frac{r_{\text{CND}}}{2 \text{ pc}} \right)^{-3} \text{ cm}^{-3}, \quad (1.6)$$

which is only met for the densest clumps with $n_{\text{CND}} \approx 10^8 \text{ cm}^{-3}$. The rest of the clumps will likely disperse on the orbital (tidal) timescale of $\tau_{\text{tidal}} \sim 7.6 \times 10^4 (r_{\text{CND}}/2 \text{ pc})^{3/2} (M_{\text{tot}}/12 \times 10^6 M_{\odot})^{-1/2}$ years. As for the minispiral, we adopt its characteristic distance from Sgr A* as the mean of the periapses of the three Keplerian bundles, $r_{\text{mini}} \sim 0.4 \text{ pc}$. This gives the limit

for the stability,

$$n_{\text{Roche}}^{\text{mini}} > 1.2 \times 10^9 \left(\frac{M_{\bullet}}{4 \times 10^6 M_{\odot}} \right) \left(\frac{r_{\text{CND}}}{0.4 \text{ pc}} \right)^{-3} \text{ cm}^{-3}, \quad (1.7)$$

where we adopted just the mass of the SMBH as this is the dominant contribution at those scales within the influence radius. According to Eq. (1.7), none of the minispiral clumps surpasses the critical density, therefore it is a transient feature with the expected tidal timescale of $\sim 60\,000$ years, which is estimated as the mean of the orbital periods of the three arms according to the orbital elements of [Zhao et al. \(2009\)](#). On the other hand, the material in the minispiral is likely being partially replenished from the inner rim of the CND ([Blank et al. 2016](#)), in particular the Western Arc and the Northern Arm. Hence, in this regard, the minispiral lifetime is set by the CND existence, whose tidal timescale is comparable to that of the minispiral. The CND material originates within the CMZ, more specifically from the molecular/neutral material orbiting along the inner stable x_2 orbit, see Fig. 1.6, which is perpendicular to the main axis of the Galactic bar. The closest giant molecular clouds to the CND are $+20 \text{ km s}^{-1}$ (M–0.13–0.08) and $+50 \text{ km s}^{-1}$ (M–0.02–0.07) clouds ([Guesten & Henkel 1983](#)), which are located $\sim 3 - 15 \text{ pc}$ from Sgr A*. There appears to be an interaction between $+20 \text{ km s}^{-1}$ cloud and the CND, which is revealed by the bridge of material between them as revealed in the position-velocity plots ([Takekawa et al. 2017](#)). This type of cloud-cloud interaction could be a mechanism for the accretion of new molecular material onto the CND and subsequently inwards towards the Central Cavity. In Fig. 1.13, we illustrate different structures and phases of the Sgr A* circumnuclear medium, in particular with the focus on their mutual relation, potential interaction, and inward material transport.

As stars belonging to the NSC occupy the same volume as the minispiral and the CND, they interact with the gas of different phases. Typically, the relative velocity between the star and the ambient medium $\mathbf{v}_{\text{rel}} = \mathbf{v}_{\star} - \mathbf{v}_{\text{a}}$ is mildly supersonic, which we can infer from the estimate of the Mach number,

$$\mathcal{M} = \frac{v_{\text{rel}}}{c_s} \approx 20.4 \left(\frac{M_{\bullet}}{4 \times 10^6 M_{\odot}} \right)^{1/2} \left(\frac{T_{\text{a}}}{10^4 \text{ K}} \right)^{-1/2} \left(\frac{r}{0.5 \text{ pc}} \right)^{-1/2}, \quad (1.8)$$

where we used $v_{\text{rel}} = [2GM_{\bullet}/r(1 - \cos \iota)]^{1/2}$ for the relative velocity at the angle ι with respect to the (minispiral) streamers. The speed of sound is calculated as $c_s \simeq [k_{\text{B}}T_{\text{a}}/(\mu m_{\text{H}})]^{1/2}$. For the estimate in Eq. (1.8), we adopted $\iota = 90^\circ$, hence the star passes through the streamer at a right angle. Wind-blowing stars with the mass-loss rate of \dot{m}_{w} and the terminal wind velocity v_{w} will drive a bow shock into the ambient medium. The shocked stellar wind is separated from the bow shock by contact discontinuity whose stagnation radius is ([Wilkin 1996](#))

$$\begin{aligned} R_{\text{bs}} &= \left(\frac{\dot{m}_{\text{w}} v_{\text{w}}}{4\pi\rho_{\text{a}} v_{\text{rel}}^2} \right)^{1/2} \simeq \left(\frac{\dot{m}_{\text{w}} v_{\text{w}} r}{8\pi G M_{\bullet} \mu m_{\text{H}} n_{\text{a}}} \right)^{1/2} \\ &\approx 4.3 \left(\frac{\dot{m}_{\text{w}}}{10^{-5} M_{\odot} \text{ yr}^{-1}} \right)^{1/2} \left(\frac{v_{\text{w}}}{10^3 \text{ km s}^{-1}} \right)^{1/2} \left(\frac{r}{0.5 \text{ pc}} \right)^{1/2} \left(\frac{M_{\bullet}}{4 \times 10^6 M_{\odot}} \right)^{-1/2} \left(\frac{n_{\text{a}}}{5 \times 10^4 \text{ cm}^{-3}} \right)^{-1/2} \text{ mpc}, \end{aligned} \quad (1.9)$$

where the second expression assumes the perpendicular interaction ($\iota = 90^\circ$) and the Keplerian orbital motion of a star around the SMBH. The numerical estimate for the stagnation radius

of a stellar bow shock, $R_{\text{bs}} \sim 4.3 \text{ mpc} \sim 883 \text{ AU}$, was calculated for the typical stellar-wind parameters of Wolf-Rayet stars that are present in the central parsec (Krabbe et al. 1995; Najarro et al. 1997; Bryant & Krabbe 2021). When we compare it with the smallest linear scales that can be studied with eight-meter class telescopes at $2 \mu\text{m}$, $x \sim (\lambda_{2\mu\text{m}}/D_{8\text{m}})d_{\text{SgrA}^*} \approx 418 \text{ AU}$, we see that such bow-shock structures should be resolved if their surface brightness is sufficiently large. Indeed, several stellar bow shocks have been found along the minispiral arms and they have been used for constraining the ambient medium properties (gas flow and density) or stellar kinematics depending on which parameters are initially better constrained (see e.g. Sanchez-Bermudez et al. 2014; Zajack et al. 2018; Karas et al. 2021, and references therein).

Sgr A* is a compact non-thermal radio source within the Sgr A West thermal region (Balick & Brown 1974). It is to a high precision associated with the SMBH of $M_{\bullet} \simeq 4 \times 10^6 M_{\odot}$ based on the correspondence of radio and infrared reference frames. The radio and infrared reference frames could have been combined with the precision of $\sim 0.03''$ thanks to a group of late-type stars with a maser emission (SiO and H_2O masers) that have been identified in both infrared and radio domains (Menten et al. 1997). With this accuracy, it was possible to infer an upper limit on the infrared luminosity of Sgr A* at $2.2 \mu\text{m}$, $\nu L_{\nu} \lesssim 1.1 \times 10^{35} \text{ erg s}^{-1}$, which implies a highly sub-Eddington accretion rate. Based on the Faraday rotation measurements at 227 and 343 GHz, Marrone et al. (2007) constrained the accretion rate within $200 r_g$ to $\dot{M} = 2 \times 10^{-9} - 2 \times 10^{-7} M_{\odot} \text{ yr}^{-1}$ for the disordered and ordered magnetic field cases, respectively. Adopting the intermediate value, $\dot{M} \sim 10^{-8} M_{\odot} \text{ yr}^{-1}$, we obtain the following Eddington ratio,

$$\begin{aligned} \dot{m} &= \frac{\dot{M}}{\dot{M}_{\text{Edd}}} = \frac{\sigma_{\text{T}} \eta_{\text{rad}} c}{4\pi G m_{\text{p}}} \frac{\dot{M}}{M_{\bullet}} \\ &\sim 1.1 \times 10^{-7} \left(\frac{\eta_{\text{rad}}}{0.1} \right) \left(\frac{\dot{M}}{10^{-8} M_{\odot} \text{ yr}^{-1}} \right) \left(\frac{M_{\bullet}}{4 \times 10^6 M_{\odot}} \right)^{-1}. \end{aligned} \quad (1.10)$$

For comparison, for the Eddington-rate limit, $\dot{m} = 1$, the actual accretion rate for Sgr A* would be $\dot{M} \sim 0.09 M_{\odot} \text{ yr}^{-1}$ or nearly 10% of the Solar mass per year. For such a low accretion rate as indicated by Eq. (1.10), the accretion flow does not cool fully via radiative losses. The energy released via viscous turbulence leads, to a dominant extent, to the entropy increase, which is transported inwards by accretion and eventually it is lost beyond the event horizon. This is so-called advective cooling and such accretion flows as in the Sgr A* system are referred to as *Advection-Dominated Accretion Flows* or ADAFs. Because only a small fraction of the viscously released energy is lost via radiation, ADAFs are radiatively inefficient and hot in comparison with standard accretion discs (Yuan & Narayan 2014). This is also related to their larger geometrical thickness and small optical depth due to more diluted plasma.

Observationally, Sgr A* is also consistent with ADAF model predictions since the peak of the spectral energy distribution (SED) is in the mm-submm domain close to 1 millimeter. This is quite different from SEDs of standard thin disc solutions (Shakura-Sunyaev, Novikov-Thorne) that peak in the UV domain for SMBHs, which is also known as the *Big Blue Bump*. The SED peak of Sgr A* close to one millimeter is also associated with the transition from optically thick synchrotron emission at lower frequencies to optically thin synchrotron and inverse Compton emission towards higher frequencies (shorter wavelengths). In Fig. 1.14, we show the ADAF model of Sgr A* for different accretion rates in the range $\dot{M} = 2 \times 10^{-9} - 2 \times 10^{-7} M_{\odot} \text{ yr}^{-1}$ as inferred from the Faraday rotation measurements (Eddington ratio of

$\dot{m} = 2 \times 10^{-8} - 2 \times 10^{-6}$; Marrone et al. 2007). In this figure, we also depict radio-mm detections of Sgr A* in the optically thick domain and close to the SED peak (see Zajaček et al. 2016, for the data collection). For the ADAF model calculations, we utilized the model by Mahadevan (1997), which has been updated by Pesce et al. (2021) and implemented in the python code LLAGNSED² that takes two basic parameters – SMBH mass and relative accretion rate (Eddington ratio). In the ADAF model, the electromagnetic emission at a given frequency depends on the electron temperature T_e , which is calculated self-consistently using the equation of energy-rate balance,

$$\delta Q^+ + Q^{ie} = Q_{\text{rad}}^- + Q_{\text{adv,e}}, \quad (1.11)$$

where on the left-hand side, δQ^+ is the fraction of the viscously dissipated energy rate that is transferred to electrons, $(1 - \delta)Q^+$ is transferred to ions, Q^{ie} is the energy rate transferred from warmer ions to electrons via Coulomb coupling. On the right-hand side, the energy losses include the advection term $Q_{\text{adv,e}}$, i.e. the electron energy rate lost via advection, and Q_{rad}^- is the energy loss rate corresponding to radiation. For the construction of the ADAF SED, the radiation term Q_{rad}^- is relevant since it consists of frequency-integrated monochromatic luminosities corresponding to synchrotron, inverse Compton, and bremsstrahlung processes,

$$Q_{\text{rad}}^- = L_{\text{synch}} + L_{\text{Comp}} + L_{\text{brems}}. \quad (1.12)$$

We show these different emission contributions in Fig. 1.14 with coloured lines (red stands for the synchrotron emission, green for inverse Compton, and blue for the bremsstrahlung component) for the case with the intermediate Eddington ratio of $\dot{m} = 2 \times 10^{-7}$. The prominent mm/submm bump in Fig. 1.14 is attributed to relativistic, thermal electrons in the inner portion of the ADAF (Dexter et al. 2010). The radio synchrotron emission at lower frequencies is attributed to a fraction of the electron thermal energy ($\sim 1.5\%$) injected into non-thermal electrons in the inner ADAF (Yuan et al. 2003). Alternatively, it could also be caused by a compact, self-absorbed jet that has a low surface-brightness (Falcke & Markoff 2000). The quiescent, faint X-ray emission at higher energies is due to the bremsstrahlung emission of colder electrons closer to the Bondi radius (Baganoff et al. 2003; Wang et al. 2013).

Although the accretion rate onto Sgr A* is very low, there is a plenty of gaseous material in its surroundings. Even without considering several $\sim 100 M_\odot$ of the minispiral gas and $\sim 10^6 M_\odot$ of the neutral/molecular gas within the CNB, stars alone can supply enough mass for accretion via their stellar winds. As reported by von Fellenberg et al. (2022), there are about 200 OB/Wolf-Rayet stars within ~ 0.4 pc from Sgr A*. Given that young, HeI-emission line massive stars typically have large mass-loss rates of $\sim 10^{-5} M_\odot \text{yr}^{-1}$ (Najarro et al. 1997), as much as $\dot{M}_{\text{wind}} \lesssim 10^{-3} M_\odot \text{yr}^{-1}$ can be available for accretion. Based on Chandra X-ray observations centered on the extended emission peaking close to Sgr A* (FWHM $\sim 1.4''$), Baganoff et al. (2003) inferred the asymptotic values of the number density and the temperature of the spherical, Bondi-like inflow, $n_B \sim 26 \text{ cm}^{-3}$ and $k_B T_B \sim 1.3 \text{ keV}$ ($T_B \sim 1.5 \times 10^7 \text{ K}$). This implies the capture (Bondi) radius where the gravitational pull of Sgr A* overcomes the thermal pressure of hot, X-ray emitting plasma,

$$\begin{aligned} r_B &\simeq \frac{2GM_\bullet}{c_s^2} = \frac{2GM_\bullet \mu m_H}{k_B T_B} \\ &\sim 0.14 \left(\frac{M_\bullet}{4 \times 10^6 M_\odot} \right) \left(\frac{T_B}{1.5 \times 10^7 \text{ K}} \right)^{-1} \text{ pc}, \end{aligned} \quad (1.13)$$

²<https://github.com/dpesce/LLAGNSED>

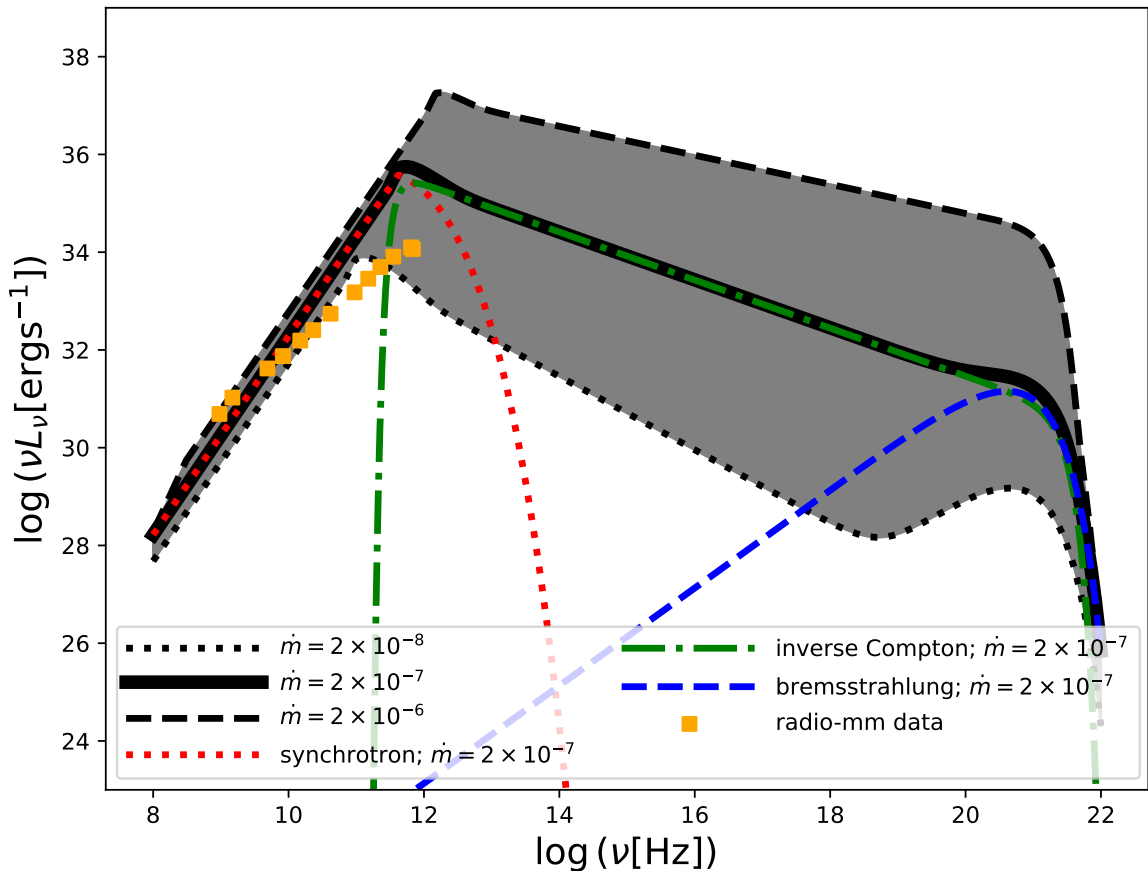


Figure 1.14: Spectral Energy Distribution (SED) of Sgr A* modelled using advection-dominated accretion flow. Different black lines correspond to ADADF continuum spectra for different relative accretion rates – Eddington ratios of $\dot{m} = 2 \times 10^{-8} - 2 \times 10^{-6}$. For the intermediate rate of $\dot{m} = 2 \times 10^{-7}$, we also depict contributions of synchrotron (red dotted line), inverse Compton (green dash-dotted line), and bremsstrahlung radiation mechanisms (blue dashed line). For comparison, radio-mm detections of Sgr A* are included as orange points (see Zajaček et al. 2016, for the collection details). For the calculations, we adopted the ADADF model according to Mahadevan (1997), which is implemented in the python code LLAGNSED by Pesce et al. (2021).

which corresponds to $r_B \sim 7.3 \times 10^5 r_g$. The accretion rate at the Bondi radius then is,

$$\begin{aligned} \dot{M}_B &\simeq \pi r_B^2 c_s \mu m_H n_B = \frac{4\pi G^2 M_\bullet^2}{c_s^3} \mu m_H n_B \\ &\sim 10^{-5} \left(\frac{M_\bullet}{4 \times 10^6 M_\odot} \right)^2 \left(\frac{T_B}{1.5 \times 10^7 \text{ K}} \right)^{-3/2} \left(\frac{n_B}{26 \text{ cm}^{-3}} \right) M_\odot \text{ yr}^{-1}, \end{aligned} \quad (1.14)$$

hence all of this material can be supplied by stellar winds of stars located within r_B or whose pericenters reach or cross r_B ($\dot{M}_B < \dot{M}_{\text{wind}}$). Since the accretion rate within $200 r_g$ is constrained to be $\dot{M} \sim 2 \times 10^{-9} - 2 \times 10^{-7} M_\odot \text{ yr}^{-1}$ based on the Faraday-rotation measurements of Sgr A* (Marrone et al. 2007), only a small fraction of $\dot{M}/\dot{M}_B \lesssim 0.02$ or $\lesssim 2\%$ of the Bondi accretion rate gets accreted through the event horizon. Therefore most of the material accreted at the Bondi radius is eventually lost via outflows. One of the properties of ADAFs

is the power-law dependence of the inflow rate on the distance from the SMBH – the inflow rate gets smaller with the radius due to an outflowing material,

$$\dot{M}_{\text{in}} = \dot{M}_{\text{B}} \left(\frac{r_{\text{in}}}{r_{\text{B}}} \right)^p \sim 1.2 \times 10^{-7} \left(\frac{\dot{M}_{\text{B}}}{10^{-5} \text{ M}_{\odot} \text{ yr}^{-1}} \right) \left(\frac{r_{\text{in}}}{100 r_{\text{g}}} \right)^{0.5} \left(\frac{r_{\text{B}}}{7.3 \times 10^5 r_{\text{g}}} \right)^{-0.5} \text{ M}_{\odot} \text{ yr}^{-1}, \quad (1.15)$$

which for $p = 0.5$ and $r_{\text{in}} = 100 r_{\text{g}}$ gives $\dot{M}_{\text{in}} \sim 10^{-7} \text{ M}_{\odot} \text{ yr}^{-1}$ that is consistent with the Faraday-rotation constraints for the ordered magnetic-field configuration (Marrone et al. 2007). The inner radius r_{in} is scaled to $\sim 100 r_{\text{g}}$, which corresponds to the distance of the transition zone between the outer convection-dominated flow and the inner region dominated by the advection of viscously generated energy density (Abramowicz et al. 2002). The power-law index p is constrained to adopt the values between ~ 0.3 and unity according to the radial density profiles based on general relativistic magnetohydrodynamic simulations (Yuan et al. 2003; Pen et al. 2003; Yuan et al. 2012; Yuan & Narayan 2014; Ressler et al. 2020). The presence of the outflow leads to the flattening of the radial density profile of the accretion flow with respect to the steady spherical Bondi inflow, which has $n_{\text{B}} \propto r^{-3/2}$. Wang et al. (2013) analyzed the obtained X-ray continuum and line spectrum and conclude that the best description is provided by an ADAF with $n_{\text{ADAF}} \propto r^{-3/2+s}$, where $s \approx 1$. This is consistent with the detected weak hydrogen-like Fe K α line. Thus the no-outflow solution can be discarded for Sgr A*.

Further support for the nuclear outflow is provided by several aligned stellar bow shocks. The closest bow-shock sources to Sgr A* are X7 (Mužić et al. 2010; Peißker et al. 2021a) and X8 (Peißker et al. 2019) located at the mean projected distances of 0.4'' (~ 0.016 pc) and 0.425'' (~ 0.017 pc), respectively. Another prominent stellar bow-shock source is X3 (Mužić et al. 2010; Peißker et al. 2023), which is located further from Sgr A* in projection at ~ 0.1 pc. Its symmetry axis is also approximately aligned with those of X7 and X8. On the other hand, these three bow-shock sources have different proper-motion directions that, at the same time, are misaligned with respect to bow-shock symmetry axes. Hence, the common symmetry axis of the bow shocks indicates the presence of a large-scale, collimated outflow directed away from Sgr A*. Mužić et al. (2010) estimated the velocity of a few 1000 km s $^{-1}$ for such an outflow. First, the nuclear outflow could be produced by the collective wind within the NSC. Second, it could be associated with the ADAF as discussed above. In the first case, if we approximate the NSC by a spherical distribution of wind-blowing stars, there have been several analytical and numerical solutions of the inflow-outflow structure of the gaseous medium around the SMBH (Quataert 2004; Cuadra et al. 2008; Generozov et al. 2015; Yalinewich et al. 2018; Ressler et al. 2019). In the steady-state 1D model, a stagnation zone develops where the radial flow velocity goes through zero and thus divides the outflow region for radii larger than the stagnation radius from the inflow region for radii that are smaller. In both regions, the radial flow velocity can reach supersonic values, especially when the mass injection rate per unit volume is sufficiently steep as a function of radial distance ($q \propto r^{-\eta}$ for $\eta > 9/4$; Yalinewich et al. 2018). Given the surface-brightness density power-law slope Γ of the NSC and the radial density profile of the circumnuclear gas $\rho \propto r^{-\nu}$, the stagnation radius can be expressed in analogy to the Bondi radius, just replacing the sound speed with the mean stellar-wind velocity v_{w} , which is valid to a good approximation for $v_{\text{w}} > \sigma_{\star}$. The estimates

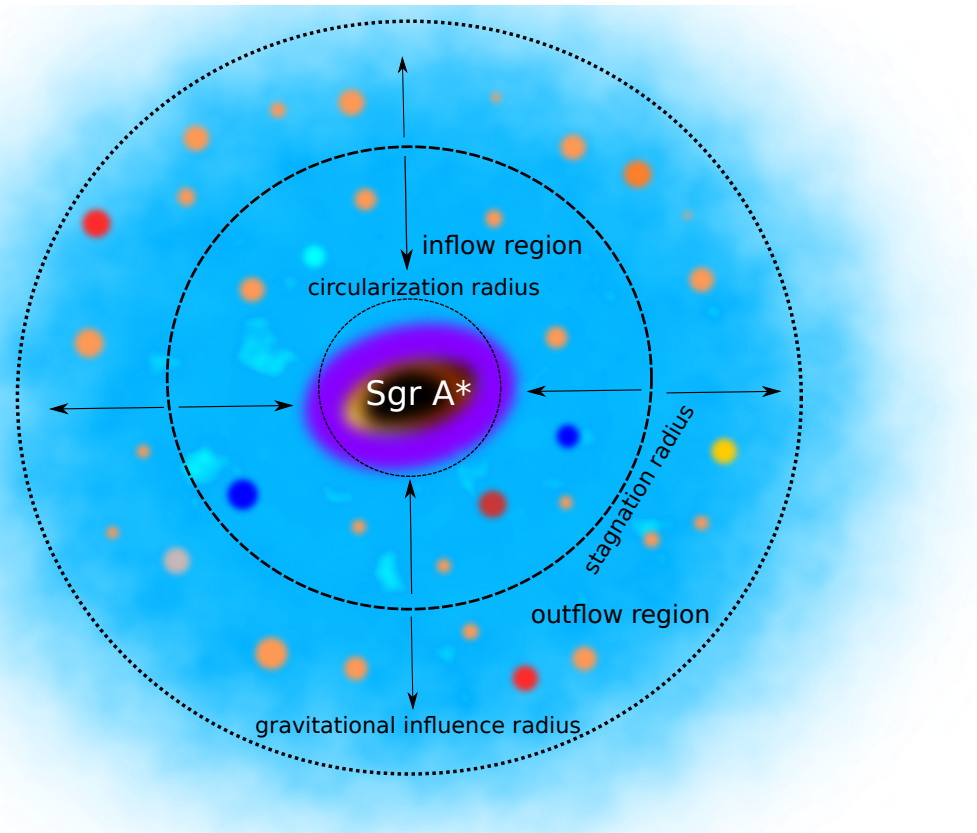


Figure 1.15: Schematic representation of the stagnation zone in the nearly spherical Nuclear Star Cluster. In addition, we also show the sphere of gravitational influence of Sgr A* ($r_{\text{st}} \sim 2$ pc), inflow, and outflow regions that are below or above the stagnation radius r_{st} . In case the stellar-wind material inside the inflow zone has a remnant angular momentum, it circularizes at the circularization radius, r_{circ} . The illustration is not drawn to the scale, it just shows a qualitative relation among different length-scales.

for the stagnation radius r_{st} in the Galactic center then are (Generozov et al. 2015),

$$\begin{aligned}
 r_{\text{st}} &\approx \left(\frac{13 + 8\Gamma}{4 + 2\Gamma} - \frac{3v_{\text{st}}}{2 + \Gamma} \right) \frac{GM_{\bullet}}{v_{\text{st}}u_{\text{w}}^2} \\
 &\approx \begin{cases} 0.30 \left(\frac{M_{\bullet}}{4 \times 10^6 M_{\odot}} \right) \left(\frac{v_{\text{w}}}{500 \text{ km s}^{-1}} \right)^{-2} \text{ pc} & , \text{ core } (\Gamma = 0.1), \\ 0.16 \left(\frac{M_{\bullet}}{4 \times 10^6 M_{\odot}} \right) \left(\frac{v_{\text{w}}}{500 \text{ km s}^{-1}} \right)^{-2} \text{ pc} & , \text{ cusp } (\Gamma = 0.8), \end{cases} \quad (1.16)
 \end{aligned}$$

where we approximated the gas density slope close to the stagnation radius $\nu_{\text{st}} = -(d \ln \rho / d \ln r)|_{r_{\text{st}}}$ according to Generozov et al. (2015), $\nu_{\text{st}} \approx 1/6[(4\Gamma + 3)]$, which for the core-like stellar distribution gives $\nu_{\text{st}} \approx 0.57$ and for the cusp-like distribution, we obtain $\nu_{\text{st}} \approx 1.03$. We illustrate the stagnation radius, inflow, outflow zones around the SMBH embedded within a nearly isotropic NSC in Fig. 1.15. Since the stagnation radius for the Galactic center appears to be located at a larger distance from Sgr A* by an order of magnitude in comparison with the location of the aligned bow-shock sources X7 and X8, see Eq. (1.16), it is more plausible that the stars interact with a nuclear outflow launched within the ADAF inflow zone. Such an outflow is likely collimated by a large-scale magnetic field, which is ordered on both larger and smaller scales and has a dominant poloidal component outside the denser clouds

as it has been inferred by several independent studies from close to the innermost stable circular orbit to the CMZ (Morris 2015; GRAVITY Collaboration et al. 2018). Hence, the nuclear outflow is expected to have a bipolar geometry. In the inner parsec, high resolution spectral studies indicate such a bipolar outflow with a small inclination with respect to the Galactic plane. Based on the ALMA mm/sub-mm spectral and continuum studies including the hydrogen recombination lines H30 α , H39 α , H52 α , and H56 α , Yusef-Zadeh et al. (2020) detected a red-/blue-shifted ionized gas outflow with the radial velocity of $\pm 500 \text{ km s}^{-1}$, with an indication of higher velocities reaching -2500 km s^{-1} and 4000 km s^{-1} on milliparsec scales (see also Murchikova et al. 2019, for the detection of a broad, double-peaked H30 α line interpreted as a rotating disc structure). On the scale from tens of milliparsecs to parsec scales, the outflow with an opening angle of $\sim 30 - 60^\circ$ and the position angle close to the Galactic plane coincides in projection with several linear and bow-shock sources detected in radio (linear features $j1 - j5$ and comet-shaped sources F1, F2, and F3; Yusef-Zadeh et al. 2016; Royster et al. 2019; Yusef-Zadeh et al. 2020) and infrared domains (bow-shock sources X7, X8, and X3; Mužić et al. 2010; Peißker et al. 2019, 2021a). In addition, it may also be related to the enhanced emission along the minicavity as well as the enhanced X-ray emission of the IRS13 region. We illustrate the mutual positions of the plausible bipolar ionized outflow, comet-shaped/linear features, the Galactic plane, the Minispiral streamers, the minicavity, and the stagnation radius in Fig. 1.16. Yusef-Zadeh et al. (2020) estimate the mass-outflow rate of the putative nuclear outflow/jet to be $\dot{M}_{\text{out}} \sim 1.4 \times 10^{-5} M_\odot \text{ yr}^{-1}$, which is consistent with the inflow rate through the event horizon being a small fraction $\lesssim 2\%$ of the inflow rate at the Bondi radius since most of it is lost in the outflow.

There are several observational signatures that the plasma that accretes towards Sgr A* or moves away from it, is magnetized. On larger scales, close to the Bondi radius, a magnetar designated as PSR J1745–2900 was detected. Based on the Faraday-rotation measurements of the magnetar radio emission, Eatough et al. (2013) put a lower limit on the line-of-sight magnetic field component, $B \gtrsim 8 \text{ mG}$, at the deprojected distance of $r \gtrsim 0.12 \text{ pc}$. On the smallest scales close to the innermost stable circular orbit, the constraints come from the multi-wavelength emission of Sgr A*. In the optically thin part of the Sgr A* SED, see the inverse Compton–bremsstrahlung components in Fig. 1.14, Sgr A* exhibits several (3-5) \sim hour-long flares in the infrared domain. About one flare per day is detected in the X-ray domain, with the one-to-one correspondence between X-ray and infrared flares (every X-ray flare has an infrared counterpart). Based on the emission properties of these synchrotron (infrared/submm/mm flares) and synchrotron-self-Compton flares (X-ray flares), it was possible to constrain the magnetic field close to the ISCO to $\sim 10 - 100 \text{ G}$ (Eckart et al. 2012; Witzel et al. 2021). A simple accretion model of the magnetized ADAF fed by stellar winds can explain the $\sim 10 - 100 \text{ G}$ field close to the ISCO due to the inflow of magnetized hot plasma that drags magnetic field lines inwards from the scales of $\sim 0.1 \text{ pc}$ (Bondi radius). To obtain some estimates of the power-law scaling of the circumnuclear magnetic field, we introduce the magnetization parameter of the plasma, $\beta_p = P_{\text{gas}}/P_{\text{mag}}$, which expresses the ratio of the plasma gas pressure to the magnetic pressure. Assuming that the magnetization parameter of the ADAF does not change significantly with the radius, we obtain the basic scaling relation $[n_p(r)T_p(r)]/B_p(r)^2 = \text{const}$, where $n_p(r)$, $T_p(r)$, and $B_p(r)$ correspond to plasma number density, temperature, and magnetic field radial profiles. Adopting the power-law scaling $T_p \propto r^{-\theta}$ and $n_p \propto r^{-3/2+s}$ according to Wang et al. (2013),

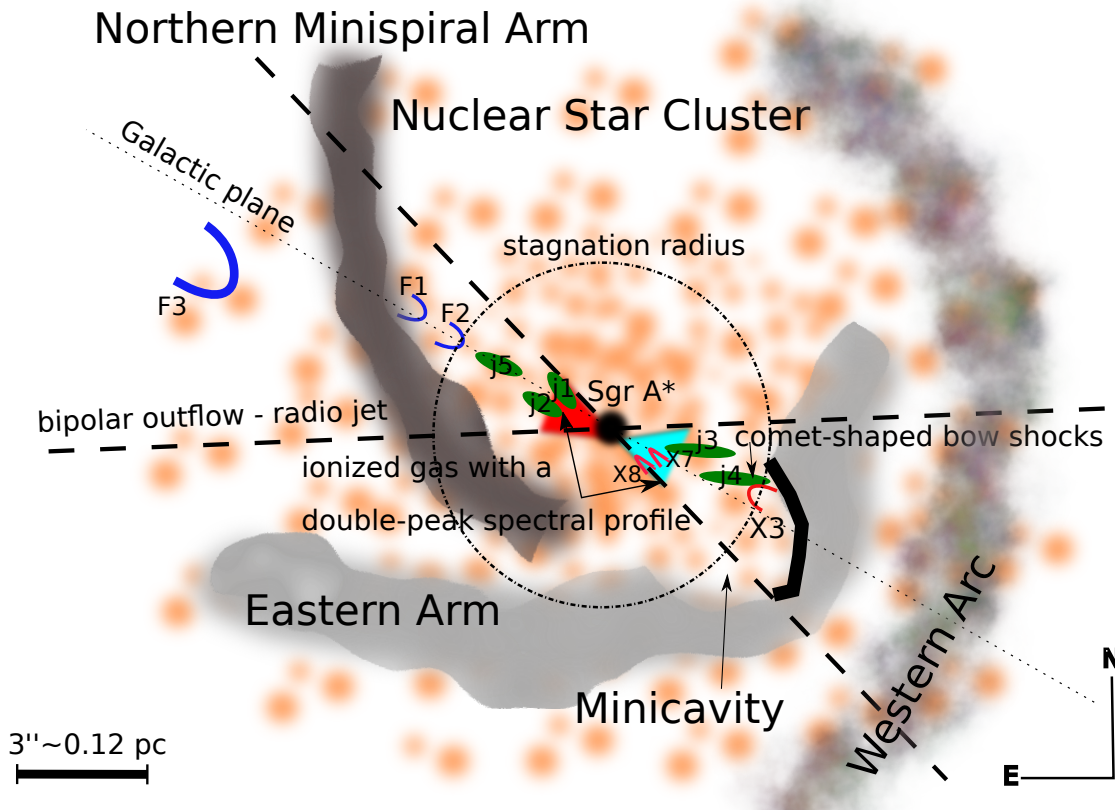


Figure 1.16: A schematic of the fast bipolar ionized outflow close to the Galactic plane coinciding with the position of several bow-shock/linear features. In particular, we show the Minispiral arms, the minicavity, the bow-shock sources X3, X7, X8, F1, F2, and F3 as well as radio linear filaments j1-j5. The position and the orientation of the bipolar ionized outflow is indicated by blue/red-shaded regions representing the Doppler shift. The stagnation radius of $r_{st} \sim 4''$ (cusp-like profile) is depicted by a dash-dotted circle.

we obtain the radial magnetic field profile as follows,

$$\begin{aligned}
 B_p(r_{in}) &= B_p(r) \left(\frac{r_{in}}{r_m} \right)^{-3/4+1/2(s-\theta)} \\
 &\sim 28 \left(\frac{r_{in}}{10 r_g} \right)^{-3/4} \left(\frac{r_m}{0.1 \text{ pc}} \right)^{3/4} \text{ G}, \tag{1.17}
 \end{aligned}$$

where the last relation is expressed for the best fit to the X-ray spectra, which leads to $s \approx 1$ and $\theta \approx 1$, i.e. the temperature radial profile is close to the virialized profile. For the Bondi flow, i.e. $s = 0$ and $\theta \approx 1$, we get $B_p(r) \propto r^{-5/4}$, which yields $B_p(r_{in}) \sim 6330 \text{ G}$ for $r_{in} = 10 r_g$ (close to the ISCO). Therefore, the outflow rate that nearly balances the inflow rate is in agreement with the magnetic field scaling across the hot flow around Sgr A*, while no-outflow Bondi flow gives too large values inconsistent with the observations.

Although Sgr A* accretes at a very low level in comparison with AGN, especially quasars, it is quite variable across all wavelengths, including radio, mm, submm, infrared, and X-ray domains. Especially in the optically thin part of its SED, in the near-infrared and X-ray domains, it exhibits several flares per day (see e.g. [Witzel et al. 2021](#), and references therein). By flares we mean an hour-long, order-of-magnitude flux excursions with the peak flux

being comparable in the near-infrared domain to relatively bright S stars. They have a multi-wavelength nature, with the simultaneous X-ray/NIR flares and time-lagged submm-mm-radio flares, which can be addressed in the framework of an adiabatically expanding self-absorbed plasmoid model (Eckart et al. 2006; Yusef-Zadeh et al. 2006; Eckart et al. 2008; Yusef-Zadeh et al. 2008, 2009a; Eckart et al. 2012). Specifically, as the blob of relativistic electrons expands and cools off on a certain timescale, the energy peak shifts towards lower frequencies (van der Laan 1966). It is not clear what the physical cause of these flares. Previously, a toy model was used to explain near-infrared/X-ray flares where a radiating, bright inhomogeneity in the inner ADAF orbits close to the ISCO. As we view this orbiting “hot spot” at a specific inclination (Broderick & Loeb 2006; Meyer et al. 2006; Zamaninasab et al. 2011), the rate at which the flux is modulated during one orbit changes due to a different amount of contribution of the Doppler boosting and strong gravitational lensing (see also Karas & Bao 1992; Stuchlík & Bao 1992, for early studies). The observed timescale of the near-infrared flares is close to one hour. If we associate this timescale with the “hot-spot” orbit, then the expected orbital radius in gravitational radii is,

$$\begin{aligned} \frac{r}{r_g} &= \left[\frac{c^3 P_{\text{flare}}}{2\pi G M_\bullet} - a_\bullet \right]^{2/3} \\ &\simeq 9.47 \left(\frac{P_{\text{flare}}}{1 \text{ hour}} \right)^{2/3} \left(\frac{M_\bullet}{4 \times 10^6 M_\odot} \right)^{-2/3}, \end{aligned} \quad (1.18)$$

where we assumed the zero spin ($a_\bullet = 0$) in the numerical estimate. Hence, since $r \approx 9 r_g$, the “hot spot” is expected to orbit close to the ISCO. In terms of the angular diameter, it corresponds to $\sim 94 \mu\text{as}$. Such tiny scales were resolved thanks to near-infrared interferometry, specifically the instrument GRAVITY utilizing the Very Large Telescope Interferometry at the European Southern Observatory, that detected the clockwise orbital motion of the emission centroid in the K -band ($2.2 \mu\text{m}$; GRAVITY Collaboration et al. 2018) during a near-infrared flare. The orbital period of the loop-like “hot spot” motion coincided with the period of the polarization rotation of the hot-spot infrared synchrotron emission (45 ± 15 minutes). This is consistent with the poloidal magnetic-field geometry since the toroidal field would lead to two polarization rotations per one orbit. Using photon ray-tracing of a hot-spot emission moving on a geodesic trajectory, GRAVITY Collaboration et al. (2020b) constrained the source diameter to $\lesssim 5 r_g$, its orbital radius to $9 r_g$, and the orbital inclination to $\sim 140^\circ$. Such a source size is consistent with the constraints given by the Very Long Baseline Interferometry observations at 1.3 mm (Doeleman et al. 2008), where the mm emission is not affected by interstellar scattering. The detected intrinsic source diameter of $37_{-10}^{+16} \mu\text{as}$, which corresponds to $7.5_{-2.0}^{+3.2} r_g$, is smaller than the apparent size of the event horizon of the SMBH of $M_\bullet \simeq 4 \times 10^6 M_\odot$ ($\theta_{\text{EH}} \simeq 6 \sqrt{3} G M_\bullet / (c^2 d_{\text{SgrA}^*}) \rightarrow \sim 51.2 \mu\text{as}$). This implies that the emitting source is not centered on Sgr A* and could correspond to the hot spot or a ring-like structure with a non-uniform surface brightness. With the involvement of more submm/mm telescopes, it was possible to reconstruct the image of Sgr A*, including the spiral-like polarized emission tracing the magnetic field structure (Event Horizon Telescope Collaboration et al. 2024). The thick emission ring has the diameter of $\sim 51.8 \pm 2.3 \mu\text{as}$ consistent with the shadow of the SMBH, however, a substructure on smaller scales cannot be excluded. In fact, using the polarized millimeter light curves of Sgr A* in 2017 obtained by ALMA, Wielgus et al. (2022) can reconstruct the polarization-angle rotation during an X-ray flare using the model of an orbiting hot spot embedded in a poloidal magnetic field and viewed at a small angle of

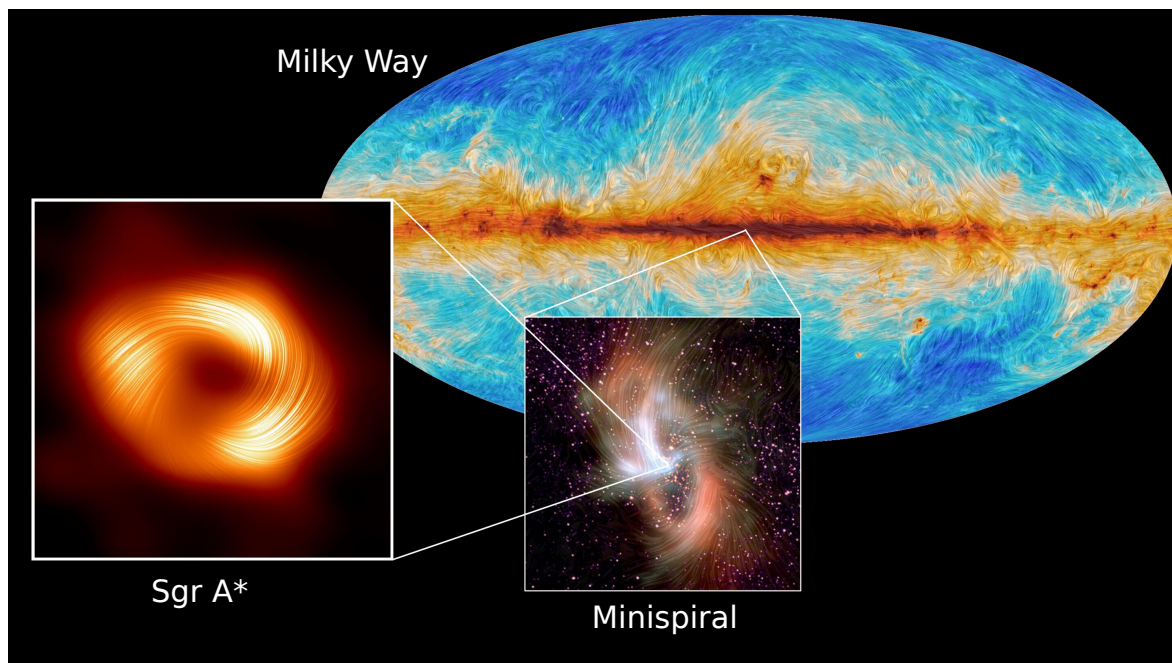


Figure 1.17: Polarized emission of gas and dust flows on different scales. In the left panel, we show the polarized millimeter emission of hot plasma along the Sgr A* ring (Event Horizon Telescope Collaboration; [Event Horizon Telescope Collaboration et al. 2024](#)). The middle panel depicts the far-infrared polarized emission of warm dust along the Minispiral arms on pc-scales (NASA/SOFIA/HST-NICMOS observations). The right top panel shows the polarized millimeter emission of dust along the whole Galactic plane (ESA/Planck Collaboration). Credit: S. Issaoun/EHT Collaboration.

$\sim 20^\circ$. The orbital radius that can reproduce the observations is $\sim 10 r_g$ and the Gaussian-like hot-spot diameter is $\sim 6 r_g$, which is overall consistent with the NIR GRAVITY results. In Fig. 1.17, we show the polarized millimeter emission of hot plasma along the Sgr A* ring (inner ADAF), the far-infrared polarized emission of warm dust along the Minispiral arms on pc-scales, and the polarized mm-emission of dust along the Galactic plane. This helps to illustrate the coherency of the magnetic field structure and its overall dynamical relevance from the largest Galactic scales to the smallest ones.

The physical mechanism behind Galactic center flares is still uncertain. Because of the dynamically relevant magnetic field that is highly ordered on both larger and smaller scales ([Morris 2015](#); [GRAVITY Collaboration et al. 2018](#)) they may be associated with heating and expansion associated with magnetic reconnection events in analogy to coronal mass ejections on the Sun ([Yuan et al. 2009](#)). This is also hinted by the power-law distribution of the flare flux-density distribution in both near-infrared and X-ray domains typical of self-criticality phenomena ([Li et al. 2015](#)). It also appears likely that the flow transitions from the so-called Standard and Normal Evolution (SANE; [Balbus & Hawley 1992](#)) where the angular momentum is transported outwards by the turbulence generated by the magneto-rotational instability to the Magnetically Arrested state ([Bisnovatyi-Kogan & Ruzmaikin 1974, 1976](#); [Narayan et al. 2003](#)), in which the magnetic pressure due to the accumulated poloidal magnetic flux dominates the flow dynamics. As magnetized plasma is accreted, poloidal magnetic flux is dragged inwards and accumulates close to the SMBH. At a certain radius r_{MAD} magnetic

energy becomes larger than the local gravitational potential energy of the flow,

$$\begin{aligned} \frac{GM_\bullet \rho_{\text{ADAF}}}{r} &= \frac{B^2}{8\pi} \\ \frac{r_{\text{MAD}}}{r_g} &\simeq \frac{(8\pi\mu m_{\text{H}} n_{\text{B}})^{2/3} c^2}{B^{4/3}} \left(\frac{r_{\text{B}}}{GM_\bullet}\right)^{1/3} \\ &\sim 56 \left(\frac{n_{\text{B}}}{26 \text{ cm}^{-3}}\right)^{2/3} \left(\frac{B}{0.5 \text{ G}}\right)^{-4/3} \left(\frac{r_{\text{B}}}{0.14 \text{ pc}}\right)^{1/3} \left(\frac{M_\bullet}{4 \times 10^6 M_\odot}\right)^{-1/3}, \end{aligned} \quad (1.19)$$

where we used the expression $\rho_{\text{ADAF}} \simeq \mu m_{\text{H}} n_{\text{B}} (r/r_{\text{B}})^{-0.5}$ for the mass density of the ADAF (Wang et al. 2013) scaled to the Bondi values (Baganoff et al. 2003). Inside the magnetospheric radius r_{MAD} the flow fragments and the accretion proceeds via diffusion through the dominant poloidal magnetic field accompanied by magnetic interchanges and reconnection events. These result in localized heating and plasma expansion whose observational demonstration could be detected flares and hot spots. The radial velocity in the MAD part is much smaller than the free-fall velocity. We illustrate the structure of the hot flow on the scale of a few hundred gravitational radii in Fig. 1.18, where we depict the MAD regime with the reconnection events as well as orbiting hot spots close to the ISCO.

Since stellar winds supplied by OB/Wolf-Rayet stars are sufficient to feed the ADAF in the Galactic center, the question where the material circularizes and forms a rotating structure arises. We consider that the gas is captured initially close to the Bondi radius, i.e. from stellar orbits close to $r_\star \sim r_{\text{B}} \sim 0.1 \text{ pc}$. At these scales, the total gas velocity (orbital+intrinsic wind velocity) cannot exceed the escape velocity from Sgr A*, that is $v_{\text{g}} \lesssim \sqrt{2GM_\bullet/r_\star}$. When the gas circularizes at the radius r_{circ} , it retains a fraction λ of the original orbital angular momentum of gas at the distance r_\star . Finally, we have

$$\begin{aligned} r_{\text{circ}} v_{\text{circ}} &\approx \lambda r_\star v_{\text{g}} \lesssim \lambda \sqrt{2GM_\bullet r_\star} \\ r_{\text{circ}} &\lesssim 2\lambda^2 r_\star \approx 0.002 \left(\frac{\lambda}{0.1}\right)^2 \left(\frac{r_\star}{0.1 \text{ pc}}\right) \text{pc}. \end{aligned} \quad (1.20)$$

Thus, assuming that the circularized gas can retain about 10% of the original angular momentum (the rest is lost via outflows and shocks), the circularized flow is expected to form at the length-scale of two orders of magnitude below the Bondi radius. This is comparable to the radial extent of the putative disc of colder material detected by Murchikova et al. (2019) as well as to the orbits of fast-moving S stars (the semi-major axis of the S2 star is $\sim 0.005 \text{ pc}$), which can in principle interact with such a rotating structure.

1.2 Mapping distant quasars

Since the discovery and identification of active galactic nuclei and especially their high-luminosity members – quasars (AGN and QSOs, respectively; Schmidt 1963), it has been obvious that the power generated is tremendous, being at least equal to the luminosity of the whole galaxy or in case of quasars exceeding it by several orders of magnitude. The model that was shortly adopted involved the conversion of gravitational potential energy of gas accreting onto the supermassive black hole (SMBH) into heat and radiation that we detect. As much as $\sim 10\%$ of the gas rest-mass energy can be converted into radiation, which follows

stars (Milky Way-like galaxy), the mass-accretion rate onto the SMBH is,

$$\dot{M} \simeq 21.1 \left(\frac{\eta_{\text{rad}}}{1/12} \right)^{-1} \left(\frac{L_{\text{acc}}}{10^{47} \text{ erg s}^{-1}} \right) M_{\odot} \text{ yr}^{-1}. \quad (1.22)$$

Assuming that the SMBH accretes at most at its Eddington limit, see Eqs. (1.1) and (1.2), that is $L_{\text{acc}} \lesssim L_{\text{Edd}}$, this gives us a lower limit on the SMBH mass,

$$\begin{aligned} M_{\bullet} &\gtrsim \frac{L_{\text{acc}} \sigma_{\text{T}}}{4\pi G m_{\text{p}} c} \\ &\simeq 8 \times 10^8 \left(\frac{L_{\text{acc}}}{10^{47} \text{ erg s}^{-1}} \right) M_{\odot}. \end{aligned} \quad (1.23)$$

The constraint given by Eq. (1.23) shows that Sgr A* with $M_{\bullet} = 4 \times 10^6 M_{\odot}$ cannot really reach the parameters of a quasar, i.e. exceeding the luminosity of all the stars in the Galaxy by several orders of magnitude. It could at most reach the luminosity level comparable to the total Galaxy output when it accretes at the Eddington limit, $L_{\text{Edd}}(\text{Sgr A}^*) \simeq 5 \times 10^{44} \text{ erg s}^{-1} \sim 10^{11} L_{\odot}$. Such lower-luminosity AGN hosted by spiral galaxies are also referred to as *Seyfert* galaxies (Seyfert 1943).

In the current Universe, nearly all massive galaxies host at least one SMBH. Most ($\sim 90\%$) of these galaxies are currently quiescent or their accretion rate is several orders of magnitude below the Eddington limit, hence the flow is rather advection dominated. Yet, their number density per comoving volume, when the expansion of the Universe is accounted for by dividing $(1+z)^3$, is comparable or nearly the same as the number density of quasars at higher redshifts. These statistical arguments lead to the conclusion that most of the current massive galaxies are “dead” quasars, which is also known as *Soltan’s argument* (Soltan 1982). This revolutionary idea, which implies the co-evolution of galaxies and SMBHs, was originally put forward by Lynden-Bell (1969) and when extended to lower luminosities of Seyfert galaxies, it also concerns the Milky Way and its past evolution (Lynden-Bell & Rees 1971).

More specifically, the studies between redshifts $z = 0$ and $z = 2$ show that the comoving number density of quasars brighter than $M_{\text{B}} = -25.9$ at $z = 2$ was ~ 1000 -times larger than today ($z = 0$). However, when the total number density of quasars is considered between $z = 2$ and $z = 0$, the value does not change significantly. In other words, the luminosity function $\phi(M)$ per comoving volume and magnitude bin is just shifted horizontally (Richards et al. 2005) - quasars are becoming fainter, which can be addressed by their evolution. Between $z = 2$ and $z = 6$, the comoving number density pattern becomes more complex – the number density has a peak at $z \approx 2.5$ and starts decreasing towards $z = 3$. The comoving number density of quasars drops by a factor of ~ 10 between the peak at $z \approx 2.5$ (the Universe age of $t = 2.645$ Gyr) and $z = 4$ (the Universe age of $t = 1.558$ Gyr). This early deficiency of quasars hints at the growth phase of SMBHs between ~ 1.5 and 2.5 Gyrs after the Big Bang, although the current James Webb Space Telescope (JWST) data in combination with deep Chandra X-ray observations seem to suggest that the SMBH formation and rapid growth took place already very early, within the first 1000 Gyrs after the Big Bang, as is revealed by the presence of “little red dots” (Matthee et al. 2024). These are small, photometrically red galaxies (in the infrared domain) that exhibit very broad Balmer emission lines, which hints at their association with AGN already in the period $\sim 0.5 - 1.5$ Gyr after the Big Bang.

One example is the galaxy UHZ1 at $z = 10.1$ or just 470 million years after the Big Bang, which has the mass of $\sim 4 \times 10^7 M_{\odot}$ assuming the Eddington rate (Natarajan et al.

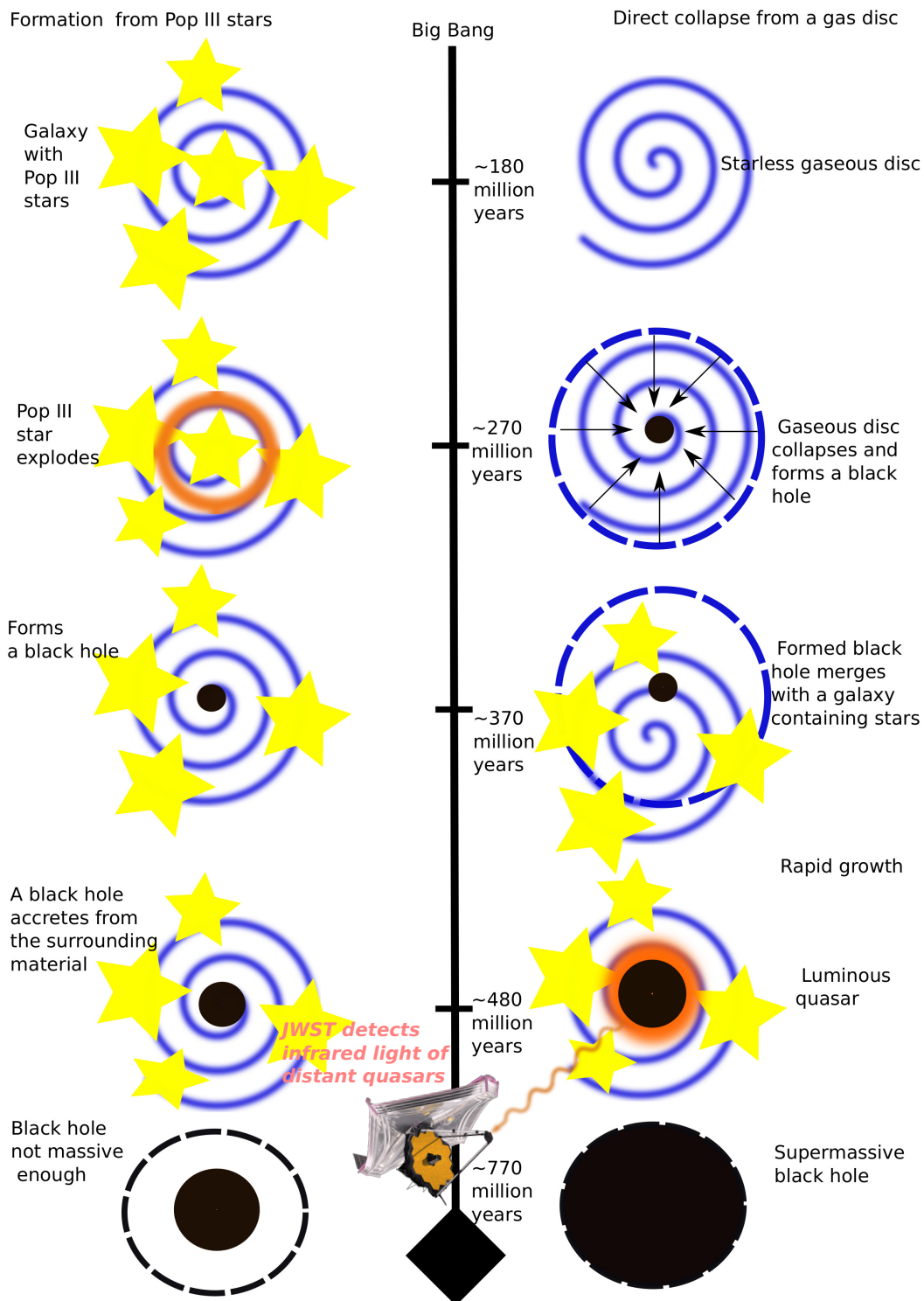


Figure 1.19: Comparison of two basic scenarios for the black-hole seed formation in the early Universe. On the left side, a seed black hole forms after a population III star explodes as a supernova type II. The black hole continues growing by accretion from the surrounding material. On the right side, the black-hole seed forms as a result of a direct collapse of a starless gaseous disc. Subsequently, this more massive seed can merge with the galaxy in the vicinity and quickly grow by accretion from the gaseous and stellar material to reach the SMBH mass. Such an early luminous quasar can be detected in the infrared domain by e.g. the James Webb Space Telescope (see [Natarajan et al. 2024](#), for the detection of an SMBH dating back to half billion years after the Big Bang).

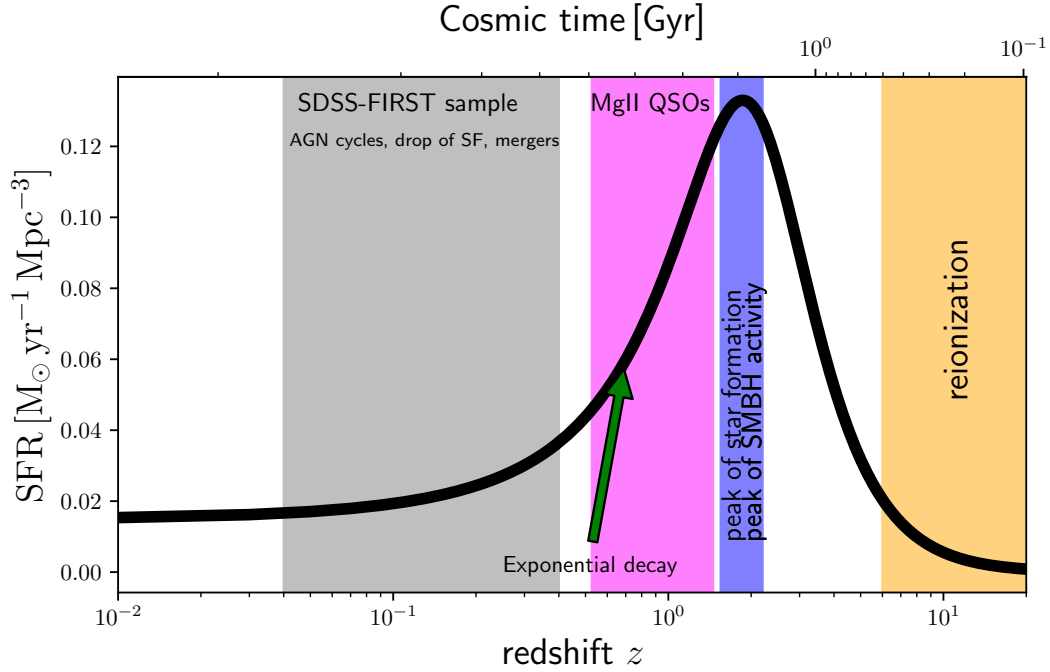


Figure 1.20: Cosmic star-formation rate per comoving volume as a function of redshift (cosmic time). The plot shows cosmic star-formation rate per comoving volume as a function of redshift. Black thick line corresponds to the best-fit relation inferred from UV and IR data according to [Madau & Dickinson \(2014\)](#). Orange-shaded area shows the epoch of the reionization of neutral hydrogen ($6 < z < 30$), while the gray-shaded area depicts the redshift range of the SDSS-FIRST sample analyzed in Section 2, and the magenta-shaded area represents quasi-stellar objects or quasars (QSOs) with a broad MgII line analyzed in Section 7.

2024). Quite surprisingly, the stellar mass derived from the JWST infrared data suggests that it is comparable to the SMBH mass. The formation of such galaxies is consistent with the direct-collapse scenario of the black-hole seed formation, in which the left-over material is consumed by the formation of a compact, dense star cluster surrounding the black hole, potentially resembling the NSC. In comparison with the conventional model of black-hole seed formation from the remnant of a population III star, the direct-collapse scenario can significantly speed up the black-hole growth by the formation of a much heavier seed, see also Fig. 1.19 for comparison. In this picture, the quasar peak density at $z \approx 2.5$ could represent the SMBH growth phase to $M_{\bullet} \sim 10^8 - 10^9 M_{\odot}$ when there was enough cold material for both star formation and the SMBH accretion since the star-formation activity also reached the peak at a comparable time period in the evolution of the Universe ([Madau & Dickinson 2014](#)), see also Fig. 1.20 for the redshift/cosmic-time dependency, which suggests a tight co-evolution between the growth of SMBHs and star formation during galaxy evolution.

This co-evolution is indicated by several significant correlations between the SMBH mass and large-scale galaxy properties. These include the SMBH mass - total galactic bulge (spheroidal component) luminosity ($M_{\bullet} - L_{\text{bulge}}$) relation, which was fitted for the K -band luminosity that is less affected by extinction ([Marconi & Hunt 2003](#)),

$$\log(M_{\bullet}/M_{\odot}) = (8.21 \pm 0.07) + (1.13 \pm 0.12)[\log(L_{K,\text{bulge}}/L_{K,\odot}) - 10.9], \quad (1.24)$$

hence the slope is close to unity. A significant correlation is also present for the SMBH mass –

bulge mass ($M_{\bullet}-M_{\text{bulge}}$) where³ $M_{\text{bulge}} \propto R_e \sigma_e^2$,

$$\log(M_{\bullet}/M_{\odot}) = (8.28 \pm 0.06) + (0.96 \pm 0.07)[\log(M_{\text{bulge}}/M_{\odot}) - 10.9], \quad (1.25)$$

which also has the slope close to unity and the rms scatter decreases to ~ 0.25 dex. For the slope set to unity, we get the *Magorrian* relation between the SMBH mass and the galaxy bulge mass, $M_{\bullet}/M_{\text{bulge}} \sim 2.4 \times 10^{-3}$, see [Magorrian et al. \(1998\)](#) for the original study with the mean ratio $\langle M_{\bullet}/M_{\text{bulge}} \rangle \sim 5 \times 10^{-3}$. In 2000, two studies ([Ferrarese & Merritt 2000](#); [Gebhardt et al. 2000](#)) were published that claimed a tight correlation between the SMBH mass and the stellar velocity dispersion in the galactic spheroidal component ($M_{\bullet} - \sigma_{\star}$ relation), which is either the galactic bulge or the whole elliptical galaxy. The $M_{\bullet} - \sigma_{\star}$ relation qualitatively states that the more massive the SMBH is, the larger the velocity dispersion in the galactic spheroid is. This result is quite profound and directly points towards the co-evolution between the SMBH and its galactic host since the stellar velocity dispersion is inferred on the large scales of kiloparsecs, hence on the length-scales that are at least one order of magnitude larger than the gravitational sphere of influence of the SMBH, see Eq. (1.4). [Ferrarese & Merritt \(2000\)](#) inferred the relation $M_{\bullet} \propto \sigma_{\star}^{4.8 \pm 0.5}$ based on the measurements in 12 galaxies. In contrast, [Gebhardt et al. \(2000\)](#) found a slightly smaller slope of 3.75 ± 0.30 based on 26 galaxies. For elliptical galaxies, the Faber-Jackson relation ([Faber & Jackson 1976](#)) had been established earlier between the luminosity of the elliptical galaxy⁴ (spheroid) and the stellar velocity dispersion, $L_{\text{spheroid}} \propto \sigma_{\star}^4$. In combination with the Magorrian relation ([Magorrian et al. 1998](#)), $M_{\bullet} \propto L_{\text{spheroid}}$, we arrive at $M_{\bullet} \propto \sigma_{\star}^4$ for elliptical galaxies. When one takes into account a slightly different scaling between the bulge/spheroid mass and its luminosity, $M_{\text{spheroid}} \propto L_{\text{spheroid}}^{5/4}$ ([Faber et al. 1987](#)), then in combination with the Faber-Jackson relation $L_{\text{spheroid}} \propto \sigma_{\star}^4$ and the Magorrian relation $M_{\bullet} \propto M_{\text{spheroid}}$, one arrives at $M_{\bullet} \propto \sigma_{\star}^5$. Hence, it is possible to recover the power-law slope between ~ 4 and ~ 5 . Therefore, the $M_{\bullet} - \sigma_{\star}$ relation as such had not been surprising, especially when one follows the simple hypothesis that a larger mass concentration within the bulge/spheroid is expected to host a more massive SMBH. It is, however, crucial to stress that the rms scatter of the $M_{\bullet} - \sigma_{\star}$ relation is smaller than for the $M_{\bullet} - L_{\text{bulge}}$ relation, which implies that M_{spheroid} and L_{spheroid} are not entirely necessary in the description. In other words, the SMBH mass–stellar velocity dispersion relation is more fundamental. The physical cause behind the tight $M_{\bullet} - \sigma_{\star}$ relation or the SMBH-spheroidal component co-evolution is likely the AGN energy and momentum feedback, via which the SMBH can impact the host galaxy on large scales. It can proceed in two basic modes ([Alexander & Hickox 2012](#)):

- (i) quasar radiative mode: accretion disc outflows/winds and radiation expel cold gas reservoir, which leads to the shut-off of star formation and SMBH rapid feeding;
- (ii) radio-mechanical kinetic mode: radio jet impacts the surrounding cooling flow, which leads to shocks that reheat the gas.

Hence, the SMBH activity (accretion/jet) is directly linked to the amount of cold gas that feeds both star formation, which affects the stellar velocity dispersion via stellar mass distribution,

³ R_e is the bulge effective radius, which contains half of its luminosity, and σ_e is the velocity dispersion at R_e .

⁴An analogous relation exists for disc galaxies, $L_{\text{disc}} \propto (\Delta V)^4$, where ΔV is the rotation curve amplitude (Tully-Fisher relation; [Tully & Fisher 1977](#)).

and accretion onto the SMBH, which contributes to the SMBH mass. There are also alternative explanations. One of them is related to the galaxy hierarchical assembly via mergers, i.e. the *bottom-up* structure formation. In the process of galaxy mergers, in which the masses of black holes and spheroidal components are initially unrelated, central black holes of different masses migrate to central regions via dynamical friction. After several mergers, the final black-hole mass tends to correlate with the galaxy bulge/spheroid mass and its velocity dispersion (see [Jahnke & Macciò 2011](#), for this statistical, non-causal argumentation).

The negative AGN feedback can effectively work just considering pure energetics of the involved processes. As the AGN accretes mass, it produces radiation that is capable of driving an outflow that interacts with the ambient cold gas in the bulge/spheroid component. Via shocks and fast radiative cooling, most of the energy associated with this interaction is preserved in the bulk motion that is driving out ambient colder gas. The energy released via the accretion onto the SMBH can be calculated as $E_{\text{acc}} \simeq \eta_{\text{rad}} M_{\bullet} c^2$, while the binding energy of the bulge is $E_{\text{bulge}} \approx GM_{\text{bulge}}^2/R_{\text{bulge}}$. The ratio of the total energy that is radiated away to the gravitational binding energy is,

$$\begin{aligned} \frac{E_{\text{acc}}}{E_{\text{bulge}}} &\approx \frac{\eta_{\text{rad}} M_{\bullet} c^2}{\frac{GM_{\text{bulge}}^2}{R_{\text{bulge}}}} = \eta_{\text{rad}} \left(\frac{M_{\bullet}}{M_{\text{bulge}}} \right) \left(\frac{c}{\sigma_{\star}} \right)^2 \\ &\sim 225 \left(\frac{\eta_{\text{rad}}}{0.1} \right) \left(\frac{M_{\bullet}/M_{\text{bulge}}}{10^{-3}} \right) \left(\frac{\sigma_{\star}}{200 \text{ km s}^{-1}} \right)^{-2} \gg 1, \end{aligned} \quad (1.26)$$

which proves at least qualitatively that the AGN activity can result in the expulsion of a significant portion of the cold gas concentrated within the bulge.

The AGN feedback can recover the $M_{\bullet} - \sigma_{\star}$ relation not only qualitatively but also quantitatively when one considers the momentum-driven nuclear outflows that become coupled to cold gas and drive it out. Considering that the outflow with the rate \dot{M}_{out} and velocity v_{out} interacts with the optically thick gas, the momentum rate is comparable to the photon momentum rate, assuming that the AGN shines at the Eddington limit,

$$\dot{M}_{\text{out}} v_{\text{out}} \approx \frac{L_{\text{Edd}}}{c}, \quad (1.27)$$

which for $\dot{M}_{\text{out}} \sim \dot{M}_{\text{Edd}}$ implies $v_{\text{out}} \sim \eta_{\text{rad}} c$. There are indeed detected nuclear outflows moving at speeds of the fraction of the light speed, such as ultrafast outflows (UFOs; [Pounds et al. 2003](#); [Tombesi et al. 2010](#)) revealed by absorption lines in the X-ray spectra. When we consider the mass shell $m(r)$ (including both gas and stars) at the radius r and the gas fraction f_{g} , the equation of motion of the gas component can be expressed as follows,

$$\begin{aligned} \frac{d[f_{\text{g}} m(r) \dot{r}]}{dt} + \frac{G f_{\text{g}} m(r) [M_{\bullet} + m(r)]}{r^2} &= \frac{L_{\text{Edd}}}{c} \\ \frac{d(\dot{r} r)}{dt} + \frac{GM_{\bullet}}{r} &= -2\sigma_{\star}^2 \left[1 - \frac{M_{\bullet}}{M_{\sigma}} \right], \end{aligned} \quad (1.28)$$

where in the second equality, we applied $m(r) \approx 2\sigma_{\star}^2 r/G$, assuming the singular isothermal sphere model. M_{σ} stands for the critical (minimum) SMBH mass that is capable of driving out the gas shell since for $M_{\bullet} > M_{\sigma}$, $\dot{r}^2 \rightarrow \sigma_{\star}^2$ for large r . For $M_{\bullet} < M_{\sigma}$, there is no outbound solution and the outflow can be referred to as failed. The critical mass M_{σ} can be numerically

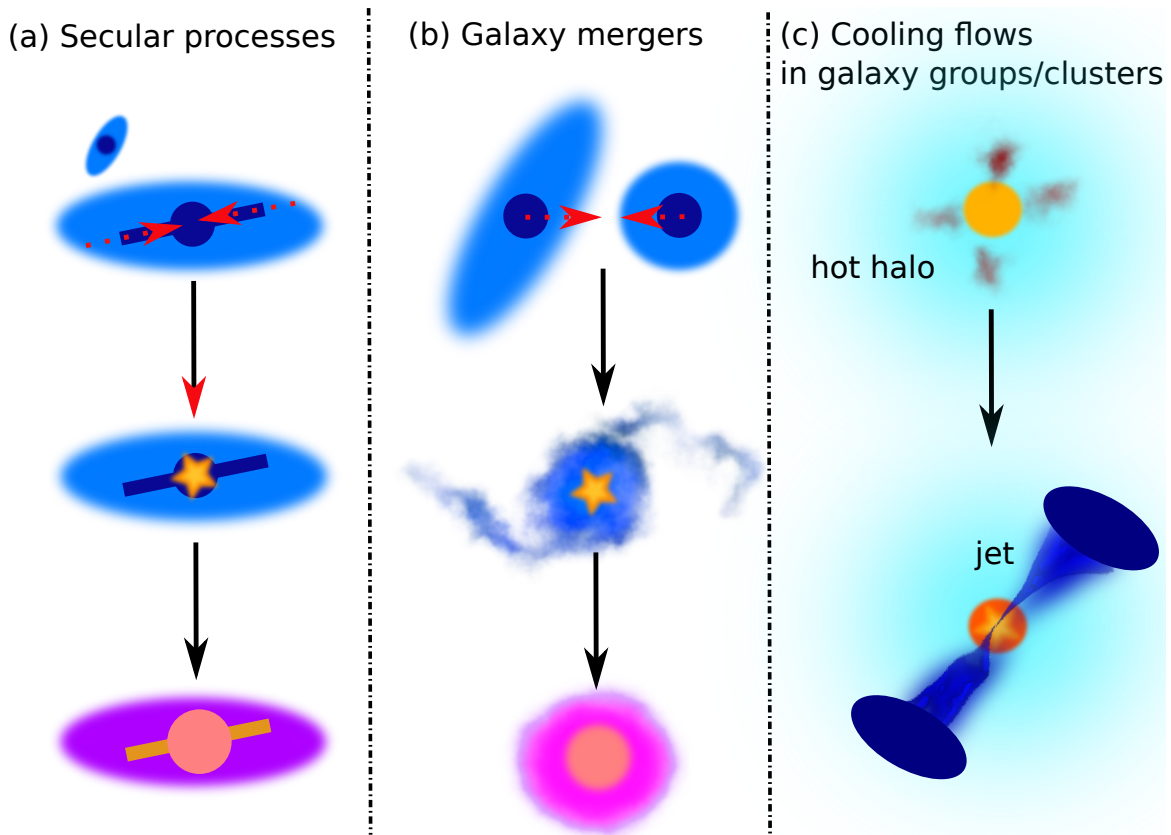


Figure 1.21: Overview of the growth processes of supermassive black holes. In the left panel (a), the SMBH grows via secular processes (galactic bar, galaxy interaction); in the middle panel (b), the SMBH growth via galaxy mergers is depicted; in the right panel (c), cooling flows in the hot halo gas of galaxy groups and clusters lead to the AGN trigger, whose activity subsequently prevents the hot halo gas from further cooling.

evaluated as,

$$\begin{aligned}
 M_\sigma &= \frac{f_g \sigma_T}{\pi G^2 m_p} \sigma_\star^4 \\
 &\simeq 2.3 \times 10^8 \left(\frac{f_g}{0.2} \right) \left(\frac{\sigma_\star}{200 \text{ km s}^{-1}} \right)^4 M_\odot,
 \end{aligned} \tag{1.29}$$

where the gas fraction f_g is scaled to the value close to the baryonic fraction of the Universe, $f_g \sim 0.16$, which is the ratio of the baryonic matter to the total matter content. The derived value for M_σ in Eq. (1.29) is very close to the current versions of the $M_\bullet - \sigma_\star$ relation, see for instance [Gültekin et al. \(2009\)](#), who inferred $M_\bullet \simeq 1.32 \times 10^8 (\sigma_\star / 200 \text{ km s}^{-1})^{4.24} M_\odot$. This adds credibility to the model of AGN negative feedback as the driving physical cause behind this tight correlation.

The SMBHs grow mostly via (a) the accretion of gas and dust channelled due to internal and external secular processes, (b) via merger processes with other SMBHs as well as smaller black holes and other compact objects, the third option is (c) the accretion of cooling flows in galaxy groups and clusters ([Alexander & Hickox 2012](#)). The processes (a), (b), (c) trigger an AGN activity, whose phases are relatively short ($\sim 10^5$ years) but they recur several times during a more extended period of the SMBH growth whose duration is estimated to be between

$\sim 10^7$ and $\sim 10^9$ years based on the Soltan argument (Schawinski et al. 2015). We illustrate the SMBH growth processes in Fig 1.21. There are multiple signatures of the mergers of two and more galaxies in the nearby Universe as well as in the earlier epochs of the galaxy evolution. Moreover, several studies point towards the correlation between the merger process and the AGN activity (Hernquist & Mihos 1995; Chiaberge et al. 2015). However, there are more recent studies of cosmological simulations that show that the SMBH growth during the whole galaxy evolution is mostly driven by secular (merger-free) processes (Martin et al. 2018; McAlpine et al. 2020; Smethurst et al. 2024), which include the angular momentum redistribution by a galactic bar (internal secular processes) or a gravitational interaction within the galactic group (external secular processes). In other words, mergers, are not the primary cause behind the co-evolution of SMBHs and their host galaxies, though they can increase the accretion rate in the galaxies undergoing a merger event (McAlpine et al. 2020) by a factor of a few. Furthermore, Garland et al. (2024) showed that strongly barred disc-dominated galaxies have a significantly larger fraction of AGN than weakly barred ones. The same holds for the weakly barred versus unbarred galaxies. Hence, the galactic bar appears to play a crucial role for the channelling of the cold gas towards the central regions of the galaxy. Within the bar potential the orbital families x_1 and x_2 can provide a way to transport the gas from the galactic disc to central regions of the galaxy, see Figs. 1.6 and 1.7 for the illustration and the depiction of different structures. This can also address the formation of the 100-pc molecular ring in our Galaxy and the associated structures of the Nuclear Stellar Disc and the Nuclear Star Cluster, see Subsection 1.1 for the discussion. Eventually, an occasional infall of a dense molecular cloud can trigger an enhanced activity of Sgr A*, potentially reaching the level of a Seyfert galaxy every few million years, see also Subsection 1.3 for details.

Since the accreting gas has a certain angular momentum, it will circularize at the circularization radius r_{circ} , see also Eq. (1.20), and form a rotating disc-like structure, generally referred to as an accretion disc. Depending on the relative accretion rate, different types of accretion flows can form. In the following subsection, we introduce the concept of reverberation mapping of the circumnuclear environment, which has proven to be instrumental not only in understanding kinematical and geometrical properties of the accreting gas and dust but also in weighting SMBH masses and thus studying their growth processes during the cosmic history.

1.2.1 Reverberation mapping of accretion discs

Based on the spectral studies of AGN/quasars in the optical/UV domains, the presence of prominent broad and narrow emission lines is one of the main characteristics of all active galaxies. However, certain patterns and differences among AGN started to be discovered. Those AGN that had both broad and narrow emission lines also exhibited a power-law continuum component as well as the soft and sometimes hard X-ray emission. In comparison, there were purely narrow-line AGN with the highly absorbed X-ray emission and a prominent infrared bump in their SEDs. The sources with both broad and narrow components on the top of the power-law continuum have been referred to as type I AGN, while the other ones with just narrow components have been denoted as type II. There have also been intermediate cases identified as well as AGN that change the type on relatively short timescales. The current consensus is that the main factor affecting the AGN type is the viewing angle towards the source: for type I sources we look close to the rotation axis, hence we can detect the accretion-disc emission and the associated broad lines, while for type II, the geometrically and optically thick dusty molecular torus obscures the view towards the center. This is a

so-called *unified model of AGN* (Antonucci 1993; Urry & Padovani 1995) that can also be extended towards the radio domain where some of the differences can also be addressed by the viewing angle with respect to the jet cone.

The accretion-disc models and their properties can be categorized based on the terms in the energy equation (Frank et al. 2002; Kato et al. 2008), $q_{\text{adv}} = q_+ + q_-$, where q_+ is the viscous heating rate per volume and q_- is the radiative cooling rate per volume. The term q_{adv} expresses the net energy advection per volume and can be expressed as (in cylindrical coordinates),

$$q_{\text{adv}} = \rho v_{\text{R}} T \frac{ds}{dR}, \quad (1.30)$$

where s is the specific entropy. Based on which terms dominate in the energy balance, the accretion flow solutions are distinguished as follows:

- *cooling-dominated flows*: $q_{\text{adv}} \ll q_+ \simeq q_-$, viscous heating is balanced by radiative cooling; standard Shakura-Sunyaev, Novikov-Thorne discs, and Shapiro, Lightman, and Eardley solutions;
- *advective flows*: $q_- < q_+ \simeq q_{\text{adv}}$, viscous heating is balanced by the advection of energy through the event horizon; these solutions include the Advection-Dominated Accretion Flows (ADAFs) for lower accretion rates and slim discs for high accretion rates close to the Eddington rate and above;
- *low-angular momentum flows*: $q_+ \ll q_- \simeq -q_{\text{adv}}$; low angular-momentum settling solutions and optically thin Bondi flows.

Specifically for AGN, we will focus on cooling-dominated and advective accretion discs. The observational spectral properties of the accretion discs in AGN depend on their relative accretion rates or Eddington ratios $\dot{m} = \dot{M}/\dot{M}_{\text{Edd}}$ and the accretion solutions can be categorized as (Kato et al. 2008),

- (a) *Advection-Dominated Accretion Flows (ADAFs)* or sometimes referred to as radiatively inefficient accretion flows that are optically thin and geometrically thick. They occur for Eddington ratios of $\dot{m} \lesssim 0.01$. They correspond to low/hard states of X-ray binaries and SMBHs (Yuan & Narayan 2014).
- (b) *Standard accretion discs* or sometimes referred to as Shakura-Sunyaev or Novikov-Thorne solutions. They correspond to the relative accretion rates of $0.01 \lesssim \dot{m} \lesssim 0.1$. They are optically thick and geometrically thin. They correspond to high/soft states of X-ray binaries and SMBHs (Shakura & Sunyaev 1973; Novikov & Thorne 1973).
- (c) *Slim discs* correspond to the accretion rates very close to the Eddington rate or above it. They are geometrically thicker than standard discs and they are optically thick. Because of large densities, photons generated close to the mid-plane are trapped within the disc and they are advected through the horizon without being radiated away. For this reason slim discs are fainter than expected from their large accretion rates and therefore rather radiatively inefficient (Abramowicz et al. 1988; Wang & Zhou 1999).

It is instructive to depict steady-state solutions of accretion discs on the local (\dot{m}, Σ) plane, i.e. for a fixed radius, see Fig. 1.22 for a schematic plot. In particular, we highlight the three fundamental viscously and thermally stable solutions with a positive slope, $d\dot{m}/d\Sigma > 0$: an

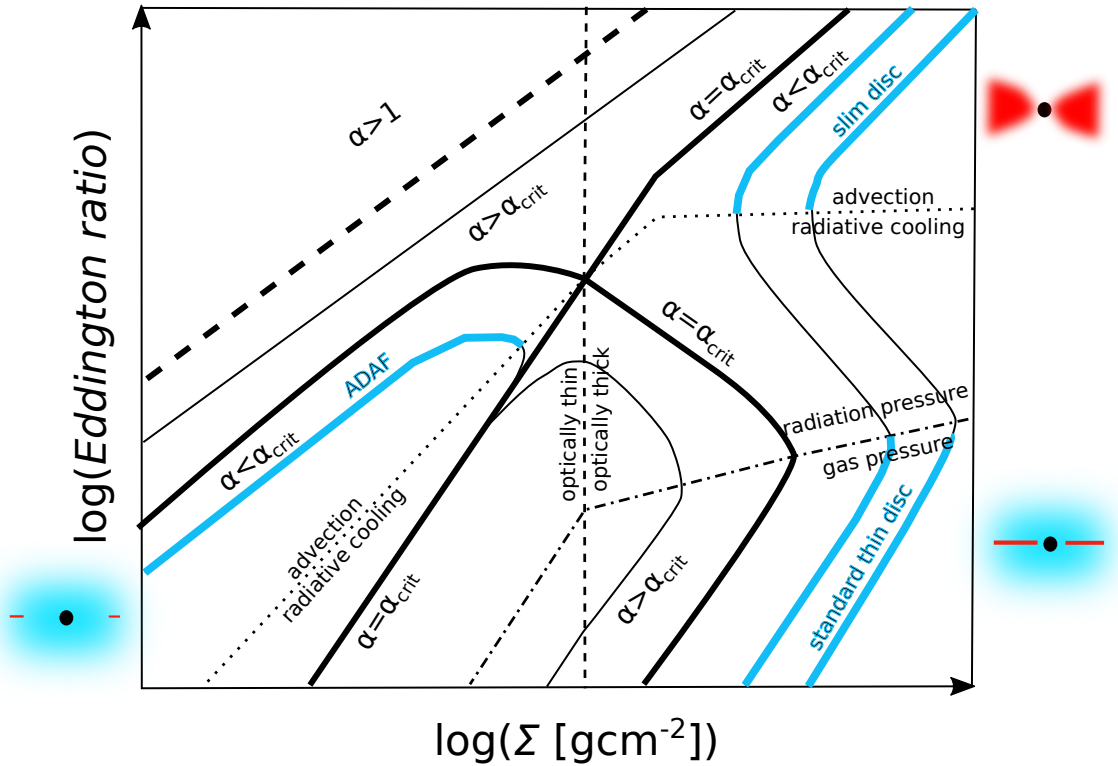


Figure 1.22: Steady-state accretion solutions on a local (\dot{m}, Σ) plot. For every radius, there is a critical value of the α parameter (α_{crit}) that divides the plane into four types of solutions. Above the thick dashed line, there are solutions with $\alpha > 1$ that are considered nonphysical. The dotted line divides the solutions dominated by advection and those dominated by radiative cooling. The dashed line divides optically thin and thick solutions. Solutions dominated by radiation pressure and gas pressure are divided by the dot-dashed line. In particular, we highlight with a thick blue colour three stable steady-state solutions– ADAF (advection-dominated, optically thin), a slim disc (advection-dominated, optically thick), and a standard thin disc (radiative cooling, gas-pressure-dominated) - that are characterized by the positive slope, i.e. $d\dot{m}/d\Sigma > 0$. The geometrical setup of these three solutions is depicted by the illustrations to the left and the right of the vertical axes.

ADAF, a slim disc, and a standard thin disc. The solutions with a negative slope, for instance a standard thin disc dominated by radiation pressure, are viscously and thermally unstable.

In an analogous manner as for X-ray binaries (Remillard & McClintock 2006), SMBHs in galactic nuclei are expected to transition from low/hard state that is dominated by an ADAF to high/soft state dominated by a standard accretion disc (Done & Gierliński 2005). These spectral transitions, however, take place on longer timescales than for X-ray binaries in proportion to the SMBH mass. There is an evidence for spectral state transitions in galactic nuclei inferred from the study of a larger sample of galaxies (Svoboda et al. 2017). The main parameter that determines spectral hardness/softness is the position of the *truncation radius*, where the standard, radiation cooling-dominated disc transitions into advection-dominated accretion flow (Yuan & Narayan 2014). The truncation radius is directly related to the relative accretion rate (Eddington ratio) of the source, being larger for a lower relative accretion rate,

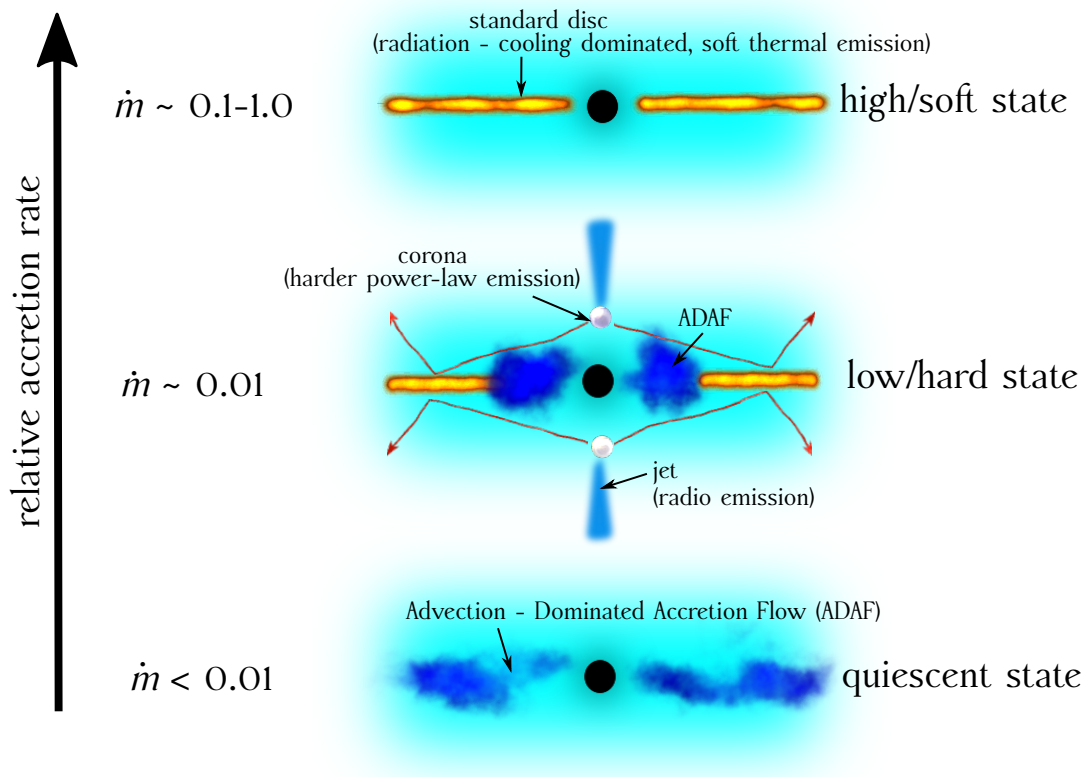


Figure 1.23: Spectral states and the associated transitions between them in supermassive black hole systems. On the right side of the illustrative figure, we show different spectral states dominated by a standard accretion disc (top), an ADAF (bottom) or an intermediate “mixed” stated (middle). On the left side, we depict the dependence of these states on the relative accretion rate. With the change in the accretion rate, the transition of the spectral state is induced.

which in the limit of quiescent nuclei, such as the Galactic center, leads to the disappearance of the standard disc with a thermal SED and the complete spectral dominance of an ADAF. Therefore, one of the best laboratories to detect state transitions in SMBH systems are tidal disruption events (TDEs; Wevers 2020), in which the relative accretion rate evolves within weeks to months from super-Eddington/Eddington values to sub-Eddington ones (see Gezari 2021, for a review as well as Subsection 1.2.3.) since the fall-back rate of the stellar debris follows the power-law temporal evolution, $\dot{M}_{\text{fb}} \propto t^{-5/3}$. There have also been detections of spectral transitions within the luminosity-hardness plot for repeating partial TDEs AT 2018fyk (Wevers et al. 2021) and eRASSt J045650.3-203750 (Liu et al. 2023). In all of the systems where a state transition has been detected there is a common pattern – during the high/soft state, the SED is dominated by soft thermal emission of an optically thick accretion disc, while in the low/hard state a power-law component emerges due to hot corona. The transition between the two states typically takes place around the Eddington ratio of a few 10^{-2} (Wevers 2020). We illustrate the spectral states and the transitions between them as a function of the relative accretion rate in Fig. 1.23.

On a quantitative level, the truncation radius r_{tr} depends on the mechanism that governs the transition. Considering a so-called *strong ADAF principle*, i.e. whenever the ADAF

solution is possible, the flow proceeds as an ADAF, the truncation radius can be estimated as (Abramowicz et al. 1995; Honma 1996; Kato & Nakamura 1998),

$$r_{\text{tr}}^{\text{ADAF}} \simeq 1600\alpha_{0.1}^4 \dot{m}_{0.05}^{-2} r_g, \quad (1.31)$$

where α is the viscosity parameter scaled to 0.1 and \dot{m} is the relative accretion rate (Eddington ratio) scaled to 0.05. If, on the other hand, the transition occurs due to evaporation induced by electron conduction between the standard disc and the hot two-temperature corona, the truncation of the standard disc is expected at (Czerny et al. 2004),

$$r_{\text{tr}}^{\text{evap}} \simeq 191\alpha_{0.1}^{0.8} \beta_{\text{mag}}^{-1.08} \dot{m}_{0.05}^{-0.53} r_g, \quad (1.32)$$

where β_{mag} is the magnetization parameter and in this case it is defined as the ratio of the gas pressure to the sum of the gas and the magnetic pressure (total pressure). When the magnetic field is negligible, $\beta_{\text{mag}} \sim 1$, while for a stronger magnetic field, β_{mag} becomes smaller and the truncation radius increases. It is thus plausible that for the intermediate relative accretion rates ($0.01 \lesssim \dot{m} < 1$) the accretion flow has a ‘‘mixed’’ structure where the standard disc has an inner hollow due to the transition into the ADAF (Štolc et al. 2023). This results in the decrement of the thermal emission at shorter wavelengths, which has also been detected in the UV spectra of some type I galactic nuclei (Dewangan et al. 2021; Kumar et al. 2023).

In the following, for studying the emission properties and variability of a nuclear region, we will focus on standard thin disc solutions, which extend across the whole radial extent of the accretion flow from the ISCO to the outer radius. Standard accretion discs can reproduce well the power-law continuum of a large portion of type I quasars. It also seems that the accretion disc can explain the general feature in SEDs of type I AGN in the optical/UV domain called the Big Blue Bump (Czerny & Elvis 1987), especially for more realistic solutions including opacity and inclination effects. The SED of a thin accretion disc represents, to the first approximation, the sum of narrow rings whose black-body temperature falls off with the distance as $T_{\text{disc}} \propto r^{-3/4}$, specifically (Frank et al. 2002),

$$T_{\text{disc}} = \left\{ \frac{3GM\bullet\dot{M}}{8\pi r^3 \sigma_{\text{SB}}} \left[1 - \left(\frac{r_{\text{isco}}}{r} \right)^{1/2} \right] \right\}^{1/4}, \quad (1.33)$$

where σ_{SB} is the Stefan-Boltzmann constant from the black-body radiation law. The AGN accretion disc SED then can be constructed by summing the rings of infinitesimal width, each having a corresponding black-body temperature $T_{\text{disc}}(r)$ and each viewed at the angle ι (Frank et al. 2002),

$$\nu L_\nu = \frac{16\pi^2 h\nu^4 \cos \iota}{c^2} \int_{r_{\text{isco}}}^{r_{\text{out}}} \frac{r dr}{\exp[h\nu/(k_B T_{\text{disc}}(r))] - 1}. \quad (1.34)$$

where we neglected any disc atmosphere in the vertical direction. The monochromatic luminosity νL_{nu} was calculated by multiplying the monochromatic flux density νF_ν by $4\pi D_L^2$ where the luminosity distance D_L can be calculated for the redshift z given the cosmological model corresponding best to the observations of standard cosmological probes, such as the cosmic microwave background radiation and its fluctuation spectrum (flat Λ CDM model with $\Omega_{\text{m}0} \simeq 0.3$; Planck Collaboration et al. 2020). The integration limits in Eq. (1.34) are the innermost stable circular orbit r_{ISCO} and the outer radius of a disc r_{out} . The outer radius for quasars is expected to be of the order of $\sim 2000 r_g$, which corresponds to ~ 12 days of light-travel time in terms of maximum observed light echos (Lobban & King 2022) and also

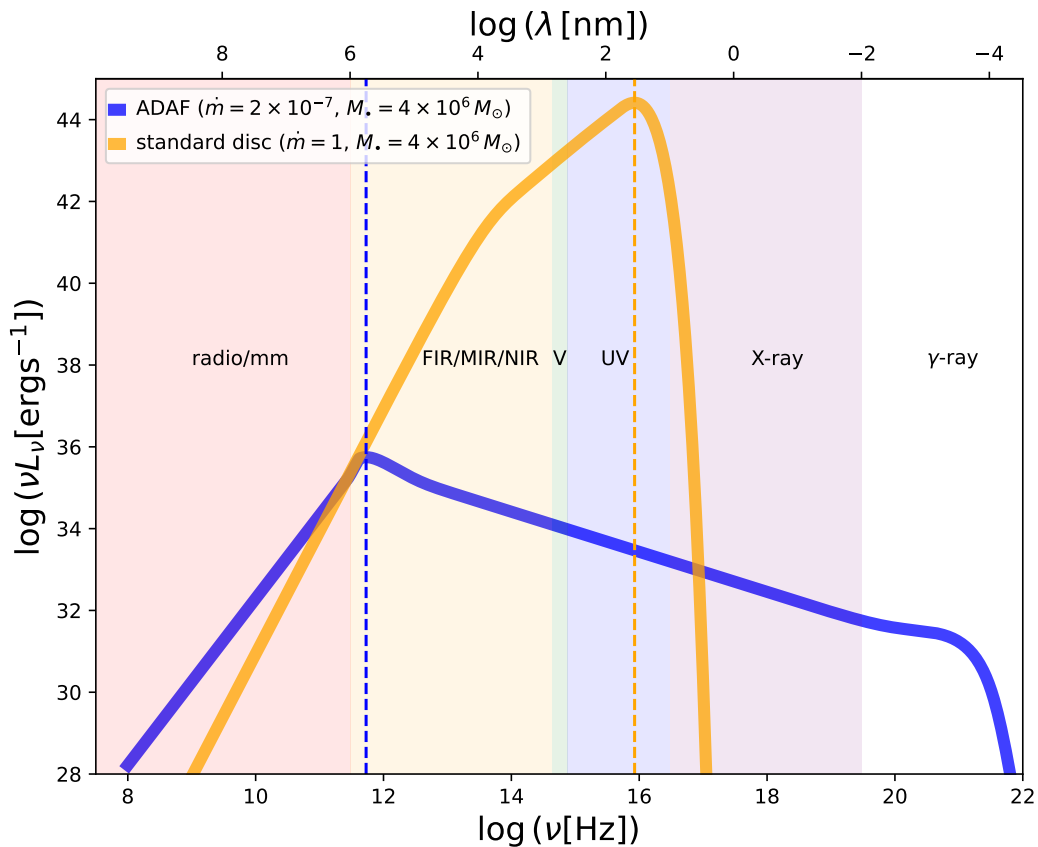


Figure 1.24: Comparison of spectral energy distributions between the standard disc and the advection-dominated accretion flow. The ADAF SED was calculated for the relative accretion rate of $\dot{m} = 2 \times 10^{-7}$ and the SMBH mass of $M_{\bullet} = 4 \times 10^6 M_{\odot}$, which represent the parameters of Sgr A*. The standard disc SED was evaluated for the same SMBH mass and $\dot{m} = 1$, i.e. the Eddington limit. We see that the shape of the SED as well as the frequency of the peak luminosity are quite different. While for the standard disc, the peak luminosity is at $\nu = 10^{15.93}$ Hz ($\lambda = 35.2$ nm), which corresponds to the far UV domain, the luminosity of the ADAF peaks at $\nu = 10^{11.73}$ Hz ($\lambda = 0.56$ mm). Hence, the difference between the frequency peaks is more than four orders of magnitude.

to the self-gravitating radius (Collin-Souffrin & Dumont 1990), where the disc is expected to break up. The outer radius is expressed for $M_{\bullet} = 10^8 M_{\odot}$, while for $M_{\bullet} = 4 \times 10^6 M_{\odot}$ we obtain $r_{\text{out}} \sim 5 \times 10^4 r_g$. We compare the standard disc SED for Sgr A* with the ADAF SED in Fig. 1.24. There is a clear difference in the SED shapes as well as the positions of the SED peaks. While for the ADAF the SED peaks in the mm domain, at $\lambda = 0.56$ mm for the case shown in Fig. 1.24, the luminosity peak for the standard disc is shifted to much shorter wavelengths in the far-UV domain, $\lambda = 35.2$ nm. Hence, the difference is more than four orders of magnitude in frequency.

The variability of type I quasars in different wavebands reflects the variability of the accretion disc at different radii since $T_{\text{disc}} \propto r^{-3/4}$, see Eq. (1.33). In this regard, the variability in the X-ray domain reflects the accretion processes close to the ISCO. A fraction of the dissipated energy can power the hard X-ray emission of hot corona that is expected to illuminate the disc at larger radii. As the material in the disc absorbs and reprocesses the harder

emission in more distant regions, we can in principle detect the delayed and blurred signal at longer wavelengths. The time delay between shorter and longer wavelengths corresponds approximately to the light-travel time, i.e. $\tau \approx \Delta r/c$. Thus, by quasi-simultaneous monitoring of an AGN at different wavelengths, we can effectively map the accretion disc and the associated circumnuclear material by cross-correlating the light curves at given wavelengths, which indicates the statistically best candidate time delay τ and thus the distance $\Delta r \approx \tau c$ between the regions in the accretion disc that emit at corresponding wavelengths. This technique is known as *reverberation mapping* and it effectively trades the spatial resolution for temporal resolution (see e.g. Cackett et al. 2021; Karas et al. 2021, for reviews). Mathematically, the reprocessed, delayed variable electromagnetic signal $\Delta F_r(t)$ can be expressed as the convolution of the driving variable radiation $\Delta F_d(t - \tau)$ with the transfer function $\psi(\tau)$, which expresses the geometry and the kinematics of the reprocessing medium,

$$\Delta F_r(t) = \int_0^{\tau_{\max}} \psi(\tau) \Delta F_d(t - \tau) d\tau, \quad (1.35)$$

where τ_{\max} is the time delay corresponding to the light-travel time $\tau_{\max} = \Delta r/c$ between the regions where the driving radiation originates and where it is reprocessed towards longer wavelengths. In Fig. 1.25, we illustrate how the X-ray emission of the hot corona (assuming the *lamp-post geometry*; Miniutti & Fabian 2004) is reprocessed further out in the disc and the circumnuclear medium, including the geometrically thicker broad-line region (BLR) clouds and the dusty molecular torus emitting in the infrared domain. Typically, to map out the whole region, one needs to employ space-based X-ray satellites (hard X-ray detectors for the corona and soft X-ray detectors for the innermost region of the accretion disc), UV and optical telescopes, performing both photometric and spectroscopic measurements (to detect reliably broad emission lines), and infrared telescopes to detect the emission of the more distant dusty torus. To combine it with the variability studies of the jet in radio AGN, radio telescopes join the multi-wavelength campaigns.

Reverberation mapping a crucial method in revealing the geometry, kinematics, and the character of the accretion flow since there are just a few galactic nuclei whose inner engine can be spatially resolved – see also Subsection 1.2.2 for more details. In particular, by monitoring an AGN in several bands, including X-ray, UV, and optical bands, interband lags can be determined. Let us denote the rest-frame time delay between the longer and shorter wavelengths as $\Delta\tau_{12}$. This time delay can be compared with the delay expected for an adopted steady-state accretion-disc solution with the radial temperature dependence $T_{\text{disc}} \propto r^{-b}$. The corresponding theoretical time delay for a specific band then is $\tau(\lambda) \propto \lambda^{1/b}$. For the standard thin disc, the slope is $b = 3/4$ and the explicit form of the interband time lag between two bands centered at the wavelengths λ_1 and λ_2 , $\lambda_2 > \lambda_1$, is

$$\Delta\tau_{12} = \tau_2(\lambda_2) - \tau_1(\lambda_1) \simeq \left(\frac{3GM_{\bullet}\dot{M}}{8\pi c^3 b^4 \sigma_{\text{SB}}} \right)^{1/3} (\lambda_2^{4/3} - \lambda_1^{4/3}) > 0, \quad (1.36)$$

where $b = 0.29 \text{ cm K}$ is the constant in the Wien's displacement law that relates the (disc) temperature to the wavelength where the black-body SED at a given radius peaks, $\lambda = b/T_{\text{disc}}(r)$.

As it can be inferred from Eq. (1.36), $\Delta\tau_{12}$ also depends on the SMBH mass and the accretion rate as $\Delta\tau_{12} \propto (M_{\bullet}\dot{M})^{1/3}$, which leads to the differences among different AGN and puts different requirements on the duration of the monitoring as well as on the cadence.

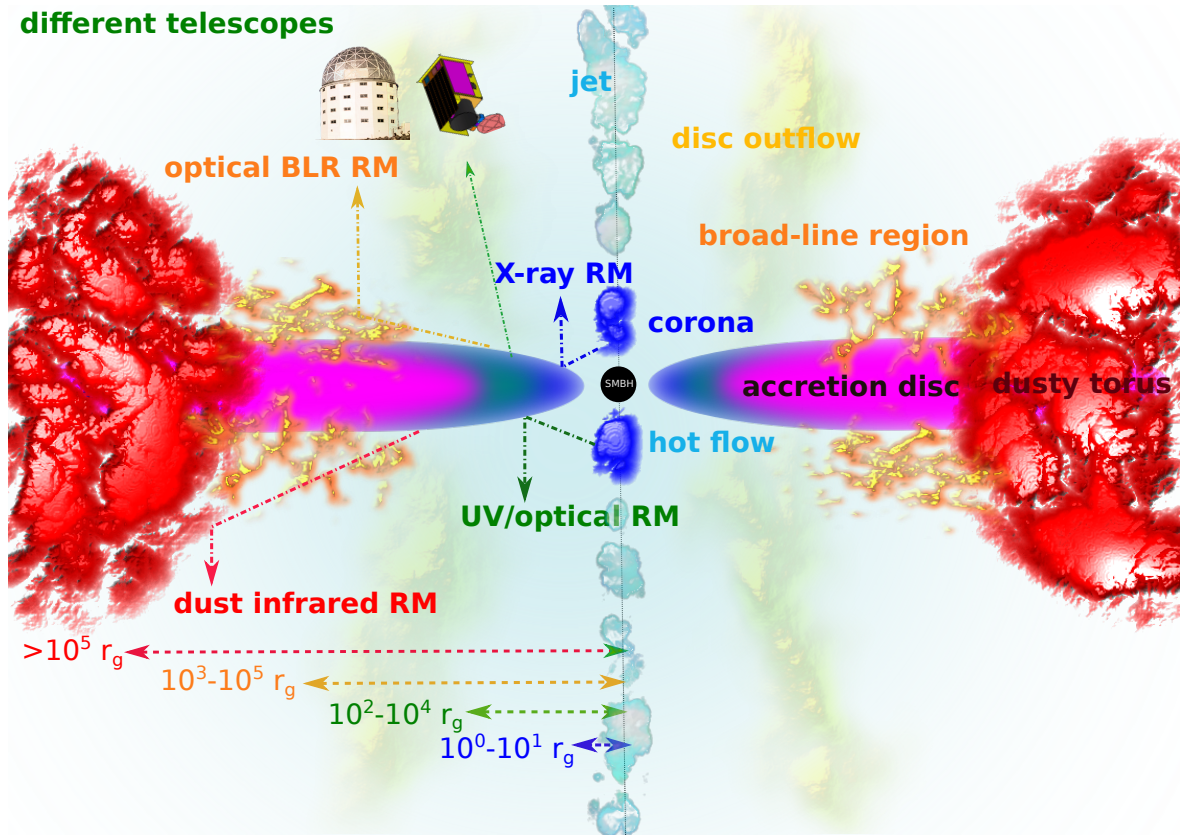


Figure 1.25: Principle of the reverberation mapping of an AGN accretion disc and the surrounding circumnuclear medium. The innermost region emits hard and soft X-ray emission that is further reprocessed in the regions more distant from the SMBH and is detected at longer wavelengths from the UV, optical, to infrared domains. Below the accretion disc/dusty torus, we indicate the typical length-scales (in gravitational radii) associated with the X-ray, UV/optical, and infrared radiation.

In Fig. 1.26, we show the time delay $\Delta\tau$ in days with respect to the U band (364 nm) as a function of wavelength in nanometers for the cases with different SMBH masses and the fixed relative accretion rate of $\dot{m} = 0.1$. The dashed lines correspond to the standard disc prediction according to Eq. (1.36), while the more observationally motivated profiles $3 \times \Delta\tau$ (Fausnaugh et al. 2016) are represented with solid lines. In the left panel of Fig. 1.26, we show the time delay for $M_{\bullet} = 10^6 - 10^7 M_{\odot}$, while in the right panel, we depict the same for $M_{\bullet} = 10^8 - 10^9 M_{\odot}$.

While most of the multi-wavelength observational campaigns imply the qualitative consistency of the wavelength-dependent time-delay with the theoretical predictions of the standard disc $\Delta\tau \propto \lambda^{4/3}$, see e.g. the results of the intense monitoring of the Seyfert 1 galaxy NGC 5548 (Edelson et al. 2015; Fausnaugh et al. 2016), a few discrepancies and systematic differences have also appeared based on the studies of several AGN (see e.g. Cackett et al. 2021, for discussion),

- the observed interband time lags tend to be $\sim 3 - 4$ times larger than the lags expected from the standard-disc model. In other words, the accretion discs appear to be larger than predicted, see also Fig. 1.26 for comparison. This systematic effect could be caused by an additional contribution of an extended medium, such as the BLR,

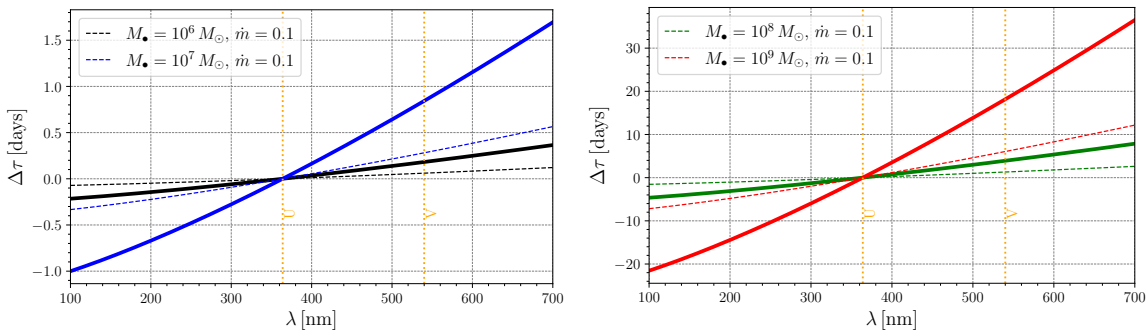


Figure 1.26: Expected time delay $\Delta\tau$ (in days) with respect to the Johnson U band (364 nm) as a function of wavelength (in nanometers). In the left panel, we show the cases for $M_{\bullet} = 10^6 - 10^7 M_{\odot}$, considering the standard disc solution (dashed lines) and the time delay that is three times longer (solid lines). The right panel is analogous to the left panel, except that we consider $M_{\bullet} = 10^8 - 10^9 M_{\odot}$. For all the cases, we adopt $\dot{m} = 0.1$. The dotted vertical lines denote U (364 nm) and V (540 nm) bands.

- the U -band time delays are systematically above the best-fit relations $\Delta\tau(\lambda)$, which can be attributed to the contribution of the Balmer continuum originating in the BLR,
- the X-ray emission is less correlated with the UV/optical light curves (the correlation coefficient is $r < 0.5$) in comparison with the correlation of UV and optical light curves among themselves ($r > 0.5$). This implies that the X-ray emission originating close to the ISCO in the hot corona may not be the main or rather the only driver of the reprocessed emission at longer wavelengths.

The first two points related to the time delay or the accretion-disc size excess, which is also confirmed by gravitational microlensing, can be explained by an additional reprocessing of the photoionizing radiation within the diffuse gas of an extended nature, such as the BLR (Cackett et al. 2018; Chelouche et al. 2019; Netzer 2022), which is supported by a large time-delay excess around the Balmer jump (364.6 nm). Furthermore, the pure scattering of photons by the ionized plasma within the BLR can also result in the prolonged time delays (Jaiswal et al. 2023).

The contribution of the BLR to the reprocessed photons detected by the observer at a given wavelength depends on its scale-height and the distance from the SMBH, i.e. on the covering factor. Netzer (2022) constrain the covering factor to be ~ 0.2 , which means that the broad-line region is consistent with being a flattened system of ionized cloudlets that orbit the SMBH predominantly in a Keplerian manner. They are photoionized by the central X-ray/far-UV source and kept at nearly the constant temperature of $\sim 10\,000 - 20\,000$ K. In combination with large velocities of BLR clouds, this gives rise to prominent broad recombination emission lines of hydrogen ($H\alpha$, $H\beta$), a resonant line of magnesium ($MgII$), as well as to higher-ionization broad lines of CIV and CIII].

The BLR can also be mapped using the reverberation mapping technique since the emission-line variability correlates significantly with the AGN continuum light curves (Blandford & McKee 1982). This allows the determination of the time lag τ_{BLR} between the BLR line light curves and the photoionizing continuum. Already these observational properties can be used to infer several BLR characteristics. A significant correlation implies that the driving photoionizing power is given by the continuum emission and the clouds must be

optically thick to the central source of irradiation. The covering factor can be estimated based on the equivalent widths of broad emission lines to be $\sim 20 - 30\%$. The scale-height of the BLR is expected to be larger than the accretion-disc scale-height to effectively intercept the continuum, though the structure should be flattened along the disc plane since the BLR clouds are only rarely detected in absorption (Czerny 2019). The reverberation mapping of the BLR using its broad emission-line variability can be applied to infer the following crucial properties of AGN:

- the size estimate of the BLR by simply using the light-travel time τ_{BLR} , $R_{\text{BLR}} = c\tau_{\text{BLR}}$ (Netzer & Peterson 1997; Kaspi et al. 2000; Peterson et al. 2004; Mejía-Restrepo et al. 2018). More precisely, depending on which line is monitored, the distance R_{BLR} corresponds to the mean radius of the given line-emitting material;
- by knowing the radius $R_{\text{BLR}} = c\tau_{\text{BLR}}$, one can also constrain the SMBH mass (Dibai 1977) by using the line width of the monitored broad line, Δv_{FWHM} (full width at half maximum), which serves as a proxy for the Keplerian speed of the BLR material around the SMBH. Since we view the system at a certain inclination and there are also effects of the BLR geometry (scale-height), the full BLR velocity is related to the observed FWHM velocity via a so-called virial factor f_{vir} , $v_{\text{BLR}} = \sqrt{f_{\text{vir}}}\Delta v_{\text{FWHM}}$. Under the assumption that the BLR clouds moving in the vicinity of the SMBH are virialized, the virial SMBH mass can be inferred using,

$$M_{\text{vir}} = \frac{R_{\text{BLR}}v_{\text{BLR}}^2}{G} \simeq f_{\text{vir}} \frac{c\tau_{\text{BLR}}(\Delta v_{\text{FWHM}})^2}{G}. \quad (1.37)$$

The virial factor f_{vir} is of the order of unity and is related to the geometry, kinematics, and line-of-sight properties of the BLR gas. Its value is mainly related to the inclination ι_{BLR} of the BLR plane with respect to the observer and the half-opening angle of the BLR ($H_{\text{BLR}}/R_{\text{BLR}}$) with respect to the source of the photoionizing continuum. The value of f_{vir} is inversely proportional to the square sum of these terms (Collin et al. 2006; Mejía-Restrepo et al. 2018; Panda et al. 2019),

$$f_{\text{vir}} = \frac{1}{4[\sin^2 \iota_{\text{BLR}} + (H_{\text{BLR}}/R_{\text{BLR}})^2]}. \quad (1.38)$$

In general, the virial factor f_{vir} is a large source of uncertainty in the SMBH mass determination and fixing its value to a specific value for single-epoch spectroscopic measurements can result in the uncertainty by a factor of $\sim 2 - 3$ (Woo et al. 2015). By comparing the SMBH masses inferred from the accretion-disc continuum fitting of AGN SEDs with those determined from the BLR reverberation mapping, see Eq. (1.37), Mejía-Restrepo et al. (2018) found out that the virial factor is inversely proportional to the line FWHM, $f_{\text{vir}} \propto \text{FWHM}^{-1}$. This can reflect the effect of the BLR inclination/viewing angle according to Eq. (1.38) or it hints at the impact of radiation pressure on the distribution of BLR clouds. A strong viewing-angle effect is expected for the flattened geometry of the BLR, which is consistent with a ‘‘bird’s nest’’ BLR model (Gaskell 2009), where higher-ionization lines originate closer to the SMBH and they thus have larger FWHMs, while lower-ionization lines originate further away and as a result, their FWHMs are smaller. Such a flattened geometry is likely related to disc outflows, which can be launched due to radiation pressure (line-driven or dust-driven)

or they can also be magnetically driven (see [Karas et al. 2021](#), for a detailed discussion). In particular, the dust-driven outflow has been able to capture several basic BLR characteristics simultaneously, including flattened geometry and kinematics dominated by a Keplerian motion with a certain turbulent (outflow-inflow) component. The dusty outflow is launched at the distance within the accretion disc where the dust can form and survive, i.e. where the temperature of the disc drops below ~ 1500 K (sublimation radius). Dust grains increase opacity and radiation pressure acting on them can lift the gaseous-dusty material above the disc plane. At the same time, as the cloudlets rise, they are exposed to the direct, harder UV irradiation of the central source, which leads to dust evaporation and a drop in radiation pressure support. The clouds then fall back onto the disc surface. In this model, the dust-driven outflow is failed, only a small fraction of the clouds can escape (Failed RAdiatively-driven Dusty Outflow – FRADO; [Czerny & Hryniewicz 2011](#); [Czerny et al. 2017](#); [Naddaf et al. 2021](#); [Naddaf & Czerny 2022](#)). The FRADO model can address the origin of low-ionization BLR lines (LIL) that have a lower ionization potential (<20 eV; $H\alpha$, $H\beta$, $MgII$, $FeII$, CII), originate in the denser gas of the accretion disc, show no significant inflow-outflow motion, and can thus be considered to be virialized. There is also a high ionization line component (HIL), which has a higher ionization potential (>40 eV; $Ly\alpha$, $HeII$, CIV , NV), exhibits signs of an outflow, specifically via the presence of asymmetric line shapes with a blue-ward tail and blue-shifted line centroids, and thus forms in the more diluted outflowing gas. However, the HIL component is still located relatively close to the SMBH since time delays can still be reliably measured (see [Kaspi et al. 2021](#), for CIV line time delays). The LIL and HIL components of the BLR are illustrated in Fig. 1.27, which depicts the two-component BLR model proposed by [Collin-Souffrin et al. \(1988\)](#);

- the radius-luminosity relation, $R_{BLR} - L$, which has a power-law form, $R_{BLR} = KL^\alpha$. Initially, for variable low-redshift sources, $R_{BLR} - L$ relation was confirmed and constrained for the broad $H\beta$ line (at 4861 \AA) and the optical monochromatic luminosity at 5100 \AA with the power-law slope $\alpha = 0.67 \pm 0.05$ ([Kaspi et al. 2005](#)), which deviated from $\alpha = 0.5$ predicted by simple photoionization arguments. With the progressive addition of more low-redshift sources ([Bentz et al. 2006, 2009, 2013](#)), and more importantly, after accounting for the host-galaxy starlight, $R_{H\beta} - L_{5100}$ was further refined and the slope was constrained to be shallower and overall consistent with the expected value close to 0.5. The best-fit $R_{BLR} - L$ relation for the $H\beta$ line for 41 sources is [Bentz et al. \(2013\)](#),

$$\log\left(\frac{\tau_{H\beta}}{1 \text{ day}}\right) = 1.527_{-0.031}^{+0.031} + 0.533_{-0.035}^{+0.035} \log\left(\frac{L_{5100}}{10^{44} \text{ erg s}^{-1}}\right), \quad (1.39)$$

which has the rms scatter of only $\sigma_{\text{rms}} = 0.19 \pm 0.02$ dex. The theoretical slope of 0.5 comes from the definition of the ionization parameter U_{ion} that relates the BLR photoionization rate with the recombination rate,

$$U_{\text{ion}} = \frac{Q(H)}{4\pi R_{BLR}^2 cn_e}, \quad (1.40)$$

where n_e is the electron number density that is related to the recombination rate. The flux of photoionizing photons is evaluated as $Q(H) = \int_{\nu_i}^{+\infty} (L_\nu/h\nu)d\nu$, where ν_i is the frequency corresponding to the ionization energy, $E_{\text{ion}} = h\nu_{\text{ion}}$. Under the assumption

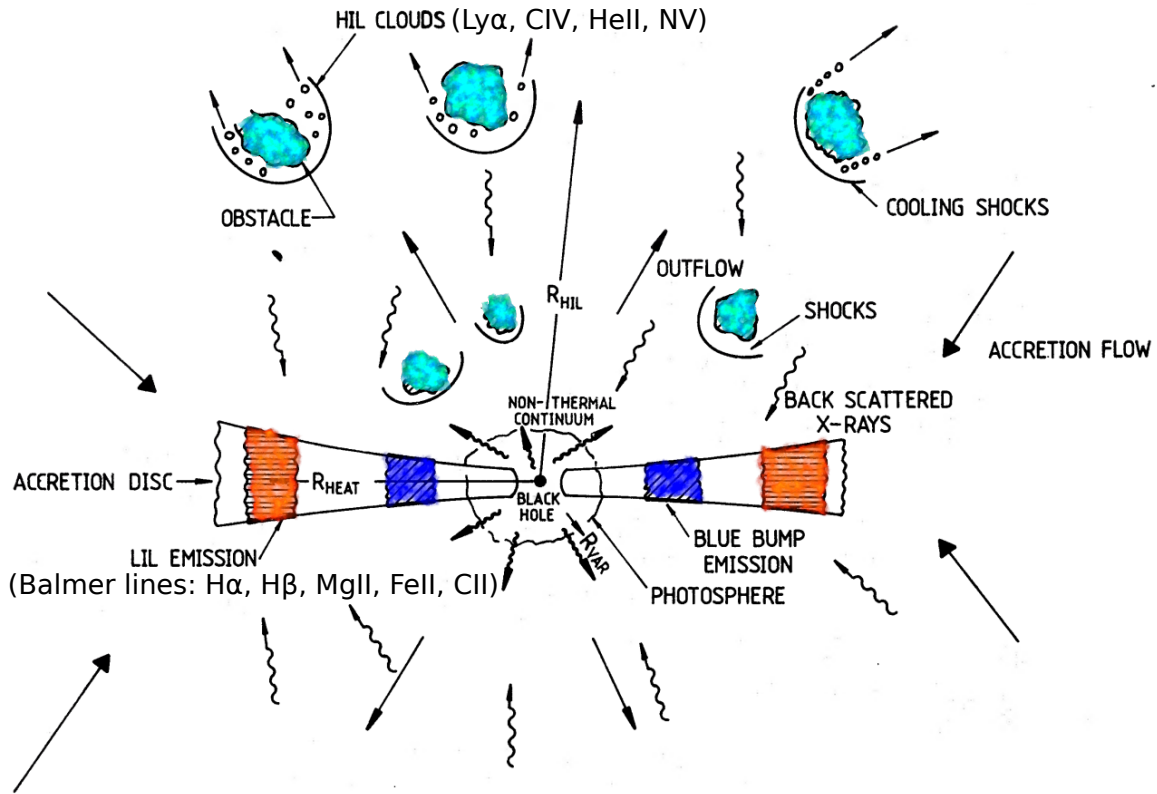


Figure 1.27: Two-component model of the Broad-line region. The low-ionization lines (LILs) originate in the denser material of the accretion disc, while the high-ionization lines (HILs) form in the more diluted outflowing gas. Figure was adopted from Collin-Souffrin et al. (1988) with some modifications.

that for all AGN the ionization parameter and the BLR electron density are constants, $U_{\text{ion}}n_e = \text{const}$, we obtain $R_{\text{BLR}} \propto Q(H)^{0.5} \propto L_v^{0.5}$. As more H β quasars have been monitored with accretion rates closer to the Eddington limit, the rms scatter of the $R_{\text{BLR}} - L$ relation has substantially increased. Using 117 H β quasars at the redshift $0.002 < z < 0.9$ and with the luminosity in the range $41.5 < \log(L_{5100} [\text{erg s}^{-1}]) < 45.9$, Martínez-Aldama et al. (2019) showed that there is a positive correlation between the departure from the best-fit $R_{\text{BLR}} - L$ relation and the relative accretion rate, i.e. the higher the Eddington ratio, the shorter the rest-frame time delay with respect to the expected one. This could be interpreted as the result of the transition towards geometrically thicker slim discs at higher accretion rates that can block a fraction of the photoionizing continuum. Using QSOs that were reverberation-mapped using the broad MgII line (at 2798 Å) from low to intermediate redshifts, several studies confirmed the existence of the MgII $R_{\text{BLR}} - L$ relation as more such sources were available (Czerny et al. 2019; Zajaček et al. 2020; Homayouni et al. 2020; Zajaček et al. 2021; Yu et al. 2023; Zajaček et al. 2024c). Zajaček et al. (2020) confirmed analogous correlation between the departure from the best-fit MgII radius-luminosity relation and the relative accretion rate as for H β QSOs. Using 194 MgII QSOs, Zajaček et al. (2024c) constrained the MgII $R_{\text{BLR}} - L$ relation as follows,

$$\log\left(\frac{\tau_{\text{MgII}}}{1 \text{ day}}\right) = 1.74^{+0.04}_{-0.04} + 0.32^{+0.04}_{-0.04} \log\left(\frac{L_{3000}}{10^{44} \text{ erg s}^{-1}}\right), \quad (1.41)$$

which has the substantial rms scatter of $\sigma = 0.30^{+0.02}_{-0.02}$ dex. We see that the MgII $R_{\text{BLR}} - L$ relation is significantly flatter than the H β $R_{\text{BLR}} - L$ relation, see Eq. (1.39). The $R_{\text{BLR}} - L$ relation has even been confirmed for the HIL CIV line (at 1549 Å) (Kaspi et al. 2021; Cao et al. 2022, 2024), which is perhaps a bit surprising because of its presumed association with the unbound outflow. For 38 CIV QSOs, the best-fit $R_{\text{BLR}} - L$ relation is (Cao et al. 2022),

$$\log\left(\frac{\tau_{\text{CIV}}}{1 \text{ day}}\right) = 1.034^{+0.097}_{-0.087} + 0.441^{+0.044}_{-0.044} \log\left(\frac{L_{1350}}{10^{44} \text{ erg s}^{-1}}\right), \quad (1.42)$$

which has the rms scatter of $0.307^{+0.039}_{-0.056}$ dex comparable to the MgII $R_{\text{BLR}} - L$ relation. Using the CIV line, one reaches quasars at the redshift of 3 and higher, whose CIV emission is redshifted to the optical domain.

The importance of the $R_{\text{BLR}} - L$ relations for different broad emission lines is that they allow the determination of the SMBH mass for one single-epoch spectrum. From such a spectrum, one can determine the continuum monochromatic flux density and for a given redshift, a monochromatic luminosity is determined. Combining this luminosity with the $R_{\text{BLR}} - L$ relation, one can infer the time-delay for a given broad emission line. With the determined FWHM of the line from the single-epoch spectrum, we can estimate the virial SMBH mass using Eq. (1.37). Having many estimated SMBH masses at different redshifts enables one to analyze the SMBH growth across the cosmic history. The power-law relation $\tau_{\text{BLR}} \propto L^\alpha$ can also be utilized for the standardization of quasars and thus for constraining cosmological parameters, see Subsection 1.4 for more details.

1.2.2 Resolving spheres of influence of extragalactic nuclei

The Galactic center is the closest galactic nucleus to us. It is also the only nucleus where we can resolve individual stars and study their proper motions and radial velocities. The sphere of influence of Sgr A* is $r_{\text{SI}} \sim 2.1$ pc according to Eq. (1.4). In order to detect the presence of a massive point mass, such as the SMBH at the center of a galaxy, one needs to be able to resolve at least the scale of one r_{SI} . In reality, to reliably determine the SMBH mass, the Keplerian rise of the stellar rms velocity along the line of sight $v_{\text{rms}} \propto r^{-1/2}$ should be detected on the scale of at least $\sim 0.1 r_{\text{SI}}$ (Merritt 2013). For the Galactic center distance of $d_{\text{SgrA*}} \sim 8$ kpc, we can actually resolve the scales of $l \sim (\lambda/D)d_{\text{SgrA*}} \sim 454 \text{ AU} \sim 0.0022 \text{ pc}$, which is $10^{-3} r_{\text{SI}}$. Therefore the gravitational potential of Sgr A* has been reliably probed by measuring the stellar rms velocity inside r_{SI} (e.g., Schödel et al. 2009). In addition to that, the presence of the SMBH of $M_\bullet \sim 4 \times 10^6 M_\odot$ has been independently confirmed by sampling several orbits of S stars (i.e. astrometry studies, see e.g., Parsa et al. 2017).

The situation in extragalactic systems is generally much worse in terms of directly resolving the sphere of the SMBH influence. The Galactic center is ~ 112.5 -times closer than M31 in the Local Group and ~ 2062.5 -times closer than the closest cluster of galaxies, the Virgo cluster. It is thus possible to resolve the sphere of influence only for a few tens of galaxies. The Keplerian rise of the stellar rms velocity was detected only for the Milky Way, M31 and its companion M32 in the Local Group. The central massive elliptical galaxy M87 in the Virgo cluster exhibits only a very gradual rms velocity increase, flatter than the typical Keplerian profile. This is most likely due to a core-like distribution of stars around the SMBH M87* caused by previous mergers (Merritt 2013). When detecting the stellar integrated

light at different projected radii, more distant slower stars contribute more to the measured line-of-sight rms velocity than the closer faster stars, which are fewer.

The stellar distribution in the nucleus of M31, the Andromeda galaxy, is asymmetric (lopsided) with two apparent photometric centers P1-P2, one brighter (P1) than the other (P2). This makes the interpretation of the Keplerian rise of the stellar rms velocity challenging, in particular it makes the SMBH mass determination uncertain. The two nuclei are separated in projection by about ~ 1.5 pc, with the fainter one coinciding with the centroid of the bulge (Lauer et al. 1993). There have been several interpretations of the Andromeda double-nucleus:

- it could be the result of the dust absorption, though this would require unusual dust properties (Lauer et al. 1993);
- the brighter offset nucleus could be the remnant of another nucleus of the galaxy that had previously merged with M31, potentially hosting another SMBH that would have stabilized it against tidal disruption by M31* (Lauer et al. 1993);
- the double-nucleus structure is created by a single eccentric stellar disc orbiting around M31* at the center of the bulge (Tremaine 1995; Kormendy & Bender 1999). The brighter second “nucleus” is an apparent effect of the accumulation of stars close to their apocenters where they move more slowly, and thus spend more time at the apocenter orbital phase than at the pericenter closer to the SMBH. Bluer, younger stars orbit around the true nucleus, close to the SMBH, which is analogous to the Galactic center and suggests that there are dynamical processes close to the SMBH that tend to catalyze star formation.

Instead of stellar kinematics, one can make use of gas motions that can more clearly trace the SMBH potential if the gas orbits in one plane, i.e. there is a thinner gas disc close to the SMBH. Then the gas velocity profile can be fitted with $v_{\text{gas}} = [G(M_{\bullet} + M_{\star}(< r))/r]^{1/2}$ with a certain inclination of the gas disc with respect to the observer. The gas motion along the line of sight is not so contaminated by the gas that is located further away, which is the case for stellar kinematics. Macchetto et al. (1997) presented the rotation curve of an ionized gas ring traced by [CII] emission close to M87* (~ 5 pc), which led to the constraining of the SMBH mass to a few $10^9 M_{\odot}$ ($3.2 \pm 0.9 \times 10^9 M_{\odot}$). In special cases, the X-ray emission of an AGN accretion disc can excite the molecular transitions in the orbiting material that lead to the stimulated *water maser* emission (Greenhill 2002). An exemplary case is NGC 4258 where the water maser emission at 22 GHz was resolved by the radio interferometry technique (Very Long Baseline Array). At the resolution of milliarcseconds, which is 100-times better than with optical telescopes, the molecular clouds were found to rotate within a thin, Keplerian disc with the radius of ~ 0.1 pc. This led to one of the most precise SMBH mass measurements of $M_{\bullet} = 3.9 \times 10^7 M_{\odot}$ (Miyoshi et al. 1995).

Radio interferometry at millimeter wavelengths can reach sufficient angular resolution to resolve event-horizon structures of M87* and Sgr A*, two SMBHs that have the largest angular sizes on the sky, when a correlated signal is combined from several stations across the whole globe. The basic condition for the imaging is the sufficient coverage of the interference fringes (visibilities) across the *uv*-plane (expressed in baseline lengths) so that the Fourier transform can be performed to produce an image on the sky (van Cittert-Zernike theorem). At the same time, because of the low relative accretion rate, both SMBHs are embedded in the geometrically thick ADAFs, whose SED becomes optically thin close to one millimeter, see

Fig. 1.14. These two factors have led to the attempt to observe M87* and Sgr A* using the global millimeter Very Long Baseline Interferometry array (mm-VLBI). The project and the collaboration utilizing mm-VLBI adopted the name *Event Horizon Telescope* (EHT)⁵. With the largest baseline of $B \sim 10^4$ km and the observing wavelength of $\lambda \sim 1$ mm, the smallest angular separation that can be resolved is $\theta_{\text{EHT}} \sim \lambda/B \sim 21 \mu\text{as}$. For a non-rotating SMBH, the accretion flow of hot thermal plasma close to the ISCO produces synchrotron radiation. Emitted photons can approach closest to the SMBH at the photon orbit and still return to the place of their origin. This last photon orbit is seen by a distant observer at the radius of $3\sqrt{3}r_g$. It is expected to create a bright ring with a darker depression at the center – SMBH *silhouette* or *shadow* (Falcke et al. 2000) – whose angular diameter is,

$$\theta_{\text{shadow}} \approx \frac{6\sqrt{3}GM_{\bullet}}{c^2 d_{\text{SMBH}}} \rightarrow 51.2 \left(\frac{M_{\bullet}}{4 \times 10^6 M_{\odot}} \right) \left(\frac{d_{\text{SMBH}}}{8 \times 10^3 \text{ pc}} \right)^{-1} \mu\text{as}, \quad (1.43)$$

which was estimated specifically for Sgr A*. For M87*, which is about thousand times heavier and ~ 2000 more distant, we get $\theta_{\text{shadow}} \sim 25.6 \mu\text{as}$. Thus, in both cases, since $\theta_{\text{EHT}} < \theta_{\text{shadow}}$, the EHT should be able to resolve the SMBH shadow and produce its brightness distribution if the uv -coverage of fringe visibilities in the baseline plane is sufficiently dense. Event Horizon Telescope Collaboration et al. (2019) report the detection of the shadow of M87* and subsequently, Event Horizon Telescope Collaboration et al. (2022) announce the detection of the Sgr A* shadow (see Fig. 1.17 for the image reconstruction, including the polarized signal). To capture the brightness distribution of Sgr A* has been more challenging since it is variable on the timescales that are shorter than the observation duration at individual stations. A typical orbital timescale close to the ISCO of Sgr A* (for a non-rotating case) is,

$$P_{\text{SgrA*}} = \frac{2\pi GM_{\bullet}}{c^3} \left(\frac{r}{r_g} \right)^{3/2} \simeq 30 \left(\frac{M_{\bullet}}{4 \times 10^6 M_{\odot}} \right) \left(\frac{r}{6 r_g} \right)^{3/2} \text{ min}, \quad (1.44)$$

while for M87*, we obtain a thousand times longer orbital timescale, $P_{\text{M87*}} \simeq 21$ days, which is much longer than the typical observing phase. In Fig. 1.28, we show the collection of multi-wavelength images of M87 from the highest energies to the lowest, capturing this elliptical galaxy with a prominent jet at the center of the Virgo cluster at all spatial scales.

The reverberation mapping of the BLR was the original and for a long time the only way to spatially map the distances via the measured time delays. The near-infrared interferometry applied to the Very Large Telescope at the European Southern observatory – the interferometer GRAVITY (GRAVITY Collaboration et al. 2017) – enabled the spatial resolution of the region for several AGN. The first resolved offset between red- and blue-photocenters of the broad Paschen α line in 3C273 was detected by Gravity Collaboration et al. (2018). Similarly, GRAVITY Collaboration et al. (2020a) spatially resolved Bry line in IRAS 09149-6206 and the radius of the line-emitting region was consistent with the value expected from the previously inferred radius-luminosity relation for the broad H β line. A spatially resolved Bry line was also reported for NGC3783 (GRAVITY Collaboration et al. 2021), where the BLR geometry, as in the previous two sources, is consistent with a thick disc of cloudlets whose density peaks at the inner radius. GRAVITY Collaboration et al. (2024) revealed near-infrared VLT/GRAVITY interferometric spectra for four more targets: Mrk509, PDS456, Mrk1239, and IC4329A. Based on these sources and the three previously reported ones, GRAVITY

⁵<https://eventhorizontelescope.org/>

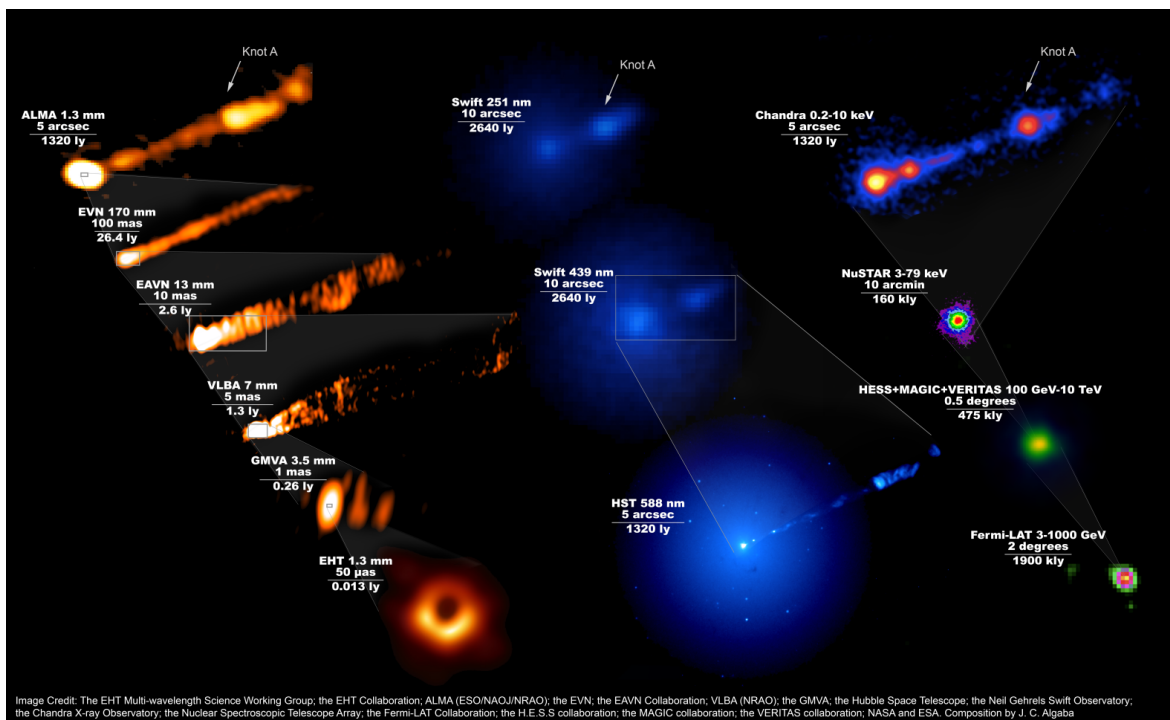


Figure 1.28: Multi-wavelength view of M87, including the mm-Very Long Baseline Interferometry image of the M87* shadow. The figure shows the composition of multi-wavelength images of M87 taken during the 2017 observing campaign when the first SMBH “photo” was taken in April. There were 19 different instruments involved. From the left to the right columns, there are mm/radio images (left; orange), UV/optical (middle; blue), and X-ray/ γ -ray images (right; green-red-yellow colours). The top row shows a series of three images (from the left to the right: 1.3 mm, 251 nm, and 0.2-10 keV) with the spatial scale of the order of 1000 light years that shows the core-jet structure, including the prominent knot A in the forward-pointed jet. Credit for the image composition: J. C. Algaba (full credit is at the bottom of the image).

[Collaboration et al. \(2024\)](#) constructed the $R_{\text{BLR}} - L$ relation independent of the previous reverberation-mapping measurements. The best-fit relation is,

$$\log\left(\frac{\tau_{\text{NIR}}}{1 \text{ day}}\right) = 1.69^{+0.23}_{-0.23} + 0.37^{+0.18}_{-0.17} \log\left(\frac{L_{5100}}{10^{44} \text{ erg s}^{-1}}\right), \quad (1.45)$$

which is flatter but within the uncertainties still consistent with the slope reported by [Bentz et al. \(2013\)](#). [GRAVITY Collaboration et al. \(2024\)](#) found an indication for shorter time delays for higher luminosity AGN, which is consistent with the trends of lag shortening for higher Eddington ratios traced along the $R_{\text{BLR}} - L$ relation inferred from reverberation-mapped data ([Martínez-Aldama et al. 2019](#); [Zajaček et al. 2020](#)). Overall, the spatially resolved BLRs by the GRAVITY instrument have confirmed the robustness of reverberation mapping so far, including the inferred virial SMBH masses and the previously determined radius-luminosity relations. These tools can thus be further employed in the studies of the SMBH growth across the cosmic history.

1.2.3 Signs of stellar-mass bodies close to extragalactic SMBHs

In the previous subsections we learned that characteristic broad and narrow optical and UV emissions lines, the power-law continuum, the infrared bump as well as the analysis of the polarized light led to the formulation of the *unified model of AGN* (Antonucci 1993; Urry & Padovani 1995), in which observed spectral properties of AGN depend largely on the viewing angle. For type I AGN that we observe close to the symmetry axis, i.e. we view an accreting SMBH close to the face-on configuration, we can detect broad components of optical and UV emission lines as well as the power-law continuum, including the X-ray emission, presumably originating in the accretion disc. For type II sources, broad components are not visible and the continuum emission has a profound infrared excess due to the emission of a more distant dusty molecular torus. For type I sources, the continuum emission varies stochastically on the timescales from days to months. Across different wavebands, these variations are more or less correlated, including the emission of broad lines, which allows us to estimate the time delays between different bands, and eventually determine the length-scales associated with a particular circumnuclear medium – this is the so-called reverberation mapping technique, see also Subsection 1.2.1. Although we have gained a basic understanding of geometrical, spectral, and temporal properties of AGN, especially via reverberation mapping campaigns (Czerny et al. 2023), some questions have still remained largely unanswered. One of them is the effect of a large number of stars within the NSC on the accretion onto the SMBH and the nuclear outflows. On the other hand, the AGN activity is expected to impact stars orbiting around the SMBH. The questions like these have been challenging to tackle due to a lack of information about orbiting stars in different galactic nuclei than the Galactic center. However, some recent detections of repeating nuclear transients (RNT) seem to indicate that stars can indeed affect noticeably the close surroundings of SMBHs.

In comparison with Sgr A* where a large number of stars within the NSC determine its low level of activity (Quataert 2004; Shcherbakov & Baganoff 2010; Ressler et al. 2020), there are several tens of detections of a rapid increase in the optical/UV luminosity by several orders of magnitude of otherwise quiescent nuclei (Gezari 2021). These optical/UV flares with the peak black-body luminosities of $\sim 10^{43} - 10^{44} \text{ erg s}^{-1}$ and typical temperatures of $\sim 10\,000 - 50\,000 \text{ K}$ are typically followed by a power-law decay. A standard interpretation of these events is the tidal disruption of a star or a tidal disruption event (TDE). TDEs were predicted before the actual discovery (Hills 1975; Rees 1988). A standard model picture is that a star moving on a parabolic/hyperbolic orbit reaches the smallest distance to the SMBH, the periape, where the acceleration due to the tidal field of the SMBH is comparable to or larger than the gravitational binding energy of the star. The critical distance for the star of mass m_\star and radius R_\star is referred to as the tidal disruption radius r_t ,

$$r_t \approx R_\star \left(\frac{M_\bullet}{m_\star} \right)^{1/3}$$

$$\frac{r_t}{r_g} \approx \frac{c^2 R_\star}{GM_\bullet^{2/3} m_\star^{1/3}} \sim 18.7 \left(\frac{R_\star}{1 R_\odot} \right) \left(\frac{M_\bullet}{4 \times 10^6 M_\odot} \right)^{-2/3} \left(\frac{m_\star}{1 M_\odot} \right)^{-1/3}, \quad (1.46)$$

where the second expression is the ratio of the tidal radius of a star to the gravitational radius of the SMBH. When the pericenter of the star is comparable to or smaller than r_t , it will be tidally perturbed. Subsequently, the debris stream forms, approximately half of which escapes the SMBH altogether while the other half falls back and powers the emission. The

fall-back rate was found to evolve with time as a power-law, $\dot{M}_{\text{fb}} \propto (t - t_p)^{-5/3}$ with respect to the time of the peak luminosity t_p , which is roughly consistent with many detections of TDEs and their evolution with time (Gezari 2021). The ratio of the tidal disruption radius r_t to the pericenter distance of the star r_p is referred to as the parameter $\beta_\star = r_t/r_p$. For different types of stars, there is a critical value of β_\star , below which the TDE is just partial. Specifically, for main-sequence stars, $\beta_{\text{crit}} \sim 2-3$ (Ryu et al. 2020), while for $\beta < \beta_{\text{crit}}$ only the upper envelopes of the star are tidally perturbed and the stellar core continues along the original orbit. When the stellar orbit is bound, i.e. elliptic, this results in repeated partial TDEs or rpTDEs (see also Suková et al. 2024, for discussion). There have been several rpTDEs detected so far with the recurrence timescale or the orbital period between tens of days to about 30 years (Payne et al. 2022; Liu et al. 2023; Wevers et al. 2023). The repetition of the TDE flares is instrumental to uncover the parameters of a given system, in particular the SMBH mass, spin, stellar type, the pericenter distance, and the orbital evolution, since they all influence the flare shape, spectrum, and the periodicity changes. The dynamics behind the orbits of rpTDEs is likely related to the disruption of binaries on nearly parabolic orbits. This three-body interaction or the so-called *Hills mechanism* (Hills 1988) leads to the binary disruption, where one component typically escapes the system as a hypervelocity star while the other component becomes bound to the SMBH and moves on orbits comparable to detected rpTDEs. Hence, rpTDEs probe not only the accretion physics but also the dynamics of the whole (extragalactic) NSC, see Fig. 1.29 for the illustration.

A novel type of short-period repeating soft X-ray transients was discovered with the recurrence timescale of a few hours to about one day (GSN069 was the first such a source; Miniutti et al. 2019), therefore about two orders of magnitude less than rpTDEs. The eruption amplitude reaches one to two orders of magnitude more than the quiescent emission. In other wavebands, including optical, UV, and hard X-ray bands, there is no significant variability. The duty cycle of the eruptions is of the order of $\sim 10\%$ of the recurrence timescale. For these reasons, such repeating nuclear transients (RNTs) were called QuasiPeriodic Erupters (QPEs; Arcodia et al. 2021). Although there have been many theoretical models presented addressing the QPEs, including accretion-disc instabilities (in particular the radiation-pressure instability; Sniegowska et al. 2020; Śniegowska et al. 2023), star-disc and black hole-disc interactions (see Suková et al. 2024, for a review), there is a preference towards models that explain the repetitive soft X-ray eruptions as a result of a smaller body orbiting in the vicinity of the SMBH. These models can be categorized into three groups according to the mechanism how the X-ray emission peaks are produced:

- perturbations of the accretion rate due to inclined perturbers (Suková et al. 2021),
- ejection of shocked, adiabatically expanding clouds above the accretion disc as the smaller body punches through the accretion disc surrounding the primary SMBH (Linial & Metzger 2023; Franchini et al. 2023),
- a Roche-lobe overflow of the stellar-envelope material onto the SMBH, which resembles rpTDEs, see Fig. 1.29, though Roche-lobe overflowing stars are expected to exhibit orbits with only mild eccentricities due to the circularization via gravitational-wave losses (Krolik & Linial 2022).

There is a preference for QPEs to be hosted by galaxies with lower-mass SMBHs ($\sim 10^5 - 10^7 M_\odot$). Adopting $M_\bullet = 10^6 M_\odot$ and assuming that the eruptions take place twice per

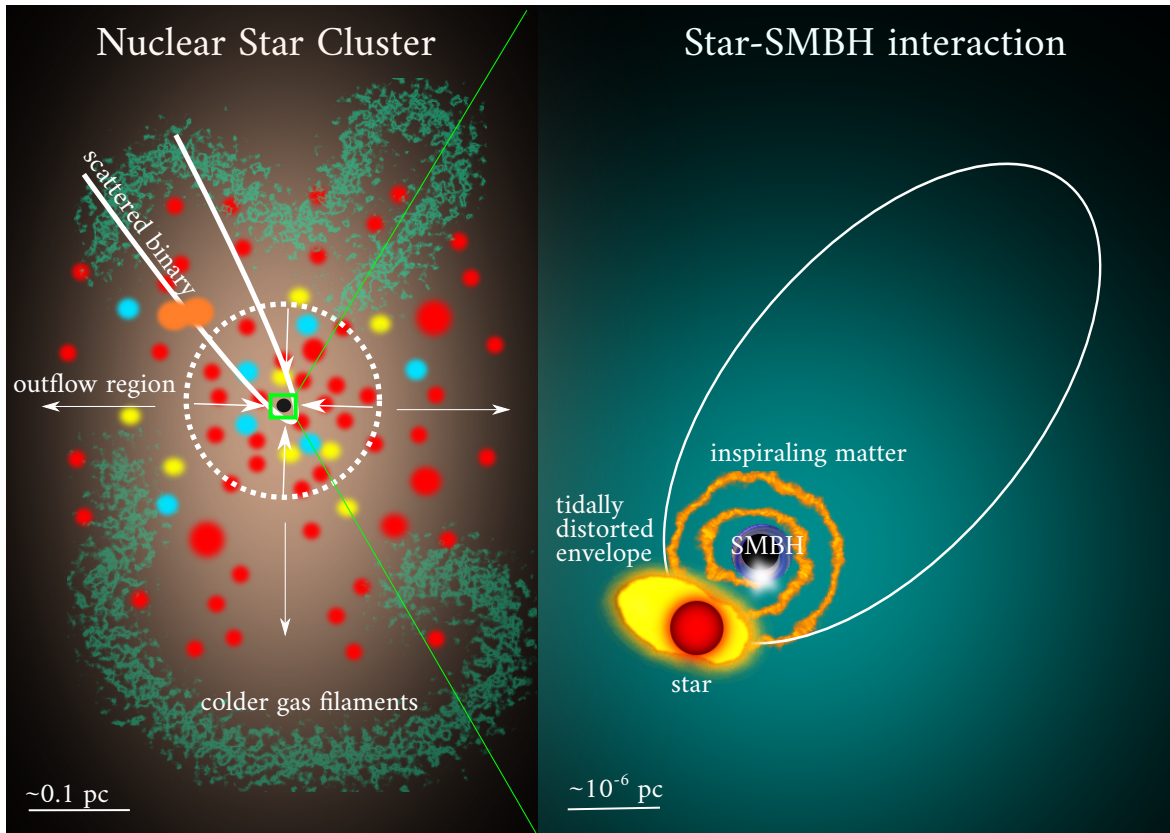


Figure 1.29: Repeating partial tidal disruption event. The left panel shows the whole NSC where two-body interactions result in the infall of binaries on nearly parabolic orbits. When the binary approaches the SMBH, it disrupts, leaving one component tightly bound to the SMBH. In the right panel, we show the tidal perturbation and stripping of such a star close to the pericenter of its orbit. This leads to repeating nuclear flares on the orbital timescale.

perturber's (mildly eccentric or nearly circular) orbit, $P_{\text{orb}} = 2P_{\text{erupt}}$, we obtain an estimate for the semi-major axis of an orbiting body in gravitational radii for P_{erupt} scaled to one hour,

$$\begin{aligned} \frac{a_{\star}}{r_g} &= \frac{c^2}{(\pi G)^{2/3}} P_{\text{erupt}}^{2/3} M_{\bullet}^{-2/3} \\ &\sim 37.9 \left(\frac{P_{\text{erupt}}}{1 \text{ hour}} \right)^{2/3} \left(\frac{M_{\bullet}}{10^6 M_{\odot}} \right)^{-2/3}. \end{aligned} \quad (1.47)$$

On the length-scales indicated by a_{\star} gravitational radiation and the related energy losses may be relevant depending on the secondary body's mass. In order for the SMBH-secondary object to merge within 10 years from now, the secondary-object mass should be at least (Peters 1964),

$$\begin{aligned} m_2 &\simeq \frac{5c^5}{256G^3} \frac{a_{\star}^4}{M_{\bullet}^2 \tau_{\text{merge}}} \\ &\approx 634 \left(\frac{M_{\bullet}}{10^6 M_{\odot}} \right)^2 \left(\frac{a_{\star}}{38r_g} \right)^4 \left(\frac{\tau_{\text{merge}}}{10 \text{ years}} \right)^{-1} M_{\odot}, \end{aligned} \quad (1.48)$$

hence in the intermediate-mass black hole range (IMBH). For smaller periods of the eruptions below half an hour, the mass of the secondary would be pushed down towards stellar-mass

black holes of $\lesssim 100 M_\odot$. Therefore, some of the current QPE sources or those detected in the future could be electromagnetic counterparts of the extreme-mass/intermediate-mass ratio inspiral (EMRI/IMRI) gravitational-wave sources to be detected by the Laser Interferometer Space Antenna (Amaro-Seoane et al. 2023; Kejriwal et al. 2024).

Recently, the Swift J0230+28 source caught attention with the period of soft X-ray eruptions of ~ 22 days, which is intermediate between QPEs and rpTDEs (Evans et al. 2023; Guolo et al. 2024). In addition to longer, regular flares, the source exhibits shorter rapid flares with a comparable recurrence timescale (Pasham et al. 2024a). Moreover, after at most ~ 536 days, the eruptions ceased to be detectable (Pasham et al. 2024a). The best interpretation is either a rpTDE of a Jupiter-like planet or a double-EMRI system consisting of two co-orbiting aligned stars. Another source – ASASSN-20qc – exhibited a TDE-like optical flare, followed by a delayed X-ray emission. When the X-ray spectrum was analysed, Pasham et al. (2024c) found the signature of an ultrafast outflow (UFO) that is periodically enhanced every 8.5 days. In contrast to the presence of the QuasiPeriodic ultrafast Outflow (QPOut), there is no significant variability of the inflow rate. These properties are consistent with an orbiting IMBH at the distance of $\sim 100 r_g$ where the inclined IMBH pushes through the ADAF and drags some matter along its orbit towards the outflow funnel where it is further accelerated by the ordered magnetic field. At the same time, the ratio of the influence radius of the IMBH to its distance is not large enough to cause significant perturbation of the inflow rate (Suková et al. 2021; Zajaček et al. 2024e). Finally, the event AT2019qiz associated with the optical TDE started to exhibit QPEs with the mean recurrence timescale of ~ 48 hours as well as QPOuts years after the TDE peak (Nicholl et al. 2024). The modeling of the detected X-ray, optical, and UV emission of the accretion disc provides support for the perturber-disc interactions. This source thus provides evidence that QPEs are associated with TDEs that eventually reveal the presence of other bound secondary bodies in the vicinity of the SMBH thanks to the supply of the fresh material that forms a new, denser accretion disc on the length-scale of the tidal radius or larger. In summary, the high-cadence time-domain surveys provide new evidence for repeating nuclear transients, many of which seem to be manifestations of the star/compact remnant interaction with the circumnuclear medium of the SMBH.

Since most spiral and elliptical galaxies with the total stellar masses of $\sim 10^8 - 10^{10} M_\odot$ host dense and massive NSCs (Neumayer et al. 2020), the question arises if the SMBH feeding by stars from the NSC cannot by itself address a large part of the SMBH growth during the galaxy evolution. The SMBH can grow when a star passes through its event horizon or by the accretion of the stellar debris after the TDE. In both cases, the critical length-scale that determines whether the star is consumed or not is the *loss-cone* radius r_{lc} (Merritt & Wang 2005). When the star approaches or goes below r_{lc} , it will eventually be consumed by the SMBH. When we approximate the NSC as a singular isothermal sphere, the stellar mass accretion rate through the radius r is,

$$\dot{M}_\star(r) \sim 4\pi r^2 \sigma_\star \rho_\star(r) \sim 2 \frac{\sigma_\star^3}{G}, \quad (1.49)$$

where the stellar mass density is $\rho_\star(r) \sim \sigma_\star^2 / (2\pi G r^2)$ for a given stellar velocity dispersion σ_\star within a singular isothermal sphere. The stellar-mass inflow rate through the loss cone is $(r_{lc}/r)\dot{M}_\star(r)$. When we set r to the radius of the SMBH gravitational influence, see Eq. (1.4), and $r_{ls} \approx 10r_g$, the loss-cone mass inflow rate can be evaluated as follows,

$$\dot{M}_{lc} \approx \frac{2\sigma_\star^3}{G} \frac{r_{lc}}{r_{SI}} \approx 20 \frac{\sigma_\star^5}{Gc^2}. \quad (1.50)$$

When we assume that the “seed” black hole is fed mostly by disrupted or swallowed stars, the resulting SMBH mass “now” after $\tau_{\text{gal}} \sim 10$ Gyr of the galaxy evolution is,

$$\begin{aligned} M_{\bullet} &\sim \dot{M}_{\text{lc}} \tau_{\text{gal}} \simeq 20 \frac{\sigma_{\star}^5}{Gc^2} \tau_{\text{gal}} \\ &\sim 1.7 \times 10^8 \left(\frac{\sigma_{\star}}{200 \text{ km s}^{-1}} \right)^5 \left(\frac{\tau_{\text{gal}}}{10 \text{ Gyr}} \right) M_{\odot}, \end{aligned} \quad (1.51)$$

which is both qualitatively and quantitatively consistent with the observed $M_{\bullet} - \sigma_{\star}$ relation (Ferrarese & Merritt 2000), see Subsection 1.2 for the discussed relation to the AGN negative feedback. The derived and evaluated relation in Eq. (1.51) implies that the SMBH “loss-cone” feeding by stars can serve as an alternative or complementary pathway for the SMBH growth and the associated feedback. The contribution of this process to the classical feeding pathways, see Fig. 1.21 for the illustration, depends on the state of the stellar nuclear environment, in particular the stellar density and the velocity dispersion of the NSC, which determine the stellar mass inflow rate.

1.3 Synergies between the Galactic center and active galactic nuclei

Currently, the Galactic center with the bolometric luminosity of $L_{\text{acc}} \sim 10^{36} - 10^{37} \text{ erg s}^{-1}$ and the accretion rate of $\dot{M} \sim 2 \times 10^{-9} - 2 \times 10^{-7} M_{\odot} \text{ yr}^{-1}$ is extremely underluminous. With the Eddington ratio of $\dot{m} \sim 10^{-7}$, it is a typical representative of quiescent nuclei that host an ADAF instead of a standard accretion disc. Therefore, the current SED with the peak close to ~ 1 mm is much softer than the SED corresponding to the cooling-dominated standard disc with the peak in far-UV domain, see Fig. 1.24. The question is how long Sgr A* has been in such a low-luminosity state. Did it reach the Eddington rate during its past evolution? If yes, for how long? Will it repeat again in the future?

Some aspects of the past evolution of Sgr A* can be inferred from its current accretion rate and its mass. Taking the present accretion rate of $\dot{M} \sim 2 \times 10^{-8} M_{\odot} \text{ yr}^{-1}$ and extrapolating it for the whole Galaxy lifetime of $\tau_{\text{gal}} \sim 10^{10} \text{ yr}$ implies that the SMBH would grow only by $\Delta M_{\bullet} \sim \dot{M} \tau_{\text{gal}} \sim 200 M_{\odot}$, which is in contradiction with the mass of $M_{\bullet} \simeq 4 \times 10^6 M_{\odot}$. This already points towards a more active past evolution unless Sgr A* was formed already very massive via a direct-collapse scenario (see e. g. Natarajan et al. 2024). Assuming that at certain epochs Sgr A* reached its Eddington luminosity, see Eq. (1.1), $L_{\text{Edd}} \sim 5 \times 10^{44} \text{ erg s}^{-1}$, it should have had an accretion rate of,

$$\dot{M}_{\text{Edd}} = \frac{4\pi G M_{\bullet} m_{\text{p}}}{\eta_{\text{rad}} \sigma_{\text{TC}}} \sim 0.09 \left(\frac{M_{\bullet}}{4 \times 10^6 M_{\odot}} \right) \left(\frac{\eta_{\text{rad}}}{0.1} \right)^{-1} M_{\odot} \text{ yr}^{-1}, \quad (1.52)$$

where we adopted the radiative efficiency of $\eta_{\text{rad}} \sim 0.1$. With the Eddington rate, the total growth phase of Sgr A* would last $\tau_{\text{g}} \sim M_{\bullet} / \dot{M}_{\text{Edd}} \sim 4.4 \times 10^7$ years or only about $\sim 0.4\%$ of the total Galaxy lifetime would be enough to reach $M_{\bullet} \sim 4 \times 10^6 M_{\odot}$ at the Eddington rate. In case the individual active phase lasts $\tau_{\text{A}} \sim 10^5$ years (Schawinski et al. 2015), there should have been about $N_{\text{A}} \sim \tau_{\text{g}} / \tau_{\text{A}} \sim 440$ such active phases during the Milky Way evolution. Since the number of non-active, quiescent phases should be comparable, $N_{\text{N}} \sim N_{\text{A}}$, the quiescent

phase is expected to last $\tau_N \sim 22.6 \times 10^6$ years. Hence, on average, every 20 million years Sgr A* is expected to reach the Eddington limit for $\sim 10^5$ years.

Although these estimates are very rough, we can try to compare the recurrence timescale of an active phase with the expected infall rate of a molecular material. An infalling/accreted mass during one active phase $\Delta M_\bullet \sim \dot{M}_{\text{Edd}} \tau_A \sim 10^4 M_\odot$ corresponds well to a smaller molecular cloud. The closest reservoir of the molecular material in the vicinity of Sgr A* is the Circum-Nuclear Disc (CND) with the total mass of $10^6 M_\odot$ (Christopher et al. 2005). The CND consists of many clumps with the radius of $r_{\text{cl}} \sim 0.1$ pc. When they reach a gas number density of $n_g \sim 10^8 \text{ cm}^{-3}$, each has a mass of $\sim 10^4 M_\odot$. According to Hsieh et al. (2021), there are about 16 sufficiently massive clumps within the radius of ~ 2 pc and the scale-height of ~ 0.5 , which yields the clump number density of $n_{\text{cl}} \sim 2.5 \text{ pc}^{-3}$. For the characteristic velocity dispersion of $\sigma_{\text{cl}} \sim 10 \text{ km s}^{-1}$, we obtain the clump-clump collisional rate as $\Gamma_{\text{col}} \sim n_{\text{cl}} \sigma_{\text{cl}} S_{\text{cl}}$, where $S_{\text{cl}} \approx \pi r_{\text{cl}}^2$ is the typical clump cross-section. When we choose one out of four final velocity directions after the collision (inwards/outwards, along/opposite the CND rotation), the characteristic infall timescale is $\tau_{\text{infall}} \sim (0.25 \Gamma_{\text{col}})^{-1} \sim 5 \times 10^6$ years, which is within all the uncertainties comparable to the mean duration of the quiescent phase.

In fact, there are several indications for an increased mass supply as well as the putative increased accretion/jet activity a few million years ago. The clockwise stellar disc of OB/Wolf-Rayet stars is likely a remnant of the massive star formation within a dense gaseous/accretion disc (Levin & Beloborodov 2003). The detected large-scale γ -ray *Fermi* bubbles (Su et al. 2010) that extend ~ 9 kpc above and below the Galactic plane seem to be associated with a massive gas outflow associated with either the starburst activity and associated supernovae or a collimated nuclear outflow-jet that took place a few million years ago. Based on the analysis of ionization properties Bland-Hawthorn et al. (2019) favour a Seyfert-like enhanced accretion activity over the mechanic outflow model. The relative accretion rate could have reached $\dot{m} \sim 0.1 - 1.0$. On a slightly larger scales than the *Fermi* bubbles, *eROSITA* identified X-ray *eROSITA* bubbles with a typical length-scale of 14 kpc (Predehl et al. 2020). In Fig. 1.30, we show the superposition of both *Fermi* and *eROSITA* bubbles. Whether these structures were all created during one event or there was a separate mechanism is still under investigation.

One of the main questions is whether we can still trace some fingerprints of the past activity of Sgr A* in the central parsec. One of the obvious targets of the nuclear outflow and the associated radiation could be the ionized and neutral/molecular gas in the sphere of influence. However, the gaseous structures such as the CND or the minispiral are rather short-lived, only of the order of $\sim 10^4 - 10^5$ years. A more promising target is the stellar population in the central parsec, especially late-type stars that must have existed during the time of the potentially enhanced Sgr A* activity. In fact, in the central ~ 0.5 pc, Sellgren et al. (1990) identified a decrease in the CO-bandhead absorption feature that is indicative of the surface-brightness of older red giants. It is still under investigation what could have caused the preferential depletion of larger, brighter red giants while smaller, fainter ones seem to be present and form a cusp-like distribution (Schödel et al. 2020). Two of the proposed scenarios involve an enhanced accretion activity a few million years ago:

- red giant-accretion disc interaction: when red giants collided with denser clumps within the self-gravitating outer disc, the outer envelopes of red giants were removed, which effectively modified their observational properties as well as the subsequent stellar evolution (Amaro-Seoane & Chen 2014; Amaro-Seoane et al. 2020);

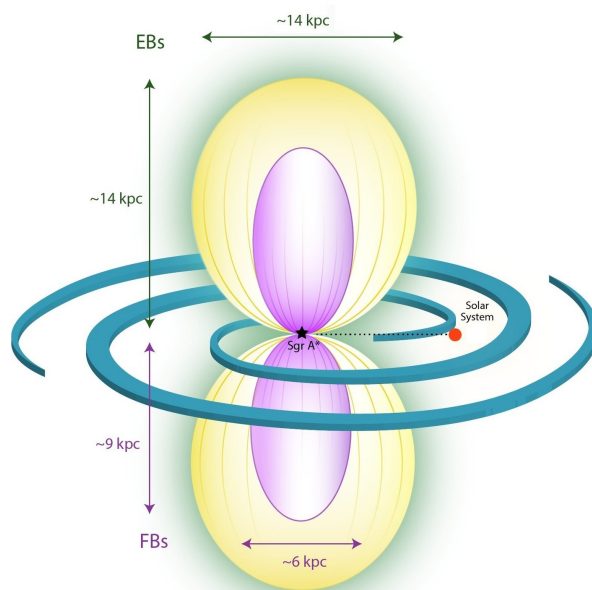


Figure 1.30: Illustration of the size of the Fermi bubbles in the γ -ray domain in comparison with the X-ray eROSITA bubbles. Fermi bubbles (FB) with the length-scale of ~ 9 kpc are more compact than eROSITA bubbles (EB) with the length-scale of ~ 14 kpc. Illustration credit: Max Planck Institute for Extraterrestrial physics.

- red giant-jet interaction, which can similarly ablate the outer layers of late-type stars. This reveals deeper, warmer layers, and thus changes the photometric colour of late-type stars and their luminosities, hence they are not classified as red giants any more, see also Fig. 1.31 for illustration. [Zajaček et al. \(2020\)](#) proposed the model and performed the first analytical estimates of the mechanism. Subsequently, [Kurfürst et al. \(2024\)](#) performed 3D hydrodynamical simulations of the jet-red giant interaction.

Even now Sgr A* exhibits order-of-magnitude near-infrared and X-ray flares lasting about one hour on a daily basis [Witzel et al. \(2021\)](#). As we already discussed, this variability may originate within the magnetically arrested disc, e.g. due to magnetic-reconnection events. The observed variable X-ray emission of molecular clouds in the vicinity of Sgr A* strongly indicates that there was a significantly enhanced emission in the Galactic center only $\sim 300 - 400$ years ago. This event was first indicated by the detected iron-line at 6.7 keV ([Koyama et al. 1989](#)). The fluorescent 6.4 keV iron line detected along the molecular cloud Sgr B2 confirmed the illumination and the reprocessing of the central-source emission by a molecular material in the CMZ ([Sunyaev & Churazov 1998](#)). This fluorescent iron line is also variable ([Inui et al. 2009](#)) and because of the reflection of the central-source emission, its X-ray emission was found to be significantly polarized ([Marin et al. 2023](#)). The variable X-ray fluorescent emission across molecular clouds in the CMZ is thus overall consistent with the reflection of the primary outburst in the direction of Sgr A*. The luminosity increase by about five orders of magnitude a few hundred years ago could have been caused by a series of discrete accretion events, for instance due to infalling compact gas clouds ([Czerny et al. 2013](#)).

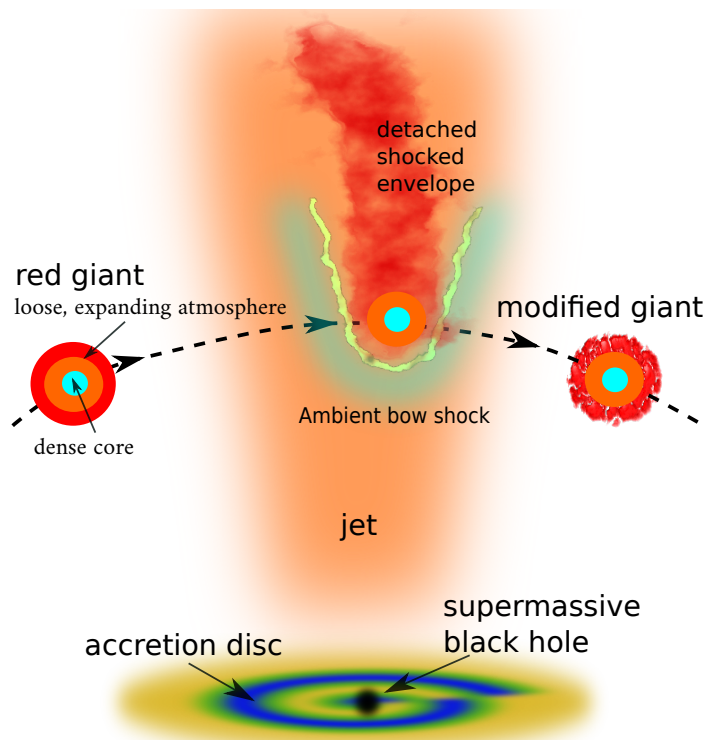


Figure 1.31: Potential effect of the jet during the period of enhanced activity of the Galactic center on the surrounding population of red giants. During repetitive jet-star collisions, the ram pressure of the jet plasma ablates the loose envelope of the red giant, which leads to an enhanced mass loss (in addition to the stellar wind) and as a result, the red giant has a higher photosphere temperature, which leads to the change in the appearance from the “red” colour to a “bluer” colour in terms of photometry.

1.4 Galactic nuclei as standardizable candles

Active galactic nuclei (AGN) are found from the local Universe to the era of reionization and even earlier when the first galaxies were just forming. It is therefore attractive to use them for cosmological studies since they in principle provide a bridge between the local, distance-ladder measurements (Cepheids, supernovae type Ia) and the early-Universe cosmic microwave background (CMB) observations (see e.g. Czerny et al. 2023; Zajaček et al. 2024b). AGN as potential alternative cosmology probes with a large redshift range are especially relevant for the resolution of current cosmological tensions between local and early-Universe measurements, such as the Hubble tension, which has become more serious over the last decade (Perivolaropoulos & Skara 2022; Abdalla et al. 2022). We illustrate the redshift ranges for the CMB, local probes used for the distance ladder (Cepheids, supernovae type Ia), and for active galactic nuclei in Fig. 1.32. While the current expansion rate of the Universe (the Hubble constant H_0) determined using the local, late-Universe distance-ladder measurements is $H_0 = 73.40 \pm 1.04 \text{ km s}^{-1} \text{ Mpc}^{-1}$ (Riess et al. 2022), the value inferred from the CMB anisotropies (power spectrum) assuming the flat Λ CDM model is $H_0 = 67.4 \pm 0.5 \text{ km s}^{-1} \text{ Mpc}^{-1}$ (Planck Collaboration et al. 2020). These two values currently differ by more than $\sim 5\sigma$ (Riess et al. 2022), which can either be caused by hidden systematic errors in at least one of the standard cosmological probes or the current standard model of cosmology (spatially flat Λ CDM) is not valid, i.e. it can only serve as a good approximation of a more complex

cosmological model. That is why searching for alternative probes, such as quasars, that cover a redshift range in between late and early Universe is needed to help reveal the cause of these tensions.

It may seem challenging to standardize AGN, i.e. to use them as standardizable ‘‘candles’’, because of their more complicated geometry in comparison with stars, a large span of SMBH masses as well as luminosities. Moreover, AGN are quite variable sources. However, two established correlations of a power-law nature related to the inner accretion engine in principle allow the determination of luminosity distances and the subsequent construction of the Hubble diagram of quasars. These are:

- the BLR radius-luminosity relation ($R_{\text{BLR}} - L$), which can further be written and parametrized as $\log\left(\frac{\tau}{\text{day}}\right) = \beta + \gamma \log\left[\frac{\nu L_\nu(z, \mathbf{p})}{10^{44} \text{ erg s}^{-1}}\right]$, where $\nu L_\nu(z, \mathbf{p}) = 4\pi D_L(z, \mathbf{p})^2 \nu F_\nu$ with $D_L(z, \mathbf{p})$ being the luminosity distance for a given QSO at the redshift z and \mathbf{p} are cosmological parameters of a given cosmological model;
- the relation between X-ray (2 keV) and UV (2500 Å) luminosities ($L_X - L_{UV}$), which can also be expressed in the log-linear form as $\log\left(\frac{L_X}{\text{erg s}^{-1} \text{Hz}^{-1}}\right) = \beta' + \gamma' \log\left(\frac{L_{UV}}{10^{29} \text{ erg s}^{-1} \text{Hz}^{-1}}\right)$, where $L_X = 4\pi D_L(z, \mathbf{p})^2 F_X$ and $L_{UV} = 4\pi D_L(z, \mathbf{p})^2 F_{UV}$.

We summarize both relations in Table 1.2, where we also specify the corresponding likelihood functions that are used to infer both the parameters of the $R_{\text{BLR}} - L$ or $L_X - L_{UV}$ relations and cosmological parameters. It was shown in a series of works that quasars can be standardized using the $L_X - L_{UV}$ relation (Risaliti & Lusso 2019), with the indication of the deviation from the standard flat Λ CDM model in the direction of a larger current relative matter content and a dynamical dark energy. However, independent analyses showed that the same set of quasars is not fully standardizable as the $L_X - L_{UV}$ parameters depended on both the redshift and the cosmological model (see e.g. Khadka & Ratra 2022).

Table 1.2: Basic methodology of the inference of cosmological parameters p for $R_{\text{BLR}} - L$ and $L_X - L_{UV}$ relations.

Relation	Dependence on cosmology	Likelihood function
$\log\left(\frac{\tau}{\text{day}}\right) = \beta + \gamma \log\left[\frac{\nu L_\nu(z, \mathbf{p})}{10^{44} \text{ erg s}^{-1}}\right]$	$\log\left(\frac{\tau}{\text{day}}\right) = \beta + \gamma \log\left[\frac{4\pi D_L^2 \nu F_\nu}{10^{44} \text{ erg s}^{-1}}\right]$	$\ln(\text{LF}) = -\frac{1}{2} \sum_{i=1}^N \left[\frac{[\log(\tau_i^{\text{obs}}) - \log(\tau_i^{\text{th}})]^2}{s_i^2} + \ln(2\pi s_i^2) \right]$
$\log\left(\frac{L_X}{\text{erg s}^{-1} \text{Hz}^{-1}}\right) = \beta' + \gamma' \log\left(\frac{L_{UV}}{10^{29} \text{ erg s}^{-1} \text{Hz}^{-1}}\right)$	$\log\left(\frac{4\pi D_L^2 F_X}{\text{erg s}^{-1} \text{Hz}^{-1}}\right) = \beta' + \gamma' \log\left(\frac{4\pi D_L^2 F_{UV}}{10^{29} \text{ erg s}^{-1} \text{Hz}^{-1}}\right)$	$\ln(\text{LF}) = -\frac{1}{2} \sum_{i=1}^N \left[\frac{[\log(F_{X,i}^{\text{obs}}) - \log(F_{X,i}^{\text{th}})]^2}{s_i^2} + \ln(2\pi s_i^2) \right]$

Concerning $R_{\text{BLR}} - L$ relation, MgII and CIV QSOs were found to be standardizable (Khadka et al. 2021, 2022b; Cao et al. 2022; Czerny et al. 2023; Cao et al. 2024), i.e. $R_{\text{BLR}} - L$ relation parameters are independent of the cosmological model. These datasets provide only weak cosmological constraints due to limited samples. The constraints are consistent with the standard flat Λ CDM model; however, a moderate dark energy dynamics as well as a small spatial curvature are also consistent with the studied QSO samples. $H\beta$ QSOs were also found to be standardizable, though those QSOs prefer a decelerated expansion of the Universe and the cosmological constraints are in the 2σ tension with the standard flat Λ CDM model (Khadka et al. 2022a).

It was possible to identify a sample of 58 X-ray detected, reverberation-mapped QSOs, for which both the MgII $R_{\text{BLR}} - L$ and $L_X - L_{UV}$ relations could be applied. Khadka et al. (2023) found systematic differences between both relations: while the cosmological parameters inferred using the MgII $R_{\text{BLR}} - L$ relation were consistent with the standard flat Λ CDM model,

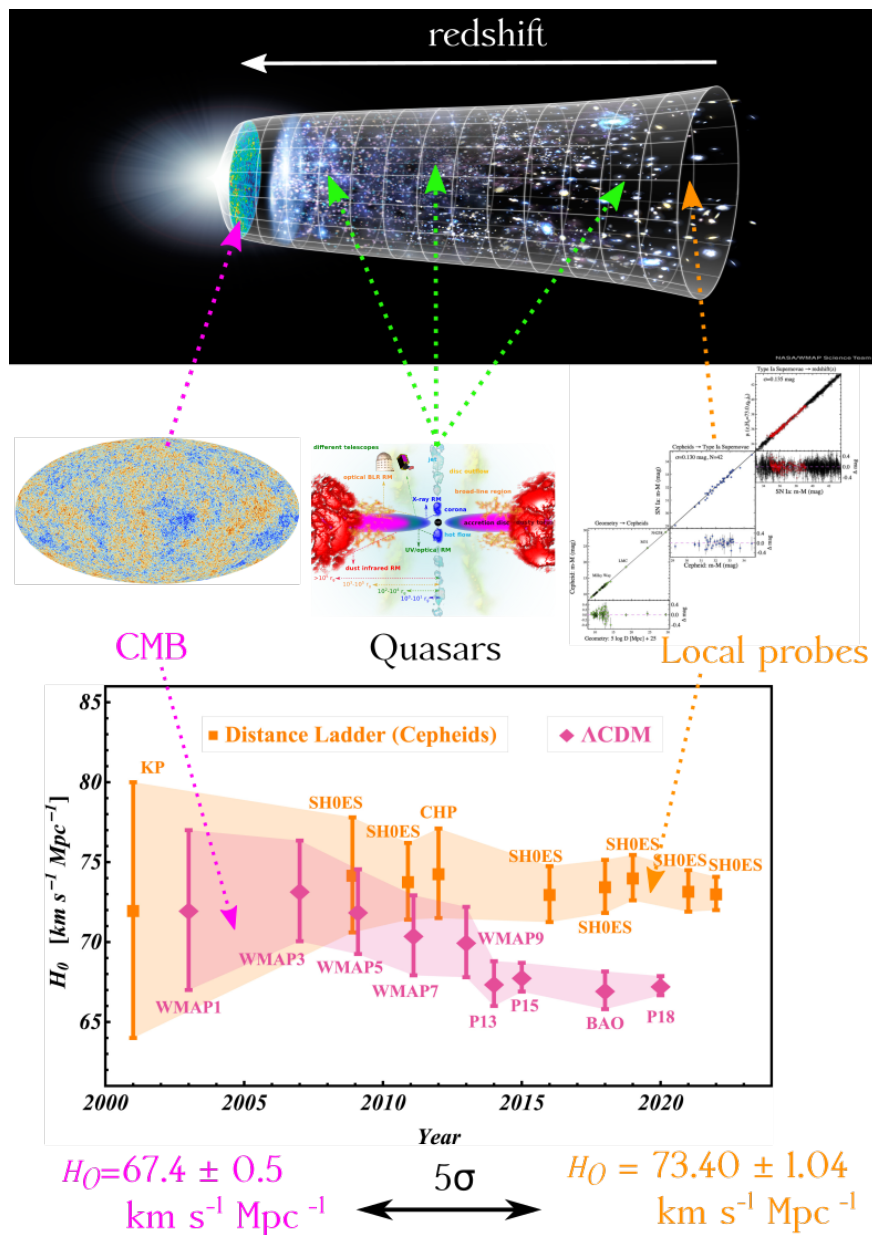


Figure 1.32: Active galactic nuclei versus standard cosmological probes and the Hubble tension. The illustration depicts the currently used standard cosmological probes – cosmic microwave background (CMB) and local, distance-ladder measurements (cepehids, supernovae of type Ia) – and their redshift range in the expanding Universe (top image; NASA/WMAP Science Team). In contrast, we show quasars that can bridge the local measurements with the distant CMB. Towards the bottom of the image, we show the values of the current expansion rate of the Universe (H_0 , the Hubble constant) as inferred from the distance-ladder measurements (orange colour; [Riess et al. 2022](#)) and the cosmic microwave background power spectrum (magenta colour; [Planck Collaboration et al. 2020](#)). The bottom plot adopted from [Perivolaropoulos & Skara \(2022\)](#) shows how the two Hubble constant values started to significantly deviate from each other after 2013 and reached the difference of as much as $\sim 5\sigma$ around 2020 as the systematic errors decreased.

the $L_X - L_{UV}$ relation preferred a larger value of the Ω_{m0} parameter. In addition, the distribution of the luminosity-distance differences, $\Delta \log D_L \equiv \log D_{L, L_X - L_{UV}} - \log D_{L, R-L}$ turned out to be asymmetric with the peak shifted towards positive values. Zajaček et al. (2024b) interpreted this systematic difference between both methods using the extinction of both UV and X-ray radiation, which affects more the $L_X - L_{UV}$ relation since the X-ray and UV luminosities are impacted differently. It is possible to show that extinction, or the optical depth difference ($\tau_X - \tau_{UV}$), always contributes to the non-zero luminosity distance difference,

$$\Delta \log D_L = \underbrace{\frac{\beta' - \gamma' \eta'}{2(1 - \gamma')} + \frac{\beta - \log \tau}{2\gamma} - \frac{\eta}{2} + 7.518}_{=0 \text{ for intrinsic quasar emission}} + \frac{\log F_{UV, \text{int}} - \log F_{X, \text{int}}}{2(1 - \gamma')} + \underbrace{\frac{(\tau_X - \tau_{UV}) \log e}{2(1 - \gamma')}}_{\text{extinction contribution}}. \quad (1.53)$$

In conclusion, the $L_X - L_{UV}$ relation should not be used for the quasar standardization, while the BLR radius-luminosity relation is less affected by extinction and is thus more promising in terms of providing tighter cosmological constraints when larger reverberation-mapped quasar datasets are available.

1.5 This Thesis

This Habilitation Thesis summarizes the research studies of galactic nuclei that span from the nearest (Galactic Center) to distant galactic nuclei close to the peak of quasar activity. At the same time, we study the circumnuclear environment of an extremely low-luminosity nucleus at the center of the Milky Way as well as the properties of active galactic nuclei accreting close to the Eddington limit. Thus we cover nearly nine orders of magnitude in the relative accretion rate. In terms of the supermassive black hole mass, we cover about three orders of magnitude. Therefore, we traverse a large portion of the parameter space, at least considering the basic quantities, such as M_\bullet , \dot{m} , and the luminosity distance (redshift). Below we list seven research papers, where the author of this thesis is the main author. Each of these papers describes studied sources, the data, the applied methodology, and the main results in detail. These works were published between 2019 and 2024,

- **Paper 1: Radio-Optical Properties of Active Galaxies.**

Description: We study a sample of SDSS-FIRST sources, specifically the distribution of their radio spectral indices across narrow-line optical diagnostic diagrams. We find that Seyfert galaxies are mostly associated with radio sources with a steeper radio spectral index and a larger radio loudness. This is caused by the presence of larger and older radio lobes and large-scale jet structures. On the other hand, low-ionization nuclear emission region (LINER) sources have a tendency to exhibit a flat to an inverted radio spectral index and a lower radio loudness. This could be interpreted by the renewed radio activity in the optically thick core region. For more details, see Chapter 2.

Importance: We found a correlation between the radio spectral index distribution and the ionization potential traced by optical line ratios. The lower ionization potential of LINERs is associated with the radio activity of the core/compact jet.

- **Paper 2: Reverberation Mapping of HE 0413-4031.**

Description: In this paper, we perform the monitoring of an intermediate-redshift,

high-luminosity quasar denoted as HE 0413-4031 located at the redshift of $z = 1.38$. A significant time delay of $302.6_{-33.1}^{+28.7}$ days is found between the variable broad line MgII and the photoionizing continuum at 3000 \AA in the rest frame. This measurement helps to confirm the existence of the MgII $R_{\text{BLR}} - L$ relation as well as the shortening of BLR time delays for high-accreting sources. For more details, see Chapter 3.

Importance: The high luminosity of HE 0413-4031 significantly contributes to constraining the MgII radius-luminosity relation, which can further be applied to infer SMBH masses from single-epoch spectra. A contribution to the MgII radius-luminosity scatter based on the accretion rate of the sources is found, in particular, the higher the accretion rate, the larger the deviation from the best-fit relation.

- **Paper 3: Red-Giant Depletion in the Galactic Center.**

Description: Bright red giants appear to be missing within the central 0.5 pc from Sgr A*. In this study, we propose a novel mechanism for the depletion of red giants in the inner half parsec from Sgr A*. An interaction of an evolved star with a powerful jet with the luminosity of $\sim 10^{42} - 10^{44} \text{ erg s}^{-1}$ is capable of ablating its upper layers and increasing its effective temperature. Thus such a modified star will deviate from the properties of typical red giants and will not be classified as a late-type star anymore. The jet-induced mass ablation is also size-dependent, affecting more large red giants located at closer separations from Sgr A*, which is consistent with the most recent observations. For more details, see Chapter 4.

Importance: Missing red giants in the Galactic center can potentially be connected to its increased activity in the past few million years.

- **Paper 4: Reverberation-Mapping of HE 0435-4312.**

Description: In this paper, we present a reverberation-mapping campaign of another intermediate-redshift luminous quasar HE 0435-4312. A significant MgII delay of 296_{-14}^{+13} days in the rest frame is found using seven time-delay determination methodologies. In combination with other 68 MgII reverberation-mapped quasars, we further constrained the MgII $R_{\text{BLR}} - L$ relation, $\log(\tau/1 \text{ day}) = (1.67 \pm 0.05) + (0.30 \pm 0.05) \log(L_{3000}/10^{44} \text{ erg s}^{-1})$, which can be used for the SMBH mass determination using single-epoch observations of intermediate-redshift quasars. Using a higher-accreting subsample, we showed that the scatter along the $R_{\text{BLR}} - L$ relations decreases significantly. We showed that the MgII $R_{\text{BLR}} - L$ relation can be applied for constraining cosmological parameters. For more details, see Chapter 5.

Importance: We provide tighter constraints on the MgII radius-luminosity relation using the reverberation-mapping of another high-luminosity quasar and other 68 sources. The relation is found to be significantly flatter than the $H\beta$ radius-luminosity relation. A high-accreting subsample exhibits a radius-luminosity relation with a smaller scatter and we demonstrate its application in cosmology.

- **Paper 5: Enhanced Doppler Beaming.**

Description: Stars orbiting the SMBH in the Galactic center within the inner S cluster with the radius of $\sim 0.04 \text{ pc}$ can reach velocities in excess of 1000 km s^{-1} . At such large velocities, the Doppler boosting of their near-infrared flux density can reach detectable values. In this manuscript, we study the effect of the continuum SED spectral index on the relative flux density variability. In case the orbiting objects are dust-enshrouded, colder or exhibit a significant inverted non-thermal spectrum, the Doppler boosting

of their light can be enhanced by as much as a factor of ~ 4 to 10. For the objects orbiting around Sgr A* with precisely measured trajectories, the amount of photometric variations could be used to constrain their spectral type/nature. For more details, see Chapter 6.

Importance: The amount of Doppler beaming depends on the SED continuum slope, which can be used to quantify it for the sources of known nature in the Galactic center. Subsequently, it can be subtracted from the overall variability. Alternatively, if the trajectory of the unknown object is constrained, the detection of the Doppler beaming along its orbit can be used to determine its nature.

- **Paper 6: Effect of Extinction on Quasar Distances.**

Description: Here we compare two methods used for turning quasars into standardizable candles for the sample of X-ray detected reverberation mapped quasars. In principle, both methods, $R_{\text{BLR}} - L$ and $L_X - L_{UV}$ relations, should give a consistent luminosity distance to the same quasar within the uncertainties. However, we find significant systematic differences, specifically the distribution of the luminosity-distance differences ($\Delta \log D_L = \log D_{L_X - L_{UV}} - \log D_{L_{R-L}}$) has a peak shifted from zero towards positive values and it also deviates from the symmetric Gaussian distribution. We interpret these effects using the model involving the extinction of quasar radiation by the dust in host galaxies. Since dust extinction affects X-ray and UV radiation differently and there are also variations among quasars, the $L_X - L_{UV}$ relation is more affected and should not be used for quasar standardization. For more details, see Chapter 7.

Importance: This work shows that the differences between cosmological constraints given by the $L_X - L_{UV}$ relation on one hand and the broad-line region $R - L$ relation as well as standard cosmological probes on the other hand are not really of a cosmological nature, i.e. a different equation of state of dark energy, but rather they can be addressed by the extinction of UV/X-ray radiation within AGN hosts.

- **Paper 7: UV FeII Emission Model and BLR Time Delays.**

Description: The stratification of the broad-line region material is an important aspect of its geometry and distribution with respect to the SMBH. This is also related to the spectral decomposition of the optical and UV domains in type I quasars. A particular problem is the blending of the MgII broad line and the FeII pseudocontinuum in the UV spectral domain in the rest frame of the source. The correct determination of the MgII line flux depends on the way how the two overlapping emission components are separated. To this goal, we revisit the intermediate-redshift luminous quasar HE 0413-4031. In addition to the eleven years of monitoring by South African Large Telescope (SALT), a near-infrared spectrum was obtained using the SOAR telescope that contained narrow emission lines of H β and [OIII]. This enabled us to obtain a much more precise redshift determination of $z = 1.39117 \pm 0.00017$, which led to a different spectral decomposition of the MgII+FeII region than previously. Overall, the MgII line properties and its time delay with respect to the continuum were not much affected, which confirms that the MgII emission is a reliable SMBH mass estimator and can additionally be applied for cosmological studies. On the other hand, the FeII pseudocontinuum was more affected – for the best-fit FeII model, the FeII rest-frame time delay of 251_{-7}^{+9} days was slightly longer than the MgII time delay of 224_{-31}^{+21} days, which was consistent with the slightly smaller FeII FWHM of $\sim 4200 \text{ km s}^{-1}$, indicating

that the FeII line-emitting material is more distant than the MgII line-emitting material by 27 light days (~ 4700 AU). Moreover, the systematic blueshift of MgII became much smaller ($\sim -200/300$ km s $^{-1}$) than for the previous decomposition and the FeII template. This shows that a precise redshift determination in combination with the more precise FeII emission model can significantly impact the overall assessment of the BLR geometry and kinematics. For more details, see Chapter 8.

Importance: We obtained a better understanding of the MgII/FeII stratification within the broad-line region. Specifically, the UV FeII line-emitting material is located a bit further with respect to the MgII-emitting material. Although the FeII emission properties are quite sensitive to the precise redshift determination and the spectral decomposition of the MgII+FeII spectral complex, the MgII line properties and its time delay are quite stable, which justifies its application for SMBH mass determination and for cosmological studies.

Paper 1: Radio-Optical Properties of Active Galaxies

Supermassive black holes (SMBHs) at the centers of galaxies affect their host galaxies via radiative and mechanical feedback. This is also supported by the correlations between the SMBH mass and the large-scale properties of their hosts, especially the SMBH mass–stellar velocity dispersion correlation ($M_{\bullet} - \sigma_{\star}$) and the relation between the SMBH mass and the bulge–spheroid mass/luminosity.

To better understand the feedback cycle, we focused on the relation between the ionization potential in host galaxies, which is traced by narrow emission-line ratios, and the radio spectral index inferred between the pairs of the following frequencies: 1.4 GHz, 4.85 GHz, and 10.45 GHz. We focused on the radio spectral index between the latter two frequencies since the corresponding flux densities were measured using the Effelsberg telescope with the comparable beam size.

Out of the initial sample of intermediate-redshift radio galaxies ($F_{1.4\text{GHz}} \geq 10$ mJy), we determined the radio spectral index distribution ($\alpha_{4.85-10.45}$) in the optical diagnostic diagrams for 209 sources. Considering how the sources are distributed in the narrow-line optical diagnostic (BPT) diagrams based on their radio spectral index ($F \propto \nu^{+\alpha}$), we found three distinct groups: (i) sources with a steep radio spectral index ($\alpha < -0.7$), with a high ionization ratio, and a large radio loudness; (ii) sources with a flat radio spectral index ($-0.7 < \alpha < -0.4$), with a lower ionization ratio, and an intermediate radio loudness; and (iii) sources with an inverted radio spectral index ($\alpha > -0.4$), a low ionization ratio, and a small radio loudness.

These three groups – (i), (ii), and (iii) – are positioned along the transition zone between the Seyfert and the low-ionization nuclear emission-line region (LINER) galaxies, with group (i) distributed mostly within the Seyfert galaxies and group (iii) among the LINER sources. We interpret these radio spectral index – ionization potential trends as a result of the recurrent nuclear-jet activity with a characteristic timescale. Seyfert galaxies are characterized by an older radio (jet) activity with optically thin large-scale radio structures (jet and lobes), while among LINERs there are sources with the recently renewed jet activity dominated by the compact, optically thick radio core.

Credit: [Zajaček et al. \(2019a\)](#), A&A 630, A83. Reproduced with permission ©ESO.

Radio spectral index distribution of SDSS-FIRST sources across optical diagnostic diagrams[★]

Michal Zajaček^{1,2,3}, Gerold Busch¹, Mónica Valencia-S.¹, Andreas Eckart^{1,2}, Silke Britzen², Lars Fuhrmann², Jana Schneeloch¹, Nastaran Fazeli¹, Kevin C. Harrington^{2,4}, and J. Anton Zensus²

¹ I. Physikalisches Institut der Universität zu Köln, Zùlpicher Strasse 77, 50937 Köln, Germany
e-mail: zajacek@cft.edu.pl

² Max-Planck-Institut für Radioastronomie (MPIfR), Auf dem Hügel 69, 53121 Bonn, Germany

³ Center for Theoretical Physics, Polish Academy of Sciences, Al. Lotnikow 32/46, 02-668 Warsaw, Poland

⁴ Argelander Institut für Astronomie, Auf dem Hügel 71, 53121 Bonn, Germany

Received 8 May 2018 / Accepted 20 June 2019

ABSTRACT

Context. The empirical relations between supermassive black holes and their host spheroids point towards the crucial role of galactic nuclei in affecting the properties of their hosts. A detailed understanding of how the activity of a galactic nucleus regulates the growth of its host is still missing.

Aims. To understand the activity and the types of accretion of supermassive black holes in different hosts, it is essential to study the radio-optical properties of a large sample of extragalactic sources. In particular, we aim to study the radio spectral index trends across the optical emission line diagnostic diagrams to search for potential (anti)correlations.

Methods. To this goal, we combined flux densities from the radio FIRST survey at 1.4 GHz (with the flux density range $10 \text{ mJy} \leq F_{1.4} \leq 100 \text{ mJy}$) for 396 SDSS sources at intermediate redshift ($0.04 \leq z \leq 0.4$) with the Effelsberg radiotelescope measurements at 4.85 GHz and 10.45 GHz. The information about the optical emission-line ratios is obtained from the SDSS-DR7 catalogue.

Results. Using the Effelsberg data, we were able to infer the two-point radio spectral index distributions for star-forming galaxies, composite galaxies (with a combined contribution to the line emission from the star formation and AGN activity), Seyferts, and low ionization narrow emission region (LINER) galaxies.

Conclusions. While studying the distribution of steep, flat, and inverted sources across optical diagnostic diagrams, we found three distinct classes of radio emitters for our sample: (i) sources with a steep radio index, high ionization ratio, and high radio loudness, (ii) sources with a flat radio index, lower ionization ratio, and intermediate radio loudness, (iii) sources with an inverted radio index, low ionization ratio, and low radio loudness. The classes (i), (ii), and (iii) cluster mainly along the transition from Seyfert to LINER sources in the optical diagnostic (Baldwin, Phillips & Telervich; BPT) diagram. We interpret these groups as a result of the recurrent nuclear-jet activity.

Key words. radio continuum: galaxies – methods: observational – techniques: spectroscopic – galaxies: active

1. Introduction

In previous decades, several correlations between the mass of supermassive black holes (SMBH) and the properties of their host spheroids (spheroidal mass, luminosity, stellar velocity dispersion) point towards the co-evolution between SMBHs and host galaxies (see Magorrian et al. 1998; Ferrarese & Merritt 2000; Gültekin et al. 2009; Kormendy & Ho 2013; Busch 2016, and references therein). There are several observational studies that point towards the relationship between black hole activity and star-formation rate in the hosts of active galactic nuclei (AGN, see e.g. Heckman & Kauffmann 2006).

In addition, the observed bimodality in the colours of local galaxies (Strateva et al. 2001; Kauffmann et al. 2003; Baldry et al. 2004; Balogh et al. 2004) points towards the correlation between the star formation activity and the morphological type of the galaxy. The more massive elliptical and lenticular galaxies are preferentially located in the massive red cloud, while less massive spiral and irregular galaxies are located in the blue

cloud. The intermediate region, the so-called “green valley”, is far less occupied (Faber et al. 2007) and the “green” sources belong to mixed types, that is, red spirals. This implies that the AGN are involved in the process of star formation quenching, which is commonly referred to as AGN feedback in galaxy evolution theories and simulations.

A useful tool for distinguishing the galaxies with different prevailing photoionization sources is the Baldwin, Phillips, and Terlevich diagram (BPT, Baldwin et al. 1981), in which the source location is determined by a pair of low-ionization, emission-line intensity ratios. A commonly used pair is the ratio $[\text{N II}]/\text{H}\alpha$ and $[\text{O III}]/\text{H}\beta$ (see Fig. 1, right panel), but ratios of other line intensities of a similar wavelength can be used as well. BPT diagrams include forbidden lines, which are for AGN sources associated with the narrow line region (NLR) and hence type 2 AGN.

The emission-line ratios depend on the strength and shape of the ionizing radiation field, as well as the physical properties of the line-emitting gas including gas density, metal abundances, dust, and cloud thickness (e.g. Veilleux & Osterbrock 1987; Komossa & Schulz 1997; Binette et al. 1997; Groves et al. 2004a,b; Richardson et al. 2016). Systematic trends and

[★] Table A.1 is also available at the CDS via anonymous ftp to [cdsarc.u-strasbg.fr](ftp://cdsarc.u-strasbg.fr) (130.79.128.5) or via <http://cdsarc.u-strasbg.fr/viz-bin/cat/J/A+A/630/A83>

correlations in different sections of the diagnostic diagrams have been traced back to systematic changes in the ionization parameter, the shape of the ionizing continuum, the fraction of matter-bound clouds, and/or the role of metal abundances.

According to a given set of ratios, four spectral classes of galaxies are commonly distinguished. In star-forming galaxies (SF), the ionizing flux is provided mostly by hot, massive, young stars and associated supernovae that are surrounded by HII regions. They have lower $[\text{OIII}]/\text{H}\beta$ and $[\text{NII}]/\text{H}\alpha$ ratios than pure AGN sources (see also Figs. 1 and 2). In between SF and AGN sources are composite (COMP) galaxies, with a mixed contribution from star formation (HII regions) and AGN. The AGN spectral class was further subdivided into Seyfert 2 sources (Sy) and low-ionization nuclear emission regions (LINERs). LINERs are characterized by a lower $[\text{OIII}]/\text{H}\beta$ ratio in comparison with Seyfert 2 AGN sources and a higher $[\text{NII}]/\text{H}\alpha$ ratio with respect to star-forming sources (both SF and COMP).

Systematic changes of line ratios across different regimes, from the HII regime across the composite region and into the AGN regime are seen in spatially-resolved spectroscopy of nearby Seyfert galaxies (e.g. Bennert et al. 2006a,b; Scharwächter et al. 2011), while Schulz & Fritsch (1994) speculated about an ionization sequence from the AGN into the LINER regime, based on systematic continuum-dilution processes.

Radio galaxies are generally considered as active galaxies that are luminous in radio bands. Strittmatter et al. (1980) argued that the radio loudness of quasars, which is typically defined as the ratio of the radio to the optical flux densities, shows a certain degree of bimodality. Kellermann et al. (1989) confirmed the bimodality in the radio loudness in the sense that radio-quiet quasars are five to ten times more frequent than radio-loud quasars, that is, they have radio emission comparable to the optical emission. A similar result was also obtained by Kellermann et al. (2016). Recent studies based on deep radio studies, namely the FIRST (Faint Images of the Radio Sky at Twenty centimeters) and the NVSS (National Radio Astronomy Observatory Very Large Array Sky Survey; Becker et al. 1995; Condon et al. 1998), in combination with sensitive optical surveys SDSS (Sloan Digital Sky Survey) and 2dF (Two Degree Field Survey; York et al. 2000; Croom et al. 2001) demonstrate the large scatter in the radio loudness. They are, however, generally inconclusive about the bimodal character of the distribution (White et al. 2000; Ivezić et al. 2002; Cirasuolo et al. 2003a,b; Laor 2003).

For a sample of galaxies, it was possible to determine the estimates of black hole masses and hence study the dependence of the radio loudness, $R = F_{\nu_R}/F_{\nu_O}$, on the Eddington ratio, $\eta \equiv L_{\text{Bol}}/L_{\text{Edd}}$, where F_{ν_R} and F_{ν_O} are monochromatic radio and optical flux densities at frequencies ν_R and ν_O , respectively, and L_{Bol} and L_{Edd} are the bolometric luminosity and the Eddington limit of the AGN. The general trend found is that the radio loudness increases with a lower Eddington ratio, that is, there seems to be an anti-correlation between R and η with a large scatter (Ho 2002; Sikora et al. 2007). This trend is so far consistent with the hardness-luminosity diagram for X-ray binaries (Fender et al. 2004; Svoboda et al. 2017) and leads to the conclusion that accretion at lower Eddington rates leads to smaller cooling rates, and hence to hot, geometrically thick, and optically thin radiatively inefficient accretion flows (RIAFs, Ichimaru 1977; Rees et al. 1982). RIAFs are often modelled as advection-dominated flows (ADAFs, Narayan & Yi 1995), which can launch jets more effectively (Rees et al. 1982) than colder, optically thick,

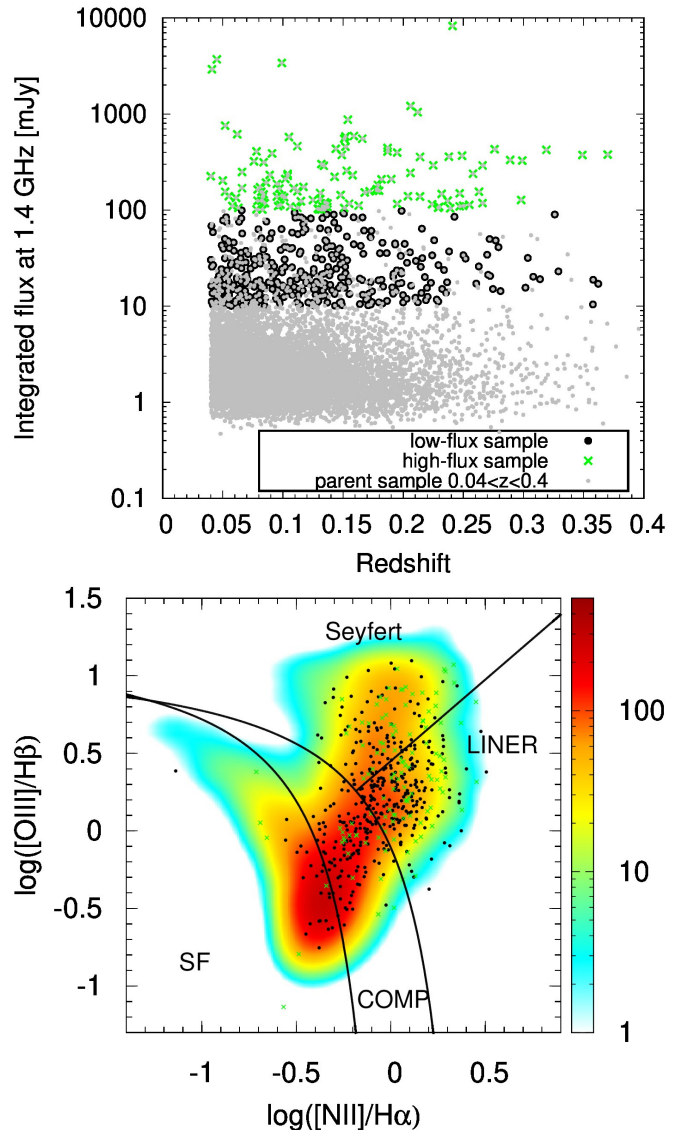


Fig. 1. Distribution of the low-flux and high-flux samples in the redshift-flux plane and in the BPT diagram. *Top panel:* two samples of radio galaxies in the redshift-flux density plane: a high-flux sample of 119 sources previously analysed by Vitale et al. (2015a) and a sample extended towards lower radio flux densities at 1.4 GHz, $10 \text{ mJy} \leq F_{1.4} \leq 100 \text{ mJy}$ (black points). The grey points represent a subset of the parent sample in the redshift range of $0.04 \leq z \leq 0.4$. *Bottom panel:* selected radio galaxies for the Effelsberg observations in the [NII]-based BPT diagnostic diagram (black points). The sample of radio galaxies with $F_{1.4} \geq 100 \text{ mJy}$ analysed by Vitale et al. (2015a) is denoted by green crosses. The parent sample is colour coded depending on the density per bin in the [OIII]–[NII] plane (bin size is set to 0.1 along both ratios).

and geometrically thin accretion discs that are associated with larger Eddington ratios due to efficient cooling (e.g. Shakura & Sunyaev 1973). This yields the trend of larger radio loudness for sources with lower Eddington ratios. However, since $R \propto 1/L_O$, where L_O is the optical luminosity, and $\eta \propto L_O$, the anti-correlation is generally expected and one should be careful when interpreting the results. Moreover, optical emission as a tracer of accretion rate only makes sense for type I AGN, since for type II sources the optical emission is influenced by obscuration and continuum dilution (Schulz & Fritsch 1994). Therefore,

M. Zajaček et al.: Radio spectral index distribution

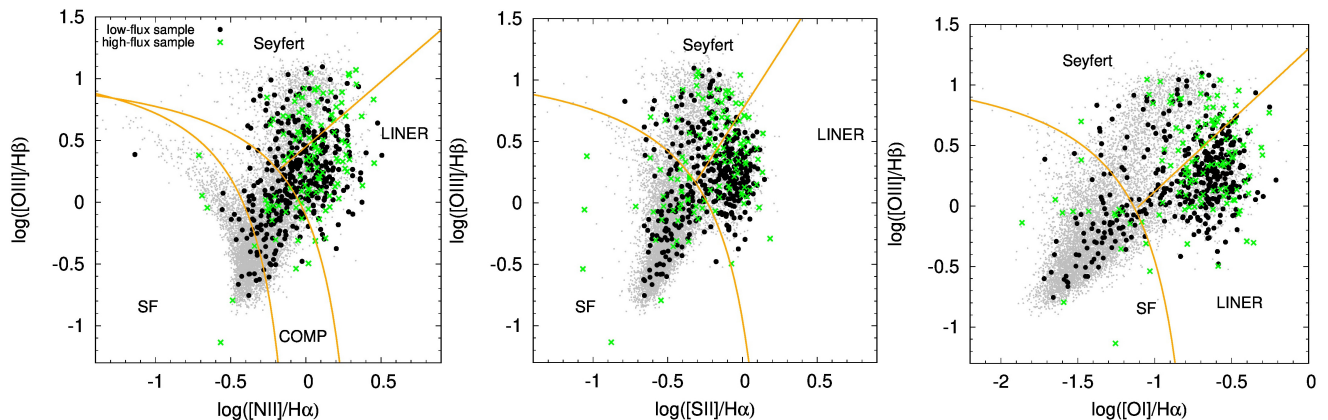


Fig. 2. Low- and high-flux sample distribution in different optical diagnostic (BPT) diagrams. *Left:* [NII]-based diagnostic diagrams of the parent (grey) and Effelsberg samples: a low-flux sample represented by black points and a high-flux sample by green crosses. Demarcation lines were derived by Kewley et al. (2001) to set an upper limit for the star-forming galaxies and by Kauffmann et al. (2003) to distinguish purely star-forming galaxies. The dividing line between Seyferts and LINERs was derived by Schawinski et al. (2007). The new Effelsberg sample (black points), extended towards lower radio fluxes, covers the whole diagnostic diagram. *Middle:* same samples as in the left panel in [SII]-based diagnostic diagram. *Right:* high- and low-flux samples in [OI]-based diagram.

adding more parameters to the study of trends, such as spectral slopes in the radio domain, may shed more light on the radio-optical properties of galaxies and the physical processes involved, namely the formation, acceleration, and collimation of jets (Sikora et al. 2007) or the effect of mergers on the radio loudness of the AGN (Chiaberge et al. 2015).

At frequencies ≤ 10 GHz, the radio-continuum spectra are dominated by non-thermal synchrotron emission with the characteristic power-law slope, $S_\nu \propto \nu^\alpha$, while the thermal bremsstrahlung (free-free) emission is negligible (Duric et al. 1988), contributing less than 10% at 10 GHz (Gioia et al. 1982), and becomes more prominent towards mm-wavelengths. Concerning the synchrotron spectral slope for radio galaxies with jets, primary components (cores) are generally self-absorbed with positive slopes of $\alpha \sim 0.4$, while secondary components have negative spectral indices with mean values $\alpha \sim -0.7$ (Eckart et al. 1986), which is consistent with optically thin synchrotron emission. The integrated radio spectrum of radio jets is typically associated with a flat spectral slope due to the superposition of self-absorbed synchrotron spectra.

The role of radio galaxies in the galaxy evolution at low to intermediate redshifts ($z < 0.7$) is unclear (Tadhunter 2016). In general, the star formation activity in their hosts is expected to be one order of magnitude smaller than for the peak of quasar and star-formation activity at $z \approx 1.9$ (Madau & Dickinson 2014). However, the AGN in these radio galaxies are expected to come through phases of intermittent accretion activity (Czerny et al. 2009), as well as mergers that influence the overall host properties, and are expected to prevent the host gas reservoirs from cooling and forming stars.

The contribution of different sources to the overall radio luminosity of galaxies remains largely unclear. The value of the radio spectral index α helps to distinguish between the prevalence of optically thin and optically thick emission mechanisms. Laor et al. (2019) made use of the high-resolution Very Large Array (VLA) observations at 5 and 8.4 GHz of optically selected radio-quiet (RQ) Palomar-Green (PG) quasars. They determined the corresponding spectral slopes $\alpha_{5/8.4}$ for 25 RQ PG sources and found a significant correlation between the slope value and the Eddington ratio. Specifically, high Eddington-ratio quasars ($L/L_{\text{Edd}} > 0.3$) have steep spectral slopes, $\alpha_{5/8.4} < -0.5$,

while lower Eddington-ratio sources ($L/L_{\text{Edd}} < 0.3$) have flat to inverted slopes, $\alpha_{5/8.4} > -0.5$. A correlation is also found with an Eigenvector I (EV1) set of properties ($\text{Fe II}/\text{H}\beta$, $\text{H}\beta_{\text{asym}}$, X-ray slope α_X ; see Boroson & Green 1992; Sulentic et al. 2000; Marziani et al. 2001), where the flat to inverted RQ PG sources have low $\text{Fe II}/\text{H}\beta$ and a flat soft X-ray slope. Laor et al. (2019) found a dichotomy between radio-quiet PG quasars and 16 radio-loud (RL) PG quasars, which in contrast with RQ sources do not exhibit the correlations with EV1 and the radio slope is instead determined by the black hole mass, which implies a different radiation mechanism for RL sources. These findings provide a motivation for the investigation of further correlations between radio slopes and optical emission-line properties for a larger sample of radio galaxies.

Previously, we performed radio continuum observations of intermediate redshift ($0.04 \leq z \leq 0.4$) SDSS-FIRST sources at 4.85 GHz and 10.45 GHz to determine their spectral index and curvature distributions (Vitale et al. 2015a). This sample included star-forming, composite, Seyfert, and LINER galaxies that obeyed the flux density cut of ≥ 100 mJy at 1.4 GHz (see Fig. 1, green crosses). Vitale et al. (2015a) searched for the radio spectral index trends in BPT diagnostic diagrams as well as for the relation between optical and radio properties of the sources. For the limited sample of 119 sources, they found a rather weak trend of spectral index flattening in the [NII]-based diagnostic diagram along the star-forming–composite–AGN Seyfert branch.

The radio spectral index flattening trend triggered the motivation to study more sources with lower radio continuum fluxes at 1.4 GHz. The sample was extended by 381 additional sources towards lower radio flux densities at 1.4 GHz, with integrated flux densities $10 \text{ mJy} \leq F_{1.4} \leq 100 \text{ mJy}$. Using the cross-scan observations conducted by the 100-m Effelsberg radio telescope, for point-like sources we determined flux densities at two frequencies, 4.85 GHz and 10.45 GHz, which enabled us to determine the spectral indices $\alpha_{[1.4-4.85]}$ (for 298 sources) and $\alpha_{[4.85-10.45]}$ (for 90 sources).

In this paper, we present the findings based on the radio-optical properties of the low-flux sample along with radio-brighter sources previously reported in Vitale et al. (2015a). We searched for any trends of the radio spectral slope in the

low-ionization diagnostic diagrams. In other words, we were interested in whether the changes in emission-line ratios across the BPT diagram are systematically reflected in the radio spectral index. Furthermore, the relation between the spectral index and the radio loudness of the sources was unknown.

The paper is structured as follows. In Sect. 2 we introduce the optical (SDSS survey) and radio (FIRST) samples used in our study. Subsequently, in Sect. 3 we present the selection of radio sources for follow-up observations with the Effelsberg 100-m telescope at two higher frequencies. The basic statistical properties of spectral index distributions are presented in Sect. 4 in combination with the optical properties of the sources. Subsequently, we describe the fundamental trends of the radio spectral slope in optical diagnostic diagrams as well as with respect to the radio loudness in Sect. 5. We continue with the interpretation of the results in Sect. 6. Finally, we summarize the main results in Sect. 7. Additional materials, specifically radio flux densities for new low-flux sources, are included in Appendix A.

2. Radio and optical samples

2.1. Sloan Digital Sky Survey

The Sloan Digital Sky Survey (SDSS) is a photometric and spectroscopic survey of celestial sources that covers one quarter of the north Galactic hemisphere (York et al. 2000; Stoughton et al. 2002). The spectra and magnitudes have been obtained by a 2.5-m wide field-of-view (FOV) telescope at Apache Point in New Mexico, USA. The spectra have an instrumental resolution of $\sim 65 \text{ km s}^{-1}$ in the wavelength range of 380–920 nm. The identified galaxies have a median redshift of 0.1. The spectra were obtained by fibers with $3''$ diameter (the linear scale of 5.7 kpc at $z = 0.1$), which makes the sample sensitive to aperture effects, that is, low-redshift galaxies are dominated by nuclear emission (see e.g. Tremou et al. 2015).

The seventh data release of SDSS (SDSS DR7, Abazajian et al. 2009) contains parameters of $\sim 10^6$ galaxies inferred from the spectral properties based on the Max Planck Institute for Astrophysics (MPIA) and Johns Hopkins University (JHU) emission-line analysis. The stellar synthesis continuum spectra (Bruzual & Charlot 2003) were applied for the continuum subtraction, after which emission line characteristics were derived. In particular, SDSS DR7 contains the emission-line characteristics of low-ionization lines that are used to distinguish star-forming galaxies from AGN (Seyfert galaxies and LINERs or high-excitation and low-excitation systems, respectively) in the diagnostic diagrams. DR7 also contains the source images as well as stellar masses inferred from the broad-band fitting of spectral energy distributions by stellar population models.

2.2. Faint Images of the Radio Sky at Twenty-centimeters Survey

The Faint Images of the Radio Sky at Twenty-centimeters Survey (FIRST Becker et al. 1995) was performed by the Very-Large-Array (VLA) in its B-configuration at 1.4 GHz. The FIRST survey covers $\sim 10\,000 \text{ deg}^2$ in the north Galactic cap, partially overlapping the region mapped by SDSS. The sky brightness was measured with a beam-size of $5.4''$ and an rms sensitivity of $\sim 0.15 \text{ mJy beam}^{-1}$. At the sensitivity level of $\sim 1 \text{ mJy}$, the FIRST survey contains $\sim 10^6$ sources, of which about a third are resolved with structures on the angular scale of $2''$ – $30''$ (Ivezić et al. 2002). The survey contains both the peak and the integrated flux densities, which allows us to distinguish

resolved and unresolved sources. The flux density measurements have uncertainties smaller than 8%. The images for each source are provided on the website.

2.3. SDSS-FIRST cross-identification

As described in Vitale et al. (2015a), we performed a cross-identification of SDSS DR7 and FIRST source catalogues using SDSS DR7 CasJobs, with a matching radius set to $1''$ (OMullane et al. 2005). This results in a total of 37 488 radio-optical emitters as a basis for further studies. This initial sample constitutes $\sim 4\%$ of SDSS sources and contains mostly active, metal-rich galaxies (see also Vitale et al. 2012, for details).

As was already done in Vitale et al. (2015a) for a high-flux sample, we apply the following selection criteria:

- the redshift limits, $0.04 \leq z \leq 0.4$,
- the signal-to-noise lower limit of $S/N > 3$ on the equivalent width EW of the emission lines used in the low-ionization optical diagnostic diagrams.

The lower redshift limit of 0.04 is due to the fact that nearby sources have angular sizes larger than the optical fiber used for the SDSS survey. Hence they are dominated by their nuclear emission (see e.g. Kewley et al. 2003). The upper redshift limit is imposed to make sure that the emission-line diagnostics concerning [N II] and H α lines is reliable, meaning that they fall into the observable spectral window. By imposing the redshift constraints, we obtain our parent sample with 9951 sources, which are shown as grey points in the redshift-flux plot (see Fig. 1). There is no evident dependency of the flux density on the redshift, apart from the expected tendency of having more radio galaxies towards lower radio flux densities.

Out of nearly 10 000 radio sources, only $\sim 1\%$ of the sources has the integrated flux density at 1.4 GHz above 100 mJy. The combined radio-optical properties of these brightest sources were investigated in Vitale et al. (2015a). By decreasing the lower boundary of the flux density cut by one order of magnitude to 10 mJy, the number of sources increases to 5.6%, that is, by a factor of five.

Most of the sources of the parent sample, 93.5%, have flux densities at 1.4 GHz below 10 mJy. Under the assumption that many of these sources have steep to flat spectra, $S_\nu \propto \nu^\alpha$, where $\alpha \leq 0$, the detection of their flux density at frequencies larger than 1.4 GHz would be beyond the detection limit of the Effelsberg telescope, which is $\sim 5 \text{ mJy}$.

In Fig. 1, the subset of the parent sample in the redshift range $0.04 < z < 0.4$ is plotted in the [N II]-diagnostic diagram with the aim of showing the source density in the [O III]–[N II] plane. We see that most of the sources are located in the star-forming composite branch, where AGN are supposed to turn on.

3. Effelsberg sample and observations

The aim of the previous study by Vitale et al. (2015a) was to analyse the radio-optical properties across the parent sample. The radio information was complemented by the radio flux density measurements at two higher frequencies – 4.85 and 10.45 GHz – using the 100-m Effelsberg radio telescope. Vitale et al. (2015a) selected the sources from the parent sample using the lower limit for the integrated flux density of $F_{1.4} \geq 100 \text{ mJy}$ at 1.4 GHz. In total, 119 sources selected according to the criteria above were observed by the Effelsberg radio telescope at two additional frequencies. Thus, for these sources it was possible to determine the spectral slopes $\alpha_{[1.4-4.85]}$ and $\alpha_{[4.85-10.45]}$. This sample is denoted as a high-flux sample and the main

properties of the sources are summarized in Table A.1 of Vitale et al. (2015a).

In Fig. 1, the sample occupies the upper part of the redshift-integrated flux plot. Due to the large radio flux, the sources are dominated by galaxies with an AGN. In the [N II]-based optical diagnostic diagram (BPT diagram) the high-flux radio-optical sample is dominated by composite sources, Seyfert, and LINER galaxies (see green points in Fig. 1). There are only few metal-rich star-forming sources whose radio emission generally originates in the shocks from supernovae and in (re)ignited AGN and jet activity.

Therefore the high-flux sample is certainly not complete in a statistical sense and the results published in Vitale et al. (2015a) are not representative of the whole radio-optical parent sample. This was the main motivation for the extension of the Effelsberg sample towards lower radio flux densities; the integrated radio flux density at 1.4 GHz was considered in the interval $10 \text{ mJy} < F_{1.4} < 100 \text{ mJy}$, that is, we decreased the upper and the lower flux limit of the high-flux sample by one order of magnitude. As shown in Figs. 1 and 2, the low-flux sample (black points) covers the whole [N II]-based diagnostic diagram and its coverage is also more uniform. It should therefore better represent the radio-optical properties of the parent sample. However, the bias towards the AGN and LINER sources is partially maintained, as can be inferred from the [N II]-, [S II]-, and [O I]-based diagrams in Fig. 2.

By imposing the redshift limits $0.04 \leq z \leq 0.4$, as well as the signal-to-noise criterion on the equivalent width of the optical emission lines, $S/N > 3$, the low-flux sample initially consisted of 381 galaxies with the integrated flux densities $10 \text{ mJy} \leq F_{1.4} \leq 100 \text{ mJy}$. These sources were first observed at 4.85 GHz with the 100-m telescope in Effelsberg. Observations were performed between April 2014 and June 2015. The receiver at 4.85 GHz is mounted on the secondary focus of the Effelsberg antenna. It has multi-feed capabilities with two horns, which allow real-time sky subtraction in every subscan measurement. The total intensity of each source was determined via scans in the azimuth and the elevation. According to the brightness of the source, several subscans were used, ranging from 6 up to 24. In the data reduction process, subscans were averaged to produce final subscans used for further processing. Each scan had a length equal to 3.5 of that of the beam size at the corresponding frequency to ensure the correct subtraction of linear baselines.

Before combining the subscans, we checked each for possible radio interference, bad weather effects, or detector instabilities. During each observational run, we observed standard bright calibration sources, such as 3C286, 3C295, and NGC 7027, which were used for correcting gain instabilities and elevation-dependent antenna sensitivity. Finally, we used these sources for the absolute flux calibration. The whole data reduction was performed using a set of Python and Fortran scripts. The flux density was obtained by fitting Gaussian functions to the signal in the averaged single-dish cross scans. Further details on the data reduction can be found in Vitale et al. (2015a), who applied the same routines for brighter sources.

From 381 sources, we managed to determine the reliable flux density at 4.85 GHz for 298 sources. The flux densities range between 350 mJy and 4 mJy with the mean and median values of 30 mJy and 17 mJy, respectively. Other sources were too faint or extended at least in one direction and therefore it was not possible to reliably determine an integrated flux density. For 10.45 GHz observations, 256 sources out of 298 were scheduled for observing based on the extrapolated flux density based on the non-simultaneous 1.4 GHz and 4.85 GHz flux den-

sities. At 10.45 GHz some sources were too faint, were extended at least in one direction, or the reliable flux density determination was not possible due to a higher sensitivity to weather effects at 10.45 GHz. In the end, we obtained flux densities at 10.45 GHz for 90 sources. The maximum and minimum flux densities are 206 mJy and 6 mJy, respectively. The mean and median values are 32 mJy and 19 mJy, respectively. The three non-simultaneous flux densities for 90 sources in the low-flux sample, $F_{1.4}$, $F_{4.85}$, and $F_{10.45}$, are listed in Table A.1, along with the radio spectra for each source as well as the mean radio spectrum for each galaxy spectral class (star-forming, composite, AGN Seyfert, and LINER galaxies).

In the following analysis, unless otherwise stated, we use the low-flux sample in combination with the high-flux sample of Vitale et al. (2015a). For the study of radio continuum properties between 1.4 and 4.85 GHz, we have 298 low-flux sources and 119 high-flux sources available. Between 4.85 and 10.45 GHz, there are 90 low-flux and 119 high-flux sources.

4. Spectral index properties

4.1. General properties of radio spectral index distributions

We present the radio flux densities at 1.4 (FIRST), 4.85, and 10.45 GHz (both Effelsberg) for 90 low-flux sources in Table A.1. The flux densities at 1.4 GHz (FIRST) and 4.85 GHz (Effelsberg) are non-simultaneous (more than one year apart from each other), while the Effelsberg observations at 4.85 GHz and 10.45 GHz were performed within one year of each other.

For high-flux sources, the analysis as well as the optical and the radio images were presented in Vitale et al. (2015a). The catalogue of the high-flux sources is available in Vitale et al. (2015b), where the (quasi)-simultaneous flux densities (obtained during a single observing session) are listed.

For the flux density in the radio domain, we assume the power-law dependency on frequency, using the notation $F(\nu) \propto \nu^{+\alpha}$, where α is the spectral index. Based on the non-simultaneous measurements of flux densities $F_{1.4}$ (FIRST) and $F_{4.85}$ (Effelsberg), we calculated the spectral index $\alpha_{[1.4-4.85]}$ using

$$\alpha_{[1.4-4.85]} = \frac{\log(F_{1.4}/F_{4.85})}{\log(1.4/4.85)}. \quad (1)$$

We note that there is a large beam-size difference between the VLA in the B-configuration and the Effelsberg telescope at 4.85 GHz: the half-power beam-width (HPBW) at 20 cm for the VLA is $\theta_{\text{HPBW}}^{1.4} \approx 4.3''$, whereas for the Effelsberg telescope at 4.85 GHz, $\theta_{\text{HPBW}}^{4.85} \approx 2.4'$. This could have led to the exclusion of extended structures for the VLA measurements for approximately one third of the sources that are clearly extended on the scales of $2''-30''$ (Ivezić et al. 2002) and thus, for such extended sources, it influences the integrated flux densities and spectral indices $\alpha_{[1.4-4.85]}$ as well. Moreover, the observations were more than one year apart from each other, thus possibly contaminated by the variability of the sources. We include the distribution of $\alpha_{[1.4-4.85]}$ for completeness, however, due to the potential beam-size effect, we exclude it from further analysis.

For the spectral index at higher frequencies, $\alpha_{[4.85-10.45]}$, which is determined analogously to Eq. (1) as

$$\alpha_{[4.85-10.45]} = \frac{\log(F_{4.85}/F_{10.45})}{\log(4.85/10.45)}, \quad (2)$$

the effect of excluding extended structures is largely diminished, since for the analysis in this paper we considered only point

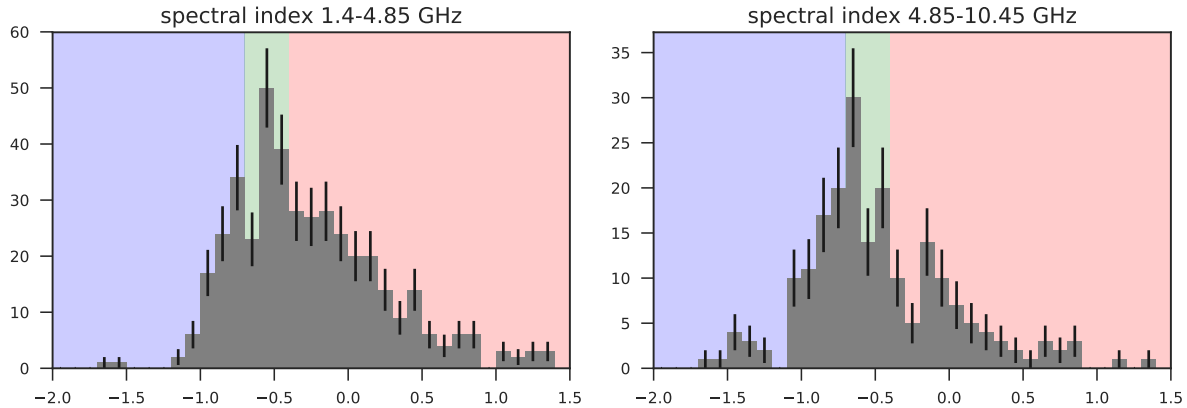


Fig. 3. Distributions of spectral indices $\alpha_{[1.4-4.85]}$ and $\alpha_{[4.85-10.45]}$. *Left panel:* a two-point spectral index ($\alpha_{[1.4-4.85]}$) distribution for the combined low-flux and high-flux sample (in total 417 sources). *Right panel:* a two-point spectral index ($\alpha_{[4.85-10.45]}$) distribution for the combined low-flux and high-flux sample (in total 209 sources).

sources that were consistent with HPBW of 2.4' and 1.1' at 4.85 GHz and 10.45 GHz, respectively. Moreover, the observations at 4.85 GHz and 10.45 GHz were performed within one year of each other, hence the spectral index $\alpha_{[4.85-10.45]}$ captures the integrated radio continuum better than the spectral index $\alpha_{[1.4-4.85]}$, which can be influenced by the core emission due to the small VLA beam width.

The uncertainty of the spectral index σ_α was calculated by propagating the measurement errors of flux densities at the corresponding frequencies,

$$\sigma_\alpha = \frac{1}{|\log(4.85/10.45)|} \sqrt{(\sigma_{4.85}/F_{4.85})^2 + (\sigma_{10.45}/F_{10.45})^2}, \quad (3)$$

where $\sigma_{4.85}$ and $\sigma_{10.45}$ are the measurement uncertainties of flux densities at the corresponding frequencies. We show exemplary error bars in Fig. 4. The median value of σ_α at higher frequencies for the joint sample is $\sigma_\alpha = 0.1$.

The distributions of spectral indices $\alpha_{[1.4-4.85]}$ and $\alpha_{[4.85-10.45]}$ for all observed sources are plotted in Fig. 3 in the left and the right panel, respectively. For the lower frequencies, the mean spectral index is $\bar{\alpha}_{[1.4-4.85]} = -0.25 \pm 0.54$ (median -0.36). For the higher frequencies, the mean spectral index is $\bar{\alpha}_{[4.85-10.45]} = -0.51 \pm 0.63$ (median -0.58). The two-dimensional distribution of spectral indices at both lower and higher frequencies is in Fig. 4.

For the general classification of radio spectra with the power-law shape $F(\nu) \propto \nu^{\alpha}$, we use the following categories based on the spectral slope α :

- (i) $\alpha < -0.7$, for short denoted as steep, which are typical for optically thin synchrotron structures, where electrons have cooled off, such as radio lobes;
- (ii) $-0.7 \leq \alpha \leq -0.4$, denoted as flat, with the mixed contribution of optically thin and self-absorbed synchrotron emission, typical for jet emission;
- (iii) $\alpha > -0.4$, denoted as inverted, which are characteristic for sources where synchrotron self-absorption becomes important, such as in AGN core components.

This division reflects the distributions of the spectral index for lower and higher frequencies as found for samples of radio-loud galaxies, such as in the S5 polar-cap sample (Eckart et al. 1986). We adopt it for all the histograms of the radio spectral index, from Fig. 3 onwards.

The mean and median radio spectra calculated for different spectral classes according to the BPT diagram – star-forming,

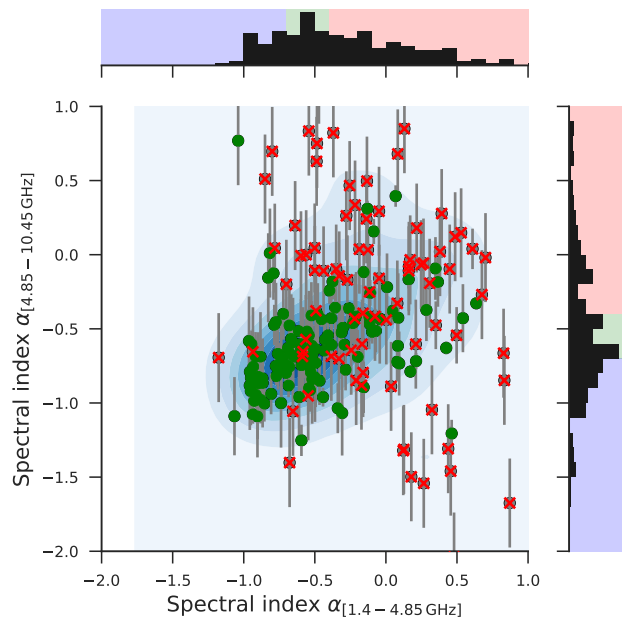


Fig. 4. Two-dimensional distribution of spectral indices at lower (x -axis) and higher frequencies (y -axis). The green points mark the high-flux sources, while the red crosses depict the low-flux sample. Some of the sources have error bars for $\alpha_{[4.85-10.45]}$ to show typical uncertainties of the spectral index.

composites, Seyferts, LINERs – are scaled for comparison in Fig. 5. The values of spectral indices for mean spectra are 0.37, 0.28, 0.39, -0.01 at smaller frequencies 1.4 GHz–4.85 GHz and -0.71 , -0.41 , -0.81 , -0.23 at higher frequencies 4.85 GHz–10.45 GHz for star-forming, composite, Seyfert, and LINER sources, respectively. Spectral indices for median spectra, which were calculated from the spectra of individual sources after the normalization with respect to the mid-frequency, are 0.46, -0.22 , -0.19 , 0.02 at smaller frequencies 1.4 GHz–4.85 GHz and -0.88 , 0.0, -0.59 , 0.13 at higher frequencies 4.85 GHz–10.45 GHz for star-forming, composite, Seyfert, and LINER sources, respectively.

The distribution of spectral indices is very reminiscent of the distribution that one finds for higher redshift quasars. The S5-survey (Kuehr et al. 1981; Gregorini et al. 1984) shows

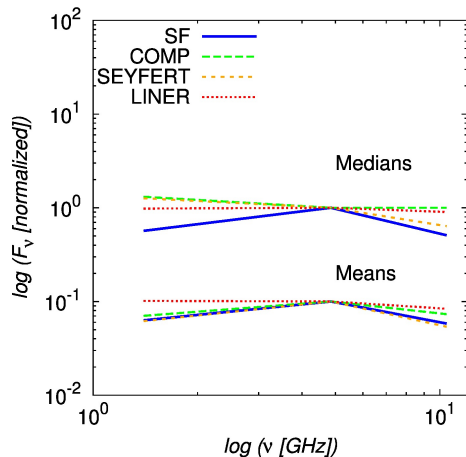


Fig. 5. Median and mean spectra for different spectral classes scaled for the common value at the mid-frequency of 4.85 GHz.

the transition between the lobe and jet-dominated structures, which are more prominent at lower radio frequencies, and the flat to inverted cores that are dominant at higher radio frequencies. Unfortunately, the spectral slope expected from the synchrotron emission of supernova remnants, which are a clear tracer of high-mass star formation, has a similar slope as the radio lobe-jet structures. The radio emission from star-forming regions can be expected to be relevant for objects on the division lines between star-forming and Seyfert/LINER objects. In the Seyfert/LINER domain of the diagnostic diagrams, objects with starburst-AGN mixing can be found (e.g. Kewley et al. 2006; Davies et al. 2016). However, a detailed and sensitive structural investigation at high angular resolution is required to differentiate between the presumably extended radio contribution from star formation and that of the core-jet-nucleus structure of a radio-active AGN. This will be possible with instruments dedicated for low-surface brightness investigations like the Square Kilometer Array (SKA; see e.g. Agudo et al. 2015).

4.2. Radio spectral index between 1.4 and 4.85 GHz

The mean and median values of the spectral index $\alpha_{[1.4-4.85]}$ for the whole low-flux and high-flux sample are in Table 1. LINER sources have the flattest median and mean radio spectral indices in comparison with galaxies in other spectral classes. This is also apparent in the histogram in Fig. 6 (left panel), where we plot the two-point spectral index distribution for each spectral class. Another way of representing this trend is shown in the plot in Fig. 6 (right panel), which combines the radio classification (steep, flat, inverted) and the optical spectral classification of galaxies (SF, Comp, Sy, LINER). While among the composites 50.5% are inverted sources and among the Seyferts 44.5% are inverted sources, most of the LINERS (58.8%) have inverted spectra. The fraction of steep sources ($\alpha < -0.7$) among LINER sources is only 17.6%, which is comparable to composite sources (17.8%). The fraction of steep Seyferts is 28.2%. In terms of the mean and median spectral slopes, LINERS have the flattest index $\alpha_{[1.4-4.85]}$ with a mean of -0.22 and a median of -0.24 , followed by the composites with a mean and median of -0.25 and -0.40 , respectively, and the Seyferts with mean and median values of -0.31 and -0.49 , respectively.

Table 1. Mean, standard deviation, median, 16%- and 84%-values of the radio spectral index $\alpha_{[1.4-4.85]}$, respectively, for each optical spectral class of galaxies and the overall sample.

Spectral class	Mean $\alpha_{[1.4-4.85]}$	σ	Median $\alpha_{[1.4-4.85]}$	16% P	84% P
SF	-0.25	0.45	-0.33	-0.66	0.24
COMP	-0.25	0.54	-0.40	-0.73	0.22
SY	-0.31	0.61	-0.49	-0.83	0.21
LINER	-0.22	0.50	-0.24	-0.72	0.26
Total	-0.25	0.54	-0.36	-0.76	0.24

4.3. Radio spectral index between 4.85 and 10.45 GHz

In an analogous way to frequencies 1.4–4.85 GHz, we determine the spectral index $\alpha_{[4.85-10.45]}$ between the non-simultaneous Effelsberg measurements at 4.85 GHz and 10.45 GHz, with the mean and median values listed in Table 2. In this case, the primary beam size is comparable, hence the resolution effects should not be so significant as for 1.4 GHz obtained from the FIRST survey. Those sources whose emission profiles in cross-scans were clearly extended were excluded from further analysis.

The distribution of the spectral index $\alpha_{[4.85-10.45]}$ for each optical spectral class is in Fig. 7 (left panel). The fractions of three radio classes – steep, flat, and inverted – are calculated for each spectral class in the right panel of Fig. 7, where composites have the largest fraction of inverted sources ($\alpha > -0.4$), 42.9%, followed by LINERs, 37.9%. In terms of the overall fraction of sources with a spectral index larger than $\alpha > -0.7$ (non-steep spectra), composites have the largest fraction with 73.9%, followed by LINERs (66.3%) and Seyferts (58.3%). In the higher frequency range 4.85–10.45 GHz, the composite sources have the flattest spectral slope $\alpha_{[4.85-10.45]}$, with a mean of -0.42 and a median of -0.43 , followed by LINERs with mean and median values of -0.46 and -0.59 , respectively, and Seyferts with a mean and median spectral slope of -0.63 and -0.64 , respectively.

The spectral-index distributions for the high-flux density sample are dominated by sources with low spectral indices as can be seen in the left column of Fig. 8 where we denote high-flux sources as HF and low-flux sources as LF. The $\alpha_{1.4/4.85}$ index distribution has a median of -0.53 and a median width of 0.50^1 . Towards higher frequencies the index even drops and the distribution becomes narrower. The $\alpha_{4.85/10.45}$ index has a median of -0.67 and a median width of 0.20 . However, the distributions have weak tails towards flatter spectra, indicating that several sources contain flat spectrum components at a flux density level lower than the fluxes for the steep components.

Therefore, the situation changes for the low-flux density sample. The flux densities are lower now and for more sources they are close to the typical fluxes of the flat components. Hence, the portion of the sources with flat spectral index increases leading to a more prominent shoulder towards the flat side of the distributions (see the middle and right columns of Fig. 8). This is very pronounced for the $\alpha_{1.4/4.85}$ index. For about 2/3 of the sources (i.e. 89 out of 289) the 10.45 GHz flux drops below the detection limit. Correspondingly, the $\alpha_{4.85/10.45}$ distribution is biased towards flat-spectrum sources. For the low-flux density sample, the $\alpha_{1.4/4.85}$ index distribution has a median of -0.26 and a median width of 0.33 . The distribution is highly skewed to the steep side and has a peak at -0.6 . The $\alpha_{4.85/10.45}$ index

¹ For the uncertainty in the median we quote the median deviation from the median or twice the value if we refer to it as the width.

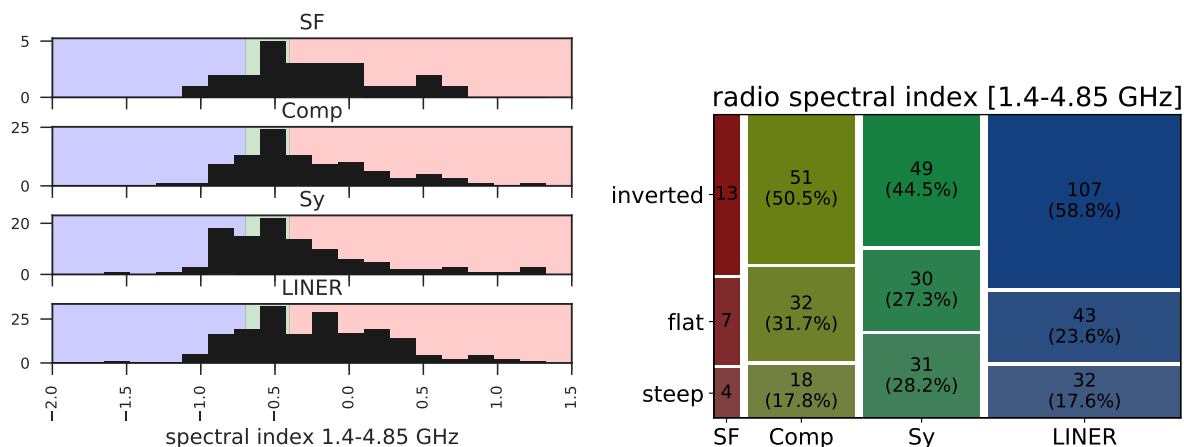


Fig. 6. Distribution of the spectral slope $\alpha_{[1.4-4.85]}$ at lower frequencies among different spectral classes of galaxies. *Left:* two-point spectral index distribution $\alpha_{[1.4-4.85]}$ for different optical spectral classes of galaxies (SF, composites, Seyferts, and LINERs). The mean and median values are listed in Table 1. *Right:* fractional distribution of steep, flat, and inverted sources among star-forming, composite, Seyfert, and LINER galaxies.

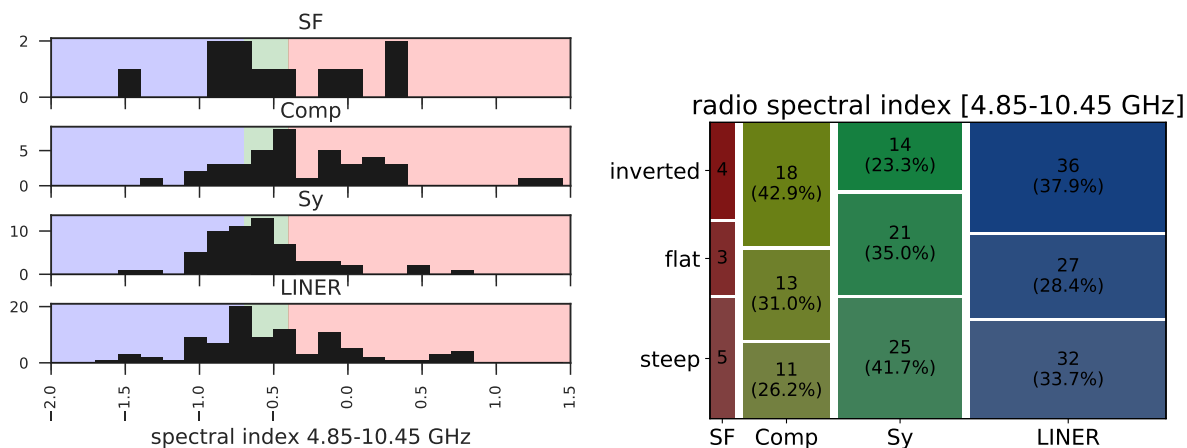


Fig. 7. Distribution of the spectral slope $\alpha_{[4.85-10.45]}$ at higher frequencies among different spectral classes of galaxies. *Left:* two-point spectral index distribution $\alpha_{[4.85-10.45]}$ for different optical spectral classes of galaxies (SF, composites, Seyferts, and LINERs). The mean and median values are listed in Table 1. *Right:* fractional distribution of steep, flat, and inverted sources among star-forming, composite, Seyfert, and LINER galaxies.

distribution has median of -0.25 and a width of 0.86 , with a similar but more pronounced 0.3 wide secondary peak around $\alpha_{4.85/10.45} = -0.10$. Separate plots of the $\alpha_{1.4/4.85}$ index for the sources with (median -0.11 , median width 0.38) and without (median -0.36 , width 0.31) a 10.45 GHz measurement show that the low-spectral index $\alpha_{1.4/4.85}$ of the 10.45 GHz detected sources is also flatter by about 0.25 .

The dropout in sources with $\alpha_{4.85/10.45}$ measurements in our low-flux sample is predominantly an effect of the flux sensitivity we reached. From the uncertainties in Table A.1 we estimate a 3σ flux density limit of 12 mJy. We find that about 70% of all sources without $\alpha_{4.85/10.45}$ measurements indeed fall below this flux density limit if one uses their low-frequency spectral index combined with the 4.85 GHz flux density to predict their 10.45 GHz flux density. A stronger spectral steeping towards 10.45 GHz and the effect of radio-source angular extension may account for the remaining 30% . For the observations at 4.85 GHz, 64 sources out of the original 381 (16.8%) were extended at least in one direction of cross-scans (larger than the HPBW at 4.85 GHz $\sim 144''$). For the subsequent observations at 10.45 GHz of 256 selected sources, we had 50 sources (19.5%) broader than the HPBW of $66''$ at least in one direction. We

excluded the extended sources from further analysis due to the fact that it was not possible to determine flux densities by Gaussian fitting to the combined cross-scan intensity profiles.

In terms of properties in the diagnostic diagrams, the sources with and without $\alpha_{4.85/10.45}$ measurements do not differ significantly. There, median $\log([\text{O III}]/\text{H}\beta)$ and $\log([\text{N II}]/\text{H}\alpha)$ values of 0.23 ± 0.19 and -0.03 ± 0.11 and values of 0.22 ± 0.22 and -0.09 ± 0.14 are reached, respectively. However, as in the high-flux density sample, the trend that the sources with flat-spectrum components show a higher excitation remains: for the sources with $\alpha_{4.85/10.45}$ measurements, we find median $\log([\text{O III}]/\text{H}\beta)$ and $\log([\text{N II}]/\text{H}\alpha)$ values of 0.26 ± 0.19 and -0.03 ± 0.11 , and for the sources without $\alpha_{4.85/10.45}$ measurements, we find $\log([\text{O III}]/\text{H}\beta)$ and $\log([\text{N II}]/\text{H}\alpha)$ values of 0.19 ± 0.26 and -0.10 ± 0.15 , respectively.

5. Trends of the spectral index in optical diagnostic diagrams

While in the previous section we looked for trends in the radio spectral index between different activity classes as traced by

M. Zajaček et al.: Radio spectral index distribution

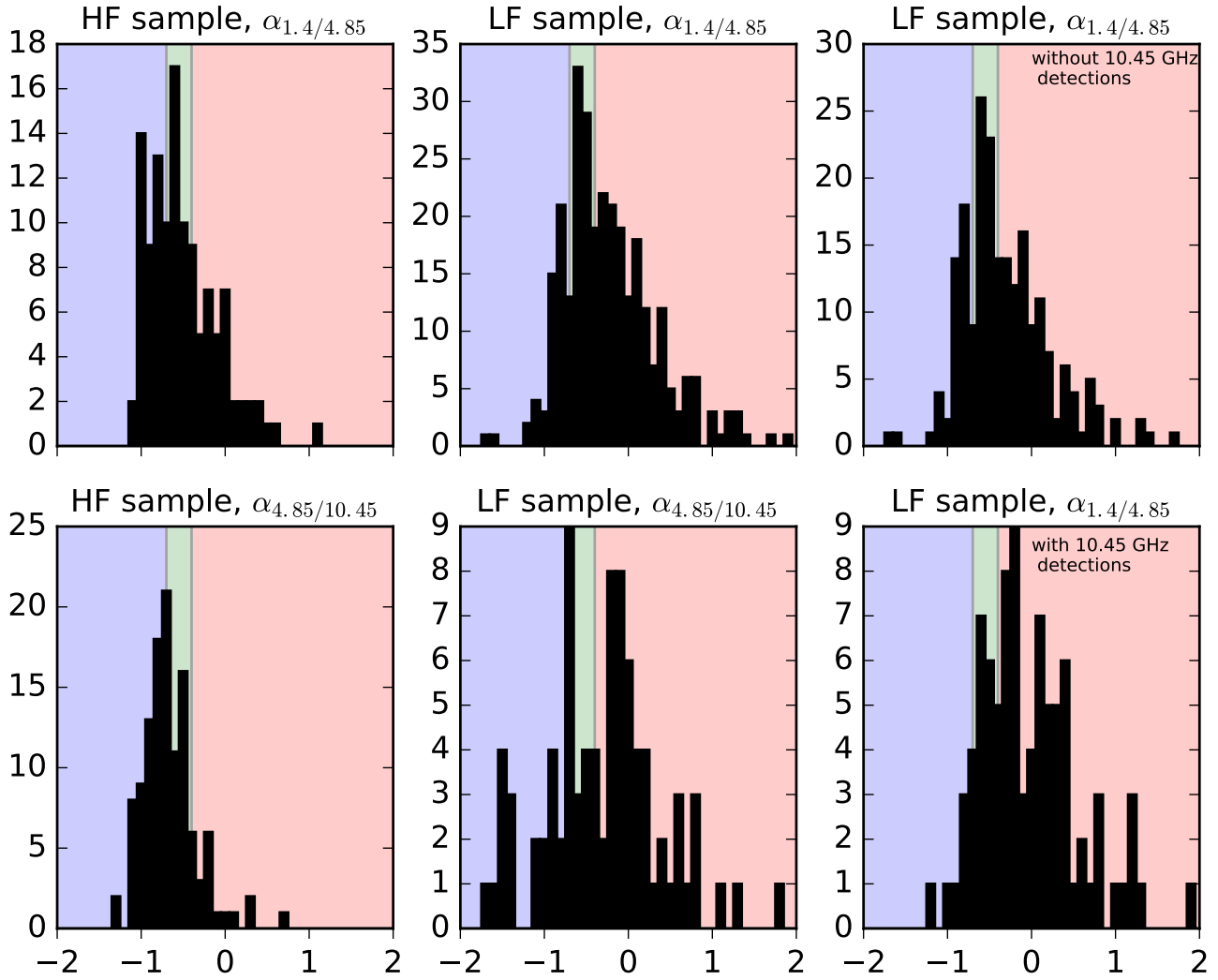


Fig. 8. Low-flux density sample experiences an increasing influence of flat-spectrum sources. *Top and bottom left:* $\alpha_{1.4/4.85}$ and $\alpha_{4.85/10.45}$ index distribution for the high-flux density sample (HF). *Top and bottom middle:* $\alpha_{1.4/4.85}$ and $\alpha_{4.85/10.45}$ index distribution for the low-flux density sample (LF) (two sources – not shown here – have a $\alpha_{4.85/10.45}$ below -3). *Top and bottom right:* $\alpha_{1.4/4.85}$ index distribution for the low-flux sources (LF) without and with 10.45 GHz measurements.

the optical diagnostic diagram, we will pursue the reverse way and investigate how different radio spectral indices are reflected in the optical diagnostic diagram. Considering the radio luminosity of the sources at 1.4 GHz, $L_{1.4\text{GHz}}$, expressed in erg s^{-1} (which traces better the radio-core emission due to a smaller beam size of the VLA), in the parent sample the general trend is that the radio luminosity increases from the star-forming, through the composites, LINERs, and up to the Seyfert sources (Fig. 9, top row). The distribution of radio luminosities implies that our source selection lacks metal-rich star-forming galaxies with radio luminosities below $\log(L_{1.4\text{GHz}}/\text{erg s}^{-1}) < 40.5$, and as redshift increases, systematically fainter sources in all luminosity bins. Hence, our radio measurements and analysis mostly trace nearby luminous, active galaxies in the composite–LINER–Seyfert regions. This is demonstrated in Fig. 9, where we first show the subsample of the parent sample with the

² The integrated flux at $\nu_0 = 1.4$ GHz in Jansky is derived from the FIRST survey. We derive the luminosity distance, D_L , from the redshift, using a standard cosmology with $H_0 = 70 \text{ km s}^{-1} \text{ Mpc}^{-1}$, $\Omega_m = 0.3$ and $\Omega_\Lambda = 0.7$. The luminosity is then given by $L_{1.4\text{GHz}} = 4\pi D_L^2 \nu_0 f_{\nu_0}$.

Table 2. Mean, standard deviation, median, 16%- and 84%- values of the spectral index $\alpha_{[4.85-10.45]}$, respectively, for each optical spectral class of galaxies and the overall sample.

Spectral class	Mean $\alpha_{[4.85-10.45]}$	σ	Median $\alpha_{[4.85-10.45]}$	16% P	84% P
SF	-0.61	0.65	-0.65	-1.02	0.05
COMP	-0.42	0.80	-0.43	-0.90	0.19
SY	-0.63	0.52	-0.64	-0.89	-0.29
LINER	-0.46	0.59	-0.59	-0.95	0.02
Total	-0.51	0.63	-0.58	-0.92	0.00

integrated flux density at 1.4 GHz greater than 10 mJy and less than 1000 mJy (middle row). For the sources detected at 4.85 GHz as well as 10.45 GHz (low + high sample, 209 sources; see the bottom row), we see distribution peaks in the Seyfert–LINER part of the optical diagram as for the flux-limited subsample for all luminosity bins, with the apparent loss of radio sources in the composite and star-forming parts in the lowest luminosity bin, $\log(L_{1.4\text{GHz}}) < 40.5$, due to source drop-outs.

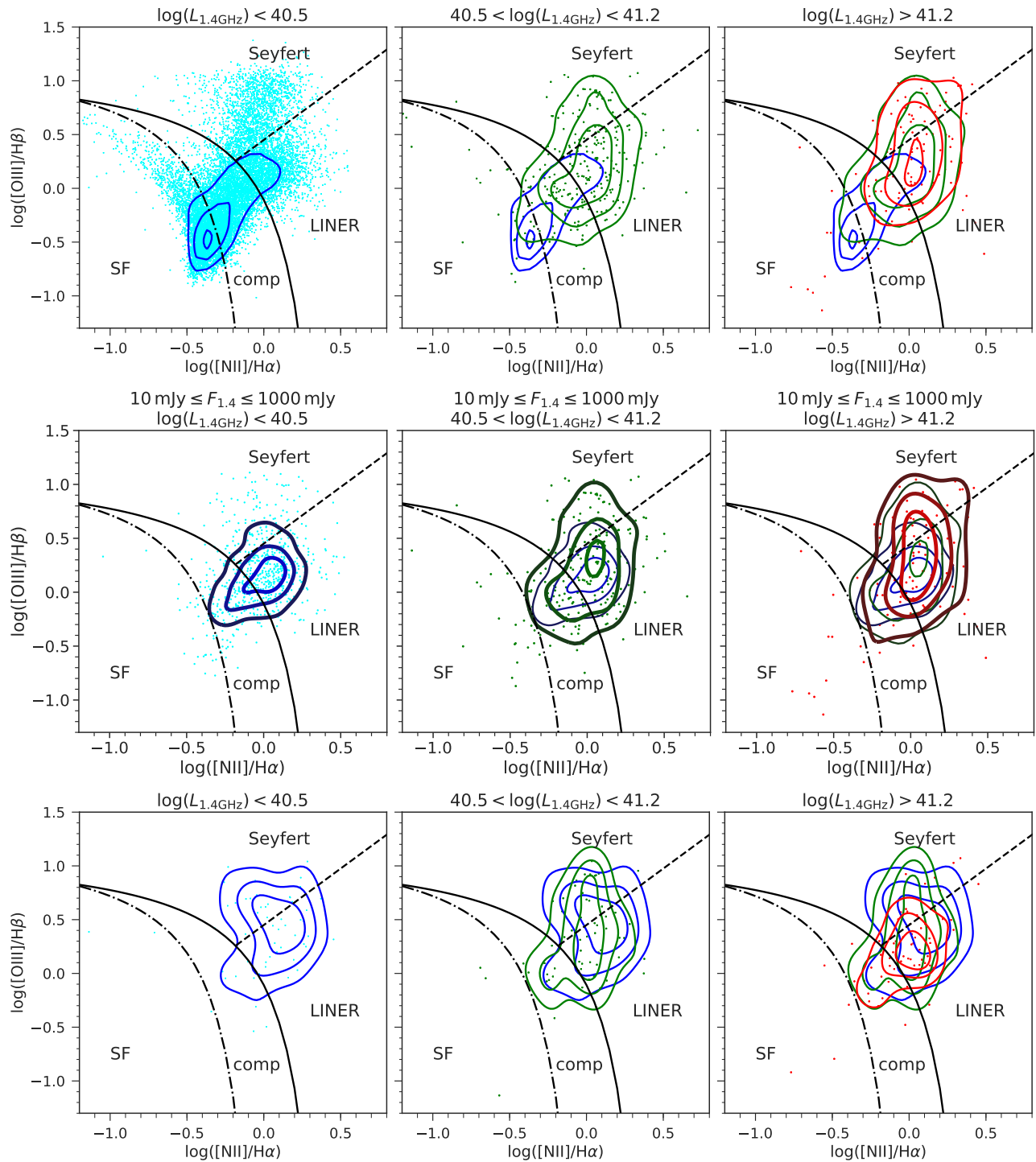


Fig. 9. Distribution of the radio luminosity at 1.4 GHz, $L_{1.4\text{GHz}}$, in optical diagnostic diagrams. *Top row:* distribution of the radio luminosity $L_{1.4\text{GHz}}$ for the parent sample. The contours correspond to the distribution of the sources for the luminosity bins, $\log(L_{1.4\text{GHz}}) < 40.5$, $40.5 < \log(L_{1.4\text{GHz}}) < 41.2$, and $\log(L_{1.4\text{GHz}}) > 41.2$, with the increasing radio luminosity from *left to right*. *Middle row:* distribution of the radio luminosity $L_{1.4\text{GHz}}$ as in the top row but for a flux-limited subsample of the parent sample, $10 \text{ mJy} \leq F_{1.4} \leq 1000 \text{ mJy}$. The luminosity bins are the same as in the *top row*. *Bottom row:* distribution of the radio luminosity $L_{1.4\text{GHz}}$ for the Effelsberg sample only (low + high flux sources). The luminosity bins are the same as in the top row.

Figure 10 shows the position of the sources in all three classical optical diagnostic diagrams, binned by the radio spectral index. Using the previous definitions, we distinguish between steep ($\alpha_{[4.85-10.45]} > -0.7$), flat ($-0.7 < \alpha_{[4.85-10.45]} < -0.4$), and

inverted radio spectra ($\alpha_{[4.85-10.45]} < -0.4$). The plots show that when going from steep via flat to inverted spectra, the optical line ratios, in particular the ratio $\log([\text{OIII}]/\text{H}\beta)$, decrease. This indicates that the ionization potential of sources with inverted

M. Zajaček et al.: Radio spectral index distribution

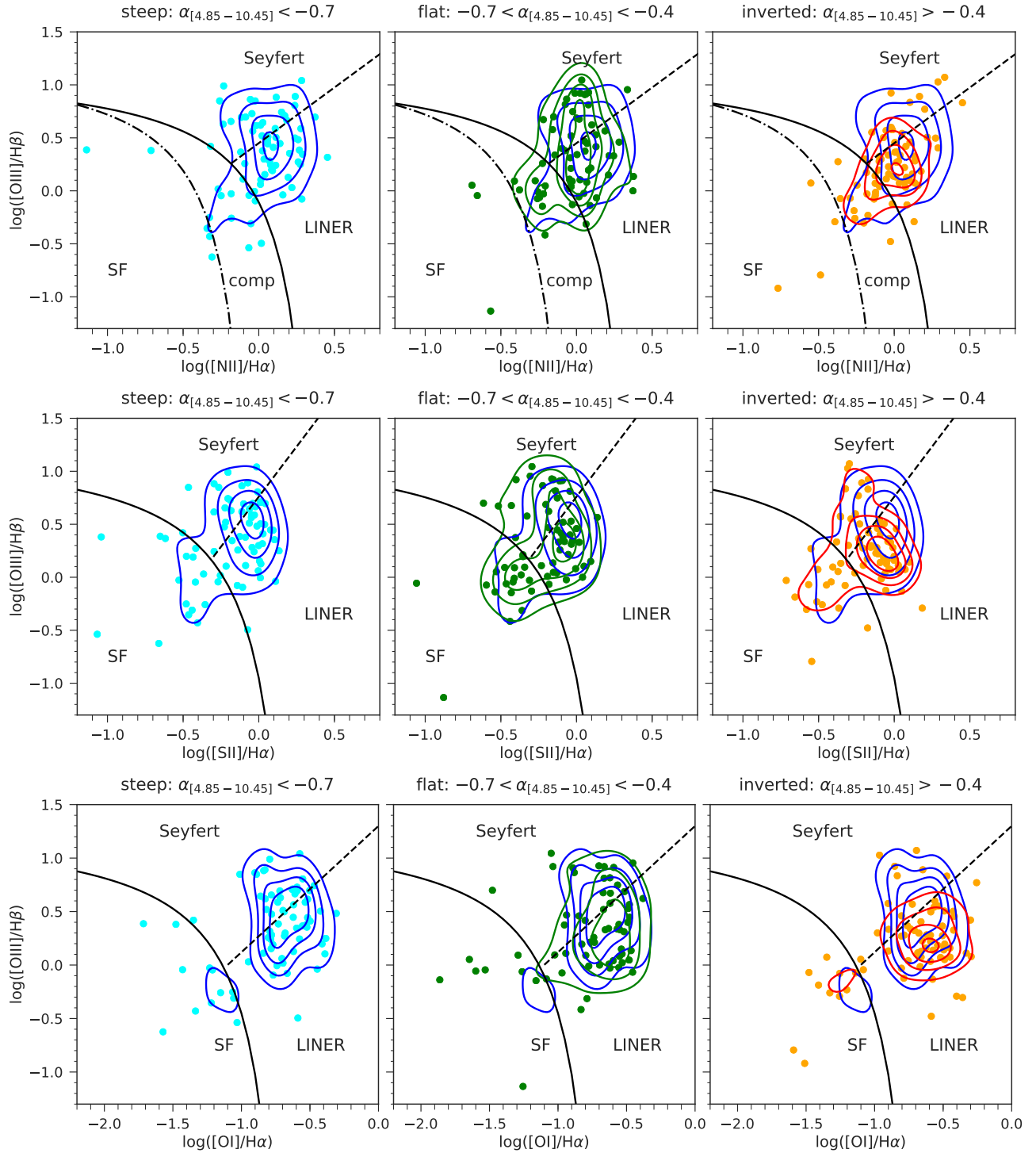


Fig. 10. Spectral index trends in the optical diagnostic diagrams. From *top to bottom panels*: [NII]-, [SII]-, and [OI]-based diagrams, respectively, with the progressively increasing spectral index from the *left to the right panels*: $\alpha_{[4.85-10.45]} < -0.7$, $-0.7 \leq \alpha_{[4.85-10.45]} \leq -0.4$, and $\alpha_{[4.85-10.45]} > -0.4$, respectively. Contours indicate Gaussian kernel density estimates.

radio spectra is weaker than that of sources with a steep radio spectrum.

Since this vertical movement in the optical diagnostic diagram follows the same direction as the usual division line between Seyfert and LINER galaxies (Kewley et al. 2006; Schawinski et al. 2007), this trend will lead to the previously

discussed increase of radio spectral index towards LINER sources, namely that steeper sources tend to fall into the Seyfert and more inverted into the LINER category. Since we select brighter radio emitters with optical counterparts, it is quite possible that all our sources have a contribution from an AGN to some extent.

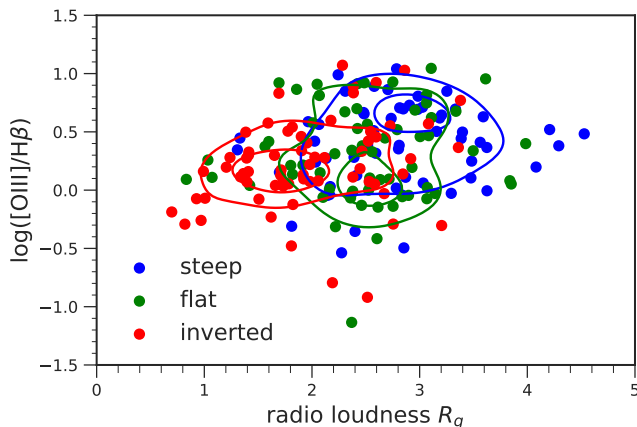


Fig. 11. Clustering of the radio sources in the radio loudness–ionization ratio plane. The galaxies are grouped with respect to the spectral index in the following categories: $\alpha_{[4.85-10.45]} < -0.7$, $-0.7 \leq \alpha_{[4.85-10.45]} \leq -0.4$, and $\alpha_{[4.85-10.45]} > -0.4$.

In the further search for general trends, we added another parameter, radio loudness, which can directly trace the energetics of AGN and their hosts rather than the purely astronomical division into low- and high-flux sources. Using the flux density at 20 cm from FIRST, $F_{1.4}$, we converted the radio flux density into the AB_g -radio magnitude system of Oke & Gunn (1983) according to Ivezić et al. (2002),

$$m_{1.4} = -2.5 \log \left(\frac{F_{1.4}}{3631 \text{ Jy}} \right), \quad (4)$$

in which the zero point 3631 Jy does not depend on the wavelength. Subsequently, the radio loudness can be calculated as the ratio of the radio flux density to the optical flux density,

$$R_g \equiv \log \left(\frac{F_{\text{radio}}}{F_{\text{optical}}} \right) = 0.4(g - m_{1.4}), \quad (5)$$

where we use the optical g -band for each source from the SDSS-DR7 catalogue.

Here we note that the optical flux density is related to the host galaxy and not to the AGN, since our sample is radio selected. An inspection of the optical spectra also shows that only a handful of sources display the typical power-law continuum shape that is associated to the accretion disk. Hence, the radio loudness derived in this way expresses the ratio between the radio power of the AGN to the optical emission of the host galaxy and can be taken as an upper limit of the intrinsic AGN radio loudness.

Figure 11 shows the location of the three radio classes, with steep, flat, and inverted radio spectra in the $R_g - \log([\text{O III}]/\text{H}\beta)$ plane where the radio loudness R_g is along the x -axis and the low-ionization ratio $\log([\text{O III}]/\text{H}\beta)$ is along the y -axis. We show that sources cluster in well-discriminated regions.

To justify these spectral-index categories, we fit a Gaussian mixture model (GMM), which is an unsupervised machine learning algorithm. For this, we consider the quantities radio loudness, R_g , low-ionization ratio, $\log([\text{O III}]/\text{H}\beta)$, and radio spectral index, $\alpha_{[4.85-10.45]}$, as a three-dimensional space; this means every galaxy is represented by a vector

$$\mathbf{x} = \begin{pmatrix} R_g \\ \log([\text{O III}]/\text{H}\beta) \\ \alpha_{[4.85-10.45]} \end{pmatrix}. \quad (6)$$

The GMM assumes that the data points can be described by a superposition of a finite number of multivariate Gaussian distributions with unknown parameters in this parameter space. The model is the probability density function represented as a weighted sum of the Gaussian component densities. Using the model, we can then give probabilities for data points belonging to one of these classes. For the fit, we assume three components and use the expectation maximization technique implemented in the PYTHON library SCIKIT-LEARN (Pedregosa et al. 2011).

In Fig. 12, we show the three classes in the $R_g - \log([\text{O III}]/\text{H}\beta)$ plane and, to represent the third dimension, we show histograms of the radio spectral index $\alpha_{[4.85-10.45]}$. In accordance with our results based on a manual cut in radio spectral index (Fig. 11), we find three distinct classes:

- (1) associated with a steep radio index, high ionization ratio, and high radio loudness;
- (2) associated with a flat radio index, lower ionization ratio, and intermediate radio loudness;
- (3) associated with an inverted radio index, low ionization ratio, and low radio loudness.

6. Interpretation of the results

6.1. General trends in radio-optical properties

By measuring flux densities with the Effelsberg radio telescope, calculating spectral indices, and analysing their distributions in the optical diagnostic diagrams, we can recover these basic trends in the radio-optical properties of our selected sources,

- (a) the radio luminosity increases in the direction of increasing low-ionization ratio $[\text{O III}]/\text{H}\beta$ (see Fig. 9) with the exception of the LINERs, which show lower radio luminosities and low ionization ratios (plus higher stellar masses) compared to the Seyferts with high radio luminosities;
- (b) there is a trend of the radio spectral index steepening in the direction of increasing $[\text{O III}]/\text{H}\beta$ (see Fig. 10);
- (c) the radio loudness increases in the same direction, as shown by Fig. 12.

Our results are representative for the nearby luminous, active SDSS-FIRST sources, which are predominantly located in the AGN (Seyfert-LINER) region of the optical diagnostic diagram. In comparison with previous studies, the determination of spectral indices allows us to connect the radio luminosity and radio-loudness trends (Kellermann et al. 1989; Sikora et al. 2007) with the radio-morphological structures, such as the activity of radio primary components (cores), jet components, and radio lobes, as is known from the studies of quasar and blazar studies (Eckart et al. 1986).

Considering the bolometric luminosities of AGN sources, for which the luminosity of the emission line $[\text{O III}]$ serves as a proxy, there is a trend of less radio-luminous galaxies being located towards lower $L_{[\text{O III}]}$ and these sources have progressively flatter to inverted radio spectra (see the top row of Fig. 13, left panel). On the other hand, more radio-luminous sources have larger $L_{[\text{O III}]}$ and steeper spectra.

To analyse the trends (a), (b), and (c) in relation with the accretion rate \dot{M}_{acc} , we calculate the Eddington ratio, defined as $\eta \equiv L_{\text{bol}}/L_{\text{Edd}}$, where the bolometric luminosity is derived from the $[\text{O III}]$ luminosity using $L_{\text{bol}} = 3500 L_{[\text{O III}]}$ (Heckman et al. 2004) and the Eddington luminosity is $L_{\text{Edd}} = 4\pi GM_{\bullet} m_p c / \sigma_T = 1.3 \times 10^{38} (M_{\bullet}/M_{\odot}) \text{ erg s}^{-1}$. The black-hole masses for SDSS-FIRST sources can be estimated from the black-hole mass–velocity dispersion $M_{\bullet} - \sigma_{\star}$ correlation, using the relation found by Gültekin et al. (2009),

M. Zajaček et al.: Radio spectral index distribution

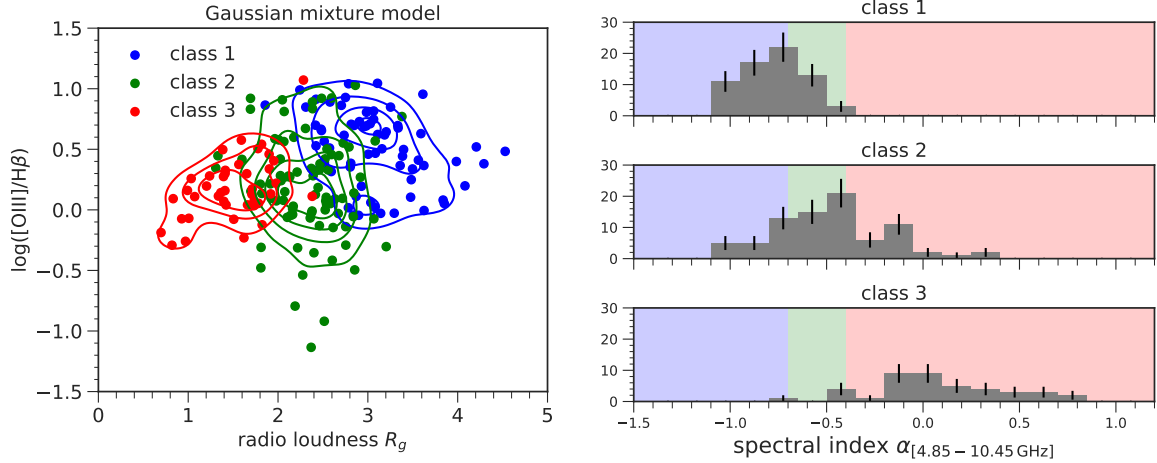


Fig. 12. Results of the Gaussian mixture model. *Left panel:* radio sources in the radio loudness–ionization ratio plane according to the spectral index divisions as found from the Gaussian fitting. *Right panel:* spectral-index histogram with three basic groups that are very similar to the manual cut with these limits: $\alpha_{[4.85-10.45]} < -0.7$, $-0.7 \leq \alpha_{[4.85-10.45]} \leq -0.4$, and $\alpha_{[4.85-10.45]} > -0.4$.

$$\log(M_{\bullet}/M_{\odot}) = 8.12 + 4.24 \log(\sigma_{\star}/200 \text{ km s}^{-1}). \quad (7)$$

In the bottom row of Fig. 13 (left panel), we depict the distribution of the spectral index $\alpha_{[4.85-10.45]}$ with respect to the radio luminosity $L_{1.4 \text{ GHz}}$ and the Eddington ratio η . All sources irrespective of their radio spectral index have very similar Eddington ratios, with 2/3 of them within $\log \eta \sim [-3, -2]$. This similarity in accretion rates is driven by the strong dependency of η on the stellar-velocity dispersion ($\eta \propto \sigma^4$) and the characteristics of our sample: the brightest radio galaxies with optical counterparts (dominated by the stellar emission) on the sky are – mostly – very massive, $M_{\star} \sim 10^{11-12} M_{\odot}$, have a large velocity dispersion, $\sigma_{\star} \sim 180-320 \text{ km s}^{-1}$, and thereby have a heavy SMBH with $\log(M_{\bullet}/M_{\odot}) \sim 8.5$.

6.2. Relation between radio emission and Eddington ratio

Our results seem to be at odds with previous findings that the radio loudness anti-correlates with the Eddington ratio (Sikora et al. 2007; Broderick & Fender 2011). Since the ionization ratio $\log([\text{O III}]/\text{H}\beta)$ is proportional to the hardness of the ionization field, which in turn depends on the accretion efficiency expressed by the Eddington ratio, we find that sources with a lower radio loudness correspond to those with lower ionization ratio and their radio spectral indices are inverted, which is indicative of self-absorbed synchrotron emission (see Fig. 12). On the other hand, the radio-louder sources are associated with larger ionization ratio and their spectral indices demonstrate optically thin synchrotron emission.

Although our sample spans shorter ranges in $L_{1.4 \text{ GHz}}$ and $\log \eta$ when compared with extended samples like that of Sikora et al. (2007), it displays similar luminosities to their broad line radio galaxies (BLRGs) and radio loud quasars (RLQs) when using only core radio powers (see Broderick & Fender 2011) indicating that our sample might represent the narrow line optical counterpart of those objects.

To estimate how our radio-loudness definition and sample selection bias our results, we study integral quantities and compare the sources selected for the Effelsberg observations to the parent sample. One main source of discrepancy could be the use of the host-galaxy optical luminosity in the radio-loudness

calculation (see Eq. (5))³. However, galaxy hosts of Effelsberg sources seem to be quite similar; $\geq 90\%$ of them have elliptical morphologies spanning only around 0.5 dex in g -band luminosities. Therefore we conclude that the main trend of decreasing radio spectral index with radio loudness is caused by the variations in the core radio luminosities.

The basic explanation of the trend of decreasing spectral indices $\alpha_{[4.85-10.45]}$ with the increasing ionization ratio $[\text{O III}]/\text{H}\beta$, which corresponds to the LINER–Seyfert transition in the optical diagnostic diagrams, might be the renewal of AGN activity in the past $\sim 10^5-10^7$ years (Tadhunter 2016; Padovani et al. 2017). At least one third of the sources that have larger $[\text{O III}]/\text{H}\beta$ and steeper radio spectral indices have extended jet structures, that is, radio emission is dominated by older radio lobes, where electrons cooled down. Since the timescales for the formation of the radio extended structures and the optical narrow-line region brightening are quite different, the observed trend can be explained by two scenarios: objects in the Seyfert region must have been optically-active for a long enough period for the radio lobes to develop, or the radio structures formed in the past and their activity has been re-triggered some decades ago.

On the other hand, only 1/8 of the sources with lower ionization ratios display jet-like structures. They might have started (or re-started) their nuclear activity very recently, which could explain inverted spectral indices corresponding to compact self-absorbed core emission. Since they did not have enough time to develop extended radio lobes, their radio luminosities are also smaller.

Visual inspection of FIRST images and literature research for each object in the Effelsberg sample allowed us to classify them as jetted or non-jetted sources. We find that 2/3 of flat and steep radio spectrum objects do not show extended structures that could be related to jet emission. Thus, we do not confirm the one-to-one relation between morphologies and spectral indices (compact/extended versus inverted/flat-steep) found by Massardi et al. (2011).

Our results seem to be in accordance with the correlations found for radio-quiet Palomar-Green quasars by Laor et al. (2019). They found an increase in the line ratio $\text{Fe II}/\text{H}\beta$ from

³ We refrain from using $L_{[\text{O III}]}$ to estimate the optical AGN emission to avoid obtaining an artificial trend by comparing $R \propto 1/L_{[\text{O III}]}$ with $\eta \propto L_{[\text{O III}]}$.

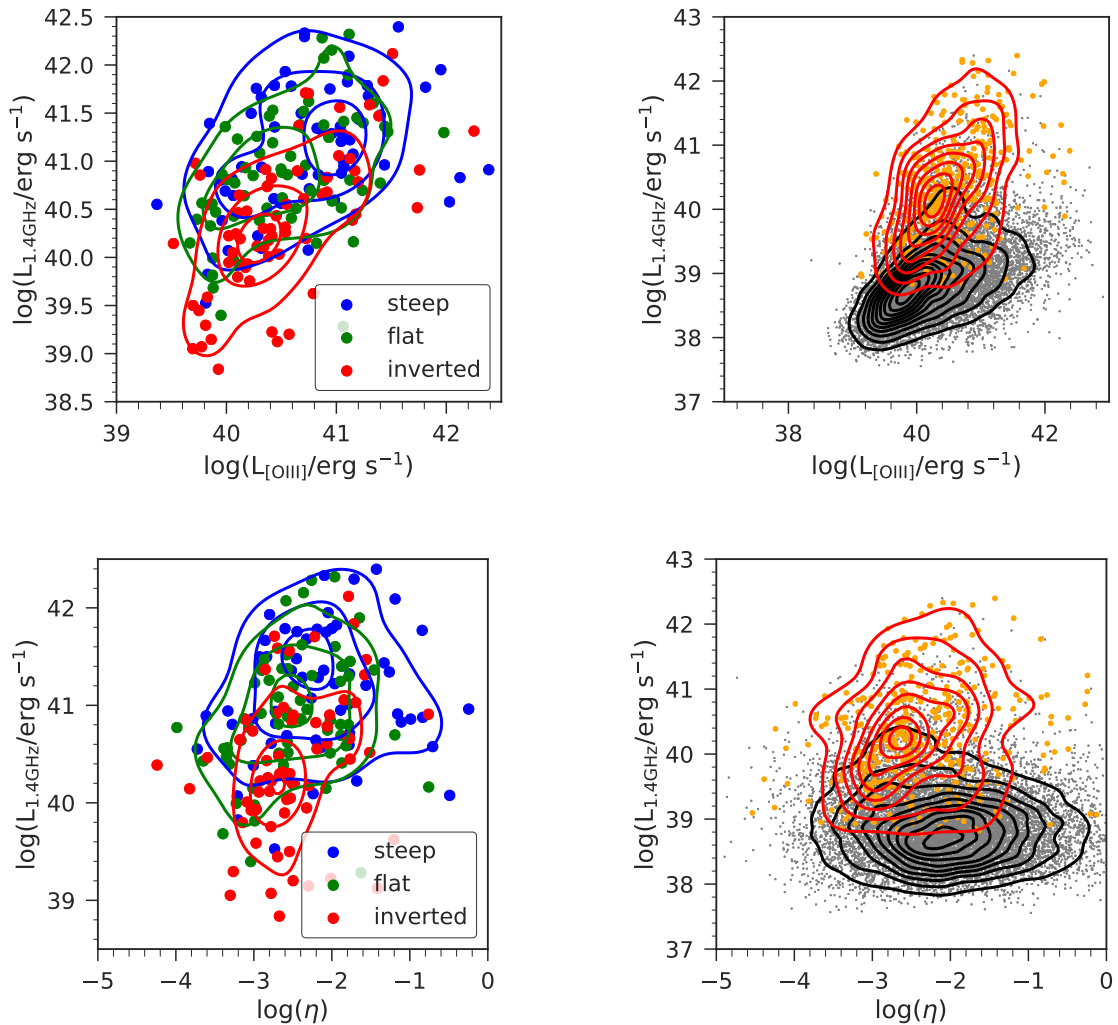


Fig. 13. Distribution of the Effelsberg sources with respect to the radio luminosity, luminosity of [O III] line, and the Eddington ratio. *Top row–left panel:* distribution of the radio spectral index $\alpha_{[4.85-10.45]}$ with respect to the radio luminosity $L_{1.4\text{GHz}}$ and the luminosity of [O III] line. *Right panel:* localization of the Effelsberg sources (low + high flux; orange points) in the plane of $L_{1.4\text{GHz}}$ and $L_{[\text{O III}]}$ with respect to the parent sample (grey points). *Bottom row–left panel:* distribution of steep, flat, and inverted radio spectral indices with respect to the radio luminosity $L_{1.4\text{GHz}}$ and the Eddington ratio η . *Right panel:* distribution of the Effelsberg sources (orange points) in the same plane as in the left figure with respect to the parent sample (grey points).

inverted, through flat, up to steep radio spectral indices, in the same way as we found for [O III]/H β . They interpret the correlations of the radio spectral index with the Eigenvector 1 parameters using the nuclear-outflow interpretation, which at least partially can be used for our findings as well. Higher excitation for steep sources, which are also radio louder (see Fig. 11) could be indicative of a large-scale nuclear outflow, which is a source of optically thin synchrotron emission. On the other hand, sources with lower [O III]/H β with flat to inverted radio slopes, which are radio weaker, could lack an outflow and the dominant source of radio emission would be the compact nucleus (coronal emission) that emits optically thick synchrotron emission.

6.3. Flat and inverted spectral index towards LINERs: Implications for their character

The interpretation and the nature of LINERs remains still unclear and several recent studies have attempted to shed more light on their characteristics and the potential effect of the environment

(Singh et al. 2013; Coldwell et al. 2017, 2018). The fact that $\geq 50\%$ of LINERs in both frequency ranges have flat to inverted spectral indices points to the activity of the nucleus and the dominant contribution of the core and the jet radio emission to the overall radio emission of LINER galaxies.

In our study of the radio-optical properties of SDSS-FIRST sources, LINERs are characterized by a lower ionization ratio [O III]/H β in comparison with Seyfert AGN sources. Keeping in mind the colour-stellar mass sequence (Schawinski 2009), LINERs have the largest stellar and black hole masses (see Fig. 14 for the distribution of stellar and black hole masses across the parent sample and Fig. 15 for the distribution of the average stellar mass across both the parent and the low+high flux sample). In addition, they are associated with redder colours and smaller star formation rates than other optical spectral classes (SF, COMP, Seyfert; Leslie et al. 2016).

The optical low-ionization emission could be explained by the presence of the extended population of hot and old post-asymptotic giant branch (AGB) stars, as is indicated by

M. Zajaček et al.: Radio spectral index distribution

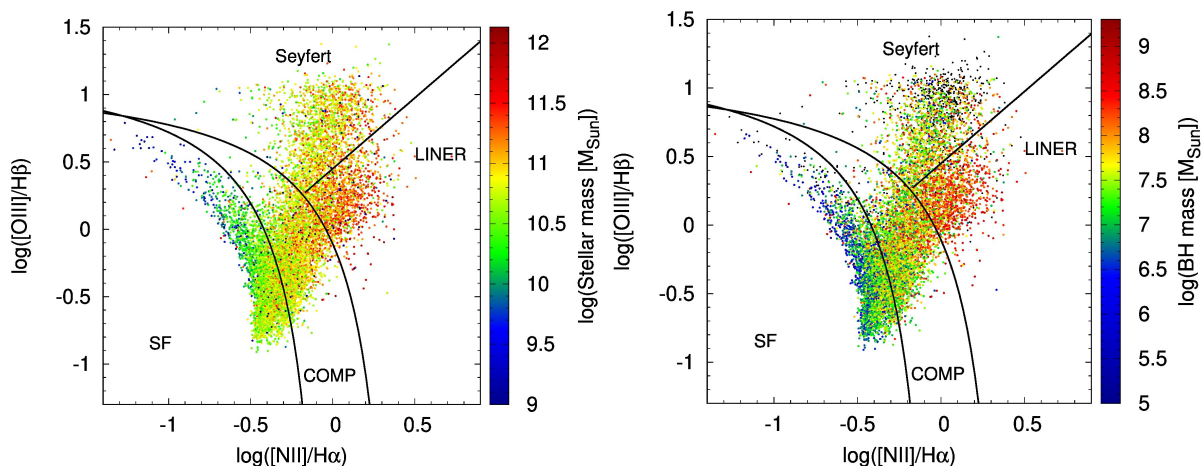


Fig. 14. Distribution of stellar and black-hole masses for the SDSS-FIRST parent sample. *Left panel:* SDSS-FIRST distribution of stellar masses in the optical BPT diagram. The colour bar indicates the logarithm of the stellar masses in units of solar masses. *Right panel:* distribution of the black hole masses inferred from the measurement of the stellar velocity dispersion in the SDSS-FIRST sources.

studying the radial brightness distribution by [Singh et al. \(2013\)](#), which is consistent with a spatially extended ionizing source (stars) rather than a point source (nucleus). However, in the radio domain, the mean spectral indices $\bar{\alpha}_{[1.4-4.85]}$ and $\bar{\alpha}_{[4.85-10.45]}$ indicate the increase in the mean radio spectral slope in comparison with Seyferts (see also the trend of the increasing spectral index in Fig. 10). This trend can be explained by the dominant contribution of the jet emission (the overall flat radio spectrum due to the collective contribution of self-absorbed structures) and the nuclear activity (inverted, optically thick synchrotron source).

Therefore, we cannot support the claim of [Singh et al. \(2013\)](#) that LINERs are defined by the lack of AGN activity, at least not for our subsample of radio-emitting LINERs. The AGN ionizing field is likely not dominant in the optical domain, but according to our statistical study, the nuclear and jet activity must be present. This is also in agreement with the studies of [Coldwell et al. \(2017, 2018\)](#) where they find that LINERs are redder and older than the control sample of galaxies in environments of different density. They also show that LINERs are likely to populate low-density regions in spite of their elliptical morphology, that is, their occurrence in low-density galaxy groups is two times higher than the occurrence of the control, non-LINER galaxies. The fact that LINERs are more likely to be found in low-density regions points towards nuclear activity, since active galaxies typically do not follow the morphology-density relation ([Popesso & Biviano 2006; Coldwell et al. 2009, 2014; Padilla et al. 2010](#)). This also indicates the relevance of major mergers in the galaxy evolution, since the low-density galaxy groups favour major mergers due to lower velocity dispersion among members. Major mergers can restart the nucleus as has been found in several studies ([Popesso & Biviano 2006; Coldwell et al. 2009; Alonso et al. 2007](#)). In addition, [Chiaberge et al. \(2015\)](#) found that major mergers are a trigger for radio-loud AGN and the launching of relativistic jets. Using the luminosity-hardness diagram, which is applied to stellar black hole binaries, [Nagar et al. \(2005\)](#) argue that LINERs seem to occupy a “low/hard” state (geometrically thick and optically thin, hot accretion flows, low Eddington ratio, launching collimated jets), while low-luminosity Seyfert sources are in a “high” state (geometrically thin and optically thick, cold accretion discs, high Eddington ratios, incapable of launching collimated jets). In this picture, LINERs would be characterized by

radiatively inefficient flows with recently (re)started nuclear and jet activity, which could explain their overall lower $[OIII]/H\beta$ ratio in the optical diagnostic diagrams and the increasing spectral index on the transition between Seyfert and LINER sources.

7. Summary

We studied the radio-optical properties of selected cross-matched SDSS-FIRST sources, with a particular focus on the spectral index trends in the optical diagnostic diagrams. Combining the high-flux sample ($S_{1.4} \geq 100$ mJy; [Vitale et al. 2015a](#)) and the low-flux sample presented in this paper ($10 \text{ mJy} \leq S_{1.4} \leq 100$ mJy), we cover a total of 417 star-forming, composite, Seyfert, and LINER sources based on the standard spectral classification using the emission-line ratios. For a total of 209 sources (90 from the low-flux sample and 119 from the high-flux sample) we have flux density measurements at 10.45 GHz.

First, we searched for potential trends of the radial spectral index between the classical optical spectral classes of galaxies. Second, we looked at how the different ranges of the radio spectral index are positioned in the optical diagnostic diagrams. While the first approach yielded basic statistics, the second approach turned out to be more appropriate for our sample in the context of radio-optical trends.

We find a scenario that is largely consistent with models in which the source population shows a dichotomy that reflects a switch between radiatively efficient and radiatively inefficient accretion modes at similarly (compared to QSOs and quasars) low accretion rates. The location of radio sources in the narrow emission-line diagnostic (BPT) diagrams shifts with the increasing importance of a radio-loud AGN away from galaxies dominated by radio emission powered by star formation. Hence, the radio weakness dominates the radio loudness over stellar mass estimate (for the stellar mass, see Fig. 15) and leads to a clear separation from the radio-loud objects. This is seen in the diagnostic diagrams in this paper and has also been put forward by similar investigations (e.g. Fig. A.1 by [Best & Heckman 2012](#)).

Comparing the $\alpha_{1.4/4.85}$ values of all the sources in the low-flux density sample with each other, one finds that while the high-flux density sources are dominated by the steep spectral index components and steepen towards higher frequencies, the low-flux density sample is significantly influenced by the

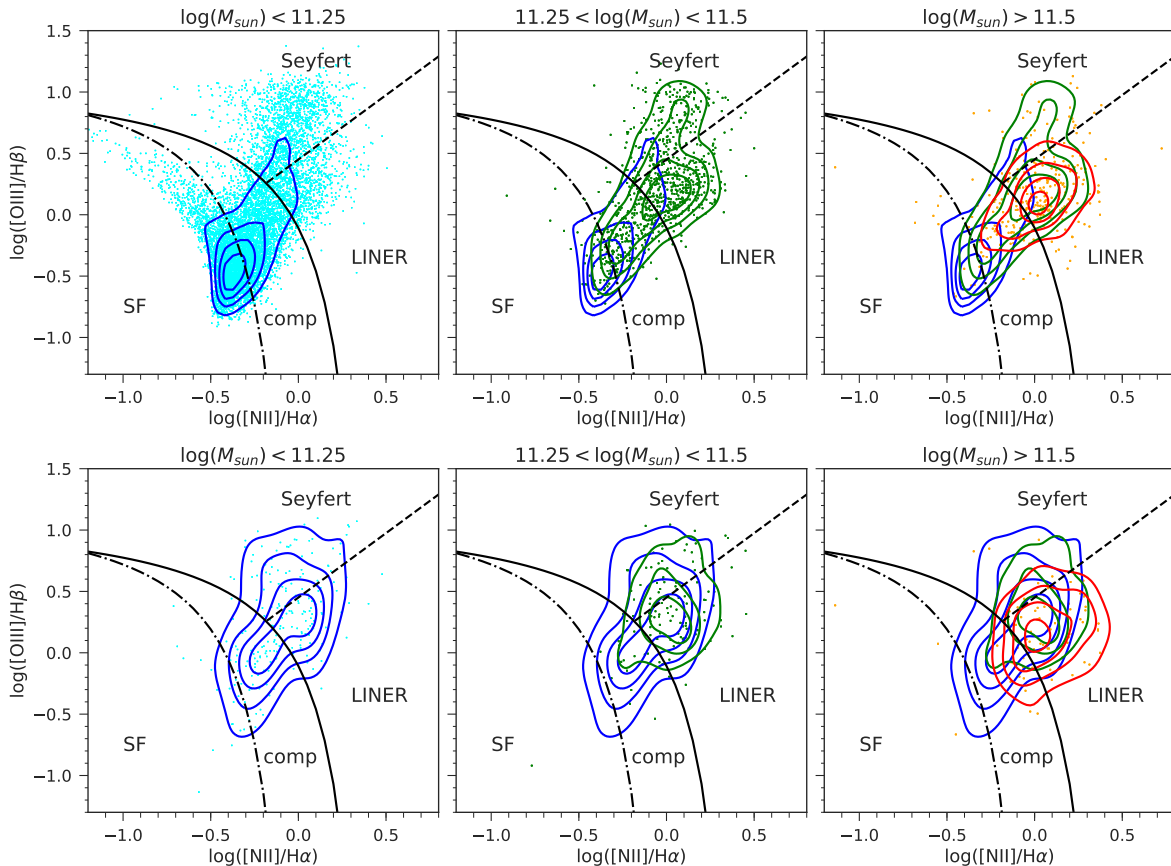


Fig. 15. Distribution of the average stellar mass across the parent and the low + high flux sample. *Top panel:* SDSS-FIRST distribution of stellar masses in the optical BPT diagram for the whole parent sample. From the *left to the right* figures: galaxies with the average stellar mass in the range $\log(M_*/[M_\odot]) < 11.25$, $11.25 < \log(M_*/[M_\odot]) < 11.5$, $\log(M_*/[M_\odot]) > 11.5$, respectively, are represented with density contours. *Bottom panel:* distribution of the average stellar mass across the BPT diagram for the same mass bins as in the *top panel*, but for the combined low + high flux sample.

increasing presence of flat-spectrum components. A detailed investigation of the spectral-index distributions of the high and low-flux density samples shows that in both samples the presence of flat-spectrum components implies a higher excitation in the optical diagnostic diagrams. In particular, the fainter sources that contain a significant contribution by a compact flat-spectrum component can be investigated through the present low-flux density sample.

If we turn to the sources from both samples that have 10.45 GHz measurements and hence a known $\alpha_{[4.85-10.45]}$ value, we find the following: considering steep ($\alpha_{[4.85-10.45]} > -0.7$), flat ($-0.7 < \alpha_{[4.85-10.45]} < -0.4$), and inverted radio spectra ($\alpha_{[4.85-10.45]} < -0.4$), we recovered three basic classes with respect to the radio loudness and ionization ratio $[\text{O III}]/\text{H}\beta$:

- (1) sources with a steep radio index, high ionization ratio, and high radio loudness;
- (2) sources with a flat radio index, lower ionization ratio, and intermediate radio loudness;
- (3) sources with an inverted radio index, low ionization ratio, and low radio loudness.

In the optical diagnostic diagrams, these three classes correspond to the transition from Seyfert to LINER classification in terms of the ionization line ratios. Seyfert sources with higher ionization ratio are dominated by older, optically thin radio emission. Towards the lower ionization ratio, LINERs exhibit a flat to inverted radio spectral index, which is indicative of the

compact, self-absorbed core and the jet emission. In the local Universe, these trends may result from re-triggered nuclear and jet activity.

Acknowledgements. We are grateful to the referee, Brent Groves, for very constructive comments that helped to improve the manuscript. We thank Stefanie Komossa (MPIfR), Pavel Kroupa (University of Bonn), Thomas Krichbaum (MPIfR), Madeleine Yttergren (University of Cologne), Bozena Czerny (CFT PAN), Mary Loli Martinez-Aldama (CFT PAN), and Swayamtrupta Panda (CFT PAN) for very helpful discussions and input. This work was done with the financial support of SFB956 – “Conditions and Impact of Star Formation: Astrophysics, Instrumentation and Laboratory Research” at the Universities of Cologne and Bonn and MPIfR, in which M.Z., G.B., A.E., N.F., S.B., J.-A.Z., K.H. are members of sub-group A2 – “Conditions for Star Formation in Nearby AGN and QSO Hosts” and A1 – “Understanding Galaxy Assembly”, with M.V. and L.F. being its former members. Michal Zajaček acknowledges the financial support by National Science Centre, Poland, grant No. 2017/26/A/ST9/00756 (Maestro 9).

References

- Abazajian, K. N., Adelman-McCarthy, J. K., Agüeros, M. A., et al. 2009, *ApJS*, **182**, 543
- Agudo, I., Boettcher, M., Falcke, H. D. E., et al. 2015, *Advancing Astrophysics with the Square Kilometre Array (AASKA14)*, 93
- Alonso, M. S., Lambas, D. G., Tissera, P., & Coldwell, G. 2007, *MNRAS*, **375**, 1017
- Baldry, I. K., Glazebrook, K., Brinkmann, J., et al. 2004, *ApJ*, **600**, 681
- Baldwin, J. A., Phillips, M. M., & Terlevich, R. 1981, *PASP*, **93**, 5

- Balogh, M. L., Baldry, I. K., Nichol, R., et al. 2004, *ApJ*, 615, L101
- Becker, R. H., White, R. L., & Helfand, D. J. 1995, *ApJ*, 450, 559
- Bennert, N., Jungwiert, B., Komossa, S., Haas, M., & Chini, R. 2006a, *A&A*, 459, 55
- Bennert, N., Jungwiert, B., Komossa, S., Haas, M., & Chini, R. 2006b, *A&A*, 456, 953
- Best, P. N., & Heckman, T. M. 2012, *MNRAS*, 421, 1569
- Binette, L., Wilson, A. S., Raga, A., & Storchi-Bergmann, T. 1997, *A&A*, 327, 909
- Boroson, T. A., & Green, R. F. 1992, *ApJS*, 80, 109
- Broderick, J. W., & Fender, R. P. 2011, *MNRAS*, 417, 184
- Bruzual, G., & Charlot, S. 2003, *MNRAS*, 344, 1000
- Busch, G. 2016, ArXiv e-prints [arXiv:1611.07872]
- Chiaberge, M., Gilli, R., Lotz, J. M., & Norman, C. 2015, *ApJ*, 806, 147
- Cirasuolo, M., Celotti, A., Magliocchetti, M., & Danese, L. 2003a, *MNRAS*, 346, 447
- Cirasuolo, M., Magliocchetti, M., Celotti, A., & Danese, L. 2003b, *MNRAS*, 341, 993
- Coldwell, G. V., Lambas, D. G., Söchting, I. K., & Gurovich, S. 2009, *MNRAS*, 399, 88
- Coldwell, G. V., Gurovich, S., Díaz Tello, J., Söchting, I. K., & Lambas, D. G. 2014, *MNRAS*, 437, 1199
- Coldwell, G. V., Pereyra, L., Alonso, S., Donoso, E., & Duplancic, F. 2017, *MNRAS*, 467, 3338
- Coldwell, G. V., Alonso, S., Duplancic, F., & Mesa, V. 2018, *MNRAS*, 476, 2457
- Condon, J. J., Cotton, W. D., Greisen, E. W., et al. 1998, *AJ*, 115, 1693
- Croom, S. M., Smith, R. J., Boyle, B. J., et al. 2001, *MNRAS*, 322, L29
- Czerny, B., Siemiginowska, A., Janiuk, A., Nikiel-Wroczyński, B., & Stawarz, Ł. 2009, *ApJ*, 698, 840
- Davies, R. L., Groves, B., Kewley, L. J., et al. 2016, *MNRAS*, 462, 1616
- Duric, N., Bourneuf, E., & Gregory, P. C. 1988, *AJ*, 96, 81
- Eckart, A., Witzel, A., Biermann, P., et al. 1986, *A&A*, 168, 17
- Faber, S. M., Willmer, C. N. A., Wolf, C., et al. 2007, *ApJ*, 665, 265
- Fender, R. P., Belloni, T. M., & Gallo, E. 2004, *MNRAS*, 355, 1105
- Ferrarese, L., & Merritt, D. 2000, *ApJ*, 539, L9
- Gioia, I. M., Gregorini, L., & Klein, U. 1982, *A&A*, 116, 164
- Gregorini, L., Mantovani, F., Eckart, A., et al. 1984, *AJ*, 89, 323
- Groves, B. A., Dopita, M. A., & Sutherland, R. S. 2004a, *ApJS*, 153, 9
- Groves, B. A., Dopita, M. A., & Sutherland, R. S. 2004b, *ApJS*, 153, 75
- Gültekin, K., Richstone, D. O., Gebhardt, K., et al. 2009, *ApJ*, 698, 198
- Heckman, T. M., & Kauffmann, G. 2006, *New Astron. Rev.*, 50, 677
- Heckman, T. M., Kauffmann, G., Brinchmann, J., et al. 2004, *ApJ*, 613, 109
- Ho, L. C. 2002, *ApJ*, 564, 120
- Ichimaru, S. 1977, *ApJ*, 214, 840
- Ivezić, Ž., Menou, K., Knapp, G. R., et al. 2002, *AJ*, 124, 2364
- Kauffmann, G., Heckman, T. M., Tremonti, C., et al. 2003, *MNRAS*, 346, 1055
- Kellermann, K. I., Sramek, R., Schmidt, M., Shaffer, D. B., & Green, R. 1989, *AJ*, 98, 1195
- Kellermann, K. I., Condon, J. J., Kimball, A. E., Perley, R. A., & Ivezić, Ž. 2016, *ApJ*, 831, 168
- Kewley, L. J., Dopita, M. A., Sutherland, R. S., Heisler, C. A., & Trevena, J. 2001, *ApJ*, 556, 121
- Kewley, L. J., Geller, M. J., & Jansen, R. A. 2003, in *Amer. Astron. Soc. Meet. Abstr.*, BAAS, 35, 1404
- Kewley, L. J., Groves, B., Kauffmann, G., & Heckman, T. 2006, *MNRAS*, 372, 961
- Komossa, S., & Schulz, H. 1997, *A&A*, 323, 31
- Kormendy, J., & Ho, L. C. 2013, *ARA&A*, 51, 511
- Kuehr, H., Witzel, A., Pauliny-Toth, I. I. K., & Nauber, U. 1981, *A&AS*, 45, 367
- Laor, A. 2003, *ApJ*, 590, 86
- Laor, A., Baldi, R. D., & Behar, E. 2019, *MNRAS*, 482, 5513
- Leslie, S. K., Kewley, L. J., Sanders, D. B., & Lee, N. 2016, *MNRAS*, 455, L82
- Madau, P., & Dickinson, M. 2014, *ARA&A*, 52, 415
- Magorrian, J., Tremaine, S., Richstone, D., et al. 1998, *AJ*, 115, 2285
- Marziani, P., Sulentic, J. W., Zwitter, T., Dultzin-Hacyan, D., & Calvani, M. 2001, *ApJ*, 558, 553
- Massardi, M., Ekers, R. D., Murphy, T., et al. 2011, *MNRAS*, 412, 318
- Nagar, N. M., Falcke, H., & Wilson, A. S. 2005, *A&A*, 435, 521
- Narayan, R., & Yi, I. 1995, *ApJ*, 444, 231
- Oke, J. B., & Gunn, J. E. 1983, *ApJ*, 266, 713
- OMullane, W., Li, N., Nieto-Santisteban, M., et al. 2005, ArXiv e-prints [arXiv:cs/0502072]
- Padilla, N., Lambas, D. G., & González, R. 2010, *MNRAS*, 409, 936
- Padovani, P., Alexander, D. M., Assef, R. J., et al. 2017, *A&ARv*, 25, 2
- Pedregosa, F., Varoquaux, G., Gramfort, A., et al. 2011, *J. Mach. Learn. Res.*, 12, 2825
- Popesso, P., & Biviano, A. 2006, *A&A*, 460, L23
- Rees, M. J., Begelman, M. C., Blandford, R. D., & Phinney, E. S. 1982, *Nature*, 295, 17
- Richardson, C. T., Allen, J. T., Baldwin, J. A., et al. 2016, *MNRAS*, 458, 988
- Scharwächter, J., Dopita, M. A., Zuther, J., et al. 2011, *AJ*, 142, 43
- Schawinski, K. 2009, in *AIP Conf. Ser.*, eds. S. Heinz, & E. Wilcots, 1201, 17
- Schawinski, K., Thomas, D., Sarzi, M., et al. 2007, *MNRAS*, 382, 1415
- Schulz, H., & Fritsch, C. 1994, *A&A*, 291, 713
- Shakura, N. I., & Sunyaev, R. A. 1973, *A&A*, 24, 337
- Sikora, M., Stawarz, Ł., & Lasota, J.-P. 2007, *ApJ*, 658, 815
- Singh, R., van de Ven, G., Jahnke, K., et al. 2013, *A&A*, 558, A43
- Stoughton, C., Lupton, R. H., Bernardi, M., et al. 2002, *AJ*, 123, 485
- Strateva, I., Ivezić, Ž., Knapp, G. R., et al. 2001, *AJ*, 122, 1861
- Strittmatter, P. A., Hill, P., Pauliny-Toth, I. I. K., Steppe, H., & Witzel, A. 1980, *A&A*, 88, L12
- Sulentic, J. W., Zwitter, T., Marziani, P., & Dultzin-Hacyan, D. 2000, *ApJ*, 536, L5
- Svoboda, J., Guainazzi, M., & Merloni, A. 2017, *A&A*, 603, A127
- Tadhunter, C. 2016, *A&ARv*, 24, 10
- Tremou, E., Garcia-Marín, M., Zuther, J., et al. 2015, *A&A*, 580, A113
- Veilleux, S., & Osterbrock, D. E. 1987, *ApJS*, 63, 295
- Vitale, M., Zuther, J., García-Marín, M., et al. 2012, *A&A*, 546, A17
- Vitale, M., Fuhrmann, L., García-Marín, M., et al. 2015a, *A&A*, 573, A93
- Vitale, M., Fuhrmann, L., García-Marín, M., et al. 2015b, *VizieR Online Data Catalog: J/A+A/573/A93*
- White, R. L., Becker, R. H., Gregg, M. D., et al. 2000, *ApJS*, 126, 133
- York, D. G., Adelman, J., Anderson, Jr., J. E., et al. 2000, *AJ*, 120, 1579

Appendix A: Table of the basic radio-optical properties

Here we summarize the information on 90 sources of the low-flux sample, for which we obtained radio flux densities at 4.85 GHz and 10.45 GHz using the 100-m Effelsberg radio telescope. In combination with the integrated flux of these sources at 1.4 GHz, we determined the corresponding spectral slopes.

In Table A.1, we include the redshift z , right ascension RA, declination Dec, integrated flux density at 1.4 GHz as adopted from the FIRST survey catalogue, the measured flux densities at 4.85 GHz and 10.45 GHz, and the corresponding errors. The final column denoted as $[\text{NII}]_d$ is the galaxy spectral type according to the [NII]-based optical diagnostic diagram (BPT diagram): SF denotes star-forming galaxies, COMP composites, SEY Seyfert AGN sources, and LIN stands for LINERs (see also Fig. A.1 for corresponding positions in the [NII]-based BPT diagram).

Table A.1. Sources with the flux densities $10\text{mJy} \leq F_{1.4} \leq 100\text{mJy}$ with measured flux densities at two higher frequencies, 4.85 GHz and 10.45 GHz.

z	RA	Dec	$F_{1.4}$ [mJy]	$F_{4.85}$ [mJy]	Err [mJy]	$F_{10.45}$ [mJy]	Err [mJy]	$[\text{NII}]_d$
0.054	37.92	-1.1677	14.250	27.5	1.3	30.8	3.3	COMP
0.062	116.18	38.6531	19.570	14.9	0.1	10.7	5.1	COMP
0.133	119.36	40.9047	12.800	10.8	0.2	13.0	2.4	COMP
0.095	129.18	53.5757	17.870	26.2	2.5	22.6	4.6	LIN
0.136	130.40	51.9057	40.580	56.5	18.0	17.3	4.2	LIN
0.127	137.97	56.9317	15.100	7.7	0.6	14.6	5.0	LIN
0.216	119.03	38.5669	63.950	20.0	0.9	12.1	2.9	LIN
0.066	119.49	39.9934	99.200	23.0	0.8	13.5	7.9	SEY
0.098	135.66	52.1874	38.440	18.3	0.8	18.2	4.6	SEY
0.069	235.62	52.9975	28.580	33.6	2.7	64.5	6.3	LIN
0.052	234.90	55.5044	31.490	16.9	1.5	17.5	3.3	COMP
0.108	242.15	53.6394	40.340	16.9	0.9	14.5	3.7	COMP
0.199	243.92	47.1866	98.080	182.0	1.9	119.9	7.5	COMP
0.195	246.83	48.5241	23.590	54.6	1.4	44.4	5.2	LIN
0.191	246.58	50.0678	15.670	9.9	1.0	18.6	5.5	LIN
0.055	10.46	-9.3032	40.200	50.2	2.8	15.9	5.5	LIN
0.077	13.03	-9.4912	29.930	51.6	12.3	18.9	3.3	LIN
0.143	20.94	-9.3843	74.240	31.8	0.4	133.1	6.7	LIN
0.103	20.99	-9.6855	14.700	43.4	3.5	12.0	2.8	LIN
0.049	21.32	-8.8737	11.570	135.9	20.4	7.8	2.8	COMP
0.049	21.87	-8.5543	24.250	44.0	5.8	9.2	2.3	SF
0.146	22.93	-8.4370	64.300	32.6	0.8	15.7	3.3	LIN
0.271	23.31	-9.5340	21.170	17.1	1.1	8.7	3.2	SF
0.136	33.21	-9.7125	47.020	22.8	1.3	13.8	2.8	LIN
0.166	31.57	-9.9549	18.720	26.0	1.4	24.9	3.4	LIN
0.081	343.62	-9.2759	27.930	16.2	1.5	14.9	4.1	LIN
0.059	185.77	63.2223	16.500	15.0	1.8	10.9	3.2	COMP
0.131	198.60	62.3294	64.520	181.7	10.3	94.8	7.9	LIN
0.099	250.46	37.3093	22.510	27.5	1.6	25.3	3.9	LIN
0.099	130.52	40.8460	24.430	20.7	1.0	30.3	4.0	LIN
0.236	126.72	39.8121	13.870	38.8	1.1	23.3	3.9	LIN
0.147	127.32	40.0373	10.850	14.2	1.0	16.3	3.8	COMP
0.167	136.84	46.3384	35.100	23.3	0.9	13.6	3.2	SEY
0.192	139.76	47.4986	13.470	7.7	0.9	18.6	4.6	COMP
0.207	145.02	51.0727	16.270	78.2	1.3	58.2	5.9	SEY
0.159	170.12	58.9371	84.050	45.6	3.5	34.1	3.4	SEY
0.234	322.42	0.0892	23.820	12.8	4.8	11.8	5.0	COMP
0.074	326.71	0.3542	10.440	18.4	2.6	6.0	2.3	SF
0.133	151.79	50.3990	30.640	24.3	0.8	25.0	5.1	LIN
0.166	157.93	52.4264	83.670	360.8	3.5	178.0	7.0	SEY
0.055	175.82	55.2777	11.720	18.8	2.8	19.1	2.8	LIN
0.091	196.40	54.0284	23.140	34.6	7.4	15.5	3.2	LIN
0.140	200.69	53.0299	22.790	106.1	74.7	8.2	3.2	SEY
0.137	232.51	43.0404	22.650	16.5	0.8	23.6	15.9	SEY
0.119	234.96	41.7237	19.630	24.0	1.0	22.6	5.0	LIN
0.066	241.43	37.1791	28.190	9.8	0.8	14.5	4.1	SEY
0.110	235.44	47.4652	83.380	68.3	1.3	37.1	5.4	SEY

Notes. Using the symbol $[\text{NII}]_d$, we denote the diagnostics according to the [NII]-based optical diagnostics diagram, where SF stands for star-forming galaxies, COMP composites, SEY represents Seyfert AGN, and LIN denotes LINER sources.

Table A.1. continued.

z	RA	Dec	$F_{1.4}$ [mJy]	$F_{4.85}$ [mJy]	Err [mJy]	$F_{10.45}$ [mJy]	Err [mJy]	[NII] $_d$
0.042	239.97	44.7090	58.810	26.1	0.7	11.6	4.7	LIN
0.173	188.57	50.9069	52.400	57.9	0.7	45.0	4.3	SEY
0.181	173.13	57.5192	35.560	25.4	1.4	22.3	3.3	SEY
0.117	179.04	56.7764	19.940	25.9	9.9	16.3	3.2	LIN
0.047	218.30	52.9631	15.190	11.6	0.9	15.0	3.7	COMP
0.150	243.84	39.9390	28.440	33.1	10.7	12.0	3.3	COMP
0.075	252.55	29.2934	10.220	13.9	1.2	13.2	5.5	LIN
0.168	211.91	40.8988	61.280	23.2	2.2	24.0	4.7	LIN
0.173	219.51	39.5710	17.760	19.7	0.9	33.2	4.8	LIN
0.237	231.28	35.5338	17.740	17.8	1.0	12.7	3.2	COMP
0.055	231.75	35.9770	13.060	12.3	1.1	15.4	3.7	COMP
0.154	239.21	32.9769	18.030	21.1	2.8	7.7	3.2	LIN
0.226	242.04	29.7541	48.500	37.4	6.6	19.5	3.7	SEY
0.112	166.28	46.8885	56.180	45.6	1.2	28.7	3.8	SEY
0.065	205.15	44.8048	82.200	86.0	48.7	43.5	4.5	SEY
0.058	245.20	24.0142	28.520	12.9	1.0	15.0	9.5	COMP
0.050	242.09	28.4787	78.160	120.9	0.2	83.9	4.5	LIN
0.201	233.72	29.1555	44.420	32.8	2.3	20.0	8.4	COMP
0.108	211.83	50.4603	58.400	29.0	1.4	18.7	3.7	SEY
0.040	229.53	42.7459	30.370	20.2	0.8	18.1	4.6	COMP
0.088	113.98	42.2034	17.720	11.0	0.2	6.5	2.3	LIN
0.052	118.18	45.9493	50.150	276.2	27.2	93.7	10.7	SEY
0.044	129.10	56.5974	10.870	17.7	2.3	21.9	4.2	SF
0.084	229.95	27.7727	15.670	28.7	1.1	31.5	8.4	LIN
0.118	238.43	23.8071	64.950	250.5	5.8	168.5	9.3	SEY
0.084	119.20	53.2156	38.980	18.8	0.3	11.1	3.3	LIN
0.122	132.05	60.7737	19.980	34.9	6.5	32.4	3.2	LIN
0.191	137.83	63.1578	13.910	68.4	11.5	11.1	2.8	COMP
0.139	208.31	35.1470	42.090	36.5	1.0	30.1	3.9	LIN
0.115	213.01	29.4671	36.970	31.6	1.4	32.4	5.7	LIN
0.126	213.75	26.8312	22.280	12.2	1.3	21.7	4.7	LIN
0.165	222.05	28.8887	42.410	15.7	1.1	26.8	6.5	LIN
0.069	226.00	24.1049	17.260	12.5	1.2	34.5	5.7	COMP
0.101	237.75	19.2783	30.570	37.8	1.5	36.8	5.2	LIN
0.110	240.91	15.9007	93.750	199.9	2.5	206.0	9.0	COMP
0.229	235.33	14.3696	11.180	26.7	1.0	26.3	4.6	SF
0.149	225.46	16.6183	32.240	26.4	1.4	19.5	4.6	LIN
0.139	214.84	21.6037	20.920	14.8	2.4	18.1	3.7	COMP
0.138	214.04	22.4760	25.650	14.0	0.9	22.7	6.0	LIN
0.151	225.88	19.6523	91.950	86.7	2.4	76.7	5.4	LIN
0.150	230.43	18.2440	93.270	40.2	4.1	13.7	4.6	LIN
0.057	245.57	50.3720	15.660	7.8	0.8	7.8	3.7	COMP
0.104	249.69	27.9109	40.920	26.5	1.4	24.6	4.2	LIN

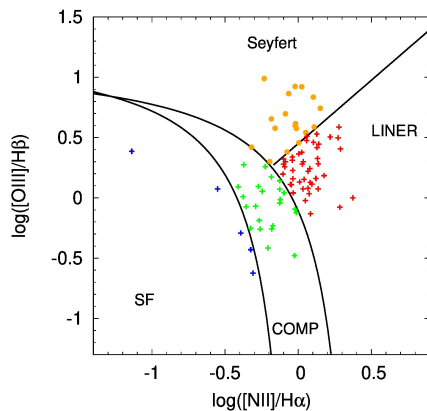


Fig. A.1. Location of the sources from Table A.1 in [NII]-based diagnostic diagram.

Paper 2: Reverberation-Mapping of HE 0413-4031

For low-redshift quasars and Seyfert galaxies, the broad-line region (BLR) radius-luminosity ($R_{\text{BLR}} - L$) relation was established for the broad $\text{H}\beta$ line (486.135 nm in the rest frame). As expected from the simple photoionization theory, the $R_{\text{BLR}} - L$ relation has a power-law form, $R_{\text{BLR}} \propto L^\gamma$, with $\gamma \sim 0.5$. This relation can be used for the estimation of the supermassive black hole masses using just one single-epoch spectrum, hence the $R_{\text{BLR}} - L$ relation has relevance for the understanding of the supermassive black hole growth across the cosmic history.

For higher-redshift quasars, the UV line of MgII is redshifted to the visible portion of the spectrum and can be used for reverberation mapping using optical telescopes. [Czerny et al. \(2019\)](#) established the existence of the MgII $R_{\text{BLR}} - L$ relation using the high-luminosity source CTS C30.10 and nine other sources with lower luminosities.

In this paper, we investigated another high luminosity source – quasar HE 0413-4031 ($z = 1.38$) with the monochromatic luminosity of $\log(L_{3000} [\text{erg s}^{-1}]) = 46.754^{+0.028}_{-0.132}$. The source was monitored for six years using the South African Large Telescope (SALT). Using seven different methods, we established the rest-frame MgII time delay of $302.6^{+28.7}_{-33.1}$ days. Using 11 quasars, we could fit the rest-frame time delay of the MgII line versus the monochromatic luminosity at 300 nm, with the result of $\log(\tau/\text{lt. days}) = (1.45 \pm 0.08) + (0.42 \pm 0.05) \log(L_{3000}/10^{44} \text{ erg s}^{-1})$. Hence, the MgII $R - L$ relation appears to be slightly flatter than the $\text{H}\beta$ relation. The MgII time delay of HE 0413-4031 lies below the best-fit relation, which is in agreement with the found correlation between the rest-frame time delay difference and the Eddington ratio – since HE 0413-4031 is a highly accreting quasar, it leads to the shortening of the BLR time delay.

In addition, we also fitted the broad-band spectral energy distribution of HE 0413-4031 using the relativistic thin accretion disc model. The inferred supermassive black hole mass, $M_{\bullet}^{\text{SED}} = 1.5 \times 10^9 - 3.5 \times 10^9 M_{\odot}$, is in agreement with the virial estimate based on the reverberation mapping, $M_{\bullet}^{\text{RM}}(f_{\text{vir}} = 1) \simeq 1.1 \times 10^9 M_{\odot}$, which provides an independent check of the reverberation-mapping analysis.

Credit: [Zajaček et al. \(2020\)](#), ApJ 896, 146. Reproduced with permission ©AAS.



Time-delay Measurement of Mg II Broad-line Response for the Highly Accreting Quasar HE 0413-4031: Implications for the Mg II-based Radius–Luminosity Relation

Michał Zajaček¹, Bożena Czerny¹, Mary Loli Martínez–Aldama¹, Mateusz Rałowski¹, Aleksandra Olejak¹, Swayamtrupta Panda^{1,2}, Krzysztof Hryniewicz², Marzena Śniegowska¹, Mohammad-Hassan Naddaf¹, Wojtek Pych², Grzegorz Pietrzyński², C. Sobrino Figaredo³, Martin Haas³, Justyna Średzińska², Magdalena Krupa⁴, Agnieszka Kurcz⁴, Andrzej Udalski⁵, Marek Gorski⁶, and Marek Sarna²

¹ Center for Theoretical Physics, Polish Academy of Sciences, Al. Lotników 32/46, 02-668 Warsaw, Poland; zajacek@cft.edu.pl

² Nicolaus Copernicus Astronomical Center, Polish Academy of Sciences, ul. Bartycka 18, 00-716 Warsaw, Poland

³ Astronomisches Institut—Ruhr Universitaet Bochum, Germany

⁴ Astronomical Observatory of the Jagiellonian University, Orla 171, 30-244 Cracow, Poland

⁵ Astronomical Observatory, University of Warsaw, Al. Ujazdowskie 4, 00-478 Warsaw, Poland

⁶ Departamento de Astronomia, Universidad de Concepcion, Casilla 160-C, Chile

Received 2019 October 29; revised 2020 May 17; accepted 2020 May 17; published 2020 June 23

Abstract

We present the monitoring of the active galactic nuclei continuum and Mg II broad-line emission for the quasar HE 0413-4031 ($z = 1.38$) based on the six-year monitoring by the South African Large Telescope (SALT). We manage to estimate a time-delay of $302.6_{-33.1}^{+28.7}$ days in the rest frame of the source using seven different methods: interpolated cross-correlation function, discrete correlation function (DCF), z -transformed DCF, JAVELIN, two estimators of data regularity (Von Neumann, Bartels), and χ^2 method. This time-delay is below the value expected from the standard radius–luminosity relation. However, based on the monochromatic luminosity of the source and the spectral energy distribution modeling, we interpret this departure as the shortening of the time-delay due to the higher accretion rate of the source, with the inferred Eddington ratio of ~ 0.4 . The Mg II line luminosity of HE 0413-4031 responds to the continuum variability as $L_{\text{line}} \propto L_{\text{cont}}^{0.43 \pm 0.10}$, which is consistent with the light-travel distance of the location of Mg II emission at $R_{\text{out}} \sim 10^{18}$ cm. Using the data of 10 other quasars, we confirm the radius–luminosity relation for the broad Mg II line, which was previously determined for the broad H β line for lower-redshift sources. In addition, we detect a general departure of higher-accreting quasars from this relation in analogy to the H β sample. After the accretion-rate correction of the light-travel distance, the Mg II–based radius–luminosity relation has a small scatter of only 0.10 dex.

Unified Astronomy Thesaurus concepts: Accretion (14); Active galaxies (17); Quasars (1319); Radio-loud quasars (1349); Supermassive black holes (1663); Quasars (1319); Spectroscopy (1558)

1. Introduction

Reverberation mapping (RM) of active galactic nuclei (AGNs) is a leading method to study the spatial scale as well as the structure of the broad-line region (hereafter BLR; see Blandford & McKee 1982; Peterson & Horne 2004; Gaskell 2009; Czerny 2019). The method is very time consuming because it requires tens or even hundreds of spectra, covering well the characteristic timescales in a given object. Collected data allow for the measurement of the time-delay of a chosen emission line with respect to the continuum. Assuming light-travel time of light propagation, we thus obtain the characteristic size of the BLR. Subsequent discovery of the relation between the size of the BLR and the source of absolute monochromatic luminosity (Kaspi et al. 2000; Peterson et al. 2004; Bentz et al. 2013) opened a way to measure black hole masses in large quasar samples using just a single-epoch spectrum (e.g., Collin et al. 2006; Vestergaard & Peterson 2006; Shen et al. 2011; Mejía-Restrepo et al. 2018).

The radius–luminosity relation based on the monitoring of the broad H β component is relatively well studied in the case of lower-redshift sources, including nearby quasars (below ~ 0.9 ; Kaspi et al. 2000; Bentz et al. 2013; Grier et al. 2017). For larger redshifts, H β moves to the infrared bands, and in the optical band, the spectrum is dominated by UV emission lines. Sources with redshifts in the range of ~ 0.4 – 1.5 , when the

spectrum is observed in the optical band, become dominated by the Mg II line, and at higher redshifts C IV moves into the optical band. Thus, the single-spectrum methods are used to scale the H β and the other line properties (mostly systematic differences in the line widths) to be able to cover a large spectral range. Direct reverberation measurements in other lines than H β are still rare. In the current paper, we show a new reverberation measurement done in the Mg II line for the redshift larger than one.

The Mg II line seems to be suitable for the black hole mass measurements because, together with H β , it belongs to the low-ionization lines (Collin-Souffrin et al. 1988), and thus should originate close to the accretion disk, where the motion of the emitting material is largely influenced by the potential of the central black hole. Therefore the motion of the Mg II-emitting material is expected to be quasi-Keplerian, i.e., the velocity field is dominantly Keplerian with a certain turbulent component. In analogy to the H β broad component, the Mg II line is virialized (Marziani et al. 2013), while high-ionization lines exhibit clear line profile asymmetries that imply the outflowing motion and the importance of the radiation force.

On the other hand, monitoring of Mg II is more difficult because the line in many sources has very low variability amplitude (Goat et al. 1999; Woo 2008; Zhu et al. 2017; Guo et al. 2020) and/or the timescales at larger redshifts and for more massive (and luminous) quasars are considerably longer.

Also the width of the Mg II line is narrower than the H β broad component, which indicates the position at larger light-travel distances (Marziani et al. 2013). In addition, the Mg II line-emitting gas is evidenced to respond to nonthermal radiation from jets, which may further complicate the RM for radio-loud and γ -ray emitting sources (León-Tavares et al. 2013; Chavushyan et al. 2020).

Successful determination of the line time-delay has been achieved only for 10 sources so far (Metzroth et al. 2006; Shen et al. 2016; Grier et al. 2017; Lira et al. 2018; Czerny et al. 2019), but it nevertheless allowed for the preliminary construction of the radius–luminosity relation based on the Mg II line (Czerny et al. 2019) with the slope close to $R \propto L^{0.5}$ (Panda et al. 2019b) being consistent with the relation for the H β line (Bentz et al. 2013). The key measurement toward larger luminosities came from the bright quasar CTS C30.10 ($z = 0.90052$, $\log [L_{3000}(\text{erg s}^{-1})] = 46.023$) monitored for 6 yr with the South African Large Telescope (SALT). The source CT252, for which the RM was also performed in Mg II line (Lira et al. 2018), alongside CIII] and C IV monitoring, so far had the largest redshift of $z = 1.890$ among Mg II sources.

In this paper, we show the results for the quasar HE 0413-4031 also monitored with the SALT, but brighter ($\log [L_{3000}(\text{erg s}^{-1})] = 46.741$) and located at the redshift of $z = 1.389$ (according to NED⁷). This quasar was found as part of the Hamburg/ESO survey for bright QSOs (Wisotzki et al. 2000). Apart from the quasar spectrum, the source is also radio-loud and belongs to the flat-spectrum radio quasars (FSRQ)—blazars (Mao et al. 2016). In fact, according to the NED database, the radio spectral slope at lower radio frequencies between 0.843 GHz and 5 GHz is inverted with $\alpha = 0.68$,⁸ which indicates a compact self-absorbed radio core. From this, we estimate the flux density at 1.4 GHz, $F_{1.4} \approx 21$ mJy, which implies the monochromatic luminosity per frequency of $L_{1.4} \approx 2.5 \times 10^{26} \text{ W Hz}^{-1} > 10^{24} \text{ W Hz}^{-1}$, based on which HE 0413-4031 can be classified as radio-loud AGN (Tadhunter 2016).

In the analysis, we determine the rest-frame time-delay of the Mg II line using different statistically robust methods—interpolated cross-correlation function (ICCF), discrete correlation function (DCF), z -transformed DCF, JAVELIN, two estimators of data regularity (Von Neumann, Bartels), and χ^2 method. The determined rest-frame time-delay of ~ 303 days turns out to be smaller than the time-delay predicted from the expected radius–luminosity relation, where the radius of the BLR is proportional to the square root of the monochromatic luminosity. Because HE 0413-4031 is a quasar with the accretion rate close to the Eddington limit, which is inferred from the detailed spectral energy distribution (SED) fitting, we demonstrate that the shortening of the measured time-delay is due to the accretion-rate effect in analogy to the H β -based radius–luminosity relation (Martínez-Aldama et al. 2019).

The paper is structured as follows. In Section 2, we present the observational analysis including both spectroscopy and photometry. Subsequently, in Section 3, we analyze the mean spectrum, rms spectrum, spectral fits of individual observations, and the variability properties of lightcurves. The focus of the paper is on the time-delay determination of the Mg II broad-line emission with respect to the continuum using different statistical methods, which is presented in detail in Section 4. In

Section 5, we present the preliminary virial black hole mass and Eddington ratio, and using other measurements of Mg II time-delay, we construct a Mg II–based radius–luminosity relation and demonstrate that the departure of the sources depends on their accretion rate, which leads to the significant time-delay shortening for the highly accreting quasar HE 0413-4031. In the discussion part in Section 6, we discuss the nature of Mg II emission in terms of the source classification along the quasar main sequence, taking into account its radio properties. In addition, we analyze the response of the Mg II line with respect to the continuum variability, which is related to the intrinsic Baldwin effect, and we perform the SED fitting to obtain independently the black hole mass and other parameters related to accretion. Finally, we summarize the main conclusions in Section 7.

2. Observations

The quasar HE 0413-4031, located at redshift $z = 1.389$ according to the NED database, is a very bright source: Véron-Cetty & Véron (2001) report the V magnitude of $M_V = 16.5$ mag. Its position on the sky ($04^{\text{h}} 15^{\text{m}} 14^{\text{s}}$; $-40^{\circ} 23' 41''$) made it a very good target for the spectroscopic monitoring with the SALT. The source was monitored from 2013 January 21 until 2019 August 8. The spectroscopic and photometric data are summarized in Section A in Tables A1–A3.

2.1. Spectroscopy

The quasar was observed using the Robert Stobie Spectrograph on SALT (RSS; Burgh et al. 2003; Kobulnicky et al. 2003; Smith et al. 2006). A slit spectroscopy mode was used, with the slit width of $2''$. Adopted medium resolution grating PG1300 and the grating angle of 28.625, with the filter PC04600, gave a configuration of a spectral resolution of 1523 at 7370 Å. The same configuration has been used in all 25 observations, covering more than six years. A single exposure usually lasted about 820 s, and two exposures were taken during each observation. All observations were performed in service mode. The observation dates are given in Table A1.

The basic reduction of the raw data was done by the SALT staff by applying a semiautomatic pipeline that was a part of the SALT PyRAF package. At the next stage the two images were combined with the aim to remove the cosmic rays as well as to increase the signal-to-noise ratio. The wavelength calibration was performed using the calibration lamp exposures taken after the source observation. In most observations argon lamp was used. Additionally, we checked the calibration using the OI sky line 6863.955 Å because in our observations of another quasar with SALT, the lamp calibration was not very accurate at early years of monitoring. However, for HE 0413-4031 the differences between the lamp calibration and the sky line position were at a level of a fraction of an Angstrom.

Due to the specific design of the SALT, correcting for vignetting is an important issue. For that purpose we used an ESO standard star LTT 4364 (white dwarf, with practically no spectral features in the interesting spectral range), which was observed with SALT in the same configuration as the quasar. Through analytic parameterization of the ratio of ESO and SALT spectrum of the star, we obtained a correction to the spectral shape of a quasar in the observed wavelength range from 6342 to 6969 Å in the observed frame. Formally, the part

⁷ <https://ned.ipac.caltech.edu/>

⁸ We use the flux-frequency convention $F_\nu \propto \nu^{+\alpha}$.

of the spectrum up to 8600 Å is available, apart from two gaps, but the correction of the spectral shape by the comparison star is not satisfactory in this spectral range. Absolute calibration of the SALT spectra was performed using the supplementary photometry.

2.2. Photometry

Spectroscopic observations were accompanied by denser photometric monitoring. For a significant part of our campaign, high-quality data were collected as part of the OGLE-IV survey done with the 1.3 m Warsaw telescope at the Las Campanas Observatory, Chile. Monitoring was performed in the *V* band, with the exposure time 240 s, and the typical error was about 0.005 mag.

We also obtained photometric measurements from the SALT on the same night as the spectroscopic observations were performed, whenever the instrument SALTICAM was available. We used the images obtained in *g* band; usually two exposures were made, with the exposure time 45 s. Because the SALT instrument is not suitable for highly accurate photometric observations, the typical error of this photometry is of the order of 0.012 mag. Because SALTICAM data were collected in a different band from OGLE, we allowed for a grayshift of the SALTICAM set using the periods when the two monitorings overlapped.

Finally, in the period between 2017 December 3 and 2019 March 24, we also performed short, denser monitoring with the 40 cm Bochum Monitoring Telescope (BMT), based at the Universitaetssternwarte Bochum, near Cerro Armazones in Chile.⁹ This monitoring was done in two bands, *B* and *V*, but for the purpose of this work only *V*-band lightcurve has been used. This data set is not entirely consistent with the OGLE + SALTICAM data; there appears to be a slight offset by 0.171 mag, when comparing the earliest BMT point with the last OGLE point. We corrected the magnitude of all the BMT points by this offset, i.e., increasing their magnitudes by 0.171 mag to match the first BMT point with the nearest OGLE point. For comparison, we performed time-delay measurements with this data subset included or not included in the photometric lightcurve. The photometric data points are listed in Tables A2 and A3.

2.3. Spectroscopic Data Fitting

We use the same approach to the modeling of the Mg II region as in Czerny et al. (2019). Because of the potential problems with the remaining vignetting effect, we concentrate only on the relatively narrow spectral band, from 2700 to 2900 Å, in the quasar rest frame. We allow for the following components: (i) power-law component of arbitrary slope and normalization, representing the continuum emission from the accretion disk; (ii) Fe II pseudo-continuum modeled using theoretical templates of Bruhweiler & Verner (2008), folded with a Gaussian of the width representing the kinematic velocity of the Fe II emitter; and (iii) the Mg II line itself. We also test other Fe II templates for completeness, but we discuss this issue separately, in Appendix C.

In our model, the Mg II line is parametrized in general by two separate kinematic components, each modeled assuming a Gaussian or a Lorentzian shape. The amplitudes, the width, and

the separation are the model parameters. Each kinematic component in turn is modeled as a doublet, and the ratio within the doublet components (varying from 1 to 2) depends on the optical depth of the emitting cloud.

The additional parameter is the source redshift, because the determination of the redshift in the NED database is not accurate enough for our data. Because we do not have an independent measure of the redshift from narrow emission lines, we assume that Fe II and one of the Mg II components represent the source rest frame.

All model parameters are fitted together; we do not first fit the continuum, because in the presence of the Fe II pseudo-continuum there is no clear continuum-dominated region and fitting all components at the same time is more appropriate. However, we differentiate between the global parameters and the parameters when modeling individual spectra. We first created a composite spectrum by averaging all observations; for such an average spectrum we determined the redshift, the best Fe II template and the Fe II smearing velocity, and the best value of the doublet ratio, and these values were later kept fixed when individual data sets were modeled.

We calculate the equivalent width (EW) of the lines with respect to the power-law component, within the limits where the model was applied (i.e., integrating between 2700 and 2900 Å). Calculation is done from the model, by numerical integration, and EW(Mg II) contains both kinematic and doublet components.

The reported errors of the fit parameters, including the errors of EWs of Mg II and Fe II, were determined by construction of the error contours—that is, computations for an adopted range of the parameter of interest, with all other parameters allowed to vary. This leads in general to asymmetric errors around the best-fit value. For the requested accuracy, we adopted the χ^2 increase by 2.706, appropriate for one parameter of interest, which represents a 90% confidence level (statistical significance 0.1).¹⁰

2.4. Spectroscopic Flux Calibration and Mg II Absolute Luminosity

The approach to data fitting outlined in Section 2.3 allows only for deriving EW of the Mg II and Fe II lines. However, computations of time-delay require the knowledge of the continuum lightcurve and the line luminosity lightcurve.

A continuum lightcurve is provided by the photometric monitoring, and we use this photometry to calibrate the SALT spectra and to determine the Mg II line flux.

Because we have three instruments providing us with the photometry, and they are of a different quality, as explained in Section 2.2, we first perform the interpolation of the photometry data points at the epochs for which the EW of Mg II is available using the weighted least-squares linear B-spline interpolation, using the inverse of photometry uncertainties as the corresponding weights in the spline interpolation algorithm.

Having established the photometric flux at the time of the spectroscopic measurements still does not allow us to obtain the calibrated spectrum easily. The *V* band does not overlap with the wavelength covered by our spectroscopy (see Section 2.1), and the redshift of our source ($z = 1.389$) corresponds to the rest-frame wavelength of 2304 Å. Therefore,

⁹ <http://www.astro.ruhr-uni-bochum.de/astro/oca>

¹⁰ <https://heasarc.gsfc.nasa.gov/xanadu/xspec/manual/XSerror.html>

we have to interpolate between the V band and the median of our fitting band, 2800 Å rest frame. Because the measurement of the continuum slope in our narrow wavelength range is not very precise, and the slope changes between observations, the use of this slope could introduce an unnecessary scatter into the line flux calibration. Therefore we decided to use the broad-band quasar continuum spectrum of Zheng et al. (1997)¹¹ as a template, and we assumed that the ratio between the flux at 2304 Å (corresponding to the V band in our quasar) and a continuum at 2800 Å in HE 0413-4031 is always the same as in the template.

This gave us a relation between the V magnitude and the 2800 Å continuum νF_ν flux at 2800 Å, F_{2800} :

$$\log F_{2800} = -0.4V - 8.234 \text{ [erg s}^{-1} \text{ cm}^{-2}] \quad (1)$$

This is of course an approximation, but the amplitude of the flux variations in our source is not very large so the issue of a spectrum becoming bluer when the quasar is brighter (see, e.g., Ulrich et al. 1997; Wilhite et al. 2005; Kokubo 2015, and the references therein) should not be critical.

3. Results: Spectroscopy

3.1. Mean Spectrum

We first combined the SALT spectra in order to establish the global source parameters, which will be fixed later in the analysis of all 25 spectra.

The mean spectrum is shown in Figure 1 (top panel). For comparison, in Figure 1 (middle panel) we also show the spectrum in the early epoch (#5), when the quasar was close to the minimum flux density, as well as the spectrum from the later epoch close to the maximum flux density (#20, bottom panel). The Mg II line shape in this quasar looks simple, immediately suggesting that HE 0413-4031 belongs to class A quasars (Sulentic et al. 2000). We checked that assuming just a single kinematic component of Lorentzian shape for Mg II is sufficient, and adding the second component does not improve the χ^2 significantly. The best fit for a 2-component model allows for 0.2% contribution from the second kinematic component, which is very broad (11,140 km s⁻¹), and the total χ^2 for such a fit is better than in a single-component fit only by 1.0. The source is thus a typical representative of class A sources. We also checked that a Lorentzian shape offers much better representation of the line shape than the Gaussian. If we assume a single kinematic component with a Gaussian shape, the reduced χ^2 of the best fit is 16.0 per degree of freedom. If we allow for 2 Gaussian kinematic components, one with no shift with respect to Fe II and the second one at arbitrary position, the fit improves (reduced $\chi^2 = 7.7$) but still does not match the one with a single Lorentzian shape, despite the higher number of parameters. We note that in the case of the 2-Gaussian fit, the component bound to Fe II dominates (contains 57% of the line flux), which happened at the expense of the overall Fe II contribution, which dropped down by a factor of 3 in comparison with a single Lorentzian fit. However, such a fit is not favored by the data. The single-component Lorentzian profile typical of population A sources (Sulentic et al. 2000) arises due to the turbulence in the line-emitting clouds, and the broadening of the line is due to the rotation (Kollatschny & Zetzl 2011; Goad et al. 2012; Kollatschny & Zetzl 2013a, 2013b).

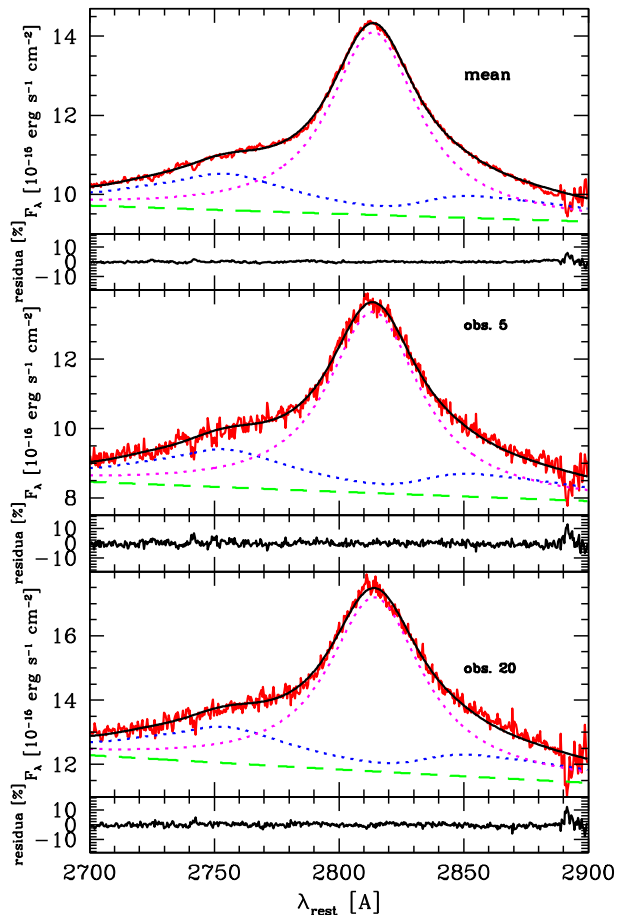


Figure 1. Top: flux-calibrated mean spectrum of HE 0413-4031. Data are shown with a red line, and the black line gives the best-fit model. Remaining lines show the spectral components: power law (green dashed line), Fe II pseudo-continuum (blue dotted line), and Mg II total flux (two doublet components, magenta dotted line). The lower panel shows the residua, which are noticeable only close to 2900 Å, where the sky line contamination was the strongest and the background subtraction did not fully correct for this effect. Middle: flux-calibrated spectrum of HE 0413-4031 for the minimum phase (epoch 5). The lines represent the same spectral components as in the top panel. Bottom: flux-calibrated spectrum of HE 0413-4031 for the maximum phase (epoch 20). The lines represent the same spectral components as in the top panel. The epochs are listed in Table A1.

Because in our full model one of the kinetic components was set at zero rest-frame velocity, together with Fe II, while the second kinematic component has an arbitrary shift in velocity space with respect to them, we eliminated the first kinematic component, leaving the second one, which allows for the flexibility of the shift between Mg II and Fe II. This model is also later used to fit individual spectra.

We tested several templates of the Fe II from Bruhweiler & Verner (2008), and the best fit was provided by the d12-m20-20-5.dat model, which assumes the cloud number density 10^{12} cm^{-3} , the turbulent velocity 20 km s^{-1} , and the hydrogen ionizing photon flux $10^{-20.5} \text{ cm}^{-2} \text{ s}^{-1}$. The same template was favored for the quasar CTS C30.10 also monitored by SALT (Czerny et al. 2019). It is not surprising, because recent modeling of the quasar main sequence also suggest values of that order for the local BLR cloud density and the turbulent

¹¹ Downloaded from https://archive.stsci.edu/prepds/composite_quasar/.

velocity (Panda et al. 2018, 2019a). The best-fit half-width of the Gaussian used for template convolution was 1200 km s^{-1} .

We calculated a grid of models for different redshift and different ratio of the doublet, and these two quantities are strongly coupled. We determined the best-fit redshift as $z = 1.37648$, and the doublet ratio as 1.9. This is a value quite close to the optically thin case, 2:1 ratio.

These parameters—the choice of the Fe II template, template smearing velocity, redshift, and doublet ratio—were later assumed to be the same in all fits of the individual spectra, while the Fe II amplitude, Mg II amplitude, line width and line shift, and power-law parameters were allowed to vary from observation to observation.

The best-fit FWHM of the Mg II line in the mean spectrum is $4380_{-15}^{+14} \text{ km s}^{-1}$, formally just above the line dividing the class A and class B source (Sulentic et al. 2000; Marziani et al. 2018). However, some trend with the mass in this division is expected, because for Seyfert galaxies the dividing line between Narrow Line Seyfert 1 galaxies and Seyfert galaxies is at 2000 km s^{-1} (Osterbrock & Pogge 1985), instead of at 4000 km s^{-1} , as in quasars. HE 0413-4031 is still more massive and brighter than most quasars in Sloan Digital Sky Survey (SDSS) catalogs (Shen et al. 2011; Pâris et al. 2017). Because we fit the single Lorentzian shape, we cannot derive the line dispersion σ from the fit, because the Lorentzian shape corresponds to the limit of $\text{FWHM}/\sigma \rightarrow 0$. We can, however, determine the line dispersion numerically because the FWHM/σ ratio is an important parameter (Collin et al. 2006). Therefore, we subtracted the fitted Fe II and the remaining underlying continuum, and integrated the line profile. We obtained $\sigma = 2849 \text{ km s}^{-1}$, and $\text{FWHM}/\sigma = 1.54$, which confirms that the source belongs to Population 2 of Collin et al. (2006), or class A of Sulentic et al. (2000).

In the mean spectrum, the $\text{EW}(\text{Mg II})$ is $27.45_{-0.10}^{+0.12} \text{ \AA}$, a bit below the average value for the Mg II from Large Bright Quasar Sample (42 \AA , Forster et al. 2001).

The most interesting part is the shift we detect between the Mg II line and the Fe II pseudo-continuum. This shift is by 15.1 \AA , or equivalently, 1620 km s^{-1} , and the Mg II line is redshifted with respect to Fe II. It may also be that Fe II is blueshifted with respect to Mg II; however, we cannot distinguish between these cases. Kovačević-Dojčinović & Popović (2015) in their study observed redshifts, not blueshifts of the Fe II. In addition, the conclusion about the relative shift strongly depends on the combination of the Fe II template used and the adopted redshift, as we discuss in Appendix C.

Unfortunately, we are unable to establish the proper position of the rest frame for our SALT observation. We failed to identify the narrow $[\text{NeV}]3426.85 \text{ \AA}$ line, which is relatively strong in the quasar spectra,¹² but this search did not yield a reliable identification.

3.2. Determination of the Mean and RMS Spectra

For constructing the mean and the rms spectra, we follow the standard procedure as explained by Peterson et al. (2004). The mean spectrum is calculated using the following relation

$$\overline{F(\lambda)} = \frac{1}{N} \sum_{i=1}^N F_i(\lambda), \quad (2)$$

¹² <http://classic.sdss.org/dr6/algorithms/linestable.html>

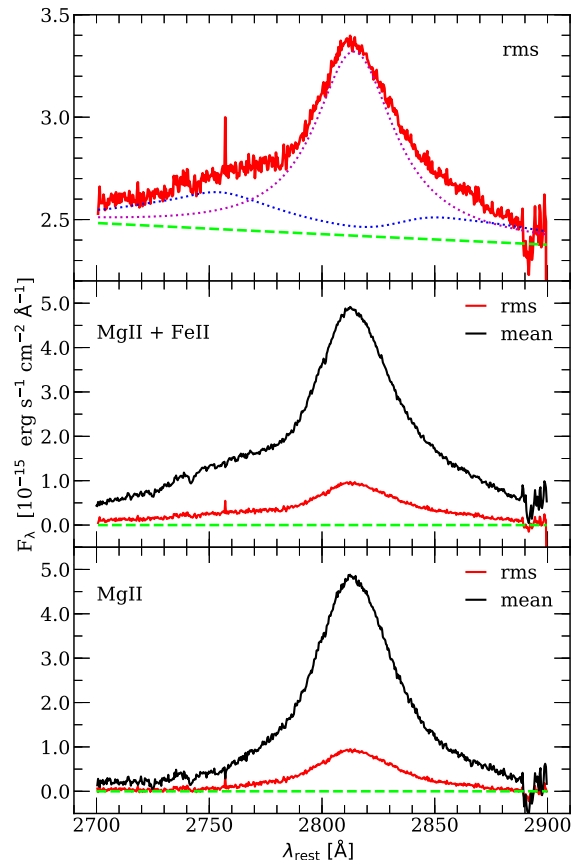


Figure 2. Decomposition of the flux-calibrated rms spectrum (top panel) and the comparison of the rms (red) and mean (black) spectra at the zero-flux level (represented by a dashed green line), first with the continuum subtracted (Mg II + Fe II; middle panel), and subsequently with the Fe II emission subtracted (Mg II; bottom panel). From the rms spectra it is clear that the core of Mg II line is the most variable, with a much smaller variability in the wings.

where $F_i(\lambda)$ are individual spectra. For studying variability phenomena, we also construct an rms spectrum using

$$S(\lambda) = \left\{ \frac{1}{N-1} \sum_{i=1}^N [F_i(\lambda) - \overline{F(\lambda)}]^2 \right\}^{1/2}. \quad (3)$$

The flux-calibrated mean and rms spectra are shown in the top panels of Figures 1 and 2, respectively. For the flux calibration we used the composite quasar spectra created by Vanden Berk et al. (2001). For the continuum, they proposed a power law with an index of $\alpha_\lambda = -1.56$. This continuum was normalized for each spectrum according to the V magnitudes reported in Table A2, which were simply converted to flux units in order to get the flux normalization.

The rms spectrum was estimated following Equation (3). Mean and rms profiles look similar, but to check this more quantitatively, we fitted the rms spectrum in the same way we fitted the mean spectrum. The result is shown in Figure 2, upper panel. The line is still well fitted when we use a single Lorentzian model. The FWHM in rms spectrum is 4337 km s^{-1} , only marginally narrower than the FWHM of the mean spectrum (4380 km s^{-1}). When the mean and rms spectra are compared at the zero-flux level, i.e., with the continuum subtracted, we see that the core of Mg II is most variable, with

the wings having a much smaller variability, which could be attributed to Fe II emission (see the central panel of Figure 2). If we subtract the Fe II pseudo-continuum from the rms and mean spectra, the only variable part of the Mg II emission is at the core of the line (see the bottom panel of Figure 2). The EW(Mg II) if measured in the rms spectrum is 21.01 Å, lower than in the mean spectrum (27.45 Å), and EW(Fe II) is lower than in the mean spectrum (8.32 Å instead of 10.13 Å), which results from the enhanced role of the continuum power law. The consistency of the rms and the mean spectra fits also supports the single-component Lorentzian fit of the line shape.

3.3. Spectral Fits of Individual Observations

For each of the spectra, the EW(Mg II), FWHM(Mg II), EW(Fe II), shift between Mg II and Fe II, and power spectrum parameters were determined. The results are given in Table A1, and Figure 3 visually shows the evolution of these properties with time.

The mean shift of the Mg II and Fe II lines, calculated from the individual spectra, is 1582 km s⁻¹, somewhat smaller than obtained from the mean spectrum. Variations from one spectrum to the other are at the level of 82 km s⁻¹ (dispersion), larger than individual errors. If we fit a linear trend, we see a systematic increase of the Mg II and Fe II separation by 109 km s⁻¹ in six years, but it is not much larger than the dispersion in the measurements; however, it seems formally significant if we use the individual measurement errors given in Table A1. The corresponding acceleration 18 km s⁻¹ yr⁻¹ is much smaller than the large value of 104 ± 14 km s⁻¹ yr⁻¹ found for the quasar HE 0435-4312 also using the SALT instrument (Średzińska et al. 2017).

The averaged FWHM is 4390.8 km s⁻¹; the dispersion is 200 km s⁻¹, again slightly larger than typical measurement error, but no interesting trends could be noticed. Thus, we observe some small variations in the line shape, but they are indeed marginal, consistent with the fact that rms spectrum is similar to the mean shape of the line.

3.4. Lightcurves: Variability and Linear Trends

The continuum photometric lightcurve and the Mg II lightcurve are presented in Figure 3. The continuum shows a mostly slow but noticeable variation. A single brightening trend dominates for most of the monitoring period, replaced with some dimming during the last 1.5 yr. The overall variability level of the continuum is $F_{\text{var}} = 13.0\%$, if BMT telescope is included, and 10.4%, if these data are not taken into account. Here we use the standard definition of the excess variance,

$$F_{\text{var}} = \sum_{i=1}^N \frac{(x_i - \bar{x})^2 - \delta x_i^2}{N\bar{x}^2}, \quad (4)$$

where \bar{x} is the average value, and δx_i is the individual measurement error. Because this linear trend seems suggestive, we also checked the shorter timescale variability by first fitting a linear trend to the lightcurve in the log space (i.e., when using magnitudes), and then subtracting this trend from the original lightcurve. We did this only for the data without BMT. The F_{var} dropped from 10.4% down to 7.4%.

The Mg II line variability is lower, $F_{\text{var}} = 7.2\%$, and $F_{\text{var}} = 7.1\%$, depending on whether BMT telescope data were or were not used for Mg II calibration, respectively. It is

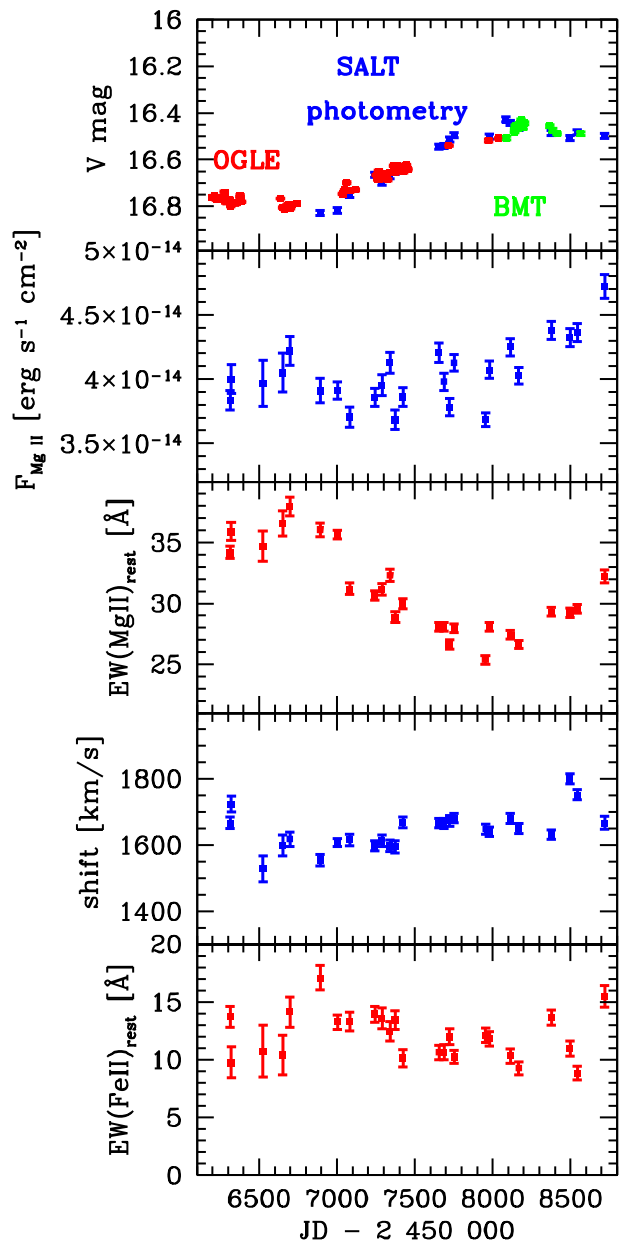


Figure 3. Temporal evolution of photometric and spectroscopic characteristics from the monitoring of the quasar HE 0413-4031. From the top to the bottom panels: photometric lightcurve (V -band magnitude) from OGLE, SALT, and BMT (color-coded; BMT data were shifted by 0.171 mag up to correct for the systematic offset with respect to the OGLE data); Mg II line-emission lightcurve (in $\text{erg s}^{-1} \text{cm}^{-2}$); the equivalent width of the Mg II line in Å; the velocity shift of the Mg II line with respect to the Fe II line in km s^{-1} ; and the equivalent width of Fe II line in Å. The time is expressed in JD-2450000.

interesting to note, however, that the levels of variability in Mg II and the continuum are comparable if the long-term trend was subtracted from the data.

We also determine Fe II lightcurve, and the variability level of Fe II seems higher, at the level of 14.7% if BMT data are neglected, and 14.9% if the BMT data are included. However, the measurement errors are large due to the coupling between the continuum and Fe II pseudo-continuum.

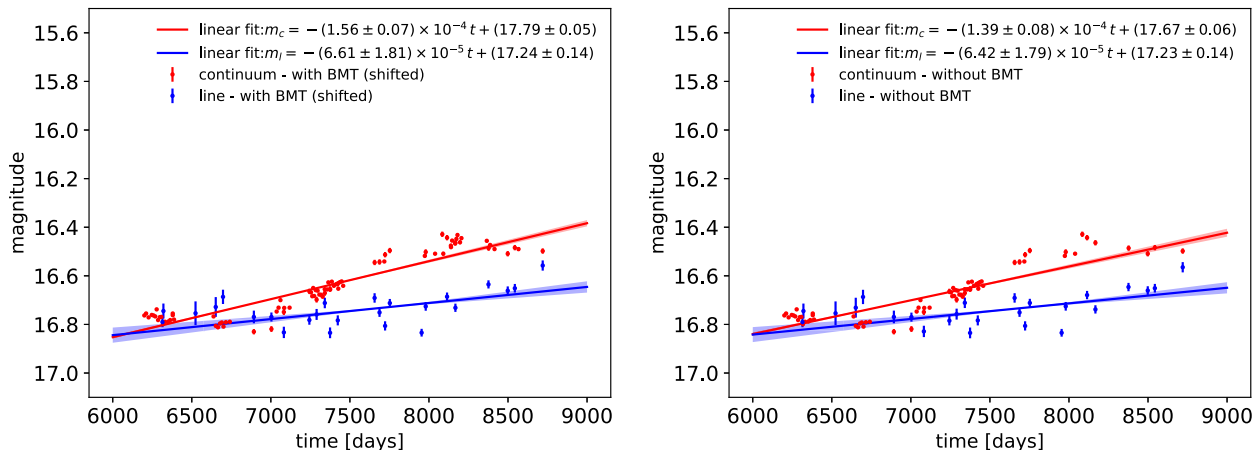


Figure 4. Linear-trend fit to both continuum and line-emission lightcurves in the log space. Left panel: the linear trend fits with BMT data included. The BMT data were shifted by 0.171 mag to correct for the systematic shift with respect to the OGLE data. The legend includes the best-fit parameters for both the continuum and the line-emission lightcurves. The fit statistics are $\chi^2 = 7121.4$ and $\chi_{\text{red}}^2 = 84.8$ for the continuum and $\chi^2 = 177.9$ and $\chi_{\text{red}}^2 = 7.7$ for the line lightcurve. Right panel: as in the left panel, but without BMT data. The fit statistics are $\chi^2 = 5609.2$ and $\chi_{\text{red}}^2 = 79.0$ for the continuum and $\chi^2 = 172.9$ and $\chi_{\text{red}}^2 = 7.5$ for the line lightcurve.

The mean monochromatic luminosity at 3000 \AA can be derived from the V -band magnitude of 16.5, using the extinction reported in NED with a value of 0.034, source redshift of 1.389, and standard cosmological parameters for the flat universe ($H_0 = 70 \text{ km s}^{-1} \text{ Mpc}^{-1}$, $\Omega_m = 0.28$, and $\Omega_\Lambda = 0.72$, see Kozłowski 2015, for details). We obtain $\log L_{3000} = 46.754$. The uncertainty of the monochromatic luminosity can be estimated from the minimum and the maximum points along the photometric lightcurve, 16.429 mag and 16.830 mag, respectively, which implies $\log L_{3000}^{\text{max}} = 46.782$ and $\log L_{3000}^{\text{min}} = 46.622$. Hence, for the further analysis, we consider $\log L_{3000} = 46.754_{-0.132}^{+0.028}$.

As already pointed out, the linear trend is present in both continuum and Mg II line emission lightcurves. In Figure 4, we show the fit of a linear function to both lightcurves, considering the case with and without BMT data in the left and right panels, respectively. The linear trend is toward smaller magnitudes, i.e., the continuum and line-emission flux densities increase during the observational run. The slope of the linear trend is larger for the continuum than for the line-emission lightcurves. The continuum slope is $s_c = 0.057 \text{ mag yr}^{-1}$ and the line slope is $s_l = 0.024 \text{ mag yr}^{-1}$ with the BMT data included; without BMT data, the continuum increase drops a little, $s_c = 0.051 \text{ mag yr}^{-1}$, while the line-emission slope is comparable, $s_l = 0.023 \text{ mag yr}^{-1}$. In other words, the decrease in the continuum magnitude is 2.38 and 2.17 larger than the decrease for the line-emission magnitude with and without BMT data, respectively.

4. Results: Time-delay Determination

As for the intermediate-redshift quasar CTS C30.10 ($z = 0.90052$) (Czerny et al. 2019), we apply several methods to determine the time-delay between the continuum V band and Mg II line emission. Apart from the standard interpolated cross-correlation function, we apply several statistically robust methods suitable for unevenly sampled, heterogeneous pairs of lightcurves (see Zajaček et al. 2019b, for an overview), namely the discrete correlation function, z -transformed discrete correlation function, JAVELIN, χ^2 method, Von Neumann, and Bartels estimator. For all seven methods, we consider the two pairs of lightcurves, those with and without magnitude-

shifted BMT data. The detailed description of the time-delay analysis is in the Appendix in Section B, with subsections B.1–B.6 describing individual methods including the corresponding plots and the tables.

4.1. Final Time-delay for Mg II Line

Due to the systematic offset of the BMT data in the continuum lightcurve, we decided to distinguish two cases for all time-delay analysis techniques. For a matter of completeness, below we summarize in Table 1 the main results for all the methods, including the cases with and without magnitude-shifted BMT data. The most prominent peak in the time-delay distributions is the peak close to 700 days in the observer’s frame. This peak is generally present in all seven methods. However, the ICCF analysis generally gives longer time-delays of 900–1000 days, which could be caused by the interpolation and hence by adding new points to the analysis. A noticeable difference is also for the JAVELIN method, where the time-delay peak is close to 1050 days. Because JAVELIN uses the damped random walk for fitting the continuum lightcurve, which is then smoothed and time-delayed to reproduce the Mg II line-emission lightcurve, extra points are introduced to the lightcurves in a similar way as for the ICCF. This can lead to biases and artifacts, especially for irregular and sparse data sets. This is why we decided to prefer the peak around 700 days, which is the most prominent for all discrete methods that do not require interpolation and are model-independent (DCF, z DCF, Von Neumann). The detected time-delay of $498.9_{-125.9}^{+170.9}$ days for the Von Neumann estimator with shifted BMT data is most likely an artifact because it is an excess given by only one point; see Figure B6 (left panel). The second minimum of the Von Neumann estimator around 700 days is then more pronounced and clearly given by more points. In addition, the minimum around 500 days is not present for the case without BMT data; see Figure B6 (right panel).

Given the arguments above, we focus on the observed time-delay around 700 days. Concerning the average value, we obtain the rest-frame time-delay of $\tau_1 = 302.2_{-61.4}^{+43.3}$ days for the case with the shifted BMT data, and $\tau_2 = 303.0_{-24.5}^{+37.8}$ days for the case without them. The final average value then is

Table 1

Summary List of the Time-delays Expressed in Light Days in the Observer's Frame between the Continuum and Mg II Line-emission Lightcurves for the Flat-spectrum Radio Quasar HE 0413-4031

Method	With Shifted BMT data	Without BMT data
ICCF interpolated continuum—centroid [days]	1004.6 ^{+196.8} _{-246.2}	1003.2 ^{+205.3} _{-235.4}
ICCF interpolated line—centroid [days]	1008.4 ^{+142.2} _{-276.9}	1034.17 ^{+139.1} _{-248.9}
ICCF symmetric—centroid [days]	1009.7 ^{+113.6} _{-211.5}	1021.7 ^{+114.5} _{-207.8}
DCF peak time-delay—bootstrap [days]	720.4 ^{+115.1} _{-147.9}	726.0 ^{+114.4} _{-145.7}
zDCF maximum likelihood	720.9 ^{+323.9} _{-527.3}	720.9 ^{+331.3} _{-100.1}
JAVELIN peak time-delay [days]	1053.7 ^{+79.8} _{-163.6}	1058.5 ^{+77.1} _{-150.7}
Von Neumann peak—bootstrap [days]	498.9 ^{+170.9} _{-125.9}	711.3 ^{+149.0} _{-139.5}
Bartels peak—bootstrap [days]	710.9 ^{+172.3} _{-173.0}	714.6 ^{+176.1} _{-164.6}
χ^2 peak—bootstrap [days]	720.4 ^{+145.6} _{-102.2}	727.7 ^{+160.0} _{-85.2}
Average of the most frequent peak—observer's frame [days]	718.2 ^{+102.8} _{-143.8}	720.1 ^{+89.8} _{-58.3}
Average of the most frequent peak—rest frame	302.2 ^{+43.3} _{-61.4}	303.0 ^{+37.8} _{-24.5}
Average of the secondary peak—observer's frame [days]	1019.1 ^{+69.9} _{-114.2}	1029.4 ^{+71.0} _{-107.0}
Average of the secondary peak—rest frame [days]	428.8 ^{+29.4} _{-48.1}	433.2 ^{+29.9} _{-45.0}

Note. We distinguish for all methods two cases—with and without magnitude-shifted BMT data.

$\bar{\tau} = 302.6^{+28.7}_{-33.1}$ days, which corresponds to the light-travel distance of $R_{\text{Mg II}} = c\bar{\tau} = 0.254^{+0.024}_{-0.028}$ pc $\sim 10^{17.9}$ cm. The inferred value of the light-travel distance $R_{\text{Mg II}}$ is larger than typical BLR length-scales inferred from other RM campaigns with time-delays of the order 10–100 light days for AGN with a broad range of black hole masses (Korista & Goad 2000, 2004; Shen et al. 2016). The length-scale of the BLR has implications for the line variability, as was shown by Guo et al. (2020), and we will specifically discuss the Mg II line–continuum variability relation in Section 6.2.

The results provided by the ICCF and the JAVELIN analyses provide a time-delay that we treat as secondary for the reasons of interpolation and the model-dependence. In the rest frame, this secondary time-delay is $428.8^{+29.4}_{-48.1}$ days for the case with the shifted BMT data and $433.2^{+29.9}_{-45.0}$ days for the case without the BMT data. The average rest-frame value is $431.0^{+21.0}_{-32.9}$ days. This secondary time-delay peak should be reevaluated when more continuum and line-emission data are available to assess if it is just an artifact of data sampling irregularity.

5. Results: Mg II–based Radius–Luminosity Relation

5.1. Preliminary Virial Black Hole Mass and Eddington Ratio

The virial black hole mass can be determined from the virial relation for the BLR, $M_{\bullet} = f_{\text{vir}} c\tau_{\text{BLR}} \text{FWHM}^2/G = (1.134^{+0.089}_{-0.072}) \times 10^9 M_{\odot}$, which was calculated assuming the virial factor equal to unity, the average time-delay for Mg II inferred earlier, and the best-fit FWHM of 4380^{+14}_{-15} km s⁻¹. In general, however, the virial factor may deviate from unity, which is indicated by the study of Mejía-Restrepo et al. (2018), which implies the anticorrelation between the virial factor and the line FWHM, which is in our case the main source of uncertainty. According to Mejía-Restrepo et al. (2018), we have

$$f_{\text{vir, Mg II}} = \left(\frac{\text{FWHM}_{\text{obs}}(\text{Mg II})}{3200 \pm 800 \text{ km s}^{-1}} \right)^{-1.21 \pm 0.24}, \quad (5)$$

which for $\text{FWHM} = 4380^{+14}_{-15}$ km s⁻¹ leads to the virial factor less than unity, $f_{\text{vir, Mg II}} = 0.42\text{--}0.92$, and the virial black hole

mass in the range of $M_{\bullet} = 4.8 \times 10^8\text{--}1.0 \times 10^9 M_{\odot}$, hence we have a factor of 2 uncertainty in the virial black hole mass. The Eddington luminosity can be estimated as

$$L_{\text{Edd}} = 1.256 \times 10^{47} \left(\frac{M_{\bullet}}{10^9 M_{\odot}} \right) \text{ erg s}^{-1}, \quad (6)$$

while the bolometric luminosity may be calculated using the bolometric correction with respect to $\lambda = 3000$ Å, $L_{\text{bol}} = (5.62 \pm 1.14)L_{3000}$ (Richards et al. 2006), which leads to the Eddington ratio of $\eta_{\text{Edd}} = L_{\text{bol}}/L_{\text{Edd}} \approx 2.18$. Using the power-law calibration of the bolometric correction by Netzer (2019), we obtain $L_{\text{bol}} \simeq 2.8L_{3000}$, which gives $\eta_{\text{Edd}} \approx 1.27$. Hence, these values imply close to the Eddington or even the super-Eddington accretion mode.

5.2. Position in the Radius–Luminosity Plane

By combining the rest-frame time-delay and the monochromatic luminosity of HE 0413-4031, we can position the source on the radius–luminosity plane alongside the other quasars to check for the potential deviation of HE 0413-4031 due to its high accretion rate, as was previously detected for super-Eddington sources monitored in the broad H β line (Wang et al. 2014a, 2014b; Martínez-Aldama et al. 2019).

With the rest-frame time-delay of $\bar{\tau} = 302.6^{+28.7}_{-33.1}$ days and the monochromatic luminosity of $\log L_{3000} = 46.754^{+0.028}_{-0.132}$, the source HE 0413-4031 lies below the expected radius–luminosity relation, $R(\text{Mg II}) - L_{3000}$ (Vestergaard & Osmer 2009). We demonstrate this in Figure 5, in which we compiled all the sources whose time-delay was determined for the Mg II line (10 sources, see Table 3 in Czerny et al. 2019), including CTS C30.10 and the new source HE 0413-4031. The list of all the sources with measured time-delays and determined monochromatic luminosities is in Table 2. With a large scatter ($\sigma = 0.246$ dex), the sources approximately follow the radius–luminosity relationship previously derived for the

THE ASTROPHYSICAL JOURNAL, 896:146 (28pp), 2020 June 20

Zajaček et al.

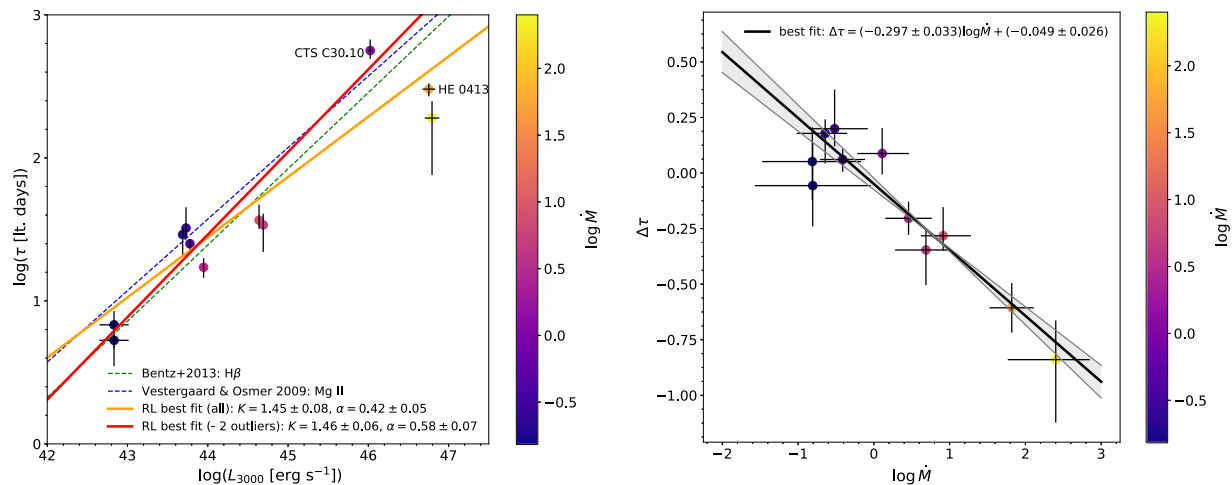


Figure 5. Radius–luminosity relation for the reverberation-mapped sources in the broad Mg II line resembles the radius–luminosity relation for the H β line. Left panel: radius–luminosity relation for the RM quasars monitored in the broad Mg II line. Clearly, the sources follow within uncertainties the scaling relationship previously derived by Vestergaard & Osmer (2009) for the Mg II line (dashed blue line) as well as the H β radius–luminosity relationship of Bentz et al. (2013) (dashed green line). The best-fit relationships are also displayed, both for the case when all the sources are included in the fitting procedure (solid orange line) and for the case when two outliers that are below the radius–luminosity relations are removed (CTS252 and HE 0413-4031) toward the higher luminosities (solid red line). Individual sources are color-coded to show the logarithm of the dimensionless accretion-rate parameter \dot{M} (see Equation (11)), according to the color bar to the right. Right panel: the strong anticorrelation (with the Pearson correlation coefficient of $p = -0.940$) of the parameter $\Delta\tau$, which expresses the rate of departure from the radius–luminosity relation (see also Equation (12)), with respect to the dimensionless accretion-rate parameter \dot{M} expressed by Equation (11).

Table 2
Characteristics of Reverberation-mapped Sources Monitored Using the Broad Mg II Line

Source	z	τ (days)	$\log(L_{3000} \text{ (erg s}^{-1}\text{)})$	FWHM (Mg II) (km s $^{-1}$)	\dot{M}	$\Delta\tau$	τ_{corr} (days)
141214.20+532546.7 ^{1,2}	0.45810	36.7 $^{+10.4}_{-4.8}$	44.63882 \pm 0.00043	2391 \pm 46	8.21 $^{+6.94}_{-5.58}$	-0.28 $^{+0.13}_{-0.07}$	80.7 $^{+22.9}_{-10.6}$
141018.04+532937.5 ^{1,2}	0.46960	32.3 $^{+12.9}_{-5.3}$	43.7288 \pm 0.0051	3101 \pm 76	0.30 $^{+0.31}_{-0.21}$	0.20 $^{+0.18}_{-0.08}$	27.1 $^{+10.8}_{-4.4}$
141417.13+515722.6 ^{1,2}	0.60370	29.1 $^{+3.6}_{-8.8}$	43.6874 \pm 0.0029	3874 \pm 86	0.23 $^{+0.15}_{-0.20}$	0.18 $^{+0.06}_{-0.14}$	22.4 $^{+2.8}_{-6.8}$
142049.28+521053.3 ^{1,2}	0.75100	34.0 $^{+6.7}_{-12.0}$	44.6909 \pm 0.0009	4108 \pm 39	4.87 $^{+3.57}_{-4.57}$	-0.35 $^{+0.09}_{-0.16}$	64.2 $^{+12.6}_{-22.6}$
141650.93+535157.0 ^{1,2}	0.52660	25.1 $^{+2.0}_{-2.6}$	43.778 \pm 0.002	4066 \pm 202	0.39 $^{+0.26}_{-0.27}$	0.06 $^{+0.05}_{-0.06}$	22.6 $^{+1.8}_{-2.3}$
141644.17+532556.1 ^{1,2}	0.42530	17.2 $^{+2.7}_{-2.7}$	43.9480 \pm 0.0011	2681 \pm 96	2.87 $^{+2.03}_{-2.03}$	-0.20 $^{+0.07}_{-0.07}$	27.8 $^{+4.4}_{-4.4}$
CTS252 ^{3,4}	1.89000	190.0 $^{+59.0}_{-114.0}$	46.79 \pm 0.09	3800 \pm 380	251.55 $^{+261.03}_{-367.22}$	-0.84 $^{+0.18}_{-0.28}$	1136.2 $^{+353.1}_{-682.0}$
NGC4151 ^{5,6}	0.00332	6.8 $^{+1.7}_{-2.1}$	42.83 \pm 0.18	4823 \pm 1105	0.15 $^{+0.23}_{-0.23}$	0.05 $^{+0.15}_{-0.17}$	4.7 $^{+1.2}_{-1.4}$
NGC4151 ^{5,6}	0.00332	5.3 $^{+1.9}_{-1.8}$	42.83 \pm 0.18	6558 \pm 1850	0.16 $^{+0.28}_{-0.27}$	-0.06 $^{+0.19}_{-0.18}$	3.7 $^{+1.3}_{-1.2}$
CTS C30.10 ^{7,7}	0.90052	564 $^{+109}_{-71}$	46.023 \pm 0.026	5009 \pm 325	1.29 $^{+1.05}_{-0.98}$	+0.09 $^{+0.11}_{-0.09}$	721.4 $^{+139.4}_{-90.8}$
HE 0413-4031 ^{8,9}	1.37648	302.6 $^{+28.7}_{-33.1}$	46.754 \pm 0.080	4380 \pm 14	66.04 $^{+44.17}_{-44.76}$	-0.61 $^{+0.11}_{-0.11}$	1223.9 $^{+116.4}_{-134.1}$

Note. From the left to the right column, the table lists the source name, redshift, measured time-delay in light days in the rest frame, the logarithm of the monochromatic luminosity at 3000 Å, FWHM of Mg II in km s $^{-1}$, the dimensionless accretion rate as defined in Equation (11), departure parameter $\Delta\tau$ defined by Equation (12), and the corrected time-delay expressed in light days in the rest frame (see also Equation (14)). The superscripts to source names indicate the sources, from which we obtained the measured time-delay (first source) and the monochromatic luminosity at 3000 Å (second source): (1) Shen et al. (2016); (2) Shen et al. (2019); (3) Lira et al. (2018); (4) NED, NUV, GALEX; (5) Metzroth et al. (2006); (6) Code & Welch (1982); (7) Czerny et al. (2019); (8) this work; and (9) a script of Kozłowski et al. (2010).

Mg II line (Vestergaard & Osmer 2009),

$$\log \left[\frac{\tau(\text{Mg II})}{1 \text{ lt-day}} \right] = 1.572 + 0.5 \log \left(\frac{L_{3000}}{10^{44} \text{ erg s}^{-1}} \right), \quad (7)$$

as well as the radius–luminosity relationship derived for the H β line for lower-redshift sources by Bentz et al. (2013),

$$\log \left[\frac{\tau(\text{H}\beta)}{1 \text{ lt-day}} \right] = 1.391 + 0.533 \log \left(\frac{L_{3000}}{10^{44} \text{ erg s}^{-1}} \right), \quad (8)$$

in which we replaced L_{5100} monochromatic luminosity by L_{3100} using $L_{5100} \simeq 0.556 L_{3000}$, using the power-law relations for

the bolometric corrections derived by Netzer (2019). The scatter of the sources around the relation by Bentz et al. (2013) is $\sigma = 0.269$ dex, which is comparable to the scatter with respect to the relation by Vestergaard & Osmer (2009).

We also fitted the general radius–luminosity relationship $\log(\tau/1 \text{ lt-day}) = K + \alpha \log(L_{3000}/10^{44} \text{ erg s}^{-1})$ to all available data. We obtained the best-fit parameters of $K = 1.45 \pm 0.08$ and $\alpha = 0.42 \pm 0.05$ with $\chi^2 = 76.6$ and $\chi^2_{\text{red}} = 8.5$. Subsequently, we removed 2 outliers—CTS252 and HE 0413-4031—that are significantly below RL relations in Equation (7) and Equation (8). This helped to improve the fit, with the best fit with $\chi^2 = 36.7$ and $\chi^2_{\text{red}} = 5.2$, and the

final relation based on Mg II data can be expressed as

$$\log \left[\frac{\tau(\text{Mg II})}{1\text{lt-day}} \right] = (1.46 \pm 0.06) + (0.58 \pm 0.07) \times \log \left(\frac{L_{3000}}{10^{44} \text{ erg s}^{-1}} \right). \quad (9)$$

Both best-fit relations are depicted in Figure 5 with solid lines.

The time-delay offset can be explained by the higher accretion rate implied by the super-Eddington luminosity. The correlation of the time-delay offset with the accretion rate was shown previously for reverberation-mapped sources in the H β line (Du et al. 2018; Martínez-Aldama et al. 2019), and we will demonstrate it in the following section for the broad Mg II line. By moving the source HE 0413-4031 back onto the radius–luminosity relation, we can estimate the corrected black hole mass using (Vestergaard & Osmer 2009)

$$M_{\bullet}^{\text{Mg II}} = 10^{z_p(\lambda)} \left[\frac{\text{FWHM}(\text{Mg II})}{1000 \text{ km s}^{-1}} \right]^2 \left(\frac{\lambda L_{\lambda}}{10^{44} \text{ erg s}^{-1}} \right)^{0.5}, \quad (10)$$

which for $\text{FWHM}(\text{Mg II}) = 4380_{-15}^{+14} \text{ km s}^{-1}$ and $z_p(\lambda) = 6.86$ ($\lambda = 3000 \text{ \AA}$) yields $M_{\bullet}^{\text{Mg II}} = 3.31 \times 10^9 M_{\odot}$ using the monochromatic luminosity of $\log L_{3000} = 46.754$.

Hence, the black hole mass obtained from the radius–luminosity relation is larger by a factor of at least ~ 3 than the maximum mass inferred from the RM time-delay, taking into account the uncertainty in the virial factor. The Eddington ratio for the higher mass then drops to $\eta_{\text{Edd}} = 0.77$ for the constant bolometric correction factor of $\text{BC} = 5.62$ (Richards et al. 2006). For the more precise luminosity-dependent bolometric correction of $\text{BC} = 25 \times (L_{3000}/10^{42} \text{ erg s}^{-1})^{-0.2} = 2.80$ for $L_{3000} = 10^{46.754} \text{ erg s}^{-1}$ (Netzer 2019), we get an even smaller Eddington ratio of $\eta_{\text{Edd}} = 0.38$, which is also consistent with the SED fitting presented in Section 6.3.

5.3. Correction of the Accretion-rate Effect along the Radius–Luminosity Relation

In the optical range, it has been observed that the accretion rate is responsible for the departure of the radius–luminosity relation more than the intrinsic scatter. Du et al. (2018, and references therein) showed that the sources with the highest accretion rates have time-delays shorter than expected from the optical radius–luminosity relation. However, the accretion-rate effect can be corrected, recovering the standard results (Martínez-Aldama et al. 2019). Following this idea, we repeated the same exercise for all Mg II reverberation-mapped data (see Table 2).

The black hole mass was estimated assuming a virial factor anticorrelated with the FWHM of the emission line (Equation (5)), which apparently corrects the orientation effect to a certain extent. Because the Eddington ratio has shown a large scatter in comparison with other expressions of the accretion rate (Martínez-Aldama et al. 2019), we will use the dimensionless accretion rate (Du et al. 2016),

$$\dot{M} = 20.1 \left(\frac{l_{44}}{\cos \theta} \right)^{3/2} m_7^{-2}, \quad (11)$$

where l_{44} is the luminosity at 3000 \AA in units of $10^{44} \text{ erg s}^{-1}$, $\theta = 0.75$ is the inclination angle of disk to the line of sight, and m_7 is the black hole mass in units of $10^7 M_{\odot}$. In Figure 5 (left

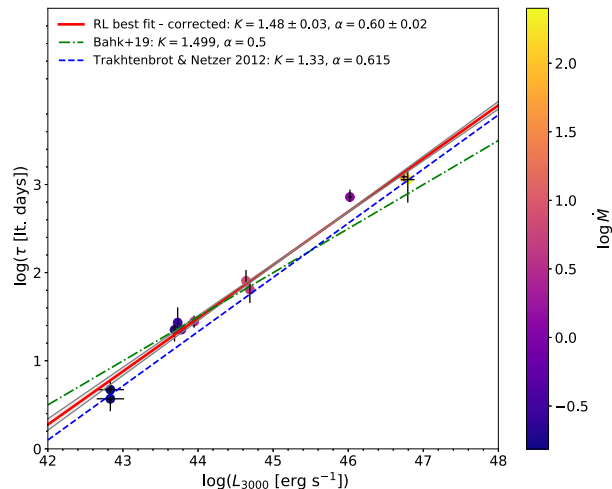


Figure 6. The radius–luminosity relation for the Mg II broad-emission line; the rest-frame time-delays were corrected for the accretion-rate effect. The best-fit linear relation in the log space is $\log(\tau/1 \text{ lt. day}) = (1.48 \pm 0.03) + (0.60 \pm 0.02) \log(L_{3000}/10^{44} \text{ erg s}^{-1})$, with $\chi^2 = 11.40$ and $\chi_{\text{red}}^2 = 1.27$. For comparison, we also show the radius–luminosity relation as inferred by Bahk et al. (2019), which has the same normalization factor as our relation, but a smaller slope of 0.5. In addition, we depict the radius–luminosity relation constructed by Trakhtenbrot & Netzer (2012), which, on the other hand, has a comparable slope of $\alpha = 0.615$, but a smaller normalization factor of $K = 1.33$.

panel), we show the variation of the dimensionless accretion rate along the radius–luminosity relation, which is similar to the observed one in the optical range.

To estimate the departure from the radius–luminosity relation, we use the parameter $\Delta\tau$, which is simply the difference between the observed time-delay and the expected one from the radius–luminosity relation,

$$\Delta\tau = \log \left(\frac{\tau_{\text{obs}}}{\tau_{\text{R-L}}} \right). \quad (12)$$

We estimate $\tau_{\text{R-L}}$ from the radius–luminosity relation described in Equation (9). Values are reported in Table 2. The largest departure from the radius–luminosity relation is associated with the highest accretion-rate sources, which is clearly evidenced in Figure 5 (right panel). The Pearson coefficient ($p = -0.940$) also indicates a strong anticorrelation between $\Delta\tau$ and \dot{M} . Performing a linear fit, we get the relation

$$\Delta\tau(\dot{M}) = (-0.297 \pm 0.033) \log \dot{M} + (-0.049 \pm 0.026), \quad (13)$$

for which $\chi^2 = 6.75$ and $\chi_{\text{red}}^2 = 0.75$. This expression can be used to recover the expected values from the radius–luminosity relation using the relation

$$\tau_{\text{corr}}(\dot{M}) = 10^{-\Delta\tau(\dot{M})} \cdot \tau_{\text{obs}}. \quad (14)$$

The corrected rest-frame time-delays are listed in Table 2. Based on them, we construct a new version of the radius–luminosity relation for the Mg II line corrected for the accretion-rate effect (see Figure 6). It shows a smaller scatter of $\sigma = 0.104$ dex in comparison with the radius–luminosity relation before the correction, which is $\sigma = 0.221$ dex when all the sources are included and $\sigma = 0.186$ dex with two outliers

THE ASTROPHYSICAL JOURNAL, 896:146 (28pp), 2020 June 20

Zajaček et al.

removed. The best-fit linear relation has smaller uncertainties with $\chi^2 = 11.40$ and $\chi_{\text{red}}^2 = 1.27$ and can be expressed as

$$\log \left[\frac{\tau(\text{Mg II})}{1\text{lt-day}} \right] = (1.48 \pm 0.03) + (0.60 \pm 0.02) \times \log \left(\frac{L_{3000}}{10^{44} \text{ erg s}^{-1}} \right). \quad (15)$$

The dispersion around the new relation is very small, equal to 0.104 dex. This is smaller than the dispersion of 0.13 dex in the original radius–luminosity relation of Bentz et al. (2013) after an artificial removal of outliers, despite the fact that the Mg II relation covers a broad range of the luminosities, redshifts, and Eddington ratios. It is not clear at this point whether the smaller dispersion is a property of the Mg II emission or it just results from the fact that the Mg II data do not come from so many different monitoring campaigns.

The normalization coefficient in Equation (15) is within uncertainties consistent with the normalization factor inferred from the Mg II–based black hole mass estimator by Bahk et al. (2019),

$$\log \left[\frac{\tau(\text{Mg II})}{1\text{lt-day}} \right] \simeq 1.499 + 0.5 \log \left(\frac{L_{3000}}{10^{44} \text{ erg s}^{-1}} \right), \quad (16)$$

where we adopted their fitting Scheme 4 and assumed the virial factor $f_{\text{vir}} \equiv 1$ while transforming $M_* \propto L_{3000}^{0.5} (\Delta V)^2$ relation to $\tau \propto L_{3000}^{0.5}$ relation. The relation 16 is also shown in Figure 6 for comparison with our best-fit relation 15.

However, the best-fit slope is larger than the slope of 0.5 in Equation (16), which is also expected from the simple photoionization arguments. Currently, this may be just a systematic effect due to a small number of reverberation-mapped sources using the Mg II line. The larger slope currently yields a significantly small scatter, because for the relation given by Equation (16) the scatter is $\sigma = 0.187$ dex for the corrected time-delays. For the uncorrected rest-frame time-delays, the scatter is $\sigma = 0.247$ dex and $\sigma = 0.189$ for the whole Mg II sample (sources in Table 2) and the Mg II sample without the two outliers (CTS252 and HE 0413-4031), respectively.

On the other hand, our best-fit slope is very similar to the value of $\alpha = 0.615$ inferred by Trakhtenbrot & Netzer (2012), who, on the other hand, have a smaller normalization factor $K = 1.33$. Our slope value is also located between the slopes derived for the $\tau(\text{Mg II})$ – L_{3000} relation by McLure & Jarvis (2002) ($\alpha = 0.47$) and by McLure & Dunlop (2004) ($\alpha = 0.62$). However, all of the above-mentioned Mg II–based radius–luminosity relations were calibrated based on the UV spectra of sources for which only H β line RM was performed. Certainly, more reverberation-mapped sources using the Mg II line are required to further constrain the $\tau(\text{Mg II})$ – L_{3000} relation.

6. Discussion

Using the SALT data and the supplementary photometric monitoring, we were able to derive the time-delay of the Mg II line with respect to the continuum in $z = 1.37648$ quasar HE 0413-4031. The source is very bright in the absolute term, but the delay is formally established as $\bar{\tau} = 302.6_{-33.1}^{+28.7}$ days in the comoving frame. Although the analysis of the Mg II complex with the underlying power-law continuum and Fe II pseudo-

continuum emission is a complex task with a certain degree of degeneracy, we showed that the peak value of the time-delay distribution is not sensitive to different Fe II templates; only its uncertainty may be affected due to a different number of parameters used in each model (see also Appendix C for a detailed discussion).

This delay is shorter than derived for CTS C30.10 (Czerny et al. 2019), but similar to the delay measured for another bright quasar by Lira et al. (2018). We show that the dispersion in the measured time-delay of the Mg II line for a given range of the monochromatic flux is related to the Eddington ratio in the source, as in the H β time-delay (Martínez-Aldama et al. 2019), and with the appropriate correction for this effect, the dispersion around the radius–luminosity is actually very small, with $\sigma = 0.104$ dex in comparison with $\sigma = 0.221$ dex before the correction (when all the sources are included; $\sigma = 0.186$ dex with two outliers removed), which opens up a possibility for the future applications of this relation for cosmology.

In this section, we discuss more generally the validity and the accuracy of using Mg II lines in black hole mass determination. Furthermore, we show that the intrinsic Baldwin effect is present in our source, which is another way of showing that the Mg II line responds to the thermal AGN continuum. To verify if the reverberating Mg II line in our source is a reliable probe of its black hole mass, we performed a fit of the accretion disk model to the optical and UV continuum data of the source SED.

6.1. Nature of Mg II Emission

Marziani et al. (2013) showed that the FWHM of the Mg II line is systematically narrower by $\sim 20\%$ than the H β line, which holds for all of its components as well as the full profile. The simple explanation is that Mg II is emitted at larger distances than H β from the photoionizing continuum source. The intrinsically symmetric profile of the Mg II line found in this work characterized by a one-component Lorentzian is consistent with the origin of the Mg II emission in the virialized BLR clouds, as for the H β broad line (Marziani et al. 2013). The Lorentzian profile may be physically explained by the turbulent motion of the emitting medium and the line broadening by its rotation (Kollatschny & Zetzl 2011; Goad et al. 2012; Kollatschny & Zetzl 2013a, 2013b). This model of the Lorentzian line profile is also consistent with the failed radiatively accelerated outflow (FRADO) model as such (Czerny & Hryniewicz 2011), in which the turbulence arises due to the failed outflow and the subsequent inflow, and the rotation is represented by the dominant Keplerian field (see also Figure 8). For Population A sources where the Mg II profile is symmetric, the Mg II gas may be considered virialized. For Population B sources, a small degree of asymmetry and the blueshift of the Mg II line may be related to outflows of the Mg II-emitting gas (Marziani et al. 2013).

Our results, in particular the studied intrinsic Baldwin effect in Section 6.2, are also consistent with the work of Yang et al. (2020), who found for the sample of 33 extreme variability quasars that the Mg II flux density responds to the variable continuum, but with a smaller amplitude. However, they also stress that the FWHM of the Mg II line does not respond to the continuum as the Balmer lines do. Therefore, black hole mass estimations based on single-epoch measurements can be luminosity-biased.

Previous works also find an overall consistency between $H\beta$ -based and Mg II-based black hole mass estimators. Trakhtenbrot & Netzer (2012) found the scatter between these two spectral regions of 0.32 dex in terms of the black hole mass estimation, smaller than for the C IV line, for which the scatter with respect to $H\beta$ is 0.5 dex. In addition, the same authors found that $\text{FWHM}(\text{Mg II}) \simeq \text{FWHM}(H\beta)$ up to 6000 km s^{-1} , beyond which the FWHM of Mg II seems to saturate. This is again different for the C IV line, which does not show any correlations with either the $H\beta$ or the Mg II line. Also, the $\text{FWHM}(\text{C IV}) \lesssim \text{FWHM}(H\beta)$ for nearly half of the studied sources (see also Shen & Liu 2012, for a similar result), which contradicts RM results. Ho et al. (2012) also showed that Mg II-based black hole masses are comparable within uncertainties to those based on $H\alpha$, while C IV-based mass estimates differed by as much as a factor of 5. Hence, the usage of the broad Mg II line for black hole mass estimating is justified for sufficiently large samples, while C IV should not be applied as a reliable virial black hole mass estimator. This is in line with the overall picture, where low-ionization lines ($H\alpha$, $H\beta$, Mg II) originate in the bound line-emitting, photoionized clouds, and high-ionization lines (C IV) originate in the unbound outflowing gas (Collin-Souffrin et al. 1988).

For the γ -ray blazar 3C 454.3, León-Tavares et al. (2013) found a significant correlation between the increase in the Mg II flux density and the γ -ray flaring emission (in 2010 fall), which could be related to the superluminal radio component in this source. This implies that Mg II-emitting gas responds to the nonthermal continuum alongside the thermal continuum of the accretion disk. This is also in agreement with the significant correlation between the Mg II flux density and the γ -ray flux increase in the blazar CTA102 (Chavushyan et al. 2020), in which the superluminal radio component was also present. In addition, the Mg II broad line was broader and blueshifted at the maximum of the γ -ray activity in comparison to the minimum. The BLR material in this source was inferred to be located $\sim 25 \text{ pc}$ from the central source. Chavushyan et al. (2020) conclude that the black hole mass estimation using Mg II is only reliable for the sources in which UV continuum is dominated by the central accretion disk, which is also the case for our source HE 0413, as we show in Section 6.3 based on the SED fitting, which is based on the thermal disk emission.

In summary, based on our findings and previous findings of other authors, a significant fraction of the Mg II-emitting gas is virialized and reverberating to the variable thermal continuum, as we also find in this work. For sources with a significant nonthermal emission due to the jet in the UV and the optical domain, outflowing gas at larger distances from the standard BLR region can respond to the nonthermal continuum, and this contributes to the broadening and a blueshifting of the Mg II line. Hence, when using the Mg II line in the reverberation studies, time-delay analysis should be complemented by SED modeling whenever possible to verify if photoionizing continuum is dominantly of thermal nature.

In terms of the quasar main sequence and the four-dimensional Eigenvector 1 (4DE1, Sulentic et al. 2000; Marziani et al. 2018), considering the equivalent width ($27.45_{-0.10}^{+0.12} \text{ \AA}$) and the FWHM ($4380_{-15}^{+14} \text{ km s}^{-1}$) exhibited by the Mg II line, HE 0413-4031 could be cataloged as a Population B1 in the 4DE1 scheme (Table 2 of Bachev et al. 2004). However, HE 0413-4031 shows a clear single-component Lorentzian profile associated with Population A sources (Section 2.3). According to the analysis presented

in Appendix C using a different model template for Fe II emission, the Mg II emission could also be modeled with two kinematic components, although their nature appears to be more problematic to interpret. Moreover, the FWHM of the 2 Gaussian components and their relative shift with respect to the Fe II emission depends strongly on the source redshift in the studied interval of $z \simeq 1.37\text{--}1.39$ (see our analysis in Appendix C, especially Figure C1).

As a high luminosity source, HE 0413-4031 can be found in the Population B spectral bins, being still a Population A source (Marziani et al. 2018). Because of its large Eddington ratio of ~ 0.4 , it can be further classified as an extreme Population A source (xA), with the $\text{Fe II}\lambda 4570$ strength larger than unity $R_{\text{Fe II}} > 1$, with the $\text{FWHM}(H\beta) > 4000 \text{ km s}^{-1}$ because the Mg II line is generally narrower than $H\beta$ line. The difficult spectral-type classification of HE 0413-4031 stems from the fact that Population A sources are typically highly accreting sources with smaller black hole masses, and Population B sources have larger black hole masses and low Eddington ratios (Marconi et al. 2009; Fraix-Burnet et al. 2017). In this sense, HE 0413-4031 has mixed properties: a large black holes mass of a few $10^9 M_{\odot}$ and a high Eddington ratio of ~ 0.4 . However, these general distinctions are based on the analyses of lower-luminosity low-redshift sources, while our source is at the intermediate redshift of $z \sim 1.4$ and of a high luminosity of $10^{47} \text{ erg s}^{-1}$. Hence the apparent discrepancy may be solved by the cosmological argumentation that the current massive black holes with low accretion rates were highly accreting sources at higher redshifts. With a black hole mass of a few billion solar masses, HE 0413 falls into the expected mass range for type 1 AGN between redshifts of 1 and 2 (see Figure 15 of Trakhtenbrot & Netzer 2012, where HE 0413 is located at the age of the universe of 4.66 Gyr for $z = 1.37$). On the other hand, HE 0413 is still an outlier in terms of the accretion rate close to the Eddington limit for a black hole mass of a few billion solar masses. Trakhtenbrot & Netzer (2012) suggest that a majority of such massive AGNs do not accrete close to their Eddington limits even at $z \simeq 2$.

Because HE 0413-4031 can be classified as a radio-loud AGN given its luminosity at 1.4 GHz, $L_{1.4} \approx 2.5 \times 10^{26} \text{ W Hz}^{-1} > 10^{24} \text{ W Hz}^{-1}$ (Tadhunter 2016), its radio-optical properties can be studied in the broader context. Ganci et al. (2019) studied the radio properties of type-1 AGNs across all main spectral types along the quasar main sequence, in particular for three classes of Kellermann's radio-loudness criterion, which is defined as the ratio of the radio and optical flux densities, $R_K = S_{\text{radio}}/S_{\text{optical}}$. We follow Ganci et al. (2019), who use 1.4 GHz flux density for S_{radio} and g -band flux density for S_{optical} and divide sources into three radio classes: radio detected (RD, $R_K < 10$), radio intermediate (RI, $10 \leq R_K < 70$), and radio-loud (RL, $R_K \geq 70$). We derive the corresponding 1.4 GHz and g -band flux densities for HE 0413-4031 by linear interpolation of the averaged SED points in the log space (see Figure 9), $S_{1.4} = 21.04 \text{ mJy}$ and $S_g = 0.434 \text{ mJy}$, which yields $R_K = 48.5$. Hence, HE 0413-4031 can be classified as an RI source with an inverted and flat radio spectrum toward higher frequencies according to Vizier SED,¹³ because the spectral index α , using the notation $S_{\nu} \propto \nu^{+\alpha}$, is $\alpha_{1-5} \simeq 0.7$, $\alpha_{5-8} \simeq 1.7$, $\alpha_{8-20} \simeq -0.02$ between 0.843 GHz, 5 GHz, 8 GHz, and 20 GHz, respectively. Sources with inverted to flat radio spectral indices are

¹³ <http://vizier.u-strasbg.fr/vizier/sed>

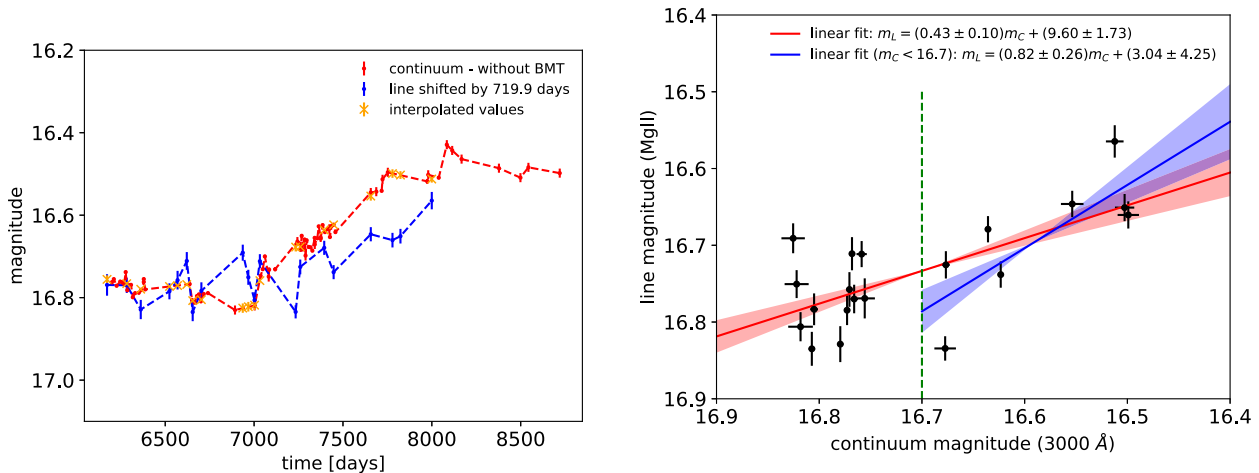


Figure 7. Determination of the continuum–line magnitude (luminosity) relation. Left panel: superposition of the continuum and the time-shifted line-emission lightcurves. Interpolated photometry points are also shown. Right panel: Mg II line-emission magnitude vs. continuum magnitude has a clear linear correlation in the logarithmic scale with the correlation coefficient of $r = 0.73$ ($R^2 = 0.53$), with the best-fit relation of $m_l = (0.43 \pm 0.10)m_c + (9.60 \pm 1.73)$. The blue line represents the linear fit to the data, with the continuum magnitude less than 16.7. In this case, the correlation coefficient is higher ($r = 0.79$, $R^2 = 0.63$) and the best-fit relation has a larger slope: $m_l = (0.82 \pm 0.26)m_c + (3.04 \pm 4.25)$.

characterized by a compact, optically thick radio core or a core-jet system (Zajaček et al. 2019a, 2019c).

Ganci et al. (2019) found that the occurrence of RD, RI, and RL sources differs along the main sequence. The classification of our source as RI with inverted-flat spectrum is consistent with its location in the extreme A population according to Ganci et al. (2019), because core-dominated sources in A3 and A4 bins are mostly RI. The source of radio emission in extreme A population can be partially due to a high star formation rate, but also the core-jet activity. In our case, the radio spectral index implies the presence of a compact core-jet system, hence the high star formation rate is not necessarily required. On the other hand, the presence of gas material is necessary to account for the high Eddington ratio of ~ 0.4 – 0.5 . The optically thick radio core could be a sign of a restarted AGN activity (Czerny et al. 2009; Padovani et al. 2017), which will eventually heat up the cold gas content and/or blow it away and slow down the star formation.

6.2. Response of Mg II Emission to Continuum Changes—*Intrinsic Baldwin Effect*

The expected properties of the Mg II line were recently modeled by Guo et al. (2020), where the authors using the CLOUDY code and the locally optimally emitting cloud (LOC) scenario showed that at the high Eddington ratio of ~ 0.4 , the Mg II line flux saturates and does not further increase with the rise of the continuum.

We confront this theoretical prediction with our observations of the quasar HE 0413-4031. We used the logarithm of both the continuum and Mg II line-emission flux densities, i.e., magnitudes. Subsequently, we applied the determined time-delay shift to the line emission, i.e., we shifted the Mg II lightcurve by 719.9 days in the observer’s frame. For the continuum lightcurve, we tried both the cases with and without BMT data, by given the fact that the BMT data are present for the epochs longer than 8000 days, they do not have a significant effect on the following analysis. As the next step, we interpolate the photometry data to the time-shifted line-emission data to have corresponding line-continuum pairs. As before, given that the photometry data come from different instruments with various uncertainties, we make use of the weighted least-squares

linear B-spline interpolation with the inverse of uncertainties as weights. We show the continuum and the time-shifted line lightcurves in Figure 7 (left panel) alongside the interpolate values, which can also serve as a cross-check that the determined time-delay of ~ 720 days in the observer’s frame represents the realistic similarity between the shapes of both lightcurves.

Finally, we plot the Mg II line magnitude with respect to the continuum magnitude in Figure 7 (right panel). This relation has a significant correlation with the correlation coefficient of $r = 0.73$. The best-fit linear relation is $m_l = (0.43 \pm 0.10)m_c + (9.60 \pm 1.73)$, which is displayed in Figure 7 with the corresponding uncertainties. Our linear fit implies directly the power-law relation between the Mg II and continuum luminosities, $L_{\text{Mg II}} \propto L_{3000}^{0.43 \pm 0.10}$. In combination with the measured time-delay of 303 days in the rest frame, we can conclude that the Mg II line responds to the continuum variability even for the source, which is highly accreting with the Eddington ratio of ~ 0.4 (see also Section 6.3 for a detailed SED modeling). Hence, our source does not exhibit a nonresponsive Mg II line with a rather constant dependency on the continuum luminosity, as was analyzed and shown by Guo et al. (2020) (see also their Figure 4). Moreover, from Figure 7 (right panel) it is apparent that the line and the continuum magnitudes consist of an uncorrelated part for continuum magnitudes of more than 16.7 mag (with the correlation coefficient of $r = 0.10$, $R^2 = 0.01$). The part of the dependency with continuum magnitudes less than 16.7 mag is strongly correlated with the correlation coefficient of $r = 0.79$ ($R^2 = 0.63$), and the best-fit linear fit is $m_l = (0.82 \pm 0.26)m_c + (3.04 \pm 4.25)$, hence the line luminosity responds even stronger to the continuum luminosity in this part with the relation $L_{\text{Mg II}} \propto L_{3000}^{0.82 \pm 0.26}$, which is marginally consistent with the linear dependency within the uncertainty.

Guo et al. (2020) analyze the LOC model and Mg II response for the smaller black hole mass and the 3000 Å luminosity ($M_* = 10^8 M_\odot$ and $L_{3000} = 10^{44-45} \text{ erg s}^{-1}$). However, their upper limit for the Eddington ratio, $\eta_{\text{Edd}} = 0.4$, is comparable to our estimated Eddington ratio and hence their flattening of

Mg II luminosity close to $L_{3000} = 10^{45} \text{ erg s}^{-1}$ is not confirmed for HE 0413-4031. On the other hand, we observe a similar dependency of the Mg II line luminosity on the continuum luminosity, as Guo et al. (2020) inferred for hydrogen recombination broad lines ($H\alpha$, $H\beta$) at lower Eddington ratios. For the luminosity range $\log [L_{3000}(\text{erg s}^{-1})] = 42\text{--}44$, the slope for $H\beta$ is $\alpha \sim 0.45$ and $\alpha \sim 0.42$ for $H\alpha$. In addition, Guo et al. (2020) show a slower rise of Mg II luminosity with respect to the continuum with the slope of ~ 0.38 , which is smaller than our value. This implies that at least for our source, the LOC model with the initial assumption of $(R_{\text{out}}, \Gamma) = (10^{17.5}, -2)^{14}$ does not apply.

The models with the larger radial extent of the BLR with $R_{\text{out}} = 10^{18} \text{ cm}$ as shown in Figure 9 of Guo et al. (2020) seem to be more consistent with our slope of 0.43, as they show a continuous rise of Mg II luminosity even for larger continuum luminosities around the Eddington ratio of ~ 0.4 . This is also in agreement with our inferred travel distance of $R_{\text{Mg II}} = c\tau = 0.254_{0.016}^{+0.020} \text{ pc} \sim 10^{17.9} \text{ cm}$. In comparison, the location of the dusty torus is still further. Its inner radius is given by the sublimation radius, $R_{\text{sub}} \sim 0.4 \text{ pc } L_{45}^{0.5} T_{1500}^{-2.6} = 5.04 \text{ pc} \sim 10^{19.2} \text{ cm}$ (Elitzur & Shlosman 2006; Nenkova et al. 2008), for our estimate of the bolometric luminosity $L_{\text{bol}} = 1.589 \times 10^{47} \text{ erg s}^{-1}$ and the dust sublimation temperature of 1500 K. The outer radius of the dusty torus is expected to be at $R_{\text{torus}} \sim YR_{\text{sub}}$, where $Y \sim 5\text{--}10$ (Elitzur & Shlosman 2006). The light-travel distance, which can serve as a proxy for the BLR location in HE 0413-4031, is also in agreement with the model of the failed radiatively accelerated dusty outflow (FRADO, Czerny & Hryniewicz 2011). The failed dusty wind requires the existence of dust in the accretion disk, which is possible at and below $\sim 1000 \text{ K}$. This sets the inner radius of the BLR to $r_{1000}/R_{\text{sub}} = 0.03M_8^{1/6}/(\dot{m}^{1/6}\eta_{0.1}^{1/2})$, where M_8 is the black hole mass scaled to $10^8 M_\odot$, $\dot{m} = \dot{M}/\dot{M}_{\text{Edd}}$ is the dimensionless accretion rate, and η is the accretion efficiency ($L_{\text{bol}} = \eta\dot{M}c^2$). Using the best-fit SED model, see Section 6.3, we adopt $M = 2.5 \times 10^9 M_\odot$, $\dot{m} = 0.51$, and $\eta = 0.1$, which leads to $r_{1000}/R_{\text{sub}} = 0.0574$ or $r_{1000} = 0.289 \text{ pc} = 10^{17.95} \text{ cm}$, which is within uncertainties consistent with the light-travel distance $R_{\text{Mg II}}$. We illustrate these basic length-scales of the quasar HE 0413-4031 in Figure 8.

For the continuum magnitudes smaller than 16.7 mag, the slope of the line-continuum dependency (0.82 ± 0.26) is even larger than for the case when the whole range is considered. Interestingly, this slope is comparable to the exponent of the line-continuum relation as studied for the sample of flat-spectrum radio quasars (Patiño Álvarez et al. 2016), which is related to the global Baldwin effect between the equivalent width of originally broad UV lines (C IV , $\text{Ly}\alpha$) and the corresponding continuum luminosities (at 1350 \AA); see the original works by Baldwin (1977), Baldwin et al. (1978), and Wampler et al. (1984). In general, the equivalent width decreases with the increasing luminosity, which can be described as a power-law relation, $\text{EW}_{\text{line}} \propto L_{\text{cont}}^\gamma$. This can be rewritten as a relation between the line and the corresponding continuum luminosities using $\text{EW} \simeq L_{\text{line}}/L_{\text{cont}}$, which yields $L_{\text{line}} \propto L_{\text{cont}}^{\gamma+1}$. The original Baldwin effect is also called global or ensemble (Baldwin 1977; Carswell & Smith 1978), which is derived based on single-epoch observations of an

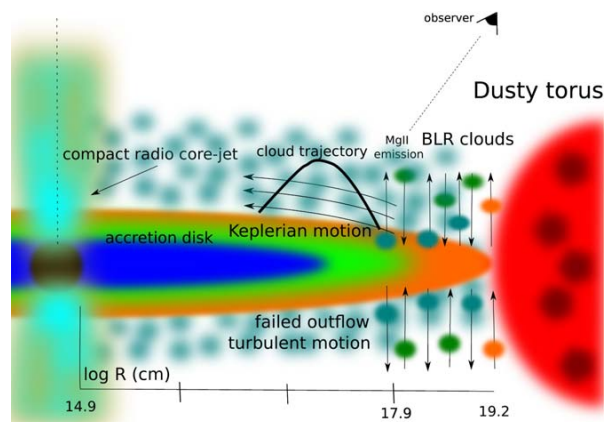


Figure 8. Illustration of the basic length-scales of the quasar HE 0413-4031. The BLR clouds are depicted with the dominantly Keplerian velocity field with a smaller outflow-inflow turbulent component according to the failed radiatively accelerated outflow model (FRADO, Czerny & Hryniewicz 2011). The axis along the bottom of the figure is expressed in the corresponding logarithms of basic radii in centimeters. From the left to the right side of the image, we include the Schwarzschild radius of $2.5 \times 10^9 M_\odot$ black hole, $\log R_{\text{Schw}} = 14.9$, the light-travel distance of Mg II emission, $\log R_{\text{Mg II}} = 17.9$, and the inner radius of the dusty torus, $\log R_{\text{sub}} = 19.2$.

ensemble of AGNs, while the analogical relation studied for individual AGNs is related to as an intrinsic Baldwin effect (Pogge & Peterson 1992).

Patiño Álvarez et al. (2016) analyze the line-continuum luminosity relation $L_{\text{line}}-L_{\text{cont}}$, including the Mg II line and 3000 \AA continuum, for a sample of 96 FSRQ sources (core-jet blazars). For FSRQ, they found the slope of 0.796 ± 0.153 , which is smaller than the slope of 0.909 ± 0.002 for the control sample of RQ AGN. Within uncertainties, their slope derived for the whole sample is comparable to our slope $L_{\text{Mg II}} \propto L_{3000}^{0.82 \pm 0.26}$. Hence, our detected intrinsic Baldwin effect is in agreement with the global one derived for the population of FSRQ. Previously, Rakić et al. (2017) studied the intrinsic Baldwin effect for 6 type-I AGN, and they detected it for the broad recombination lines, $H\alpha$ and $H\beta$. They found that the intrinsic Baldwin effect is not related to the global one. Patiño Álvarez et al. (2016) found the difference of the global Baldwin effect between the radio-loud (blazar) and radio-quiet AGN, which could imply the importance of the nonthermal component, i.e., boosted jet emission, to the ionizing continuum for radio-loud sources. Apparently, more data for our quasar as well as more radio-loud and radio-quiet sources are needed to study in detail both the intrinsic and global Baldwin effect and their potential relation, especially taking into account the potential nonthermal contribution for radio-loud sources.

In summary, we detect a significant correlation between Mg II and the 3000 \AA continuum after the removal of the light-travel time effect. The relation $L_{\text{line}}-L_{\text{cont}}$ is not linear, but has a slope of 0.43 ± 0.10 when all the corresponding line-luminosity points are combined. The slope is larger, $\gamma + 1 = 0.82 \pm 0.26$, when only a higher correlated part of the points is selected. These results are consistent with the Mg II broad-line emission being at least partially driven by the underlying continuum.

6.3. SED Fitting

Our determination of the black hole mass in Section 5.1 is not unique, because it requires additional assumptions about

¹⁴ Locally optimally emitting cloud (LOC) models assume the power-law radial distribution of clouds, $f(r) \propto r^\Gamma$.

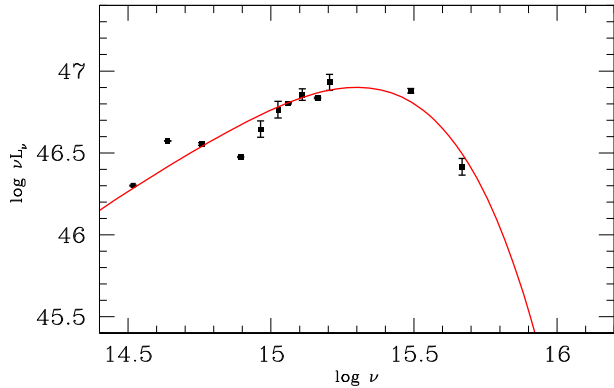


Figure 9. The SED data and the accretion disk model for HE 0413-4031 shown as the dependency of the luminosity νL_ν (in erg s^{-1}) on the frequency ν (in Hz) in the log space. The data are taken from the Vizier SED data (see <http://vizier.u-strasbg.fr/vizier/sed>). For the fitting, we use error-weighted averages of the data. The best-fit SED model is represented by a solid red line and is based on the parameters $M = 3.0 \times 10^9 M_\odot$, $\dot{m} = 0.35$ (here measured in units of $1.678 \times 10^{18} (M/M_\odot \text{ g s}^{-1})$), $a = 0.31$, and $\iota = 34$ deg.

the virial factor. As a test of the mass range we obtained, we attempted to obtain the constraints for the black hole mass directly, from the accretion disk fitting to the continuum.

We used the data points available from Vizier SED photometric viewer.¹⁵ After removal of the multiple entries and converting the measurements to the rest frame (assuming $z = 1.37648$ as determined in Section 3.1), and adopting $H_0 = 69.5$, $\Omega_m = 0.286$, $\Omega_L = 0.714$ (Bennett et al. 2014), we obtain the IR to UV SED (see Figure 9). We corrected the data for the Galactic extinction, although the effect is not strong in the direction of HE 0413-4031. The data points come from various epochs. Therefore, we added an additional error of 0.08 (in log space) to the measurements to account for the variability. For disk fitting, we used only points at the frequencies above 14.5 in the log scale, rest frame, because the rest frame near-IR emission in quasars comes from the hot dust component. We did not assume any presence of the blazar component because the data point did not seem to suggest its need.

We used the fully relativistic Novikov–Thorne model (Novikov & Thorne 1973), with all propagation effects as described in Czerny et al. (2011). The model is characterized by the black hole mass, accretion rate (in Eddington units, assuming the fixed efficiency of 1/12 in the definition, i.e., in units of $1.678 \times 10^{18} (M/M_\odot \text{ g s}^{-1})$), spin, and viewing angle. We performed the fitting without constraints for any of those parameters. First, we performed the fitting for all the data points available, and we obtained the best-fit model with the parameters: $M = 3.0 \times 10^9 M_\odot$, $\dot{m} = 0.35$, $a = 0.31$, and $\iota = 34$ deg. We present this fit in Figure 9. Second, we also performed the fitting for the error-weighted averages of the data, and for the uncertainties we used error-weighted standard deviations. In this case, the best-fit solution was formally with the parameters: $M = 2.5 \times 10^9 M_\odot$, $\dot{m} = 0.51$, $a = 0.025$, and $\iota = 33.8$ deg. However, fits are highly degenerate, so the χ^2 allows for a broad mass range from $1 \times 10^9 M_\odot$ to masses even above $5 \times 10^9 M_\odot$ (see Table 3). Large masses, however, do not provide an acceptable solution because they also require a very high viewing angle. A high viewing angle is not expected because the unification scheme of AGN excludes it due to the

¹⁵ <http://vizier.u-strasbg.fr/vizier/sed/>

Table 3

Best-fitted Parameters for the Black Mass in the Range of $1\text{--}5 \times 10^9 M_\odot$

$M (10^9 M_\odot)$	Spin	\dot{m}	ι (deg)	χ^2
1	−0.99	1.81	0.0	31.57
1.5	−0.94	1.08	0.0	19.38
2	−0.13	0.60	0.0	19.54
2.5	0.025	0.51	33.8	19.17
3	0.46	0.31	25.8	19.31
3.5	0.52	0.26	33.6	19.23
4	0.44	0.29	49.8	20.20
4.5	0.0062	0.54	68.2	20.31
5	0.044	0.50	69.5	20.30

Note. The parameters include the spin, the accretion rate \dot{m} (here measured in units of $1.678 \times 10^{18} (M/M_\odot \text{ g s}^{-1})$), and the viewing angle ι . The smallest χ^2 of 19.17 is for the case with the parameters $M = 2.5 \times 10^9 M_\odot$, $\dot{m} = 0.51$, $a = 0.025$, and $\iota = 33.8$ deg.

presence of the dusty/molecular torus (see, e.g., Padovani et al. 2017 for a recent review), and the clear excess in the near-IR shows that the torus is present in HE 0413-4031.

If we constrain the allowed parameters to $\iota < 45$ deg, the upper limit for the black hole mass is $M = 3.5 \times 10^9 M_\odot$. In our fits, the black hole spin is never large. For very small black hole masses, the accretion rate is super-Eddington and the spin is retrograde; the highest value of the spin we get is 0.52. However, this determination highly relies on one data point—the far-UV Galaxy Evolution Explorer measurement, which is in the spectral range where relativistic effects are important. If there is some internal reddening in the quasar, the allowed spin probably could be higher, but the SED data quality is not good enough to attempt more complex modeling.

The obtained black hole mass range $1.5 \times 10^9 M_\odot\text{--}3.5 \times 10^9 M_\odot$ is consistent with those presented in Section 5.1.

By integrating the best-fit SED, we can derive the bolometric correction BC for the monochromatic luminosity at 3000 \AA . We obtain $L_{\text{bol}} = 2.8 L_{3000}$, which is smaller than the mean value of 5.62 ± 1.14 provided by Richards et al. (2006) for the same wavelength. However, it is consistent with the luminosity-dependent relation for the bolometric correction derived by Netzer (2019), which gives $\text{BC} = 25 \times (L_{3000}/10^{42} \text{ erg s}^{-1})^{-0.2} = 2.80$ for $L_{3000} = 10^{46.754} \text{ erg s}^{-1}$. The consistency with the power-law relation of Netzer (2019) stems from the fact that they used essentially the same model of an optically thick, geometrically thin accretion disk that is used in this work to fit the SED.

In summary, the SED fitting showed that the canonical thin, optically thick accretion disk can still account for the dominant part of the continuum in our highly accreting quasar. At higher accretion rates, the inner parts of the accretion flow are expected to become geometrically and optically thick, as in slim accretion disks, which can account for the reduction of the ionizing flux and shortening of time-delays (Wang et al. 2014b). This is indeed supported by the existence of stable geometrically thick and optically thick “puffy” accretion disks in global 3D GRMHD simulations for sub-Eddington accretion rates comparable to our values of $\dot{m} = 0.3\text{--}0.6$ (Lančová et al. 2019). However, the current computational facilities still do not allow a self-consistent treatment of the accretion disk-BLR dynamics on the scales of as much as 1000 gravitational radii, while the analytical and semi-analytical models explain the main observational features (Czerny et al. 2011; Czerny & Hryniewicz 2011).

7. Conclusions

We summarize the main findings of the paper as follows:

1. Using seven different methods, we found a rest-frame time-delay between the continuum and Mg II line emission for the bright quasar HE 0413-4031, $\tau = 302.6^{+28.7}_{-33.1}$ days, which was the most frequent peak in time-delay distributions.
2. In combination with the data for 10 other sources monitored in the Mg II line, we construct a radius–luminosity relation, which is consistent with the theoretically expected dependency, $R \propto L^{1/2}$. The new quasar HE 0413-4031 with the monochromatic luminosity of $\log L_{3000} = 46.754^{+0.028}_{-0.132}$ lies below the expected relation, which can be explained by its higher accretion rate. In general, for all Mg II sources, the departure from the radius–luminosity relation, i.e., the shortening of their time-delays, is larger for higher-accreting sources. The same effect was previously observed for the sources monitored in H β .
3. We determined the response of the Mg II line luminosity to the photoionizing continuum luminosity, $L_{\text{line}} \propto L_{\text{cont}}^{0.43 \pm 0.10}$, which is comparable to the response of recombination emission lines H α and H β , according to theoretical photoionization models. This is consistent with the outer radius of the BLR at $R_{\text{out}} = 10^{18}$ cm, which is in turn in agreement with the light-travel distance inferred from the rest-frame time-delay.
4. The virial black hole mass determined based on the measured rest-frame time-delay, $M_{\text{RM}}^{\text{uncorr}}(f=1) \simeq 1.1 \times 10^9 M_{\odot}$, is smaller by a factor of 4 than the value expected from the radius–luminosity relation, $M_{\text{RM}}^{\text{corr}}(f=1) \simeq 4.6 \times 10^9 M_{\odot}$.

The black hole mass inferred from fitting a thin accretion disk model to the source SED, $M_{\text{SED}} = 1.5 \times 10^9 M_{\odot} - 3.5 \times 10^9 M_{\odot}$, is in agreement with these values within the uncertainty. Other best-fitted parameters for the source are the Eddington ratio of $0.26 \leq \dot{m} \leq 1.08$, the black hole spin of $-0.94 \leq a \leq 0.52$, and the viewing angle of $0 \leq \iota \leq 34$ degrees.

We thank the referee for constructive comments that helped to improve the clarity of the manuscript. The authors acknowledge the financial support by the National Science Centre, Poland, grant No. 2017/26/A/ST9/00756 (Maestro 9), and by the Ministry of Science and Higher Education (MNiSW) grant DIR/WK/2018/12. G.P. acknowledges the grant MNiSW DIR/WK/2018/09. K.H. acknowledges support by the Polish National Science Centre grant 2015/18/E/ST9/00580. The OGLE project has received funding from the National Science Centre, Poland, grant MAESTRO 2014/14/A/ST9/00121. The Polish participation in SALT is funded by grant No. MNiSW DIR/WK/2016/07.

Software: IRAF (Tody 1986, 1993), JAVELIN (Zu et al. 2011, 2013, 2016), PyCCF (Sun et al. 2018), vnrm.py (Chelouche et al. 2017), zdcf_v2.f90 (Alexander 1997), plike_v4.f90 (Alexander 1997), delay_chi2.f (Czerny et al. 2013).

Appendix A Photometric and Spectroscopic Data

In this section, we summarize the characteristics of Fe II and Mg II lines in Table A1, where we specifically list the Fe II and

Table A1
Table of Fe II and Mg II Equivalent Widths in Å, Velocity Shift in km s⁻¹, Line Width in Å, and the Mg II Flux Density in erg s⁻¹ cm⁻² Å⁻¹

Obs. No.	JD -2 450 000	EW(Fe II) Å	EW(Mg II) Å	Shift km s ⁻¹	Width Å	Flux density erg s ⁻¹ cm ⁻² Å ⁻¹
1	6314.4087	13.71 ^{+0.91} _{-0.93}	34.18 ^{+0.51} _{-0.49}	1666.98 ^{+17.04} _{-16.65}	2149.29 ^{+28.50} _{-40.08}	(3.836 ± 0.074) × 10 ⁻¹⁴
2	6320.3859	9.75 ^{+1.34} _{-1.32}	35.89 ^{+0.79} _{-0.74}	1723.70 ^{+23.73} _{-23.96}	2196.68 ^{+54.72} _{-52.86}	(4.000 ± 0.114) × 10 ⁻¹⁴
3	6523.5954	10.73 ^{+2.28} _{-2.22}	34.67 ^{+1.25} _{-1.20}	1529.11 ^{+39.28} _{-39.12}	2165.96 ^{+88.44} _{-81.07}	(3.966 ± 0.178) × 10 ⁻¹⁴
4	6651.4751	10.38 ^{+1.77} _{-1.72}	36.59 ^{+1.04} _{-1.02}	1598.83 ^{+31.86} _{-31.09}	2289.73 ^{+81.43} _{-64.80}	(4.051 ± 0.152) × 10 ⁻¹⁴
5	6697.3600	14.13 ^{+1.32} _{-1.34}	37.93 ^{+0.78} _{-0.76}	1617.81 ^{+22.58} _{-22.60}	2316.05 ^{+46.37} _{-43.77}	(4.219 ± 0.114) × 10 ⁻¹⁴
6	6892.5678	17.07 ^{+1.11} _{-1.03}	36.06 ^{+0.56} _{-0.58}	1554.76 ^{+18.02} _{-18.05}	2218.54 ^{+41.03} _{-38.86}	(3.911 ± 0.094) × 10 ⁻¹⁴
7	7003.5182	13.25 ^{+0.58} _{-0.64}	35.64 ^{+0.36} _{-0.34}	1608.01 ^{+11.37} _{-11.35}	2307.95 ^{+24.90} _{-23.98}	(3.908 ± 0.067) × 10 ⁻¹⁴
8	7082.2985	13.29 ^{+0.83} _{-0.82}	31.20 ^{+0.48} _{-0.44}	1615.91 ^{+17.11} _{-17.14}	2300.84 ^{+46.54} _{-35.14}	(3.702 ± 0.080) × 10 ⁻¹⁴
9	7243.6124	13.93 ^{+0.69} _{-0.72}	30.65 ^{+0.41} _{-0.36}	1597.95 ^{+14.64} _{-14.64}	2250.33 ^{+34.74} _{-28.81}	(3.856 ± 0.069) × 10 ⁻¹⁴
10	7289.4741	13.57 ^{+0.89} _{-0.86}	31.14 ^{+0.47} _{-0.46}	1613.10 ^{+17.51} _{-17.45}	2213.75 ^{+45.45} _{-31.14}	(3.953 ± 0.082) × 10 ⁻¹⁴
11	7341.3298	12.46 ^{+0.82} _{-0.87}	32.33 ^{+0.45} _{-0.49}	1597.92 ^{+16.98} _{-17.10}	2296.71 ^{+40.25} _{-39.59}	(4.127 ± 0.082) × 10 ⁻¹⁴
12	7374.4950	13.43 ^{+0.83} _{-0.83}	28.87 ^{+0.43} _{-0.45}	1594.19 ^{+19.07} _{-17.77}	2200.05 ^{+36.00} _{-35.27}	(3.681 ± 0.075) × 10 ⁻¹⁴
13	7423.3702	10.12 ^{+0.74} _{-0.72}	29.97 ^{+0.41} _{-0.44}	1669.13 ^{+16.79} _{-16.53}	2331.95 ^{+34.35} _{-39.93}	(3.860 ± 0.073) × 10 ⁻¹⁴
14	7656.2474	10.64 ^{+0.63} _{-0.61}	28.06 ^{+0.36} _{-0.33}	1664.97 ^{+14.98} _{-13.65}	2290.71 ^{+35.96} _{-30.11}	(4.204 ± 0.075) × 10 ⁻¹⁴
15	7687.3943	10.65 ^{+0.65} _{-0.62}	28.08 ^{+0.36} _{-0.35}	1664.77 ^{+15.31} _{-14.89}	2288.94 ^{+37.67} _{-30.63}	(3.979 ± 0.067) × 10 ⁻¹⁴
16	7722.5591	11.90 ^{+0.66} _{-0.66}	26.62 ^{+0.38} _{-0.34}	1672.60 ^{+16.16} _{-15.95}	2254.84 ^{+29.84} _{-40.84}	(3.781 ± 0.066) × 10 ⁻¹⁴
17	7752.4673	10.26 ^{+0.58} _{-0.58}	27.94 ^{+0.34} _{-0.32}	1682.02 ^{+14.26} _{-14.03}	2298.09 ^{+29.95} _{-33.91}	(4.125 ± 0.065) × 10 ⁻¹⁴
18	7953.6598	12.10 ^{+0.64} _{-0.64}	25.37 ^{+0.33} _{-0.34}	1648.26 ^{+15.85} _{-15.69}	2208.36 ^{+32.51} _{-31.79}	(3.683 ± 0.054) × 10 ⁻¹⁴
19	7979.5920	11.83 ^{+0.59} _{-0.62}	28.05 ^{+0.35} _{-0.34}	1640.45 ^{+14.78} _{-14.73}	2363.17 ^{+33.85} _{-35.90}	(4.072 ± 0.067) × 10 ⁻¹⁴
20	8114.4800	10.35 ^{+0.56} _{-0.65}	27.40 ^{+0.36} _{-0.32}	1681.22 ^{+14.14} _{-14.81}	2337.25 ^{+33.20} _{-37.38}	(4.250 ± 0.067) × 10 ⁻¹⁴
21	8167.3265	9.26 ^{+0.53} _{-0.58}	26.59 ^{+0.34} _{-0.27}	1649.54 ^{+14.75} _{-14.32}	2358.10 ^{+33.34} _{-34.15}	(4.025 ± 0.063) × 10 ⁻¹⁴
22	8376.5021	13.63 ^{+0.65} _{-0.62}	29.30 ^{+0.36} _{-0.35}	1631.38 ^{+14.73} _{-14.41}	2326.37 ^{+30.10} _{-29.91}	(4.380 ± 0.069) × 10 ⁻¹⁴
23	8498.4167	10.98 ^{+0.61} _{-0.65}	29.25 ^{+0.37} _{-0.37}	1800.13 ^{+15.32} _{-14.75}	2343.83 ^{+30.65} _{-41.66}	(4.323 ± 0.070) × 10 ⁻¹⁴
24	8543.3100	8.85 ^{+0.61} _{-0.62}	29.55 ^{+0.38} _{-0.36}	1751.82 ^{+15.48} _{-14.00}	2368.61 ^{+33.36} _{-42.12}	(4.361 ± 0.071) × 10 ⁻¹⁴
25	8719.5708	15.47 ^{+0.94} _{-0.91}	32.19 ^{+0.54} _{-0.52}	1667.05 ^{+19.55} _{-19.16}	2359.25 ^{+52.31} _{-40.14}	(4.722 ± 0.092) × 10 ⁻¹⁴

Note. The flux density was calculated for the case without the BMT data; see the text for the description.

Table A2
Table of Continuum Magnitudes with Uncertainties

JD −2450,000	Magnitude (V band) mag	Error mag	Instrument No.
6199.79634	16.763	0.005	1
6210.81464	16.755	0.003	1
6226.67656	16.771	0.004	1
6246.69516	16.761	0.004	1
6257.74660	16.763	0.005	1
6268.68051	16.767	0.004	1
6277.68239	16.738	0.003	1
6286.66584	16.782	0.004	1
6297.61482	16.770	0.004	1
6307.57245	16.769	0.004	1
6317.63928	16.799	0.004	1
6330.65489	16.789	0.003	1
6351.54598	16.788	0.004	1
6363.57130	16.782	0.003	1
6379.48424	16.762	0.004	1
6379.49181	16.755	0.004	1
6387.50984	16.780	0.003	1
6637.66923	16.767	0.003	1
6651.62009	16.806	0.003	1
6665.60325	16.812	0.004	1
6678.59717	16.796	0.003	1
6689.67132	16.792	0.003	1
6700.63473	16.809	0.004	1
6715.57393	16.791	0.003	1
6740.48864	16.789	0.004	1
6892.59242	16.830	0.011	2
7003.54330	16.819	0.012	2
7036.65108	16.747	0.004	1
7048.65280	16.731	0.003	1
7060.60356	16.700	0.004	1
7082.30016	16.749	0.012	2
7084.53369	16.732	0.005	1
7118.50567	16.731	0.005	1
7243.61293	16.664	0.011	2
7253.88913	16.668	0.003	1
7261.88037	16.684	0.004	1
7267.91217	16.650	0.004	1
7273.84457	16.683	0.004	1
7283.84655	16.659	0.004	1
7289.47056	16.698	0.012	2
7295.84011	16.661	0.004	1
7306.77839	16.677	0.004	1

Note. The epoch is given in Julian dates (−2450,000). The last column denotes three different instruments used to obtain the photometry data: 1. OGLE, 2. SALTICAM, 3. BMT. The BMT photometry points were shifted by 0.171 mag to larger magnitudes to match the last OGLE point with the closest BMT point in the lightcurve.

Table A3
Table of Continuum Magnitudes with Uncertainties

JD −2450,000	Magnitude (V band) mag	Error mag	Instrument No.
7317.73770	16.678	0.004	1
7327.77204	16.686	0.004	1
7340.70393	16.655	0.003	1
7341.32488	16.671	0.011	2
7355.69184	16.656	0.004	1
7363.66368	16.627	0.003	1
7374.49091	16.654	0.011	2
7374.70619	16.657	0.003	1

Table A3
(Continued)

JD −2450,000	Magnitude (V band) mag	Error mag	Instrument No.
7385.55446	16.624	0.003	1
7398.61439	16.641	0.003	1
7415.58224	16.634	0.003	1
7423.36782	16.633	0.011	2
7426.56315	16.653	0.003	1
7436.52206	16.626	0.004	1
7447.52422	16.623	0.003	1
7457.51899	16.641	0.003	1
7656.47709	16.545	0.011	2
7687.38749	16.543	0.011	2
7717.70291	16.541	0.003	1
7722.55378	16.513	0.011	2
7752.46369	16.496	0.011	2
7973.91046	16.518	0.006	1
7979.59391	16.502	0.011	2
8038.85902	16.509	0.004	1
8084.30756	16.429	0.011	2
8090.70000	16.338	0.008	3
8114.47660	16.193	0.011	2
8138.70000	16.305	0.008	3
8139.60000	16.311	0.004	3
8146.60000	16.284	0.003	3
8165.60000	16.296	0.005	3
8167.32241	16.464	0.011	2
8173.60000	16.277	0.007	3
8180.50000	16.261	0.006	3
8196.50000	16.291	0.008	3
8205.50000	16.274	0.006	3
8365.90000	16.285	0.006	3
8377.50208	16.486	0.011	2
8386.90000	16.302	0.008	3
8414.80000	16.319	0.005	3
8498.41249	16.509	0.011	2
8543.30431	16.484	0.011	2
8566.50000	16.319	0.008	3
8719.57089	16.498	0.011	2

Note. The epoch is given in Julian dates (−2450 000). The last column denotes three different instruments used to obtain the photometry data: 1. OGLE, 2. SALTICAM, 3. BMT. The BMT photometry points were shifted by 0.171 mag to larger magnitudes to match the last OGLE point with the closest BMT point in the lightcurve.

Mg II equivalent widths in Å, velocity shift in km s^{-1} , line width in Å, and the Mg II flux density in $\text{erg s}^{-1} \text{cm}^{-2} \text{Å}^{-1}$. The continuum magnitudes (V band) from the three instruments—OGLE, SALTICAM, and BMT—are included in Tables A2 and A3.

Appendix B

Overview of Time-delay Determination Methods

B.1. Interpolated Cross-correlation Function (ICCF)

The ICCF is a standard method for determining the time-delay between the continuum and line-emission lightcurves. In general, both lightcurves are unevenly sampled, while the ICCF by its definition requires regular sampling with a certain time-step, which is achieved by the interpolation of the continuum lightcurve with respect to the line-emission lightcurve or vice versa (asymmetric ICCF). The definition of the ICCF

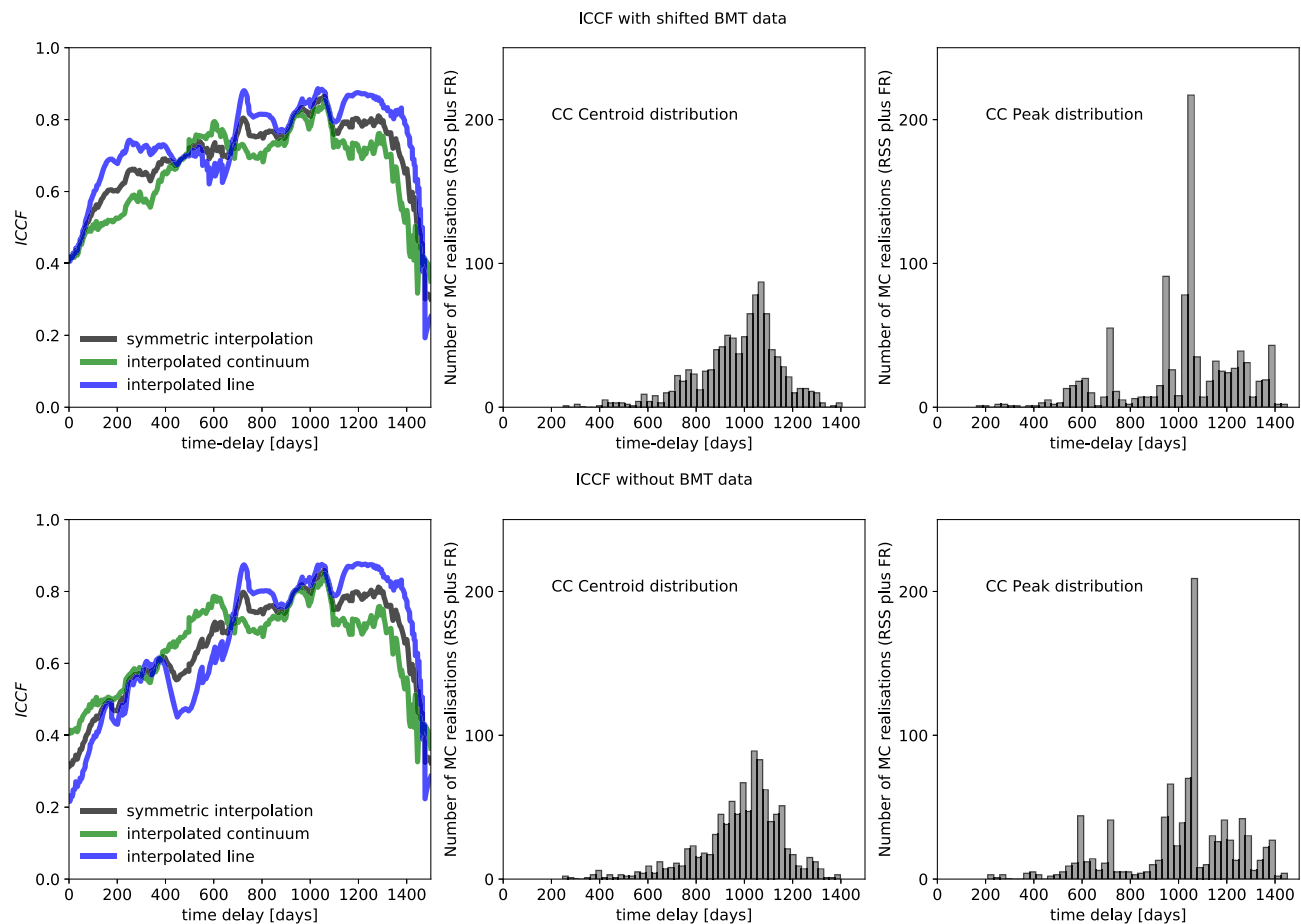


Figure B1. Interpolated cross-correlation coefficient as a function of time-delay in the observer’s frame. Top panel: the interpolated cross-correlation function (ICCF) as a function of time-delay, including shifted BMT points. The middle panel displays the distribution of cross-correlation centroids, while the right panel shows the distribution of cross-correlation peaks. Bottom panel: the same as in the top panel but without BMT data.

between the two lightcurves, x_i and y_i , with the step-size of $\Delta t = t_{i+1} - t_i$, is

$$CCF(\tau_k) = \frac{(1/N) \sum_{i=1}^{N-k} (x_i - \bar{x})(y_{i+k} - \bar{y})}{\left[(1/N) \sum_{i=1}^N (x_i - \bar{x})^2 \right]^{1/2} \left[(1/N) \sum_{i=1}^N (y_i - \bar{y})^2 \right]^{1/2}}, \quad (\text{B1})$$

where τ_k is the time-shift $\tau_k = k\Delta t$, where the index $k = 1, \dots, N - 1$, of the second lightcurve with respect to the first one, and where \bar{x} and \bar{y} are the means of the two lightcurves x_i and y_i . The final, symmetric ICCF is obtained by averaging the ICCFs from both interpolations.

We apply the Python implementation of ICCF, the script PYCCF (Sun et al. 2018) based on an earlier ICCF analysis of Peterson et al. (1998), which calculates the ICCF including the continuum, line-emission, and symmetric interpolation. Using 1,000 Monte Carlo realizations of random subset selection (RSS) and flux randomization (FR), we obtained ICCF peak and centroid distributions, including their corresponding uncertainties.

First, we cross-correlated the full continuum lightcurve, which included SALTICAM, OGLE, and flux-shifted BMT data, in total 86 points, with the Mg II lightcurve (25 points). In

addition, given the systematic offset of the BMT flux densities from SALTICAM points, we decided to perform the ICCF analysis also without them, which reduced the photometric lightcurve to 73 points. The ICCF values with respect to the time-delay, for which we separately calculated the continuum-interpolated, line-interpolated, and symmetric ICCF, with the corresponding peak and centroid distributions (for symmetric CCF) are displayed in Figure B1 with and without BMT points in the top and bottom panels, respectively. We summarize the peak and centroid values of the ICCF for the interpolated continuum, interpolated line-emission, and symmetric case in Table B1, where the cases with and without BMT data points are separated as well. When comparing these two cases in Table B1, the peak and centroid values for the case without the BMT data are generally comparable within the uncertainties, which is also visible in centroid and peak distributions in Figure B1.

The maximum values of the ICCF are about 0.8 (for the interpolation of the photometry), which for such a relatively short emission-line lightcurve is a high value, supporting the view that the delay determination should be in general reliable because the line and continuum are well correlated. For comparison, the maximum value of the ICCF for the quasar CTS C30.10, with similar formal data quality, was only 0.65 (Czerny et al. 2019; Zajaček et al. 2019b).

Table B1
Results of the Interpolated Cross-correlation Function Applied to HE 0413-84031 Lightcurves

	With Shifted BMT Data	Without BMT Data
Interpolated continuum—centroid [days]	1004.6 ^{+196.8} _{-246.2}	1003.2 ^{+205.3} _{-235.4}
Interpolated continuum—peak [days]	1060.0 ^{+228.0} _{-342.6}	1061.0 ^{+228.2} _{-270.8}
Interpolated line—centroid [days]	1008.4 ^{+142.2} _{-276.9}	1034.17 ^{+139.1} _{-248.9}
Interpolated line—peak [days]	984.0 ^{+227.6} _{-349.0}	1001.0 ^{+252.3} _{-282.0}
Symmetric—centroid [days]	1009.7 ^{+113.6} _{-211.5}	1021.7 ^{+114.5} _{-207.8}
Symmetric—peak [days]	1056.0 ^{+197.0} _{-332.1}	1057.0 ^{+196.0} _{-343.8}

Note. We include centroids and peaks with uncertainties for interpolated continuum lightcurve, interpolated emission lightcurve, and symmetric ICCF. Cases with and without BMT data are separated. The time-delays are expressed in light days in the observer’s frame.

Table B2
Time-delay in Light Days Corresponding to the Peak Values of DCF in the Observer’s Frame

	With Shifted BMT Data	Without BMT Data
Time-delay at the DCF peak (0,1500; 120)	812.7 (DCF = 0.82)	812.7 (DCF = 0.80) ¹
Time-delay at the DCF peak (200,1100; 20)	730.0 (DCF = 0.93)	730.0 (DCF = 0.92)
Peak time-delay—bootstrap [days]	720.4 ^{+115.1} _{-147.9}	726.0 ^{+114.4} _{-145.7}
Mean time-delay—bootstrap [days]	658.7 ^{+116.2} _{-139.2}	665.4 ^{+115.0} _{-142.8}

Note. Two time intervals are analyzed: between 0 and 1500 days, and the narrower interval between 200 and 1100 days. The bottom two lines show the peak and the mean time-delay as inferred from 500 bootstrap realizations. (1) This is the value for the maximum DCF for time-delays less than 1300 days; the time-delay at 1315 days has the larger DCF of 0.82, but this value can be excluded as it approaches the end of the observational run.

We also tested if the linear trend present in the continuum should be eventually subtracted before the time-delay is measured. However, we noticed that such a trend subtraction decreases the maximum value of the correlation in ICCF. For example, for the interpolated continuum, without BMT data points, r_{\max} decreases from 0.85 down to 0.61. Thus we conclude that the trend subtraction is not beneficial for the time-delay analysis. The presence of the trend is natural if the lightcurve of the red noise character, as here, covers the period shorter than the maximum timescale present in the system. The time-delay measurement is not strongly affected anyway; we obtain for the same case the peak time-delay of 1037.0 days instead of 1061.0 days. Thus, in further analysis, we do not consider the trend subtraction.

B.2. Discrete Correlation Function (DCF)

Edelson & Krolik (1988) suggested using the DCF because the ICCF by definition introduces additional interpolated data points and can thus distort the time-delay determination, especially for the unevenly and sparsely sampled pairs of lightcurves. The basic algorithm is to search for data pairs (x_i, y_j) between the two lightcurves that fall into the time-delay bin $\tau - \delta\tau/2 \leq \Delta t_{ij} < \tau + \delta\tau/2$, where τ is the time-delay, $\delta\tau$ is the chosen time-delay bin, and $\Delta t_{ij} = t_j - t_i$. Given M such pairs, we can calculate the unbinned discrete correlation coefficient for each of them,

$$\text{UDCF}_{ij} = \frac{(x_i - \bar{x})(y_j - \bar{y})}{\sqrt{(s_x - \sigma_x^2)}\sqrt{(s_y - \sigma_y^2)}}, \quad (\text{B2})$$

where \bar{x} and \bar{y} are the lightcurve means in the given time-delay bin; s_x , s_y are the variances; and σ_x , σ_y are the mean measurement errors for a given bin. The discrete correlation function for a given time-delay is calculated by averaging over

M data point pairs,

$$\text{DCF}(\tau) = \frac{1}{M} \sum_{ij} \text{UDCF}_{ij}. \quad (\text{B3})$$

The error of the DCF can be formally inferred from the relation

$$\sigma_{\text{DCF}}(\tau) = \frac{1}{M-1} \sqrt{\sum [\text{UDCF}_{ij} - \text{DCF}(\tau)]^2}. \quad (\text{B4})$$

For our DCF analysis, we make use of the Python code `pyDCF` by Robertson et al. (2015) with the possibility of applying the Gaussian weighting scheme to matching pairs of both lightcurves. We also tested different time-delay bins as well as the searched time-delay intervals. In addition, we extended the DCF analysis by including the bootstrap technique to construct time-delay distributions and to infer the actual peaks and their uncertainties.

We explore the correlation of the two lightcurves on two timescales:

1. Between 0 and 1500 days, with a time-step of 120 days,
2. Between 200 and 1100 days, with a smaller time-step of 20 days.

As before for the ICCF analysis, we perform the DCF analysis with and without flux-shifted BMT data. The time-delays for the peak values of the DCF are shown in Table B2. The figures of the DCF versus the time-delay are in Figure B2 for the case with and without BMT data points in the left and right panels, respectively. In the top panels of Figure B2, we show the whole explored time-range between 0 and 1500 days (with a time-step of 120 days); in the bottom panels, we display the DCF analysis in the time-range (200, 1100) days with a smaller time-step of 20 days.

To determine the uncertainty of the DCF peaks as well as the mean values for the time-delay, we perform 500 bootstrap simulations by randomly selecting subsamples of the

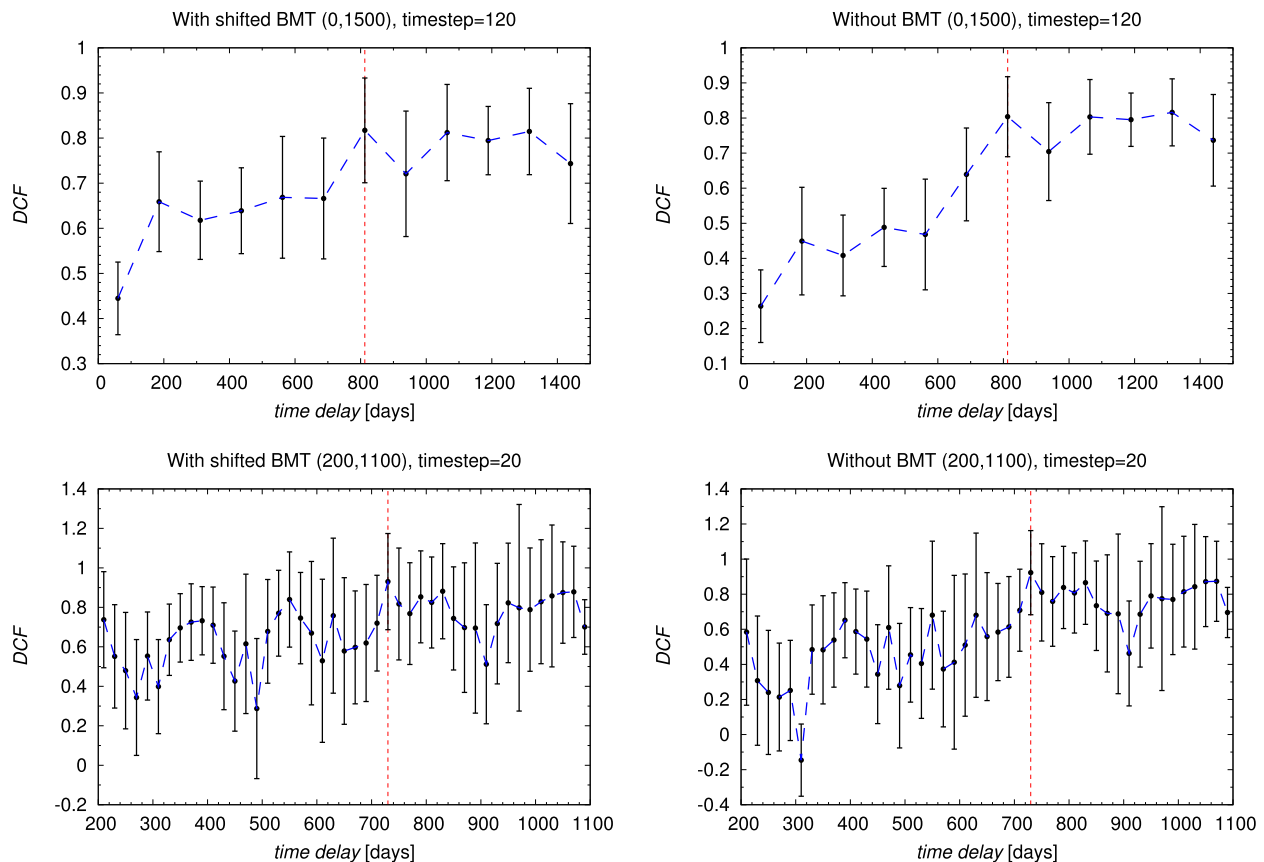


Figure B2. The discrete correlation function (DCF) as a function of the time-delay in the observer’s frame. Top panels: the DCF determined between 0 and 1500 days, with a time-step of 120 days. To the left we include the shifted BMT flux densities for the continuum; to the right, they are omitted. The vertical dashed line denotes the time-delay for the maximum DCF. Bottom panels: similar to the panel above, the DCF analysis was performed for the time-interval of 200–1100 days with a smaller time-step of 20 days. The vertical dashed line denotes the time-delay for the maximum DCF.

lightcurves for both the cases with the flux-shifted BMT data and without them. The values of the peak and mean time-delays are in Table B2. The peak time-delay (for the largest DCF value) is clearly in the interval around 720–730 days, as is also visible in the histograms in Figure B3 for both the cases with and without BMT data in the left and right panels, respectively.

B.3. z -transformed Discrete Correlation Function (z DCF)

Alexander (1997) proposed the z DCF to correct several biases of the classical DCF (Edelson & Krolik 1988); namely, it replaces equal time-lag binning with equal population binning and uses Fisher’s z -transform. The minimum required number of observed points is 11; therefore, the z -transformed DCF is specially suited for undersampled, sparse and heterogeneous pairs of lightcurves, which is the case for our continuum and line-emission lightcurves, as they are combined from different instruments. In addition, z DCF does not assume any lightcurve properties, such as smoothness, or any AGN variability process. Moreover, from Monte Carlo generated pairs of lightcurves with randomized errors, it is possible to infer the uncertainty from the averaged z DCF values.

For our z DCF analysis, we first used 86 continuum measurements (including data from OGLE, SALTICAM, and flux-corrected BMT) and 25 Mg II line-emission points (from SALT spectral observations). The z DCF values as a function of

the time-delay are displayed in Figure B4, including both errors for the time-delay and the z DCF value. Two peaks are apparent, $\tau_1 = 720.9$ days with z DCF = 0.92, and $\tau_2 = 1059$ days with z DCF = 0.91. To evaluate the uncertainties of these peaks, we ran the maximum-likelihood (ML) analysis for the surroundings of each peak, between 500 and 1000 days for the peak at 721 days and 1000 and 1500 days for the peak at 1059 days. In the next step, we performed global ML analysis of the time-delay peaks between 0 and 2000 days, with the most likely peak at 721^{+324}_{-527} days. The results are shown in Table B3 (left column).

In the continuum lightcurve, the BMT points needed to be systematically shifted toward smaller flux densities to match OGLE and SALTICAM values. Therefore we also performed z DCF analysis without BMT points, with the total of 73 continuum points and 25 Mg II line-emission points. The overall results concerning the time-delay peaks were not affected; see Table B3 (right column) and Figure B4 (right panel). The global peak remained at $720.9^{+331.3}_{-100.1}$ days with a smaller lower uncertainty interval than for the case including BMT data points, but with a comparable likelihood value.

B.4. The JAVELIN Code Package

Another way of estimating the time-delay is to model the AGN continuum variability as a stochastic process via the

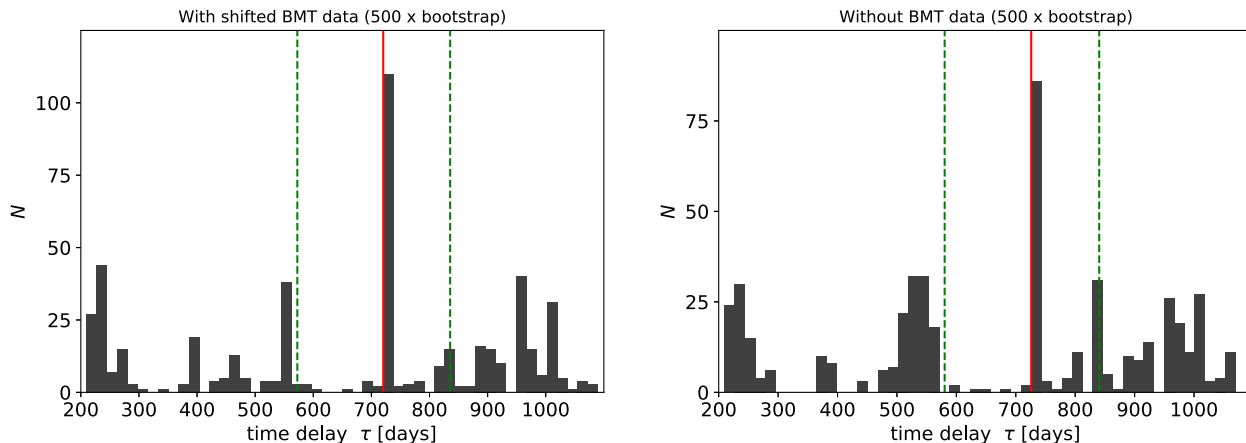


Figure B3. Histograms of the time-delays constructed from 500 bootstrap realizations of the DCF analysis. Left panel: with flux-shifted BMT data included. Right figure: without BMT data. In both panels, the red vertical line marks the histogram peak value, and the two green horizontal lines stand for 1σ uncertainties of the peak.

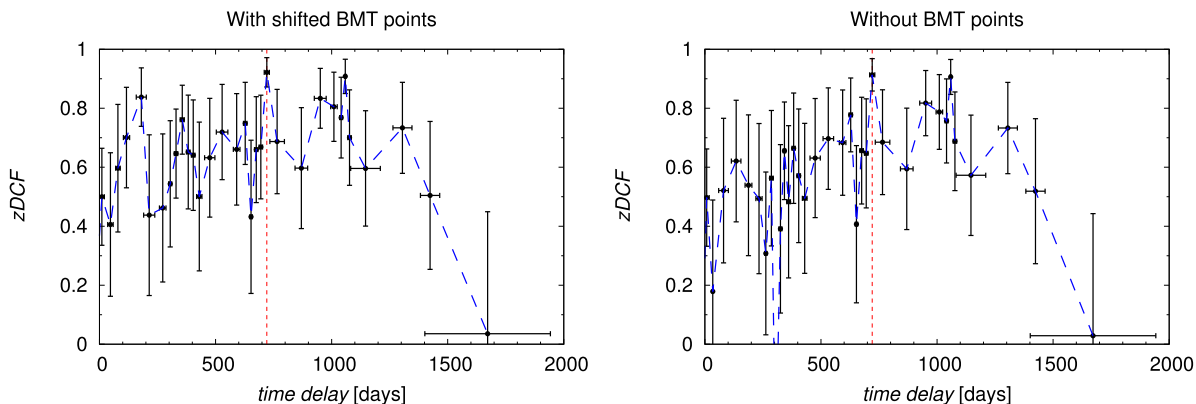


Figure B4. The z DCF values as a function of the time-delay, including the uncertainties for the time-delay and the z DCF values. Left panel: z DCF values as a function of the time-delay in the observer's frame based on the continuum lightcurve (including OGLE, SALTICAM, and flux-corrected BMT data) and Mg II line-emission lightcurve (SALT telescope). The red dashed vertical line denotes the most prominent peak at 721 days. Right panel: z DCF values vs. the time-delay in the observer's frame as in the left panel, but without BMT data points.

Table B3

Maximum-likelihood (ML) Analysis for the z DCF Time-delay Values with and Without Flux-shifted BMT Points Included

Time-delay Interval	With Shifted BMT Data	Without BMT Data
500–1000 days	$720.9^{+78.8}_{-24.1}$, $\mathcal{L} = 0.51$	$720.9^{+80.6}_{-84.5}$, $\mathcal{L} = 0.48$
1000–1500 days	$1059.0^{+219.5}_{-22.09}$, $\mathcal{L} = 0.53$	$1059.0^{+224.9}_{-19.6}$, $\mathcal{L} = 0.54$
0–2000 days	$720.9^{+323.9}_{-527.3}$, $\mathcal{L} = 0.1434$	$720.9^{+331.3}_{-100.1}$, $\mathcal{L} = 0.12$

Note. The time-delays are expressed in light days in the observer's frame. The table contains results for the localized ML analysis, taking into account the surroundings of the two most prominent peaks at 721 and 1059 days. The lower part contains the peak of the global ML analysis in the searched interval between 0 and 2000 days. The actual maximum likelihood is denoted as \mathcal{L} and its value is listed for the time-delay in each interval.

damped random walk process (DRW; Kelly et al. 2009; Kozłowski et al. 2010; MacLeod et al. 2010; Kozłowski 2016). The emission-line lightcurve is then modeled as a time-delayed, scaled, and smoothed response to the continuum stochastic

variability. Based on this model assumption, JAVELIN (Just Another Vehicle for Estimating Lags In Nuclei) code was developed (Zu et al. 2011, 2013, 2016).¹⁶ The JAVELIN package employs Markov Chain Monte Carlo (MCMC) to obtain posterior probabilities of the continuum variability timescale and amplitude. With these two parameters, distributions of three parameters—time-delay, smoothing width of the top-hat function, and scaling factor (ratio of the continuum and line-emission amplitudes $A_{\text{line}}/A_{\text{cont}}$)—that describe the line-emission lightcurve are searched for.

In Figure B5, we show the distributions of the time-delay and scaling factor in the top panels with and without (magnitude-shifted) BMT data in the left and the right panels, respectively. Both the peak and the mean of the distributions are consistent within the uncertainties, with the peak close to 1050 days.

To estimate the uncertainties for these time-delays, we ran 200 bootstrap realizations, generating randomly subsets of both

¹⁶ Please visit <https://bitbucket.org/nye17/javelin/src/develop/> for more information on the code usage and application.

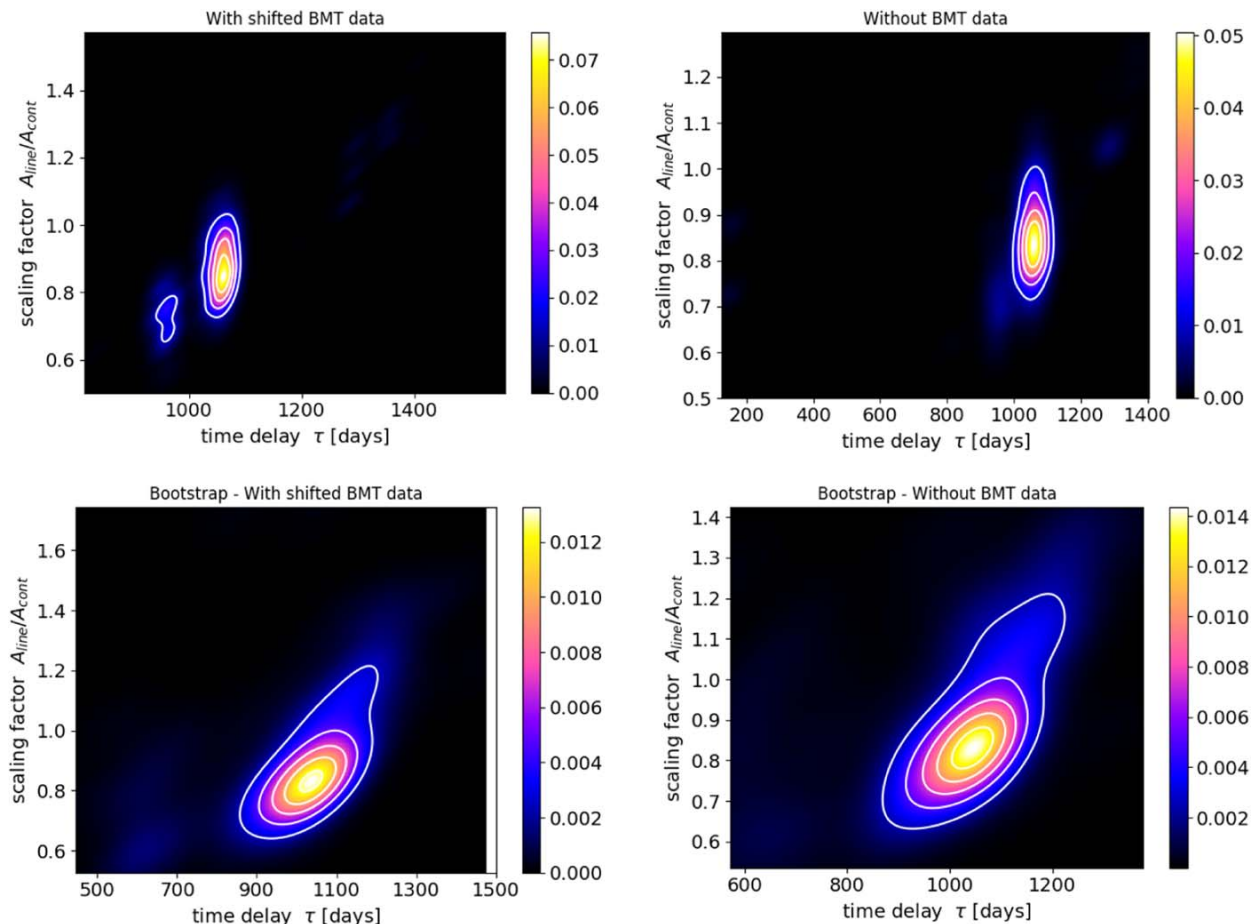


Figure B5. Color-coded plots of JAVELIN code results in the time-delay/scaling factor plane. Top row: time-delay distribution including magnitude-shifted BMT data (left panel) and without them (right panel). Bottom row: distribution of the time-delay mean values from 200 bootstrap realizations—including shifted BMT data (left panel) and without them (right panel).

lightcurves. The distributions of the means of time-delays are shown in the bottom panels of Figure B5 both with shifted BMT data (left panel) and without them (right panel). The peak and mean time-delays with corresponding uncertainties are listed in Table B4.

B.5. Measures of Regularity/Randomness—Von Neumann Estimator

A novel technique to investigate time-delays is to measure regularity or randomness of data (Chelouche et al. 2017), which has previously been extensively applied in cryptography or electronic data compression. This method does not require interpolation of lightcurves as the ICCF, nor does it require binning in the correlation space as for DCF and τ DCF. Moreover, the analysis is not based on any assumptions concerning the AGN variability in a way as the JAVELIN assumes for the continuum lightcurve. One of the most robust measures of the data regularity is an optimized Von Neumann scheme, which uses the combined lightcurve $F(t, \tau) = \{(t_i, f_i)\}_{i=1}^N = F_1 \cup F_2^\tau$, where F_1 is the continuum lightcurve and F_2^τ is the time-delayed line-emission lightcurve. Based on the combined lightcurve, the Von Neumann estimator is defined as the mean successive

difference of $F(t, \tau)$,

$$E(\tau) \equiv \frac{1}{N-1} \sum_{i=1}^{N-1} [F(t_i) - F(t_{i+1})]^2. \quad (\text{B5})$$

The minimum of the estimator E is reached for a certain time-delay $\tau = \tau'$, which is expected to be close to the actual time-delay, $\tau' = \tau_0$.

We applied the estimator to the data of HE 0413-4031 to estimate the time-delay between the continuum and Mg II line lightcurves. We made use of the Python implementation of the estimator in Equation (B5), which was demonstrated in Chelouche et al. (2017).¹⁷ In Figure B6, we show the estimator value as a function of the time-delay with and without magnitude-shifted BMT data in the left and the right panels, respectively. For the case with shifted BMT data, we obtain the minimum of $E(\tau)$ at 499.3 days, while without BMT data, the minimum is for the time-delay of 715.18 days.

To construct distributions of the estimator minima, we perform 10,000 bootstrap realizations for both cases with and without shifted BMT data. For both of these cases, the peak and the mean of the distributions are listed in Table B5. The

¹⁷ For the script, visit www.pozonunez.de/astro_codes/python/vnrm.py.

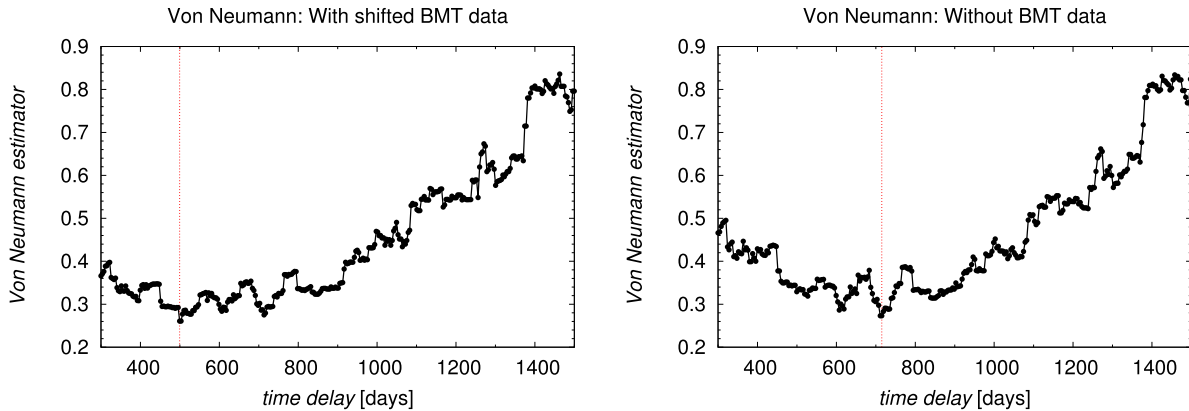


Figure B6. The Von Neumann estimator as a function of the time-delay. Left figure: the case with magnitude-shifted BMT data; the minimum at 499.33 days is depicted by a red vertical line. Right panel: the case without BMT data; the minimum at 715.18 days is represented by a red vertical line.

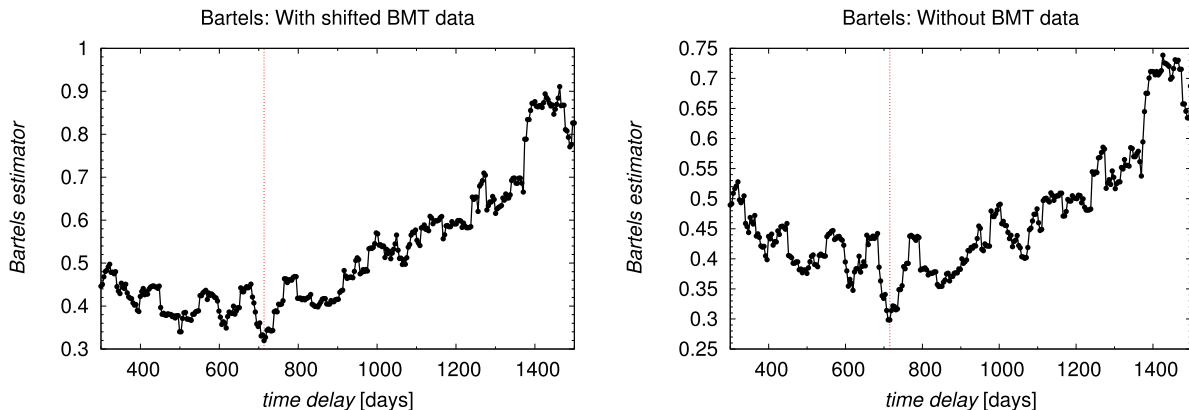


Figure B7. Bartels estimator as a function of the time-delay. Left figure: the case with magnitude-shifted BMT data; the minimum at 713.43 days is depicted by a red vertical line. Right panel: the case without BMT data; the minimum at 715.18 days is represented by a red vertical line.

Table B4

The Peak and Mean Values of the Time-delay Distribution (in the Observer's Frame) from 200 Bootstrap Realizations of JAVELIN

	With Shifted BMT Data	Without BMT Data
Peak time-delay [days]	$1053.7^{+79.8}_{-163.6}$	$1058.5^{+77.1}_{-150.7}$
Mean time-delay [days]	$1002.1^{+77.0}_{-161.8}$	$1016.0^{+70.5}_{-148.2}$

Note. Time-delays are expressed in light days.

minima and the peaks differ by about 200 days for the cases with and without BMT data. However, the minimum around 710 days is present for both cases, being a local minimum for the case with BMT data. This makes the peak at 710 days more robust, while we do not obtain any significant result for the peak at 1060–1070 days, which we obtained using JAVELIN and ICCF methods.

In addition, we perform the same analysis using the Bartels estimator, which is a modification of the Von Neumann estimator using the ranked unified lightcurve $F_R(t, \tau)$ (Bartels 1982). In comparison with the pure Von Neumann scheme, the Bartels modification of the estimator has a consistent global minimum at 713.43 and 715.18 days for both cases with and without BMT photometry data, respectively; see

Figure B7 (left and right panels, respectively). The peak values of the time-delay distribution in the observer's frame are also comparable; see Table B5. The mean value of the time-delay distribution is smaller for the case with the BMT data included, but within uncertainties the mean values of the time-delay are still comparable.

B.6. χ^2 Method

As for the quasar CTS C30.10 (Czerny et al. 2019), we also apply the χ^2 method to the lightcurves. It was found that the χ^2 method, which is frequently used in quasar lensing studies, works better than the ICCF for the AGN variability modeled as a red noise process (Czerny et al. 2013). The lightcurves were prepared as for the standard ICCF, that is, mean values were subtracted from them and they were normalized by their corresponding variances. Subsequently, the spectroscopic lightcurve was time-shifted with respect to the photometry lightcurve. The data points were linearly interpolated, but because the photometry lightcurve is denser than the spectroscopic lightcurve, we interpolated the photometry to the spectroscopy, i.e., we performed an asymmetric interpolation. Finally, we estimated the degree of similarity between shifted lightcurves by calculating the χ^2 , whose minimum may be considered as the most likely time-delay between the continuum and the line emission.

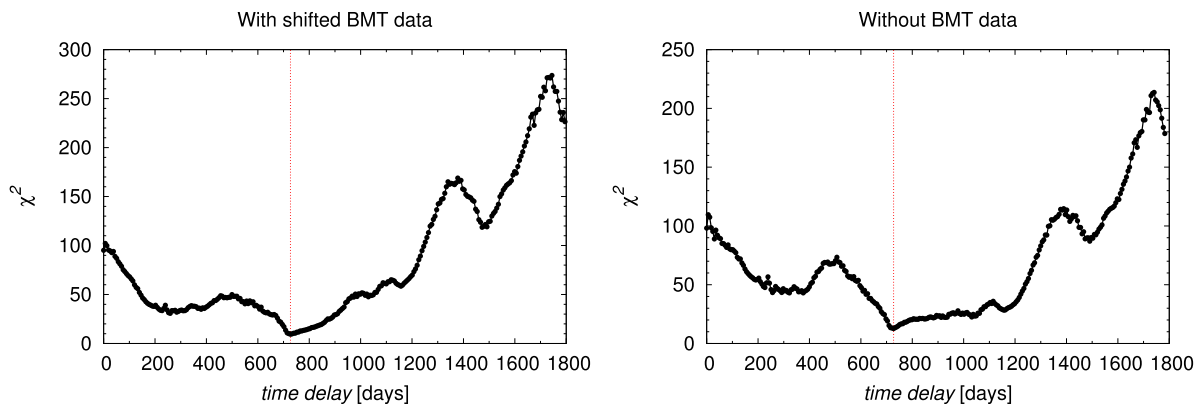


Figure B8. The values of the χ^2 statistic as a function of the time-delay expressed in days with respect to the observer's frame of reference. Left panel: the χ^2 values calculated for the case with the shifted BMT photometry data. Right panel: the χ^2 values calculated for the case without the BMT photometry data.

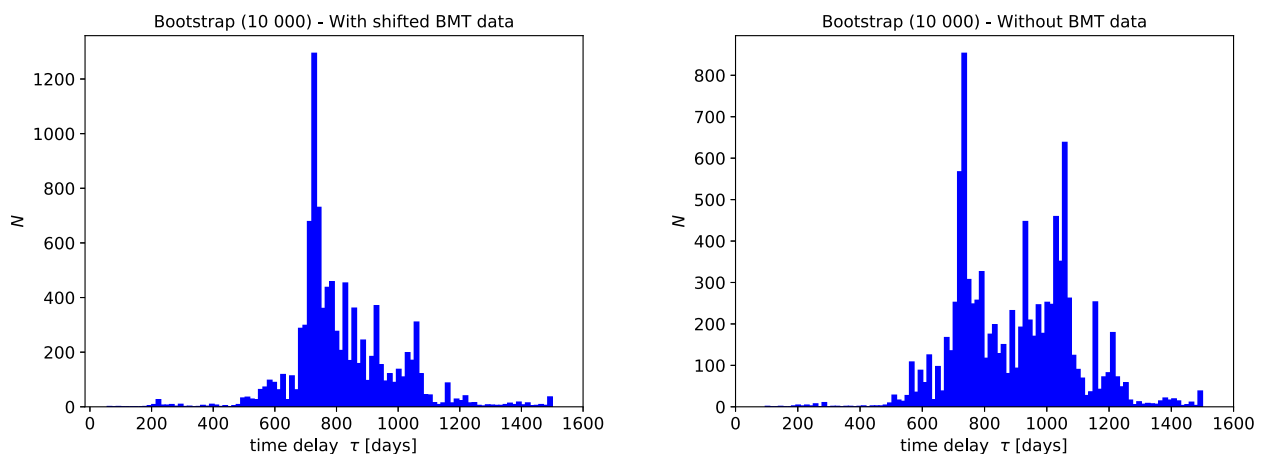


Figure B9. Distributions of the time-delays expressed in days in the observer's frame of reference for 10,000 bootstrap realizations. Left panel: the time-delay distribution based on the χ^2 analysis calculated for the case with the shifted BMT photometry data. Right panel: the time-delay distribution based on the χ^2 analysis calculated for the case without the BMT photometry data.

Table B5

The Upper Part of the Table Shows the Minima of the Von Neumann Estimator, the Peak and the Mean of Minimum Distributions for the Case With and Without Magnitude-shifted BMT Data in the Left and the Right Columns Respectively

Estimator	With Shifted BMT Data	Without BMT Data
Von Neumann: Minimum of $E(\tau)$ [days]	499.33	715.18
Von Neumann: Bootstrap (10,000) –peak [days]	$498.9^{+170.9}_{-123.9}$	$711.3^{+149.0}_{-139.5}$
Von Neumann: Bootstrap (10,000) –mean [days]	$588.5^{+157.3}_{-108.0}$	$708.1^{+147.0}_{-137.9}$
Bartels: Minimum of $E(\tau)$ [days]	713.43	715.18
Bartels: Bootstrap (10,000) –peak [days]	$710.9^{+172.3}_{-173.0}$	$714.6^{+176.1}_{-164.6}$
Bartels: Bootstrap (10,000) –mean [days]	$634.6^{+161.9}_{-159.9}$	$725.5^{+172.8}_{-150.3}$

Note. The lower part displays the same information as above, but for the Bartels estimator, which is the modification of the Von Neumann scheme using the ranked combined lightcurve. Time-delays are expressed in light days in the observer's frame.

In Figure B8, we show the χ^2 values as a function of the time-delay in the observer's frame of reference for the case with the magnitude-shifted BMT data included (left panel) and without them (right panel). In both cases, the global minimum of χ^2 is close to $\tau = 727$ days. To determine the uncertainty of this minimum, we construct the distributions of the time-delay by performing 10,000 bootstrap realizations, i.e., by creating randomly selected subsets of both lightcurves and using the χ^2

method for each new pair. The distributions are displayed in Figure B9. Both cases with and without the BMT data have one main peak and secondary peaks toward longer time-delays. The peak and mean values of the distributions are listed in Table B6. The peak and mean values are within uncertainties consistent, with the mean values shifted toward larger values with respect to the peak values because of the presence of secondary peaks at larger time-delays.

Table B6Results of the χ^2 Analysis of the Time-delay for Two Cases: With and Without Shifted BMT Data

Statistic	With Shifted	Without BMT Data
	BMT Data	
χ^2 minimum [days]	726.86	727.41
Bootstrap (10,000)– peak [days]	$720.4^{+145.6}_{-102.2}$	$727.7^{+160.0}_{-85.2}$
Bootstrap (10,000)– mean [days]	$818.6^{+133.0}_{-85.2}$	$900.0^{+110.8}_{-91.3}$

Note. We list the χ^2 minima, the peaks, and the means of the time-delay distributions expressed for the observer’s frame of reference. Time-delays are expressed in light days.

Appendix C

Tests of Complementary UV Fe II Templates

We used the theoretical Fe II templates from Bruhweiler & Verner (2008) (hereafter **d12** template) in our basic modeling, because one of these templates, **d12-m20-20-5.dat**, allowed us to get very nice and simple fits to all data sets. However, other Fe II templates are also used. Therefore, for our mean spectrum, we additionally tested two other templates. The first one was a semiempirical template of Tsuzuki et al. (2006) (hereafter **T06**) based on a combination of 14 low-redshift quasars and CLOUDY modeling of the Fe II emission to disentangle the Fe II and Mg II contribution. This template combined the advantage of the previously used purely observational template of Vestergaard & Wilkes (2001) and a theoretical modeling. The results are given in Table C1. The fits obtained with this template had the same number of free parameters as the fits with **d12-m20-20-5.dat**, if a single Lorentzian is used for Mg II, but the fit quality is always lower. The fits do not depend strongly on the doublet ratio, because the Mg II line is unresolved, and the change of the doublet ratio is easily compensated with the change of the redshift and the shift of the Mg II line with respect to the Fe II emission. Even if we add the second kinematic component, fits do not improve considerably, and final χ^2 is higher than for our canonical fits.

Next we incorporate the semiempirical UV Fe II template¹⁸ (hereafter referred to as the KDP15 template, Kovačević-Dojčinović & Popović 2015; Popović et al. 2019) to fit the Fe II pseudo-continuum in spectral window 2700–2900 Å. This model includes overall 7 free parameters, which includes 5 multiplets, namely, 60 ($a^4D-z^6F^o$), 61 ($a^4D-z^6P^o$), 62 ($a^4D-z^4F^o$), 63 ($a^4D-z^4D^o$), and 78 ($a^4P-z^4P^o$). Additionally, there is an empirically added component, “I Zw 1 lines,” that is represented with two Gaussians (at $\lambda\lambda 2720, 2840$ Å). This additional empirical set of lines was included in the model because they were not identified in the emission within ~ 2825 – 2860 Å and 2690 – 2725 Å. The remaining parameter is the line width (see Appendix A1 in Popović et al. 2019, for more details).

The fits with this template, also given in Table C1. In the case of a single kinematic component, the provided fits are again not better in comparison with our standard fits. However, if we allow for two kinematic components for Mg II, indeed the resulting χ^2 is lower, particularly if we optimize the redshift to the new template. Although during the fitting we allowed for all the six template components to vary, we noticed in the final fits

that the multiplets 61, 63, and 78 converge to values close to zero, and only the multiplets 60 and 62 and the “I Zw 1 lines” return nonzero values. This is consistent with the Figure A1 in the paper of Popović et al. (2019). In their figure, the multiplets 60 and 78 are outside our spectral window, and the multiplet 63 has a very weak contribution (by a factor ~ 3 – 3.5 times with respect to multiplet 62).

This new best fit implies a different shape of the Mg II line and different kinematics of the Fe II– and Mg II–emitting region. With **d12-m20-20-5.dat**, the Mg II line was represented by a single Lorentzian, and FWHM of the Mg II line was somewhat broader than the requested FWHM of the Fe II (4380 km s^{-1} , and 2800 km s^{-1} , respectively), implying that Fe II emission comes on average from a little more distant part of the BLR. In the case of the new best fit, the requested FWHM of Fe II is larger, 4000 km s^{-1} , and the two components of Mg II, if treated as separate components, have the corresponding values of FWHM of 3100 km s^{-1} and 9050 km s^{-1} , respectively, thus considerable part of the Mg II emission should originate at a larger distance than Fe II. If the two Mg II components are treated as a single asymmetric line, then the FWHM of Mg II is 4250 km s^{-1} just above that for Fe II emission in this model, but effectively similar to the FWHM of Mg II from the basic model. However, the overall line shape is widely different, and we present the new fit in Figure C1. The very broad Mg II component is then located at the same position as the Fe II emission, but the narrower Mg II component is again shifted considerably by 1545 km s^{-1} with respect to Fe II, which is comparable to the shift of 1620 km s^{-1} in our basic fits using a single Lorentzian component discussed in Section 3.1.

In addition, we verify statistically whether the fit using the KDP15 template provides an overall improvement. We compare the KDP15 template with the original fit using the **d12** Fe II template, which has $p_1 = 8$ parameters (2 for Fe II, 3 for the Mg II single Lorentzian component, 2 for the power-law continuum, and 1 for the redshift). The KDP15 template uses 7 parameters for the Fe II pseudo-continuum, 5 parameters for the Mg II line with 2 Gaussian components, 2 for the power-law continuum, and 1 for the redshift, overall $p_2 = 15$ parameters. Given the $\chi_1^2 = 2088.42$ for the **d12** fitting, $\chi_2^2 = 1711.34$ for the KDP15 template, and the total number of data points of $n = 579$, we can calculate the F statistic with the null hypothesis that the apparently better fit using the KDP15 template does not lead to an improvement. The F statistic can be calculated as follows

$$F = \frac{(\chi_1^2 - \chi_2^2)/(p_2 - p_1)}{\chi_2^2/(n - p_2)}, \quad (C1)$$

which for the values above gives $F = 17.75$. When the three parameters in the KDP15 template that converge to zero are removed from the calculation, we get $F' = 31.23$. Because these values are larger than the test statistic critical value, which is between 1 and 2 for our F distribution with (7564) degrees of freedom,¹⁹ the null hypothesis is rejected and formally, the fit using the KDP15 template with 2 Gaussian components for the Mg II line is better.

The new fit still implies a considerable shift between Fe II and Mg II components, which is not expected according to

¹⁸ http://servo.aob.rs/FeII_AGN/link7.html

¹⁹ <http://www.itl.nist.gov/div898/handbook/eda/section3/eda3673.htm>

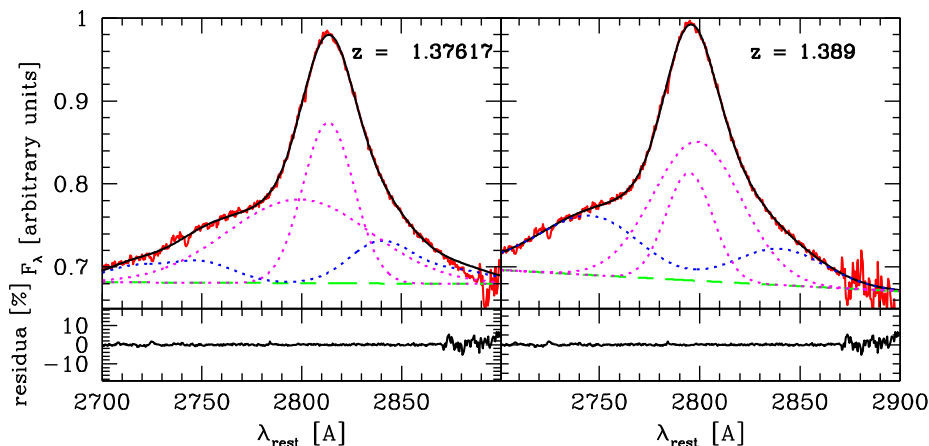


Figure C1. Left panel: the best fit to the mean spectrum with the Fe II template (Kovačević-Dojčinović & Popović, 2015; Popović et al. 2019) and 2 Gaussian components, for the best-fit redshift of 1.37617. Visually, the residuals are similar, but the implied shape of the Mg II line (dashed magenta) is very different from our standard fit shown in Figure 1. Right panel: fit of the same model but for the redshift from NED, $z = 1.389$.

Table C1
An Overview of the Parameters Used for Fitting Different Fe II Templates to the Mean Spectrum as Well as the Inferred Best-fit Parameters

Fe II Template	Mg II Shape Shape	Redshift	Doublet Ratio	Fe II Smear Velocity [km s ⁻¹]	EW(Mg II)	χ^2
d12	1 Lorentz	1.37648	1.6	2800	27.44	2088.42
T06	1 Lorentz	1.38205	1.0	4500	29.64	2476.92
T06	1 Lorentz	1.38323	1.7	4700	29.77	2482.84
T06	2 Lorentz	1.38323	1.7	4700	29.74	2299.37
KDP15	1 Lorentz	1.37648*	1.6	5000	25.45	2921.12
KDP15	2 Gauss	1.37648*	1.6	4000	22.13	1749.18
KDP15	2 Gauss	1.37617	1.6	4000	22.46	1711.34
KDP15	2 Gauss	1.389 (NED)	1.6	5600	19.02	1991.62

Note. From left to right, the parameters are the template name (d12 according to Bruhweiler & Verner 2008, T06 according to Tsuzuki et al. 2006, and the KDP15 template based on Kovačević-Dojčinović & Popović, 2015; Popović et al. 2019), the Mg II shape (number of either Lorentzian or Gaussian profiles), the redshift (the star * for the KDP15 template means that the redshift was fixed in this case based on the best-fit d12 value), the Mg II doublet ratio (between one and two), Fe II smear velocity, the equivalent width of the Mg II line, and χ^2 in the last column.

Kovačević-Dojčinović & Popović (2015) and Marziani et al. (2013). However, with the KDP15 Fe II template, the fitting results highly depend on the adopted redshift. When we performed the analysis assuming that the redshift value given by NED is the right one, the decomposition of the spectrum changed significantly. Now the two Gaussians are rather similar; the dominating Gaussian coincides with the position of Fe II emission, and the second one is shifted only by 404 km s⁻¹ toward shorter wavelengths. This happened because now the Fe II contribution peaks at shorter wavelengths than before, and the ratio of the multiplet 63 to multiplet 62 is 0.49, while in the previous fits the contribution from the multiplet 63 was negligible. On the other hand, formally this fit is worse, with χ^2 of 1991.62 versus 1711.34 for the redshift 1.37617. This stresses the importance of an independent and precise measurement of the redshift in this source.

Because the χ^2 for the new fit of the mean spectrum is better than our basic fit, we also refitted all individual 25 spectra using this model. Because three of the six parameters were unimportant for the mean spectrum fit, we optimize our model fitting and reduce the parameter space to account only for the contribution from these three nonzero Fe II components. The result is shown in Figure C2. The overall trend of the higher values followed with the decrease in the second part of the data

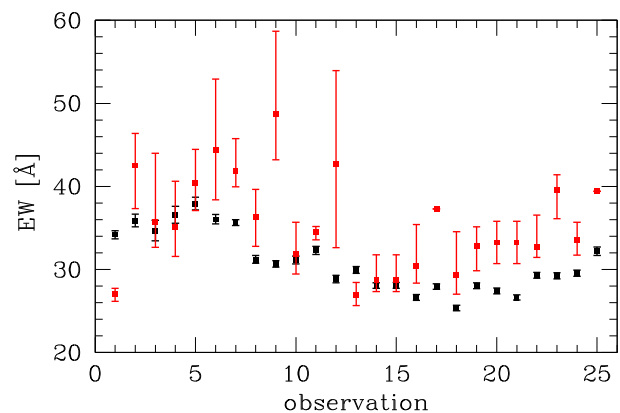


Figure C2. The equivalent width of the Mg II line in each of 25 observations measured from the standard d12 model (black points, Bruhweiler & Verner 2008) and from the new model based on the Fe II template (Kovačević-Dojčinović & Popović, 2015; Popović et al. 2019) and 2 Gaussian components. The equivalent width based on the KDP15 template has noticeably larger errors.

is still seen, but the errors are much larger. This is directly related to the larger number of parameters, and the Mg II error is determined allowing for all the other parameters to vary

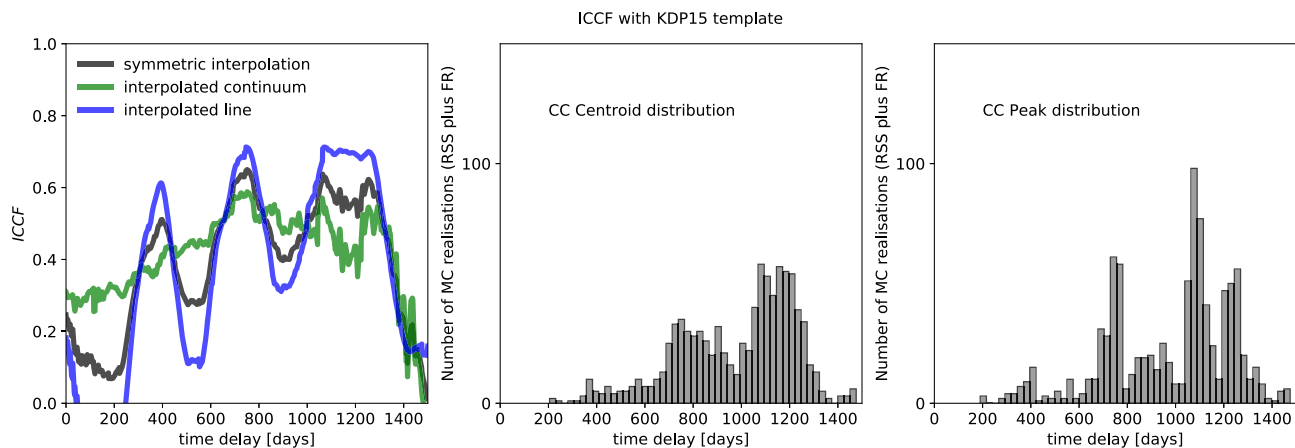


Figure C3. The ICCF values based on the KDP15 template for different interpolation cases according to the legend as a function of the time-delay in light days in the observer’s frame. In the central and the right panels, we show the centroid and the peak distributions, respectively.

Table C2

The Centroid and the Peak Time-delays in Light Days in the Observer’s Frame for the Mg II Lightcurve Derived from the KDP15 Template

	Centroid (days)	Peak (days)
Interpolated continuum	$1062.9^{+228.0}_{-362.3}$	$1057.5^{+247.9}_{-354.5}$
Interpolated line emission	$1070.2^{+136.9}_{-352.9}$	$1060.0^{+147.0}_{-345.6}$
Symmetric interpolation	$1058.9^{+149.0}_{-326.5}$	$1063.5^{+166.5}_{-334.5}$

Note. The values are expressed in the observer’s frame for the case of the interpolated continuum lightcurve (with respect to the line emission), the interpolated line emission, and the symmetric interpolation.

(apart from the redshift, the doublet ratio, and the Fe II width, kept at values optimized for the mean spectrum). In particular, the parameters of the second, very broad component of the Mg II line are considerably degenerate with respect to the underlying power law and Fe II parameters.

The new Mg II lightcurve was used again to measure the time-delay using different methods. The values are comparable, but as expected the uncertainties are generally larger and the correlation coefficient between the two lightcurves is lower. For the ICCF, we include the centroid and the peak values for the interpolated continuum, the interpolated line emission, and the symmetric case in Table C2. In Figure C3, we show the correlation coefficient as a function of the time-delay in the observer’s frame with the centroid as well as the peak distributions in the central and the right panels, respectively. The peak value of the correlation coefficient is 0.65 for the time-delay of 751 days, whereas for the d12 template, we previously got the peak value of 0.86 for the time-delay of 1058 days for the case without BMT points. For the z DCF method, we obtain the peak at $\tau_{0-1000} = 382.3^{+401.1}_{-59.1}$ days according to the ML analysis in the interval of 0–1000 days. When the interval is narrowed down to 500–1000 days, the ML peak is at $\tau_{500-1000} = 765.3^{+70.2}_{-79.8}$ days, which is comparable within uncertainties to $\tau_{500-1000} = 720.9^{+80.6}_{-84.5}$ days using the d12 template without the BMT data in the same interval. The χ^2 -based method gives $\tau_{d12} = 721^{+57}_{-45}$ days for the original d12 template, while for the Mg II lightcurve inferred from the KDP15 template fitting, we obtained $\tau_{KDP15} = 751^{+104}_{-150}$ days. In summary, the basic result of our

analysis—the time-delay of the response of the Mg II line—is comparable to the previous analysis based on d12 template, only the uncertainty is larger for the KDP15 template.

ORCID iDs

Michal Zajaček <https://orcid.org/0000-0001-6450-1187>
 Bożena Czerny <https://orcid.org/0000-0001-5848-4333>
 Mary Loli Martinez–Aldama <https://orcid.org/0000-0002-7843-7689>
 Mateusz Rałowski <https://orcid.org/0000-0002-0297-3346>
 Aleksandra Olejak <https://orcid.org/0000-0002-6105-6492>
 Swayamtrupta Panda <https://orcid.org/0000-0002-5854-7426>
 Krzysztof Hryniewicz <https://orcid.org/0000-0002-2005-9136>
 Marzena Śniegowska <https://orcid.org/0000-0003-2656-6726>
 Mohammad-Hassan Naddaf <https://orcid.org/0000-0002-7604-9594>
 Grzegorz Pietrzyński <https://orcid.org/0000-0002-9443-4138>
 C. Sobrino Figaredo <https://orcid.org/0000-0001-9704-690X>
 Martin Haas <https://orcid.org/0000-0002-7284-0477>
 Andrzej Udalski <https://orcid.org/0000-0001-5207-5619>
 Marek Gorski <https://orcid.org/0000-0002-3125-9088>
 Marek Sarna <https://orcid.org/0000-0003-4745-3923>

References

- Alexander, T. 1997, in *Astronomical Time Series*, Vol. 218, ed. D. Maoz, A. Sternberg, & E. M. Leibowitz (Dordrecht: Kluwer), 163
 Bachev, R., Marziani, P., Sulentic, J. W., et al. 2004, *ApJ*, 617, 171
 Bahk, H., Woo, J.-H., & Park, D. 2019, *ApJ*, 875, 50
 Baldwin, J. A. 1977, *ApJ*, 214, 679
 Baldwin, J. A., Burke, W. L., Gaskell, C. M., & Wampler, E. J. 1978, *Natur*, 273, 431
 Bartels, R. 1982, *Journal of the American Statistical Association*, 77, 40
 Bennett, C. L., Larson, D., Weiland, J. L., & Hinshaw, G. 2014, *ApJ*, 794, 135
 Bentz, M. C., Denney, K. D., Grier, C. J., et al. 2013, *ApJ*, 767, 149
 Blandford, R. D., & McKee, C. F. 1982, *ApJ*, 255, 419
 Bruhweiler, F., & Verner, E. 2008, *ApJ*, 675, 83
 Burgh, E. B., Nordsieck, K. H., Kobulnicky, H. A., et al. 2003, *Proc. SPIE*, 4841, 1463
 Carswell, R. F., & Smith, M. G. 1978, *MNRAS*, 185, 381

- Chavushyan, V., Patiño-Álvarez, V. M., Amaya-Almazán, R. A., & Carrasco, L. 2020, *ApJ*, **891**, 68
- Chelouche, D., Pozo-Núñez, F., & Zucker, S. 2017, *ApJ*, **844**, 146
- Code, A. D., & Welch, G. A. 1982, *ApJ*, **256**, 1
- Collin, S., Kawaguchi, T., Peterson, B. M., & Vestergaard, M. 2006, *A&A*, **456**, 75
- Collin-Souffrin, S., Dyson, J. E., McDowell, J. C., & Perry, J. J. 1988, *MNRAS*, **232**, 539
- Czerny, B. 2019, *OAsT*, **28**, 200
- Czerny, B., & Hryniewicz, K. 2011, *A&A*, **525**, L8
- Czerny, B., Hryniewicz, K., Maity, I., et al. 2013, *A&A*, **556**, A97
- Czerny, B., Hryniewicz, K., Nikolajuk, M., & Sadowski, A. 2011, *MNRAS*, **415**, 2942
- Czerny, B., Olejak, A., Rałowski, M., et al. 2019, *ApJ*, **880**, 46
- Czerny, B., Siemiginowska, A., Janiuk, A., Nikiel-Wroczyński, B., & Stawarz, L. 2009, *ApJ*, **698**, 840
- Du, P., Lu, K.-X., Zhang, Z.-X., et al. 2016, *ApJ*, **825**, 126
- Du, P., Zhang, Z.-X., Wang, K., et al. 2018, *ApJ*, **856**, 6
- Edelson, R. A., & Krolik, J. H. 1988, *ApJ*, **333**, 646
- Elitzur, M., & Shlosman, I. 2006, *ApJL*, **648**, L101
- Forster, K., Green, P. J., Aldcroft, T. L., et al. 2001, *ApJS*, **134**, 35
- Fraix-Burnet, D., Marziani, P., D'Onofrio, M., & Dultzin, D. 2017, *FrASS*, **4**, 1
- Ganci, V., Marziani, P., D'Onofrio, M., et al. 2019, *A&A*, **630**, A110
- Gaskell, C. M. 2009, *NewAR*, **53**, 140
- Goad, M. R., Koratkar, A. P., Axon, D. J., Korista, K. T., & O'Brien, P. T. 1999, *ApJL*, **512**, L95
- Goad, M. R., Korista, K. T., & Ruff, A. J. 2012, *MNRAS*, **426**, 3086
- Grier, C. J., Trump, J. R., Shen, Y., et al. 2017, *ApJ*, **851**, 21
- Guo, H., Shen, Y., He, Z., et al. 2020, *ApJ*, **888**, 58
- Ho, L. C., Goldoni, P., Dong, X.-B., Greene, J. E., & Ponti, G. 2012, *ApJ*, **754**, 11
- Kaspi, S., Smith, P. S., Netzer, H., et al. 2000, *ApJ*, **533**, 631
- Kelly, B. C., Bechtold, J., & Siemiginowska, A. 2009, *ApJ*, **698**, 895
- Kobulnicky, H. A., Nordsieck, K. H., Burgh, E. B., et al. 2003, *Proc. SPIE*, **4841**, 1634
- Kokubo, M. 2015, *MNRAS*, **449**, 94
- Kollatschny, W., & Zetzl, M. 2011, *Natur*, **470**, 366
- Kollatschny, W., & Zetzl, M. 2013a, *A&A*, **549**, A100
- Kollatschny, W., & Zetzl, M. 2013b, *A&A*, **558**, A26
- Korista, K. T., & Goad, M. R. 2000, *ApJ*, **536**, 284
- Korista, K. T., & Goad, M. R. 2004, *ApJ*, **606**, 749
- Kovačević-Dojčinović, J., & Popović, L. Č. 2015, *ApJS*, **221**, 35
- Popović, L. Č., Kovačević-Dojčinović, J., & Marčeta-Mandić, S. 2019, *MNRAS*, **484**, 3180
- Kozłowski, S. 2015, *AcA*, **65**, 251
- Kozłowski, S. 2016, *ApJ*, **826**, 118
- Kozłowski, S., Kochanek, C. S., Udalski, A., et al. 2010, *ApJ*, **708**, 927
- Lančová, D., Abarca, D., Kluźniak, W., et al. 2019, *ApJL*, **884**, L37
- León-Tavares, J., Chavushyan, V., Patiño-Álvarez, V., et al. 2013, *ApJL*, **763**, L36
- Lira, P., Kaspi, S., Netzer, H., et al. 2018, *ApJ*, **865**, 56
- MacLeod, C. L., Ivezić, Ž., Kochanek, C. S., et al. 2010, *ApJ*, **721**, 1014
- Mao, P., Urry, C. M., Massaro, F., et al. 2016, *ApJS*, **224**, 26
- Marconi, A., Axon, D. J., Maiolino, R., et al. 2009, *ApJL*, **698**, L103
- Martínez-Aldama, M. L., Czerny, B., Kawka, D., et al. 2019, *ApJ*, **883**, 170
- Marziani, P., Dultzin, D., Sulentic, J. W., et al. 2018, *FrASS*, **5**, 6
- Marziani, P., Sulentic, J. W., Plauchu-Frayn, I., & del Olmo, A. 2013, *A&A*, **555**, A89
- McLure, R. J., & Dunlop, J. S. 2004, *MNRAS*, **352**, 1390
- McLure, R. J., & Jarvis, M. J. 2002, *MNRAS*, **337**, 109
- Mejía-Restrepo, J. E., Lira, P., Netzer, H., Trakhtenbrot, B., & Capellupo, D. M. 2018, *NatAs*, **2**, 63
- Metzroth, K. G., Onken, C. A., & Peterson, B. M. 2006, *ApJ*, **647**, 901
- Neškova, M., Sirocky, M. M., Ivezić, Ž., & Elitzur, M. 2008, *ApJ*, **685**, 147
- Netzer, H. 2019, *MNRAS*, **488**, 5185
- Novikov, I. D., & Thorne, K. S. 1973, in *Black Holes (Les Astres Occlus)*, ed. C. DeWitt & B. S. DeWitt (New York: Gordon and Breach), 343
- Osterbrock, D. E., & Pogge, R. W. 1985, *ApJ*, **297**, 166
- Padovani, P., Alexander, D. M., Assef, R. J., et al. 2017, *A&ARv*, **25**, 2
- Panda, S., Czerny, B., Adhikari, T. P., et al. 2018, *ApJ*, **866**, 115
- Panda, S., Czerny, B., Done, C., & Kubota, A. 2019a, *ApJ*, **875**, 133
- Panda, S., Martínez-Aldama, M. L., & Zajaček, M. 2019b, *FrASS*, **6**, 75
- Pâris, I., Petitjean, P., Ross, N. P., et al. 2017, *A&A*, **597**, A79
- Patiño Álvarez, V., Torrealba, J., Chavushyan, V., et al. 2016, *FrASS*, **3**, 19
- Peterson, B. M., Ferrarese, L., Gilbert, K. M., et al. 2004, *ApJ*, **613**, 682
- Peterson, B. M., & Horne, K. 2004, *AN*, **325**, 248
- Peterson, B. M., Wanders, I., Horne, K., et al. 1998, *PASP*, **110**, 660
- Pogge, R. W., & Peterson, B. M. 1992, *AJ*, **103**, 1084
- Rakić, N., la Mura, G., Ilić, D., et al. 2017, *A&A*, **603**, A49
- Richards, G. T., Lacy, M., Storrie-Lombardi, L. J., et al. 2006, *ApJS*, **166**, 470
- Robertson, D. R. S., Gallo, L. C., Zoghbi, A., & Fabian, A. C. 2015, *MNRAS*, **453**, 3455
- Shen, Y., Hall, P. B., Horne, K., et al. 2019, *ApJS*, **241**, 34
- Shen, Y., Horne, K., Grier, C. J., et al. 2016, *ApJ*, **818**, 30
- Shen, Y., & Liu, X. 2012, *ApJ*, **753**, 125
- Shen, Y., Richards, G. T., Strauss, M. A., et al. 2011, *ApJS*, **194**, 45
- Smith, M. P., Nordsieck, K. H., Burgh, E. B., et al. 2006, *Proc. SPIE*, **6269**, 62692A
- Średzińska, J., Czerny, B., Hryniewicz, K., et al. 2017, *A&A*, **601**, A32
- Sulentic, J. W., Marziani, P., & Dultzin-Hacyan, D. 2000, *ARA&A*, **38**, 521
- Sun, M., Grier, C. J., & Peterson, B. M. 2018, PyCCF: Python Cross Correlation Function for reverberation mapping studies, Astrophysics Source Code Library, ascl:1805.032
- Tadhunter, C. 2016, *A&ARv*, **24**, 10
- Tody, D. 1986, *Proc. SPIE*, **627**, 733
- Tody, D. 1993, in *ASP Conf. Ser. 52, IRAF in the Nineties*, ed. R. J. Hanisch, R. J. V. Brissenden, & J. Barnes (San Francisco, CA: ASP), 173
- Trakhtenbrot, B., & Netzer, H. 2012, *MNRAS*, **427**, 3081
- Tsuzuki, Y., Kawara, K., Yoshii, Y., et al. 2006, *ApJ*, **650**, 57
- Ulrich, M.-H., Maraschi, L., & Urry, C. M. 1997, *ARA&A*, **35**, 445
- Vanden Berk, D. E., Richards, G. T., Bauer, A., et al. 2001, *AJ*, **122**, 549
- Véron-Cetty, M. P., & Véron, P. 2001, *A&A*, **374**, 92
- Vestergaard, M., & Osmer, P. S. 2009, *ApJ*, **699**, 800
- Vestergaard, M., & Peterson, B. M. 2006, *ApJ*, **641**, 689
- Vestergaard, M., & Wilkes, B. J. 2001, *ApJS*, **134**, 1
- Wampler, E. J., Gaskell, C. M., Burke, W. L., & Baldwin, J. A. 1984, *ApJ*, **276**, 403
- Wang, J.-M., Du, P., Li, Y.-R., et al. 2014a, *ApJL*, **792**, L13
- Wang, J.-M., Qiu, J., Du, P., & Ho, L. C. 2014b, *ApJ*, **797**, 65
- Wilhite, B. C., Vanden Berk, D. E., Kron, R. G., et al. 2005, *ApJ*, **633**, 638
- Wisotzki, L., Christlieb, N., Bade, N., et al. 2000, *A&A*, **358**, 77
- Woo, J.-H. 2008, *AJ*, **135**, 1849
- Yang, Q., Shen, Y., Chen, Y.-C., et al. 2020, *MNRAS*, **493**, 5773
- Zajaček, M., Busch, G., Valencia-S., M., et al. 2019a, *A&A*, **630**, A83
- Zajaček, M., Czerny, B., Martínez-Aldama, M. L., & Karas, V. 2019b, *AN*, **340**, 577
- Zajaček, M., Eckart, A., Britzen, S., & Czerny, B. 2019c, arXiv:1911.12901
- Zheng, W., Kriss, G. A., Telfer, R. C., Grimes, J. P., & Davidsen, A. F. 1997, *ApJ*, **475**, 469
- Zhu, D., Sun, M., & Wang, T. 2017, *ApJ*, **843**, 30
- Zu, Y., Kochanek, C. S., Kozłowski, S., & Peterson, B. M. 2016, *ApJ*, **819**, 122
- Zu, Y., Kochanek, C. S., Kozłowski, S., & Udalski, A. 2013, *ApJ*, **765**, 106
- Zu, Y., Kochanek, C. S., & Peterson, B. M. 2011, *ApJ*, **735**, 80

Paper 3: Red-Giant Depletion in the Galactic Center

While performing near-infrared observations, it was found that the carbon-monoxide (CO) bandhead absorption is decreasing inside ~ 0.5 pc (Sellgren et al. 1990). Since the CO bandhead feature is a proxy of the surface-brightness of late-type stars, it was recognized that this signifies the drop in the number of late-type stars (red giants and supergiants, asymptotic giant-branch stars). It has triggered several discussions and the formation of models how this could have arisen close to the compact radio source Sgr A*, which is associated with the supermassive black hole. The proposed red-giant depletion models include their collisions with other stars, red giant-accretion disc interactions, and the tidal disruption of red-giant envelopes. In this paper, we propose novel mechanism – the interaction of red giants with the nuclear jet – which is capable of ablating the upper layers of red-giant envelopes. The ablation by the jet has been motivated by the recent indications that the Galactic center was much more active several million years ago (Bland-Hawthorn et al. 2019). This increased Seyfert-like activity may be linked to the formation of the large-scale γ -ray *Fermi* bubbles as well as X-ray *eROSITA* bubbles above and below the Galactic plane.

Depending on the duration of the active jet phase, the number of stellar passages through the jet can vary, but typically it reaches $\sim 10^3 - 10^4$ interactions with the jet when it is active at least for 0.5 million years. For the moderate jet luminosity of $L_j \sim 10^{42}$ erg s $^{-1}$, the stagnation radius can in principle be only ~ 30 Solar radii at ~ 0.04 pc from Sgr A* and the detached mass per one passage is in the range $10^{-10} - 10^{-2} M_\odot$. Since the detached mass after one passage depends steeply on the stellar radius and the distance, $\Delta M_1 \propto R_\star^4 z^{-2}$, large red giants that orbit Sgr A* within the S cluster are affected the most, which is consistent with the flattened surface-density profiles of bright late-type stars. We also constructed surface-density profiles of a mock nuclear star cluster composed of late-type stars. Initially, the stars have a cusp-like distribution resulting from the two-body relaxation. Once the jet activity starts, late-type stars brighter than 14 mag develop a core-like distribution. For the largest possible jet luminosities of $L_j = 10^{44}$ erg s $^{-1}$ close to the Eddington luminosity of Sgr A*, red giants brighter than 12 mag develop a core-like distribution up to ~ 0.4 pc, while fainter red giants keep their initial cusp-like profiles. This is qualitatively consistent with the findings of Schödel et al. (2020), who found similar surface-density distributions: core-like for the brightest late-type stars and cusp-like for the fainter ones.

Credit: Zajaček et al. (2020), ApJ 903, 140. Reproduced with permission ©AAS.



Depletion of Bright Red Giants in the Galactic Center during Its Active Phases

Michal Zajaček¹, Anabella Araudo^{2,3}, Vladimír Karas³, Božena Czerny¹, and Andreas Eckart^{4,5}¹Center for Theoretical Physics, Polish Academy of Sciences, Al. Lotnikow 32/46, 02-668 Warsaw, Poland; zajacek@cft.edu.pl²ELI Beamlines, Institute of Physics, Czech Academy of Sciences, CZ-25241 Dolní Břežany, Czech Republic³Astronomical Institute of the Czech Academy of Sciences, Boční II 1401, CZ-14100 Prague, Czech Republic⁴I. Physikalisches Institut der Universität zu Köln, Zùlpicher Strasse 77, D-50937 Köln, Germany⁵Max-Planck-Institut für Radioastronomie (MPIfR), Auf dem Hùgel 69, D-53121 Bonn, Germany

Received 2020 February 25; revised 2020 September 10; accepted 2020 September 29; published 2020 November 12

Abstract

Observations in the near-infrared domain showed the presence of the flat core of bright late-type stars inside ~ 0.5 pc from the Galactic center supermassive black hole (Sgr A*), while young massive OB/Wolf–Rayet stars form a cusp. Several dynamical processes were proposed to explain this apparent paradox of the distribution of the Galactic center stellar populations. Given the mounting evidence on the significantly increased activity of Sgr A* during the past million years, we propose a scenario based on the interaction between the late-type giants and a nuclear jet, whose past existence and energetics can be inferred from the presence of γ -ray Fermi bubbles and bipolar radio bubbles. Extended, loose envelopes of red giant stars can be ablated by the jet with kinetic luminosity in the range of $L_j \approx 10^{41}–10^{44}$ erg s⁻¹ within the inner ~ 0.04 pc of Sgr A* (S-cluster region), which would lead to their infrared luminosity decrease after several thousand jet–star interactions. The ablation of the atmospheres of red giants is complemented by the process of tidal stripping that operates at distances of $\lesssim 1$ mpc, and by the direct mechanical interaction of stars with a clumpy disk at $\gtrsim 0.04$ pc, which can explain the flat density profile of bright late-type stars inside the inner half parsec from Sgr A*.

Unified Astronomy Thesaurus concepts: Galactic center (565); Red giant stars (1372); Red supergiant stars (1375); Relativistic jets (1390); Stellar dynamics (1596)

1. Introduction

The Galactic center supermassive black hole (hereafter SMBH) with the mass of $4.1 \times 10^6 M_\odot$ is located at the distance of 8.1 kpc (Boehle et al. 2016; Gillessen et al. 2017; Parsa et al. 2017; Gravity Collaboration et al. 2018) and provides a unique laboratory for studying detailed dynamical processes and the mutual interaction between a nuclear star cluster (NSC) and a central massive black hole (Alexander 2005; Genzel et al. 2010; Eckart et al. 2017; Ali et al. 2020) as well as with the multiphase gaseous-dusty circumnuclear medium (Morris & Serabyn 1996; Rózańska et al. 2017). The compact radio source Sgr A* associated with the SMBH is embedded in the Milky Way NSC, which is one of the densest stellar systems in the Galaxy (Alexander 2017; Schödel et al. 2014), and in addition, it is surrounded by an ionized, neutral, and molecular gas and dust (see, e.g., Moser et al. 2017 and references therein).

The NSC consists of both late-type (red giants, supergiants and asymptotic giant branch stars) and early-type stars of O and B spectral classes (Krabbe et al. 1991; Buchholz et al. 2009; Do et al. 2009; Gallego-Cano et al. 2018), which imply star formation during the whole Galactic history, albeit most likely episodic (Pfuhl et al. 2011; Schödel et al. 2020) with the star formation peak at 10 Gyr, the minimum at 1–2 Gyr, and a recent increase in the last few hundred million years.

In the innermost parsec of the Galactic center, there is a surprising abundance of young massive OB/Wolf–Rayet stars that have formed in situ in the last 10 million years (Ghez et al. 2003). These young stars form an unrelaxed cusp-like distribution. On the other hand, previous studies of the distribution of late-type stars showed that they exhibit a core-like distribution inside the inner ~ 0.5 pc, which has a projected flat or even decreasing profile toward the center (Buchholz et al. 2009; Do et al. 2009; Sellgren et al. 1990). More recent studies provided a precise

analysis of the distribution of late-type stars because of increasing their sensitivity toward larger magnitudes, i.e., fainter giants (Gallego-Cano et al. 2018; Habibi et al. 2019). Using photometric number counts and diffuse light analysis, Gallego-Cano et al. (2018) found that fainter late-type stars with magnitudes of $K \approx 18$ exhibit a cusp-like distribution within the sphere of influence of Sgr A* with a 3D power-law exponent of $\gamma \simeq 1.43$. In comparison, there is an apparent lack of bright red giants with $K = 12.5–16$ at the projected radii of $\lesssim 0.3$ pc from Sgr A*. Gallego-Cano et al. (2018) estimate the number of missing giants to 100 for this distance range. The study of Habibi et al. (2019) also finds a cusp-like distribution for late-type stars with $K < 17$ within 0.02–0.4 pc. In agreement with Gallego-Cano et al. (2018), they found a core-like distribution for the brightest giants with $K < 15.5$, although the number of missing giants appears to be lower than 100 according to their analysis. Although the surface-brightness distribution of late-type stars brighter than 15.5 mag appears to be rather flat, already in Figure 11 of Buchholz et al. (2009) the inner point at $0''.5$ (where $1'' \sim 0.04$ pc at the Galactic center) of the distribution of late-type stars as well as of the distribution of all stars indicates the presence of a cusp.

In summary, there appears to be an internal mechanism within the NSC that preferentially depleted bright, large red giants on one hand, which has led to their apparent core-like distribution, and at the same time has been less efficient for early-type as well as fainter late-type stars, on the other hand. Such a mechanism has altered either the spatial, luminosity, or the temperature distribution of the bright red giant stars so that they effectively fall beyond the detection limit or they instead mimic younger, “bluer” stars. So far, it is mainly the following four mechanisms that have been discussed to explain the apparent lack of bright red giants:

1. complete or partial tidal disruption of red giants by the SMBH (Hills 1975; Bogdanović et al. 2014; King 2020; envelope removal),
2. envelope stripping by the collisions of red giants with the dense clumps within a self-gravitating accretion disk (Armitage et al. 1996; Amaro-Seoane & Chen 2014; Kieffer & Bogdanović 2016; Amaro-Seoane et al. 2020; envelope removal),
3. collisions of red giants with field stars and compact remnants (Phinney 1989; Morris 1993; Genzel et al. 1996; Bailey & Davies 1999; Alexander 2005; Davies & King 2005; Dale et al. 2009; envelope removal),
4. mass segregation effects: the dynamical effect of a secondary massive black hole (Baumgardt et al. 2006; Merritt & Szell 2006; Portegies Zwart et al. 2006; Matsubayashi et al. 2007; Löckmann & Baumgardt 2008; Gualandris & Merritt 2012) or of an infalling massive cluster (Kim & Morris 2003; Ernst et al. 2009; Antonini et al. 2012) or of stellar black holes (Morris 1993; altered spatial distribution),

where in parentheses we include the mechanism responsible for altering the population of late-type stars. The importance of star–star and star–disk interactions was also analyzed generally for active galactic nuclei (AGNs) in terms of the effects on the accretion disk and broad-line region structure as well as the NSC orbital distribution (Zurek et al. 1994; Armitage et al. 1996; Karas & Šubr 2001; Vilkoviskij & Czerny 2002; Kieffer & Bogdanović, 2016; MacLeod & Lin 2020).

We propose here another mechanism based on the jet–star interactions (Barkov et al. 2012a; Araudo et al. 2013; Araudo & Karas 2017), which most likely coexisted with the mechanisms proposed above. In particular, the star–accretion disk collisions are expected to be accompanied by star–jet crossings during previous active phases of Sgr A*. Because red giant stars have typically large, loosely bound tenuous envelopes, dense compact cores, and slow winds with the terminal velocity $\lesssim 100 \text{ km s}^{-1}$, they are in particular susceptible to mass removal in encounters with higher-pressure material (MacLeod et al. 2012; Amaro-Seoane & Chen 2014; Kieffer & Bogdanović 2016).⁶ Therefore, during the red giant–jet interactions, the jet ram pressure will remove the outer layers of the stellar envelope during the passage. We illustrate this idea in Figure 1.

After several star–jet crossings, the atmosphere is removed similarly as for repetitive star–disk crossings (Amaro-Seoane et al. 2020), and the giant is modified in a way that it follows an evolutionary track in the Hertzsprung–Russell (HR) diagram approximately along the constant absolute magnitude toward higher effective temperatures. We show that this mechanism quite likely operated in the vicinity of Sgr A* during its active Seyfert-like phase in the past few million years (Bland-Hawthorn et al. 2019) when the jet kinetic luminosity could have reached $\sim 10^{44} \text{ erg s}^{-1}$. In principle, even in the quiescent state, a tidal disruption event (TDE) every $\sim 10^4 \text{ yr}$, which can be estimated for the Galactic center (Syer & Ulmer 1999; Alexander 2005), can temporarily reactivate the jet of Sgr A*, and some of the bright red giants could be depleted during its existence. This makes the red giant–jet interaction in the

⁶ The estimate of the terminal wind velocity is given by the escape velocity $v_{\text{esc}} = 62 \left(\frac{M_*}{1 M_\odot} \right)^{1/2} \left(\frac{R_*}{100 R_\odot} \right)^{-1/2} \text{ km s}^{-1}$.

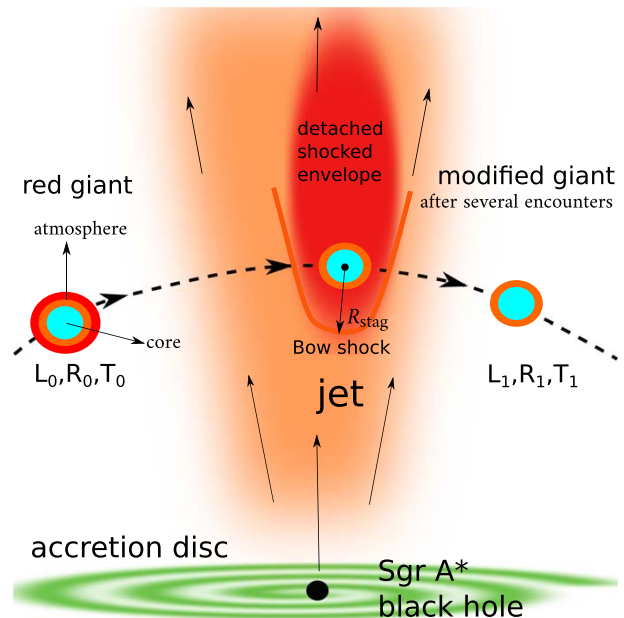


Figure 1. Illustration of the jet–red giant interaction in the vicinity of Sgr A* during its active phase. The large, loosely bound envelope of the red giant (colored as red and orange), which has an initial luminosity, radius, and temperature (L_0, R_0, T_0), is ablated by the jet ram pressure during several encounters as the lifetime of the jet $t_{\text{jet}} \sim 0.5 \text{ Myr}$ is much longer than the orbital timescale in the inner $\sim 0.5 \text{ pc}$, $P_{\text{orb}} \sim 1500(a/0.1 \text{ pc})^{3/2} \text{ yr}$. After a few hundred encounters, star has modified parameters (L_1, R_1, T_1), which change the overall outlook of the giant in the near-infrared domain. Inspired by Barkov et al. (2012a) and Bosch-Ramon et al. (2012).

Galactic center relevant and highly plausible in its recent history, and the dynamical consequences can be inferred based on the so-far detected traces of the past active phase of Sgr A* as well as the currently observed stellar density distribution.

Previous jet–star interaction studies were focused on the emergent nonthermal radiation, in particular in the gamma-ray domain, and mass-loading and chemical enrichment of jets by stellar winds (see e.g., Komissarov 1994; Barkov et al. 2012a; Bosch-Ramon et al. 2012; Araudo et al. 2013; Bednarek & Banasiński 2015; de la Cita et al. 2016). Here we focus on the effect of the jet on the stellar population. In most jetted AGNs, this is perhaps a secondary problem because stellar populations in the host bulge cannot be resolved out, i.e., one can only analyze the integrated starlight. In contrast, within the Galactic center NSC, one can not only disentangle late- and early-type stars, but it is also possible to study their distribution as well as the kinematics of individual stars. Although in the current low-luminosity state there is no firm evidence for the presence of a relativistic jet, there are nowadays several multiwavelength signatures of the past active Seyfert-like state of Sgr A* that occurred a few million years ago (Bland-Hawthorn et al. 2019; Heywood et al. 2019; Ponti et al. 2019). However, even in the current quiescent state of Sgr A*, studies by Yusef-Zadeh et al. (2012) and Li et al. (2013) indicate the existence of a low-surface-brightness parsec-scale jet. In addition, the presence of the cometary-shaped infrared-excess bow-shock sources X3, X7 (Mužić et al. 2010), and recently X8 (Peißker et al. 2019) indicates that the star–outflow interaction is ongoing even in a very low state of the Sgr A* activity. The morphology of these sources can be explained by the interaction with a strong

accretion wind originating from Sgr A* or with the collective wind of the cluster of young stars.

This paper proposes a new mechanism that could have affected the current population of bright late-type stars, namely their appearance as well as number counts in specific magnitude bins, in the Galactic center. We apply analytical and semianalytical calculations to assess whether the potential past jet–star interactions could have had an effect on the stellar population in the sphere of influence of Sgr A*. Although the analytical calculations introduce several simplifications, we show that the mechanism could have operated and the estimated number of affected red giants is in accordance with the most sensitive, up-to-date studies (Gallego-Cano et al. 2018; Habibi et al. 2019). A more detailed computational treatment including magnetohydrodynamic numerical simulations as well as a stellar evolution will be presented in our future studies.

The paper is structured as follows. In Section 2, we derive the stagnation radius, basic timescales, and the envelope mass removed for red giant stars interacting with the jet of Sgr A* during its past active phase. In Section 3, we discuss the observational signatures in the near-infrared domain. Subsequently, in Section 4, we estimate the number of red giants that could be affected by the jet interaction and visually depleted from the immediate vicinity of Sgr A*. In Section 6, we discuss additional processes related to the red giant–jet interaction in the Galactic center. Finally, we summarize the main results and conclude with Section 7.

2. Derivation of the Jet–Star Stagnation Radius and the Jet-induced Stellar Mass Loss

The evidence for the active phase of Sgr A* that is estimated to have occurred 4 ± 1 Myr ago is based on the X-ray/ γ -ray bubbles with a total energy content of 10^{56} – 10^{57} erg (Bland-Hawthorn et al. 2019). The first evidence for the nuclear outburst was the kiloparsec-scale 1.5 keV ROSAT X-ray emission that originated in the Galactic center (Bland-Hawthorn & Cohen 2003). The X-ray structure coincides well with the more recently discovered Fermi γ -ray bubbles extending 50° north and south of the Galactic plane at 1–100 GeV (Su et al. 2010). The X-ray/ γ -ray bubbles are energetically consistent with the nuclear AGN-like activity associated with the jet and/or disk-wind outflows with jet power $L_j = 2.3^{+5.1}_{-0.9} \times 10^{42}$ erg s $^{-1}$ and age $4.3^{+0.8}_{-1.4}$ Myr (Miller & Bregman 2016). In comparison, the starburst origin of the Fermi bubbles is inconsistent with the bubble energetics by a factor of ~ 100 (Bland-Hawthorn & Cohen 2003). On intermediate scales of hundreds of parsecs, the base of the Fermi bubbles coincides with the bipolar radio bubbles (Heywood et al. 2019) as well as with the X-ray chimneys (Ponti et al. 2019).

Using hydrodynamic simulations, Guo & Mathews (2012) reproduce the basic radiative characteristics of the Fermi bubbles with the AGN jet duration of ~ 0.1 – 0.5 Myr, which corresponds to the jet luminosity $L_j \approx 10^{56-57}$ erg/(0.1 – 0.5 Myr) = $6.3 \times 10^{42} - 3.2 \times 10^{44}$ erg s $^{-1}$. The jet is dominated by the kinetic luminosity $L_j = \eta_j L_{\text{acc}}$, where η_j is the conversion efficiency from the accretion luminosity L_{acc} to the jet kinetic luminosity. The accretion luminosity is $L_{\text{acc}} \lesssim L_{\text{Edd}}$, where the Eddington luminosity is

$$L_{\text{Edd}} = 5.03 \times 10^{44} \left(\frac{M_\star}{4 \times 10^6 M_\odot} \right) \text{erg s}^{-1}, \quad (1)$$

and $\eta_j < 0.7$ for most radio sources (Ito et al. 2008). This yields the maximum jet kinetic luminosity for Sgr A* of $L_j \approx 3.5 \times 10^{44}$ erg s $^{-1}$. We will consider $L_j \approx 10^{41} - 10^{44}$ erg s $^{-1}$, where the lower limit is given by the putative jet present in the current quiescent state (Yusef-Zadeh et al. 2012), with the inferred kinetic luminosity of $L_{\text{min}} \sim 1.2 \times 10^{41}$ erg s $^{-1}$, and the upper limit is given by the Eddington luminosity.

We assume a conical jet with a half-opening angle θ and width $R_j = z \tan \theta$, where z is the distance to Sgr A*. The jet footpoint for Sgr A* can be estimated to be located at $z_0 \sim 2 \times 10^{-5} (M_\star / 4 \times 10^6 M_\odot) \text{pc} = 52 R_{\text{Schw}}$ (Junor et al. 1999), where $R_{\text{Schw}} = 2GM_\star / c^2 = 3.8 \times 10^{-7} (M_\star / 4 \times 10^6 M_\odot) \text{pc}$ is the Schwarzschild radius. Any red giant or supergiant with radius⁷ R_\star and mass m_\star is not expected to plunge below z_0 as the tidal disruption radius $r_t = R_\star (2M_\star / m_\star)^{1/3}$ (Hills 1975; Rees 1988) is at least a factor of 2 larger,

$$\frac{r_t}{R_{\text{Schw}}} = 1.20 \left(\frac{R_\star}{10 R_\odot} \right) \left(\frac{M_\star}{4 \times 10^6 M_\odot} \right)^{1/3} \left(\frac{m_\star}{M_\odot} \right)^{-1/3}. \quad (2)$$

$R_\star = 10 R_\odot$ and $m_\star = 1 M_\odot$ are typical intermediate values for the evolved late-type giants with extended envelopes (Merritt 2013). For numerical estimates, we consider the range of radii for red giants and supergiants, $R_\star \sim 4$ – $1000 R_\odot$, as indicated by the HR diagram. These late-type stars have a large range of bolometric luminosities, $L_\star \sim 10$ – $72,000 L_\odot$, and the temperature range of $T_\star \sim 5000$ – 3000 K, which corresponds to the spectral classes K and M, respectively. The K-band magnitude range is $K \sim 15.2$ mag for $R_\star = 4 R_\odot$, $T_\star = 5000$ K, and $K \sim 4.4$ mag for $R_\star = 1000 R_\odot$, $T_\star = 3000$ K. More specifically, we focus on late-type stars of $K = 16$ mag and brighter, which appear to form a core-like density distribution in the central 0.5 pc. Using the isochrones obtained with the Parsec code (Bressan et al. 2012), these stars have $R_\star \sim 4 R_\odot$ and larger for an age of 5 Gyr. The late-type stars that are completely absent in the S cluster (inner ~ 0.04 pc) were inferred to have $R_\star = 30 R_\odot$ and larger (Habibi et al. 2019). Therefore, numerical estimates are typically scaled to $R_\star = 30 R_\odot$ unless otherwise indicated.

We will further focus on the region between the tidal radius of red giants and the outer edge of the S cluster, which approximately corresponds to the Bondi radius of the hot bremsstrahlung plasma (Baganoff et al. 2003; Wang et al. 2013),

$$R_B = \frac{GM_\star}{c_s^2} = 0.12 \left(\frac{M_\star}{4 \times 10^6 M_\odot} \right) \left(\frac{T_p}{10^7 \text{ K}} \right)^{-1} \text{pc}, \quad (3)$$

which is two to three orders of magnitude larger than the tidal radius of red giants, $R_B \sim 3.1 \times 10^5 R_{\text{Schw}}$. More generally speaking, the population of predominantly B-type stars lies within the innermost arcsecond (~ 0.04 pc, S cluster), while the population of young massive OB/Wolf–Rayet stars stretches from ~ 0.04 pc up to ~ 0.5 pc, a fraction of which forms a warped stellar disk (Genzel et al. 2010).

The stellar-wind ram pressure at a distance r from the center of the star can be estimated as $P_{\text{sw}} \sim \rho_w v_w^2 = \dot{m}_w v_w / (4\pi r^2)$,

⁷ The stellar radius is the sum of the core radius and the envelope radius, $R_\star = R_c + R_{\text{env}}$.

where \dot{m}_w is the mass-loss rate and v_w is the terminal wind velocity. Using typical values for red giants with $\dot{m}_w \approx 10^{-8} M_\odot \text{ yr}^{-1}$ and $v_w \approx 10 \text{ km s}^{-1}$ (e.g., Reimers 1987; de la Cita et al. 2016),⁸

$$P_{sw} = 0.012 \left(\frac{\dot{m}_w}{10^{-8} M_\odot \text{ yr}^{-1}} \right) \left(\frac{v_w}{10 \text{ km s}^{-1}} \right) \times \left(\frac{r}{30 R_\odot} \right)^{-2} \text{ erg cm}^{-3}. \quad (4)$$

The ram pressure of a relativistic jet with bulk motion Lorentz factor Γ is $P_j = \Gamma \rho_j v_j^2$, where the jet density is $\rho_j = L_j / [(\Gamma - 1)c^2 \sigma_j v_j]$ and $\sigma_j = \pi R_j^2$ is the jet cross-sectional area. By assuming $v_j \sim c$ and $\Gamma \sim 10$, the jet kinetic pressure for Sgr A* can be written as

$$P_j \approx \frac{L_j}{\sigma_j c} = \frac{L_j}{\pi c z^2 \tan^2 \theta} = 0.014 \left(\frac{L_j}{10^{42} \text{ erg s}^{-1}} \right) \left(\frac{z}{0.04 \text{ pc}} \right)^{-2} \text{ erg cm}^{-3}, \quad (5)$$

where we have assumed $\theta \simeq 12^\circ.5$, which corresponds to the jet sheath half-opening angle estimated for the current candidate jet of Sgr A* (Li et al. 2013). Note that the innermost arcsecond ($z \sim 0.04 \text{ pc}$) is also the outer radius of fast-moving stars in the S cluster (Genzel et al. 2010; Eckart et al. 2017).

By equating $P_{sw} = P_j$, we obtain the stagnation distance

$$\frac{R_{\text{stag}}}{R_\odot} = 27 \left(\frac{z}{0.04 \text{ pc}} \right) \left(\frac{\dot{m}_w}{10^{-8} M_\odot \text{ yr}^{-1}} \right)^{\frac{1}{2}} \times \left(\frac{v_w}{10 \text{ km s}^{-1}} \right)^{\frac{1}{2}} \left(\frac{L_j}{10^{42} \text{ erg s}^{-1}} \right)^{-\frac{1}{2}}, \quad (6)$$

which characterizes by how much the red giant envelope can be ablated by the jet in one encounter. Note that $R_{\text{stag}} < R_*$ for late-type giants and supergiants with $R_* \sim 100\text{--}1000 R_\odot$ (see Figure 2). The very tenuous wind of red giants cannot balance the jet ram pressure, and therefore, the jet plasma impacts on the stellar surface. As a consequence, a fraction of the stellar envelope is removed as estimated by Equation (6).

Interestingly, giant stars with $R_* \gtrsim 30 R_\odot$ appear to be missing in the S cluster. Only late-type stars with R_* between 4 and $30 R_\odot$ (with absolute bolometric magnitudes between -1.05 and 3.32 , respectively, for the effective temperature of 4000 K) were detected by Habibi et al. (2019; see their Figure 2). Stars with $4 \leq R_*/R_\odot \leq 30$ within 0.02 pc have $R_{\text{stag}}/R_* \sim 1$ when $2 \times 10^{41} \leq L_j/\text{erg s}^{-1} \leq 1.1 \times 10^{43}$, as indicated in Figure 2. This is in agreement with the estimated jet power $L_j \sim 2.3 \times 10^{42} \text{ erg s}^{-1}$ from X- and γ -ray bubbles (Miller & Bregman 2016). Therefore, an apparent lack of late-type giant stars with envelopes $R_* \gtrsim 30 R_\odot$ in the inner $\sim 0.04 \text{ pc}$ of Galactic center could result from the jet-induced ablation of the stellar envelope during the last active phase of Sgr A*, a few million years ago.

⁸ For red giants, $\dot{m}_w \approx 10^{-6}\text{--}10^{-9} M_\odot \text{ yr}^{-1}$ according to Reimers (1987).

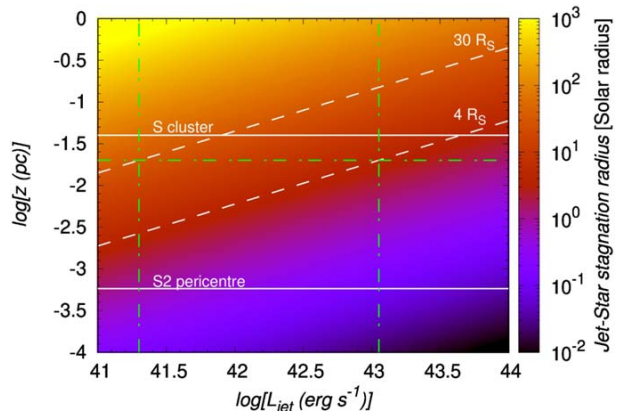


Figure 2. Stagnation radius R_{stag}/R_\odot . The two horizontal white solid lines indicate the radial extent of the S cluster between the S2 pericenter distance and the outer radius at $\sim 0.04 \text{ pc}$. The two white dashed lines stand for the atmosphere radius limits of late-type stars in the S cluster, $4R_\odot$ and $30R_\odot$ (Habibi et al. 2019). The dotted-dashed green lines indicate the jet luminosity limits that would yield the stellar atmosphere ablation at 30 and $4R_\odot$ at $z = 0.02 \text{ pc}$.

2.1. Basic Timescales of the Jet–Star Interaction

The red giant will enter the jet and not mix with its sheath layers on the surface if $v_{\text{orb}} \gtrsim v_{\text{sc}}$, where $v_{\text{orb}} \sim (GM_*/z)^{1/2}$ is the Keplerian orbital velocity of the star around Sgr A* and $v_{\text{sc}} \sim c(\Gamma \rho_j / \rho_*)$ is the sound speed inside the shocked obstacle. This condition can be written as

$$\frac{\rho_*}{\rho_j} \gtrsim 5.2 \times 10^5 \left(\frac{z}{0.01 \text{ pc}} \right) \left(\frac{\Gamma}{10} \right) \left(\frac{M_*}{4 \times 10^6 M_\odot} \right)^{-1}, \quad (7)$$

which means that stellar atmosphere layers of comparable density or greater than indicated by Equation (7) will enter the jet, and the less dense upper layers will mix with the jet surface layers.

Once inside, the bow shock is formed inside the jet on the very short timescale of $t_{\text{bs}} \sim R_*/c \sim 232(R_*/100 R_\odot) \text{ s}$. A shock also propagates through the red-giant atmosphere on the shock-crossing or dynamical timescale, $t_d \sim R_*/v_{\text{sc}}$, whose lower limit is imposed by the condition of penetration, $v_{\text{orb}} \gtrsim v_{\text{sc}}$, which leads to $t_d \gtrsim R_*/v_{\text{orb}} = R_* \sqrt{z/(GM_*)} \sim 53063(R_*/100 R_\odot)(z/0.01 \text{ pc})^{1/2}(M_*/4 \times 10^6 M_\odot)^{-1/2} \text{ s}$. The dynamical, shock-crossing time is at least ~ 10 times longer than the bow-shock formation time close to the footpoint of the jet, but the ratio becomes larger with the distance from Sgr A* as $t_d/t_{\text{bs}} \gtrsim 229(z/0.01 \text{ pc})^{1/2}(M_*/4 \times 10^6)^{-1/2}$.

The star-crossing time through the jet can be estimated as $t_* \sim 2R_j/v_{\text{orb}}$. Using $R_j = z \tan \theta$ and the condition $v_{\text{sc}} \lesssim v_{\text{orb}}$, we obtain

$$\frac{t_*}{t_d} \lesssim \frac{2z \tan \theta}{R_*} \sim 1966, \quad (8)$$

which implies that the shock propagates throughout the detached envelope, which is dragged by the jet and mixed with its material. Eventually, after several t_d , the envelope material will reach the velocity of $v_j \sim c$. Note that $t_*/t_d \sim 1$ when $z \sim 10^{-5} \text{ pc}$; hence, the removed envelope material should be dragged by the jet throughout the whole NSC.

The ablated red giant after the first crossing through the jet would first expand adiabatically to the original size on the

thermal expansion timescale $t_{\text{exp}} \sim R_*/c_s = R_* \sqrt{\mu m_{\text{H}} / (k_{\text{B}} T_{\text{atm}})} = 0.2(R_*/100 R_{\odot})(T_{\text{atm}}/10^4 \text{ K})^{-1/2}$ yr because of the pressure of the warmer, underlying layers as the star adjusts its size to reach a hydrodynamic equilibrium. This expansion timescale is shorter than the orbital timescale

$$P_{\text{orb}} = 2\pi \left(\frac{z^3}{GM_*} \right)^{1/2} = 47 \left(\frac{z}{0.01 \text{ pc}} \right)^{3/2} \left(\frac{M_*}{4 \times 10^6 M_{\odot}} \right)^{-1/2} \text{ yr.} \quad (9)$$

Kieffer & Bogdanović (2016) infer a similar timescale for the envelope expansion using the hydrodynamic simulations of red giant–accretion-clump collisions. According to their Figure 7, the envelope expands to a larger size than the original stellar radius in $t_{\text{exp}} \sim 1.5 t_{\text{dyn}}$ after the star emerges from the accretion clump, where t_{dyn} is a dynamical timescale of the star,

$$t_{\text{dyn}} \sim 0.32 \left(\frac{R_*}{100 R_{\odot}} \right)^{3/2} \left(\frac{m_*}{1 M_{\odot}} \right)^{-1/2} \text{ yr,} \quad (10)$$

which leads to $t_{\text{exp}} \sim 1.5 \times 0.32 \text{ yr} \approx 0.5 \text{ yr}$.

The timescale of the thermal evolution of a star after the jet–star interaction is expressed by the Kelvin–Helmholtz (KH) or thermal timescale,

$$t_{\text{KH}} \approx \frac{Gm_*^2}{R_* L_*} = 210 \left(\frac{m_*}{1 M_{\odot}} \right)^2 \left(\frac{R_*}{100 R_{\odot}} \right)^{-1} \left(\frac{L_*}{1500 L_{\odot}} \right)^{-1} \text{ yr,} \quad (11)$$

where we estimated the stellar luminosity using $L_* = 4\pi R_*^2 \sigma T_*^4$ for $T_* = 3500\text{--}3700$ K typical of red giants. For the whole range of stellar radii $R_* \sim 4\text{--}1000 R_{\odot}$ and stellar luminosities $L_* \sim 10\text{--}7.2 \times 10^3 L_{\odot}$, t_{KH} differs considerably—from $\sim 10^6$ yr for the smallest giants to ~ 0.43 yr for the largest ones.

Based on the comparison between the time between jet–star collisions $t_c = P_{\text{orb}}/2$ and the KH timescale, one can distinguish cool colliders when $t_c \gtrsim t_{\text{KH}}$, i.e., the star had enough time to radiate away the accumulated collisional heat, and it cools down and shrinks before the next collision. For the case when $t_c < t_{\text{KH}}$, there is not enough time to radiate away the excess collisional heat, and the star is warmer and larger at the time of the subsequent collision—these are the so-called warm colliders. In the nuclear star cluster when the jet was active, there were both types of colliders with the approximate division given by $t_c \approx t_{\text{KH}}$, which leads to

$$z_c \approx \frac{Gm_*^{4/3} M_*^{1/3}}{R_*^{2/3} L_*^{2/3} \pi^{2/3}} = 0.04 \left(\frac{m_*}{1 M_{\odot}} \right)^{4/3} \left(\frac{M_*}{4 \times 10^6 M_{\odot}} \right)^{1/3} \times \left(\frac{R_*}{100 R_{\odot}} \right)^{-2/3} \left(\frac{L_*}{1500 L_{\odot}} \right)^{-2/3} \text{ pc.} \quad (12)$$

The length scale z_c implies that red giants located inside the inner S cluster were collisionally heated up and bloated, which increased their mass removal during repetitive encounters with the

jet. Stars orbiting at larger distances managed to cool down and shrink in size before the next collision, which has subsequently diminished their overall mass loss. However, note that Equation (12) is a function of the stellar parameters m_* , R_* , and L_* , hence z_c differs depending on the red giant stage and its mass. For the smallest late-type stars with $R_* \sim 4 R_{\odot}$ and $L_{\odot} \sim 8.9 L_{\odot}$, $z_c \sim 10.5$ pc; therefore, they can be classified as warm colliders throughout the nuclear star cluster. On the other hand, the late-type supergiants with $R_* \sim 10^3 R_{\odot}$ and $L_{\odot} \sim 7.2 \times 10^4 L_{\odot}$ have $z_c \sim 0.7$ mpc, hence they can be classified as cool colliders beyond milliparsec distances.

2.2. Jet-induced Envelope Removal

The stellar evolution after a jet–star encounter is generally complicated given that the envelopes of red giants become bloated after the first passage through the jet. This is because of the pressure of lower, hotter layers and their subsequent nearly adiabatic expansion, which can make the red giant even larger and brighter (Kieffer & Bogdanović 2016). Note that the number of encounters $n_{\text{cross}} = 2t_{\text{jet}}/P_{\text{orb}}$, where $t_{\text{jet}} \sim 0.5$ Myr is the jet lifetime, is typically $\gg 1$. In particular,

$$n_{\text{cross}} \sim 2 \times 10^4 \left(\frac{t_{\text{jet}}}{0.5 \text{ Myr}} \right) \left(\frac{M_*}{4 \times 10^6 M_{\odot}} \right)^{1/2} \left(\frac{z}{0.01 \text{ pc}} \right)^{-3/2}. \quad (13)$$

The number of encounters is also at least two orders of magnitude larger than the one expected from the star–accretion-clump interaction investigated by Kieffer & Bogdanović (2016) and Amaro-Seoane et al. (2020). After the first passage, the bloated red giant has an even larger cross section than before the encounter, which increases the mass removed during subsequent encounters (Armitage et al. 1996; Kieffer & Bogdanović 2016). The jet–star interaction phase proceeds during the red giant lifetime, which is $t_{\text{rg}} \sim 10^8$ yr (MacLeod et al. 2012). During the red giant phase, there are $n_{\text{orb}} = t_{\text{rg}}/P_{\text{orb}} \sim 2.1 \times 10^6 (z/0.01 \text{ pc})^{-3/2}$ orbits around Sgr A*, out of which $n_{\text{cross}}/n_{\text{orb}} = 2t_{\text{jet}}/t_{\text{rg}} \sim 1\%$ involve the interaction with the jet, assuming there was only one period of increased activity of Sgr A* in the last 100 million years. This ensures that the repetitive jet–red giant interaction leads to substantial mass loss, and the upper layer of the envelope is eventually removed.

The mass removal in a single passage due to atmosphere ablation ΔM_1 can be estimated through the balance of the jet ram force and the gravitational force acting on the envelope, i.e., $P_j \pi R_*^2 \approx G \Delta M_1 m_*/R_*^2$, giving (Barkov et al. 2012a)

$$\frac{\Delta M_1^{\text{max}}}{M_{\odot}} \approx 4 \times 10^{-10} \left(\frac{L_j}{10^{42} \text{ erg s}^{-1}} \right) \left(\frac{R_*}{100 R_{\odot}} \right)^4 \times \left(\frac{z}{0.04 \text{ pc}} \right)^{-2} \left(\frac{\theta}{0.22} \right)^{-2} \left(\frac{m_*}{M_{\odot}} \right)^{-1}. \quad (14)$$

In Figure 3, we plot ΔM_1 . Note that $\Delta M_1 \ll m_*$ and, therefore, the orbital dynamics is not significantly affected by a single passage through the jet. However, given that $\Delta M_1 \propto R_*^4 z^{-2}$, the mass loss can be about one-thousandth to one-hundredth of the mass of a star for the largest giants on the asymptotic giant branch with $R_* \sim 10^3 R_{\odot}$ and distances an order of magnitude smaller than $z \approx 0.04$ pc (see the yellowish region in Figure 3). In fact, the

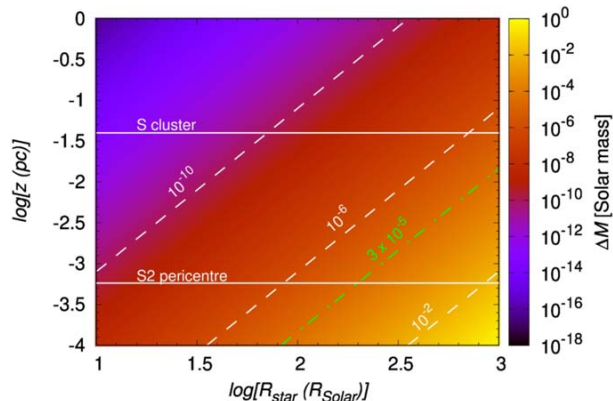


Figure 3. Mass removed from the red giant envelope for a single jet–star interaction, ΔM in Equation (14), for the case with $L_j = 10^{42}$ erg s $^{-1}$, $m_* = 1 M_\odot$, and $\theta = 12^\circ 5$. The two horizontal lines indicate the radial extent of the S cluster between the S2 pericentre distance and the outer radius at $z \sim 0.04$ pc. Dashed lines indicate $\Delta M/M_\odot = 10^{-10}$, 10^{-6} , and 10^{-2} . The dotted-dashed green line corresponds to $\Delta M = 3 \times 10^{-5} M_\odot$, which is equivalent to $\Delta M = 6 \times 10^{28}$ g in Equation (6) of Barkov et al. (2012a).

value of $\Delta M_1 = 6 \times 10^{28}$ g = $3 \times 10^{-5} M_\odot$ discussed by Barkov et al. (2012a) for powerful blazars in connection to their very high-energy γ -ray emission can be reached in the Galactic center for red giants with radii $R_* > 200 R_\odot$ at $z < 0.01$ pc. Such a large mass-loss with a certain momentum with respect to the star can already have an effect on the orbital dynamics, taking into account repetitive encounters of the red giant with the jet. In other words, the mass removal takes place at the expense of the kinetic energy of the star, which has implications for the dynamics of the NSC; see also Kieffer & Bogdanović (2016) for discussion. In addition, already for jets with a lower power corresponding to the active phase of the Galactic center, jet–red giant interactions can affect the short-term TeV emission in these sources. These effects are beyond the scope of the current paper and will be investigated in our future studies.

The mass removal during a single jet encounter given by Equation (14) can be considered as an upper limit as we assume that the cross section of the star is given by its radius during the entire passage of the star through the jet, hence $\Delta M_1^{\max} \approx P_j \pi R_*^4 / (Gm_*)$. However, this is only an approximation as realistically, during a few shock-crossing or dynamical timescales t_d , the ram pressure of the jet will shape the red giant and its detached envelope into a comet-like structure (see Figure 1) for which the interaction cross section is given by R_{stag} rather than by R_* , which gives us a lower limit on the mass removal, $\Delta M_1^{\min} \approx P_j \pi R_{\text{stag}}^4 / (Gm_*) \leq \Delta M_1^{\max}$. Using Equation (6), ΔM_1^{\min} can be expressed in terms of the basic parameters of the star and the jet, and it can numerically be expressed by the same units as in Equations (14) and (6),

$$\begin{aligned} \frac{\Delta M_1^{\min}}{M_\odot} &\approx \frac{c(\dot{m}_w v_w z \tan \theta)^2}{16Gm_* L_j} \\ &= 2.1 \times 10^{-12} \left(\frac{L_j}{10^{42} \text{ erg s}^{-1}} \right)^{-1} \left(\frac{m_*}{M_\odot} \right)^{-1} \\ &\quad \times \left(\frac{\dot{m}_w}{10^{-8} M_\odot \text{ yr}^{-1}} \right)^2 \left(\frac{v_w}{10 \text{ km s}^{-1}} \right)^2 \left(\frac{z}{0.04 \text{ pc}} \right)^2, \end{aligned} \quad (15)$$

where we adopted $\theta \sim 12^\circ 5$ as before. In comparison with ΔM_1^{\max} in Equation (14), which is proportional to z^{-2} , ΔM_1^{\min} in Equation (15) increases as z^2 . This implies that $\Delta M_1^{\min} \leq \Delta M_1^{\max}$ holds for $z \leq z_{\text{stag}}$, where at z_{stag} , $R_* = R_{\text{stag}}$. In other words, only at $z < z_{\text{stag}}$ is the mass removal due to the jet activity from the red giant atmosphere possible, while at distances larger than z_{stag} , the jet ablation is limited to the stellar-wind material, as is the case for the observed comet-shaped sources X3, X7, and X8 (Mužić et al. 2010; Peiřker et al. 2019). From Equation (6), the relation for z_{stag} follows as

$$\begin{aligned} z_{\text{stag}} &\approx 0.15 \left(\frac{R_*}{100 R_\odot} \right) \left(\frac{\theta}{0.22} \right)^{-1} \left(\frac{L_j}{10^{42} \text{ erg s}^{-1}} \right)^{\frac{1}{2}} \\ &\quad \times \left(\frac{\dot{m}_w}{10^{-8} M_\odot \text{ yr}^{-1}} \right)^{-\frac{1}{2}} \left(\frac{v_w}{10 \text{ km s}^{-1}} \right)^{-\frac{1}{2}} \text{ pc}. \end{aligned} \quad (16)$$

The dependence of z_{stag} on the stellar radius and the mass-loss rate is shown in Figure 4 (left panel). It is apparent that the volume around the reactivated Sgr A*, where the jet ablation can occur for a particular red giant, depends considerably on \dot{m}_w , which spans over three orders of magnitude depending on the evolutionary stage, $\dot{m}_w \approx 10^{-9} - 10^{-6} M_\odot \text{ yr}^{-1}$ (Reimers 1987). In particular, for red giants with $R_* = 10 R_\odot$, z_{stag} shrinks from 0.047 pc to 0.0015 pc as the mass-loss rate increases from $\dot{m}_w = 10^{-9} M_\odot \text{ yr}^{-1}$ to $10^{-6} M_\odot \text{ yr}^{-1}$.

In Figure 4 (right panel), we show an exemplary case for the mass removal range from the red giant atmosphere (red giant with the parameters of $R_* = 100 R_\odot$, $\dot{m}_w = 10^{-8} M_\odot \text{ yr}^{-1}$, and $v_w = 10 \text{ km s}^{-1}$) due to the single crossing through the jet with the luminosity of $L_j = 10^{42}$ erg s $^{-1}$ and the opening angle of 25° . Toward z_{stag} , the mass removal due to a single encounter approaches the mean value of $\overline{\Delta M_1} = \Delta M_1^{\max}$ ($z = z_{\text{stag}} = \Delta M_1^{\min}$ ($z = z_{\text{stag}}$),

$$\begin{aligned} \frac{\overline{\Delta M_1}}{M_\odot} &= \frac{\dot{m}_w v_w R_*^2}{4Gm_*} \\ &= 2.9 \times 10^{-11} \left(\frac{\dot{m}_w}{10^{-8} M_\odot \text{ yr}^{-1}} \right) \left(\frac{v_w}{10 \text{ km s}^{-1}} \right) \\ &\quad \times \left(\frac{R_*}{100 R_\odot} \right)^2 \left(\frac{m_*}{1 M_\odot} \right)^{-1}. \end{aligned} \quad (17)$$

Because of the estimated several thousands of red giant–jet encounters according to Equation (13), the cumulative mass loss from the red giant can be derived as $\Delta M \sim n_{\text{cross}} \Delta M_1$, giving

$$\begin{aligned} \frac{\Delta M}{M_\odot} &\approx 10^{-4} \left(\frac{L_j}{10^{42} \text{ erg s}^{-1}} \right) \left(\frac{R_*}{100 R_\odot} \right)^4 \left(\frac{z}{0.01 \text{ pc}} \right)^{-\frac{7}{2}} \\ &\quad \times \left(\frac{\theta}{0.22} \right)^{-2} \left(\frac{m_*}{M_\odot} \right)^{-1} \left(\frac{t_{\text{jet}}}{0.5 \text{ Myr}} \right) \left(\frac{M_*}{4 \times 10^6 M_\odot} \right)^{\frac{1}{2}}. \end{aligned} \quad (18)$$

In Figure 5, we plot ΔM for $L_j = 10^{42}$ and 10^{44} erg s $^{-1}$, and $R_* = 50$ and $100 R_\odot$. Additionally, we plot ΔM for the longer jet lifetime of $t_{\text{jet}} = 1$ Myr and $L_j = 10^{44}$ erg s $^{-1}$ and $R_* = 100 R_\odot$, which can be considered as an upper limit of ΔM for a red giant orbiting Sgr A*. We find that ΔM within the S cluster is comparable to the mass removal inferred from

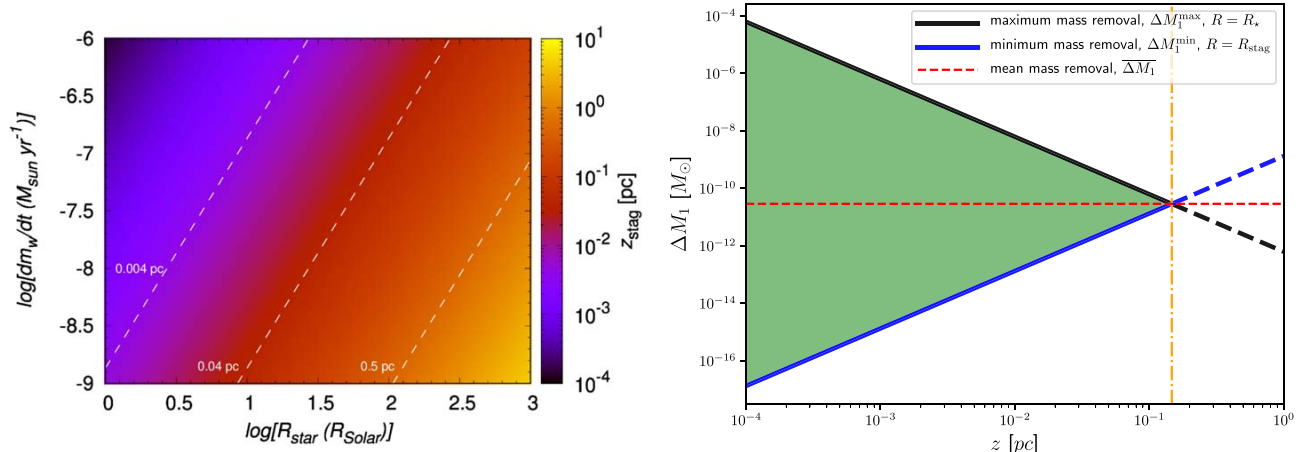


Figure 4. Mass removal during a single encounter of the red giant with the jet. Left panel: the color-coded distance in parsecs from Sgr A*, where $R_* = R_{\text{stag}}$ as a function of \dot{m}_w and R_* . The dashed white lines mark z_{stag} equal to 0.004 pc, 0.04 pc, and 0.5 pc from the left to the right, respectively. Right panel: an exemplary mass removal range $\Delta M_1^{\text{min}} - \Delta M_1^{\text{max}}$ (green-shaded region) for $R_* = 100 R_{\odot}$, $\dot{m}_w = 10^{-8} M_{\odot} \text{ yr}^{-1}$, $v_w = 10 \text{ km s}^{-1}$, $L_j = 10^{42} \text{ erg s}^{-1}$, and $\theta = 12.5^\circ$. The dotted-dashed vertical orange line marks z_{stag} (see Equation (16)), where $R_* = R_{\text{stag}}$. The red dashed line marks the mean mass removal $\overline{\Delta M}_1$ (see Equation (17)), $\overline{\Delta M}_1 = \Delta M_1^{\text{max}}(z = z_{\text{stag}}) = \Delta M_1^{\text{min}}(z = z_{\text{stag}})$.

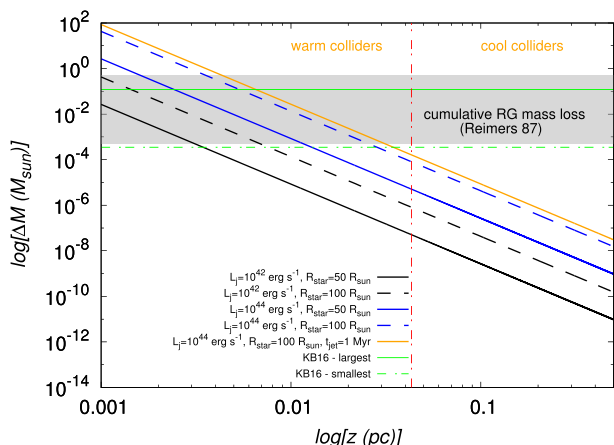


Figure 5. Cumulative mass removal ΔM due to the repetitive red giant–jet encounters as a function of the distance from Sgr A*. We fixed $L_j = 10^{42}$ and $10^{44} \text{ erg s}^{-1}$ and $R_* = 50$ and $100 R_{\odot}$. In addition, we plot ΔM for $L_j = 10^{44} \text{ erg s}^{-1}$, $R_* = 100 R_{\odot}$, and a longer duration of the jet activity, $t_{\text{jet}} = 1 \text{ Myr}$. For comparison, we also show the mass removal limits as inferred by Kieffer & Bogdanović (2016) for the red giant–clump collisions and the mass range as expected from the cumulative red giant (RG) mass loss due to stellar winds analyzed by Reimers (1987). The red dotted–dashed line marks the division between warm and cool colliders according to Equation (12).

the red giant–clump collision simulations by Kieffer & Bogdanović (2016). In Figure 5, we plot the upper and lower limits of ΔM obtained by Kieffer & Bogdanović (2016). Beyond $z = 0.03 \text{ pc}$, ΔM for the star–jet interaction is progressively smaller than $3.5 \times 10^{-4} M_{\odot}$, which implies that the jet impact on the stellar evolution is the most profound for S-cluster red giants. In this region, there also lies the division between the warm and the cool colliders as discussed in Section 2.1, with warm colliders present inside $z_c \sim 0.04 \text{ pc}$, which is also marked in Figure 5 with a vertical dotted–dashed line. Because warm colliders are warmer and bigger, this

further enhances the mass removal inside the S cluster. In addition, the mass removal due to the jet interaction is of a comparable order of magnitude to the mass loss expected from cool winds during the time interval of the active jet $\Delta M_w \approx \dot{m}_w t_{\text{jet}} \sim 0.5\text{--}5 \times 10^{-4} M_{\odot}$ when $\dot{m}_w \approx 10^{-6}\text{--}10^{-9} M_{\odot} \text{ yr}^{-1}$ (Reimers 1987), as indicated by the shaded rectangle in Figure 5. This implies that the jet–star interaction perturbs the stellar evolution of passing red giants, in particular in the innermost parts of the NSC.

Note that, on one hand, ΔM is supposed to be a lower limit as after the first passage through the jet, the giant is expected to expand to an even larger radius before the next encounter, which increases the mass removal efficiency (Kieffer & Bogdanović 2016). On the other hand, the resonant relaxation of stellar orbits as well as a jet precession may change the frequency of the jet–star interactions (see Sections 4 and 6.1), and therefore, n_{cross} should be considered as an upper limit of the number of encounters. Overall, ΔM in Equation (18) can be applied as an approximation for the total mass removal due to the red giant–jet interactions. Hence, the truncation of stellar envelopes of late-type stars by the jet during active phases of Sgr A* appears to be efficient and complementary to other previously proposed processes, mainly tidal disruptions of giants and stellar collisions with other stars and/or the accretion disk.

3. Missing Red Giants in the Near-infrared Domain

Red giants are post-main-sequence evolutionary stages of stars with initial mass $0.5 M_{\odot} \lesssim m_* \lesssim 10 M_{\odot}$. These stars exhausted hydrogen supplies in their cores, and the hydrogen fusion into helium continues in the shell. As a result, the mass of the helium core gradually increases, and this is linked to the increase in the atmosphere radius as well as luminosity. Stellar evolutionary models of red giants show that their atmosphere radius and bolometric luminosity depend primarily on the mass of the helium core m_c as (Refsdal & Weigert 1971;

Joss et al. 1987)

$$\frac{L_\star}{L_\odot} \approx \frac{10^{5.3} \mu_c^6}{1 + 10^{0.4} \mu_c^4 + 10^{0.5} \mu_c^5},$$

$$\frac{R_\star}{R_\odot} \approx \frac{3.7 \times 10^3 \mu_c^4}{1 + \mu_c^3 + 1.75 \mu_c^4}, \quad (19)$$

where $\mu_c \equiv m_c/M_\odot$. This also holds for red supergiants with carbon–oxygen cores and burning hydrogen and helium in their shells (Paczynski 1970). In the red giant stage, the dominant energy source is the p–p process, and hence, the luminosity is mainly determined by the growth rate of the helium core \dot{m}_c ,

$$\frac{L_\star}{L_\odot} \approx 1.02 \left(\frac{\dot{m}_c}{10^{-11} M_\odot \text{ yr}^{-1}} \right). \quad (20)$$

Equations (19) and (20) imply that the bolometric luminosity is not significantly affected by the jet–red giant interaction, as only the tenuous shell is ablated by the jet, and the dense core is left untouched. Then, the effective temperature T_1 of the ablated giant is

$$\frac{T_1}{T_0} = \left(\frac{R_0}{R_1} \right)^{\frac{1}{2}}, \quad (21)$$

where T_0 is the original effective temperature, and R_0 and R_1 are the atmosphere radii before and after the truncation, respectively. Here we implicitly assume that the red giant underwent n_{coll} interactions with the jet during the active phase given by Equation (13), which eventually leads to the decreased radius of $R_1 \approx R_{\text{stag}}$ according to Equation (6). The luminosity in the infrared domain between frequencies ν_1 and ν_2 can be expressed using the Rayleigh–Jeans approximation⁹ as $L_{\text{IR}} \lesssim 8/3(\pi/c)^2 R_\star^2 k_B T_\star (\nu_2^3 - \nu_1^3) \propto R_\star^2 T_\star$ (see Alexander 2005 for a similar analysis), which using Equation (21) leads to

$$\frac{L_1}{L_0} \sim \left(\frac{R_1}{R_0} \right)^{\frac{3}{2}}. \quad (22)$$

For instance, the ablation of a red giant atmosphere from 120 to 30 R_\odot would result in the increase of effective temperature by a factor of 2 and a decrease by a factor of 8 in the IR luminosity or ~ 2.26 mag. The ablation of the envelope from 120 to 4 R_\odot would result in the decrease by as much as ~ 5.5 mag. The difference of 2–5 mag can already affect the count rate of late-type stars in the near-infrared domain in the central arcsecond of the Galactic center.

As an exemplary case, we set up a simplified temporal evolution of a red giant using Equations (19) and (20). We perform this calculation to estimate the potential difference in near-infrared magnitudes, and the color change for late-type stars before and after the active jet phase—it does not represent realistic stellar evolution tracks, but can provide insight into the basic trends in the near-infrared magnitude evolution and the effective temperature. We evolve the stellar luminosity and the radius for an increasing core mass $\mu_c = \mu_{c,0} + \dot{\mu}_c dt$, where $\mu_{c,0} = 0.104$ and the time step is $dt = 10^4$ yr. The overall

evolution from $\mu_{c,0}$ to $\mu_c = 0.55$ takes $\sim 8.41 \times 10^9$ yr, when neither the effect of stellar winds nor that of rotation is taken into account. The initial and the final core masses were chosen according to the limiting values for lighter stars, $m_\star < 2 M_\odot$, in which case $\mu_c^{\text{min}} \sim 0.1$ and $\mu_c^{\text{max}} \sim 0.5$. These are stars with degenerate helium cores and hydrogen-burning shells (Refsdal & Weigert 1971). The lower core-mass value of 0.1 also approximately corresponds to the Schönberg–Chandrasekhar limit. The total duration is comparable to the time that stars of 1 M_\odot spend on the giant and asymptotic giant branches, which is of the order of 10^9 yr according to MacLeod et al. (2012).

To assess the observational effects of the star–jet collision in the near-infrared domain, we calculate the effective temperature at each step using $T_\star = T_\odot (L_\star/L_\odot)^{1/4} (R_\star/R_\odot)^{-1/2}$. Subsequently, we calculate the monochromatic flux density in K band ($2.2 \mu\text{m}$) and L' band ($3.8 \mu\text{m}$) using $F_\nu = (R_\star/d_{\text{GC}})^2 \pi B_\nu(T_\star)$, where $B_\nu(T_\star)$ is the spectral brightness given by the Planck function at the given effective temperature. The corresponding magnitudes are calculated using $m_K = -2.5 \log(F_K/653 \text{ Jy})$ and $m_{L'} = -2.5 \log(F_{L'}/253 \text{ Jy})$, from which the color index follows as $CI = m_K - m_{L'}$.

For the analysis in this section as well as in Section 5, we calculate intrinsic stellar magnitudes m_K and $m_{L'}$. The calculated magnitudes and colors can then be compared to extinction-corrected magnitudes and the derived surface-brightness profiles of the nuclear star cluster, i.e., those corrected for the foreground extinction. To compare our results to observed magnitudes and derived surface profiles that are just corrected for the differential extinction but not for the foreground extinction (Buchholz et al. 2009; Habibi et al. 2019; Schödel et al. 2020), it is necessary to increase the magnitudes using the corresponding mean extinction coefficients (see, e.g., Schödel et al. 2010), in particular $A_K = 2.54 \pm 0.12$ mag and $A_{L'} = 1.27 \pm 0.18$ mag.

The imprint of the ablation of the stellar atmosphere by a jet, whose kinetic luminosity is fixed to $L_j = 2.3 \times 10^{42} \text{ erg s}^{-1}$, is modeled by assuming that the radius of an interacting red giant keeps evolving according to Equation (19) when $R_\star < R_{\text{stag}}$ at a given distance z from Sgr A*. After the stellar radius reaches the scale of the stagnation radius at a given distance z , we set $R_\star = R_{\text{stag}}$ for the rest of the evolution, which can be justified by the fact that the red giant propagates through the jet n_{coll} times and the envelope is removed after repetitive encounters. The expected number of encounters is 6×10^5 , 2×10^4 , and 632 for $z = 0.001$ pc, 0.01 pc, and 0.1 pc, respectively; see Equation (13). In Figure 6, we show three magnitude–effective temperature curves of the ablated red giants that underwent repetitive encounters with the jet at their orbital distances of 0.001, 0.01, and 0.1 pc from Sgr A*, which led to their truncation to a smaller radius close to the corresponding stagnation radius at a given distance. In addition, we compare the magnitude–temperature curves of ablated giants with an unaffected evolution. We list the stellar parameters at the time of the atmosphere truncation when $R_\star = R_{\text{stag}}$ at the corresponding distance as well as the parameters for the final state of ablated giants in Table 1. This is compared to an unaffected final state with the core mass of $0.55 M_\odot$; see the bottom row of Table 1. The basic signature of the jet–star interaction is that the star gets progressively warmer (with a bluer, more negative color index) and fainter in the near-infrared K_s band in comparison with the normal evolution without any atmosphere ablation. This trend is more apparent for red giants that are

⁹ Strictly speaking, for $T_\star = 5000$ K, the condition $k_B T_\star > h\nu$ applies for wavelengths longer than $2.9 \mu\text{m}$.

Table 1
Parameters at the Time of the Jet Ablation and Those of the Final State of a Red Giant, which is Evolved from the Core Mass of $\mu_c = 0.104$ to 0.55

Ablation Distance (pc)	Ablation Time (yr)	R_*^{abl} (R_\odot)	T_*^{abl} (K)	T_*^{fin} (K)	m_K^{abl} (mag)	m_K^{fin} (mag)	CI ^{fin}
0.001	3.0×10^8	0.45	6205	68 759	19.6	16.4	-0.14
0.01	8.0×10^9	4.45	4662	21 744	15.2	12.8	-0.09
0.1	8.4×10^9	44.51	3526	6 876	10.7	9.4	-0.09
Normal Evolution	...	255.21 (final radius)	...	2 871	...	7.47	0.51

Note. The upper three lines contain parameters of the ablated red giants orbiting at distances 0.001, 0.01, and 0.1 pc (first column). The second column lists the time, at which the ablation occurred with respect to the initial state of $\mu_c = 0.104$. The third column lists the truncation radius, when $R_* = R_{\text{stag}}$. The fourth column lists the effective temperature at the time of truncation. The fifth column lists the final effective temperature at the final stage of their evolution (when $\mu_c = 0.55$). The sixth and seventh columns contain dereddened magnitudes at the ablation and final times, respectively. The last column contains dereddened color indices, $\text{CI} = m_K - m_L$, at the final state. The bottom line corresponds to the final state of a normal, unaffected evolution.

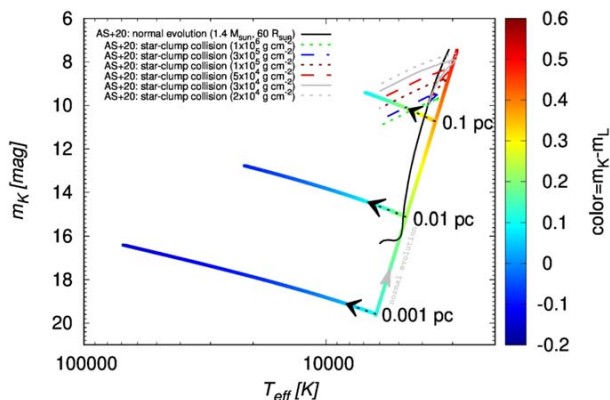


Figure 6. Near-infrared magnitude (K band, $2.2 \mu\text{m}$, dereddened) and temperature (or color index that is color-coded) of a red giant after crossing the jet n_{coll} times. We compare three temperature- K_s -band magnitude curves affected by a series of collisions with the jet at $z = 0.001$, 0.01, and 0.1 pc (marked by black arrows) with a normal, unaffected evolution (marked by a gray arrow). The evolution is driven by an increase in the helium core mass from $\mu_c = 0.104$ to $0.55 M_\odot$ with a time step of 10^4 yr. At each time step, we calculate R_* and L_* using Equations (19). The overall evolution takes $\sim 8 \times 10^9$ yr. For comparison, we also show the evolutionary tracks for the normal evolution (black solid line) and the evolution affected by the star-clump collisions (lines according to the legend for different clump surface densities listed in parentheses) as calculated by Amaro-Seoane et al. (2020), abbreviated as AS+20 using the CESAM code (Morel & Lebreton 2008).

closer to Sgr A* because of the smaller jet-star stagnation radius and hence a larger fraction of the stellar atmosphere that is removed.

Although we do not calculate stellar evolutionary tracks, only basic trends in terms of near-infrared magnitude and effective temperature, our results are consistent with those of Amaro-Seoane et al. (2020) who calculated evolutionary tracks specifically for late-type stars ablated due to the red giant-accretion-clump collisions. They show in their Figure 2 that the collision affects the stellar evolution of a red giant in a way that after repetitive encounters it follows a track along a nearly constant absolute bolometric magnitude toward higher effective temperatures. The constant absolute bolometric magnitude or bolometric luminosity in combination with an increasing effective temperature results in the drop in the near-infrared luminosity, because $L_{\text{IR}}/L_{\text{bol}} \propto T_*^{-3}$. We used their evolutionary tracks calculated using the CESAM code (Morel & Lebreton 2008) for estimating K_s -band near-infrared magnitudes. These tracks are depicted in Figure 6 for the case of a

normal evolution of a star with $M_* = 1.4 M_\odot$ and $R_* = 60 R_\odot$ (black solid line) and different collision cases for clumps with surface densities in the range $\Sigma = 2 \times 10^4$ – 10^6 g cm^{-2} (see the legend). Qualitatively, the perturbed stellar evolutionary tracks follow the temperature trends that we can also observe for giant-jet collisions: ablated giants move toward higher effective temperature. Also, they become fainter in the near-infrared domain in comparison with an unperturbed evolution. The main difference in comparison with the analysis of Amaro-Seoane et al. (2020) is their trend toward larger magnitudes (stars become fainter), while we see a small gradual increase in brightness. This difference is due to our simplifying assumption of a constant radius after the series of collisions with the jet, while in reality the radius should evolve, especially after the jet ceases to be active. Because $L_{\text{IR}} \propto R_*^2 T_*$, the near-infrared luminosity grows linearly with increasing temperature for the fixed stellar radius. This motivates further exploration of the effect of star-jet collisions using a modified stellar evolutionary code.

For asymptotic giant branch stars, an extreme transition from a red, cool luminous giant to a hot and faint white dwarf is possible when it is completely stripped of its envelope. This was studied by King (2020) for tidal stripping close to the SMBH but cannot be excluded also for asymptotic giant branch stars and jet collisions for a case when the giant star is at milliparsec separation from Sgr A* and less, in which case the stagnation radius is typically a fraction of the solar radius. In fact, an active jet can enlarge the volume around the SMBH where asymptotic giant branch stars are turned into white dwarfs. Considering Equation (6), we can derive that in order for R_{stag} to be of the order of a white-dwarf radius $R_{\text{wd}} \sim 0.01 R_\odot$, the giant needs to orbit the SMBH at $z \approx 0.15 \text{ mpc}$ so that the jet with $L_j = 10^{44} \text{ erg s}^{-1}$ can truncate it down to the white-dwarf size. The stellar interior that is not affected by tidal forces is characterized by the Hill radius

$$r_{\text{Hill}} \approx z \left(\frac{m_*}{3M_*} \right)^{\frac{1}{3}} = 29 \left(\frac{z}{0.15 \text{ mpc}} \right) \times \left(\frac{m_*}{1 M_\odot} \right)^{\frac{1}{3}} \left(\frac{M_*}{4 \times 10^6 M_\odot} \right)^{-\frac{1}{3}} R_\odot, \quad (23)$$

from which we see that tidal forces alone will not truncate the giant down to its white-dwarf core because $r_{\text{Hill}} > R_{\text{stag}}$ at z .

In summary, the jet-star interaction could have affected the appearance of late-type giants in the central arcsecond by making them warmer or bluer in terms of color and hence fainter in the near-infrared domain.

4. Fraction of Red Giants Interacting with the Jet

We estimate the number of late-type stars, i.e., stars that form a cusp, that could have passed and interacted with the jet during its estimated lifetime of $\sim 0.1\text{--}0.5$ Myr (Guo & Mathews 2012). For the density distribution of late-type stars in the inner 0.5 pc, we adopt a cusp-like power-law distribution $n_{\text{RG}} \approx n_0(z/z_0)^{-\gamma}$, with $n_0 \simeq 52 \text{ pc}^{-3}$, $z_0 \simeq 4.9 \text{ pc}$, and $\gamma \simeq 1.43$ (Gallego-Cano et al. 2018). The expected number of late-type stars within a certain distance z_{out} is

$$N_*(\langle z_{\text{out}} \rangle) = \int_0^{\langle z_{\text{out}} \rangle} n_{\text{RG}}(z) 4\pi z'^2 dz' = 4\pi n_0 \frac{z_0^\gamma \langle z_{\text{out}} \rangle^{3-\gamma}}{3-\gamma} \quad (24)$$

giving $N_* \approx 610$ and 25.8 inside 0.3 and 0.04 pc, respectively. The number of stars inside the jet at any time is given by the jet covering factor f_j in a spherical volume $V_* = (4/3)\pi z_{\text{out}}^3$. By considering a conical jet and a counter-jet with the total volume $V_j = 2/3\pi R_j^2 z_{\text{out}}$, the covering factor is $f_j = V_j/V_* \sim (R_j/z_{\text{out}})^2$ and the number of red giants inside the jet is $N_j(\langle z_{\text{out}} \rangle) = f_j N_*(\langle z_{\text{out}} \rangle) \sim N_*(\langle z_{\text{out}} \rangle) \tan^2(\theta)/2$. Then, the average number of red giants that are simultaneously inside the jet is $N_j \approx 14.8$ and 0.62 inside 0.3 pc and 0.04 pc, respectively.

To estimate the number of stars crossing the jet per orbital timescale, we first calculate the jet-crossing rate per unit of time. Because we focus on the region $z \lesssim 0.5 \text{ pc}$, which is well inside the radius of influence of Sgr A*, $r_h \sim 2 \text{ pc}$ (Merritt 2013), we approximate the stellar velocity dispersion by the local Keplerian velocity, $\sigma_* \sim v_{\text{orb}} = \sqrt{GM_*/z}$; see, e.g., Šubr & Haas (2014). With the jet cross section $S_{\text{jet}} \approx zR_j \sim z^2 \tan \theta$, the number of late-type stars entering both the jet and counter-jet per unit of time is

$$\dot{N}_{\text{RG}} \approx 2n_{\text{RG}}\sigma_*S_{\text{jet}} \simeq 2n_0z_0^\gamma \sqrt{GM_*} \tan \theta z^{3-\gamma}. \quad (25)$$

The number of red giants crossing the jet per orbital timescale is

$$N_{\text{RG}} = \dot{N}_{\text{RG}}P_{\text{orb}} = 4\pi n_0z_0^\gamma \tan \theta z^{3-\gamma}, \quad (26)$$

where the orbital period in the sphere of influence of the SMBH follows from the third Keplerian law, $P_{\text{orb}} = 2\pi z^{3/2}/\sqrt{GM_*}$. In Figure 7, we plot N_{RG} . The average number of crossing giants per orbital period in the region with an outer radius z_{out} is

$$\bar{N}_{\text{RG}} = \frac{4\pi}{4-\gamma} n_0z_0^\gamma \tan \theta z_{\text{out}}^{3-\gamma}. \quad (27)$$

In particular, $\bar{N}_{\text{RG}} \simeq 3.5$ and $\bar{N}_{\text{RG}} \simeq 82$ when $z_{\text{out}} = 0.04 \text{ pc}$ (S cluster) and $z_{\text{out}} = 0.3 \text{ pc}$, respectively (see Figure 7).

In this case, \bar{N}_{RG} represents all late-type stars that cross the jet sheath per orbital period on average. The fraction of giants whose envelopes could have been stripped off by the jet can be estimated by comparing the radii of stars with the corresponding stagnation radius at a certain distance from Sgr A*. The basic condition for the ablation is that $R_* \gtrsim R_{\text{stag}}$ at a given z from Sgr A*. In particular, for $z = 0.04 \text{ pc}$ and the jet luminosity of $L_j = 10^{42} \text{ erg s}^{-1}$, the minimum stellar parameters for ablation are $R_* = 27 R_\odot$, $\mu_c = 0.3$, $L_* = 129 L_\odot$, $T_* = 3743 \text{ K}$, and $m_{\text{abl}} = 11.7 \text{ mag}$, where m_{abl} denotes the upper magnitude limit, below which stars are expected to be affected by the jet. Using the *K*-band luminosity function

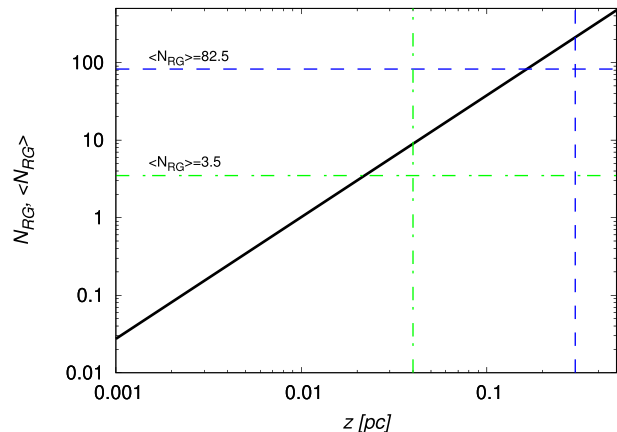


Figure 7. Number of red giants crossing the jet per orbital period (black solid line; see Equation (26)). The average number of red giant/jet interactions at $z \leq 0.04 \text{ pc}$ and 0.3 pc are plotted in green dotted-dashed and blue-dashed lines, respectively.

approximated by the power law, $d \log N/dm_K = \beta$ with $\beta \simeq 0.3$ for late-type stars (Buchholz et al. 2009; Pfuhl et al. 2011) between 12 and 18 mag, we can estimate the fraction of ablated stars as $\eta = N_{\text{abl}}/N_{\text{tot}} \times 100 = 10^{\beta(m_{\text{abl}} - m_{\text{max}}) + 2\%}$, where m_{max} is the limiting magnitude, which we set to 18 mag according to Pfuhl et al. (2011). Then, for $z = 0.04 \text{ pc}$ and $L_j = 10^{42} \text{ erg s}^{-1}$, we get $\eta = 1.27\%$. For the larger distance $z = 0.5 \text{ pc}$ and $L_j = 10^{42} \text{ erg s}^{-1}$, we obtain the minimum parameters of ablated stars as follows, $R_* = 338 R_\odot$, $\mu_c = 0.6$, $L_* = 6081 L_\odot$, $T_* = 2775 \text{ K}$, $m_{\text{abl}} = 6.95 \text{ mag}$ with $\eta = 0.05\%$. The limiting values and the percentage of ablated giants are quite sensitive to the jet luminosity. Increasing L_j to $10^{44} \text{ erg s}^{-1}$, we get $R_* = 2.7 R_\odot$, $\mu_c = 0.16$, $L_* = 3.97 L_\odot$, $T_* = 4960 \text{ K}$, $m_{\text{abl}} = 16.1 \text{ mag}$ with $\eta = 26.5\%$ for $z = 0.04 \text{ pc}$ and $R_* = 33.8 R_\odot$, $\mu_c = 0.31$, $L_* = 181 L_\odot$, $T_* = 3645 \text{ K}$, $m_{\text{abl}} = 11.3 \text{ mag}$ with $\eta = 0.95\%$ for $z = 0.5 \text{ pc}$. We summarize the relevant values in Table 2. Although the fraction of affected late-type stars is small, it significantly affects brighter stars with smaller magnitudes—stars brighter than 14 mag constitute $\sim 6.3\%$ of the total observed sample and stars brighter than 12 mag constitute only 1.6%. We explicitly show the change in the projected brightness distribution for brighter stars in Section 5.

The jet ablation could partially have contributed to the inferred four to five missing late-type giants in the region with $z_{\text{out}} = 0.04 \text{ pc}$ (Habibi et al. 2019) as well as to the ~ 100 missing late-type giants in the larger region with $z_{\text{out}} = 0.3 \text{ pc}$ (Gallego-Cano et al. 2018), especially for higher luminosities of the jet.

The number of stars that can interact with the jet is increased via dynamical processes in the dense nuclear star cluster. In particular, the vector resonant relaxation (VRR) changes the direction of the orbital angular momentum (Alexander 2005; Merritt 2013), and therefore, stars that were not passing through the jet can do so on the resonant relaxation timescale. More precisely, in the sphere of influence of the SMBH, stars move on Keplerian ellipses, and the gravitational interactions between stars are correlated. Given the finite number of stars, there is a nonzero torque on a test star. During the time interval

Table 2

 Limiting Minimal Stellar Radii, Maximum Apparent K -band Magnitudes (dereddened), and the Fraction of Ablated Giants for Two Distances from Sgr A* (0.04 and 0.5 pc) and Two Luminosities of Its Jet (10^{42} erg s^{-1} and 10^{44} erg s^{-1})

Distance	$L_j = 10^{42}$ erg s^{-1}	$L_j = 10^{44}$ erg s^{-1}
0.04 pc	$R_* = 27 R_\odot$, $m_{\text{abl}} = 11.7$, $\eta = 1.27\%$	$R_* = 2.7 R_\odot$, $m_{\text{abl}} = 16.1$, $\eta = 26.5\%$
0.5 pc	$R_* = 338 R_\odot$, $m_{\text{abl}} = 6.95$, $\eta = 0.05\%$	$R_* = 33.8 R_\odot$, $m_{\text{abl}} = 11.3$, $\eta = 0.95\%$

Δt , for which $P_{\text{orb}} \ll \Delta t \ll T_{\text{coh}}$ and the coherence timescale

$$T_{\text{coh}} = \frac{P_{\text{orb}}}{2\pi\sqrt{N_*}} \frac{M_*}{m_*} = \sqrt{\frac{3-\gamma}{4\pi G n_0 z_0^\gamma}} \frac{M_*^{\frac{1}{2}}}{m_* z^{\frac{\gamma}{2}}} \quad (28)$$

is inversely proportional to the square root of the number of enclosed stars, the angular momentum of a test star changes linearly with time.

The inclination of stellar orbits would change by $\sim\pi$ only when $T_{\text{coh}}(z) \lesssim t_j \sim 0.1\text{--}0.5$ Myr and hence essentially all late-type stars could interact with the jet during its lifetime. The estimated number of enclosed stars in the S cluster ($z_{\text{out}} \sim 0.04$ pc) is $26 < N_* < 10,000$, where the lower limit considers only late-type stars according to the analysis by Habibi et al. (2019) and the upper limit stands for all the stars including compact remnants. The upper limit is supposed to be closer to the actual number of stellar objects because the number of old neutron stars and stellar black holes in the central arcsecond could be of that order of magnitude (Morris 1993; Deegan & Nayakshin 2007; Zhu et al. 2018). The total number of massive objects naturally affects the coherence timescale by more than an order of magnitude. In Figure 8, we plot T_{coh} . We see that when $N_* \sim 1000$ and more, T_{coh} is comparable to the lifetime of the jet in the inner parts of the S cluster. In summary, the coherent resonant relaxation makes the number of affected giants bigger and the estimates per orbital timescale \bar{N}_{RG} can be considered as a lower limit. Another more hypothetical effect that can enlarge the number of affected giants is the jet precession (see Section 6.1).

The VRR can affect the number of encounters, n_{cross} ; see Equation (13). In case $T_{\text{coh}} > t_{\text{jet}}$, i.e., for a smaller number of enclosed objects ($N_* \lesssim 100$), n_{cross} is still mainly determined by t_{jet} ; see Equation (13). However, then the mean number of interacting giants \bar{N}_{RG} is also not significantly enlarged. On the other hand, if $T_{\text{coh}} \lesssim t_{\text{jet}}$, then n_{cross} is reduced approximately by a factor of $2\theta/\pi$, which assumes that the angular momentum vector shifts linearly with time during T_{coh} . In that sense, the interaction timescale with the jet is $t_{\text{int}} \sim T_{\text{coh}}(2\theta/\pi)$. Considering $T_{\text{coh}} \sim t_{\text{jet}}$, the number of crossings is

$$n_{\text{cross}}^{\text{RR}} \sim 2800 \left(\frac{T_{\text{coh}}}{0.5 \text{ Myr}} \right) \left(\frac{M_*}{4 \times 10^6 M_\odot} \right)^{\frac{1}{2}} \left(\frac{z}{0.01 \text{ pc}} \right)^{-\frac{3}{2}}, \quad (29)$$

which is smaller by an order of magnitude in comparison with n_{cross} .

5. Effect of Jet Ablation on the Surface-brightness Profile of a Nuclear Star Cluster

To assess the observational signatures of the jet ablation of late-type stars, we generate a mock spherical cluster of stars. Their initial spatial distribution follows $n_{\text{RG}} = n_0(z/z_0)^{-\gamma}$ with $n_0 = 52 \text{ pc}^{-3}$, $z_0 = 4.9 \text{ pc}$, and $\gamma \sim 1.43$ (Gallego-Cano et al. 2018). This spatial profile suggests that there are in total ~ 4000

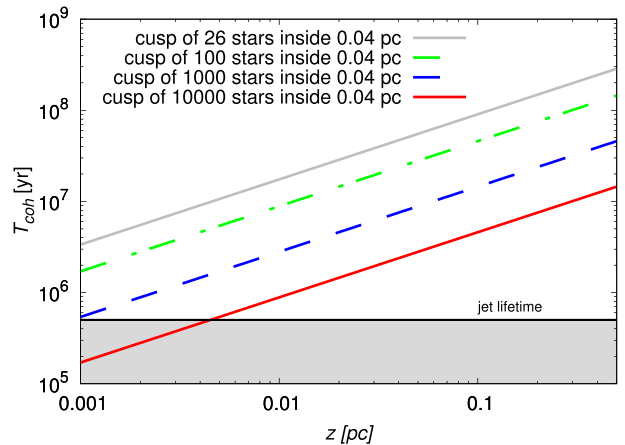


Figure 8. The coherence timescale T_{coh} for different numbers of stars in the S cluster according to the legend. The shaded area stands for the expected lifetime of the jet during the previous Seyfert-like activity of Sgr A*.

late-type stars inside the inner 1 pc, which we generate using the Monte Carlo approach to form a mock NSC; see Figure 9 (left panel) for illustration.

Each star is assigned its mass in the range from $0.08 M_\odot$ to $100 M_\odot$ following the initial mass function (IMF) according to Kroupa (2001), i.e.,

$$\zeta(m_*) = m_*^{-\alpha}, \quad \text{where} \quad \begin{cases} \alpha = 0.03, & m_* < 0.08 M_\odot, \\ \alpha = 1.3, & 0.08 M_\odot < m_* < 0.5 M_\odot, \\ \alpha = 2.3, & m_* > 0.5 M_\odot. \end{cases} \quad (30)$$

The Chabrier/Kroupa IMF is a good approximation for the observed mass distribution of the late-type NSC population (Pfuhl et al. 2011).

In the next step, we assigned the core mass to each star of the mock cluster. Here, we fix the ratio between the core mass and the stellar mass to $\mu_c/m_* = 0.4$, which is in between the value inferred from the Schönberg–Chandrasekhar limit¹⁰ and the final phases of the stellar evolution, where the white-dwarf core constitutes most of the mass for solar-type stars. For more precise simulations, core masses from the stellar evolution of the NSC should be adopted; however, here we are interested in the first-order effects of the jet activity on the surface-brightness distributions.

To construct the surface-brightness profiles of the late-type population after the active jet phase in different magnitude bins, we followed these steps:

¹⁰ The Schönberg–Chandrasekhar limit expresses the ratio between the isothermal core mass and the stellar mass, $m_{\text{ic}}/m_* \simeq 0.37(\mu_{\text{env}}/\mu_{\text{ic}})^2 \sim 0.1$, where μ_{env} and μ_{ic} are the mean molecular weights for the envelope and the isothermal core, respectively.

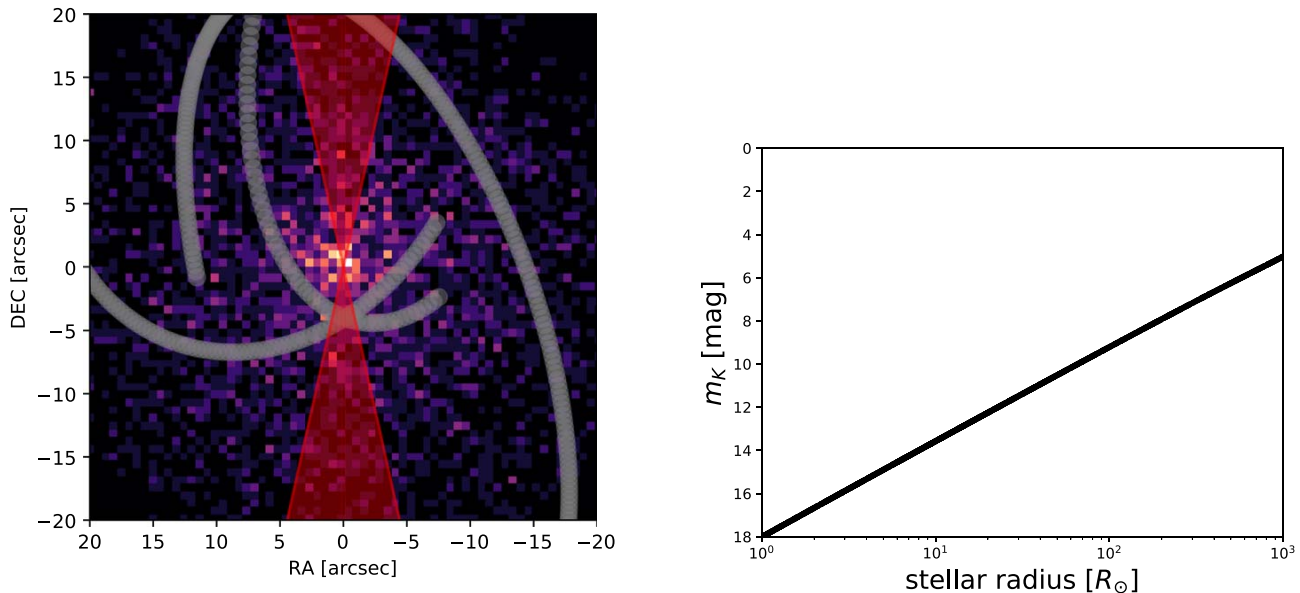


Figure 9. Initial properties of the Monte-Carlo-generated mock NSC. Left panel: the projected surface density distribution of 4000 stars with the illustrated active jet with the half-opening angle of $\theta = 12^\circ.5$. The gray streamers illustrate the mini-spiral arms according to the Keplerian model of Zhao et al. (2009). Right panel: the K -band magnitude (dereddened)–stellar radius relation for our generated NSC.

1. We calculated $L_*(\mu_c)$ and $R_*(\mu_c)$ using Equation (19).
2. If the jet was set active with a certain luminosity L_j , we compared R_* and R_{stag} for a given distance z of the star. If $R_* \geq R_{\text{stag}}$, then we set $R_* = R_{\text{stag}}$. In this case, we also implicitly assumed that at a given distance, all of the stars, for which $R_* \geq R_{\text{stag}}$, are eventually ablated by the jet; hence, the resonant relaxation was assumed to be efficient and hence $T_{\text{coh}} < l_{\text{jet}}$.
3. We estimated the effective temperature of a star using $T_* = T_\odot (L_*/L_\odot)^{1/4} (R_*/R_\odot)^{-1/2}$.
4. From the Planck function $B_\nu(T_*)$, we calculated the monochromatic flux in the K_s band ($2.2 \mu\text{m}$) $F_\nu(R_*, T_*) = (R_*/d_{\text{GC}})^2 \pi B_\nu(T_*)$ and the corresponding apparent magnitude m_K (dereddened).

The initial relation between the K_s -band magnitude and the stellar radius is shown in Figure 9 in the right panel. We calculate the projected stellar density using concentric annuli with mean radius R and width of ΔR , $\sigma_* = N_*/(2\pi R \Delta R)$, where N_* is the number of stars in an annulus. We estimate the uncertainty of the stellar number counts as $\sigma_N \approx \sqrt{N_*}$. Subsequently, we construct the surface stellar profiles in two-magnitude bins starting at $m_K = 18$ mag up to $m_K = 10$ mag, i.e., in total, four bins; see Figure 10. In the top-left panel of Figure 10, we plot the nominal projected distribution without considering the effect of the jet. The brightness profile for all four magnitude bins can be approximated by simple power-law functions, $N(R) = N_0 (R/R_0)^{-\Gamma}$, whose slopes are listed in Table 3. Hence, the initial cluster distribution is cusp like. In the top-right panel, we show the case with an active jet with the luminosity of $L_j = 10^{42} \text{ erg s}^{-1}$. We see that the profile for the brightest stars in the 10–12 mag bin becomes flat in the inner arcsecond and can be described as a broken power-law function, $N(R) = N_0 (R/R_{\text{br}})^{-\Gamma} [1 + (R/R_{\text{br}})^\Delta]^{\Gamma-\Gamma_0}/\Delta$, where R_{br} is a break radius, Γ is a slope of the inner part, Γ_0 marks the slope of an outer part, and Δ denotes the sharpness of the transition. The larger surface-brightness values for this magnitude bin may be interpreted as an extra input of ablated giants with

initial magnitudes $m_K < 10$ mag that after the ablation fall into bins with a larger magnitude. Finally, we increase the jet luminosity to $L_j = 10^{44} \text{ erg s}^{-1}$, which makes the flattening of the brightest giants even more profound. The stars in the 12–14 mag bin also exhibit a flatter profile inside the inner arcsecond for this case, which shows the significance of the jet luminosity in affecting the observed surface profile of the NSC. We list the power-law slopes for both a simple and a broken power-law function and the break radii, where available, for all the magnitude bins and the three jet-activity cases in Table 3.

Figure 10 demonstrates a potential signature of the jet activity on the surface profile of the NSC. It is important to study differential profiles, i.e., the distribution in different magnitude bins, because the lower-luminosity jet starts affecting the profile of bright stars (smaller magnitudes), while with an increasing jet luminosity, the fainter stars become affected as well, starting at smaller projected radii ($< 1''$). Our Monte Carlo simulation suggests that the active jet phase with $L_j \lesssim 10^{44} \text{ erg s}^{-1}$ likely affected late-type stars with $m_K \leq 14$ mag that exhibit the flat profile inside the inner arcsecond. The fainter stars of $m_K > 14$ mag can still keep a cusp-like profile after the jet ceased its enhanced activity.

For better quantitative comparisons with observations, it is necessary to include the stars of different ages and hence different core masses. This is rather complex as there were recurrent star formation episodes in the NSC, with 80% of the stellar mass being formed 5 Gyr ago, the minimum in the star formation rate close to 1 Gyr, and the renewed star formation in the last 100–200 million years, although with the $10\times$ lower star formation rate than at earlier episodes (Pfuhl et al. 2011). These findings were confirmed by Schödel et al. (2020), who estimate that 80% of stars formed 10 Gyr ago or earlier, then about 15% formed 3 Gyr ago, and the remaining fraction in the last 100 Myr. Furthermore, the dynamical effects such as the mass segregation and the relaxation processes could also have played a role in shaping the final observed profile of the NSC, and in addition, we might expect other bright-giant depletion

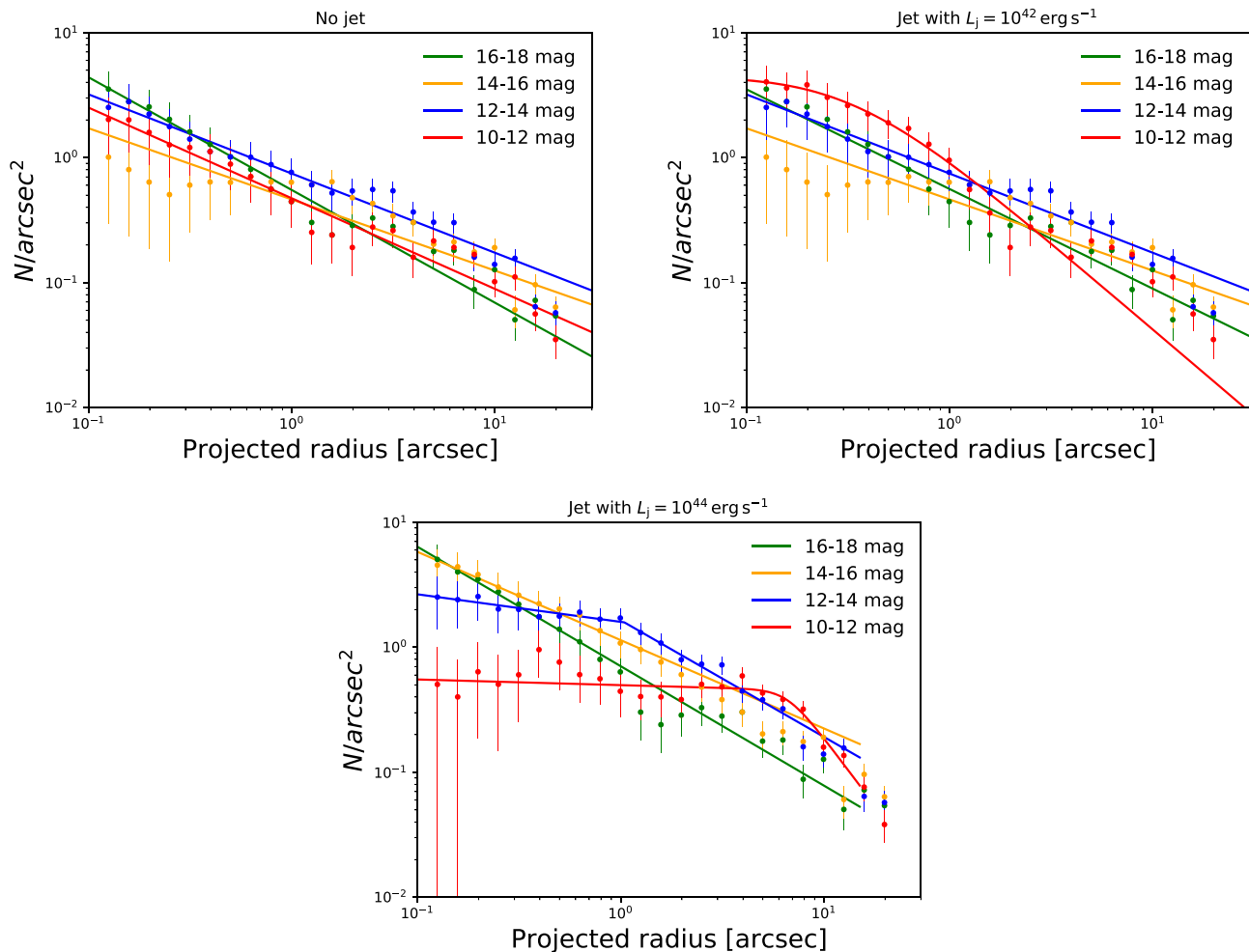


Figure 10. Potential effect of the jet activity on the surface distribution of the initially cuspy late-type NSC. The calculations assume that the coherent resonant relaxation timescale is comparable to or shorter than the jet lifetime (~ 0.5 Myr) within the S-cluster region. In all panels, the magnitude bins are dereddened. Top-left panel: the projected profile of an initial cusp of late-type stars with the surface slope of $\Gamma \sim 0.6$ – 0.9 across all magnitude bins (2 mag bins). Top-right panel: a modified projected profile for the jet luminosity of $10^{42} \text{ erg s}^{-1}$. The 10–12 mag surface profile flattens inside the inner arcsecond, while the fainter stars (12–18 mag) keep a cusp-like profile. Bottom panel: a modified surface profile for the jet luminosity of $L_j = 10^{44} \text{ erg s}^{-1}$. The profile of the brightest stars (10–12 mag) flattens even more and decreases inside the inner arcsecond. The stars with 12–14 mag exhibit a flat profile as well in the inner arcsecond. The stars in the 14–16 mag and 16–18 mag bins keep the cuspy profile. For all three panels, the solid lines represent the single and the broken power-law function fits to the surface stellar distribution in four magnitude bins. The slopes and the break radii are listed in Table 3.

Table 3

Summary of the Power-law Slopes (for Both Single and Broken if Relevant) for the Four Magnitude Bins (2 mag Intervals Starting at 18 mag up to 10 mag in the Near-infrared K_s Band; Magnitudes are Dereddened) and Three Jet-activity Cases (No Jet, $L_j = 10^{42} \text{ erg s}^{-1}$, $L_j = 10^{44} \text{ erg s}^{-1}$)

Magnitude Bin	No Jet	Jet $L_j = 10^{42} \text{ erg s}^{-1}$	Jet $L_j = 10^{44} \text{ erg s}^{-1}$
18–16 mag	single: $\Gamma = 0.9$	single: $\Gamma = 0.8$	single: $\Gamma = 1.0$
16–14 mag	single: $\Gamma = 0.6$	single: $\Gamma = 0.6$	single: $\Gamma = 0.7$
14–12 mag	single: $\Gamma = 0.6$	single: $\Gamma = 0.6$	broken: $\Gamma = 0.2$, $\Gamma_0 = 0.9$, $R_{\text{br}} = 1''$
12–10 mag	single: $\Gamma = 0.7$	broken: $\Gamma = -0.08$, $\Gamma_0 = 1.4$, $R_{\text{br}} = 0''.3$	broken: $\Gamma = 0.04$, $\Gamma_0 = 2.2$, $R_{\text{br}} = 6''.6$

processes (Alexander 2005). Despite these difficulties in comparing theoretical and observed profiles, the basic trend shown in Figure 10, in particular for $L_j = 10^{44} \text{ erg s}^{-1}$ (bottom panel), is consistent with the observational findings of Schödel et al. (2020), who found cusp-like profiles for all magnitude bins apart from the $m_K = 14.5$ – 14 mag bin (including foreground field extinction), which shows a flat/decreasing

profile in their analysis. In our panels in Figure 10, this corresponds to the dereddened 10–12 and 12–14 mag bins, whose profiles become affected for $L_j = 10^{42} \text{ erg s}^{-1}$ starting from the projected radii below $1''$. However, Schödel et al. (2020) also note that precise surface profiles for late-type stars are difficult to construct due to the contamination at all magnitude bins by an unrelaxed population of young stars.

Habibi et al. (2019) report a cusp-like profile for late-type stars of $m_K < 17$ mag (including foreground extinction), which approximately corresponds to our bin of 14–16 mag (yellow points) that maintains a cusp-like profile even for the largest jet luminosity (bottom panel). In conclusion, the expected trend of preferential depletion of bright late-type stars by the jet is confirmed.

6. Discussion

We investigated the effects of a jet during an active phase of Sgr A* in the last million years on the appearance of late-type giant stars with atmosphere radii more than $30R_\odot$. We found that especially in the innermost arcsecond of the Galactic center (the S cluster), the upper layers of the stellar envelope could be removed by the jet ram pressure. Hence, the jet–red giant interactions during the active phase of Sgr A* could have contributed to the depletion of bright late-type stars. In other words, the atmosphere ablation by the jet would alter the red giant appearance in a way that would make them look bluer and fainter in the near-infrared bands (mainly K' and L bands), in which stars in the Galactic center region are generally monitored. In the following, we outline several additional effects that could be associated with the jet/red giant interaction.

6.1. Enlarging the Number of Affected Stars by the Jet Precession

Jet precession is a phenomenon that accompanies the launching of jets during the evolution of galaxies and stellar binaries. It is caused by perturbations due to the misalignment of the accretion flow and the black hole spin, the so-called Lense–Thirring precession, or by a secondary black hole. The jet precession was proposed to explain a long-term flux variability in radio galaxies, e.g., OJ 287 (Britzen et al. 2018), 3C 84 (Britzen et al. 2019b), 3C 279 (Abraham & Carrara 1998), the neutrino emission from TXS 0506+056 (Britzen et al. 2019a), as well as in X-ray binaries (Monceau-Baroux et al. 2015; Miller-Jones et al. 2019).

For the Galactic center, the Lense–Thirring precession of the hot thick accretion flow was analyzed by Dexter & Fragile (2013) in relation to the near-infrared and millimeter variability of Sgr A*. This effect would also translate to the precession of the jet under the assumption that it is coupled to the disk via the launching mechanism (Blandford–Payne mechanism; see Blandford & Payne 1982). The jet precession is also suggested by wide UV ionization cones with the opening angle of 60° (Bland-Hawthorn et al. 2019), which is larger by a factor of a few expected for the jet opening angle of $\sim 25^\circ$ (Li et al. 2013).

We estimate the factor by which the volume of the affected red giants is enlarged. We adopt the jet precession half-opening angle of $\Omega_p \approx 30^\circ$ based on the scale of UV ionization cones (Bland-Hawthorn et al. 2019). During the precession motion, the jet circumscribes a cone with the radius $R_p = z \sin \Omega_p$. The factor by which the volume at given distance z enlarges is given by

$$f_{\text{prec}} = \frac{2\pi R_p}{2R_j} = \pi \frac{\sin \Omega_p}{\tan \theta} \sim 7.1, \quad (31)$$

when $\theta = 12.5^\circ$ and $\Omega_p = 30^\circ$. The number of affected late-type stars would then increase by the same factor to $N_j \approx 105$ and 4.4 within 0.3 and 0.04 pc, respectively, which is comparable to the number of missing bright red giants at these scales—100 at $z < 0.3$ pc (Gallego-Cano et al. 2018) and 4 at

$z < 0.04$ pc (Habibi et al. 2019). The factor derived in Equation (31) should be treated as an upper limit on the volume enlargement as it assumes that the precession period is comparable to or less than the jet lifetime, but it could also be longer. On the other hand, a larger volume means that the stars are affected correspondingly less (over a shorter period of time) by the jet action, which is spread in different directions with the precession duty cycle.

6.2. High-energy Particle Acceleration and Jet Mass Loading due to Jet/Star Interactions

The detection of the Fermi bubbles in the GeV domain indicates the presence of relativistic particles emitting gamma rays. Guo & Mathews (2012) considered that particles can be accelerated in the jet-launching region or in the jet termination shocks. Note, however, that the coexistence of the jet with the dense NSC in the Galactic center makes jet/star interactions very likely. The NSC is composed of both early- and late-type stars. In the former case, the powerful wind of OB and Wolf–Rayet stars makes the stagnation distance $R_{\text{stag}} \gg R_*$, and therefore, a double bow-shock structure is formed (Araudo et al. 2013). In the latter case, the slow winds of low-mass stars cannot create a big bow shock around the stars, but a shock in the jet will be formed anyway. In both cases, particles can be accelerated through the Fermi I acceleration mechanism in the bow shocks (Bell 1978). Even when the interaction with massive stars is a better scenario to accelerate particles up to highest energies (given that the size of the acceleration region is $\sim R_{\text{stag}}$), acceleration of particles up to GeV energies is not difficult to achieve.

Barkov et al. (2010, 2012b) consider the interaction of AGN jets with red giant stars to explain the TeV emission in radio galaxies and blazars. The mass stripped from the red giant forms clouds moving in the jet direction; see also our Figure 1. Particles are accelerated in the bow shock around the cloud formed by the pressure exerted by the jet from below. Another shock propagates into the cloud, and as a consequence, it will heat up and expand. After a certain time, there will be a population of relativistic particles in the jet as well as chemical enrichment by stellar envelopes (Perucho et al. 2017). These effects were previously not taken into account in the jet models of the Fermi bubbles.

6.3. Chemically Peculiar Stars as Remnant Cores of Ablated Red Giants

The past ablation of red giants by the jet would contribute to the apparent lack of late-type stars in the central region of the Galactic center. Another potential imprint of the past jet–red giant interaction would be the presence of chemically peculiar, high-metallicity stars in the NSC. This can be predicted from the fact that as the jet ram pressure removes upper hydrogen- and helium-rich parts of the stellar atmosphere, the lower metal-rich parts as well as the denser core are exposed. In fact, two late-type stars at ~ 0.5 pc from Sgr A* were reported as having a supersolar metallicity (Do et al. 2018) with an anomalous abundance of scandium, vanadium, and yttrium. A detailed modeling of the stellar evolution in combination with the treatment of the jet–star interaction is needed to confirm or exclude the previous interaction with the jet for these and similar candidate stars with supersolar metallicities.

6.4. A Collimated Jet or a Broad-angle Disk Wind?

In the current analysis, we took into account mainly highly collimated nuclear outflow—jet—with the small half-opening angle close to $\sim 10^\circ$. The analysis of the UV ionization cones by Bland-Hawthorn et al. (2019) indicates a half-opening angle of $\sim 30^\circ$, which could be a signature of jet precession as we discussed in Section 6.1 or alternatively disk winds with a larger opening angle. In case the jet would be absent and the disk wind would be present with the larger half-opening angle, the expected stagnation radius would be proportionally larger because $R_{\text{stag}} \propto \tan \theta$. Assuming the same kinetic luminosity $L_j = 10^{42} \text{ erg s}^{-1}$ and the outflow velocity close to c (ultrafast outflows), the ratio of the stagnation radii is $R_{\text{stag}}^{\text{wind}}/R_{\text{stag}}^{\text{jet}} = \tan \theta_{\text{wind}}/\tan \theta_{\text{jet}} \approx 2.6$, which yields for $R_{\text{stag}}^{\text{wind}} \sim 70 R_\odot$ using Equation (6). The ablation effect would still take place but only for the largest red giants with $R_* \gtrsim 100 R_\odot$ at the outer radius of the S cluster. The stagnation radius of $30 R_\odot$ would be reached at the distance of $z \sim 0.017 \text{ pc}$ for the same stellar parameters as we assumed in Equation (6) and a larger outflow half-opening angle of 30° .

6.5. Recurrent Seyfert-like Activity and TDEs

The X-ray/ γ -ray Fermi bubbles were created during the increased Seyfert-like activity about $3.5 \pm 1 \text{ Myr}$ ago (Bland-Hawthorn et al. 2019) with total duration of $\sim 0.1\text{--}0.5 \text{ Myr}$ (Guo & Mathews 2012). Currently, it is unclear whether this increased activity is related to the star formation event that led to the formation of massive OB/Wolf-Rayet stars a few million years ago, a fraction of which forms a stellar disk that is a remnant of a former massive gaseous disk (Levin & Beloborodov 2003). In case a correlation between the episodic star formation and the accretion activity exists, the Seyfert-like phase could occur every 100 million years based on the currently observed stellar populations in the Galactic center region (Pfuhl et al. 2011). In the context of this work, this could provide a mechanism for the recurrent depletion of large red giants by the increased jet activity. However, the most relevant episode in terms of currently observed stellar populations is the most recent episode a few million years ago. There is evidence for even more recent activity $\sim 400 \text{ yr}$ ago, which is inferred from the X-ray reflections or propagating brightening of molecular clouds in the Central Molecular Zone (Sunyaev et al. 1993; Sunyaev & Churazov 1998). However, these repetitive events occur stochastically based on the presence of infalling clumps and lead to the increase by only several orders of magnitude and last for several years depending on the exact viscous timescale (Czerny et al. 2013).

Another possibility of a recurrent launching of the jet is a TDE, which can occur in the Galactic center every $\sim 10^4\text{--}10^5 \text{ yr}$ depending on the stellar type (Syer & Ulmer 1999; Alexander 2005; Komossa 2015). For completeness, we note that the jet is not always formed during the TDE (Komossa 2015). However, for a few months to years, the TDE can trigger a jet activity similar to the Seyfert sources (Hills 1975). Due to the short duration of the TDE between several months to years given by the steep dependency of the luminosity on time, $L \propto t^{-5/3}$, the average number of interacting stars would be given by the estimates calculated in Section 4. In general, the number of ablated red giants in the S cluster would be of the order of unity. The jet precession driven by the Lense-Thirring effect

(Lodato & Pringle 2006) could enlarge this number depending on the precession period and Ω_p (see Section 6.1).

6.6. Comparison with Other Mechanisms—the Region of Efficiency

The jet-induced alternation of the population of late-type stars is not necessarily an alternative to other proposed mechanism, listed in the introductory, Section 1. In reality, it could have coexisted simultaneously during the past few million years with other previously proposed mechanisms, in particular the tidal disruption of red giant envelopes as well as direct star-disk interactions. This follows from the fact that these mechanisms have different length scales of their efficiency, as we further outline in the paragraphs below.

First, the tidal disruption of red giant envelopes takes place on the smallest scales—less than 1 mpc from Sgr A*—as given by the tidal radius, $r_t \approx R_*(2M_*/m_*)^{1/3}$,

$$\begin{aligned} r_t &\lesssim 6000 \left(\frac{R_*}{30 R_\odot} \right) \left(\frac{m_*}{1 M_\odot} \right)^{-1/3} \left(\frac{M_*}{4 \times 10^6 M_\odot} \right)^{1/3} R_\odot \\ &= 0.14 \text{ mpc} = 354 R_{\text{Schw}}. \end{aligned} \quad (32)$$

The resonant relaxation process (discussed in Section 4), in particular the scalar resonant relaxation, can cause an increase in orbital eccentricities and thus effectively induce the tidal disruption of giants as their orbital distance decreases below r_t close to the pericenter of their orbits. This could have contributed to the dearth of brighter red giants in the inner $\sim 0.1 \text{ pc}$ (Madigan et al. 2011), which is a larger scale than given by r_t but still smaller than the total extent of 0.5 pc of the red giant hole.

Then, the jet-induced mass removal is clearly the most efficient in the S-cluster region, $z \lesssim 0.04 \text{ pc}$, according to the cumulative mass removal distance profile in Figure 5. Another way to constrain the region of the maximum efficiency is to use the relation in Equation (6) for the stagnation radius, from which we derive the distance z . It follows that for the maximum jet luminosity of $L_j = 10^{44} \text{ erg s}^{-1}$ and the stagnation radius range of $R_{\text{stag}} = 4\text{--}30 R_\odot$, we obtain the distance range $z_{\text{jet}} = 0.06\text{--}0.44 \text{ pc}$. Hence, within the S cluster, $z \lesssim 0.04 \text{ pc}$, R_{stag} would be effectively below $4 R_\odot$, which corresponds to $K \sim 16 \text{ mag}$ stars for a typical age of 5 Gyr. Therefore, the jet luminosities close to the Eddington limit for Sgr A* are required to truncate the atmospheres of late-type stars of $K \lesssim 16 \text{ mag}$. For the moderate jet luminosity of $L_j = 10^{42} \text{ erg s}^{-1}$, the distance range decreases by an order of magnitude to $z_j = 0.006\text{--}0.04 \text{ pc}$; hence, only brighter giants with $R_* = 30 R_\odot$ ($K \sim 13.5 \text{ mag}$) would be effectively truncated within the S cluster, while the smaller and fainter giants with $K \sim 16 \text{ mag}$ would remain largely unaffected by the jet.

Finally, the star-clumpy disk collisions are the most efficient for the disk surface densities $\Sigma > 10^4 \text{ g cm}^{-2}$ typical of self-gravitating clumps (Kieffer & Bogdanović 2016; Amaro-Seoane et al. 2020), which can form at larger distance scales where the condition for gravitational instability is met as given by the Toomre instability criterion (Milosavljević & Loeb 2004). In the Galactic center, this region likely corresponds to $0.04 \lesssim z \lesssim 0.5 \text{ pc}$, where the disk population of young massive stars is observed, and they are believed to have formed in situ in a massive gaseous disk (Levin & Beloborodov 2003).

Hence, we speculate that the dearth of bright red giants for $z \lesssim 0.5$ pc is due to the combination of the three processes—tidal stripping, jet-induced atmosphere ablation, and star–disk interactions—that operated the most efficiently at complementary length scales up to ~ 0.5 pc.

6.7. Observational Signatures and Falsifiability

The jet-ablation mechanism likely operated in the central S-cluster region (< 0.04 pc) for stars of large atmosphere radii of $10 R_\odot$, and especially for supergiants of $\sim 100 R_\odot$ even at larger distances up to ~ 0.1 pc. However, as the enhanced jet activity and the resulting atmosphere ablation took place a few million years ago, any direct observational trace of the jet–star interaction is difficult to find. Here we list tentative observational signatures of the jet ablation on the preexisting cusp of late-type stars. Some of them have more possible interpretations due to other mechanisms operating simultaneously in the complex NSC around Sgr A*. The signatures proposed here can serve as a guideline toward confirming the jet activity and in particular the jet–star interaction in the central parsec. On the other hand, if other explanations become more likely, these can also serve as suitable falsifiability criteria for the jet-ablation theory. The signatures can be outlined as follows:

- (i) Flattening of the density distribution for brighter late-type stars. This is a classical signature of the preferential bright late-type star depletion, which has more interpretations due to mechanisms, which likely operated on different scales; see Section 6.6. Therefore, this signature should be treated with caution. However, we have shown in Section 5 that the jet active for a sufficiently long time can have an impact on the surface-brightness profile of the NSC when it reaches the kinetic luminosity at least 10^{42} erg s $^{-1}$; see also Section 5 and Figure 10. In particular, brighter giants with $m_K < 14$ mag could exhibit a flat profile due to the jet activity inside the inner arcsecond ($z \lesssim 0.04$ pc). Such a trend has also been recently reported by the high-sensitivity photometric analysis of Schödel et al. (2020).
- (ii) Detection of high-metallicity stars. The jet ablation of red giant and supergiant shells could reveal deeper metal-rich layers. A jet-ablation mechanism can be considered as one of the explanations for the occurrence of stars with anomalous metal concentrations in their atmospheres, as was found by Do et al. (2018); see also Section 6.3.
- (iii) Cluster of remnant white dwarfs at millipasec scales. In relation to point (ii), an extreme case of jet ablation could lead to the exposure of degenerate cores for asymptotic giant branch (AGB) stars. This is analogous to the ablation by tidal stripping (King 2020); however, the jet ablation has a larger length scale for Sgr A*. As we derived in Section 3, the AGB stars could be jet-ablated down to the white-dwarf cores for $z < 0.015$ – 0.15 mpc for $L_j = 10^{42}$ – 10^{44} erg s $^{-1}$. The tidal stripping to the size of $10^{-2} R_\odot$ is only possible essentially below the event horizon. There has not been a direct observation of white dwarfs at such small distances from Sgr A*; however, the hard X-ray flux peaking at Sgr A* was hypothesized to originate in the cluster of accreting white dwarfs (Perez et al. 2015).
- (iv) Cusp of remnant blue OB stars. As we have shown in Section 3, the late-type stars could be turned to blue stars of spectral type OB by the jet-ablation mechanism. In

Table 1, we show that the effective temperature could be of a few $\times 10^4$ K, and with the stagnation radius of $R_{\text{stag}} = 4.45 R_\odot$, the K -band magnitude was estimated to reach $m_K \sim 13$ mag, which is comparable to an S2 star ($m_K \sim 14.1$ mag, Habibi et al. 2017). In this sense, we hypothesize that the fraction of S stars could be produced via the jet ablation of older stars; however, the production rate within the S cluster was of the order of unity, as we showed in Section 4. Hence, the majority of B-type S stars was most likely formed in situ in the circumnuclear gaseous material (Mapelli & Gualandris 2016), and the current location and the kinematic structure of the S cluster are a result of different dynamical processes, most likely the Kozai–Lidov mechanism and the resonant relaxation (Ali et al. 2020).

- (v) Presence of bow-shock and comet-shaped sources. The presence of bow-shock sources X3 and X7 (Mužić et al. 2010) as well as X8 (Peißker et al. 2019) in the mini cavity implies the interaction of these sources with a nuclear outflow in the current state of activity of Sgr A*. The present nuclear outflow could be a signature of a low-surface-brightness jet (Yusef-Zadeh et al. 2020), which was much more luminous a few million years ago. The infrared-excess sources X3, X7, and X8 thus directly reveal the interaction of a nuclear outflow/jet with stars at the scale of ~ 0.2 pc.
- (vi) Nonspherical distribution of stars. In the broader context, the activity of the Seyfert-like jet at the scales of ~ 0.1 pc could be imprinted on the nonspherical stellar structures, e.g., by affecting the distribution of denser star-forming material and its temperature via the jet feedback. Recently, Ali et al. (2020) revealed an X-shape structure of the S cluster formed by two, nearly perpendicular stellar disks. Because S stars formed a few million years ago, their formation could be linked to the phase of higher accretion and enhanced jet activity. Also, the X-structure implies that the resonant relaxation process (see Section 4), in particular the VRR, is not as fast; otherwise, the kinematic structure of the S cluster would be rather isotropic. However, the potential relation between the jet activity and the stellar kinematics needs to be verified via the detailed hydrodynamical/ N -body or smooth-particle-hydrodynamics simulations.
- (vii) Nonspherical distribution of ionization tracers around Sgr A*. In a similar way as we discussed in point (vi) in terms of the nonspherical stellar distribution, the jet interaction with the surrounding gas could also be revealed via the nonisotropic distribution of ionization tracers. In particular, the shock-tracer line [Fe III] seems to be preferentially located in the direction of the mini cavity (Peißker et al. 2020), which suggests either current or past interaction of the gas with the high-velocity outflow/jet (Yusef-Zadeh et al. 2020). On scales larger than 1 pc, the nonisotropic distribution is manifested by bipolar radio lobes (Heywood et al. 2019) and X-ray (Ponti et al. 2019) and γ -ray bubbles (Su et al. 2010; Ackermann et al. 2014). Recently, the analysis of the tilted, partially ionized disk in the inner Galactic latitudes has shown that its optical line ratios are characteristic of low-ionization nuclear emission regions (LINERs; Krishnarao et al. 2020). The bipolar ionization structure is energetically in favor of the Seyfert-like jet activity rather

than the star formation event (Bland-Hawthorn et al. 2019).

In summary, the jet-activity signs listed in points (i)–(vii) indicated the past enhanced activity of the jet and its interaction with the surrounding circumnuclear medium, including the nuclear star cluster. Although each of the above-mentioned points can have alternative explanations, the absence of all of these signatures would suggest that the jet did not operate in the past, and our hypotheses would then be strongly disfavored. Future detailed observations by the Extremely Large Telescope (ELT) in combination with detailed numerical simulations of the jet–star interactions close to Sgr A* will help to reveal the signatures of current and past jet–star interactions.

7. Summary and Conclusions

We presented a novel scenario to explain the lack of bright red giants in the inner regions of the Galactic center in the sphere of influence of the currently quiescent, but previously active, radio source Sgr A*. Taking this increased activity into account, we focused on the effect of the jet on late-type stars at $\lesssim 0.3$ pc. By adopting the scenario of the recent active period of Sgr A*, we considered the interaction of red giants with a jet of a typical active Seyfert-like nucleus with the expected kinetic luminosity $L_j = 10^{41}–10^{44}$ erg s $^{-1}$. Given that red giants have a very slow wind, the jet can significantly ablate the stellar envelope down to at least $\sim 30 R_\odot$ within the S cluster ($z \lesssim 0.04$ pc) after repetitive encounters. Specifically, at $z = 0.02$ pc, the stagnation radius is $4 \leq R_{\text{stag}}/R_\odot \leq 30$ for $2.0 \times 10^{41} \leq L_j/\text{erg s}^{-1} \leq 1.1 \times 10^{43}$. Hence, the higher luminosity end that corresponds to the less frequent events that formed the Fermi bubbles can ablate the stellar atmospheres of late-type giants by a factor of ~ 7.5 more than the more frequent, less energetic outbursts of Sgr A*.

This truncation is accompanied by the removal of a large fraction of matter, reaching as much as $\Delta M_1 \approx 3 \times 10^{-5} M_\odot \approx 10 M_{\text{Earth}}$ for red giants with radii $R_* > 200 R_\odot$ at distances smaller than 0.01 pc for a single encounter. After at least a thousand red giant–jet encounters, we expect the cumulative mass loss of at least $\Delta M \approx 10^{-4} M_\odot$ at the orbital distance of 0.01 pc. This is comparable to the values inferred from red giant–accretion-clump simulations. The proposed mechanism can thus help to explain the presence of late-type stars with the maximum atmosphere radius of $\sim 30 R_\odot$ within the S cluster as inferred from the near-infrared observations.

The reduction in the mass and radius of the red giant atmosphere after repetitive jet–star crossings will produce an estimated decrease in the near-infrared *K*-band magnitude by 1.9, 5.3, and 8.9 mag with respect to the normal evolution at 0.1, 0.01, and 0.001 pc from Sgr A*, respectively. Simultaneously, the color index would decrease to negative values, i.e., the stars should appear bluer with a higher effective temperature. The mean expected number of red giant–jet crossings per orbital period is 3.5 within 0.04 pc, and 82.5 within 0.3 pc, respectively. For the jet kinetic luminosity of 10^{44} erg s $^{-1}$, $\sim 26.5\%$ of currently detectable late-type stars located at $z = 0.04$ pc (S cluster) with radii larger than $2.7 R_\odot$ and *K*-band magnitudes smaller than ~ 16 mag could be affected by the jet ablation. The estimated numbers of interacting giants can be considered as lower limits because various dynamical effects, such as the coherent resonant relaxation within the nuclear star cluster as well as a potential jet precession would enlarge the number of affected giants.

Constructed surface-brightness profiles of the mock NSC affected by the jet with the luminosity of $10^{42}–10^{44}$ erg s $^{-1}$ show that profiles of mainly brighter late-type stars with $m_K < 14$ mag (dereddened, < 16 mag with the foreground extinction included) are flattened by the jet inside the inner arcsecond ($\lesssim 0.04$ pc). Fainter stars keep the initially assumed cusp-like projected profile.

In summary, the interaction of red giants with the jet of Sgr A* during its enhanced activity could contribute to the observed lack of bright red giants and hence affect their surface-brightness profile in the central parts of the NSC. More likely, this mechanism operated in parallel with other previously proposed mechanisms, such as the star–disk interactions, star–star collisions, and TDEs that have different spatial scales of efficiency. Detailed numerical computations of red giant–jet interactions in combination with a modified stellar evolution will help to verify our analytical estimates.

We thank the referee for constructive comments that helped us improve our manuscript. M.Z., B.C., and V.K. acknowledge the continued support by the National Science Center, Poland, grant No. 2017/26/A/ST9/00756 (Maestro 9), and the Czech-Polish mobility program (MSMT 8J20PL037). A.A. and V.K. acknowledge the Czech Science Foundation under grant GACR 20-19854S titled “Particle Acceleration Studies in Astrophysical Jets,” and the European Space Agency PRODEX project eXTP in the Czech Republic. This work was carried out partly also within the Collaborative Research Center 956, sub-project [A02], funded by the Deutsche Forschungsgemeinschaft (DFG) project ID184018867. The work on this project was partially carried out during the short-term stay of M.Z. within the Polish-Czech bilateral exchange program supported by NAWA under agreement PPN/BCZ/2019/1/00069. M.Z. also acknowledges the NAWA financial support under agreement PPN/WYM/2019/1/00064 to perform a three-month exchange stay at the Astronomical Institute of the Czech Academy of Sciences in Prague.

ORCID iDs

Michal Zajaček  <https://orcid.org/0000-0001-6450-1187>
 Anabella Araudo  <https://orcid.org/0000-0001-7605-5786>
 Vladimír Karas  <https://orcid.org/0000-0002-5760-0459>
 Božena Czerny  <https://orcid.org/0000-0001-5848-4333>
 Andreas Eckart  <https://orcid.org/0000-0001-6049-3132>

References

- Abraham, Z., & Carrara, E. A. 1998, *ApJ*, 496, 172
 Ackermann, M., Albert, A., Atwood, W. B., et al. 2014, *ApJ*, 793, 64
 Alexander, T. 2005, *PhR*, 419, 65
 Alexander, T. 2017, *ARA&A*, 55, 17
 Ali, B., Paul, D., Eckart, A., et al. 2020, *ApJ*, 896, 100
 Amaro-Seoane, P., & Chen, X. 2014, *ApJL*, 781, L18
 Amaro-Seoane, P., Chen, X., Schödel, R., & Casanellas, J. 2020, *MNRAS*, 492, 250
 Antonini, F., Capuzzo-Dolcetta, R., Mastrobuono-Battisti, A., & Merritt, D. 2012, *ApJ*, 750, 111
 Araudo, A. T., Bosch-Ramon, V., & Romero, G. E. 2013, *MNRAS*, 436, 3626
 Araudo, A. T., & Karas, V. 2017, in Proc. RAGtime 17–19: Workshops on Black Holes and Neutron Stars (Opava: Silesian Univ.), 1
 Armitage, P. J., Zurek, W. H., & Davies, M. B. 1996, *ApJ*, 470, 237
 Baganoff, F. K., Maeda, Y., Morris, M., et al. 2003, *ApJ*, 591, 891
 Bailey, V. C., & Davies, M. B. 1999, *MNRAS*, 308, 257
 Barkov, M. V., Aharonian, F. A., Bogovalov, S. V., Kelner, S. R., & Khangulyan, D. 2012a, *ApJ*, 749, 119
 Barkov, M. V., Aharonian, F. A., & Bosch-Ramon, V. 2010, *ApJ*, 724, 1517

- Barkov, M. V., Bosch-Ramon, V., & Aharonian, F. A. 2012b, *ApJ*, **755**, 170
- Baumgardt, H., Gualandris, A., & Portegies Zwart, S. 2006, *MNRAS*, **372**, 174
- Bednarek, W., & Banasiński, P. 2015, *ApJ*, **807**, 168
- Bell, A. R. 1978, *MNRAS*, **182**, 147
- Blandford, R. D., & Payne, D. G. 1982, *MNRAS*, **199**, 883
- Bland-Hawthorn, J., & Cohen, M. 2003, *ApJ*, **582**, 246
- Bland-Hawthorn, J., Maloney, P. R., Sutherland, R., et al. 2019, *ApJ*, **886**, 45
- Boehle, A., Ghez, A. M., Schödel, R., et al. 2016, *ApJ*, **830**, 17
- Bogdanović, T., Cheng, R. M., & Amaro-Seoane, P. 2014, *ApJ*, **788**, 99
- Bosch-Ramon, V., Perucho, M., & Barkov, M. V. 2012, *A&A*, **539**, A69
- Bressan, A., Marigo, P., Girardi, L., et al. 2012, *MNRAS*, **427**, 127
- Britzen, S., Fendt, C., Böttcher, M., et al. 2019a, *A&A*, **630**, A103
- Britzen, S., Fendt, C., Witzel, G., et al. 2018, *MNRAS*, **478**, 3199
- Britzen, S., Fendt, C., Zajaček, M., et al. 2019b, *Galax*, **7**, 72
- Buchholz, R. M., Schödel, R., & Eckart, A. 2009, *A&A*, **499**, 483
- Czerny, B., Kunneriath, D., Karas, V., & Das, T. K. 2013, *A&A*, **555**, A97
- Dale, J. E., Davies, M. B., Church, R. P., & Freitag, M. 2009, *MNRAS*, **393**, 1016
- Davies, M. B., & King, A. 2005, *ApJL*, **624**, L25
- de la Cita, V. M., Bosch-Ramon, V., Paredes-Fortuny, X., Khangulyan, D., & Perucho, M. 2016, *A&A*, **591**, A15
- Deegan, P., & Nayakshin, S. 2007, *MNRAS*, **377**, 897
- Dexter, J., & Fragile, P. C. 2013, *MNRAS*, **432**, 2252
- Do, T., Ghez, A. M., Morris, M. R., et al. 2009, *ApJ*, **703**, 1323
- Do, T., Kerzendorf, W., Konopacky, Q., et al. 2018, *ApJL*, **855**, L5
- Eckart, A., Hüttemann, A., Kiefer, C., et al. 2017, *FoPh*, **47**, 553
- Ernst, A., Just, A., & Spurzem, R. 2009, *MNRAS*, **399**, 141
- Gallego-Cano, E., Schödel, R., Dong, H., et al. 2018, *A&A*, **609**, A26
- Genzel, R., Eisenhauer, F., & Gillessen, S. 2010, *RvMP*, **82**, 3121
- Genzel, R., Thatte, N., Krabbe, A., Kroker, H., & Tacconi-Garman, L. E. 1996, *ApJ*, **472**, 153
- Ghez, A. M., Duchêne, G., Matthews, K., et al. 2003, *ApJL*, **586**, L127
- Gillessen, S., Plewa, P. M., Eisenhauer, F., et al. 2017, *ApJ*, **837**, 30
- Gravity Collaboration, Abuter, R., Amorim, A., et al. 2018, *A&A*, **615**, L15
- Gualandris, A., & Merritt, D. 2012, *ApJ*, **744**, 74
- Guo, F., & Mathews, W. G. 2012, *ApJ*, **756**, 181
- Habibi, M., Gillessen, S., Martins, F., et al. 2017, *ApJ*, **847**, 120
- Habibi, M., Gillessen, S., Pfuhl, O., et al. 2019, *ApJL*, **872**, L15
- Heywood, I., Camilo, F., Cotton, W. D., et al. 2019, *Natur*, **573**, 235
- Hills, J. G. 1975, *Natur*, **254**, 295
- Ito, H., Kino, M., Kawakatu, N., Isobe, N., & Yamada, S. 2008, *ApJ*, **685**, 828
- Joss, P. C., Rappaport, S., & Lewis, W. 1987, *ApJ*, **319**, 180
- Junor, W., Biretta, J. A., & Livio, M. 1999, *Natur*, **401**, 891
- Karas, V., & Šubr, L. 2001, *A&A*, **376**, 686
- Kieffer, T. F., & Bogdanović, T. 2016, *ApJ*, **823**, 155
- Kim, S. S., & Morris, M. 2003, *ApJ*, **597**, 312
- King, A. 2020, *MNRAS*, **493**, L120
- Komissarov, S. S. 1994, *MNRAS*, **269**, 394
- Komossa, S. 2015, *JHEAp*, **7**, 148
- Krabbe, A., Genzel, R., Drapatz, S., & Rotaciuc, V. 1991, *ApJL*, **382**, L19
- Krishnarao, D., Benjamin, R. A., & Haffner, L. M. 2020, *SciA*, **6**, 9711
- Kroupa, P. 2001, *MNRAS*, **322**, 231
- Levin, Y., & Beloborodov, A. M. 2003, *ApJL*, **590**, L33
- Li, Z., Morris, M. R., & Baganoff, F. K. 2013, *ApJ*, **779**, 154
- Löckmann, U., & Baumgardt, H. 2008, *MNRAS*, **384**, 323
- Lodato, G., & Pringle, J. E. 2006, *MNRAS*, **368**, 1196
- MacLeod, M., Guillochon, J., & Ramirez-Ruiz, E. 2012, *ApJ*, **757**, 134
- MacLeod, M., & Lin, D. N. C. 2020, *ApJ*, **889**, 94
- Madigan, A.-M., Hopman, C., & Levin, Y. 2011, *ApJ*, **738**, 99
- Mapelli, M., & Gualandris, A. 2016, in *Star Formation and Dynamics in the Galactic Centre*, ed. F. Haardt et al., Vol. 905 (Berlin: Springer)
- Matsubayashi, T., Makino, J., & Ebisuzaki, T. 2007, *ApJ*, **656**, 879
- Merritt, D. 2013, *Dynamics and Evolution of Galactic Nuclei* (Princeton, NJ: Princeton Univ. Press)
- Merritt, D., & Szell, A. 2006, *ApJ*, **648**, 890
- Miller, M. J., & Bregman, J. N. 2016, *ApJ*, **829**, 9
- Miller-Jones, J. C. A., Tetarenko, A. J., Sivakoff, G. R., et al. 2019, *Natur*, **569**, 374
- Milosavljević, M., & Loeb, A. 2004, *ApJL*, **604**, L45
- Monceau-Baroux, R., Porth, O., Meliani, Z., & Keppens, R. 2015, *A&A*, **574**, A143
- Morel, P., & Lebreton, Y. 2008, *Ap&SS*, **316**, 61
- Morris, M. 1993, *ApJ*, **408**, 496
- Morris, M., & Serabyn, E. 1996, *ARA&A*, **34**, 645
- Moser, L., Sánchez-Monge, Á., Eckart, A., et al. 2017, *A&A*, **603**, A68
- Mužić, K., Eckart, A., Schödel, R., et al. 2010, *A&A*, **521**, A13
- Paczyński, B. 1970, *AcA*, **20**, 47
- Parsa, M., Eckart, A., Shahzamanian, B., et al. 2017, *ApJ*, **845**, 22
- Peißker, F., Hosseini, S. E., Zajaček, M., et al. 2020, *A&A*, **634**, A35
- Peißker, F., Zajaček, M., Eckart, A., et al. 2019, *A&A*, **624**, A97
- Perez, K., Hailey, C. J., Bauer, F. E., et al. 2015, *Natur*, **520**, 646
- Perucho, M., Bosch-Ramon, V., & Barkov, M. V. 2017, *A&A*, **606**, A40
- Pfuhl, O., Fritz, T. K., Zilka, M., et al. 2011, *ApJ*, **741**, 108
- Phinney, E. S. 1989, in *IAU Symp. 136, The Center of the Galaxy*, ed. M. Morris (Dordrecht: Kluwer), **543**
- Ponti, G., Hofmann, F., Churazov, E., et al. 2019, *Natur*, **567**, 347
- Portegies Zwart, S. F., Baumgardt, H., McMillan, S. L. W., et al. 2006, *ApJ*, **641**, 319
- Rees, M. J. 1988, *Natur*, **333**, 523
- Refsdal, S., & Weigert, A. 1971, *A&A*, **13**, 367
- Reimers, D. 1987, in *IAU Symp. 122, Circumstellar Matter*, ed. I. Appenzeller & C. Jordan (Dordrecht: Reidel), **307**
- Różańska, A., Kunneriath, D., Czerny, B., Adhikari, T. P., & Karas, V. 2017, *MNRAS*, **464**, 2090
- Schödel, R., Feldmeier, A., Neumayer, N., Meyer, L., & Yelda, S. 2014, *CQGra*, **31**, 244007
- Schödel, R., Najarro, F., Muzic, K., & Eckart, A. 2010, *A&A*, **511**, A18
- Schödel, R., Noguera-Lara, F., Gallego-Cano, E., et al. 2020, *A&A*, **641**, A102
- Sellgren, K., McGinn, M. T., Becklin, E. E., & Hall, D. N. 1990, *ApJ*, **359**, 112
- Su, M., Slatyer, T. R., & Finkbeiner, D. P. 2010, *ApJ*, **724**, 1044
- Šubr, L., & Haas, J. 2014, *ApJ*, **786**, 121
- Sunyaev, R., & Churazov, E. 1998, *MNRAS*, **297**, 1279
- Sunyaev, R. A., Markevitch, M., & Pavlinsky, M. 1993, *ApJ*, **407**, 606
- Syer, D., & Ulmer, A. 1999, *MNRAS*, **306**, 35
- Vilkoviskij, E. Y., & Czerny, B. 2002, *A&A*, **387**, 804
- Wang, Q. D., Nowak, M. A., Markoff, S. B., et al. 2013, *Sci*, **341**, 981
- Yusef-Zadeh, F., Arendt, R., Bushouse, H., et al. 2012, *ApJL*, **758**, L11
- Yusef-Zadeh, F., Royster, M., Wardle, M., et al. 2020, *MNRAS*, **499**, 3909
- Zhao, J.-H., Morris, M. R., Goss, W. M., & An, T. 2009, *ApJ*, **699**, 186
- Zhu, Z., Li, Z., & Morris, M. R. 2018, *ApJS*, **235**, 26
- Zurek, W. H., Siemiginowska, A., & Colgate, S. A. 1994, *ApJ*, **434**, 46

Paper 4: Reverberation-Mapping of HE 0435-4312

From the studies of the spatial distribution of late-type stars in the Galactic center, we refocused on distant luminous quasars, specifically HE 0435-4312 ($z = 1.2231$). We analyzed the variability of the broad MgII line (in the UV part of the spectrum in the rest frame) and mainly how this variability is driven by the photoionizing continuum at 300 nm.

We found that, despite some predictions, MgII line is quite variable with the fractional variability of $\sim 5.4\%$, which is comparable to the continuum variability of 4.8%. Using seven time-delay methodologies, we inferred the MgII time delay of 296^{+13}_{-14} days in the rest frame. We dedicated some effort to the removal of false peaks and aliases using the bootstrap method and the light-curve pair weighting probability function.

With its high luminosity at 300 nm ($L_{3000} = 10^{46.4}$ erg s $^{-1}$), the source is beneficial for decreasing the rms scatter of the $R_{\text{BLR}} - L$ relation, while at the same time, it increases its correlation. Using 58 SDSS-RM sources (Homayouni et al. 2020), we put together a sample of 69 sources including HE 0435-4312. For the whole sample, the MgII relation is surprisingly flat with the best-fit $R_{\text{BLR}} - L$ relation, $\log(\tau/\text{lt.day}) = (1.67 \pm 0.05) + (0.30 \pm 0.05) \log(L_{3000}/10^{44} \text{ erg s}^{-1})$, which has a considerable scatter of 0.30 dex.

When we restrict ourselves to the high-accreting sources (dimensionless accretion rate \dot{M} larger than the median value), the scatter of the high-accreting sources around their best-fit $R_{\text{BLR}} - L$ relation, $\log(\tau/\text{lt.day}) = (1.37 \pm 0.08) + (0.42 \pm 0.06) \log(L_{3000}/10^{44} \text{ erg s}^{-1})$ is significantly smaller, $\sigma \sim 0.20$, than the scatter for the whole sample. This indicates that the $R_{\text{BLR}} - L$ relation for especially high-accreting quasars could be applied for constraining cosmological parameters. For the current sample of 27 high-accreting sources (with 8 outliers removed), the fitting of general non-flat Λ CDM model yields the best-fit parameters $(\Omega_m, \Omega_\Lambda) = (0.19, 0.62)$, which is within 1σ confidence interval consistent with the values based on better established cosmological probes (CMB; Planck Collaboration et al. 2020).

Credit: Zajaček et al. (2021), ApJ 912, 10. Reproduced with permission ©AAS.



Time Delay of Mg II Emission Response for the Luminous Quasar HE 0435-4312: toward Application of the High-accretor Radius–Luminosity Relation in Cosmology

Michał Zajaček¹, Bożena Czerny¹, Mary Loli Martínez–Aldama¹, Mateusz Rałowski², Aleksandra Olejak³, Robert Przyłuski¹, Swamyamtrupta Panda^{1,3}, Krzysztof Hryniewicz⁴, Marzena Śniegowska^{1,3}, Mohammad-Hassan Naddaf¹, Raj Prince¹, Wojtek Pych³, Grzegorz Pietrzyński³, Catalina Sobrino Figaredo⁵, Martin Haas⁵, Justyna Średzińska³, Magdalena Krupa², Agnieszka Kurcz², Andrzej Udalski⁶, Vladimír Karas⁷, Marek Sarna³, Hannah L. Worters⁸, Ramotholo R. Sefako⁸, and Anja Genade⁸

¹ Center for Theoretical Physics, Polish Academy of Sciences, Al. Lotników 32/46, 02-668 Warsaw, Poland; zajacek@cft.edu.pl

² Astronomical Observatory of the Jagiellonian University, Orla 171, 30-244 Cracow, Poland

³ Nicolaus Copernicus Astronomical Center, Polish Academy of Sciences, ul. Bartycka 18, 00-716 Warsaw, Poland

⁴ National Centre for Nuclear Research, Pasteura 7, 02-093 Warsaw, Poland

⁵ Astronomisches Institut—Ruhr Universitaet Bochum, Germany

⁶ Astronomical Observatory, University of Warsaw, Al. Ujazdowskie 4, 00-478 Warsaw, Poland

⁷ Astronomical Institute of the Czech Academy of Sciences, Boční II 1401, CZ-14100 Prague, Czech Republic

⁸ South African Astronomical Observatory, P.O. Box 9, Observatory, 7935 Cape Town, South Africa

Received 2020 December 21; revised 2021 February 10; accepted 2021 February 23; published 2021 April 29

Abstract

Using six years of spectroscopic monitoring of the luminous quasar HE 0435-4312 ($z = 1.2231$) with the Southern African Large Telescope, in combination with photometric data (CATALINA, OGLE, SALTICAM, and BMT), we determined a rest-frame time delay of 296_{-14}^{+13} days between the Mg II broad-line emission and the ionizing continuum using seven different time-delay inference methods. Time-delay artifact peaks and aliases were mitigated using the bootstrap method and prior weighting probability function, as well as by analyzing unevenly sampled mock light curves. The Mg II emission is considerably variable with a fractional variability of $\sim 5.4\%$, which is comparable to the continuum variability ($\sim 4.8\%$). Because of its high luminosity ($L_{3000} = 10^{46.4}$ erg s⁻¹), the source is beneficial for a further reduction of the scatter along the Mg II-based radius–luminosity relation and its extended versions, especially when the highly accreting subsample that has an rms scatter of ~ 0.2 dex is considered. This opens up the possibility of using the high-accretor Mg II-based radius–luminosity relation for constraining cosmological parameters. With the current sample of 27 reverberation-mapped sources, the best-fit cosmological parameters (Ω_m, Ω_Λ) = (0.19; 0.62) are consistent with the standard cosmological model within the 1σ confidence level.

Unified Astronomy Thesaurus concepts: Accretion (14); Galaxy accretion disks (562); Active galactic nuclei (16); Quasars (1319); Emission line galaxies (459); Reverberation mapping (2019); Galaxy spectroscopy (2171); Galaxy photometry (611)

1. Introduction

Broad emission lines with line widths of several thousand km s⁻¹ are one of the main characteristic features of the optical and UV spectra of active galactic nuclei (AGNs; Seyfert 1943; Woltjer 1959; Schmidt 1963), specifically of type I, where the broad-line region (BLR) is not obscured by the dusty molecular torus (Antonucci 1993; Urry & Padovani 1995). However, the scattered polarized light can reveal broad lines even for obscured type II AGNs (type II NGC 1068 was the first case, Antonucci & Miller 1985), which implies the universal presence of the BLR for accreting supermassive black holes (SMBHs). Low-luminosity systems, such as the Galactic Center (Genzel et al. 2010; Eckart et al. 2017; Zajaček et al. 2018) or M87 (Sabra et al. 2003), do not reveal the presence of broad lines. But broad lines can be present even for some sources with lower accretion rates (Bianchi et al. 2019), and the exact accretion limit for their appearance was analyzed to some extent by, e.g., Elitzur & Ho (2009), who estimated a bolometric luminosity limit of $5 \times 10^{39} (M/10^7 M_\odot)^{2/3}$ erg s⁻¹, where M is the black hole mass in units of 10^7 solar masses (M_\odot). However, several crucial questions remain unanswered. Mainly the transition from geometrically thin disk accretion flows to geometrically thick advection-dominated accretion flows at lower accretion rates is

still unclear and is likely related to the boundary conditions, the ability of the flow to cool, the feeding mechanism (warm stellar winds or an inflow of cold gas from larger scales), the associated initial angular momentum, and the resulting circularization radius. In addition, not only the formation of the BLR but also its properties seem to depend on the accretion rate, which motivates the study of more highly accreting sources (Du et al. 2015, 2018), such as HE 0413-4031 in particular (Zajaček et al. 2020).

The BLR has mostly been studied indirectly via reverberation mapping, i.e., by inferring the time delay between the ionizing UV continuum emission of an accretion disk and the broad-line emission (Blandford & McKee 1982; Peterson & Horne 2004; Gaskell 2009; Czerny 2019; Popović 2020) using typically the interpolated cross-correlation function (Peterson et al. 1998, 2004; Sun et al. 2018) or other methods (see, e.g., Zajaček et al. 2019, 2020, for an overview and an application of seven methods in total). The high correlation between the continuum and the line-emission fluxes implies that the line emission is mostly reprocessed thermal emission from an accretion disk. From the rest-frame time delay τ_{BLR} , it is straightforward to estimate the size of the BLR, $R_{\text{BLR}} = c\tau_{\text{BLR}}$, and in combination with the single-epoch line FWHM or the line dispersion σ , which serve as proxies for the BLR virial

velocity, one can infer the central black hole mass, $M_{\bullet} = f c \tau_{\text{BLR}} \text{FWHM}^2 G^{-1}$. The factor f is known as the virial factor and takes into account the geometrical and kinematic characteristics of the BLR. Although f is typically of the order of unity, it introduces a factor of ~ 2 – 3 uncertainty in the black hole mass. By comparing the black hole masses inferred from accretion-disk spectra with the masses from single-epoch spectroscopy, Mejía-Restrepo et al. (2018) found that the value of f is approximately inversely proportional to the broad-line FWHM,⁹ which provides a way to better estimate f for individual sources.

Optical reverberation mapping studies using the $\text{H}\beta$ line showed that there is a simple power-law relation between the size of the BLR and the monochromatic luminosity of AGNs at 5100 Å (Kaspi et al. 2000; Peterson et al. 2004), the so-called radius–luminosity (RL) relation. After a proper removal of the host galaxy starlight (Bentz et al. 2013), the slope of the power law is close to 0.5, which is expected from simple photoionization arguments. The importance of the radius–luminosity relation lies in its application to infer black hole masses from single-epoch spectroscopy, where FWHM or the line dispersion σ serves as a proxy for the velocity of virialized BLR clouds, and the monochromatic luminosity of the source serves as a proxy for the rest-frame time delay, and hence the BLR radius, via the RL relation.

Another, more recent application of the RL relation is the possibility to utilize it for obtaining absolute monochromatic luminosities. From the measured flux densities, one can calculate luminosity distances and use them for constraining cosmological parameters (Haas et al. 2011; Watson et al. 2011; Czerny et al. 2013, 2020; Martínez-Aldama et al. 2019; Panda et al. 2019). The problem for cosmological applications is that the RL relation exhibits a scatter, which has increased with the accumulation of more sources, especially those with higher accretion rates (super-Eddington accreting massive black holes—SEAMBHs; Du et al. 2015, 2018).

The scatter is present both for lower-redshift $\text{H}\beta$ sources (Grier et al. 2017) and for higher-redshift Mg II sources, which follow an analogous RL relation (Czerny et al. 2019; Homayouni et al. 2020; Zajaček et al. 2020). The scatter was attributed to the accretion-rate intensity, with the basic trend that the largest departure from the nominal RL relation is exhibited by the highly accreting sources (Du et al. 2018). The correction to the time delay was proposed based on the Eddington ratio and the dimensionless accretion rate (Martínez-Aldama et al. 2019); however, these two quantities depend on the time delay via the black hole mass. To break down the interdependence, Fonseca Alvarez et al. (2020) proposed to make use of independent, observationally inferred quantities related to the optical/UV spectral energy distribution (SED). The relative Fe II strength correlated with the accretion-rate intensity is especially efficient in reducing the scatter for $\text{H}\beta$ sources to only 0.19 dex (Du & Wang 2019; Yu et al. 2020a). The same effect is observed for the extended radius–luminosity relations for Mg II reverberation-mapped sources (68 sources; Martínez-Aldama et al. 2020). Martínez-Aldama et al. (2020) divide the sources into low and high accretors, where the high

accretors show a much smaller scatter of only ~ 0.2 dex. The extended RL relation including the relative Fe II strength further reduces the scatter down to 0.17 dex for the highly accreting subsample.

Large reverberation monitoring campaigns are currently performed by several groups, for instance the Australian Dark Energy Survey (OzDES, Hoormann et al. 2019), the Sloan Digital Sky Survey Reverberation Mapping project (SDSS-RM, Shen et al. 2015, 2019), the Dark Energy Survey (DES, Abbott et al. 2018; Diehl et al. 2018; Yang et al. 2020), the SEAMBHs (Du et al. 2015, 2018), but monitoring of an individual source can also contribute significantly, especially if its luminosity is an extreme value in the radius–luminosity relation. This is because the most luminous quasars have very low sky densities, so they are not suitable for reverberation mapping multi-object spectroscopy (MOS-RM) programs, and instead require monitoring of individual objects. This is why programs such as the one presented here are necessary. Luminous sources are expected to be beneficial in terms of increasing the RL correlation coefficient, and this can also lead to a reduction in the scatter. In the current paper, we present results of the time delay of the Mg II line for the last of three very luminous quasars at intermediate redshift monitored for several years with the Southern African Large Telescope (SALT). The source HE 0435-4312 ($z=1.2231$) hosts a supermassive black hole of $2.2 \times 10^9 M_{\odot}$ that is highly accreting with an Eddington ratio of 0.58 according to the SED best-fit of Sredzińska et al. (2017). The peculiarity of the source is a smooth shift of the peak of the Mg II line first toward longer wavelengths, while currently the shift proceeds toward shorter wavelengths. This line shift could hint at the presence of a supermassive black hole binary (Sredzińska et al. 2017).

In this paper, we measure the time delay of HE 0435-4312 using seven methods. Subsequently, we study the position of the source in the RL relation, including its extended versions, and how the source affects the correlation coefficient as well as the scatter. Finally, we look at the potential applicability of the Mg II highly accreting subsample for cosmological studies.

The paper is structured as follows. In Section 2, we describe observations including both spectroscopy and photometry. In Section 3, we analyze the mean and the rms spectra, spectral fits of individual observations, and the variability of the continuum and the line-emission light curves. The core of the paper is Section 4, where we summarize the mean rest-frame time delay between the Mg II emission and the continuum as inferred from seven different methods. The position of the source in the RL relation and its extended versions is also analyzed in this section. Subsequently, in Section 5, we discuss the aspect of variability of the Mg II emission as well as the application of the highly accreting Mg II subsample in cosmology. Finally, we present our conclusions in Section 6.

2. Observations

Here we present the optical photometric and spectroscopic observations of the quasar HE 0435-4312 ($z=1.232$, $V=17.1$ mag) with J2000 coordinates R.A. = $04^{\text{h}}37^{\text{m}}11^{\text{s}}.8$, decl. = $-43^{\circ}06'04''$ according to the NED database.¹⁰ Due to its large optical flux density, it was found during the Hamburg ESO quasar survey (Wisotzki et al. 2000). Previously,

⁹ More precisely, using the general dependence of f on the line FWHM in the form $f = (\text{FWHM}_{\text{obs}}(\text{line})/\text{FWHM}_{\text{obs}}^0)^{\beta}$, with $\text{FWHM}_{\text{obs}}^0$ and β being the searched parameters, Mejía-Restrepo et al. (2018) obtained $\text{FWHM}_{\text{obs}}^0 = 3200 \pm 800 \text{ km s}^{-1}$, $\beta = -1.21 \pm 0.24$ for Mg II and $\text{FWHM}_{\text{obs}}^0 = 4550 \pm 1000 \text{ km s}^{-1}$, $\beta = -1.17 \pm 0.11$ for $\text{H}\beta$ measurements.

¹⁰ NASA/IPAC Extragalactic Database: <http://ned.ipac.caltech.edu/>.

THE ASTROPHYSICAL JOURNAL, 912:10 (25pp), 2021 May 1

Zajaček et al.

Sredzińska et al. (2017) reported ten spectroscopic observations performed by SALT Robert Stobie Spectrograph (RSS) over the course of three years (from 2012 December 23/24 to 2015 December 7/8). The main result of their analysis was the detection of the fast displacement of the Mg II line with respect to the quasar rest frame by $104 \pm 14 \text{ km s}^{-1} \text{ yr}^{-1}$. In this paper the number of spectroscopic observations increased to 25, which together with 81 photometric measurements allows for the analysis of the time-delay response of the Mg II line with respect to the variable continuum. Previously we detected a time delay for two other luminous quasars: 562^{+116}_{-68} days for CTS C30.10 (Czerny et al. 2019) and 303^{+29}_{-33} days for HE 0413-4031 (Zajaček et al. 2020), both in the rest frames of the corresponding source. These intermediate-redshift sources are very important for constraining the Mg II-based radius–luminosity relation. Especially sources with either low or high luminosities are needed to constrain the slope of the RL relation and evaluate the scatter along it (Martínez-Aldama et al. 2020).

2.1. Photometry

The photometric data were combined from a few dedicated monitoring projects, described in more detail in Zajaček et al. (2020). The source has been monitored in the *V* band as part of the OGLE-IV survey (Udalski et al. 2015) done with the 1.3 m Warsaw telescope at the Las Campanas Observatory, Chile. The exposure times were typically around 240 s, and the photometric errors were small, of the order of 0.005 magnitude (see Table 3). In the later epochs the quasar was observed, again in the *V* band, with the 40 cm Bochum Monitoring Telescope (BMT).¹¹ These data showed a systematic offset of 0.2 magnitudes toward larger magnitudes with respect to the overlapping OGLE data, which we corrected for by the shift of all of the BMT points. SALT spectroscopic observations were also supplemented, whenever possible with SALTICAM imaging in the *g* band. We have analyzed all of these data; however, two data sets (2013 August 20 and 2019 January 27) showed a significant discrepancy with the other measurements. The first of the two sets of observations was done during full moon, and with the moon–target separation relatively large; spectroscopic observations were not affected, but the photometric observations were. During the second set of observations the night was dark but seeing was about 2.5" during the photometry, dropping down to 2" during the spectroscopic exposures. We were unable to correct the data for these effects, and we did not include these data points in further considerations. Because of the collection of the data in the *g* band, we allowed for the grayshift of all the SALTICAM data, and the shift was determined using epochs when they coincided with the more precise OGLE set collected in the *V* band. Finally, we supplemented our photometry with the light curve from the Catalina Sky Survey,¹² which is not of a very high quality (with uncertainties of 0.02–0.03 mag) but nicely covers the early period from 2005 until 2013. We have binned these data to reduce the scatter. Table 3 contains only the data points that were used in time-delay measurements. All the data points are presented in the upper panel of Figure 1.

Recently, the quasar was monitored in the *V* band with a median sampling of 14 days using Lesedi, a 1 m telescope at

the South African Astronomical Observatory (SAAO), with the Sutherland High Speed Optical Camera (SHOC). SHOC has a $5.7 \times 5.7 \text{ arcmin}^2$ field of view (FoV). Each observation consists of nine dithered 60 s exposures. They are corrected for bias and flatfields (using dusk or dawn sky flats). Astrometry is obtained using the SCAMP tool.¹³ The resulting median-combined image has a $7.5 \times 7.5 \text{ arcmin}^2$ FoV centered on the quasar. The light curves were created using five calibration stars located on the same image as the quasar. The preliminary results are consistent with the last photometric point from SALT/SALTICAM.

2.2. Spectroscopy

Spectroscopic observations of HE 0435-4312 were performed with the 11 m telescope SALT, with the RSS (Burgh et al. 2003; Kobulnicky et al. 2003; Smith et al. 2006) in a long-slit mode and a slit width of 2". We used the RSS PG1300 grating with a grating tilt angle of $26^\circ 75'$. Order blocking was done with the blue PC04600 filter. Two exposures were always made, each of about 820 s. The same setup has been used throughout the whole monitoring period, from 2012 December 23 until 2020 August 20. Observations were always performed in the service mode.

The raw data reduction was performed by the SALT observatory staff, and the final reduction was performed by us with the use of the IRAF package. All the details were given in Sredzińska et al. (2017), where the results from the first three years of this campaign were presented. We followed exactly the same procedure for all 25 observations to minimize the possibility of unwanted systematic differences.

In order to get the flux calibration, we performed a weighted spline interpolation of the first order (with inverse measurement errors as weights) between the epochs of photometric and spectroscopic observations, thus an apparent *V* magnitude was assigned to each spectrum. Taking as a reference the composite spectrum and the continuum with a slope of $\alpha_\lambda = -1.56$ from Vanden Berk et al. (2001), we just normalized each spectrum to the *V* magnitudes (5500 Å).

2.3. Spectroscopic Data Fitting

The reduced and calibrated spectra were fitted in the 2700–2900 Å range in the rest frame. The basic model components were as in Sredzińska et al. (2017). The data were represented by (i) continuum in the form of a power law with arbitrary slope and normalization, (ii) the Fe II pseudocontinuum, and (iii) two kinematic components representing the Mg II line; each of the kinematic components was represented by two doublet components. The line is unresolved, and the doublet ratio could not be well constrained, so it was fixed at 1:1 (see Sredzińska et al. 2017 for the discussion). For the kinetic shapes we used Lorentzian profiles since they provided somewhat better representation of the data in χ^2 terms than Gaussian ones. All the parameters were fitted simultaneously. In order to determine the redshift and the most appropriate Fe II template, we studied in detail observation 23, which also covered the region around 3000 Å in the rest frame (see Appendix B). Thus for the adopted redshift $z = 1.2231$, the Fe II template was very slightly modified in comparison with Sredzińska et al. (2017), and the pseudocontinuum was kept at

¹¹ BMT is a part of the Universitätssternwarte Bochum located near Cerro Armazones in Chile. For more information, see Ramolla et al. (2013).

¹² http://nunu.ku.caltech.edu/cgi-bin/getcssconedb_release_img.cgi

¹³ <https://www.astromatic.net/software/scamp>

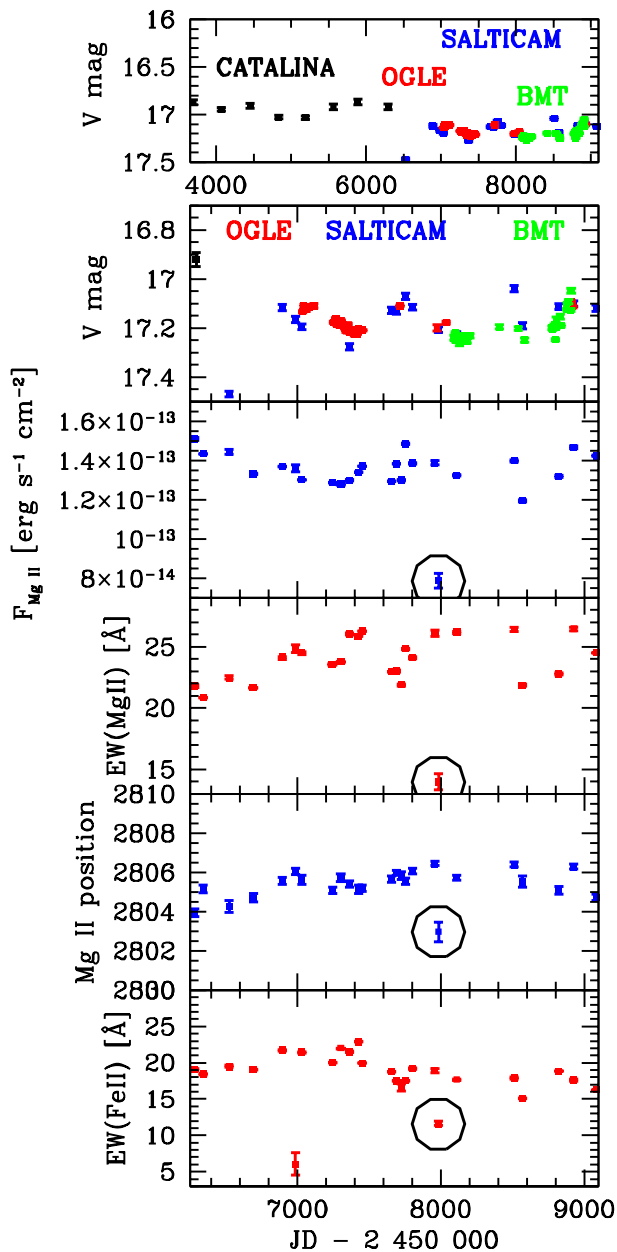


Figure 1. Light curves and the time evolution of emission line properties measured in the rest frame. Points marked with a black circle (obs. 19) were removed from the analysis.

FWHM of 3100 km s^{-1} . Thus there were eight free parameters in the model: power-law normalization and slope, normalization of the Fe II pseudocontinuum, the width and normalizations of the two kinematic components of Mg II, and the position of the second component, with the other one set at the quasar rest frame, together with Fe II.

3. Results: Spectroscopy

3.1. Determination of the Mean and the rms Spectra

We determined the mean and the rms spectra for HE 0435-4312 as we did previously for quasar HE 0413-4031 (Zajaček et al. 2020). Due to the particularly low signal-to-noise ratio

(~ 7.5) shown by spectrum no. 19, which is clearly an outlier in the light curve (Figure 1), we do not consider it for the estimation of the mean and rms spectra. We followed the methodology for constructing the mean and the rms spectra as outlined in Peterson et al. (2004). In particular, we formed the mean spectrum (without spectrum no. 19) using

$$\overline{F(\lambda)} = \frac{1}{N} \sum_{i=1}^N F_i(\lambda), \quad (1)$$

where $F_i(\lambda)$ is the i th spectrum out of a total of N spectra in the measured database. Subsequently, the rms spectrum, initially taking into account all spectral components (Mg II line + continuum + Fe II pseudocontinuum), was constructed using

$$S(\lambda) = \left\{ \frac{1}{N-1} \sum_{i=1}^N [F_i(\lambda) - \overline{F(\lambda)}]^2 \right\}^{1/2}. \quad (2)$$

The constructed mean and rms spectra are shown in Figure 2 (black solid lines) in the upper and upper middle panels, respectively. The quasar is not strongly variable, so the normalization of the rms is very low, and the spectrum is noisy, with visible effects of occasional imperfect sky subtraction. However, the overall quality of the rms spectrum is still suitable for the analysis. In both the mean and the rms spectra, the Mg II line modeling required two kinematic components, since line asymmetry is clearly visible. The result is shown in Figure 2 with spectral components depicted with different colored lines described in the figure caption. For the fitting, we finally used the redshift as determined by Sredzińska et al. (2017), but with a slightly modified Fe II template based on the d11 template of Bruhweiler & Verner (2008). We also compared and analyzed other Fe II templates based on the updated CLOUDY model (Ferland et al. 2017) as well as the six-transition model by Kovačević-Dojčinović & Popović (2015) and Popović et al. (2019). For a detailed discussion of different Fe II templates—a total of eight setups with different redshifts as well as Lorentzian or Gaussian line component profiles—see Appendix B.

The overall shapes of the mean and the rms spectra are similar (see Figure 2). The FWHM of the Mg II line in the mean spectrum is $3695_{-21}^{+21} \text{ km s}^{-1}$; the line in the rms spectrum might be slightly broader, $3886_{-341}^{+143} \text{ km s}^{-1}$, but is consistent within the error margins. A much larger difference is seen in the line dispersion, which is much smaller in the mean spectrum than in the rms spectrum ($2707_{-6}^{+10} \text{ km s}^{-1}$ versus $3623_{-412}^{+76} \text{ km s}^{-1}$). The FWHM and σ are larger in the rms spectrum, most likely due to its noisy nature, although there is an indication of a trend of both Mg II FWHM and σ being larger in the rms spectrum than in the mean spectrum based on the analysis of the SDSS-RM sample (Wang et al. 2019). However, the ratio of FWHM to σ for both the mean and the rms spectra is far from the value 2.35 expected for a Gaussian shape. The source can be classified as A-type according to the classification of Sulentic et al. (2000). This is consistent with the Eddington ratio 0.58 determined by Sredzińska et al. (2017) for this object. There is also an interesting change in the line position between the mean and the rms spectra, as determined from the first moment of the distribution: 2805 Å versus 2792 Å .

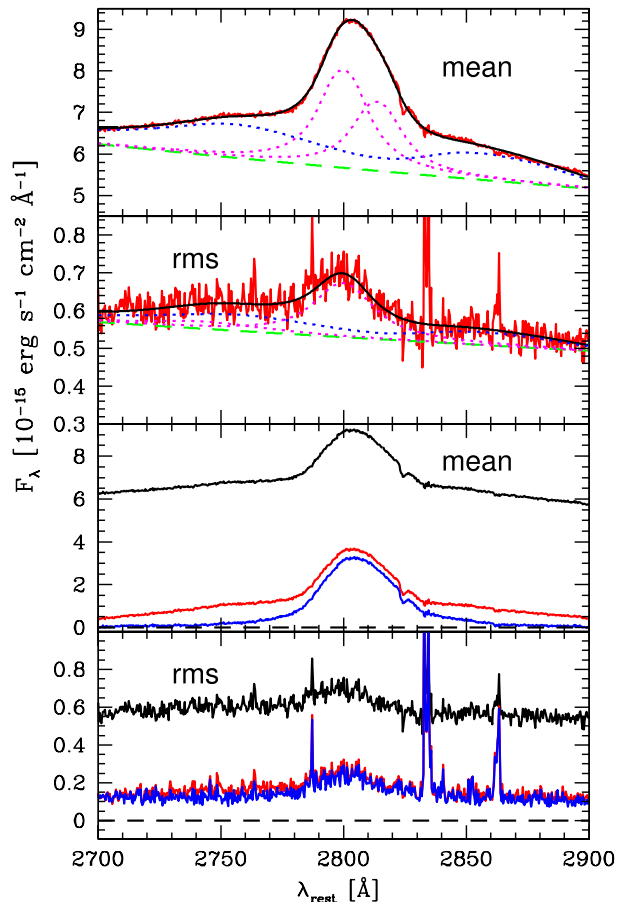


Figure 2. Upper panel: mean spectrum (red curve) obtained without observation 19. We also show its decomposition into two Lorentzian components of the Mg II line (dotted magenta), Fe II pseudocontinuum (dotted blue line), and a power law (green dashed line). Upper middle panel: rms spectrum and its decomposition. The notation of spectral components is the same as for the mean spectrum in the upper panel. Lower middle panel: the mean spectrum in absolute calibration. The solid black line denotes the mean spectrum including all the components (line, continuum, and Fe II pseudocontinuum). The red solid line indicates the mean spectrum constructed after removal of the continuum contribution from each spectrum. The blue solid line indicates the line-only mean spectrum after the additional removal of Fe II pseudocontinuum. Lower panel: a properly calibrated rms spectrum, with the black line denoting the total rms (line + continuum + Fe II pseudocontinuum). The rms spectrum after the subtraction of the continuum is shown by the red line, while the line-only rms is depicted by the blue line.

Following the spectral studies by Barth et al. (2015) and Wang et al. (2019), we show in Figure 2 (lower middle and lower panels) the mean and the rms spectra constructed taking into account all the spectral components (black lines; Mg II line + continuum + Fe II pseudocontinuum), the mean and the rms spectra that have the continuum power law subtracted from each spectrum (red lines), and finally the spectra with Fe II pseudocontinuum subtracted from individual spectra, which represents the true, line-only mean and the rms spectrum (blue lines). For the rms spectra, we do not detect any significant difference in the line width, which is expected to be smaller for the total-flux rms than for the line-only rms spectrum (Barth et al. 2015; Wang et al. 2019). This can be attributed to

the overall noisy nature of our rms spectra, which are constructed from only 24 individual spectra. According to Barth et al. (2015) and Wang et al. (2019), the difference in the line width becomes smaller for a sufficiently long duration of the campaign. However, in our case, the spectroscopic monitoring was only ~ 4.25 times longer than the emission-line time lag in the observer’s frame (see Section 4). For such a short duration, the distribution of the ratios of line width between the total-flux and the line-only rms spectra is broad—between 0.5 and 1.0, with the peak close to 1.0; see Appendix C in Barth et al. (2015).

3.2. Spectral Fits of Individual Observations

The fits to individual spectroscopic data sets were done in the same way as for the mean spectrum. In all 25 data sets, two kinematic components of the Mg II line were needed to represent the line shape well. The normalization of Fe II pseudocontinuum was allowed to vary for each individual spectrum, while the Fe II width was fixed to $\text{FWHM} = 3100 \text{ km s}^{-1}$. The Mg II component kinematically related to the Fe II is slightly narrower, having an average $\text{FWHM} = 2128 \pm 28 \text{ km s}^{-1}$, while the second shifted component is somewhat broader, with $\text{FWHM} = 2262 \pm 90 \text{ km s}^{-1}$. However, we stress here that the broadband modeling by Sredzińska et al. (2017) did not support any identification of these components with separate regions, so the two components are just a mathematical representation of the slightly asymmetric line shape.

The parameters for observation 19 were considerably different, but as we already mentioned in Section 3.1, this observation was of a particularly low quality despite the fact that actually three exposures were made this time. Cirrus clouds were present during the whole night, and even more clouds started arriving during the second exposure of the quasar, so the third exposure was done. Nevertheless, all the parameters were determined with errors a few times larger than for the remaining observations.

The average value of the equivalent width of the Mg II line is $23.6 \pm 0.5 \text{ \AA}$ if observation 19 is included. If observation 19 is not taken into account, the mean value increases to $24.1 \pm 0.6 \text{ \AA}$, and this is similar to the value determined from the mean spectrum: 23.9 \AA . Such values are perfectly in agreement with the properties of the bright quasar sample studied by Forster et al. (2001), where the mean EW of the Mg II broad component was found to be $27.4^{+8.5}_{-6.3} \text{ \AA}$. We do not see any traces of the narrow component in either the mean spectrum or the individual data sets.

The average value of the EW of Fe II, $18.2 \pm 0.7 \text{ \AA}$, is also similar to the value in the mean spectrum, 18.9 \AA . The relative error is larger than for the Mg II line since Fe II pseudocontinuum is more strongly coupled to the power-law continuum during the fitting procedure.

The dispersion in the measurements between observations partially represents the statistical errors, but partially reflect the intrinsic evolution of the source in time. This evolution is studied in the next section.

3.3. Light Curves: Variability and Trends

The quasar HE 0435-4312 is not strongly variable in terms of the continuum emission. The whole photometric light curve, including the CATALINA data, covers 14 yr, and the fractional

variability amplitude for the continuum is 8.9% in flux. During the period covered by SALT data (7 yr) it is $\sim 4.9\%$. Fortunately, the Mg II line flux shows significant variability, comparable to the continuum, at the level of 5.4% during this period. We do not observe a suppressed Mg II variability in this source, unlike that seen in much larger samples (Goad et al. 1999; Woo 2008; Zhu et al. 2017). Yang et al. (2020) also detect the response of Mg II emission to the continuum for 16 extreme-variability quasars, but with a smaller variability amplitude, $\Delta \log L(\text{Mg II}) = (0.39 \pm 0.07) \Delta \log L(3000 \text{ \AA})$. A low Mg II variability was modeled to be the result of a relatively large Eddington ratio (Guo et al. 2020) but HE 0435-4312 is also a source with a rather large Eddington ratio of 0.58 (Sredzińska et al. 2017). Overall, the fractional variability of the Mg II line for our source is comparable to a variability of $\sim 10\%$ on 100 day timescales as inferred for the SDSS-RM ensemble study (Sun et al. 2015).

The variations in quasar parameters are smooth overall. The quality of observation 6 was not very high, as discussed in Sredzińska et al. (2017), but it still allowed the Mg II line parameters to be obtained properly. However, observation 19 created considerable problems. The registered number of photons was much lower (by a factor of a few) than in typical observations, even the background was rather low, and clouds were apparently present in the sky. We did the data fitting, and the derived values of the model parameters form clear outliers when compared with the trends (see Figure 1). Therefore, we did not use this observation in the remaining analysis and the determination of the time delay.

In Sredzińska et al. (2017) the change of the line position was discussed in much detail, since during the first three years the Mg II line seems to move systematically toward longer wavelength with a surprising speed of $104 \pm 14 \text{ km s}^{-1} \text{ yr}^{-1}$ with respect to the quasar rest frame. However, now this trend has seemingly stopped, and in recent observations it seems to have reversed. Such emission line behavior is frequently considered as a signature of a binary black hole (e.g., Popović 2012 for a review). However, to claim such a phenomenon would require extensive tests that are beyond the current paper, which is aimed at measurement of the time delay of the Mg II line.

4. Results: Time-delay determination

To determine the most probable time delay between the continuum and Mg II line emission, we applied several methods as previously in Czerny et al. (2019) and Zajaček et al. (2020), namely:

1. interpolated cross-correlation function (ICCF),
2. discrete correlation function (DCF),
3. z -transformed discrete correlation function (zDCF),
4. the JAVELIN package,
5. measures of data regularity/randomness—von Neumann and Bartels estimators,
6. χ^2 method.

These seven methods are described in detail in Appendix C, including their strengths over other methods. It is beneficial to compare more methods since our light curves are irregularly sampled and the continuum light curve is heterogeneous, i.e., coming from four different instruments (CATALINA, OGLE, SALTICAM, and BMT). After the exclusion of low-quality

Table 1
Overview of the Best Time Delays for Different Methods

Method	Time Delay in the Observer's Frame (days)
ICCF	672^{+49}_{-37}
DCF	656^{+18}_{-73}
zDCF	646^{+63}_{-57}
JAVELIN	645^{+55}_{-41}
von Neumann estimator	635^{+32}_{-66}
Bartels estimator	644^{+27}_{-45}
χ^2 method	706^{+70}_{-61}
Observer's frame mean	658^{+29}_{-31}
Rest-frame mean ($z = 1.2231$)	296^{+13}_{-14}

Note. The time delay is expressed in light-days in the observer's frame. The last two rows contain the mean time delays in the observer's frame and in the rest frame for a redshift of $z = 1.2231$.

data points and outliers, we finally obtained 79 continuum measurements with a mean cadence of 69.0 days (maximum 597.6 days, minimum 0.75 days) and 24 Mg II light-curve data points with a mean cadence of 121.6 days (maximum 398.9 days, minimum 25.9 days).

For our set of light curves, there were several candidate time delays present for different methods. A significant time delay between 600 and 700 days in the observer's frame was present for all the methods and we summarize the obtained values for this peak in Table 1 for the $d11_{\text{mod}}$ Fe II template and the redshift of $z = 1.2231$. The time delay is not affected significantly by a different Fe II template, in particular the template of Kovačević-Dojčinović & Popović (2015) and Popović et al. (2019) (hereafter denoted as KDP15) with a slightly different best-fit redshift of $z = 1.2330$. The ICCF peak for KDP15 is at 692 days for the observer's frame; see Figure 13 in Appendix C.

The significance of the peak between 600 and 700 days was evaluated using the bootstrap method for several time-delay techniques, i.e., by randomly selected light-curve subsets. In addition, for the JAVELIN method, we applied alias mitigation using downweighting by the number of overlapping data points; see Appendix C.4. With this technique (see also Grier et al. 2017), secondary peaks for a time delay longer than 700 days could effectively be suppressed. For the assessment of other time-delay artifact peaks, we generated mock light curves using the Timmer–Koenig algorithm (Timmer & Koenig 1995) with the same light-curve cadence as the observed one; see Appendix D for a detailed discussion. From the constructed time-delay probability distributions for all the seven methods, we could identify clear artifacts due to the sampling for time delays $\lesssim 200$ days as well as for $\gtrsim 800$ days in the observer's frame. The recovery of the true time delay appears to be challenging for the given cadence and the duration of the observations, but the combination of more methods is beneficial in identifying the best candidate for the true time delay.

4.1. Final Time Delay for the Mg II Line

Combining all the seven methods listed in Table 1, the mean value in the observer's frame is $\bar{\tau}_{\text{obs}} = 658^{+29}_{-31}$ days. We visually compare the continuum light curve and the original as

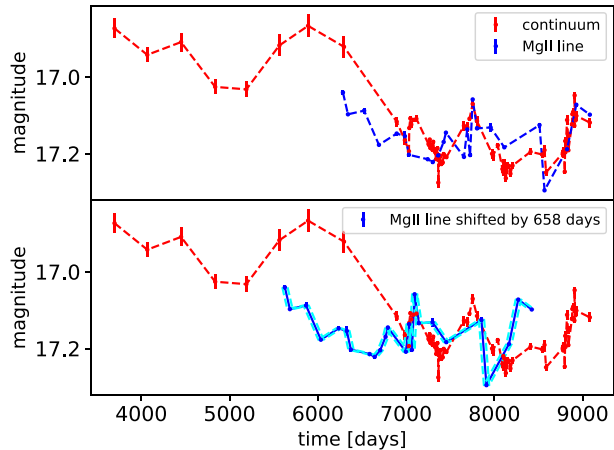


Figure 3. Comparison of the continuum and the shifted Mg II light curves. Top: the continuum and the original Mg II light curve. Bottom: the continuum and the Mg II light curve shifted by the mean time delay of 658 days in the observer’s frame.

well as the time-shifted light curve of the Mg II line in Figure 3. For an easier comparison, the Mg II line is shifted toward larger magnitudes by the difference in the mean values of the two light curves (1.74 mag). The correlation between the continuum and the shifted Mg II light curve, although present, is not visually improved with respect to the zero time lag. This is not unexpected since our source does not exhibit such a large variability amplitude as sources with a low Eddington ratio. In addition, even when the line-emission light curve is shifted by the fiducial time delay, it can intrinsically exhibit periods when the line emission is decorrelated with respect to the continuum emission, which is referred to as the emission-line or the BLR holiday (studied in more detail for NGC 5548, Dehghanian et al. 2019). This justifies the need to use several robust statistical methods to assess the best time delay. We also tried to subtract a linear trend from both light curves, but since for both of them the slope is consistent with zero within fitting uncertainties, it did not yield an improvement. Even for a noticeable linear trend, as for instance for HE 0413-4031 (Zajaček et al. 2020), detrending actually led to a decrease in the correlation coefficient at the fiducial time delay. Hence, the subtraction of a linear trend should be tested on a larger set of sources to assess statistical relevance in terms of time-delay determination.

Subsequently, we obtain the mean rest-frame value of $\bar{\tau}_{\text{rest}} = \bar{\tau}_{\text{obs}} / (1 + z) = 296_{-14}^{+13}$ days for the redshift of $z = 1.2231$. The light-travel distance of the Mg II emission zone can then be estimated as $R_{\text{Mg II}} \sim c\bar{\tau}_{\text{rest}} = 7.7_{-0.4}^{+0.3} \times 10^{17}$ cm = $0.249_{-0.012}^{+0.011}$ pc. The rest-frame time delay is comparable within uncertainties to the time delay of the previously analyzed highly accreting quasar HE 0413-4031 ($z = 1.38$, Zajaček et al. 2020).

4.2. Estimate of Black Hole Mass

Taking into account the rest-frame time delay of $\bar{\tau}_{\text{rest}} = 296_{-14}^{+13}$ days and the Mg II FWHM in the mean spectrum of $\text{FWHM}_{\text{Mg II}} = 3695_{-21}^{+21}$ km s⁻¹, we can estimate the central black hole mass under the assumption that Mg II emission clouds are virialized. Using the anticorrelation

between the virial factor and the line FWHM according to Mejía-Restrepo et al. (2018),

$$f_{\text{MR}} = \left(\frac{\text{FWHM}_{\text{Mg II}}}{3200 \pm 800 \text{ km s}^{-1}} \right)^{-1.21 \pm 0.29}, \quad (3)$$

we obtain $f_{\text{MR}} \sim 0.84$. The virial black hole mass can then be calculated using the Mg II FWHM in the mean spectrum and the measured time delay as $M_{\text{vir}}^{\text{FWHM}}(f_{\text{MR}}) = (6.6_{-0.3}^{+0.3}) \times 10^8 M_{\odot}$. Adopting the virial factor according to Woo et al. (2015), $f_{\text{Woo}} = 1.12$ (based on FWHM of the H β line), we obtain the virial black hole mass $M_{\text{vir}}^{\text{FWHM}}(f_{\text{Woo}}) = (8.8_{-0.4}^{+0.4}) \times 10^8 M_{\odot}$. Here we adopted the FWHM from the mean spectrum since it is better constrained than the rms FWHM. The mean values, however, are consistent within uncertainties, which is in agreement with the general correlation of Mg II line widths measured in the mean and the rms spectra using the SDSS-RM sample (Wang et al. 2019).

Using instead the Mg II line dispersion in the mean spectrum, $\sigma = 2707_{-6}^{+10}$ km s⁻¹, and the associated virial factor $f_{\sigma} = 4.47$ (based on the H β line dispersion) according to Woo et al. (2015), the black hole mass is estimated as $M_{\text{vir}}^{\sigma}(f_{\sigma}) = (1.89_{-0.09}^{+0.08}) \times 10^9 M_{\odot}$. This value is consistent with the value inferred from the broadband SED fitting using the model of a thin accretion disk according to Sredzińska et al. (2017), where they obtained $M_{\text{SED}} = 2.2 \times 10^9 M_{\odot}$. Hence for our source, using the line dispersion inferred from the mean spectrum (the rms spectrum is too noisy to reliably measure σ) appears to be beneficial for constraining the virial SMBH mass. Using the FWHM yields a virial mass below that inferred from broadband fitting.

Next, we estimate the Eddington ratio. Using our continuum light curve, the mean V-band magnitude is 17.15 ± 0.09 mag. With the redshift of $z = 1.2231$ and the mean Galactic foreground extinction in the V band of 0.045 mag according to NED,¹⁴ we determine the luminosity at 3000 Å, $\log(L_{3000}[\text{erg s}^{-1}]) = 46.359_{-0.034}^{+0.038}$, for which we apply the conversions of Kozłowski (2015). To estimate the bolometric luminosity, the corresponding bolometric correction can be obtained via the simple power-law scaling by Netzer (2019), $\kappa_{\text{bol}} = 25 \times [L_{3000}/10^{42} \text{ erg s}^{-1}]^{-0.2} \sim 3.36$, which yields $L_{\text{bol}} = 3.36 L_{3000} \sim 7.68 \times 10^{46} \text{ erg s}^{-1}$. The Eddington limit can be estimated for $M_{\bullet} \simeq 2 \times 10^9 M_{\odot}$, which was obtained via the SED fitting as well as the virial mass using the line dispersion, $L_{\text{Edd}} \simeq 2.5 \times 10^{47} \times (M_{\bullet}/(2 \times 10^9 M_{\odot})) \text{ erg s}^{-1}$. Finally, the Eddington ratio is $\eta = L_{\text{bol}}/L_{\text{Edd}} \sim 0.31$, which is about a factor of two smaller than the Eddington ratio of 0.58 obtained by Sredzińska et al. (2017) using the SED fitting. Still, the source is highly accreting, with η comparable to HE 0413-4031 ($\eta = 0.4$, Zajaček et al. 2020).

The highly accreting sources exhibit the largest scatter with respect to the standard RL relation, with a trend of shorter time delays by a factor of a few than expected based on their monochromatic luminosity. This was studied for the H β reverberation-mapped sources (Du et al. 2015, 2016; Martínez-Aldama et al. 2019), and confirmed for the higher-redshift Mg II reverberation-mapped sources as well (Homayouni et al. 2020; Martínez-Aldama et al. 2020; Zajaček et al. 2020), which suggests a common mechanism for time-delay shortening driven by the accretion rate. The relation between the rest-frame time

¹⁴ <https://ned.ipac.caltech.edu/>

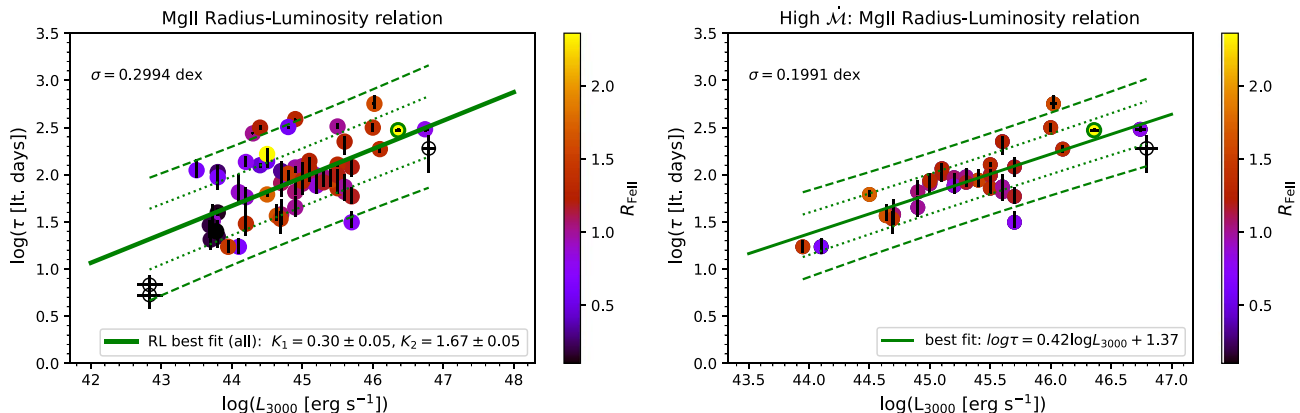


Figure 4. Left panel: Mg II-based radius–luminosity relation including all 68 Mg II reverberation-mapped sources studied in Martínez-Aldama et al. (2020) and the new source HE 0435-4312 denoted by a green circle. The relative UV Fe II strength $R_{\text{Fe II}}$ is color-coded for each source according to the color axis on the right (except for NGC 4151 and CTS 252, for which $R_{\text{Fe II}}$ was not available, and these sources are denoted by empty circles). For HE 0435-4312, we obtained $R_{\text{Fe II}} = \text{EW}(\text{Fe II}) / \text{EW}(\text{Mg II}) \sim 2.36$. Right panel: the same as the left panel, but for highly accreting sources with $\log \dot{M} > 0.2167$, where the division of high accretors was taken from Martínez-Aldama et al. (2020) according to the median value of their full sample. The scatter along the RL relation is noticeably lower for high accretors than for the full sample. In both panels, dashed and dotted lines denote the 68% and 95% confidence intervals, respectively.

delay of the $\text{H}\beta$ line and the linear combination of the monochromatic luminosity at 5100 \AA and the relative strength of the Fe II line (flux ratio between Fe II and $\text{H}\beta$ lines) yields a low scatter of only $\sigma_{\text{rms}} = 0.196$ dex (Du & Wang 2019), which suggests that the relative Fe II strength and hence the accretion rate can account for most of the scatter.

In addition, highly accreting Mg II reverberation-mapped sources exhibit a generally lower scatter along the multi-dimensional RL relations (Martínez-Aldama et al. 2020). This motivates us to further study how high-luminosity and highly accreting sources such as HE 0435-4312 affect the scatter along the radius–luminosity relation on their own as well as in combination with independent observables, such as the Mg II line FWHM, the Fe II strength $R_{\text{Fe II}}$, and the fractional variability F_{var} of the continuum, where the latter two parameters are correlated with the accretion rate.

4.3. Position in the Radius–Luminosity Plane

The high luminosity of HE 0435-4312 is expected to be beneficial for constraining the Mg II-based radius–luminosity relation. We add HE 0435-4312 to the original sample of 68 Mg II reverberation-mapped sources studied in Martínez-Aldama et al. (2020). To characterize the accretion rate of our source and in order to compare it with other sources, we make use of the dimensionless accretion rate \dot{M} expressed specifically for 3000 \AA as (Wang et al. 2014; Martínez-Aldama et al. 2020)

$$\dot{M} = 26.2 \left(\frac{L_{44}}{\cos \theta} \right)^{3/2} m_7^{-2}, \quad (4)$$

where L_{44} is the luminosity at 3000 \AA expressed in units of $10^{44} \text{ erg s}^{-1}$ and m_7 is the central black hole mass expressed in units of $10^7 M_{\odot}$. The angle θ is the inclination angle with respect to the accretion disk and we set $\cos \theta = 0.75$, which represents the mean inclination angle for type I AGNs according to studies of the covering factor of the dusty torus (see, e.g., Lawrence & Elvis 2010; Ichikawa et al. 2015).

Using Equation (4) and the estimate of black hole mass based on the line dispersion in the mean spectrum and the broadband SED fitting, we obtain $\dot{M} = 4.0^{+0.7}_{-0.6}$ or $\log \dot{M} = 0.61^{+0.07}_{-0.06}$ for HE 0435-4312, which puts it into the high-accretor category according to Martínez-Aldama et al. (2020), where all the Mg II reverberation-mapped sources with $\log \dot{M} > 0.2167$ (median value of their Mg II sample). Using the smaller SMBH mass based on Mg II FWHM in the mean spectrum yields a larger \dot{M} by a factor of a few, $\log \dot{M} = 1.51^{+0.07}_{-0.06}$ (based on f_{MR}) and $\log \dot{M} = 1.26^{+0.07}_{-0.06}$ (based on f_{WOO}). In the further analysis, we adopt the \dot{M} value based on the line dispersion in the mean spectrum because of the consistency of $M_{\text{vir}}^{\sigma}(f_{\sigma})$ with the SMBH mass inferred from the broadband fitting of Sredzińska et al. (2017). In Figure 4 (left panel), we plot the RL relation for all 69 sources including HE 0435-4312 (green circle). In the right panel of Figure 4, we restrict the RL relation to only highly accreting sources, which results in a significantly reduced rms scatter of $\sigma_{\text{rms}} = 0.1991$ dex versus $\sigma_{\text{rms}} = 0.2994$ dex for the full sample. Adding HE 0435-4312 results in a small but detectable reduction of scatter for both the full sample (0.2994 versus 0.3014) and the highly accreting subsample (0.1991 versus 0.2012) with respect to the original Mg II sample of 68 sources (Martínez-Aldama et al. 2020).

In the extended RL relations that include other independent observables in the linear combination of logarithms, namely Mg II line FWHM, the relative Fe II strength with respect to the Mg II line $R_{\text{Fe II}}$, and the continuum fractional variability F_{var} , HE 0435-4312 lies within 1σ of the mean relation for both the full sample and the highly accreting subsample; see Figure 5 for the combination with FWHM, Figure 6 that includes $R_{\text{Fe II}}$, and Figure 7 that utilizes the continuum F_{var} . When one restricts the analysis to the highly accreting subsample, the rms scatter drops below 0.2 dex in all combinations, with the smallest scatter exhibited by the RL relation including $R_{\text{Fe II}}$ ($\sigma_{\text{rms}} = 0.1734$ dex). In Table 2, we summarize the best-fit parameters as well as the rms scatter for all the RL relations for the highly accreting subsample including HE 0435-4312. Our high-luminosity source is

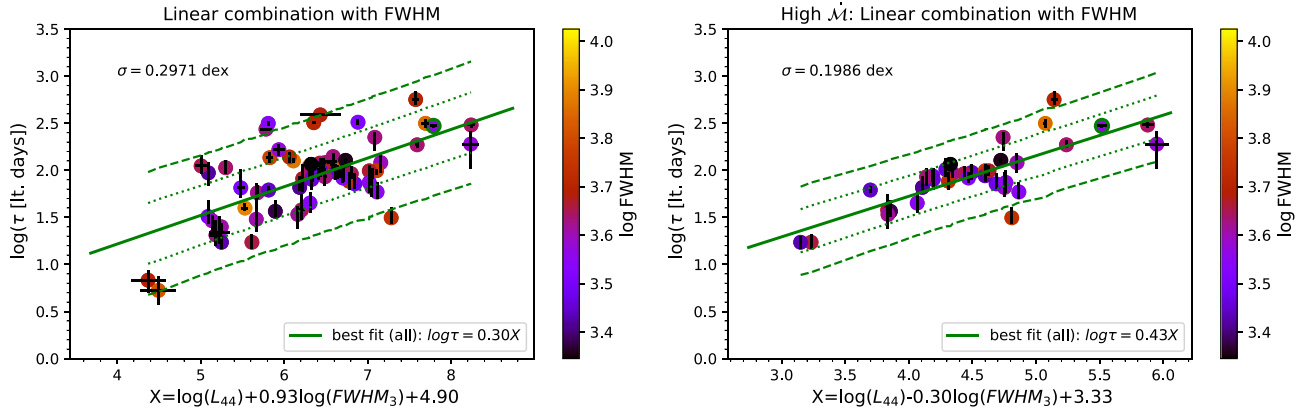


Figure 5. Rest-frame time delay expressed as a function of $\log(L_{44})$ and $\log(FWHM_3)$. Left panel: the linear combination studied for all 68 Mg II reverberation-mapped sources studied in Martínez-Aldama et al. (2020) and a new source HE 0435-4312 denoted by a green circle. Right panel: as in Figure 4, the linear combination is restricted to highly accreting sources with the same division according to \dot{M} . In both panels, each source is color-coded according to the corresponding Mg II FWHM.

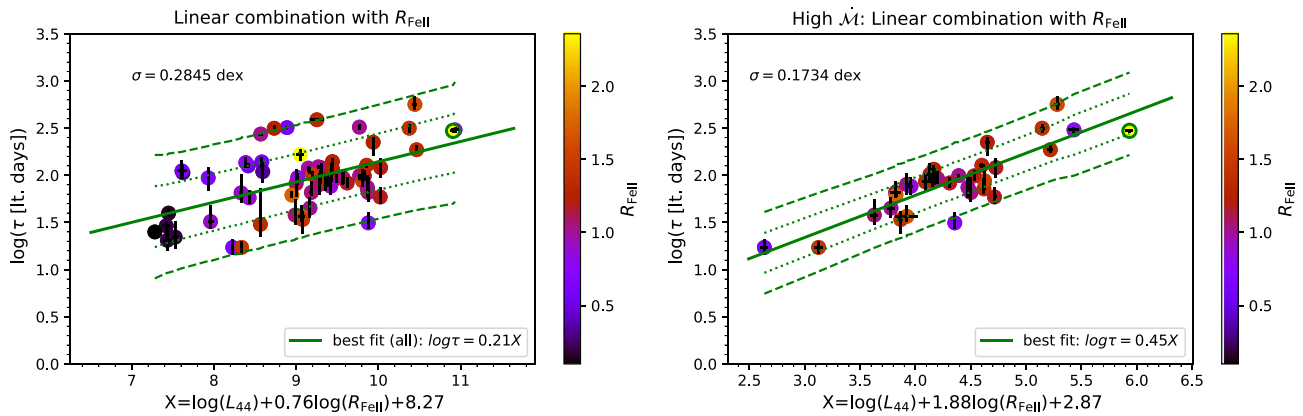


Figure 6. Rest-frame time delay expressed as a function of $\log(L_{44})$ and $\log(R_{FeII})$. Left panel: the linear combination studied for all 68 Mg II reverberation-mapped sources studied in Martínez-Aldama et al. (2020) and a new source HE 0435-4312 denoted by a green circle. Right panel: as in Figure 4, the linear combination is restricted to highly accreting sources with the same division according to \dot{M} . In both panels, each source is color-coded according to the corresponding relative UV Fe II strength R_{FeII} .

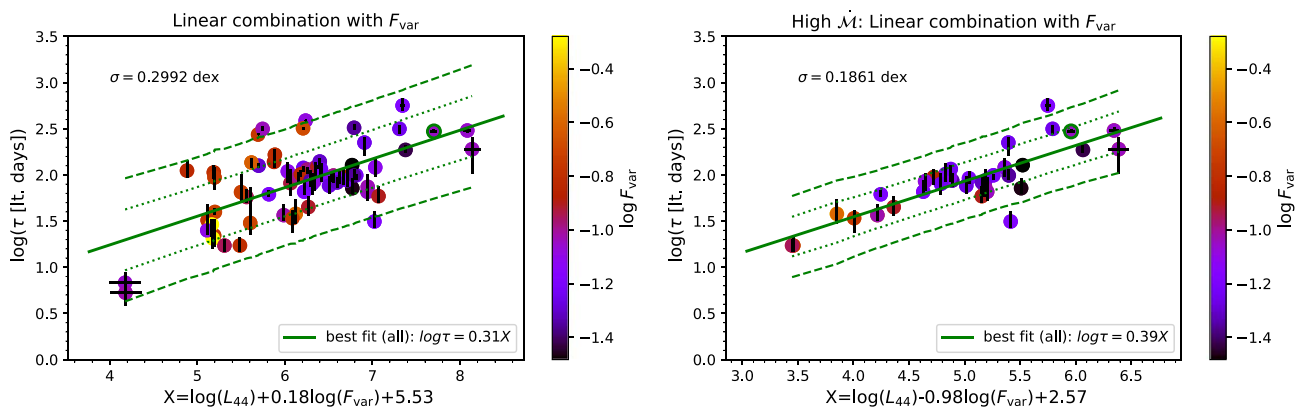


Figure 7. Rest-frame time delay expressed as a function of $\log(L_{44})$ and $\log(F_{var})$. Left panel: the linear combination studied for all 68 Mg II reverberation-mapped sources studied in Martínez-Aldama et al. (2020) and a new source HE 0435-4312 denoted by a green circle. Right panel: as in Figure 4, the linear combination is restricted to highly accreting sources with the same division according to \dot{M} . In both panels, each source is color-coded according to the corresponding continuum fractional variability F_{var} .

Table 2

Parameters for The Standard RL Relation as Well as Multidimensional RL Relations Including Independent Observables, Namely FWHM, $R_{\text{Fe II}}$, and F_{var} , for the Highly Accreting Subsample (35 Sources Including HE 0435-4312)

$\log \tau_{\text{obs}}$	K_1	K_2	K_3	σ_{rms} [dex]	r	σ_{rms} [dex] (without)	r (without)
$K_1 \log L_{44} + K_2$	0.422 ± 0.055	1.374 ± 0.082	...	0.1991	0.80	0.2012	0.78
$K_1 \log L_{44} + K_2 \log \text{FWHM}_3 + K_3$	0.43 ± 0.06	-0.13 ± 0.31	1.44 ± 0.17	0.1986	0.80	0.2007	0.78
$K_1 \log L_{44} + K_2 \log R_{\text{Fe II}} + K_3$	0.45 ± 0.05	0.84 ± 0.29	1.28 ± 0.08	0.1734	0.85	0.1718	0.84
$K_1 \log L_{44} + K_2 \log F_{\text{var}} + K_3$	0.39 ± 0.06	-0.38 ± 0.18	0.99 ± 0.19	0.1861	0.83	0.1863	0.82

Note. The last four columns show rms scatter and Pearson's correlation coefficient with and without HE 0435-4312 for comparison.

beneficial for the reduction of rms scatter, except for the combination including $R_{\text{Fe II}}$, where the rms scatter marginally increases in comparison with the best-fit result of Martínez-Aldama et al. (2020). For all RL relations, adding the new quasar leads to an increase in the Pearson correlation coefficient. For the comparison of the rms scatter and the correlation coefficients with and without the inclusion of HE 0435-4312, see the last four columns of Table 2.

The dimensionless accretion rate \dot{M} of Mg II sources defined by Equation (4) is intrinsically correlated with the rest-frame time delay via the black hole mass ($\dot{M} \propto \tau^{-2}$, while the Eddington ratio $\eta \propto \tau^{-1}$) as discussed by Martínez-Aldama et al. (2020). Therefore we do not use \dot{M} in extended RL relations, because the correlation would be artificially enhanced. We merely use \dot{M} for the division of the sample into the high and low accretors. For the extended RL relations, we prefer the independent observables Mg II FWHM, UV $R_{\text{Fe II}}$, and F_{var} . Characterizing the accretion-rate intensity by \dot{M} is justified by its correlation with the relative UV Fe II strength $R_{\text{Fe II}}$, which in turn is related to the accretion rate (Dong et al. 2011; Martínez-Aldama et al. 2020), which was analogously shown for optical Fe II strength (Shen & Ho 2014; Du & Wang 2019). For the whole sample of Mg II sources, including HE 0435-4312, for which $R_{\text{Fe II}}$ can be estimated (in total 66 sources), the Spearman correlation coefficient between \dot{M} and $R_{\text{Fe II}}$ is positive with $\rho = 0.440$ (with a p -value of 2.19×10^{-4}). For the same sample, the relative Fe II strength is in turn positively correlated with the Eddington ratio $\eta = L_{\text{bol}}/L_{\text{Edd}}$ with $\rho = 0.447$ ($p = 1.71 \times 10^{-4}$). This justifies the division into low and high accretors according to \dot{M} .

On the other hand, \dot{M} is anticorrelated with respect to the continuum variability F_{var} with $\rho = -0.480$ ($p = 2.97 \times 10^{-5}$, 69 sources). Furthermore, the parameter \dot{M} is anticorrelated with Mg II FWHM, although the (anti)correlation is weaker than for $R_{\text{Fe II}}$ and F_{var} with $\rho = -0.386$ ($p = 1.05 \times 10^{-3}$, 69 sources). The anticorrelation between Mg II FWHM and \dot{M} , and hence also $R_{\text{Fe II}}$, is expected from optical studies of eigenvector 1 of the quasar main sequence (Boroson & Green 1992; Sulentic et al. 2000), which can be traced in the UV plane as well (Kozłowski et al. 2020). These (anti) correlations between \dot{M} and other quantities across classical and extended RL relations are also apparent in the color-coded plots in Figures 4–7. The reduction in scatter for the high- \dot{M} subsample could therefore arise due to a lower variability and the stabilisation of the luminosity and black hole mass ratio for the sources accreting close to the Eddington limit as discussed in detail in Martínez-Aldama et al. (2020); see also Ai et al. (2010) and Marziani & Sulentic (2014).

In order to clarify our idea of the sample division quantitatively, we divided the sample analyzed by Martínez-Aldama et al. (2020), with the studied source HE 0435-4312 included, considering the median values of $R_{\text{Fe II}}$ and F_{var} ($\log R_{\text{Fe II}} = 0.02$, $\log F_{\text{var}} = -1.05$) instead of \dot{M} ($\log \dot{M} = 0.23$). Since the correlation between \dot{M} and $R_{\text{Fe II}}$ is positive, we expect that the high Fe II emitters show the highest \dot{M} values, i.e., above the corresponding median value. On the other hand, the correlation between F_{var} and \dot{M} is negative, hence highly accreting AGNs show a lower variability or F_{var} values with respect to the median value of each parameter. In the case of the \dot{M} - $R_{\text{Fe II}}$ correlation, we find that $\sim 70\%$ of the sample satisfies the criteria with respect to the median values of $R_{\text{Fe II}}$ and \dot{M} . Meanwhile, for the \dot{M} - F_{var} correlation, $\sim 72\%$ of our sources are within the median values considered. This is graphically shown in Figure 8, where we depict the correlation \dot{M} - $R_{\text{Fe II}}$ (left panel) and the anticorrelation \dot{M} - F_{var} (right panel) for the studied sample of Mg II sources. Therefore, we can conclude that the division into low and high accretors based on \dot{M} is analogous to a division based on the independent parameters $R_{\text{Fe II}}$ and F_{var} . To illustrate this, in Figure 4 we use $R_{\text{Fe II}}$ for color-coding individual sources in the RL relation for the whole sample (left panel) and the high-accretor subsample (right panel).

5. Discussion

By combining the SALT spectroscopy and the photometric data from more instruments, we were able to determine the rest-frame time delay of 296_{-14}^{+13} days between the Mg II broad line and the underlying continuum at 3000 Å. Fitting the Mg II line with the underlying continuum and Fe II pseudocontinuum is rather complex, but we show in Appendix B that the time-delay distribution for a different Fe II template is comparable and does not affect the main time-delay analysis presented in this paper.

The rest-frame time delay is essentially the same as for another luminous and highly accreting quasar, HE 0413-4031, analyzed in Zajaček et al. (2020). While the RL relation for the collected sample of 69 Mg II reverberation-mapped sources has a relatively large scatter of ~ 0.3 dex, it is significantly reduced to 0.2 dex when we consider only high accretors, where HE 0435-4312 also belongs with an Eddington ratio of ~ 0.31 – 0.58 (the corresponding dimensionless accretion rate is $\dot{M} = 4.0_{-0.6}^{+0.7}$). Further reduction of the scatter is achieved in the 3D RL relations that include independent observables (FWHM, $R_{\text{Fe II}}$, and F_{var}). Especially, the linear combination including the relative strength of Fe II leads to the smallest scatter of 0.17 dex. Because of the correlation between $R_{\text{Fe II}}$ and \dot{M} (Martínez-Aldama et al. 2020), this indicates that the

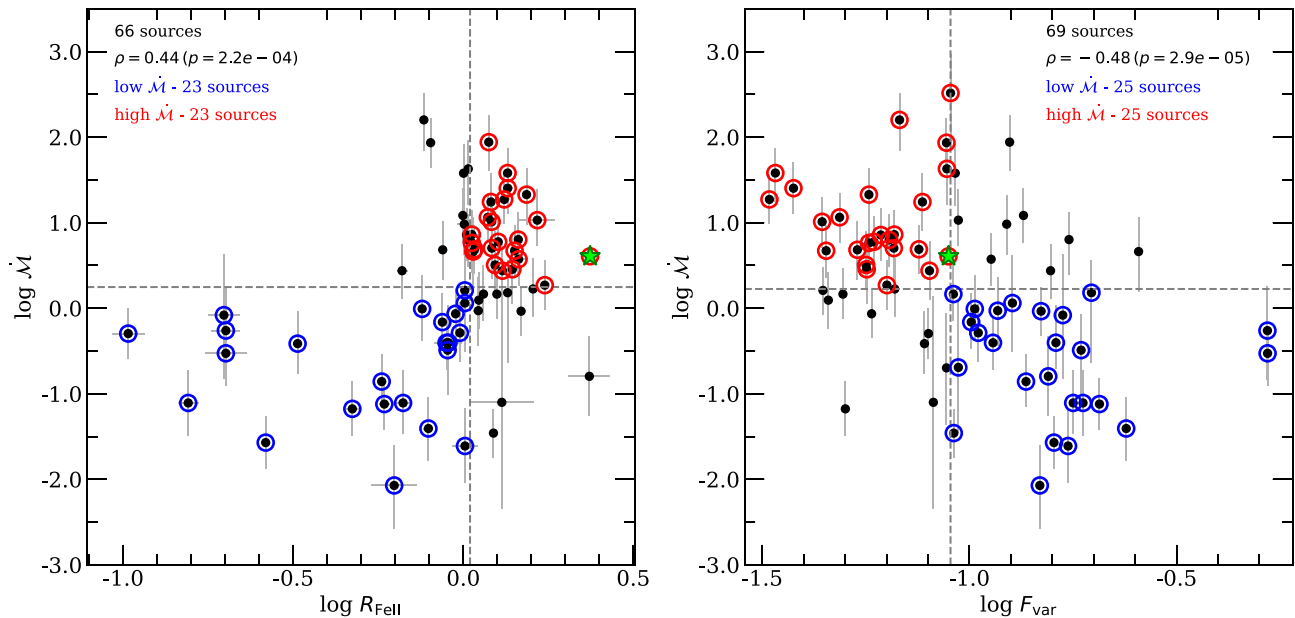


Figure 8. Relation between the dimensionless accretion rate \dot{M} and the relative UV Fe II strength $R_{\text{Fe II}}$ and the continuum fractional variability F_{var} . Left panel: the positive correlation between \dot{M} and $R_{\text{Fe II}}$ (Spearman correlation coefficient $\rho = 0.44$; $p = 2.2 \times 10^{-4}$). The dashed lines mark the median values of each parameter. When the sample is divided according to the median of $R_{\text{Fe II}}$, $\sim 70\%$ of high-/low- \dot{M} sources are present. The star symbol marks HE 0435-4312. Right panel: the anticorrelation between \dot{M} and F_{var} (Spearman correlation coefficient $\rho = -0.48$; $p = 2.9 \times 10^{-5}$). The dashed lines mark the median values of each parameter. When the Mg II sample is divided according to the median value of F_{var} , $\sim 72\%$ of high-/low- \dot{M} sources are included. The star symbol depicts HE 0435-4312.

scatter along the RL relation is driven by the accretion rate, as we already showed in Zajaček et al. (2020) for a sample of only 11 Mg II sources.

In the following subsection, we further discuss some aspects of the Mg II variability, focusing on the interpretation of a relatively large variability of the Mg II line for our source. Then, using the sample of 35 high accretors that exhibit a small scatter along the RL relation, we show how it is possible to apply the radius–luminosity relation to constrain cosmological parameters.

5.1. Variability of Mg II Emission

The fractional variability of the Mg II line of HE 0435-4312 is $F_{\text{var}}^{\text{line}} \simeq 5.4\%$ (excluding observation 19). The continuum fractional variability is larger, $F_{\text{var}}^{\text{cont}} \simeq 8.8\%$ over 14.74 yr. However, when the continuum light curve is separated into the first 7 yr (CATALINA), $F_{\text{var}}^{\text{cont1}} \simeq 4.8\%$, and the last 6 yr (SALT monitoring), $F_{\text{var}}^{\text{cont2}} \simeq 4.8\%$, then both values are comparable to the fractional variability of Mg II emission. This implies that Mg II-emitting clouds reprocess the continuum emission very well for our source. In other words, the triggering continuum and a line echo have similar amplitudes, suggesting that sharp echoes are present and that the Mg II-emitting region lies on (or close to) an isodelay surface, which is an important geometrical condition. In addition, the variability timescale of the continuum must be long enough, i.e., longer than the light-travel time through the locally optically emitting cloud (LOC) model of the BLR. It seems that both conditions are fulfilled for our source.

This is in contrast with the study of Guo et al. (2020), who used the CLOUDY code and the LOC model to study the

response of Mg II emission to the variable continuum. They found that at the Eddington ratio of ~ 0.4 , the Mg II emission saturates and does not further increase with the rise in the continuum luminosity. Observationally, Yang et al. (2020) found for extreme-variability quasars that Mg II emission responds to the continuum but with a smaller amplitude, $\Delta \log L(\text{Mg II}) = (0.39 \pm 0.07) \Delta \log L(3000 \text{ \AA})$. Although our source has a high Eddington ratio comparable to that studied in Guo et al. (2020), $\eta \sim 0.3\text{--}0.6$, its Mg II emission responds very efficiently to the variable continuum. For the previous highly accreting luminous quasar HE 0413-4031 that we studied (Zajaček et al. 2020), we also showed that the Mg II line can respond strongly to the increase in the continuum, $\Delta \log L(\text{Mg II}) = (0.82 \pm 0.26) \Delta \log L(3000 \text{ \AA})$, as shown by the intrinsic Baldwin effect.

A possible interpretation of the discrepancy between the saturation of Mg II emission at larger Eddington ratios modeled nominally by Guo et al. (2020) and our two highly accreting sources, HE 0435-4312 and HE 0413-4031, which exhibit a strong response of the Mg II emission to the continuum, is an order-of-magnitude difference in the black hole mass as well as in the studied luminosity at 3000 Å. In Guo et al. (2020), they used $M_{\bullet} = 10^8 M_{\odot}$ and $L_{3000} = 10^{44}\text{--}10^{45} \text{ erg s}^{-1}$ as well as $(R_{\text{out}}, \Gamma) = (10^{17.5}, -2)$ for the outer radius and the slope of the LOC model, respectively. For our source, all of the characteristic parameters are increased: $M_{\bullet} \simeq 2 \times 10^9 M_{\odot}$, $L_{3000} \simeq 10^{46.36} \text{ erg s}^{-1}$, and $R_{\text{Mg II}} = 10^{17.9} \text{ cm}$. Mainly the larger outer radius implies that not all of the Mg II-emitting gas is fully ionized at these scales and can exhibit “partial breathing,” as is also shown by Guo et al. (2020) for the case with $R_{\text{out}} = 10^{18} \text{ cm}$, when the Mg II line luminosity continues to rise with the increase in the continuum luminosity.

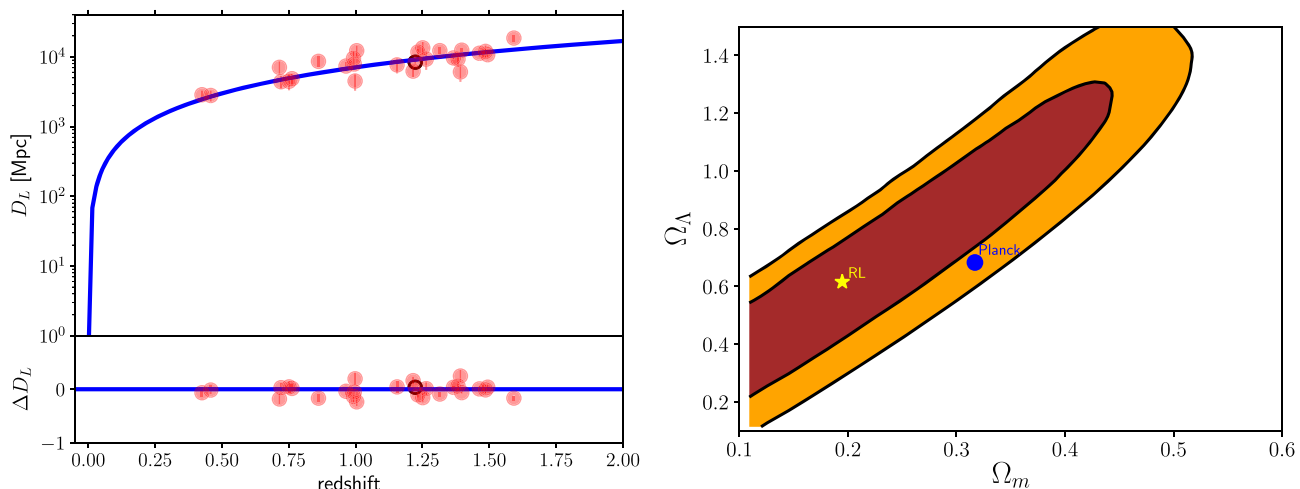


Figure 9. Constraining cosmological parameters using the highly accreting subsample of Mg II reverberation-mapped sources, including HE 0435-4312. Left panel: the quasar Hubble diagram using 27 sources (red points), after removal of eight outliers, with the best-fit standard Λ CDM model (black solid line; $\Omega_m = 0.252^{+0.051}_{-0.044}$ with fixed $H_0 = 67.36 \text{ km s}^{-1} \text{ Mpc}^{-1}$ according to Planck Collaboration et al. (2020)). The bottom panel shows the residuals $\Delta D_L = \log(D_L^{\text{exp}}/D_L)$, where D_L^{exp} is the expected luminosity distance and D_L is the measured one. HE 0435-4312 is marked by a black circle. Right panel: contour plot showing the confidence levels at 68% (orange) and 95% (brown) for the general Λ CDM model based on χ^2 fitting. The yellow star depicts the best-fit $(\Omega_m, \Omega_\Lambda) = (0.19, 0.62)$ and the blue filled circle shows the cosmological constraints as provided by Planck Collaboration et al. (2020).

5.2. Constraining Cosmological Parameters Using an Mg II Highly Accreting Subsample

Since the RL relation for a highly accreting Mg II subsample showed a relatively small scatter of ~ 0.2 dex, we attempt to use it for cosmological purposes. We adopt the general approach outlined in Martínez-Aldama et al. (2019), that is we assume a perfect relation between the absolute luminosity and the measured time delay, and having absolute luminosity and the observed flux we can determine the luminosity distance for each source. We do not use here the best-fit relation given in Figure 4, right panel, since this relation was calibrated for a specific assumed cosmology. Therefore we assume a relation in a general form,

$$\log L_{3000} = \alpha \log \tau - \beta + 44, \quad (5)$$

and we treat α and β as free parameters. We consider first the case of a flat cosmology, and we assume the value of the Hubble constant $H_0 = 67.36 \text{ km s}^{-1} \text{ Mpc}^{-1}$ adopted from Planck Collaboration et al. (2020), and we minimize the fits to the predicted luminosity distance by varying Ω_m , α , and β . The preliminary fit was highly unsatisfactory, and we used a sigma-clipping method to remove the outliers (eight sources). The final sample was well fitted with the standard Λ CDM model for $\Omega_m = 0.252^{+0.051}_{-0.044}$ (1σ error). This result is fully consistent with the data from Planck Collaboration et al. (2020) with $\Omega_m^{\text{Planck}} = 0.3153 \pm 0.0073$. The values obtained for the remaining two parameters were $\alpha = 1.8$ and $\beta = 2.1$, which would correspond to a slightly different RL relation, $\log \tau = 0.56 \log L_{3000} + 1.18$. The results are illustrated in Figure 9, left panel. We also attempted to constrain both Ω_Λ and Ω_m , waiving the assumption of a flat space. The parameters α and β in Equation (5) were kept fixed to the values inferred from the flat-cosmology fit, i.e., $\alpha = 1.8$ and $\beta = 2.1$. The result

is given in the right panel of Figure 9. The best fit in this case implies a slightly lower Ω_m , but the contour error is large and covers the best fit from Planck Collaboration et al. (2020) within the 1σ confidence level. The data do not yet tightly constrain the cosmological parameters, but the Mg II highly accreting subsample does not imply any departures from the standard model, and the data quality is much higher, and constrains the parameters better than the larger sample based on the H β line and discussed in Martínez-Aldama et al. (2019), and somewhat better than the mixed sample discussed in Czerny et al. (2020).

6. Conclusions

Our main conclusions from the reverberation mapping analysis of the source HE 0435-4312 ($z = 1.2231$, $\log(L_{3000}[\text{erg s}^{-1}]) = 46.359^{+0.038}_{-0.034}$) can be summarized as follows.

1. Using seven different methods, we determined the mean rest-frame time delay of 296^{+13}_{-14} days, with all the methods giving a consistent time-delay peak within uncertainties that were determined using the bootstrap or the maximum-likelihood method. By combining the bootstrap method, the weighting by the number of overlapping data points, and the analysis of mock light curves, we could classify the other prominent time-delay peaks as artifacts due to the particular sampling and a limited observational duration.
2. The fractional variability of Mg II emission ($\sim 5.4\%$) is comparable to the continuum variability, hence the Mg II line flux for our source has not reached the saturation level despite the high Eddington ratio of ~ 0.3 – 0.6 . This is most likely due to the large black hole mass of $\sim 2 \times 10^9 M_\odot$ and the large extent of the Mg II-emitting region, $R_{\text{Mg II}} = 10^{17.9}$ cm.

3. The large luminosity of HE 0435-4312 is beneficial for decreasing the scatter and increasing the correlation coefficient for the Mg II-based radius–luminosity relation. The scatter is ~ 0.2 dex for the highly accreting subsample of Mg II sources, where HE 0435-4312 belongs. A further reduction in the scatter is achieved using linear combinations with independent observables (FWHM, relative Fe II strength, and fractional variability), which indicates that the scatter along the radius–luminosity relation is mainly driven by the accretion rate.
4. A low scatter of the radius–luminosity relation for the highly accreting subsample motivates us to apply these sources for constraining cosmological parameters. Given the current number of sources (27, after removal of eight outliers) and the data quality, the best-fit values of the cosmological parameters $(\Omega_m, \Omega_\Lambda) = (0.19; 0.62)$ are consistent with the standard cosmological model within the 1σ confidence level.

The project is based on observations made with the SALT under programs 2012-2-POL-003, 2013-1-POL-RSA-002, 2013-2-POL-RSA-001, 2014-1-POL-RSA-001, 2014-2-SCI-004, 2015-1-SCI-006, 2015-2-SCI-017, 2016-1-SCI-011, 2016-2-SCI-024, 2017-1-SCI-009, 2017-2-SCI-033, 2018-1-MLT-004 (PI: B. Czerny). The authors acknowledge the financial support by the National Science Centre, Poland, grant No. 2017/26/A/ST9/00756 (Maestro 9), and by the Ministry of Science and Higher Education (MNiSW) grant DIR/WK/2018/12. G.P. acknowledges the grant MNiSW DIR/WK/2018/09. K.H. acknowledges support by the Polish National Science Centre grant 2015/18/E/ST9/00580. M.Z. was supported by the NAWA under the agreement PPN/WYM/2019/1/00064 to perform a three-month exchange stay at the Charles University and the Astronomical Institute of the Czech Academy of Sciences in Prague. M.H. and C.S.F. are supported by Deutsche Forschungsgemeinschaft grants CH71/33 and CH71/34. The OGLE project has received funding from the National Science Centre, Poland, grant MAESTRO 2014/14/A/ST9/00121. The Polish participation in SALT is funded by grant No. MNiSW DIR/WK/2016/07. M.Z., V.K., and B.C. acknowledge PPN/BCZ/2019/1/00069 (MŠMT 8J20PL037) for the support of the Polish-Czech mobility program. This paper uses observations made at the South African Astronomical Observatory (SAAO).

Software: IRAF (Tody 1986, 1993), JAVELIN (Zu et al. 2011, 2013, 2016), PyCCF (Sun et al. 2018), vnrm.py (Chelouche et al. 2017), zdcf_v2.f90 (Alexander 1997), plike_v4.f90 (Alexander 1997), delay_chi2.f (Czerny et al. 2013), sklearn (Pedregosa et al. 2011), statsmodels (Seabold & Perktold 2010), numpy (Oliphant 2015), matplotlib (Hunter 2007).

Appendix A Photometric and Spectroscopic Data

Continuum magnitudes with uncertainties are shown in Table 3.

Table 3
Continuum Magnitudes with Uncertainties

JD – 2,450,000	Magnitude (V band) [mag]	Error [mag]	Instrument No.
3696.98828	16.8733330	2.51584481E-02	1
4067.76562	16.9422932	1.88624337E-02	1
4450.48828	16.9090614	2.42404137E-02	1
4837.18359	17.0258694	1.94998924E-02	1
5190.14453	17.0322189	2.00808570E-02	1
5564.26562	16.9177780	2.75434572E-02	1
5889.63672	16.8666668	2.98607871E-02	1
6296.05078	16.9212513	2.82704569E-02	1
6893.60449	17.1165180	1.20000019E-02	2
6986.31592	17.1647282	1.20000019E-02	2
7032.45020	17.1936970	1.20000019E-02	2
7035.63428	17.1329994	4.0000019E-03	3
7047.64209	17.1079998	4.0000019E-03	3
7058.61475	17.1240005	8.0000038E-03	3
7083.54346	17.1119995	4.9999989E-03	3
7116.50684	17.1089993	8.0000038E-03	3
7253.89209	17.1749992	4.0000019E-03	3
7261.88330	17.1779995	4.0000019E-03	3
7267.91504	17.1630001	4.9999989E-03	3
7273.84717	17.1849995	4.9999989E-03	3
7283.84912	17.1779995	4.0000019E-03	3
7295.84277	17.1889992	6.0000005E-03	3
7306.78125	17.1690006	4.0000019E-03	3
7317.74023	17.1889992	4.9999989E-03	3
7327.77490	17.1959991	6.0000005E-03	3
7340.70654	17.2140007	4.0000019E-03	3
7355.69482	17.1860008	4.9999989E-03	3
7363.66650	17.2159996	4.0000019E-03	3
7364.53760	17.2753944	1.20000019E-02	2
7374.70947	17.2080002	4.0000019E-03	3
7385.55762	17.2049999	4.0000019E-03	3
7398.61768	17.2269993	4.0000019E-03	3
7415.58545	17.2229996	4.0000019E-03	3
7426.56641	17.2010002	4.0000019E-03	3
7436.52539	17.2049999	4.9999989E-03	3
7447.52783	17.2080002	4.0000019E-03	3
7457.52246	17.2089996	4.0000019E-03	3
7655.49414	17.1270580	1.20000019E-02	2
7692.38037	17.1313496	1.20000019E-02	2
7717.70557	17.1089993	4.0000019E-03	3
7754.46582	17.0703278	1.20000019E-02	2
7803.32959	17.1150951	1.20000019E-02	2
7973.91357	17.2000008	1.3000003E-02	3
7984.59424	17.2056389	1.20000019E-02	2
8038.86182	17.1779995	6.0000005E-03	3
8091.25000	17.2399998	9.9999978E-03	4
8102.25000	17.2199993	4.0000019E-03	4
8104.25000	17.2430000	8.9999961E-03	4
8105.00000	17.2430000	4.9999989E-03	4
8107.25000	17.2509995	6.0000005E-03	4
8112.48926	17.2262497	1.20000019E-02	2
8130.25000	17.2639999	8.9999961E-03	4
8138.00000	17.2459984	7.0000022E-03	4
8147.00000	17.2319984	8.0000038E-03	4
8166.00000	17.2319984	2.0000009E-03	4
8182.00000	17.2519989	8.0000038E-03	4
8206.00000	17.2309990	8.9999961E-03	4
8410.25000	17.1949997	8.9999961E-03	4
8540.00000	17.2019997	8.0000038E-03	4
8568.24609	17.1906471	1.20000019E-02	2
8585.50000	17.2489986	8.0000038E-03	4
8775.75000	17.1980000	7.0000022E-03	4
8778.75000	17.2049999	4.0000019E-03	4

Table 3
(Continued)

JD – 2,450,000	Magnitude (V band) [mag]	Error [mag]	Instrument No.
8788.75000	17.1889992	4.99999989E-03	4
8797.75000	17.2469997	4.99999989E-03	4
8802.50000	17.1669998	1.09999999E-02	4
8805.50000	17.1959991	3.00000003E-03	4
8823.55176	17.1121445	1.20000001E-02	2
8834.75000	17.1529999	9.99999978E-03	4
8838.75000	17.1910000	4.00000019E-03	4
8878.75000	17.1229992	3.00000003E-03	4
8883.50000	17.0970001	2.00000009E-03	4
8892.50000	17.0909996	8.99999961E-03	4
8906.50000	17.1269989	6.00000005E-03	4
8909.50000	17.0479984	8.99999961E-03	4
8913.50293	17.0949993	4.99999989E-03	3
8920.50293	17.1130009	4.00000019E-03	3
8928.26728	17.1011489	0.012	2
9081.58692	17.1188643	0.012	2

Note. The epoch is given as the Julian Dates (–2,450,000). The last column denotes four different instruments used to obtain the photometric data: 1. CATALINA, 2. SALTICAM, 3. OGLE, 4. BMT. The BMT photometric points were shifted by 0.2 mag toward lower magnitudes to optimize the match with the OGLE photometry.

Appendix B Redshift and Fe II Template

Precise determination of the redshift for quasar HE 0435-4312 is challenging, although its spectrum is not affected by absorption. The original redshift for the quasar, $z = 1.232 \pm 0.001$, was reported by Wisotzki et al. (2000) from the position of the Mg II line. Marziani et al. (2009) measured the redshift on the basis of the H β line from VLT/ISAAC IR spectra, deriving $z = 1.2321 \pm 0.0014$. A narrow [O III] line was also visible in the spectrum, but it was strongly affected by atmospheric absorption, so it could not serve as a reliable redshift mark. Sredzińska et al. (2017) determined the redshift as $z = 1.2231$ using the data from SALT collected during the first three years of the SALT monitoring of this source. In this paper, two kinematic components were used to fit the Mg II line: one component at the systemic redshift, together with the Fe II template, and the shift of the second was a model parameter. What is more, Sredzińska et al. (2017) showed that the Mg II line position systematically changes with time. Thus the redshift was mostly determined by the location of the strong Fe II emission at 2750 Å.

In the currently available set of observations, one set, obtained on 2019 December 5 (observation 23), was obtained with a slightly shifted setup, so it covered the spectral range almost up to 3000 Å in the rest frame (in all other observations, this region overlaps with a CCD gap). Observed quasar spectra usually have a clear gap just above 2900 Å, which could serve as additional help in constraining the redshift, as well as the optimum Fe II template.

The basic template d11-m20-20.5-735 (marked later as d11) of Bruhweiler & Verner (2008) (with parameters: plasma density 10^{11} cm^{-3} , turbulence velocity 20 km s^{-1} , and log of ionization parameter in $\text{cm}^{-2} \text{ s}^{-1}$ of 20.5) favored by Sredzińska et al. (2017) does not fit well the dip in the region of 2900 Å (see Figure 10). We also checked other theoretical

Table 4
Summary of the Redshift and Fe II Templates Used to Fit Observation 23

Mg II Model	Fe II Template	Redshift	FWHM (Fe II)	χ^2	Panel in Figure 10
LL	d11	1.2231	3100	1377.59436	a
LL	d11BV08-C17	1.2231	3100	1818.21631	b
GG	d11BV08-C17	1.2231	3100	1505.38	c
GG	d12-MaFer-C17	1.2321	2800	1517.13757	
LL	d11 _{mod}	1.2231	3100	1296.09912	d
LL	KDP15	1.2321	3600	1408.91748	
LL	KDP15	1.2321	4000	1400.57812	e
LL	KDP15	1.2330	4000	1370.64978	f

templates provided by Bruhweiler & Verner (2008), but all of them predicted considerable emissivity in that spectral region. Since the CLOUDY code has been modified over the years, we calculated new Fe II templates using the newest version of the code (Ferland et al. 2017), but with the same input as in the template d11, including the spectral shape of the incident continuum. New results did not solve the problem, and actually gave a much worse fit (see Table 4), if the two-Lorentzian model was assumed for the Mg II line, as in Sredzińska et al. (2017). If, instead, we used two Gaussians for the line fitting, the resulting χ^2 became much better (see Table 4) but still higher than with the older template, and the emission above 2900 Å was still overproduced. We thus experimented with simple removal of a few transitions from the original d11 template. We removed transitions at $\lambda\lambda 2896.32, 2901.96, 2907.61,$ and 2913.28 , creating the d11_{mod} template. This clearly allowed a satisfactory representation of the data to be achieved, and favored the same redshift as in Sredzińska et al. (2017).

Next, we tried the KDP15 Fe II templates (Kovačević-Dojčinović & Popović 2015; Popović et al. 2019), which have fewer transitions but an additional flexibility of arbitrarily changing the normalization of each of the six transitions. This template provided a good fit for another of the quasars monitored with SALT (Zajaček et al. 2020). The clear disadvantage is that fitting these templates is much more time-consuming, since then the spectral model has 13 free parameters instead of eight, when the Fe II template has just one normalization as a free parameter. Nevertheless, we fitted all parameters at the same time, as in our standard approach.

The KDP15 template gave a rather poor fit for the low values of redshift favored by Sredzińska et al. (2017), but the model gave much lower χ^2 values for the redshift range suggested by Marziani et al. (2009) (see Table 4). The best fit for this template was achieved for the redshift $z = 1.2330$, even slightly higher than in Marziani et al. (2009). However, formal χ^2 is still higher than for the d11_{mod} template. Since the two redshifts and the Fe II templates used for modeling in these two cases are so different, we checked how this difference in the spectrum decomposition actually affects the Mg II line. For that purpose, we subtracted the fitted Fe II template and continuum from the original spectrum. The result is displayed in Figure 11 (left panel) in the observer’s frame. As we see, the difference in the actual Mg II shape is not large, despite large differences in the Fe II templates. The FWHM of the line is only slightly broader for KDP15, 3632 km s^{-1} versus 3507 km s^{-1} , as determined from the total line shape. Line dispersion σ measured as the second moment differs more (3060 km s^{-1} versus

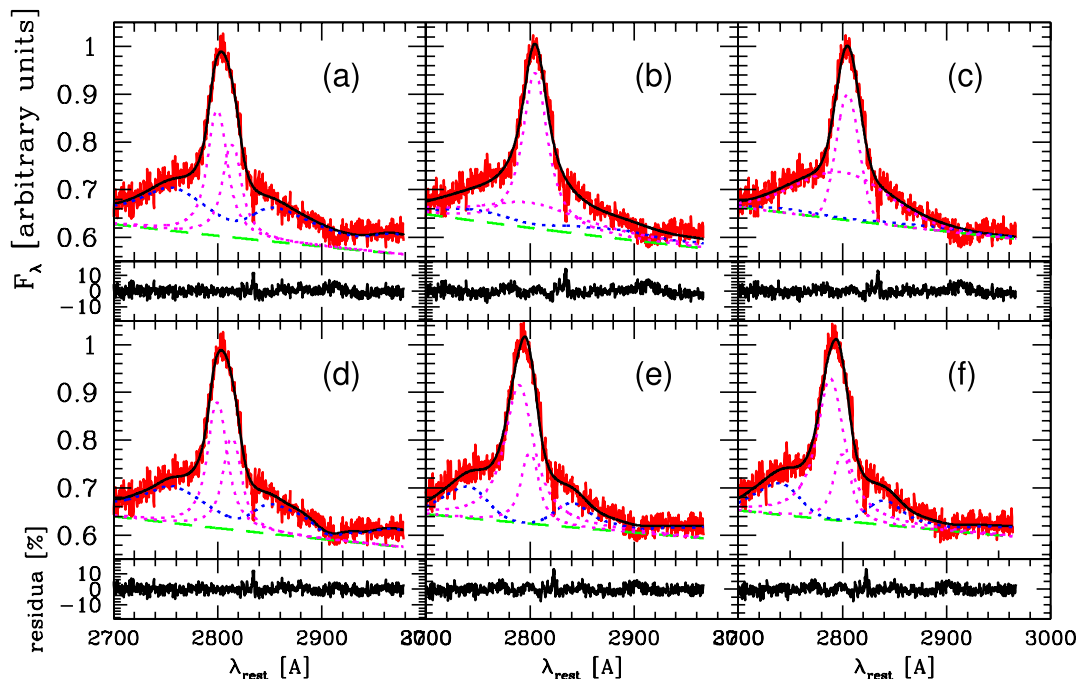


Figure 10. Selected models of observation 23 from Table 4.

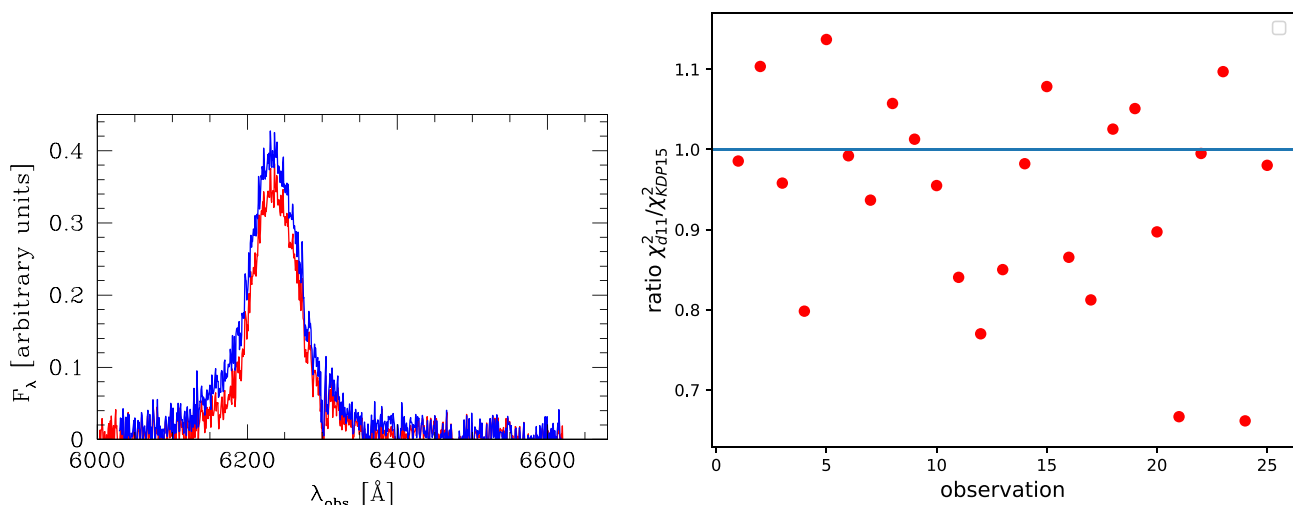


Figure 11. Comparison between the fits of the observed Mg II and Fe II complexes performed using $d11_{\text{mod}}$ and KDP15 models. Left panel: Mg II line shape in the observer's frame after subtraction of Fe II and a power law with models $d11_{\text{mod}}$ from panel (d) of Figure 10 (red line) and KDP15 from panel (f) of Figure 10 (blue line). The normalization is the same as in Figure 10, so the slight difference in the line normalization between the two models is visible. Right panel: the ratio of χ^2 values between the fits performed using the $d11_{\text{mod}}$ model ($z = 1.2231$) and the KDP15 model ($z = 1.2330$) for available observational epochs. For 17 epochs out of 25, $\chi^2_{d11_{\text{mod}}} < \chi^2_{\text{KDP15}}$.

3423 km s⁻¹) but in both cases the ratio FWHM/ σ is much smaller than expected for a Gaussian profile.

Since fitting the full six-transition KDP15 template is time-consuming, and we do not expect considerable changes in Fe II shape in the SALT data, we constructed a new single-parameter template based on KDP15, taking the relative values of the six components from the best fit of observation 23 in the extended wavelength range, and using the (best) Fe II broadening of

4000 km s⁻¹. With this new template KDP15, we refitted all SALT observations in the range 2700–2900 Å. For 17 observations $\chi^2_{d11_{\text{mod}}} < \chi^2_{\text{KDP15}}$, and for eight KDP15 fitted the data better, but generally not significantly; see Figure 11 (right panel). We thus perform most of the time-delay computations with the $d11_{\text{mod}}$ template, and we illustrate the role of the template in the time-delay determination for the ICCF method—see Appendix C.1, where we show that the

KDP15 template is associated with a comparable cross-correlation function and similar peak and centroid distributions as those for $d11_{\text{mod}}$; see Figure 13.

Appendix C Overview of Methods for Time-delay Determination

C.1. Interpolated Cross-correlation Function

We first analyzed the continuum and Mg II line-emission light curves using the interpolated cross-correlation function, which is a standard and well-tested method for assessing the time delay between the continuum and the line emission flux density (Peterson et al. 1998). Light curves are typically unevenly sampled, while the ICCF works with the continuum–line emission pairs with a certain time step of $\Delta t = t_{i+1} - t_i$. The cross-correlation function for two light curves, x_i and y_i , with the same time step of Δt achieved by interpolation, evaluated for a time shift of $\tau_k = k\Delta t$ ($k = 1, \dots, N - 1$), is defined as

$$\text{CCF}(\tau_k) = \frac{(1/N) \sum_{i=1}^{N-k} (x_i - \bar{x})(y_{i+k} - \bar{y})}{\left[(1/N) \sum_{i=1}^N (x_i - \bar{x})^2 \right]^{1/2} \left[(1/N) \sum_{i=1}^N (y_i - \bar{y})^2 \right]^{1/2}}. \quad (\text{C1})$$

The same time step Δt can be achieved by interpolating the continuum light curve with respect to the line-emission light curve and vice versa (asymmetric ICCF). Typically, both interpolations are averaged to obtain the symmetric ICCF.

For the time-delay analysis, we use the Python implementation of ICCF in code PYCCF by Sun et al. (2018), which is based on the algorithm by Peterson et al. (1998). The code allows one to perform both asymmetric and symmetric interpolation. Based on the Monte Carlo techniques of random subset selection and flux randomization, one can obtain the centroid and the peak distributions and their corresponding uncertainties.

We studied the time delay between the continuum light curve consisting of 81 measurements, with eight Catalina-survey averaged detections, 16 SALTICAM measurement, 27 BMT data, and 30 OGLE data. Two SALTICAM measurements were excluded based on their poor quality. The emission-line light curve consists of 25 SALT measurements, where the 19th measurement has a poor quality due to weather conditions and is excluded from the further analysis. Hence, we have 79 continuum points with a mean cadence of 69.0 days and 24 Mg II flux-density measurements with a mean cadence of 121.6 days. We set the interpolation interval to one day. For the redshift of $z = 1.2231$ and the $d11_{\text{mod}}$ template, we display the ICCF as a function of time delay in the observer’s frame in Figure 12 (left panel) for both asymmetric and symmetric interpolation. In the middle and right panels, we show the centroid and the peak distributions for the symmetric interpolation based on 3000 Monte Carlo realizations of random subset selection and flux randomization. The centroid and the peak are generally not well defined. The peak value of the correlation function for the symmetric interpolation is 0.32 for a time delay of 635 days, which is less than for our previous quasars CTS C30.10 (peak CCF of ~ 0.65 , Czerny et al. 2019; Zajaček et al. 2019) and HE 0413-4031 (peak CCF of 0.8, Zajaček et al. 2020). In the next step, we focus on the surroundings of this peak and we analyze the CCF centroid and peak distributions in the interval between 500 and 1000 days. The results for all interpolations are summarized in Table 5. For the symmetric interpolation, we obtain a centroid time delay of $\tau_{\text{cent}} = 663^{+66}_{-40}$ days and a peak time delay of $\tau_{\text{peak}} = 672^{+49}_{-37}$ days.

We also performed the time-delay analysis using the ICCF for the Mg II light curve derived using the KDP15 template (case f in Table 4). For the symmetric ICCF, the CCF peak value is 692 days with $\text{CCF} = 0.36$, which is comparable to the analysis performed for the $d11_{\text{mod}}$ template. The CCF peak and centroid distributions also contain the same subpeaks, with the peak close to 700 days being the most prominent; see Figure 13.

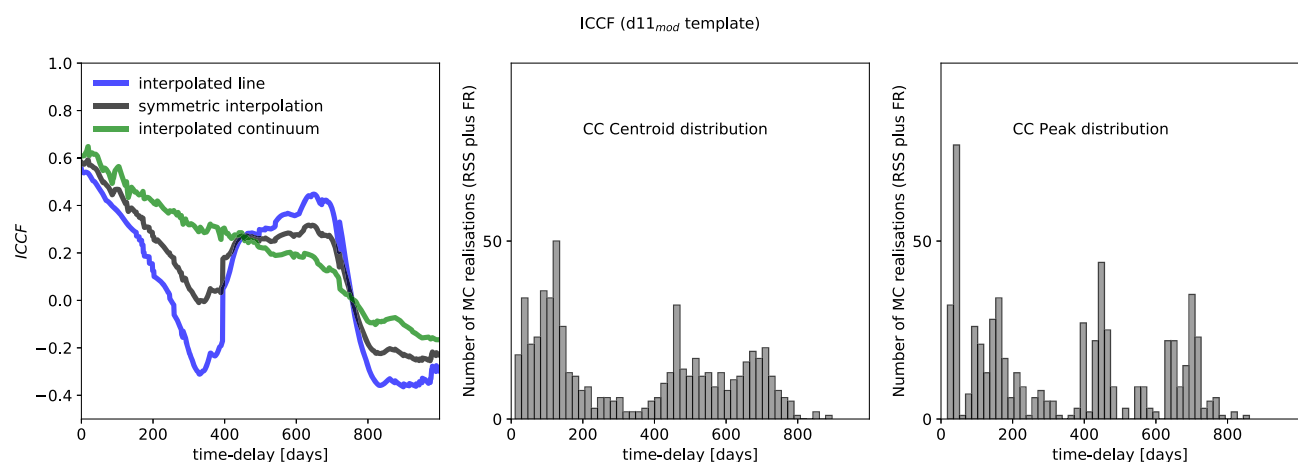


Figure 12. The interpolated cross-correlation function as a function of the time delay expressed in days in the observer’s frame. The calculation is performed for the $d11_{\text{mod}}$ template and the redshift of $z = 1.2231$. Left panel: the ICCF as a function of the time delay expressed in days in the observer’s frame for three types of interpolation: interpolated continuum light curve (green solid line), interpolated line light curve (blue solid line), and the symmetric interpolation (black solid line). Middle panel: the distribution of the cross-correlation centroids for the symmetric interpolation. Right panel: the distribution of the cross-correlation peaks for the symmetric interpolation.

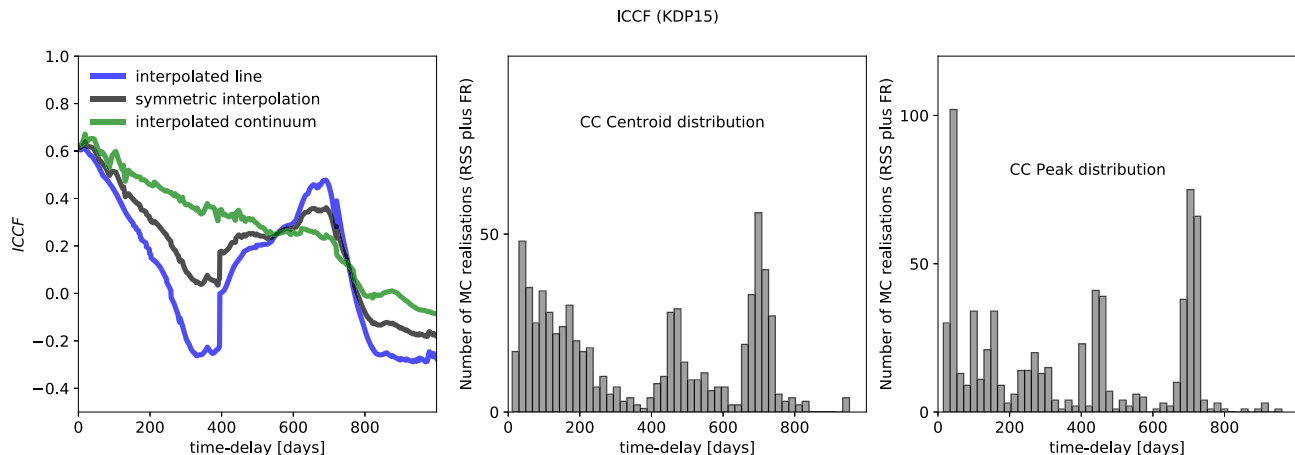


Figure 13. The same ICCF analysis as in Figure 12 but for the KDP15 template (case f in Table 4) and the redshift of $z = 1.2330$.

Table 5

Summary of the Time-delay Determination for the Quasar HE 0435-4312
Using the ICCF

Interpolation Method	Time Delay ($z = 1.2231$)
Interpolated continuum—centroid [days]	635^{+31}_{-34}
Interpolated continuum—peak [days]	630^{+42}_{-46}
Interpolated line—centroid [days]	673^{+60}_{-50}
Interpolated line—peak [days]	683^{+38}_{-48}
Symmetric—centroid [days]	663^{+66}_{-40}
Symmetric—peak [days]	672^{+49}_{-37}

Note. We list the centroids as well as the peaks for the interpolated continuum light curve, the interpolated line emission light curve, and the symmetric interpolation. Time delays are expressed in days in the observer’s frame of reference.

C.2. Discrete Correlation Function

For unevenly sampled and sparse light curves, the ICCF can distort the best time delay by adding additional data points to one or both light curves. In that case, the discrete correlation function (DCF) introduced by Edelson & Krolik (1988) is better suited to determine the best time lag.

In general, the DCF value is determined for any pair of light curves (x_i, y_j) whose time difference Δt_{ij} falls into the time-delay bin of size $\delta\tau$, $\tau - \delta\tau/2 < \Delta t_{ij} < \tau + \delta\tau/2$, where τ is a given time delay. First, one calculates the unbinned DCF,

$$\text{UDCF}_{ij} = \frac{(x_i - \bar{x})(y_j - \bar{y})}{\sqrt{s_x - \sigma_x^2} \sqrt{s_y - \sigma_y^2}}, \quad (\text{C2})$$

where \bar{x} and \bar{y} are light-curve means in a given time-delay bin, s_x and s_y are corresponding light curve variances, and σ_x and σ_y are the mean measurement errors of the light-curve points in the given time-delay interval.

The DCF is then calculated as a mean over M light-curve points that are located in a given bin,

$$\text{DCF}(\tau) = \frac{1}{M} \sum_{ij} \text{UDCF}_{ij}. \quad (\text{C3})$$

The uncertainty can be estimated using the relation

$$\sigma_{\text{DCF}} = \frac{1}{M-1} \sqrt{\sum [\text{UDCF}_{ij} - \text{DCF}(\tau)]^2}. \quad (\text{C4})$$

We made use of the Python script pyDCF (Robertson et al. 2015), where the general procedure described using Equations (C2), (C3), and (C4) is implemented. We searched for the DCF peak in the time interval from 100 to 1000 days, with a time step of 50 days. We obtained a better defined DCF peak using the Gaussian weighting scheme than using the slot weighting. In Figure 14 (left panel), we show the DCF versus time delay in the observer’s frame. The time delay with the highest DCF value of 0.41 ± 0.16 is at 675 days. To determine the uncertainty of the peak, we ran 1000 bootstrap simulations, where at each step we constructed a pair of new light curves by randomly selecting a light-curve subset. The histogram of peak DCF time delays constructed from 1000 bootstrap realizations is shown in Figure 14 (right panel). The peak of the distribution is at $\tau_{\text{DCF}} = 656^{+18}_{-73}$ days in the observer’s frame. The left and right uncertainties represent standard deviations, where we included the area within 30% of the main peak.

C.3. z-Transformed Discrete Correlation Function

In the following, we applied the z -transformed discrete correlation function (Alexander 1997), which improves the classical DCF by replacing equal time binning by equal population binning. This is achieved by applying Fisher’s z -transform. With this property, the z DCF processes satisfactorily especially undersampled, sparse, and heterogeneous light curves, which to some extent is the case here, since the continuum light curve originates from three different instruments and the Mg II light curve is relatively sparse with respect to the continuum (24 versus 79 points). In our analysis, we applied the z DCF method several times, changing the minimum number of light-curve pairs per population bin. Finally, we set the minimum number of light-curve pairs to eight and used 5000 Monte Carlo-generated pairs of light curves to determine the errors in each bin. In Figure 15, we show the z DCF values as a function of time delay in the observer’s frame. There are some peaks with a large DCF value within the first 200 days in the rest frame, e.g., 190.3 days

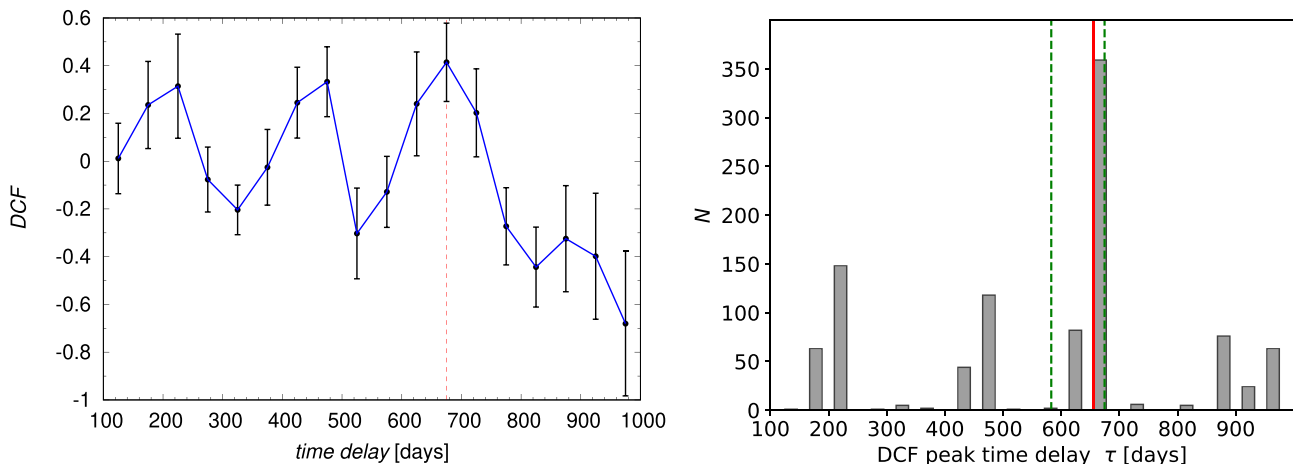


Figure 14. Discrete correlation function vs. a time delay in the observer’s frame using the $d11_{\text{mod}}$ template. Left panel: a DCF vs. time delay in the observer’s frame. A red vertical line denotes the peak DCF. Right panel: histogram of peak DCF time delays constructed from 1000 bootstrap realizations. The red and dashed green vertical lines denote the histogram peak and its left and right standard deviations within 30% of it, respectively.

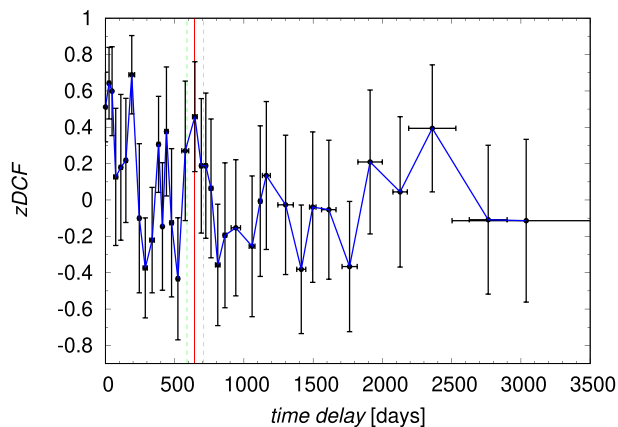


Figure 15. The zDCF as a function of the time delay in the observer’s frame. The uncertainties in each population bin were inferred from 5000 Monte Carlo-generated pairs of light curves (using the observed measurement errors). The red vertical line marks the most prominent, maximum-likelihood peak of 646^{+63}_{-57} days, while the green vertical dashed lines mark the uncertainties.

(DCF = 0.69). These are, however, too short to correspond to the realistic rest-frame time delay for our highly luminous quasar. The most prominent peak at larger time delays is at 646 days (DCF = 0.46).

Next we calculate the maximum likelihood (ML) using the zDCF values and we focus on the prominent peak in the interval between 500 and 800 days. From the ML analysis, we obtain the ML peak of $\tau_{\text{zDCF}} = 646^{+63}_{-57}$ days in the observer’s frame. This peak and the corresponding uncertainties are also highlighted in Figure 15 by vertical lines.

C.4. The JAVELIN Package

Another technique to evaluate the time-delay distribution is to model the continuum variability of AGNs as a stochastic process using the damped random walk process (Kelly et al. 2009; Kozłowski et al. 2010; MacLeod et al. 2010; Kozłowski 2016). Subsequently, the line emission is assumed to be time-delayed, smoothed, and a scaled version of the continuum emission. This method is implemented in the

JAVELIN package (Just Another Vehicle for Estimating Lags in Nuclei; Zu et al. 2011, 2013, 2016)¹⁵. The package uses Markov Chain Monte Carlo (MCMC) methods to first determine the posterior probabilities for the continuum variability timescale and the amplitude. Based on that, the variability of the line emission is modeled to obtain the posterior probabilities for the time lag, smoothing width of the top-hat function, and the scaling ratio (the ratio between the line and the continuum amplitudes, $A_{\text{line}}/A_{\text{cont}}$).

First, we searched for the time delay in the longer interval between 0 and 2000 days in the observer’s frame. There are four distinct peaks (see Figure 16, left panel) at ~ 100 , ~ 650 , ~ 1300 , and ~ 2000 days. The first peak is too short, while the last two appear too long for our data set. In the zDCF analysis in Section C.3, the time-delay peaks at 1000 days and more also have large uncertainties. Therefore, in the next search, we perform a time-delay search in the narrower interval between 0 and 1000 days to focus on the intermediate peak at ~ 650 days. We obtain a prominent peak at ~ 652 days; see Figure 16 (right panel).

To determine the precise position of the time-delay peak, we performed 200 bootstrap simulations—i.e., generating 200 subsets of the original continuum and Mg II light curves. Then we applied the JAVELIN to determine the peak time delay for each individual pair of light curves. From 200 best time delays, we first construct a density plot in the plane of the time delay and the scaling factor; see Figure 17 (left panel). We see that there is a peak in the distribution close to 600 days in the observer’s frame. In Figure 17 (right panel), we show the histogram of the best time delays with the peak value of $\tau_{\text{peak}} = 645^{+55}_{-41}$ days, where the uncertainties were determined within 30% of the peak value.

For the JAVELIN time-delay determination, we typically notice several narrow comparable peaks in the histogram of time delays for a single MCMC run as can be seen in Figure 16. These secondary peaks typically arise due to a limited duration of observational runs and a sparse and/or nonuniform sampling of continuum and line-emission light curves. However, they might also reflect the complex BLR geometry seen in advanced

¹⁵ <http://www.astronomy.ohio-state.edu/~yingzu/codes.html#javelin>

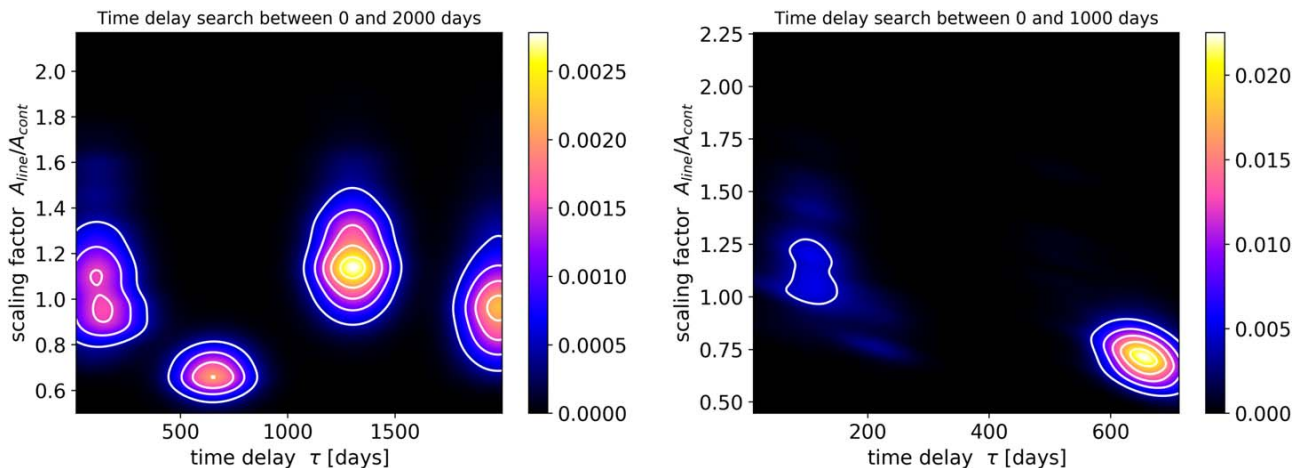


Figure 16. The time-delay determination for HE 0435-4312 using the JAVELIN package. Left panel: the time-delay search in the interval between 0 and 2000 days in the observer’s frame. There are four distinct peaks at ~ 100 , ~ 650 , ~ 1300 , and ~ 2000 days. Right panel: the time-delay search in the narrower interval between 0 and 1000 days yields a clear peak at ~ 652 days.

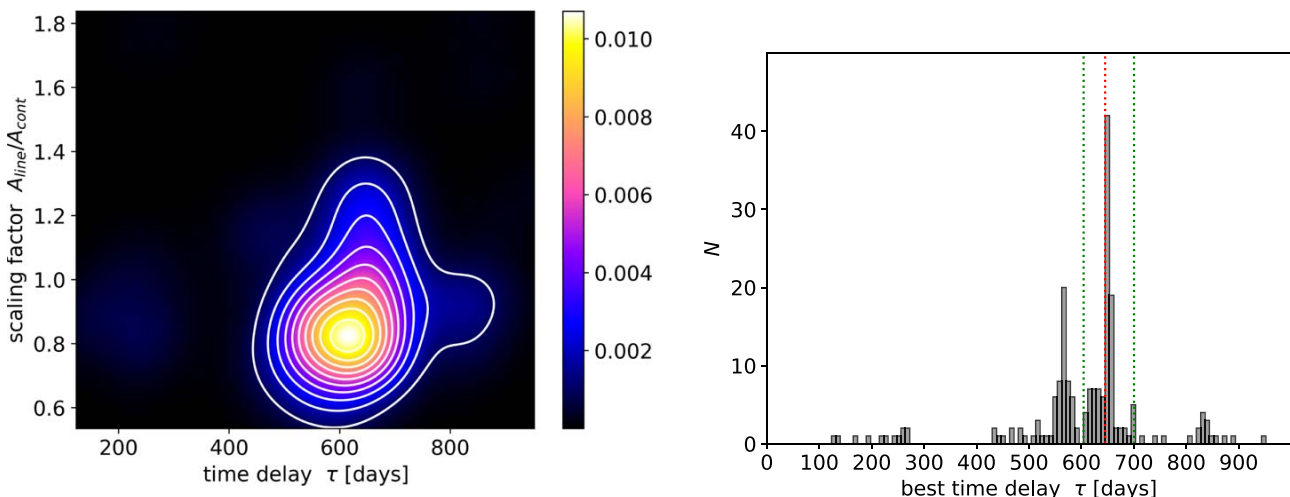


Figure 17. Bootstrap analysis of the BLR time delay in HE 0435-4312 using the JAVELIN package. Left panel: the distribution of 200 best time delays in the plane of the time delay (in the observer’s frame) and the scaling factor A_{line}/A_{cont} . There is a prominent peak in the distribution close to 600 days. Right panel: the histogram of 200 best time delays. The peak value is at $\tau_{peak} = 645^{+55}_{-41}$ days, which is marked by the vertical red and green dotted lines. The uncertainty is determined as the standard deviation within 30% of the main peak.

data analysis or models (e.g., Grier et al. 2017; Hu et al. 2020; Horne et al. 2021; Naddaf et al. 2021). As mentioned in Grier et al. (2017), these alias peaks can be of a comparable significance to the true peak in the time-delay distribution, which is also the case here; see Figure 18 (right panel, black line), where time delays at ~ 105 , ~ 1300 , and ~ 1980 days appear to have a larger significance than the fiducial peak of ~ 650 days in the observer’s frame.

Following Grier et al. (2017), we weight the posterior probability distribution of time delays by the number of overlapping light-curve points, where the prior probability distribution is given by $P(\tau) = [N(\tau)/N(0)]^2$, where $N(\tau)$ denotes the number of overlapping light-curve points for the time delay τ , and $N(0)$ is the number of data points in the overlap region for zero time lag. Hence, the weight is $P(\tau) = 1$

by definition for zero time lag and it will decrease for larger positive and negative time lags, being zero when there is no overlap. For our light curves, we construct the prior probability distribution $P(\tau)$, which is shown in Figure 18 (left panel).

Using $P(\tau)$, we weight the posterior time-delay distribution based on the number of overlapping light-curve points. This is demonstrated in Figure 18 (right panel, red line). The alias mitigation based on $P(\tau)$ helps to effectively suppress longer time-delays, which drop in significance below the fiducial time lag at ~ 655 days. However, this technique is not efficient to suppress aliases at shorter time delays of ~ 100 days, where the decrease is negligible due to the definition of $P(\tau)$. This peak at smaller time delays is effectively mitigated by the bootstrap or random subset selection technique. As we showed in Figure 17, this peak is not further represented in the posterior time-delay

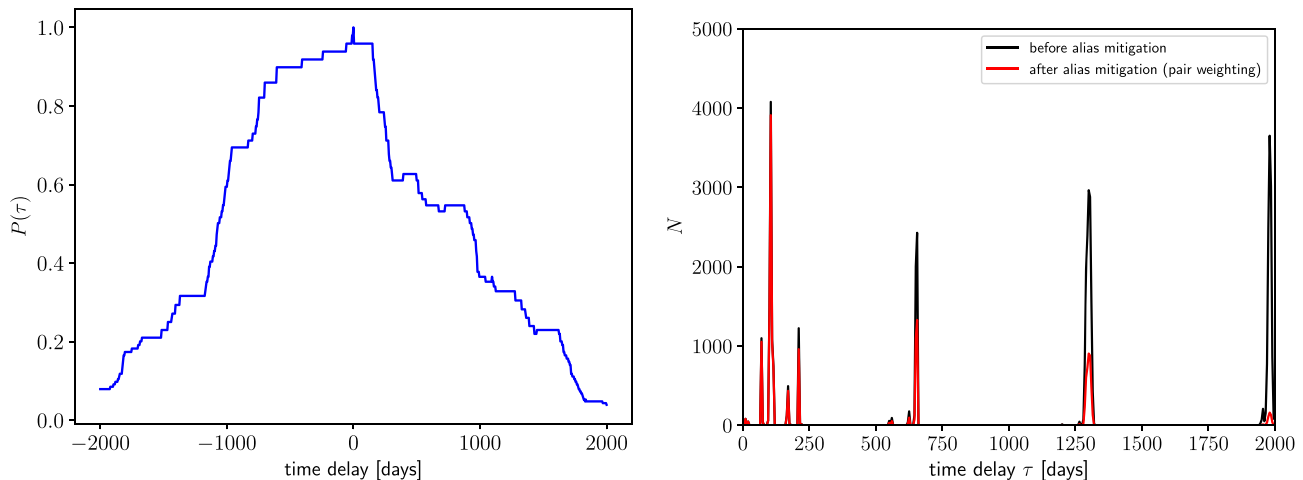


Figure 18. Alias mitigation for the JAVELIN time-delay distribution. Left panel: prior probability distribution $P(\tau) = [N(\tau)/N(0)]^2$ based on the number of overlapping data points for a given time delay. Right panel: posterior time-delay distributions before alias mitigation (black line) and after alias mitigation by using $P(\tau)$ as an effective weight for individual time-delay peaks.

distribution, which leaves us with the fiducial peak close to ~ 650 days. In addition, in Appendix D we show that the artifact peaks at $\lesssim 200$ days arise in the probability density distributions (see Figures 22 and 23) constructed from mock light curves that are sampled with the same cadence as the original continuum and line-emission light curves.

C.5. Measures of Data Regularity/Randomness—von Neumann and Bartels Estimators

We also analyzed the time-delay between the continuum and Mg II light curves using a novel technique of the measures of the data regularity or randomness (Chelouche et al. 2017), which were previously applied extensively in cryptography and data compression. The advantage of these regularity measures is that they do not require the interpolation as for the ICCF or χ^2 technique and neither do they require binning in the correlation space like the DCF and zDCF methods. In addition, no AGN variability model is needed for the continuum light curve as for the JAVELIN.

One of the suitable estimators to analyze the time delay between two light curves is the optimized von Neumann scheme, which works with the combined light curve $F(t, \tau) = (t_i, f_i)_{i=1}^N = F_1 \cup F_2^\tau$, where F_1 is the continuum light curve and F_2^τ is the time-shifted line-emission light curve. The optimized von Neumann estimator for a given time delay τ is defined as the mean of the successive differences of $F(t, \tau)$,

$$E(\tau) = \frac{1}{N-1} \sum_{i=1}^{N-1} [F(t_i) - F(t_{i+1})]^2. \quad (\text{C5})$$

The aim of the von Neumann scheme is to find the minimum $E(\tau')$, where $\tau' \sim \tau_0$ is supposed to correspond to the actual time delay.

In Figure 19 (left panel), we calculate $E(\tau)$ for HE 0435-4312 using the Python script based on Chelouche et al. (2017).¹⁶ The minimum is reached for a time delay between 300 and 400 days in the observer’s frame (333–334 days and 391–392 days), and then for 690 days, which is consistent with

¹⁶ For the script and the corresponding documentation, see www.pozonunez.de/astro_codes/python/vnm.py.

the results of previous methods. To determine the peak value and its uncertainty close to this minimum, we performed $\sim 10,000$ bootstrap realizations, from which we constructed the histogram of the best von Neumann time delays; see Figure 19 (right panel). In this histogram, we detect two prominent peaks at ~ 27 days and ~ 1200 days and a smaller peak at ~ 635 days. After focusing on the interval between 150 and 1100 days, the best peak is at 635^{+32}_{-66} days in the observer’s frame, where the uncertainties correspond to standard deviations within 30% of the best peak.

For comparison, we also applied the Bartels estimator to both light curves; it uses the ranked version of the combined light curve $F_R(t, \tau)$. In Figure 20 (left panel), we show the Bartels estimator as a function of the time delay in the observer’s frame. The minimum is clearer than for the von Neumann estimator and is located at 690 days. After running 10,000 bootstrap realizations, we detect three peaks as for the von Neumann estimator. Between 100 and 1100 days, there is a peak of 644^{+27}_{-45} days (see Figure 20, right panel), where the uncertainties were calculated within 30% of this time-delay peak.

C.6. The χ^2 Method

Inspired by the time-delay analysis in quasar lensing studies, we applied the χ^2 method to our set of light curves. The χ^2 method performed well and consistently in comparison with other time-delay analysis techniques for the previous two SALT quasars—CTS C30.10 (Czerny et al. 2019) and HE 0413-4031 (Zajaček et al. 2020). It also performs better than the classical ICCF for the case when the AGN variability can be interpreted as a red-noise process (Czerny et al. 2013). We subtracted the mean from both the continuum and the line-emission light curves, and subsequently they were normalized by their corresponding variances. The similarity between the continuum and the time-shifted line-emission light curves is evaluated using χ^2 . We make use of symmetric interpolation.

In Figure 21 (left panel), we show χ^2 as a function of the time delay in the observer’s frame. There is a global minimum at 696 days. The exact position and the uncertainty of this peak are inferred from the histogram of the best time delays

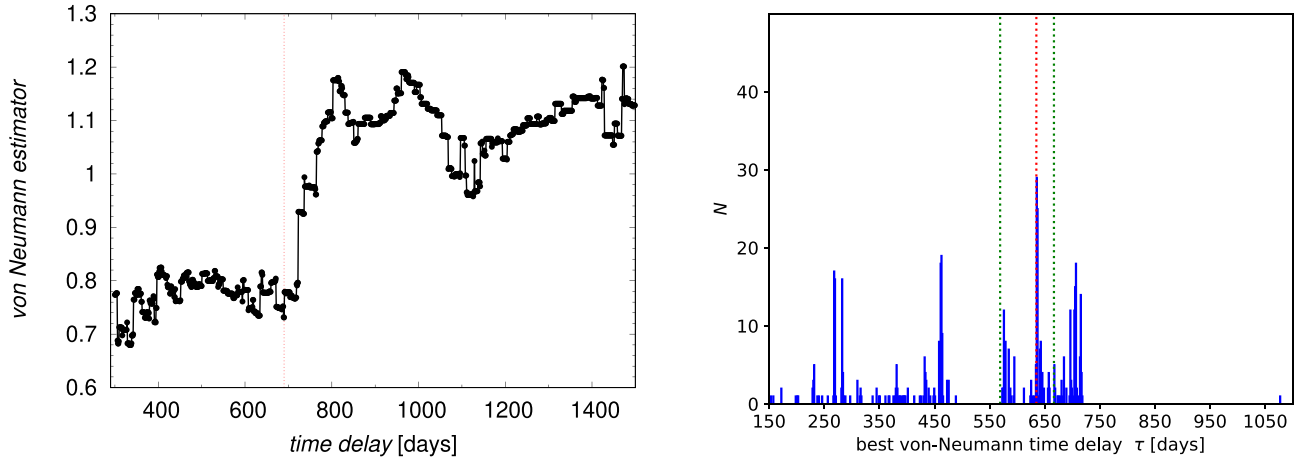


Figure 19. The results of the time-delay analysis using the von Neumann estimator. Left panel: the value of the von Neumann estimator as a function of the time delay in the observer's frame. The red vertical line denotes the minimum at 690 days. Right panel: the histogram of best von Neumann time delays constructed from 10,000 bootstrap simulations of random subset selections of both continuum and line-emission light curves. The red and green dotted vertical lines mark the peak value of 635^{+32}_{-66} days and the corresponding uncertainties.

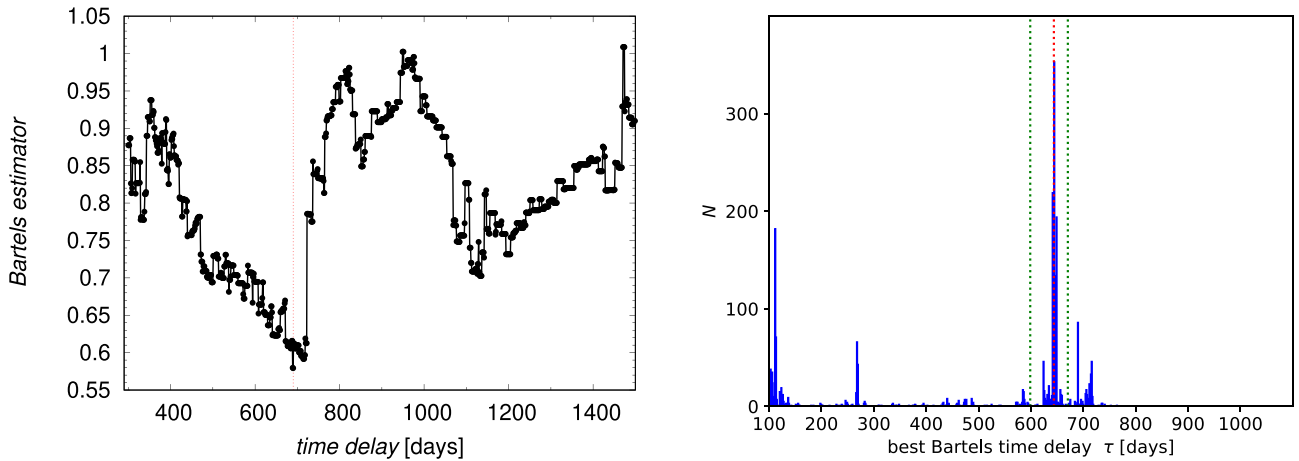


Figure 20. The results of the time-delay analysis using the Bartels estimator. Left panel: the value of the Bartels estimator as a function of the time delay in the observer's frame. The minimum estimator value is reached for a time delay of 690 days. Right panel: the histogram of best Bartels time delays constructed from 10,000 bootstrap simulations of random subset selections of both continuum and line-emission light curves. The red and green dotted vertical lines mark the peak value of 644^{+27}_{-47} days and the corresponding uncertainties.

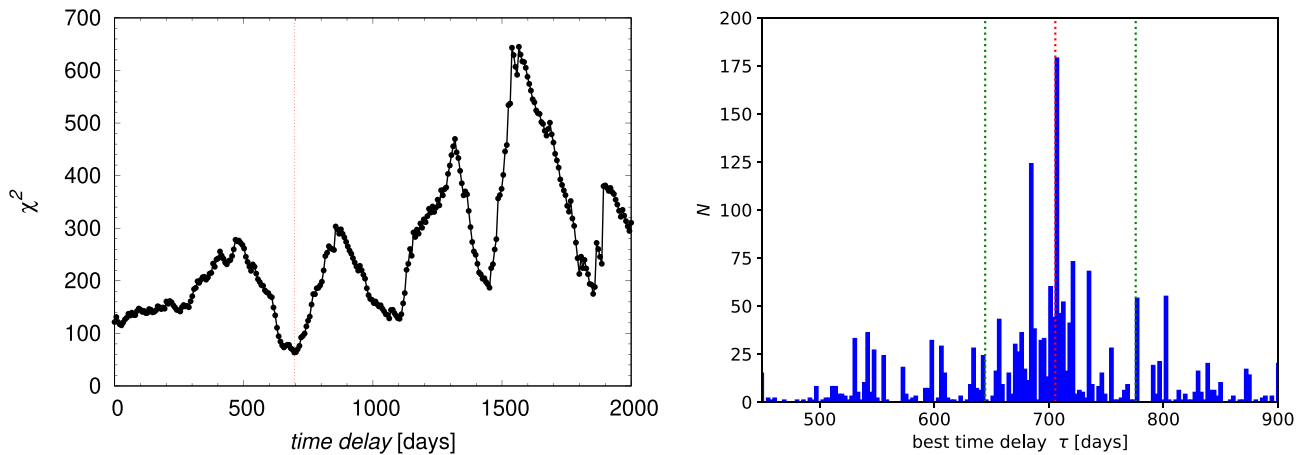


Figure 21. Time-delay determination using χ^2 method. Left panel: the χ^2 value as a function of the time delay in the observer's frame. The global minimum is at ~ 696 days, which is marked by a red vertical line. Right panel: the histogram of best time delays constructed from 10,000 bootstrap simulations around the global χ^2 minimum of ~ 700 days. The peak value is 706^{+70}_{-61} days, which is shown using vertical red and green dotted lines.

constructed from 10,000 bootstrap realizations. We obtain 706^{+70}_{-61} days, where the uncertainties were determined as the left and the right standard deviations from the time delays that are positioned within 30% of the main peak; see Figure 21 (right panel).

Appendix D Alias Mitigation Using Generated Light Curves

In this appendix, we investigate the alias problem, i.e., the occurrence of secondary peaks in the time-delay distribution from a different perspective than presented in Appendix C.4, where we applied the downweighting technique on the posterior time-delay distribution based on the number of data points in the overlap region. Here we instead generate a large set of synthetic light curves similar in basic temporal properties to those of our studied quasar, while the line-emission light curve has a known prior time delay with respect to the continuum light curve. Then we apply several methods for time-delay determination to see how well we can recover the true time delay and what the distribution width is close to the assumed time delay.

To generate mock light curves, we use the method of Timmer & Koenig (1995) (hereafter TK) to produce synthetic light curves from the assumed shape and the normalization of the power density spectrum (PDS). The TK method can generate mock light curves based on any shape of PDS, unlike the damped random walk approach (Kelly et al. 2009; MacLeod et al. 2010; Zu et al. 2011, 2013, 2016), which generates light curves with the PDS slope close to -2 . The assumed shape of the PDS is a broken power-law function with two break frequencies corresponding to $\sim 10,000$ days at lower frequencies and to ~ 700 days at higher frequencies. The slopes from lower to higher frequencies vary consequently from 0.0, through -1.2 , up to -2.5 . The line-emission light curve is first time-shifted by the assumed time delay, here fixed to 600 days in the observer's frame. Then the line emission is smeared by a timescale equal to 10% of the time delay, where we adopt the Gaussian shape of the BLR transfer function. Finally, dense continuum and line emission light curves are interpolated to the actual observational epochs of our observed light curves. We generate in total 1000 mock light curves with the actual observational cadence, which has the potential to reveal artifact peaks in the time-delay probability distributions due to the particular sampling pattern of our observations (see also Max-Moerbeck et al. 2014, for a similar analysis of cross-correlation artifacts). These corresponding continuum–line pairs are further analyzed by seven different time-delay methods. Subsequently, we construct histograms of best time delays, which are utilized as probability density distributions to determine the peak time delays and the corresponding 1σ uncertainties; see Figure 22 for the ICCF method and Figure 23 for the zDCF, JAVELIN, von Neumann, Bartels, DCF, and χ^2 methods. In particular, we focus on how well we can determine the prior (true) time delay and what its uncertainty is. In Table 6, we list for individual methods the most prominent peaks and their uncertainties in the interval between 500 and 800 days in the observer's frame.

In general, the cadence of our observed light curves appears to produce two or three secondary peaks besides the prior peak close to 600 days, which are often more prominent than the assumed peak. Two peaks at $\lesssim 200$ days and ~ 900 – 1000 days are especially apparent. For the ICCF, DCF, and zDCF methods, the prior time-delay peak is not well defined, i.e.,

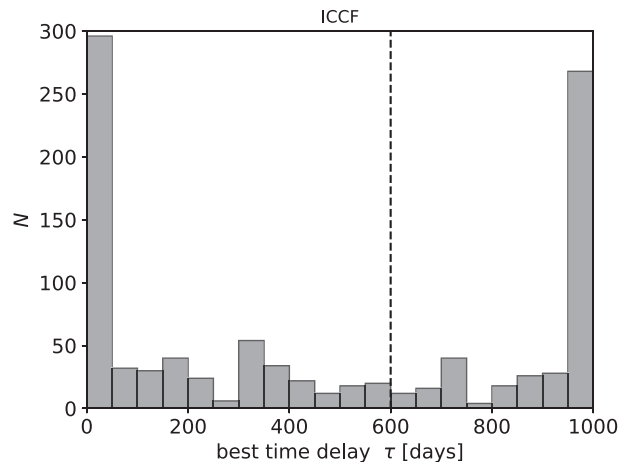


Figure 22. Best time-delay distribution constructed from the analysis of 1000 pairs of light curves generated using the Timmer–Koenig algorithm (Timmer & Koenig 1995) and subsequently analyzed by the interpolated cross-correlation function. The histogram of the best time delays has a bin size of 50 days. The dashed vertical line marks the time delay of 600 days in the observer's frame assumed for the time-shifted line-emission light curve.

Table 6
Peaks Close to $\tau = 600$ days (in the Range between 500 and 800 days in the Observer's Frame) in the Time-delay Distributions (see Figure 23) for Individual Methods

Method	Time-delay peak (days)
ICCF	720^{+79}_{-218}
zDCF	724^{+79}_{-221}
JAVELIN	564^{+131}_{-165}
Von Neumann	594^{+143}_{-115}
Bartels	707^{+78}_{-199}
DCF	525^{+127}_{-109}
χ^2	632^{+128}_{-178}

the distribution is highly smeared and broad in the interval between 500 and 800 days. For other methods, the peak close to 600 days is better defined, however, with a large standard deviation of the order of 100 days. The true peak at ~ 600 days is best recovered using the JAVELIN method, which also suppresses effectively the secondary peaks detected in other methods. This result is consistent with the study of Yu et al. (2020b), who report that the JAVELIN outperforms the ICCF in terms of estimating time-delay error. Furthermore, Li et al. (2019) used mock light curves to compare the time-lag recovery and error estimation of the JAVELIN, ICCF, and zDCF and concluded that the JAVELIN produces higher quality time-delay estimations than both the ICCF and the zDCF. In Table 6, we list the inferred peaks in the range between 500 and 800 days, i.e., close to the true peak of 600 days in the observer's frame. We see that due to the sparse cadence of our observations, the detected peak can be shifted by as much as ~ 100 days shortward or longward of the assumed peak.

The time-delay analysis of the generated light curves thus shows that secondary peaks can be created in the time-delay distribution due to the specific cadence and duration of the observed light curves. The secondary peaks longward of the

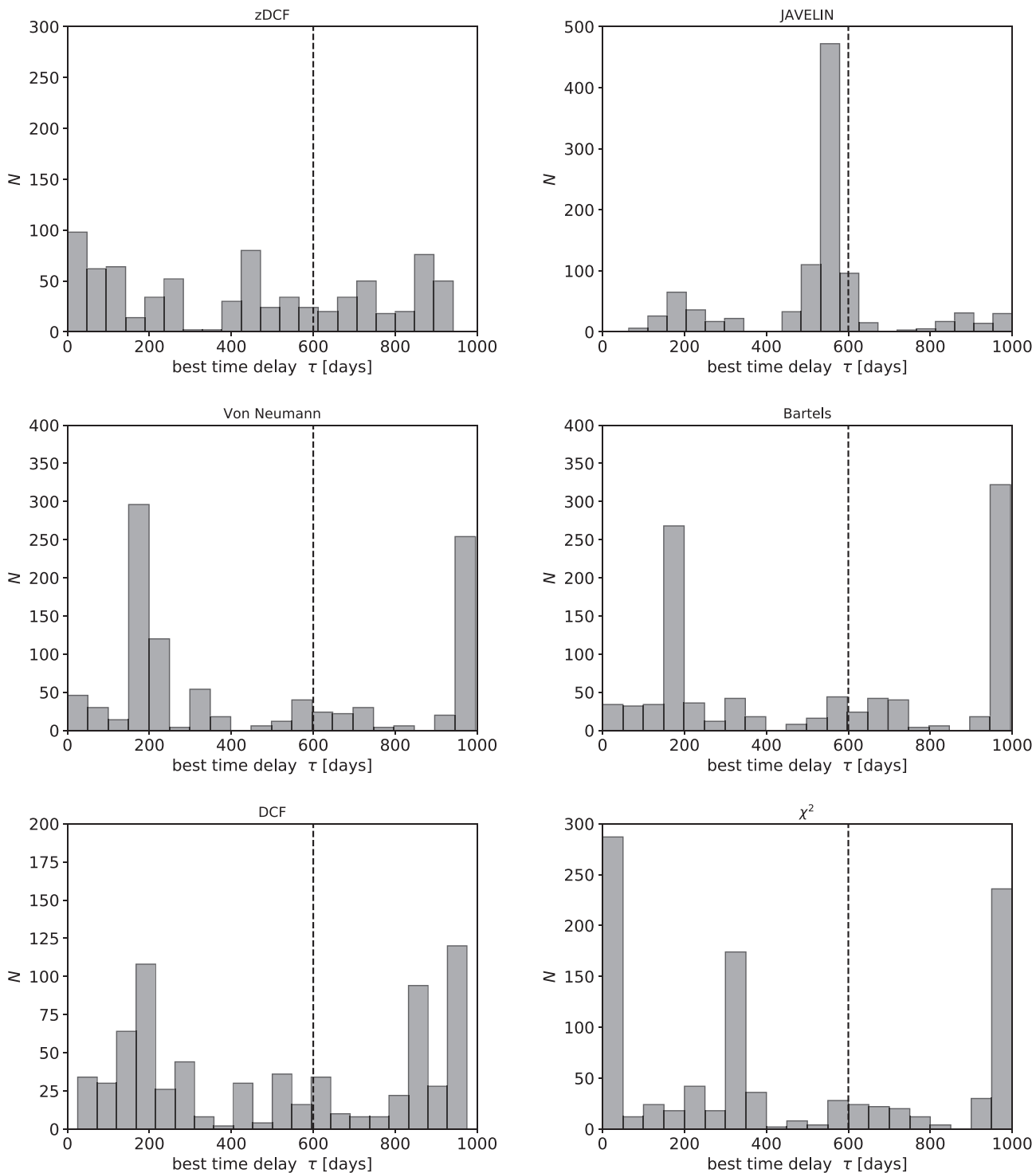


Figure 23. Best time-delay distributions constructed from 1000 pairs of light curves generated using the Timmer–Koenig algorithm (Timmer & Koenig 1995). Top left: the histogram of the best time delays constructed for the zDCF method. The bin size is 50 days. The dashed vertical line marks the time delay of 600 days in the observer’s frame assumed for the time-shifted line-emission light curve. The other panels show analogous histograms of the best time delays constructed for the JAVELIN method (top right), the von-Neumann estimator (middle left), the Bartels estimator (middle right), the DCF method (bottom left), and the χ^2 method (bottom right).

true peak at 600 days can be mitigated using the down-weighting technique as we showed in Appendix C.4 for the JAVELIN method; see also Grier et al. (2017). Here we show

that the prominent peaks between 0 and ~ 200 days, which are not mitigated by the downweighting due to a large number of overlapping light-curve pairs, can arise due to a lower cadence

of our light curves, especially the line-emission light curve with only 24 points. Hence, they do not reflect the physical response of the BLR transfer function. In this sense, the reported mean peak time-delay of 658_{-31}^{+29} days in the observer's frame (296_{-14}^{+13} days in the rest frame for $z = 1.2231$) for the quasar HE 0435-4312 can be considered as the best candidate for the true time delay, albeit with a large uncertainty up to ~ 100 days. The other peaks appear to be aliases due to the specific cadence and the duration of our light curves.

ORCID iDs

Michal Zajaček  <https://orcid.org/0000-0001-6450-1187>
 Bożena Czerny  <https://orcid.org/0000-0001-5848-4333>
 Mary Loli Martínez–Aldama  <https://orcid.org/0000-0002-7843-7689>
 Mateusz Rałowski  <https://orcid.org/0000-0002-0297-3346>
 Aleksandra Olejak  <https://orcid.org/0000-0002-6105-6492>
 Swayamtrupta Panda  <https://orcid.org/0000-0002-5854-7426>
 Krzysztof Hryniewicz  <https://orcid.org/0000-0002-2005-9136>
 Marżena Śniegowska  <https://orcid.org/0000-0003-2656-6726>
 Mohammad-Hassan Naddaf  <https://orcid.org/0000-0002-7604-9594>
 Grzegorz Pietrzyński  <https://orcid.org/0000-0002-9443-4138>
 Catalina Sobrino Figaredo  <https://orcid.org/0000-0001-9704-690X>
 Martin Haas  <https://orcid.org/0000-0002-7284-0477>
 Andrzej Udalski  <https://orcid.org/0000-0001-5207-5619>
 Vladimír Karas  <https://orcid.org/0000-0002-5760-0459>
 Marek Sarna  <https://orcid.org/0000-0003-4745-3923>
 Ramotholo R. Sefako  <https://orcid.org/0000-0003-3904-6754>

References

- Abbott, T. M. C., Abdalla, F. B., Allam, S., et al. 2018, *ApJS*, **239**, 18
 Ai, Y. L., Yuan, W., Zhou, H. Y., et al. 2010, *ApJL*, **716**, L31
 Alexander, T. 1997, in *Astrophysics and Space Science Library*, Vol. 218, *Astronomical Time Series*, ed. D. Maoz, A. Sternberg, & E. M. Leibowitz (Dordrecht: Kluwer), 163
 Antonucci, R. 1993, *ARA&A*, **31**, 473
 Antonucci, R. R. J., & Miller, J. S. 1985, *ApJ*, **297**, 621
 Barth, A. J., Bennert, V. N., Canalizo, G., et al. 2015, *ApJS*, **217**, 26
 Bentz, M. C., Denney, K. D., Grier, C. J., et al. 2013, *ApJ*, **767**, 149
 Bianchi, S., Antonucci, R., Capetti, A., et al. 2019, *MNRAS*, **488**, L1
 Blandford, R. D., & McKee, C. F. 1982, *ApJ*, **255**, 419
 Boroson, T. A., & Green, R. F. 1992, *ApJS*, **80**, 109
 Bruhweiler, F., & Vermer, E. 2008, *ApJ*, **675**, 83
 Burgh, E. B., Nordsieck, K. H., Kobulnicky, H. A., et al. 2003, *Proc. SPIE*, **4841**, 1463
 Chelouche, D., Pozo-Núñez, F., & Zucker, S. 2017, *ApJ*, **844**, 146
 Czerny, B. 2019, *OAsT*, **28**, 200
 Czerny, B., Hryniewicz, K., Maity, I., et al. 2013, *A&A*, **556**, A97
 Czerny, B., Olejak, A., Rałowski, M., et al. 2019, *ApJ*, **880**, 46
 Czerny, B., Martínez-Aldama, M. L., Wojtkowska, G., et al. 2020, arXiv:2011.12375
 Dehghanian, M., Ferland, G. J., Peterson, B. M., et al. 2019, *ApJL*, **882**, L30
 Diehl, H. T., Neilsen, E., Gruendl, R. A., et al. 2018, *Proc. SPIE*, **10704**, 107040D
 Dong, X.-B., Wang, J.-G., Ho, L. C., et al. 2011, *ApJ*, **736**, 86
 Du, P., Hu, C., Lu, K.-X., et al. 2015, *ApJ*, **806**, 22
 Du, P., Lu, K.-X., Zhang, Z.-X., et al. 2016, *ApJ*, **825**, 126
 Du, P., & Wang, J.-M. 2019, *ApJ*, **886**, 42
 Du, P., Zhang, Z.-X., Wang, K., et al. 2018, *ApJ*, **856**, 6
 Eckart, A., Hüttemann, A., Kiefer, C., et al. 2017, *FoPh*, **47**, 553
 Edelson, R. A., & Krolik, J. H. 1988, *ApJ*, **333**, 646
 Elitzur, M., & Ho, L. C. 2009, *ApJL*, **701**, L91
 Ferland, G. J., Chatzikos, M., Guzmán, F., et al. 2017, *RMxAA*, **53**, 385
 Fonseca Alvarez, G., Trump, J. R., Homayouni, Y., et al. 2020, *ApJ*, **899**, 73
 Forster, K., Green, P. J., Aldcroft, T. L., et al. 2001, *ApJS*, **134**, 35
 Gaskell, C. M. 2009, *NewAR*, **53**, 140
 Genzel, R., Eisenhauer, F., & Gillessen, S. 2010, *RvMP*, **82**, 3121
 Goad, M. R., Koratkar, A. P., Axon, D. J., Korista, K. T., & O'Brien, P. T. 1999, *ApJL*, **512**, L95
 Grier, C. J., Trump, J. R., Shen, Y., et al. 2017, *ApJ*, **851**, 21
 Guo, H., Shen, Y., He, Z., et al. 2020, *ApJ*, **888**, 58
 Haas, M., Chini, R., Ramolla, M., et al. 2011, *A&A*, **535**, A73
 Homayouni, Y., Trump, J. R., Grier, C. J., et al. 2020, *ApJ*, **901**, 55
 Hoormann, J. K., Martini, P., Davis, T. M., et al. 2019, *MNRAS*, **487**, 3650
 Horne, K., De Rosa, G., Peterson, B. M., et al. 2021, *ApJ*, **907**, 76
 Hu, C., Li, S.-S., Guo, W.-J., et al. 2020, *ApJ*, **905**, 75
 Hunter, J. D. 2007, *CSE*, **9**, 90
 Ichikawa, K., Packham, C., Ramos Almeida, C., et al. 2015, *ApJ*, **803**, 57
 Kaspi, S., Smith, P. S., Netzer, H., et al. 2000, *ApJ*, **533**, 631
 Kelly, B. C., Bechtold, J., & Siemiginowska, A. 2009, *ApJ*, **698**, 895
 Kobulnicky, H. A., Nordsieck, K. H., Burgh, E. B., et al. 2003, *Proc. SPIE*, **4841**, 1634
 Kovačević-Dojčinović, J., & Popović, L. Č. 2015, *ApJS*, **221**, 35
 Kozłowski, S. 2015, *AcA*, **65**, 251
 Kozłowski, S. 2016, *ApJ*, **826**, 118
 Kozłowski, S., Kochanek, C. S., Udalski, A., et al. 2010, *ApJ*, **708**, 927
 Kozłowski, M., Czerny, S., Panda, B., Hryniewicz, S., & Śniegowska, K. 2020, *ApJ*, **900**, 64
 Lawrence, A., & Elvis, M. 2010, *ApJ*, **714**, 561
 Li, J. I.-H., Shen, Y., Brandt, W. N., et al. 2019, *ApJ*, **884**, 119
 MacLeod, C. L., Ivezić, Ž., Kochanek, C. S., et al. 2010, *ApJ*, **721**, 1014
 Martínez-Aldama, M. L., Czerny, B., Kawka, D., et al. 2019, *ApJ*, **883**, 170
 Martínez-Aldama, M. L., Zajaček, M., Czerny, B., & Panda, S. 2020, *ApJ*, **903**, 86
 Marziani, P., & Sulentic, J. W. 2014, *MNRAS*, **442**, 1211
 Marziani, P., Sulentic, J. W., Stirpe, G. M., Zamfir, S., & Calvani, M. 2009, *A&A*, **495**, 83
 Max-Moerbeck, W., Richards, J. L., Hovatta, T., et al. 2014, *MNRAS*, **445**, 437
 Mejía-Restrepo, J. E., Lira, P., Netzer, H., Trakhtenbrot, B., & Capellupo, D. M. 2018, *NatAs*, **2**, 63
 Naddaf, M.-H., Czerny, B., & Szczerba, R. 2021, arXiv:2102.00336
 Netzer, H. 2019, *MNRAS*, **488**, 5185
 Oliphant, T. 2015, *NumPy: A Guide to NumPy* (2nd ed.; USA: CreateSpace Independent Publishing Platform), <http://www.numpy.org/>
 Panda, S., Martínez-Aldama, M. L., & Zajaček, M. 2019, *FoPh*, **6**, 75
 Pedregosa, F., Varoquaux, G., Gramfort, A., et al. 2011, *JMLR*, **12**, 2825
 Peterson, B. M., Ferrarese, L., Gilbert, K. M., et al. 2004, *ApJ*, **613**, 682
 Peterson, B. M., & Horne, K. 2004, *AN*, **325**, 248
 Peterson, B. M., Wanders, I., Horne, K., et al. 1998, *PASP*, **110**, 660
 Planck Collaboration, Aghanim, N., Akrami, Y., et al. 2020, *A&A*, **641**, A6
 Popović, L. Č. 2012, *NewAR*, **56**, 74
 Popović, L. Č. 2020, *OAsT*, **29**, 1
 Popović, L. Č., Kovačević-Dojčinović, J., & Marčeta-Mand, S. 2019, *MNRAS*, **484**, 3180
 Ramolla, M., Drass, H., Lemke, R., et al. 2013, *AN*, **334**, 1115
 Robertson, D. R. S., Gallo, L. C., Zoghbi, A., & Fabian, A. C. 2015, *MNRAS*, **453**, 3455
 Sabra, B. M., Shields, J. C., Ho, L. C., Barth, A. J., & Filippenko, A. V. 2003, *ApJ*, **584**, 164
 Schmidt, M. 1963, *Natur*, **197**, 1040
 Seabold, S., & Perktold, J. 2010, in *Proc. IX Python in Science Conf.* 92, ed. S. van der Walt & J. Millman (Austin, TX: SciPy)
 Seyfert, C. K. 1943, *ApJ*, **97**, 28
 Shen, Y., Brandt, W. N., Dawson, K. S., et al. 2015, *ApJS*, **216**, 4
 Shen, Y., Hall, P. B., Horne, K., et al. 2019, *ApJS*, **241**, 34
 Shen, Y., & Ho, L. C. 2014, *Natur*, **513**, 210
 Smith, M. P., Nordsieck, K. H., Burgh, E. B., et al. 2006, *Proc. SPIE*, **6269**, 62692A
 Średzińska, J., Czerny, B., Hryniewicz, K., et al. 2017, *A&A*, **601**, A32
 Sulentic, J. W., Marziani, P., & Dultzin-Hacyan, D. 2000, *ARA&A*, **38**, 521
 Sun, M., Grier, C. J., & Peterson, B. M. 2018, *PyCCF: Python Cross Correlation Function for reverberation mapping studies*, Astrophysics Source Code Library, ascl:1805.032
 Sun, M., Trump, J. R., Shen, Y., et al. 2015, *ApJ*, **811**, 42
 Timmer, J., & Koenig, M. 1995, *A&A*, **300**, 707

THE ASTROPHYSICAL JOURNAL, 912:10 (25pp), 2021 May 1

Zajaček et al.

- Tody, D. 1986, [Proc. SPIE](#), **627**, 733
- Tody, D. 1993, in ASP Conf. Ser. 52, IRAF in the Nineties, ed. R. J. Hanisch, R. J. V. Brissenden, & J. Barnes (San Francisco, CA: ASP), 173
- Udalski, A., Szymański, M. K., & Szymański, G. 2015, [AcA](#), **65**, 1
- Urry, C. M., & Padovani, P. 1995, [PASP](#), **107**, 803
- Vanden Berk, D. E., Richards, G. T., Bauer, A., et al. 2001, [AJ](#), **122**, 549
- Wang, J.-M., Du, P., Hu, C., et al. 2014, [ApJ](#), **793**, 108
- Wang, S., Shen, Y., Jiang, L., et al. 2019, [ApJ](#), **882**, 4
- Watson, D., Denney, K. D., Vestergaard, M., & Davis, T. M. 2011, [ApJL](#), **740**, L49
- Wisotzki, L., Christlieb, N., Bade, N., et al. 2000, [A&A](#), **358**, 77
- Woltjer, L. 1959, [ApJ](#), **130**, 38
- Woo, J.-H. 2008, [AJ](#), **135**, 1849
- Woo, J.-H., Yoon, Y., Park, S., Park, D., & Kim, S. C. 2015, [ApJ](#), **801**, 38
- Yang, Q., Shen, Y., Chen, Y.-C., et al. 2020, [MNRAS](#), **493**, 5773
- Yu, L.-M., Zhao, B.-X., Bian, W.-H., Wang, C., & Ge, X. 2020a, [MNRAS](#), **491**, 5881
- Yu, Z., Kochanek, C. S., Peterson, B. M., et al. 2020b, [MNRAS](#), **491**, 6045
- Zajaček, M., Czerny, B., Martínez-Aldama, M. L., & Karas, V. 2019, [AN](#), **340**, 577
- Zajaček, M., Czerny, B., Martínez-Aldama, M. L., et al. 2020, [ApJ](#), **896**, 146
- Zajaček, M., Tursunov, A., Eckart, A., & Britzen, S. 2018, [MNRAS](#), **480**, 4408
- Zhu, D., Sun, M., & Wang, T. 2017, [ApJ](#), **843**, 30
- Zu, Y., Kochanek, C. S., Kozłowski, S., & Peterson, B. M. 2016, [ApJ](#), **819**, 122
- Zu, Y., Kochanek, C. S., Kozłowski, S., & Udalski, A. 2013, [ApJ](#), **765**, 106
- Zu, Y., Kochanek, C. S., & Peterson, B. M. 2011, [ApJ](#), **735**, 80

Paper 5: Enhanced Doppler Beaming

Most spiral and elliptical galaxies with the total stellar mass larger than $10^8 M_{\odot}$ host dense nuclear star clusters in their centers (Neumayer et al. 2020). The Galactic center is the only galactic nucleus where one can study the motion and variability of individual stars as well as the properties of the nuclear star cluster as a whole. The closest stars to the supermassive black hole Sgr A*, so-called S stars, move at the velocities of several thousand km/s. During the last 30 years, several of them have already completed at least one orbit around the supermassive black hole. In this sense, these are special or rather extreme-mass binary systems, where the heavier component is the supermassive black hole of $4 \times 10^6 M_{\odot}$.

When being close enough, the S stars can move around the common center of mass, which is close to the supermassive black hole, at the fraction of a light speed. More specifically, to reach $\sim 3\%$ of the light speed, the star needs to be at ~ 44 AU or ~ 1100 gravitational radii. When the star is located at ~ 4 AU or 100 gravitational radii, it already reaches as much as $\sim 10\%$ of the light speed. There are stellar candidates in the S cluster that can reach such a fraction of the light speed close to their pericenters (Peißker et al. 2020a, 2022).

Rafikov (2020) suggested that due to high velocities, the stellar light is expected to be Doppler-boosted, hence the star would appear temporarily brighter or fainter in a narrow infrared photometry band. The variability amplitude due to Doppler boosting for the S2 star is about 2%, while for some of the newly discovered S stars (S62 and S4714), it can reach $\sim 6\%$.

In this paper, we investigated the possibility that the broad-band continuum spectral energy distribution of S cluster objects does not necessarily have to correspond to main-sequence stars (positive spectral indices close to $\alpha = 2$), but also to colder objects (dust-enshrouded objects, brown dwarfs) or pulsars with generally negative spectral indices in the infrared domain. In that case, the photometric variability is significantly enhanced by a factor of ~ 4 for pulsars and by an order of magnitude for dust-enshrouded stars, which can reach the variability amplitude due to Doppler beaming of $\sim 10\%$. One of the main applications, given that future instruments have a sufficient photometric precision, is to infer the nature of S cluster objects in case their orbits have already been precisely determined. The photometric variability amplitude can thus provide important clues whether the object is a main-sequence star, a dust-enshrouded object, or an exotic pulsar.

Credit: Zajaček (2021), ApJ 915, 111. Reproduced with permission ©AAS.



Enhanced Doppler Beaming for Dust-enshrouded Objects and Pulsars in the Galactic Center

Michal Zajaček^{1,2,3} ¹ Center for Theoretical Physics, Polish Academy of Sciences, Al. Lotników 32/46, 02-668 Warsaw, Poland; zajacek@cft.edu.pl
² Department of Theoretical Physics and Astrophysics, Faculty of Science, Masaryk University, Kotlářská 2, 611 37 Brno, Czech Republic
³ L. Novomeského 4, 901 01 Malacky, Slovakia

Received 2021 April 5; revised 2021 May 7; accepted 2021 May 21; published 2021 July 15

Abstract

Stars within the innermost part of the nuclear star cluster can reach orbital velocities up to a few percent of the light speed. As analyzed by Rafikov, Doppler boosting of stellar light may be of relevance at the pericenter of stellar orbits, especially with the upcoming high-precision photometry in the near- and mid-infrared bands. Here we analyze the previously neglected effect of the infrared spectral index of monitored objects on the Doppler-boosted continuum emission in a narrow photometric band. In contrast to main-sequence stars, the detected compact infrared-excess dust-enshrouded objects have an enhanced Doppler-boosting effect by as much as an order of magnitude, with the variability amplitude of the order of 10% for the most eccentric orbits. In a similar way, pulsars dominated by nonthermal synchrotron emission are also expected to exhibit a stronger Doppler-boosted signal by a factor of at least 4 in comparison with canonical S stars. In case the stellar orbit is robustly determined, the relative flux variation can thus provide hints about the nature of the objects. For extended dust-enshrouded objects, such as G1, that are variable due to tidal, ellipsoidal, bow-shock, and irradiation effects, the subtraction of the expected Doppler-boosting variations will help to better comprehend their internal physics. In addition, the relative flux variability due to higher-order relativistic effects is also modified for different negative spectral indices in a way that it can obtain both positive and negative values with the relative variability of the order of 1%.

Unified Astronomy Thesaurus concepts: Galactic center (565); Stellar photometry (1620); Relativistic binary stars (1386)

1. Introduction

The Galactic center nuclear star cluster (NSC) is a unique dynamical testbed, where it is possible to monitor the motion of stars in the potential of the compact radio source Sgr A* (Balick & Brown 1974), which is associated with the supermassive black hole of $\sim 4 \times 10^6 M_\odot$ (SMBH; Genzel et al. 2010; Schödel et al. 2014; Eckart et al. 2017). In particular, the innermost part of the NSC, the S cluster, contains several tens of bright B-type stars with inferred orbits (Ghez et al. 2005; Gillessen et al. 2009, 2017; Ali et al. 2020), which has been utilized for tests of gravitational theories in the strong-field regime (Hees et al. 2017; Parsa et al. 2017) as well as for N -body cluster dynamics in the potential dominated by the SMBH (see, e.g., Merritt 2013, and references therein).

For the S2 star on a highly elliptical orbit with the period of ~ 16 yr, the combined general relativistic gravitational redshift and transverse Doppler shift of $\sim 200 \text{ km s}^{-1}/c$ was measured using its spectral absorption lines (Gravity Collaboration et al. 2018; Do et al. 2019b). The general theory of relativity was also confirmed to a high precision by the measurement of its Schwarzschild precession of $\delta\phi \sim 12'$ per orbital period (Parsa et al. 2017; Gravity Collaboration et al. 2020).

Recently, Rafikov (2020) analyzed the effect of nonrelativistic and relativistic Doppler boosting on the detected photometric flux density of S stars. The study was inspired by the analysis of the photometric light curve of the S2 star in L' -band (Hosseini et al. 2020) that found no intrinsic variability at the level of $\sim 2.5\%$. Rafikov (2020) concluded that the Doppler boosting of the continuum stellar light is especially of relevance for stars that reach the pericenter velocities of a few percent of the light speed. The amplitude of the relative flux

change due to the Doppler beaming is $\sim 2.0\%$ for the S2 star ($\Delta m \sim 0.02$ mag), and reaches $\sim 5.6\%$ for the newly analyzed S62 ($\Delta m \sim 0.06$ mag) and $\sim 6.4\%$ for the recently discovered S4714 star ($\Delta m \sim 0.07$ mag) (Peißker et al. 2020a, 2020b). This is at the sensitivity limit of ~ 0.01 mag of current infrared adaptive optics instruments. The detection and the timing of the Doppler beaming for these sources is achievable with an order of magnitude improved sensitivity of 30+ meter telescopes (Do et al. 2019a; Hosseini et al. 2020). The higher-order corrections to the Doppler-beamed stellar light due to general relativistic redshift and transverse Doppler shift have the amplitude of the relative flux change at the level of 0.7×10^{-3} mag for S2, $\sim 2.6 \times 10^{-3}$ mag for S62, and $\sim 2.6 \times 10^{-3}$ mag for S4714, which is close to the sensitivity limit of upcoming infrared instruments. However, they will hardly be detectable due to stellar crowding and confusion in the innermost parts of the NSC (Rafikov 2020). In principle, if the Doppler boosting effect and its temporal profile is detected, it could be utilized to verify and constrain orbital elements in case the photometry and the spectroscopy of the source is confused (Rafikov 2020).

However, the overall uncertainty of the infrared spectral index of the Galactic center sources was not quantitatively analyzed by Rafikov (2020). Since their study focused on B-type stars, such as S2, fixing the spectral index to $\alpha = 2$ (using the convention for the radiation intensity as $I_\nu \propto \nu^{+\alpha}$) can be justified in the infrared domain. However, the S cluster also hosts several dust-enshrouded objects with a negative spectral index in the near-infrared domain due to the dust emission with the effective temperature of ~ 500 – 600 K (Ciurlo et al. 2020; Peißker et al. 2020c). In addition, the emission of compact remnants, in particular energetic pulsars,

is expected to be dominated by optically thin synchrotron emission in infrared bands with $\alpha \sim -1$ (see, e.g., Zajaček et al. 2017, and references therein). Future surveys using 30 + meter telescopes will likely reveal cold brown dwarfs with infrared spectral properties similar to dusty objects (Do et al. 2019a). Since the relative flux change due to the Doppler boosting is $(\Delta F/F_{\text{em}})_1 \approx (\alpha - 3)v_{\text{LOS}}/c$ (Rafikov 2020), where v_{LOS} is a line-of-sight velocity (positive for receding objects), dust-enshrouded objects as well as pulsars are expected to exhibit a larger variability due to the beaming effect by at least a factor of a few in comparison with main-sequence stars.

In this study, we consider different negative values of a stellar spectral index in the infrared domain to quantify the relative flux variability due to the Doppler boosting. Since the S cluster hosts different types of objects, we focus on the enhanced variability with respect to main-sequence stars.

The paper is structured as follows. In Section 2, we introduce the basic formalism of the continuum Doppler boosting and compare the relative flux variability among dust-enshrouded objects, pulsars, and main-sequence stars. Subsequently, we evaluate the relative variability due to the Doppler boosting for four monitored dust-enshrouded objects in Section 3 to demonstrate the importance of the spectral index for the actual objects in the S cluster. In Section 4, we discuss other internal processes for extended dust-enshrouded objects that can lead to significant continuum variations. We also consider the potential detection of longer beaming flares and dimming events. Finally, we conclude in Section 5.

2. Doppler Boosting of Stellar Light: Effect of Spectral Index

Stars orbiting the SMBH in the Galactic center can reach pericenter distances of a few 1000 gravitational radii (r_g), reaching velocities of a few percent of the light speed. Two stars, S62 and S4714, are candidates to reach only a few 100 r_g with pericenter velocities up to $\sim 10\%$ of the light speed (Peißker et al. 2020b). As stars approach the SMBH, they are subject to time dilation, light aberration, and the frequency shift due to a stellar motion and a general relativistic redshift as well as a special relativistic transverse Doppler shift. All of these effects add up and lead to the Doppler boosting of stellar emission (Zucker et al. 2006, 2007; Rafikov 2020) that can make a star appear both fainter and brighter depending on the line-of-sight velocity.

The flux density of a star as detected by an observer on the Earth in a narrow frequency band $w(\nu)$ can be expressed as a power-law function of the ratio of observed and emitted frequencies ν_{obs} and ν_{em} , respectively, as $F_{\text{obs}} = F_{\text{em}}(\nu_{\text{obs}}/\nu_{\text{em}})^{3-\alpha}$, where $F_{\text{em}} = \int_0^\infty I_{\text{em}}(\nu)w(\nu)d\nu$ is the emitted flux density.

As shown by Rafikov (2020), the relative flux variability due to $\mathcal{O}(v/c)$ terms (nonrelativistic Doppler beaming) for $v \ll c$ can be expressed as,

$$\left(\frac{\Delta F}{F_{\text{em}}}\right)_1 \approx (\alpha - 3) \frac{v_{\text{LOS}}}{c}. \quad (1)$$

If we consider main-sequence B-type stars with $\alpha \sim 2$, in particular S2, the variability amplitude is 2.13% and 2.07% in K (2.2 μm) and L (3.8 μm) bands, respectively, see Table 1. More exotic objects within the S cluster, namely monitored

dusty objects (Ciurlo et al. 2020; Peißker et al. 2020c) as well as putative pulsars (Pfahl & Loeb 2004; Wharton et al. 2012), have a broadband spectral energy distribution (SED) with the negative spectral index $\alpha < 0$. Hence, the variability amplitude due to the Doppler boosting will be increased for them as the factor in Equation (1) is at least ~ 3 in absolute terms while for main-sequence stars with $\alpha \sim 2$ it is effectively equal to unity. As soon as more sensitive near- and mid-infrared detectors mounted at 30 + telescopes are operational, it will be possible to probe the stellar initial mass function toward the low-mass end where brown dwarfs of spectral type L and T are positioned (Do et al. 2019a). Old brown dwarfs have effective temperatures $\lesssim 1000$ K (Basri 2000) and their SED slopes are thus comparable to dust-enshrouded objects and therefore the presented analysis is relevant for them as well.

We take into account different negative values of the spectral index in the infrared K and L bands. First, we take into account the SED of dust-enshrouded objects D2, D23, D3, and DSO/G2 as analyzed by Peißker et al. (2020c). Their SEDs are plotted in Figure 1. In most cases, for D2, D23, and D3 sources, the broadband SED can be described well as a one-component blackbody spectrum with the effective temperature of ~ 500 K and the radius of ~ 1 au. For the DSO/G2 source, the two-component blackbody fit is preferred since at the shortest wavelengths the stellar emission appears to dominate, see Figure 1 for the spectral decomposition and Peißker et al. (2020c) for a detailed discussion. The dominant contribution in K , L , and M bands is due to the optically thick dusty envelope with the temperature of $T \sim 500$ K. The corresponding spectral indices between K and L bands as well as L and M bands— α_{KL} and α_{LM} —are listed in Table 1. The mean values for the four studied dust-enshrouded objects are $\bar{\alpha}_{\text{KL}} = -6.31 \pm 1.23$ and $\bar{\alpha}_{\text{LM}} = -4.30 \pm 2.75$. We use these average values for a representative case of a dust-enshrouded object orbiting the SMBH on the S2 orbit, for which we obtain the variability amplitude of 18.16% and 14.24% in K and L bands, respectively. Hence, the variability due to the Doppler boosting is increased by a factor of ~ 9 and ~ 7 in K and L bands, respectively. If we define the characteristic half-maximum timescale $\tau_{1/2}$ between the epochs where the relative flux variability reaches half of the maximum value, we obtain $\tau_{1/2} = 2.8$ yr independent of the spectral index, which by definition affects only the amplitude of the relative flux variability.

Furthermore, the higher-order corrections to the Doppler boosting due to $\mathcal{O}(v^2/c^2)$ terms (gravitational redshift and the transverse Doppler shift) are also affected by the spectral index. If we consider the relative flux variability $\Delta F/F_{\text{em}}$ up to $\mathcal{O}(v^2/c^2)$ terms, then we get (Rafikov 2020),

$$\begin{aligned} \frac{\Delta F}{F_{\text{em}}} &= \frac{F_{\text{obs}} - F_{\text{em}}}{F_{\text{em}}} \\ &= \left(\frac{1 + \frac{v_{\text{LOS}}}{c}}{1 + (\phi_{\text{BH}} - v^2/2)/c^2} \right)^{\alpha-3} - 1, \end{aligned} \quad (2)$$

where $\phi_{\text{BH}} = -GM_*/r$ is the gravitational potential of the SMBH. Using Equations (2) and (1), the higher-order corrections to the first-order Doppler boosting can be calculated as $(\Delta F/F_{\text{em}})_2 = \Delta F/F_{\text{em}} - (\Delta F/F_{\text{em}})_1$. In contrast to $\alpha = 2$ considered by Rafikov (2020), $(\Delta F/F_{\text{em}})_2$ can reach positive

Table 1
Near-infrared Spectral Indices between K and L Bands and L and M Bands for the Selected Infrared-excess Sources Analyzed by Peißker et al. (2020c)

Source	α_{KL}	α_{LM}	$\delta(\Delta F/F_{em})_1^{KL}$ [%]	$\delta(\Delta F/F_{em})_1^{LM}$ [%]	$\delta(\Delta F/F_{em})_2^{KL}$ [%]	$\delta(\Delta F/F_{em})_2^{LM}$ [%]
D2	-6.02	-2.64	3.95	2.47	0.026	0.011
D23	-5.69	-8.59	3.65	4.86	0.019	0.033
D3	-8.38	-1.32	4.30	1.63	0.032	0.0056
DSO/G2	-5.15	-4.65	16.79	15.76	0.66	0.60
G1	(-9.07, 1.17)	(-5.50, 0.89)	18.33	12.51	1.02	0.49
S2	+1.91	+1.94	2.13	2.07	0.066	0.064
Pulsar (S2 orbit)	-1.00	-1.00	7.80	7.80	0.26	0.26
Dust-enshrouded object (S2 orbit)	-6.31	-4.30	18.16	14.24	0.98	0.65
Dust-enshrouded object (S62 orbit)	-6.31	-4.30	60.27	47.26	12.25	7.86
Dust-enshrouded object (S4714 orbit)	-6.31	-4.30	59.15	46.38	12.56	7.61

Note. For comparison with main-sequence stars, we also include the S2 star whose blackbody SED was calculated using the radius and the effective temperature from Habibi et al. (2017). We also modified the spectral index of S2 to demonstrate the impact on the beamed flux density for a dust-enshrouded object (slopes determined as mean values of four studied objects: D2, D23, D3, and DSO/G2) as well as a pulsar. In a similar way, we also estimated the Doppler beaming for putative dust-enshrouded objects on S62- as well as S4714-like orbits. The amplitudes of relative flux variability due to $\mathcal{O}(v/c)$ terms, $\delta(\Delta F/F_{em})_1$, as well as $\mathcal{O}(v^2/c^2)$ terms, $\delta(\Delta F/F_{em})_2$, are calculated for both K and L infrared bands.

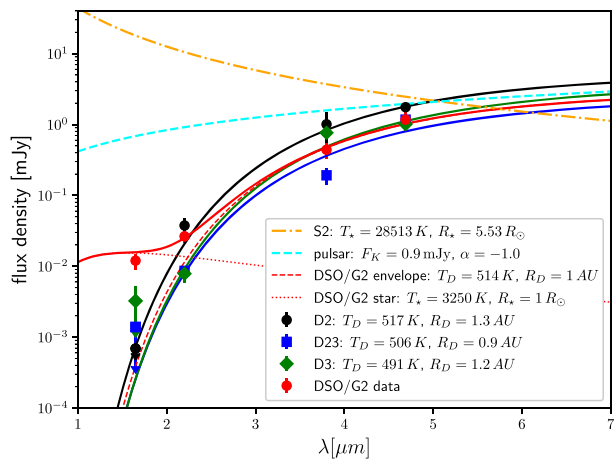


Figure 1. Representative spectral energy distributions (SED) of four dusty sources in the S cluster (D2, D23, D3, and DSO/G2) studied in Peißker et al. (2020c), see the legend. We include measured flux densities in H , K , L , and M bands as well as best-fit blackbody SEDs characterized by the temperature and the radius of the optically thick photosphere. For the DSO/G2 source, a two-component blackbody fit is preferred consisting of a stellar blackbody emission as well as a more extended dusty envelope. Hot main-sequence B-type stars in the S cluster are represented by the S2 star (dotted-dashed orange line; Habibi et al. 2017). A putative pulsar, whose energetic analog is PSR B0540-69 (Mignani et al. 2012), with the spectral slope $\alpha = -1.0$ is depicted by a cyan dashed line. Spectral slopes between K and L bands as well as L and M bands are listed in Table 1 for selected sources.

values (negative magnitude change), which is unique for exotic objects within the S cluster, such as dusty objects, pulsars or brown dwarfs. The overall amplitude of the relative flux variability is also increased. For $\bar{\alpha}_{KL} = -6.31$ on the S2 orbit, we obtain $(\Delta F/F_{em})_2 = 0.98\%$, while for $\bar{\alpha}_{LM} = -4.30$, we get $(\Delta F/F_{em})_2 = 0.65\%$.

In Figure 2, we show the line-of-sight velocity, v_{LOS} (top panel), the relative flux variability due to the Doppler boosting $(\Delta F/F_{em})_1$ (middle panel) for different spectral indices, and the associated higher-order relative flux variability $(\Delta F/F_{em})_2$ as a function of time for the exemplary orbit of the S2 star.

Finally, we also consider a putative case of an energetic pulsar orbiting within the S cluster, which could mimic near-infrared excess sources in terms of the broadband SED

(Zajaček et al. 2017). As an analog, we adopt the energetics of PSR B0540-69 that has a prominent near-infrared emission (Mignani et al. 2012) with the K -band luminosity of $L_K \approx 10^{34}$ erg s $^{-1}$. For the spectral index, we adopt $\alpha = -1$ that is typical of synchrotron-dominated young pulsars (Mignani et al. 2012). The SED of such a putative pulsar is shown in Figure 1. The amplitude of the relative flux variability is 7.80%, hence by about a factor of 4 larger than for the main-sequence star. The temporal evolution of $(\Delta F/F_{em})_1$ is shown among other cases in Figure 2. The amplitude of the relative variability due to higher-order corrections is also increased by a factor of $\sim 4\%$ to $\sim 0.26\%$. The flux density minimum of $(\Delta F/F_{em})_2$ is at $+2.63 \times 10^{-3}$ magnitudes, while the maximum is at -0.23×10^{-3} magnitudes. The characteristic amplitudes of the Doppler boosting for both the first- and the second-order effects in K and L bands are summarized in Table 1 for the case of a main-sequence star, a dust-enshrouded object, as well as a pulsar assuming the same S2 orbit.

3. Results

In this section, we describe the analysis of the relative flux variability due to Doppler beaming for monitored dust-enshrouded objects within the S cluster, specifically D2, D23, D3, and DSO/G2 objects. We adopt the infrared flux densities as determined by Peißker et al. (2020c). The SEDs of these sources and the corresponding blackbody fits are shown in Figure 1. All of these sources are on long-period orbits with periods of a few hundred years. Therefore the detection of a significant Doppler-boosted signal within the observational duration of a few years is unlikely with the upcoming monitoring or in archival data. However, we estimate the Doppler beaming effect for these sources to illustrate that the overall photometric amplitude of relative variations can be comparable to or even exceed the values expected for a short-period star S2 on a tight orbit. This is especially relevant in case such an infrared-excess source will be approaching or going through its pericenter during the future more sensitive photometric monitoring, such as previous G1 and DSO/G2 sources (Witzel et al. 2014; Valencia-S. et al. 2015).

Below we list relevant values of $(\Delta F/F_{em})_1$, $(\Delta F/F_{em})_2$ and their amplitudes for individual objects.

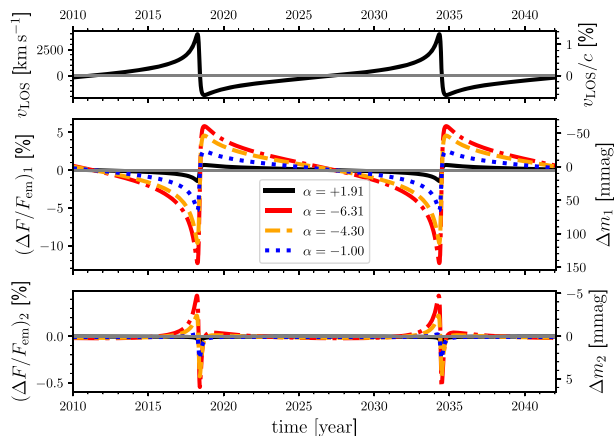


Figure 2. Effect of the near-infrared spectral slope on the Doppler-boosting effect of stellar light calculated for the star on the S2 orbit. Top panel: a line-of-sight (LOS) velocity (in km s^{-1}) as a function of time. The right y-axis shows the LOS velocity in the percent of the light speed. Middle panel: the Doppler boosting due to the leading $\mathcal{O}(v/c)$ term (nonrelativistic) expressed as the relative flux change in percent. Different lines stand for different types of stellar objects present in the S cluster: B-type hot star (black solid line; $\alpha = +1.91$), a dust-enshrouded NIR-excess source observed in K band (red dotted-dashed line; $\alpha_{KL} = -6.31$), a dust-enshrouded NIR-excess source observed in L band (orange dashed line; $\alpha_{LM} = -4.30$), and a pulsar (blue dotted line; $\alpha = -1.00$). The y-axis on the right shows the relative flux change in millimagnitudes (mmag). Bottom panel: the relative flux change in percent due to $\mathcal{O}(v^2/c^2)$ terms (gravitational redshift and transverse Doppler shift). The y-axis on the right shows the relative change in millimagnitudes (mmag).

D2. The source is on a mildly eccentric orbit with the eccentricity of $e \sim 0.15$ and the semimajor axis of $a \sim 30$ mpc. The pericenter distance is $r_p \sim 130,000 r_g$ and the corresponding velocity is $v_p \sim 900 \text{ km s}^{-1}$. Therefore the resulting continuum variations are rather small, with the amplitudes $\delta(\Delta F/F_{em})_1^{KL} = 3.95\%$ and $\delta(\Delta F/F_{em})_1^{LM} = 2.47\%$ for the first-order Doppler boosting. The amplitudes of the higher-order flux variations in the near-infrared K and L bands are $\delta(\Delta F/F_{em})_2^{KL} = 0.026\%$ and $\delta(\Delta F/F_{em})_2^{LM} = 0.011\%$, respectively.

D23. This dusty source is the least eccentric from the selected sources, with $e = 0.06 \pm 0.01$. Orbiting the SMBH with the long period of ~ 431 yr, its pericenter distance is as much as $\sim 212,000 r_g$ with the corresponding velocity of $\sim 670 \text{ km s}^{-1}$. The first-order Doppler-boosting flux variations have the amplitude of 3.65% and 4.86% in K and L bands, respectively, while the relativistic corrections are 2 orders of magnitude smaller, $\delta(\Delta F/F_{em})_2^{KL} = 0.019\%$ and $\delta(\Delta F/F_{em})_2^{LM} = 0.033\%$.

D3. This dusty source is on a mildly eccentric orbit with $e = 0.24 \pm 0.02$ and the semimajor axis of $a = 35.20 \pm 0.01$ mpc (orbital period of ~ 306 yr). Its smallest distance to SgrA* is $\sim 137,000 r_g$ and the corresponding maximum velocity is $\sim 904 \text{ km s}^{-1}$. Because of the measured steep slope between K and L bands, implying $\alpha \sim -8.4$, the amplitude of the first-order flux variability is $\delta(\Delta F/F_{em})_1^{KL} = 4.30\%$. Between L and M bands, the SED becomes flatter, which results in the smaller amplitude of $\delta(\Delta F/F_{em})_1^{LM} = 1.63\%$. The higher-order relativistic corrections are again at least 2 orders of magnitude smaller, with amplitudes of 0.032% and 0.0056% in K and L bands, respectively.

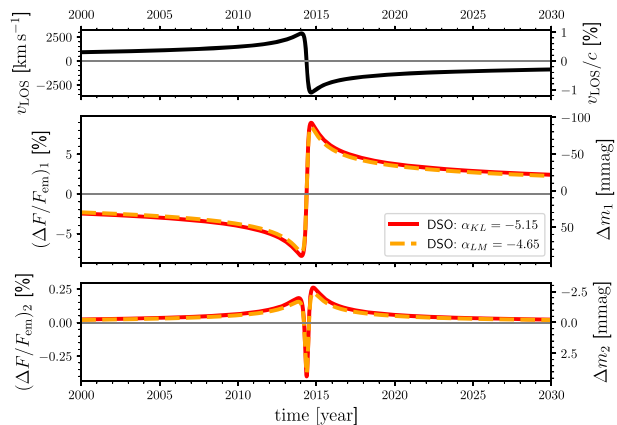


Figure 3. The same panels as in Figure 2 for the infrared-excess source DSO/G2. In the middle and the bottom panels, we plot the relative flux variability separately for the spectral index between K and L bands (red solid line) and for the spectral index between L and M bands (orange dashed line).

DSO/G2. The most eccentric source among the recently monitored dusty objects is DSO/G2 with $e = 0.976$ (Valencia-S, et al. 2015). Having a semimajor axis of $a \sim 33$ mpc, it went through the pericenter of its orbit around 2014.39, with the smallest distance of $r_p \sim 4042 r_g$ and the maximum orbital velocity of $\sim 6600 \text{ km s}^{-1}$. Given the high eccentricity and the resulting small pericenter distance, the amplitudes of the relative flux variability due to the leading-order Doppler beaming are the largest among the monitored infrared-excess sources, specifically $\delta(\Delta F/F_{em})_1^{KL} = 16.79\%$ (0.182 mag) and $\delta(\Delta F/F_{em})_1^{LM} = 15.76\%$ (0.171 mag). The amplitudes of the second-order relativistic variations are at the level of $\sim 1\%$, $\delta(\Delta F/F_{em})_2^{KL} = 0.66\%$ and $\delta(\Delta F/F_{em})_2^{LM} = 0.60\%$. The relative flux variations are depicted in Figure 3 as functions of time for the epochs close to the pericenter. The changes at the level of ~ 0.2 mag are still challenging to detect in the crowded environment of the Galactic center. The L -band light curve of the DSO/G2 as analyzed by Witzel et al. (2014) is constant within the observational uncertainties that reach as much as ~ 0.5 mag. The mean value of the flux slightly increased close to the pericenter and then dropped; however, this cannot be claimed as significant (Witzel et al. 2014).

The compact dusty sources on highly eccentric orbits such as DSO/G2 provide the best prospects for detecting longer “beaming flares” or dimming events, i.e., the phases when the star is expected to appear brighter or fainter for at least several months. While for D2, D23, and D3 sources we obtain the half-maximum timescales of $\tau_{1/2} = 89, 143,$ and 111 yr, respectively, the DSO/G2 source has $\tau_{1/2} = 3.55$ yr, with the peak of $(\Delta F/F_{em})_1 \sim 8.4\% - 9.0\%$ (-0.088 and -0.093 mag, respectively) at ~ 2014.67 or ~ 3.36 months after reaching the pericenter.

We summarize the variability amplitudes $\delta(\Delta F/F_{em})_1$ and $\delta(\Delta F/F_{em})_2$ for the monitored dust-enshrouded objects in Table 1.

4. Discussion

We studied the effect of the infrared spectral index on the Doppler-beamed continuum emission of stars within the S cluster. The relative variability can be enhanced by a factor of a few up to an order of magnitude for negative values of the

THE ASTROPHYSICAL JOURNAL, 915:111 (7pp), 2021 July 10

spectral index, which is exhibited by observed dust-enshrouded objects as well as putative young pulsars and older brown dwarfs.

However, especially the extended dust-enshrouded objects are prone to an order of magnitude variation due to tidal, irradiation, bow-shock, and ellipsoidal effects. These will prevent the detection of the clear Doppler-beamed signal. On the other hand, the expected Doppler-beaming variations can be subtracted to study the internal processes of these sources in more detail. We will discuss some of those other internal effects in the upcoming subsection. Subsequently, we also mention the possibility of detection of beaming flares at the position of Sgr A* due to high-velocity dusty and other cold objects (brown dwarfs) as well as pulsars.

4.1. Internal Variations of Dust-enshrouded Objects

There is an ongoing debate concerning the source of the continuum emission of dust-enshrouded objects, some of which are spatially extended. Currently, they appear to be internally heated due to the presence of a stellar core (Witzel et al. 2017; Zajaček et al. 2017; Ciurlo et al. 2020; Peißker et al. 2020c). However, the contribution of an external irradiation cannot be excluded. Below we discuss several processes that can likely contribute to the internal photometric variations of these objects, in particular those that are extended beyond their corresponding tidal (Hill) radii. Subtraction of the expected flux density changes due to Doppler beaming, provided that the orbital trajectory is well constrained, is relevant for the further assessment of these effects.

- (a) *External irradiation.* Considering that there are $N_S \sim 100$ stars within the S cluster of radius $R_S \sim 1'' \sim 0.04$ pc, we obtain the mean stellar volume number density of $n_S \sim 4 \times 10^5 \text{ pc}^{-3}$. The mean distance of an S star from any dusty object thus is $\bar{d}_S = (n_S)^{-1/3} \sim 3000$ au. Assuming that there is an embedded star inside the dusty object, its flux is greater than the flux from an S star by a factor of

$$\frac{F_*}{F_S} = \left(\frac{T_*}{T_S}\right)^4 \left(\frac{R_*}{R_S}\right)^2 \left(\frac{\bar{d}_S}{R_{\text{DSO}}}\right)^2, \quad (3)$$

where F_* is the flux of an embedded star, T_* and R_* are its temperature and radius, respectively, F_S is the flux of an external S star, T_S and R_S are its temperature and radius, respectively, and finally R_{DSO} is the characteristic DSO/G2 radius. Considering $T_* = 3250$ K and $R_* = 1R_\odot$ from the two-component blackbody fit, see Figure 1, $T_S \sim 30,000$ K, $R_S \sim 5R_\odot$ (Habibi et al. 2017), and $R_{\text{DSO}} \sim 1$ au (Figure 1), we obtain using Equation (3), $F_*/F_S \sim 50$. The ratio F_*/F_S is unity for the S star approach to the dusty object with the separation of $\bar{d}_S \sim 424$ au. The total bolometric magnitude change due to the external irradiation can approximately be estimated from the extreme approach of an S star within a few hundred astronomical units, when its flux reprocessed by the gaseous-dusty envelope is comparable to the embedded star, $\Delta m \lesssim -2.5 \log 2 \sim -0.8$ mag, which is greater than or comparable to the variations due to the Doppler-boosting effect.

- (b) *Ellipsoidal variations.* Due to tidal stretching and compression of the gaseous-dusty envelope, dusty objects are expected to have an ellipsoidal shape. As the object

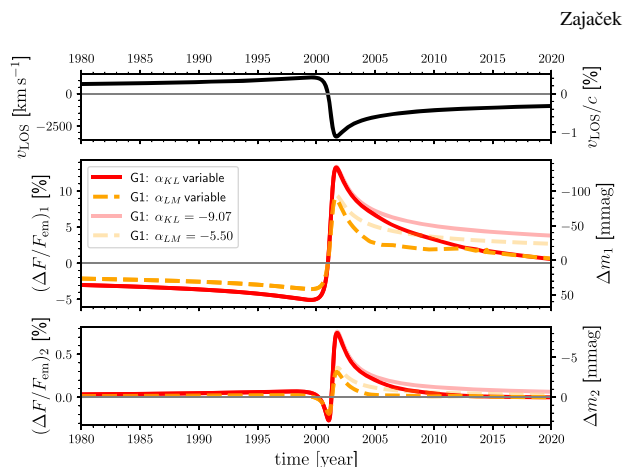


Figure 4. Effect of a variable spectral index on the Doppler beaming effect. The same panels as in Figure 2 for the infrared-excess source G1. In the middle and the bottom panels, we plot the relative flux variability separately for the spectral index between K and L bands (red solid line) and for the spectral index between L and M bands (orange dashed line). In particular, we consider increasing spectral indices as indicated by the observations of Witzel et al. (2017). For comparison, we also show, in fainter colors, the case with fixed spectral indices in K and L bands.

orbits around SMBH, the projected area seen by the observer changes, which leads to photometric variations. This effect was observed for a tidally distorted star orbiting the microquasar GRO J1655-40 (Greene et al. 2001), where the amplitude of the optical and infrared continuum variations reaches ~ 0.2 – 0.4 mag.

- (c) *Bow-shock radiation.* Due to their supersonic motion at the pericenter, dust-enshrouded objects are expected to develop a bow shock, in which electrons are accelerated in the amplified magnetic field and emit broadband synchrotron radiation. This can lead to the flux density enhancement close to the pericenter, which, however, depends on the ambient density as well as magnetic field. Hosseini et al. (2020) constrain the contribution of the nonthermal bow-shock emission to $\lesssim 0.1$ mag in near-infrared L' -band for the S2 star.
- (d) *Tidal truncation: Case of G1.* A prominent and extended L -band emission source passed close to Sgr A* around 2001.0 (Clénet et al. 2004, 2005). It was subsequently named G1 and analyzed in detail by Witzel et al. (2017) during its post-pericenter phase; see also Pfuhl et al. (2015). The source was more extended and resolved out before 2006 and afterwards got more compact and appeared as a point source, which was interpreted by the tidal truncation of its large gaseous-dusty envelope. Its L -band emission flux density also dropped by about two magnitudes (Witzel et al. 2017). The first-order and second-order Doppler beaming as a function of time is depicted in Figure 4. We compare two cases: the Doppler beaming for a gradually increasing spectral index (bright red and orange lines) as indicated by the analysis of Witzel et al. (2017) and the case that assumes fixed spectral indices (fainter red and orange lines). The main effect that we see is that the evolving spectral slope in the post-pericenter phase effectively shortens the duration of the beaming “flare” (see also Section 4.2), while the amplitude is not significantly affected. For the leading-term Doppler boosting effect, we obtain the amplitudes $\delta(\Delta F/F_{\text{cm}})_{\text{I}}^{KL} = 18.33\%$ (~ 0.192 mag) and

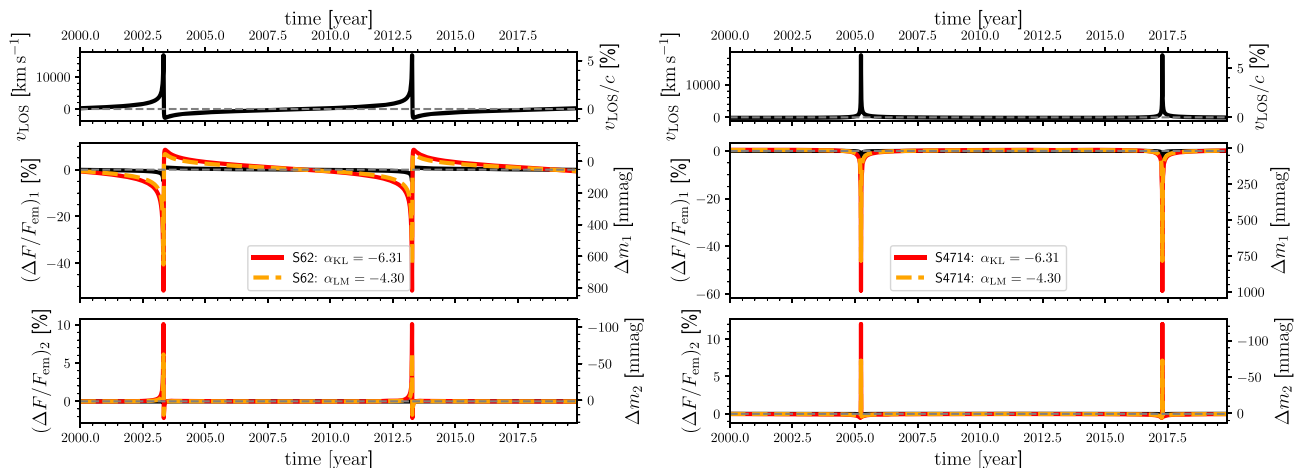


Figure 5. The same panels as in Figure 2 for a dust-enshrouded object on an S62-like orbit (left panel) and on an S4714-like orbit (right panel). In the middle and the bottom panels, we plot the relative flux variability separately for the spectral index between K and L bands (red solid line) and for the spectral index between L and M bands (orange dashed line).

$\delta(\Delta F/F_{\text{em}})_{1}^{LM} = 12.51\%$ (~ 0.132 mag). The higher-order relativistic corrections have the overall amplitudes of $\delta(\Delta F/F_{\text{em}})_{2}^{KL} = 1.02\%$ (~ 0.011 mag) and $\delta(\Delta F/F_{\text{em}})_{2}^{LM} = 0.49\%$ (~ 0.005 magnitudes). Since there is no L -band light curve of G1 close to its pericenter passage available and the L -band flux density drops by nearly 2 magnitudes due to structural changes in the post-pericenter phase of the orbit, the Doppler-boosting effect cannot be practically traced for this object. On the other hand, the subtraction of nearly ~ 0.1 – 0.2 mag variations due to the Doppler boosting is of relevance for studying internal changes of the source close to the pericenter passage.

For future monitoring, compact dusty sources, whose intrinsic K - and L -band flux densities are rather stable within at least 0.1 mag, such as the DSO/G2 object, appear suitable for the detection of the Doppler beaming effect, especially due to the fact that the overall amplitude of the boosting effect can be larger by an order of magnitude in comparison with B-type S stars. Cold brown dwarfs orbiting Sgr A* that are even more compact and are expected to be photometrically stable are even more suitable for a detailed monitoring of the Doppler beaming. Observations by future 30+ telescopes equipped with adaptive optics in near- and mid-infrared bands should be sensitive enough to detect faint objects orbiting Sgr A* down to the brown-dwarf level (Do et al. 2019a).

4.2. Beaming Flares and Dimming of ~ 0.1 – 1 mag Close to Sgr A*

Faint dust-enshrouded objects, pulsars, and brown dwarfs on highly eccentric orbits observed in near-infrared bands are expected to cause brightening events or beaming “flares” with an increase of ~ 0.1 – 1 magnitudes and lasting for a few days to years, depending on the pericenter distance. Having these properties, the events would be unique and could be distinguished from the near-infrared flares of Sgr A* that last approximately 1 hour and occur a few times per day (Witzel et al. 2020).

Specifically, focusing on K -band observations, for a dust-enshrouded object on the S2 orbit we get the peak relative flux

of 5.83% ($\Delta m = -0.062$ mag) with the timescale of $\tau_{1/2} = 2.79$ yr. For a pulsar on the same orbit, we get the relative flux maximum of 2.50% ($\Delta m = -0.027$ mag) with the same timescale. For the DSO/G2 object, the relative flux density increases up to 8.97% ($\Delta m = -0.093$ mag) with the half-maximum timescale of $\tau_{1/2} = 3.55$ yr.

Even more prominent Doppler beaming can occur at the pericenter distances 1 order of magnitude less than for the S2 star. Recently, Peißker et al. (2020a) and Peißker et al. (2020b) reported the detection of faint S stars, some of which, in particular S62 and S4714, can approach Sgr A* at a distance as small as $\sim 439 r_g$ and $\sim 312 r_g$, respectively. Rafikov (2020) predicted the variability of $\sim 6\%$ for both S62 and S4714. In case a dust-enshrouded object with the K -band spectral index of $\bar{\alpha}_{KL} = -6.31$ would be moving on an orbit comparable to S62 and S4714, the variability could reach as much as $\sim 60\%$ for S62-like orbit and $\sim 59\%$ for S4714-like orbit, see Table 1 for the summary of amplitudes and Figure 5 for the temporal profiles of $(\Delta F/F_{\text{em}})_1$ and $(\Delta F/F_{\text{em}})_2$ for both stars.

As we can see in light curves of the relative variability in Figure 5, both for S62 and S4714 orbits the Doppler dimming by a few ~ 0.1 mag would be more prominent than the Doppler brightening. Especially for faint dusty objects, brown dwarfs, or pulsars on similar orbits, there would be an epoch of dimming or potentially a complete disappearance of the object in case its infrared flux would be at the sensitivity limit. For the S62-like orbit, the minimum relative flux is $\sim -52\%$ ($\Delta m \sim 0.8$ magnitudes) and the half-minimum timescale is $\tau_{1/2} \sim 0.036$ yr or ~ 13 days. In the case of S4714, the dimming minimum is $\sim 59\%$ ($\Delta m \sim 1$ mag) and the half-minimum timescale is $\tau_{1/2} = 4.75$ days.

5. Conclusions

Motivated by the occurrence of colder dust-enshrouded objects among main-sequence B-type stars, we explored the effect of the infrared spectral index on the Doppler beaming effect within the S cluster. For three dust-enshrouded objects on mildly eccentric orbits, D2, D23, and D3, we found the relative variability amplitudes of 3.95%, 3.65%, and 4.30% in K band, respectively. The most prominent variability is for highly eccentric dusty objects DSO/G2 and G1 with K -band

amplitudes of 16.79% and 18.33%, respectively, where the latter object has a gradually increasing spectral index. In general, dust-enshrouded objects with steep spectral indices are expected to exhibit an enhanced Doppler beaming effect by as much as an order of magnitude in comparison with B-type S stars. Putative synchrotron-powered pulsars would have a stronger Doppler-beaming variability by a factor of about 4.

Therefore, the best prospects for detecting a Doppler beaming effect within the S cluster with future sensitive instruments, such as Extremely Large Telescope, are for compact dusty objects, brown dwarfs, and pulsars that are expected to have stable intrinsic continuum flux densities. For extended dusty objects, such as G1, variations due to tidal, ellipsoidal, bow-shock, and irradiation effects are generally larger. The subtraction of the expected Doppler-beaming variations will help us to better comprehend their internal physics, especially close to the pericenter passage.

In case the Doppler-beamed emission is detected for objects with well-determined orbits, the temporal profiles of the first- and second-order Doppler boosting could be utilized to constrain the spectral index, and hence, the nature of the objects. Moreover, with the expected detection of fainter cold compact objects within the S cluster (dust-enshrouded objects and brown dwarfs) using the upcoming sensitive infrared photometry, we expect that the Doppler boosting will lead to episodic beaming “flares” or dimming by a few 0.1 magnitudes on the timescale of a year within ~ 15 milliarcseconds of Sgr A*.

The author thanks the referee for constructive comments that helped to improve the manuscript. The project was partially supported by the Polish Funding Agency National Science Centre, project 2017/26/A/ST9/00756 (MAESTRO 9). MZ also acknowledges the NAWA financial support under the agreement PPN/WYM/2019/1/00064 to perform a three-month exchange stay at the Charles University in Prague and the Astronomical Institute of the Czech Academy of Sciences in Prague. A part of the presented research was performed within the Polish-Czech mobility program (MŠMT 8J20PL037 and NAWA PPN/BCZ/2019/1/00069).

ORCID iDs

Michal Zajaček  <https://orcid.org/0000-0001-6450-1187>

References

- Ali, B., Paul, D., Eckart, A., et al. 2020, *ApJ*, 896, 100
 Balick, B., & Brown, R. L. 1974, *ApJ*, 194, 265
 Basri, G. 2000, *ARA&A*, 38, 485
 Ciurlo, A., Campbell, R. D., Morris, M. R., et al. 2020, *Natur*, 577, 337
 Clénet, Y., Rouan, D., Gendron, E., et al. 2004, *A&A*, 417, L15
 Clénet, Y., Rouan, D., Gratadour, D., et al. 2005, *A&A*, 439, L9
 Do, T., Ghez, A., Becklin, E., et al. 2019a, *BAAS*, 51, 530
 Do, T., Hees, A., Ghez, A., et al. 2019b, *Sci*, 365, 664
 Eckart, A., Hüttemann, A., Kiefer, C., et al. 2017, *FoPh*, 47, 553
 Genzel, R., Eisenhauer, F., & Gillessen, S. 2010, *RvMP*, 82, 3121
 Ghez, A. M., Salim, S., Hornstein, S. D., et al. 2005, *ApJ*, 620, 744
 Gillessen, S., Eisenhauer, F., Trippe, S., et al. 2009, *ApJ*, 692, 1075
 Gillessen, S., Plewa, P. M., Eisenhauer, F., et al. 2017, *ApJ*, 837, 30
 Gravity Collaboration, Abuter, R., Amorim, A., et al. 2018, *A&A*, 615, L15
 Gravity Collaboration, Abuter, R., Amorim, A., et al. 2020, *A&A*, 636, L5
 Greene, J., Bailyn, C. D., & Orosz, J. A. 2001, *ApJ*, 554, 1290
 Habibi, M., Gillessen, S., Martins, F., et al. 2017, *ApJ*, 847, 120
 Hees, A., Do, T., Ghez, A. M., et al. 2017, *PhRvL*, 118, 211101
 Hosseini, S. E., Zajaček, M., Eckart, A., Sabha, N. B., & Labadie, L. 2020, *A&A*, 644, A105
 Merritt, D. 2013, *Dynamics and Evolution of Galactic Nuclei* (Princeton, NJ: Princeton Univ. Press)
 Mignani, R. P., De Luca, A., Hummel, W., et al. 2012, *A&A*, 544, A100
 Parsa, M., Eckart, A., Shahzamanian, B., et al. 2017, *ApJ*, 845, 22
 Peißker, F., Eckart, A., & Parsa, M. 2020a, *ApJ*, 889, 61
 Peißker, F., Eckart, A., Zajaček, M., Ali, B., & Parsa, M. 2020b, *ApJ*, 899, 50
 Peißker, F., Hosseini, S. E., Zajaček, M., et al. 2020c, *A&A*, 634, A35
 Pfahl, E., & Loeb, A. 2004, *ApJ*, 615, 253
 Pfuhl, O., Gillessen, S., Eisenhauer, F., et al. 2015, *ApJ*, 798, 111
 Rafikov, R. R. 2020, *ApJL*, 905, L35
 Schödel, R., Feldmeier, A., Neumayer, N., Meyer, L., & Yelda, S. 2014, *CQGra*, 31, 244007
 Valencia-S., M., Eckart, A., Zajaček, M., et al. 2015, *ApJ*, 800, 125
 Wharton, R. S., Chatterjee, S., Cordes, J. M., Deneva, J. S., & Lazio, T. J. W. 2012, *ApJ*, 753, 108
 Witzel, G., Ghez, A. M., Morris, M. R., et al. 2014, *ApJL*, 796, L8
 Witzel, G., Martinez, G., Willner, S. P., et al. 2020, *ApJS*, in press (arXiv:2011.09582)
 Witzel, G., Sitarski, B. N., Ghez, A. M., et al. 2017, *ApJ*, 847, 80
 Zajaček, M., Britzen, S., Eckart, A., et al. 2017, *A&A*, 602, A121
 Zucker, S., Alexander, T., Gillessen, S., Eisenhauer, F., & Genzel, R. 2006, *ApJL*, 639, L21
 Zucker, S., Mazeh, T., & Alexander, T. 2007, *ApJ*, 670, 1326

Paper 6: Effect of Extinction on Quasar Distances

Currently, they are two methods that are used to standardize quasars, i.e. use them as standard candles in analogy to type Ia supernovae: one method is based on the BLR radius-luminosity ($R_{\text{BLR}} - L$) relation and the other on the correlation between X-ray (2 keV) and UV (250 nm) luminosities or $L_X - L_{\text{UV}}$ relation. These two methods were previously applied to quasar samples separately. In [Khadka et al. \(2023\)](#), we collected for the first time a sample of 58 X-ray emitting reverberation-mapped quasars, which allowed to compare luminosity distances based on $L_X - L_{\text{UV}}$ and $R_{\text{BLR}} - L$ relations as well as the corresponding cosmological constraints.

Quite surprisingly, luminosity distances to the same quasars were not identical within uncertainties. The distribution of the luminosity distance differences $\Delta \log D_L \equiv \log D_{L, L_X - L_{\text{UV}}} - \log D_{L, R - L}$ for this sample deviates from the Gaussian distribution - the distribution peak is positively shifted and the whole distribution is significantly asymmetric. These are common characteristics for all the six cosmological models we have considered (flat and non-flat Λ CDM, XCDM, and ϕ CDM models, i.e. cold dark matter models with different equations of state for dark energy: $P_{\text{DE}} = w_{\text{DE}} \epsilon_{\text{DE}}$).

In this paper, we propose that the properties of the $\Delta \log D_L$ distribution can be explained by invoking standard extinction due to dust in host galaxies. In other words, the extinction of X-ray and UV emission always contributes to the non-zero difference by the term we derive: $(\Delta \log D_L)_{\text{ext}} = (\tau_X - \tau_{\text{UV}}) \log e / [2(1 - \gamma')]$, where $\tau_X - \tau_{\text{UV}}$ is the difference in the optical depths between X-ray and UV domains, e is the Euler number, and γ' is the slope of the $L_X - L_{\text{UV}}$ relation for a given sample of galaxies. Inversely, since we measured the positive shift of the distribution, we can estimate the average X-ray/UV colour index $\bar{E}_{X - \text{UV}} \equiv A_X - A_{\text{UV}} \sim 5(1 - \gamma')(\Delta \log D_L)_{\text{ext}}$, which is between 0.03 and 0.28 mag when the median and the peak values of the distributions are considered, respectively. This amount of extinction is rather moderate and corresponds to the extrapolated standard optical reddening of the population of quasars. It can arise due to the presence of dust in the circumnuclear media of galaxies. When we make use of standard hard X-ray and far UV extinction cuts, we obtain a quasar subsample for which the extinction outliers are absent but the distribution positive shift is nevertheless still present. We also notice that the $L_X - L_{\text{UV}}$ relation is generally more influenced since the effect arises due to the different amount of extinction in the UV and the X-ray domains.

Credit: [Zajaček et al. \(2024b\)](#), ApJ 961, 229. Reproduced with permission ©AAS.



Effect of Extinction on Quasar Luminosity Distances Determined from UV and X-Ray Flux Measurements

Michal Zajaček¹, Božena Czerny², Narayan Khadka^{3,4}, Mary Loli Martínez-Aldama^{5,6}, Raj Prince², Swayamtrupta Panda^{7,9}, and Bharat Ratra⁸

¹ Department of Theoretical Physics and Astrophysics, Faculty of Science, Masaryk University, Kotlářská 2, 611 37 Brno, Czech Republic; zajacek@physics.muni.cz

² Center for Theoretical Physics, Polish Academy of Sciences, Al. Lotników 32/46, 02-668 Warsaw, Poland

³ Department of Physics, Bellarmine University, 2001 Newburg Rd, Louisville, KY 40205, USA

⁴ Department of Physics and Astronomy, Stony Brook University, Stony Brook, NY 11794, USA

⁵ Astronomy Department, Universidad de Concepción, Casilla 160-C, Concepción 4030000, Chile

⁶ Instituto de Física y Astronomía, Facultad de Ciencias, Universidad de Valparaíso, Gran Bretaña 1111, Playa Ancha, Valparaíso, Chile

⁷ Laboratório Nacional de Astrofísica—MCTI, R. dos Estados Unidos, 154—Nações, Itajubá—MG, 37504-364, Brazil

⁸ Department of Physics, Kansas State University, 116 Cardwell Hall, Manhattan, KS 66506, USA

Received 2023 August 23; revised 2023 November 16; accepted 2023 December 2; published 2024 January 31

Abstract

In Khadka et al., a sample of X-ray-detected reverberation-mapped quasars was presented and applied for the comparison of cosmological constraints inferred using two well-established relations in active galactic nuclei—the X-ray/UV luminosity (L_X – L_{UV}) relation and the broad-line region radius–luminosity (R – L) relation. L_X – L_{UV} and R – L luminosity distances to the same quasars exhibit a distribution of their differences that is generally asymmetric and positively shifted for the six cosmological models we consider. We demonstrate that this behavior can be interpreted qualitatively as arising as a result of the dust extinction of UV/X-ray quasar emission. We show that the extinction always contributes to the nonzero difference between L_X – L_{UV} -based and R – L -based luminosity distances and we derive a linear relationship between the X-ray/UV color index E_{X-UV} and the luminosity-distance difference, which also depends on the value of the L_X – L_{UV} relation slope. Taking into account the median and the peak values of the luminosity-distance difference distributions, the average X-ray/UV color index falls in the range of $\bar{E}_{X-UV} = 0.03$ – 0.28 mag for the current sample of 58 sources. This amount of extinction is typical for the majority of quasars and can be attributed to the circumnuclear and interstellar media of host galaxies. After applying the standard hard X-ray and far-UV extinction cuts, heavily extinguished sources are removed but overall the shift toward positive values persists. The effect of extinction on luminosity distances is more pronounced for the L_X – L_{UV} relation since the extinction of UV and X-ray emissions both contribute.

Unified Astronomy Thesaurus concepts: Cosmology (343); Cosmological parameters (339); Observational cosmology (1146); Active galaxies (17); Quasars (1319); Interstellar dust extinction (837)

1. Introduction

The spatially flat Λ CDM cosmological model (Peebles 1984) is largely consistent with most lower-redshift, $z \lesssim 2.3$, observations (Yu et al. 2018; eBOSS Collaboration 2021; Brout et al. 2022) as well as with high-redshift cosmic microwave background (CMB) data at $z \sim 1100$ (Planck Collaboration 2020). However, there are several potential tensions between flat Λ CDM parameter values inferred using different techniques (Abdalla et al. 2022; Moresco et al. 2022; Perivolaropoulos & Skara 2022; Hu & Wang 2023). These can be addressed by improving the accuracy and precision of established cosmological probe measurements, and also by looking for alternative cosmological probes, especially in the redshift range between nearby data and CMB data.

Active galactic nuclei (AGN), especially bright quasars (quasi-stellar objects (QSOs); Karas et al. 2021; Zajaček et al. 2023), appear to be promising alternative probes due to their broad redshift coverage, ranging from the nearby Universe

($z = 0.00106$ for NGC4395; Brum et al. 2019) to $z \approx 7.642$ (J0313-1806; Wang et al. 2021). For cosmological applications, so far three types of QSO data have been more widely utilized: (i) QSO angular size observations (Cao et al. 2017; Ryan et al. 2019; Cao et al. 2020, 2021a, 2021b; Lian et al. 2021; Cao et al. 2022b); (ii) data based on the nonlinear relation between QSO X-ray and UV luminosities, the L_X – L_{UV} relation (Risaliti & Lusso 2015, 2019; Khadka & Ratra 2020a, 2020b; Lusso et al. 2020; Khadka & Ratra 2021; Li et al. 2021; Colgáin et al. 2022; Dainotti et al. 2022; Hu & Wang 2022; Khadka & Ratra 2022; Petrosian et al. 2022; Rezaei et al. 2022; Khadka et al. 2023); and (iii) data based on the correlation between the rest-frame broad-line region (BLR) time delay and the monochromatic luminosity, the R – L relation (Panda et al. 2019a, 2019b; Martínez-Aldama et al. 2019; Khadka et al. 2021b, 2022a, 2022b; Czerny et al. 2021; Zajaček et al. 2021; Cao et al. 2022c, 2023; Cao & Ratra 2022; Panda 2022; Cao & Ratra 2023a; Czerny et al. 2023a; Panda & Marziani 2023). In addition to these methods, Elvis & Karovska (2002) suggested using angular diameters of the BLR to measure the cosmological constant Λ (also see Wang et al. 2020) and Collier et al. (1999) as well as Cackett et al. (2007) discussed the application of continuum reverberation mapping (RM) to measure the Hubble constant. Also, the H0LICOW (H0 Lenses in COSMOGRAIL’s Wellspring)

⁹ CNPq Fellow.

program based on time delays between lensed images of QSOs has measured the Hubble constant (Birrer et al. 2020).

QSO standardization based on the L_X - L_{UV} relation and the constructed Hubble diagram has led to claims of strong cosmological constraints and tension with the Λ CDM model with the nonrelativistic matter density parameter $\Omega_{m0} \sim 0.3$ (Risaliti & Lusso 2019; Lusso et al. 2020). However, the analyses of Risaliti & Lusso (2019) and Lusso et al. (2020) were approximate and based on incorrect assumptions (Khadka & Ratra 2020a, 2020b; Banerjee et al. 2021; Khadka & Ratra 2021, 2022; Petrosian et al. 2022), i.e., cosmological parameters and L_X - L_{UV} relation parameters were constrained within the non-flat Λ CDM model; hence, the results were model dependent. The correct technique for the analysis of these data was developed by Khadka & Ratra (2020a) and here we outline it as follows: given the current quality of these data, one must use them to simultaneously determine the L_X - L_{UV} relation parameters and the cosmological model parameters, and one must also study a number of different cosmological models to determine whether the L_X - L_{UV} relation parameter values are independent of the assumed cosmological model. If the L_X - L_{UV} relation parameter values are independent of the assumed cosmological model, the QSOs are standardizable and the circularity problem is circumvented. We emphasize, however, that when correctly analyzed, the most recent Lusso et al. (2020) data compilation is not standardizable (Khadka & Ratra 2021, 2022) because the L_X - L_{UV} relation parameters depend on the assumed cosmological model as well as on redshift (Khadka & Ratra 2021, 2022). Khadka & Ratra (2022) discovered that the largest of the seven subsamples in the Lusso et al. (2020) QSO compilation, the Sloan Digital Sky Survey (SDSS)-4XMM one that contains about 2/3 of the total QSOs, has an L_X - L_{UV} relation that depends on the cosmological model and on redshift and is the main source of the problem with the Lusso et al. (2020) data.

On the other hand, the BLR R - L relation parameters generally appear independent of the adopted cosmological model (Khadka et al. 2021b, 2022a, 2022b; Cao et al. 2022c). Cosmological constraints are weak, but for Mg II (at 2798 Å in the rest frame) and C IV QSOs (at 1549 Å in the rest frame) they are consistent with those from better established probes (Khadka et al. 2022b; Cao et al. 2022c). However, there is a 2σ tension between the constraints given by lower-redshift H β QSOs (at 4861 Å in the rest frame) and those from the better established probes (Khadka et al. 2022a). The H β QSO sample yields weak cosmological constraints with a preference for decelerated cosmological expansion. This tension, and possible systematic issues, related to H β QSOs will need to be addressed when more reverberation-mapped QSOs are available, e.g., from the upcoming Vera C. Rubin telescope and its Legacy Survey of Space and Time (LSST; see, e.g., Panda et al. 2019a; Ivezić et al. 2019; Czerny et al. 2023b) and the SDSS-V black hole Mapper (Almeida et al. 2023).

In summary, both the L_X - L_{UV} relation and R - L relation data provide cosmological constraints, which is encouraging, but they have systematic problems that require further study. To uncover the systematic issues we looked for a sample of X-ray-detected quasars that have been reverberation mapped in the UV domain using the Mg II line. For such a sample, in principle, both L_X - L_{UV} and R - L relations should be applicable. To this goal, we provided a sample of 58 X-ray-detected reverberation-mapped Mg II QSOs in Khadka et al. (2023),

from which we measured both the L_X - L_{UV} relation and the R - L relation parameter values that are consistent with values measured using larger samples. The sample was quite limited but we stress that for each of the sources we could determine the luminosity distance from these two methods independently. The goal was to compare cosmological constraints inferred from the QSOs for both of these relations not just in the overall statistical study of two independent samples but for the same sample. Using six cosmological models, we found that both R - L and L_X - L_{UV} relations are standardizable. The main result of this study was that while the R - L relation measurements favored a smaller Ω_{m0} value consistent with the $\Omega_{m0} \sim 0.3$ value measured using better established cosmological probes, the L_X - L_{UV} relation measurements favored a value of Ω_{m0} larger than that inferred from the better established cosmological probes.

In Khadka et al. (2023), we showed that this is in agreement with the tendency for luminosity distances based on L_X - L_{UV} relation data to have a mean value smaller than luminosity distances based on R - L relation data for the same QSOs. The median L_X - L_{UV} relation luminosity-distance values, on the other hand, are mostly larger except for the flat and non-flat Λ CDM models. We note that these results are based on the distribution of the luminosity-distance difference ($\log D_{L,R-L} - \log D_{L,L_X-L_{UV}}$) normalized by the square root of the quadratic sum of the corresponding uncertainties.

Here we revisit the nonzero median (mean) of the difference in the luminosity distances based on the L_X - L_{UV} relation and R - L relation data sets. It is expected that, in the absence of systematic effects, the median (mean) of the distance-difference distribution should vanish within uncertainties since we construct the distribution from the same sample of sources and the luminosity distance to a particular source must be the same for both methods. The offset from zero hints at a systematic effect in one or both data sets and demands further analysis.

We propose that the offset in the $\Delta \log D_L \equiv \log D_{L,L_X-L_{UV}} - \log D_{L,R-L}$ distribution may be attributed to the extinction (absorption and scattering) of UV and X-ray photons along the line of sight. Since the extinction curve generally increases from the UV (2500 Å) to the soft X-ray bands (2 keV), we evaluate the differential extinction or the difference in optical depth between the X-ray and UV bands, $\tau_X - \tau_{UV}$. Specifically, we derive a simple analytical relation between $\tau_X - \tau_{UV}$ and the slope γ' of the L_X - L_{UV} relation as well as the luminosity-distance difference $\Delta \log D_L$, i.e., $\tau_X - \tau_{UV} \simeq 4.6(\gamma' - 1)\Delta \log D_L$. This way the mean differential extinction effect, or the X-ray/UV color index, can be directly inferred for the current sample of 58 X-ray reverberation-mapped QSOs as well as any future sample of such sources.

We show that the asymmetry and the positive shift of $\Delta \log D_L$ distributions for all the considered cosmological models, including the flat Λ CDM model, with prevailing positive medians, can be explained by a mild extinction of the UV and X-ray flux densities from QSOs. From all the median and the peak values of the $\Delta \log D_L$ distributions, the X-ray/UV color index falls in the range of ~ 0.03 - 0.28 mag for the sample of 58 X-ray detected, reverberation-mapped sources (Khadka et al. 2023). We demonstrate that this amount of extinction is typical for the majority of QSOs, originates in the circumnuclear and interstellar media of host galaxies

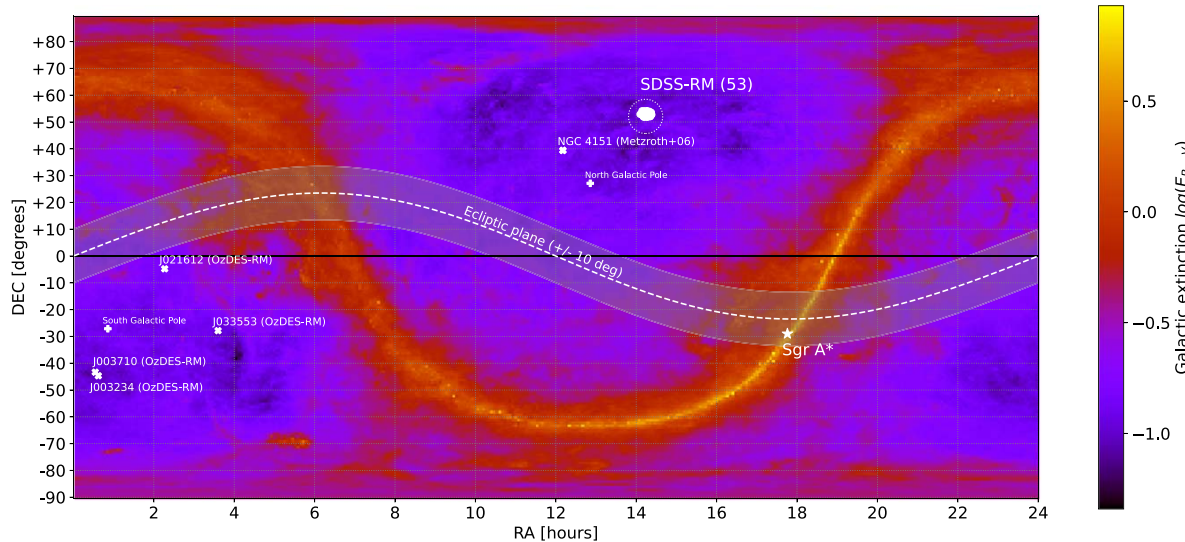


Figure 1. The position of the sample of 58 X-rays detected reverberation-mapped sources on the sky. Right ascension (R.A. expressed in hours) is along the x -axis, while decl. (decl. expressed in degrees) is along the y -axis. The white-dotted circle in the northern hemisphere denotes the sample of 53 SDSS-RM sources (Shen et al. 2016, 2019; Homayouni et al. 2020), while the five remaining sources (Metzroth et al. 2006; Yu et al. 2021) are more scattered to the south. The figure also shows the dust extinction map of the Milky Way (red-orange band) color coded using the logarithm of the $(B - V)$ color index E_{B-V} according to Schlegel et al. (1998). The position of the Galactic center (Sgr A*) is marked by a white star, while the north and the south Galactic poles are depicted by plus signs. The ecliptic plane and the surrounding band of $\pm 10^\circ$ are represented by the white-dashed line and the gray-shaded area, respectively.

(Czerny et al. 2004), and is only slightly alleviated by standard hard X-ray and far-UV extinction cuts (Lusso et al. 2020). Since the L_X - L_{UV} relation employs both UV and X-ray flux density measurements, it turns out to be more affected by extinction, which can address some of the previously mentioned problems with its standardization.

Our paper is structured as follows. In Section 2, we describe the characteristics of the data set of X-ray reverberation-mapped QSOs. In Section 3, we summarize the calculation method for luminosity distances and the different cosmological models we utilize. Subsequently, in Section 4, we derive the relation between the X-ray and UV optical depth difference (color index) and the luminosity-distance difference. Our main results are presented in Section 5. We provide an additional discussion of the source selection and our results in Section 6 and conclude in Section 7.

The reader may also find additional derivations of luminosity distances, including the extinction law in Appendix A, whereas the distributions related to the luminosity-distance difference formula are presented in Appendix B. Additional distributions of the X-ray/UV color index for different cosmological models are shown in Appendix C and the detailed investigation of reddening using SDSS magnitudes is presented in Appendix D.

2. Data Description

Our sample consists of 58 sources that were both (i) reverberation mapped using UV continuum and Mg II emission-line light curves, and (ii) X-ray detected at 2 keV. In this regard, the sample is complete, and due to its small size, we are not imposing further selection criteria unless stated otherwise. There are altogether 59 measurements of BLR time delays since the time delay for NGC 4151 was measured twice (Metzroth et al. 2006). The sample is described in detail in Khadka et al. (2023), and we list the main observables, i.e., the redshift z , the rest-frame Mg II time delay τ , 2 keV flux density

per frequency F_X , 2500 Å flux density per frequency F_{UV} , and 3000 Å flux density F_{3000} , in Appendix A of Khadka et al. (2023). The sample consists of 53 sources from the SDSS-RM program (Shen et al. 2016, 2019; Homayouni et al. 2020), NGC 4151 (Metzroth et al. 2006), and four sources from the OzDES RM program (Yu et al. 2021). These sources are also detected in the X-ray domain and are listed in the XMM-Newton X-ray source catalog (4XMMDR11). The sample position on the sky to the Galactic plane and the Galactic center (Sgr A*; Eckart et al. 2017) is shown in Figure 1, which is color coded using the decadic logarithm of the $(B - V)$ color index $\log E_{B-V}$ according to Schlegel et al. (1998).

We summarize the main properties of the main sample in Table 1. In Khadka et al. (2023), we also estimated the α_{OX} parameter, finding that our sample is not heavily obscured. An alternative verification that the Mg II quasars are not intrinsically obscured sources (or red quasars) is presented in Appendix D using $ugriz$ magnitudes from the SDSS database.

In addition, we analyze a subsample of 21 sources that meet the hard X-ray index and far-UV slope criteria of Lusso et al. (2020).¹⁰ The selection methodology and the subsample were described in detail in Khadka et al. (2023).¹¹ The properties of the subsample are also described in Table 1.

3. Cosmological Models and Parameters

The application of these QSO observations in cosmology depends on the empirical measurement of the QSO luminosity distances. This requires the assumption of a cosmological model. However, to determine whether or not the QSOs are

¹⁰ The hard X-ray photon index should lie between 1.7 and 2.8 and the far-UV spectral slope should lie between -0.7 and 1.5 (Lusso et al. 2020). The extinction cuts are applied to the sources that are outside these limits.

¹¹ Using the source identification (ID) of Khadka et al. (2023; see their Appendix A), the IDs of the sources are the following: 18, 28, 44, 118, 159, 185, 260, 280, 301, 303, 338, 440, 449, 459, 522, 588, 675, J141214, J141018, J141650, and J141644.

Table 1
Selected Properties of the Main Sample of X-Ray Detected Reverberation-mapped QSOs and the Subsample of 21 Sources

Property	Main Sample	Subsample
Source number	58	21
Redshift range	(0.0041, 1.686)	(0.418, 1.587)
Redshift (16th, 50th, 84th) percentiles	(0.527, 0.990, 1.454)	(0.4810, 0.919, 1.3394)
2 keV luminosity range [erg s ⁻¹]	(1.9 × 10 ⁴¹ , 6.1 × 10 ⁴⁴)	(1.6 × 10 ⁴³ , 1.5 × 10 ⁴⁴)
2 keV luminosity median [erg s ⁻¹]	4.4 × 10 ⁴³	4.8 × 10 ⁴³
2500 Å luminosity range [erg s ⁻¹]	(1.2 × 10 ⁴³ , 1.3 × 10 ⁴⁶)	(5.9 × 10 ⁴³ , 4.8 × 10 ⁴⁵)
2500 Å luminosity median [erg s ⁻¹]	9.3 × 10 ⁴⁴	9.5 × 10 ⁴⁴
Mg II time delay range [days]	(5.3, 387.9)	(17.2, 387.9)
Mg II time delay median [days]	92.0	99.1

Note. The luminosities are computed for the flat Λ CDM model with $\Omega_{m0} = 0.3$ and $H_0 = 70$ km s⁻¹ Mpc⁻¹. Mg II time delays are expressed in the rest frames of the sources. See Section 2 for the details of the subsample of 21 sources.

standardizable requires that we study them in several different cosmological models to see whether or not the empirical correlation relation used to determine their luminosities is independent of the assumed cosmological model (Khadka & Ratra 2020c). In this paper, we use three spatially flat and three spatially non-flat¹² cosmological models to determine QSO luminosity distances. In any cosmological model, the luminosity distance can be computed as a function of redshift (z) and cosmological parameters (p) in the following way:

$$D_L(z, p) = \begin{cases} \frac{c(1+z)}{H_0\sqrt{\Omega_{k0}}} \sinh \left[\frac{H_0\sqrt{\Omega_{k0}}}{c} D_C(z, p) \right] & \text{if } \Omega_{k0} > 0, \\ (1+z)D_C(z, p) & \text{if } \Omega_{k0} = 0, \\ \frac{c(1+z)}{H_0\sqrt{|\Omega_{k0}|}} \sin \left[\frac{H_0\sqrt{|\Omega_{k0}|}}{c} D_C(z, p) \right] & \text{if } \Omega_{k0} < 0. \end{cases} \quad (1)$$

Here c is the speed of light, H_0 is the Hubble constant, Ω_{k0} is the current value of the spatial curvature energy density parameter, and $D_C(z, p)$ is the comoving distance. $D_C(z, p)$ is computed as a function of z and p for a given cosmological model as follows:

$$D_C(z, p) = c \int_0^z \frac{dz'}{H(z', p)}, \quad (2)$$

where $H(z, p)$ is the Hubble parameter that is given next for the six cosmological models we use in this paper.

In a compact form, the Hubble parameter for all the six models (spatially flat/non-flat Λ CDM model, XCDM parameterization, and ϕ CDM model) can be written as

$$H(z) = H_0 \sqrt{\Omega_{m0}(1+z)^3 + \Omega_{k0}(1+z)^2 + \Omega_{DE}(z)}, \quad (3)$$

where Ω_{k0} vanishes in the spatially flat models. For the Λ CDM models and XCDM parameterizations, $\Omega_{DE}(z) = \Omega_{DE0}(1+z)^{1+\omega_X}$, where Ω_{DE0} is the current value of the dark energy density parameter and ω_X is the dark energy equation of state parameter. For the Λ CDM models $\omega_X = -1$ and the XCDM parameterizations, ω_X is a free parameter to be determined from

¹² For discussions of the constraints on spatial curvature see Rana et al. (2017), Ooba et al. (2018a), Park & Ratra (2019a), DES Collaboration (2019), Efstathiou & Gratton (2020), Di Valentino et al. (2021), Khadka et al. (2021a), Dhawan et al. (2021), Vagnozzi et al. (2021a, 2021b), Renzi et al. (2022), Geng et al. (2022), Cao et al. (2022a), Mukherjee & Banerjee (2022), Glanville et al. (2022), Wu et al. (2023), de Cruz Pérez et al. (2023), Dahiya & Jain (2023), Stevens et al. (2023), Favale et al. (2023), and references therein.

observational data. For the ϕ CDM models (Peebles & Ratra 1988; Ratra & Peebles 1988; Pavlov et al. 2013), $\Omega_{DE}(z) = \Omega_\phi(z, \alpha)$ can be obtained by solving the equations of motion of a spatially homogeneous scalar field model numerically. Here α is a positive parameter characterizing the inverse power-law potential energy density of the dynamical dark energy scalar field (ϕ) and can be constrained by using observational data.¹³

To determine QSO luminosity distances using empirical correlation relations, in particular, those expressed by Equations (4) and (6) below, we perform a likelihood analysis of predicted luminosity distances in a given cosmological model using Equation (1) and the observational luminosity distances obtained from Equations (5)–(7) below. This allows us to measure the nuisance parameters involved in the correlation relation (and check whether they are independent of cosmological model parameters), and that ultimately leads us to the determination of the QSO luminosity distances. For a detailed description of the computational method and the determination of QSO luminosity distances used in this paper, see Khadka et al. (2023).

4. UV and X-Ray Extinction and Luminosity Distances

The source intrinsic UV and X-ray flux densities (per frequency) at 2500 Å and 2 keV are $F_{UV,int}$ and $F_{X,int}$, respectively, and originate in the very central parts of galaxies during the accretion process and as such are assumed to be unaffected by dust at the place of their origin. The corresponding luminosities are calculated as $L_{UV,int} = 4\pi D_L^2 F_{UV,int}$ and $L_{X,int} = 4\pi D_L^2 F_{X,int}$, where D_L is the luminosity distance of a given QSO.

For the R – L relation, the corresponding UV luminosity is expressed at 3000 Å, $L_{3000,int} = 4\pi D_L^2 F_{3000,\nu} \nu_{3000} = 4\pi D_L^2 F_{UV,int} (2500/3000)^{\alpha_\nu} \nu_{3000}$, where $\alpha_\nu \simeq -0.45$ is the mean QSO continuum slope in the frequency domain, $F_\nu \propto \nu^{\alpha_\nu}$ (Vanden Berk et al. 2001) and ν_{3000} is the frequency corresponding to 3000 Å. Since the relation between the mean radius of the BLR region R and the corresponding time delay τ in the rest frame of the source is given by the light–travel relation, $R = c\tau$,

¹³ For discussions of the constraints on the ϕ CDM model see Zhai et al. (2017), Ooba et al. (2018b, 2019), Park & Ratra (2018, 2019b, 2020), Solà Peracaula et al. (2019), Singh et al. (2019), Ureña-López & Roy (2020), Sinha & Banerjee (2021), Xu et al. (2022), de Cruz Pérez et al. (2021), Jesus et al. (2022), Adil et al. (2023), Dong et al. (2023), Van Raamsdonk & Waddell (2023), Cao & Ratra (2023b), and references therein.

the R - L relation can be expressed in the form using τ instead of R ,

$$\log\left(\frac{\tau}{\text{days}}\right) = \beta + \gamma \log\left(\frac{L_{3000,\text{int}}}{10^\eta \text{ erg s}^{-1}}\right), \quad (4)$$

where γ , β , and η represent the slope, intercept, and normalization coefficients, respectively. From Equation (4), we can derive an expression for the luminosity distance $D_{L,R-L}$ as a function of τ , $F_{\text{UV, int}}$, and the coefficients of the R - L relation

$$\log D_{L,R-L} = \frac{1}{2\gamma} \{\log \tau - \beta - \gamma[\log(4\pi) + \log F_{\text{UV, int}} + 15.04 - \eta]\}, \quad (5)$$

where the term 15.04 results from the evaluation of $\log[(2500/3000)^{\alpha_\nu} \nu_{3000}]$. The L_X - L_{UV} relation considering the intrinsic X-ray and UV luminosities of the sources $L_{X,\text{int}}$ and $L_{\text{UV, int}}$ located at the luminosity distance $D_{L,L_X-L_{\text{UV}}}$ can be expressed as

$$\log\left(\frac{L_{X,\text{int}}}{\text{erg s}^{-1} \text{ Hz}^{-1}}\right) = \beta' + \gamma' \log\left(\frac{L_{\text{UV, int}}}{10^{\eta'} \text{ erg s}^{-1} \text{ Hz}^{-1}}\right), \quad (6)$$

where β' , γ' , and η' denote quantities analogous to those in Equation (4). The luminosity distance, $D_{L,L_X-L_{\text{UV}}}$, inferred from the L_X - L_{UV} relation given in Equation (6) is

$$\begin{aligned} \log D_{L,L_X-L_{\text{UV}}} &= \frac{1}{2(1-\gamma')} [\beta' + (\gamma' - 1)\log(4\pi) \\ &+ \gamma'(\log F_{\text{UV, int}} - \eta') - \log F_{X,\text{int}}]. \end{aligned} \quad (7)$$

Taking into account just the intrinsic UV and X-ray flux densities, we can evaluate the luminosity-distance difference, $\Delta \log D_L$, as

$$\begin{aligned} &(\log D_{L,L_X-L_{\text{UV}}} - \log D_{L,R-L})_{\text{int}} \\ &= \delta + \frac{\log F_{\text{UV, int}} - \log F_{X,\text{int}}}{2(1-\gamma')}, \end{aligned} \quad (8)$$

where the factor δ is a function of γ , β , γ' , β' , and τ ,

$$\delta = \frac{\beta - \log \tau}{2\gamma} + \frac{\beta' - \gamma'\eta'}{2(1-\gamma')} + 7.52 - \frac{\eta}{2}, \quad (9)$$

where the term 7.52 results from the evaluation of $0.5 \log[(2500/3000)^{\alpha_\nu} \nu_{3000}]$.

In the following, we adopt the assumption that, in the absence of a systematic effect, the luminosity-distance difference for a given source, or the statistical mean (median) of the luminosity-distance differences for a source sample, vanish, i.e., $(\Delta \log D_L)_{\text{int}} \equiv 0$; hence, $\delta + (\log F_{\text{UV, int}} - \log F_{X,\text{int}})/[2(1-\gamma')] = 0$. However, during the propagation of light through the circumnuclear and interstellar medium of the host galaxy, both UV and X-ray photons are absorbed and scattered with wavelength-dependent optical depths τ_{UV} and τ_X , respectively. The observed flux densities are therefore attenuated following the exponential law, $F_{\text{UV}} = F_{\text{UV, int}} \exp(-\tau_{\text{UV}})$ and $F_X = F_{X,\text{int}} \exp(-\tau_X)$. Hence, the resulting luminosity-distance difference under the influence of

extinction in both the UV and X-ray domains is

$$\begin{aligned} &(\Delta \log D_L)_{\text{ext}} \\ &= \delta + \frac{\log F_{\text{UV, int}} - \log F_{X,\text{int}}}{2(1-\gamma')} + \frac{(\tau_X - \tau_{\text{UV}})\log e}{2(1-\gamma')} \\ &= \frac{(\tau_X - \tau_{\text{UV}})\log e}{2(1-\gamma')}, \end{aligned} \quad (10)$$

where the second equation follows because the sum of the first two terms on the right-hand side of the first part of Equation (10) is intrinsically zero. In Equation (10), $\log e$ denotes the decadic logarithm of Euler's number, i.e., $\log e \simeq 0.434$. We outline a more detailed, step-by-step derivation of Equation (10) in Appendix A. The relation among the distributions of δ , $(\log F_{\text{UV}} - \log F_X)/[2(1-\gamma')]$, and $\Delta \log D_L$ for our sample is discussed in Appendix B.

Consequently, the optical depth difference $\tau_X - \tau_{\text{UV}}$ can be expressed as a function of the luminosity-distance difference and the slope γ' of the L_X - L_{UV} relation

$$\tau_X - \tau_{\text{UV}} = \frac{2(1-\gamma')}{\log e} (\Delta \log D_L)_{\text{ext}}. \quad (11)$$

The extinction in magnitude at a given wavelength is directly proportional to the optical depth, $A_\lambda = 1.086\tau_\lambda$. Hence, we can express the X-ray/UV color excess as

$$\begin{aligned} E_{X-\text{UV}} &\equiv A_X - A_{\text{UV}} \simeq \\ &5.001(1-\gamma') \langle (\Delta \log D_L)_{\text{ext}} \rangle, \end{aligned} \quad (12)$$

where the angular brackets represent the median/mean/peak value of the luminosity-distance difference for a given population of QSOs.

5. Results

In Khadka et al. (2023), we simultaneously measured the R - L or L_X - L_{UV} relation parameters and the cosmological model parameters for six different cosmological models—flat and non-flat Λ CDM, XCDM, and ϕ CDM. Based on the cosmological parameter values, we computed the R - L -based and L_X - L_{UV} -based luminosity distances, $D_{L,R-L}$ and $D_{L,L_X-L_{\text{UV}}}$, respectively. In Figure 2 we show the distributions of $\Delta \log D_L$. The plot shows that the difference between the luminosity distances can be positive or negative. If extinction plays the dominant role in measurement accuracy, the difference should always be positive. The presence of negative values implies that other measurement errors dominate. On the other hand, if no extinction effect is present, the mean/median values should be consistent with zero. Establishing the systematic shift is important, particularly from the point of view of future measurements coming from very large samples, when the stochastic net error for the entire sample will become small but the systematic shift will persist. With this aim, we concentrate on tracing this systematic shift in the present sample.

In comparison with Khadka et al. (2023), here we construct distributions of non-normalized luminosity-distance differences, from which $E_{X-\text{UV}}$ can be inferred using Equation (12). The normalized luminosity-distance distributions computed in Khadka et al. (2023) are appropriate for comparing the R - L -based and L_X - L_{UV} -based luminosity distances for each source. For the graphical representation in Figure 2, we binned $\Delta \log D_L$ using Knuth's rule (Knuth 2006).

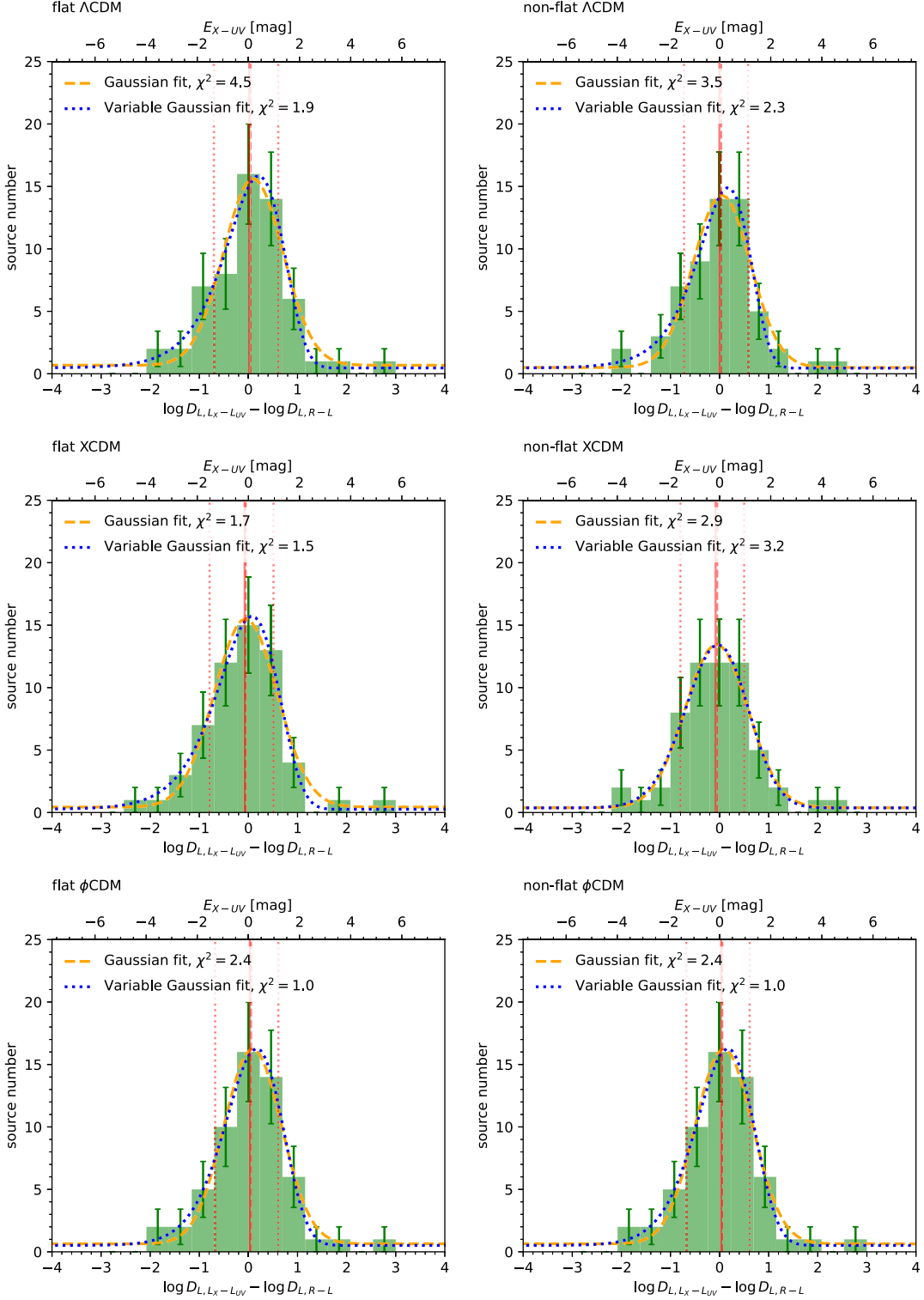


Figure 2. Distributions of the quasar luminosity-distance differences $\Delta \log D_L = \log D_{L,LX-LUV} - \log D_{L,R-L}$ for 58 sources for flat and non-flat Λ CDM, XCDM, and ϕ CDM cosmological models (from top to bottom row). The X-ray/UV color index $E_{X-UV} = 5.001(1 - \gamma^2)\Delta \log D_L$ is enumerated along the top x-axis in each panel. Solid red vertical lines indicate the mean difference, red-dashed vertical lines indicate the median difference, and red-dotted vertical lines denote the 16th and 84th percentiles. The bin width is determined based on the Knuth binning algorithm and the source number uncertainties for each bin are $\sigma_{y,i} = \sqrt{N_i}$, where N_i is the number of points in each bin. The orange-dashed line depicts the best-fit Gaussian function and the blue-dotted line shows the best-fit variable Gaussian function.

Table 2
Characteristics of the Distributions $\Delta \log D_L = \log D_{L,LX-UV} - \log D_{L,R-L}$ for the Six Cosmological Models Considered in This Paper

Model	Median	16th Percentile	84th Percentile	Mean	Skewness	Fisher's Kurtosis	Kurtosis Test	K-S test
Flat Λ CDM	0.0423	-0.7036	0.6080	0.0167	0.2369	1.7366	2.1136, $p = 0.035$	0.0000, $p = 1.0000$
Non-flat Λ CDM	0.0310	-0.7229	0.5806	-0.0030	0.2194	1.7271	2.1068, $p = 0.035$	0.0690, $p = 0.9993$
Flat XCDM	-0.0539	-0.7911	0.5106	-0.0768	0.2418	1.7391	2.1154, $p = 0.034$	0.1034, $p = 0.9192$
Non-flat XCDM	-0.0490	-0.7969	0.5003	-0.0812	0.2228	1.7290	2.1082, $p = 0.035$	0.1034, $p = 0.9192$
Flat ϕ CDM	0.0534	-0.6766	0.6097	0.0293	0.2390	1.7376	2.1144, $p = 0.034$	0.0345, $p = 1.0000$
Non-flat ϕ CDM	0.0556	-0.6780	0.6128	0.0307	0.2375	1.7369	2.1139, $p = 0.035$	0.0517, $p = 1.0000$
Flat Λ CDM—21	0.1869	-0.4825	0.5173	0.0114	-0.8175	0.2430	0.4899, $p = 0.624$	0.1552, $p = 0.7855$

Note. The distributions are graphically depicted in Figure 2. From the left to the right columns, we list the distribution median, 16th and 84th percentiles, mean, skewness, and Fisher's kurtosis parameters (both corrected for statistical bias), the kurtosis test, and the K-S test statistic including the corresponding p -values.

Table 3
Parameters of the X-Ray/UV Extinction E_{X-UV} in Magnitude for Six Cosmological Models Inferred Using the Variable Gaussian Function That Fits the E_{X-UV} Distributions Better than a Normal Gaussian Function

Model (1)	γ' (2)	E_{X-UV} (mag) (median) (3)	E_{X-UV} (mag) (peak) (4)	σ_+ (mag) (5)	σ_- (mag) (6)
Flat Λ CDM	0.616 ± 0.074	0.081	0.29 ± 0.13	1.06 ± 0.11	1.29 ± 0.12
Non-flat Λ CDM	0.609 ± 0.073	0.061	0.31 ± 0.10	0.95 ± 0.09	1.25 ± 0.10
Flat XCDM	0.614 ± 0.075	-0.104	0.17 ± 0.13	1.02 ± 0.12	1.29 ± 0.13
Non-flat XCDM	0.608 ± 0.075	-0.096	0.20 ± 0.11	0.89 ± 0.10	1.20 ± 0.11
Flat ϕ CDM	0.609 ± 0.073	0.104	0.34 ± 0.11	1.03 ± 0.10	1.28 ± 0.11
Non-flat ϕ CDM	0.610 ± 0.073	0.108	0.34 ± 0.11	1.03 ± 0.10	1.28 ± 0.11
Flat Λ CDM—21	0.610 ± 0.100	0.364	0.50 ± 0.12	0.82 ± 0.09	1.20 ± 0.13

Note. We transform the luminosity-distance difference $\Delta \log D_L$ to the color excess E_{X-UV} using Equation (12) with the best-fit slope of the L_X-L_{UV} relation (column (2)) adopted from Khadka et al. (2023). Columns (3)–(6) (from the left to the right) list the E_{X-UV} median and peak values, and the standard deviations to the positive and the negative sides of the distributions, respectively. The quoted errors are the errors of the fit of the variable Gaussian function to the E_{X-UV} histograms

The uncertainty in the number of sources falling into the bin is estimated as $\sigma_{y,i} = \sqrt{N_i}$.

The distributions of the luminosity-distance differences have several common characteristics. At first glance, the peak of each distribution is shifted to the positive side, which hints at positive values of $\tau_X - \tau_{UV}$, and hence, also E_{X-UV} . We summarize the main characteristics, specifically the median distribution, 16th and 84th percentiles, mean, skewness, Fisher's kurtosis, kurtosis test, and the Kolmogorov–Smirnov (K-S) test statistic, in Table 2. More specifically, for calculating the distribution skewness, we correct for the statistical bias and use the Fisher–Pearson standardized moment $\sqrt{N(N-1)/(N-2)}m_3/m_2^{3/2}$, where N is the sample size and m_2 and m_3 denote the second and the third central moments, respectively. All of the distributions are positively skewed, which is caused by the presence of tails on the positive side. For four out of six models, the median is positive; it is negative for the flat and non-flat XCDM models. The mean value is positive for the flat Λ CDM, flat, and non-flat ϕ CDM models, while for the other cosmological models, it is negative. Since the mean is more sensitive to the outliers in the distribution tails, we consider the median values to be more representative of the quasar sample. Fisher's kurtosis, which is also corrected for the statistical bias, is greater than zero, which implies a heavier tail than for the normal distribution. We verify the deviation from the normal distribution by performing the kurtosis test, whose z -scores and the corresponding p -values confirm the deviation. The two-sample K-S test is applied between each model and the flat Λ CDM model. All of the K-S p -values are close to 1; hence, the null hypothesis that

the $\Delta \log D_L$ distributions are drawn from the same underlying distribution as the one for the flat Λ CDM model is valid.

Furthermore, we analyze the $\Delta \log D_L$ distributions in Figure 2 by fitting a Gaussian function and a variable Gaussian function to them.¹⁴ The comparison of the fits based on the χ^2 value shows that the variable Gaussian function fits the distributions better, with the peak value shifted to the positive side and with $\sigma_- > \sigma_+$, i.e., the distributions are asymmetric to the peak. Qualitatively the same behavior is traced for the distributions of the X-ray/UV color index E_{X-UV} (in magnitude), which is calculated using Equation (12) and its value is greater than the luminosity-distance offset by about a factor of 2. We show the corresponding histograms binned according to Knuth's rule, including the Gaussian and the variable Gaussian fits, for all the flat and non-flat Λ CDM, XCDM, and ϕ CDM cosmological models in Figure 9 in Appendix C. In Figure 9, the distribution means are represented by red solid vertical lines, medians are represented by red vertical dashed lines, and the 16th and 84th percentiles are shown with red vertical dotted lines. The basic statistical properties of these distributions, specifically the E_{X-UV} median and peak values, the right and the left standard deviations, σ_+ and σ_- , respectively, are summarized in Table 3. For all the cosmological models, we obtain $\sigma_+ < \sigma_-$, which implies a significant asymmetry. The median values are predominantly positive (except for the flat and non-flat XCDM models), with an average value of

¹⁴ For the variable Gaussian function, we use the form according to Barlow (2004). The variable Gaussian function is introduced as $G_{\text{var}} = a \exp(-(x - x_0)^2 / [2\sigma(x)]) + b$, where $\sigma(x) = \sigma_1 + \sigma_2(x - x_0)$, $\sigma_1 = (2\sigma_+ \sigma_-) / (\sigma_+ - \sigma_-)$, and $\sigma_2 = (\sigma_+ - \sigma_-) / (\sigma_+ + \sigma_-)$.

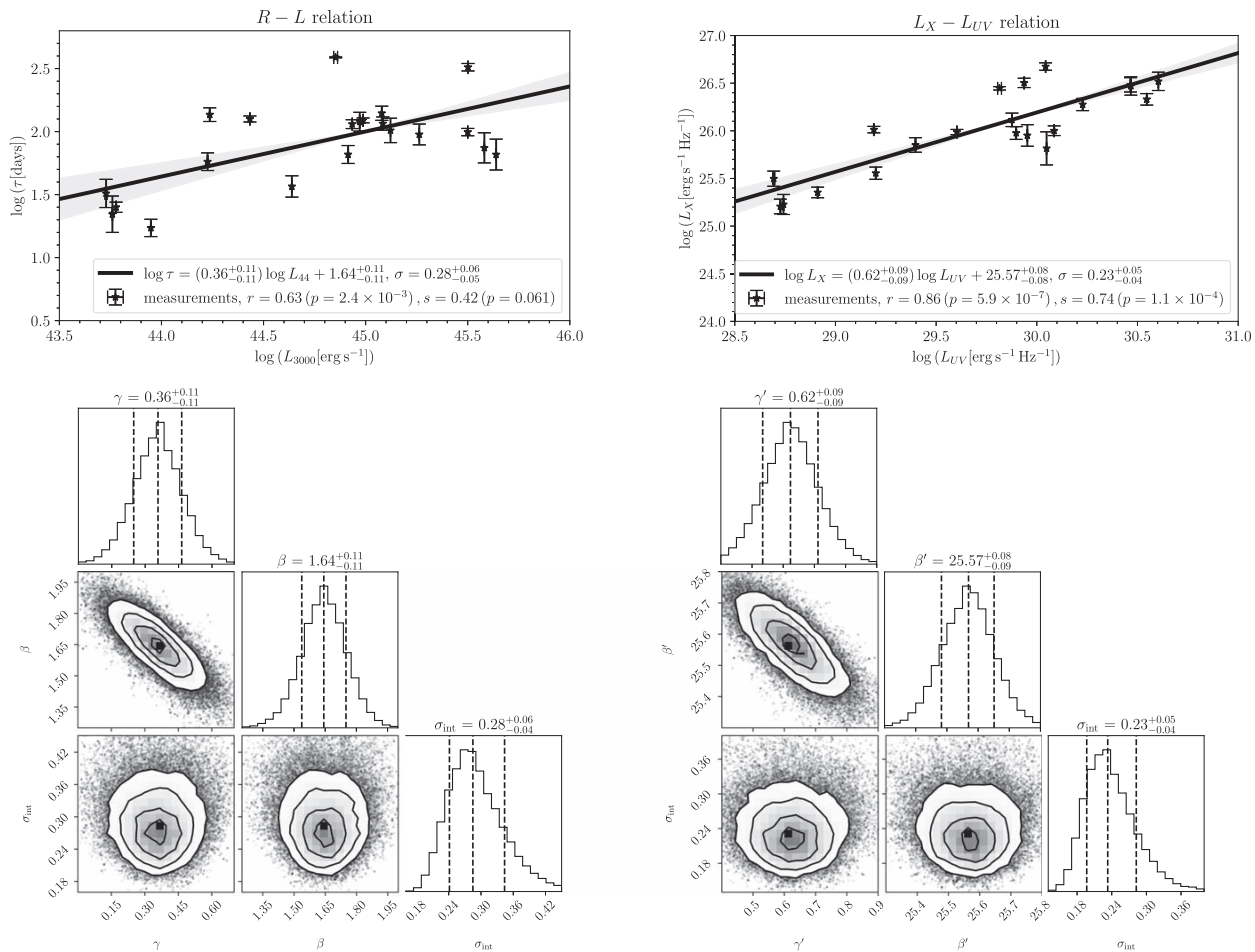


Figure 3. $R-L$ and L_X-L_{UV} relations in the flat Λ CDM model ($\Omega_{m0} = 0.3$) in the left and the right panels, respectively, for the subsample of 21 sources. The top row depicts the measurements alongside the best-fit relations, including the intrinsic scatter σ , while the bottom row shows the likelihood distributions for the slopes γ and γ' , the intercepts β and β' , as well as the intrinsic scatter σ_{int} for the corresponding relations.

Table 4
Marginalized One-dimensional Best-fit Parameters with 1σ Confidence Intervals for the 21 L_X-L_{UV} and $R-L$ QSOs in the Flat Λ CDM Model

Model	Data	Ω_{m0}	σ_{int}	β, β'	γ, γ'
Flat Λ CDM	$R-L$ QSOs	...	$0.301^{+0.041}_{-0.069}$	1.660 ± 0.120	0.360 ± 0.120
	L_X-L_{UV} QSOs	...	$0.244^{+0.031}_{-0.054}$	25.541 ± 0.090	0.610 ± 0.100

$\bar{E}_{X-UV} = 0.03$ mag, which is comparable in magnitude to the value inferred from the mean for the flat Λ CDM model. The inferred peak values of E_{X-UV} are positive for all the cosmological models. The average value is $\bar{E}_{X-UV} = 0.28 \pm 0.07$ mag, and hence, is larger than the value inferred from the medians. Overall, based on the average median and the peak values, we estimate the X-ray/UV color index of $\bar{E}_{X-UV} \sim 0.03-0.28$ mag for our sample.

The positive peak value of the E_{X-UV} distributions for all the cosmological models implies that the extinction is present in the sample, and the effect is stronger in the X-ray band than in the UV band. As we show by the comparison of distributions of δ and $(\log F_{UV} - \log F_X)/[2(1 - \gamma')]$ in Appendix B, the positive difference between $\tau_X - \tau_{UV}$ results in the shift of their sum to positive values due to the extinction term. In other

words, extinction causes the drop of the X-ray flux to the UV flux density, i.e., $\log F_{UV} - \log F_X$ is positive, which is correlated with the positive difference in optical depths, $\tau_X - \tau_{UV}$. If we assume zero extinction in the UV domain, we can convert $\bar{E}_{X-UV} = 0.03-0.28$ mag to the hydrogen column density N_H which is customarily used in X-ray studies. Assuming just electron scattering, we derive the mean intrinsic column density of $N_H = 4.2 \times 10^{22} - 3.9 \times 10^{23} \text{ cm}^{-2}$, which is moderate and in the Compton-thin regime. It can even be lower if the effect is partially due to X-ray absorption. If UV extinction is also present, then the corresponding N_H would be higher since we determine only the difference between the two effects. However, it is not likely that the two effects just compensate, so both X-ray and UV extinction effects are noticeable but not dramatically strong in our sample.

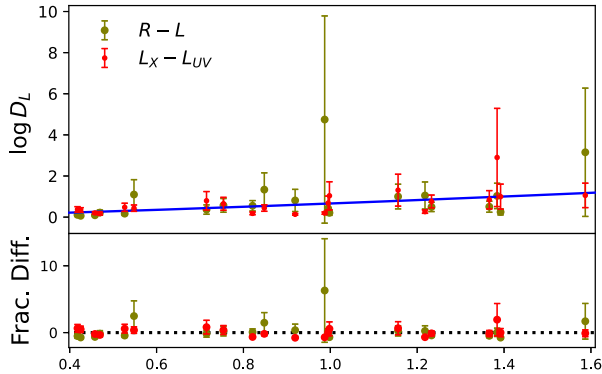


Figure 4. Upper panel: luminosity distances for 21 sources (expressed in 10^4 Mpc) inferred using the $R-L$ and L_X-L_{UV} relations in the flat Λ CDM model. The blue solid line represents the prediction for the flat Λ CDM model with $\Omega_{m0} = 0.3$. Lower panel: fractional difference between the observed and model-predicted luminosity distances for 21 sources. The colors follow the upper panel convention. The black-dotted line indicates zero fractional difference.

Assuming that in our sample UV extinction is negligible, we can use the mean X-ray extinction determined from our sample to correct the measured values of the $\log D_{L,L_X-L_{UV}}$. All actual values should be larger by 0.032 if corrected for X-ray extinction. When used for the flat Λ CDM cosmology, it systematically pushes the best solution toward significantly higher values of Ω_{m0} , roughly by 0.14, as estimated from the standard cosmology calculator for a median redshift of 0.99, as in our sample. As we show in the derivations in Appendix A, see Equations (A3) and (A7), the extinction affects $\log D_{L,R-L}$ by a factor of $+0.2\tau_{UV}$, while the effect is more pronounced for $\log D_{L,L_X-L_{UV}}$, which is modified by $+0.54\tau_X - 0.33\tau_{UV}$. Hence, for a negligible UV extinction, only the L_X-L_{UV} luminosity distance is affected.

Our analysis result is just the difference between the extinction effect in the X-ray and UV bands and we cannot correct the sample without additional spectral studies.

6. Discussion

We have shown that the $\Delta \log D_L$, and hence, the E_{X-UV} distributions are also significantly asymmetric and their peaks are shifted to the positive side for all the cosmological models considered. We attribute this to the extinction in the X-ray and UV domains with the average value in the range of $\bar{E}_{X-UV} = 0.03-0.28$ mag based on the average median and peak values of the E_{X-UV} distributions for all six cosmological models.

This implies that the effect is not very strong but it is present, and it can bias the cosmological results. Our sample of 58 sources contains all sources for which we have luminosity-distance measurements with both methods, and we did not apply any preselection aimed at removing extinction based on spectral studies of individual sources. By calculating the α_{OX} index (Khadka et al. 2023) and considering the $ugriz$ magnitudes from the SDSS catalog (see Appendix D), we can conclude that our sample is, for the most part, not heavily obscured and shares properties with the normal (blue) quasar population.

Nevertheless, even though our sample is not heavily obscured, we test the effect of extinction for our sample. By applying X-ray and UV selection cuts, we arrive at a subsample

of 21 sources, for which the heavily absorbed sources were removed. Furthermore, we connect E_{X-UV} color index to the more standard E_{B-V} in the optical domain.

6.1. Subsample without Absorbed Sources

To test the extinction effect further, we attempt to remove sources with larger extinction. In our original sample of 58 quasars (Khadka et al. 2023) no preselection was made since the sample of X-ray-detected reverberation-mapped quasars is already limited in size. In the new test, we apply the criteria of Lusso et al. (2020), as described in Khadka et al. (2023), to remove absorbed sources based on available hard X-ray photon indices and far-UV slopes. According to Lusso et al. (2020), the hard X-ray photon index should lie between 1.7 and 2.8, which is satisfied for 41 sources, and the far-UV slope should lie between -0.7 and 1.5, which is satisfied for 27 out of 31 sources for which GALEX EUV magnitudes are available. Combining both criteria yields a subsample of 21 sources, which supposedly does not contain heavily extincted quasars; see Section 2 for the description of the subsample.

For these 21 sources, we construct $R-L$ and L_X-L_{UV} relations in the flat Λ CDM model ($\Omega_{m0} = 0.3$), see Figure 3, whose parameters are consistent with those for the corresponding relations in the main sample of 58 sources, with a slightly decreased intrinsic scatter of 0.28 and 0.23 dex for the $R-L$ and L_X-L_{UV} relations, respectively. The removal of absorbed sources is also beneficial for increasing the correlation in both relations. For the $R-L$ relation, we obtain a Pearson correlation coefficient of $r = 0.63$ ($p = 2.38 \times 10^{-3}$), while for the whole sample of 58 sources, it is $r = 0.56$ ($p = 4.42 \times 10^{-6}$). For the L_X-L_{UV} relation of the subsample of 21 sources, we get $r = 0.86$ ($p = 5.90 \times 10^{-7}$), while for the whole sample, we have $r = 0.78$ ($p = 6.54 \times 10^{-13}$).

We also performed the simultaneous fitting of the L_X-L_{UV} or $R-L$ relation parameters as well as cosmological parameters for the flat Λ CDM model. For both relations, we list the parameters in Table 4, including their 1σ confidence intervals. The $R-L$ and L_X-L_{UV} relation parameters for the 21 and 58 sources are consistent within the uncertainties. The differences in γ and β for the $R-L$ relation are 0.62σ and 0.15σ , respectively. The differences in γ' and β' for the L_X-L_{UV} relation are 0.04σ and 0.88σ , respectively.

Luminosity distances for the 21 sources inferred using the two relations are shown in Figure 4. We show the unnormalized distributions of the luminosity-distance difference in Figure 5 (left panel). We list the basic statistical parameters of the unnormalized distribution in the last line of Table 2. The removal of extincted sources does affect the distribution by decreasing the mean value of the luminosity-distance difference. In addition, skewness becomes negative since the positive tail of the distribution disappears. Fisher's kurtosis also gets smaller because the obscured sources in the tails are removed. On the other hand, the median value increases, which may be the effect of the small size of the subsample. We also fit the $\Delta \log D_L$ and E_{X-UV} distributions using the normal Gaussian and the variable Gaussian functions, see the left and the right panels in Figure 5, respectively, with the variable Gaussian fitting the distributions better according to the χ^2 statistic. Actually, the distribution of E_{X-UV} becomes even more asymmetric with $\sigma_+ < \sigma_-$, see Table 3, and the peak is positively shifted with $E_{X-UV} = 0.50 \pm 0.12$ mag, while the median is at ~ 0.4 mag. We thus see that the source preselection

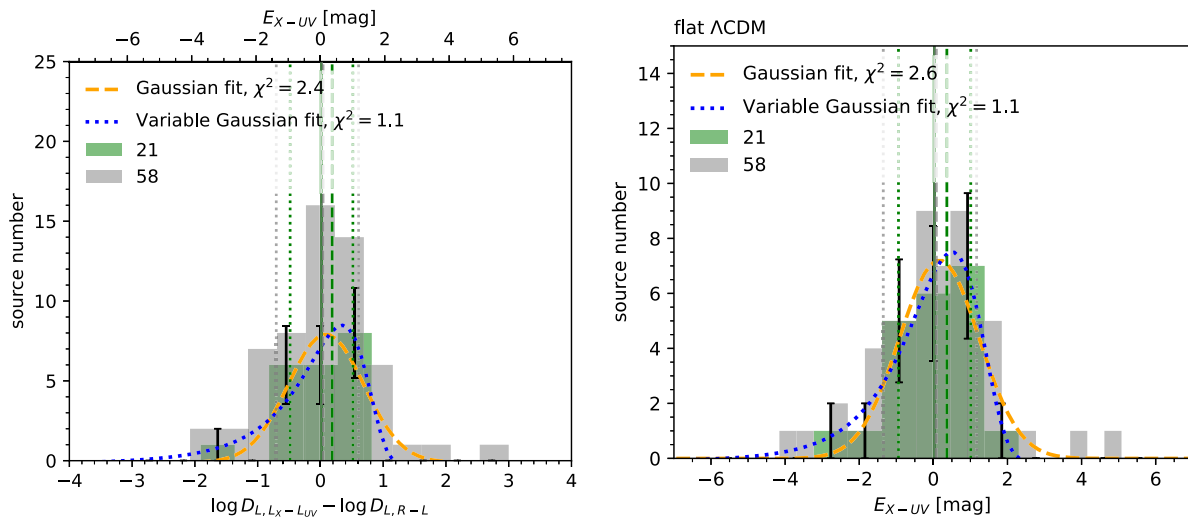


Figure 5. Unnormalized distributions of $\Delta \log D_L = \log D_{L,LX-LUV} - \log D_{L,R-L}$ and E_{X-UV} for the sample of 21 (58) sources in the flat Λ CDM model in green (gray). Left panel: distribution of the unnormalized luminosity-distance difference $\Delta \log D_L = \log D_{L,LX-LUV} - \log D_{L,R-L}$ for the subsample of 21 sources. The solid vertical green (gray) line denotes the distribution mean, the green-dashed vertical (gray) line represents the median, and the green-dotted vertical (gray) lines denote the 16th and 84th percentiles. The best-fit Gaussian function is depicted by an orange-dashed line, while the best-fit variable Gaussian function is represented by a blue-dotted line. Right panel: the distribution of E_{X-UV} (in magnitude) in green (gray) for the sample of 21 (58) sources. The vertical lines as well as the blue-dotted and the orange-dashed lines have the same meaning as in the left panel.

alleviates the problem of extinction by removing the outliers and reducing the tails. The change in the distribution characteristics between the samples of 58 and 21 sources indicates that extinction plays a role in increasing the distribution tails consisting of outliers and inducing a positive skewness. However, even after the application of hard X-ray and far-UV cuts, the positive shift of the distribution peak still indicates a contribution from extinction.

The normalized distribution of luminosity-distance differences shown in Figure 6 remains negatively skewed as in the bigger sample of 58 sources analyzed in Khadka et al. (2023). For the sample of 58 sources, the mean of the normalized distribution is negative (-0.116), which indicates that luminosity distances inferred from the L_X-L_{UV} relation are smaller than those inferred from the $R-L$ relation. This is consistent with the overall preference of larger Ω_{m0} for the L_X-L_{UV} relation constructed for 58 sources. The removal of extinguished sources and the final subsample of 21 sources exhibit the normalized distribution with a positive mean value ($+0.075$); hence, this indicates an opposite trend. However, since the subsample of 21 sources is more than a factor of 2 smaller in size, the change in the sign of the mean value may be the result of limited statistics and it does not reflect the trend in the larger samples. However, as for the unnormalized distribution, the absolute value of the mean decreases, which implies that the removal of extinguished sources is beneficial for decreasing the luminosity-distance difference between the L_X-L_{UV} and $R-L$ relations.

6.2. Relation to the Extinction Curve and E_{B-V}

Galactic extinction is generally corrected since the $(B-V)$ color excess is known for the whole range of Galactic coordinates (see, e.g., Schlegel et al. 1998). Our sample of 58 sources is in a region in the sky that is far from the Galactic plane, which has a Galactic extinction of $E_{B-V} \sim 0.1$ mag, see Figure 1. However, there still may be uncertainty in the applied

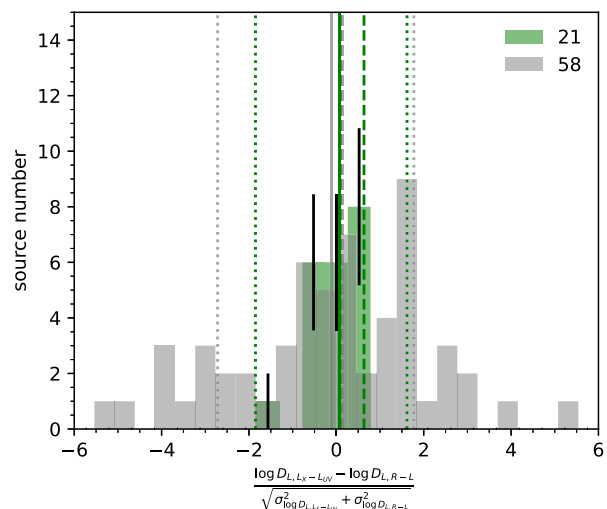


Figure 6. The distribution of $\Delta \log D_L = \log D_{L,LX-LUV} - \log D_{L,R-L}$ normalized by the square root of the sum of the luminosity-distance uncertainties. The distributions are shown for the whole sample of 58 sources (gray) and the subsample of 21 sources (green). The vertical lines denote the same statistical properties as in Figure 5.

Galactic extinction correction at the level of $E_{B-V} \sim 0.001$ mag. For instance, for NGC 4151 the color index is $E_{B-V} \sim 0.024$ mag according to Schlafly & Finkbeiner (2011), while it was measured to be $E_{B-V} \sim 0.027$ mag according to Schlegel et al. (1998); see the NASA/IPAC Extragalactic Database¹⁵ for the extinction values and their scatter for the other sources.

The more uncertain extinction contribution is due to the QSO optical, UV, and X-ray continuum emissions being affected by intrinsic extinction. For the SDSS data (4576 QSOs), Richards et al. (2003) constructed composite

¹⁵ <https://ned.ipac.caltech.edu/>

spectra, which they categorized into six composite spectral classes (Composites 1–6). Composite 1 corresponds to sources with intrinsically blue (or optically flat) power-law continua, while Composite 5 corresponds to reddened sources with optically steep power-law continua. Most of the quasars belong to rather bluer composite classes with a color excess of $E_{B-V} < 0.04$ mag, while only $\sim 10\%$ are reddened.

Based on the composite spectra constructed by Richards et al. (2003), Czerny et al. (2004) derived the extinction curve of QSOs, which is generally similar to the Small Magellanic Cloud extinction curve (Prevot et al. 1984), e.g., lacking the absorption feature at 2200 \AA except for the shortest UV wavelengths. The QSO extinction curve can generally be attributed to a circumnuclear dusty shell composed of amorphous carbon grains that lack both silicate and graphite grains based on the corresponding missing spectral features.

In the following, we use the simplified analytical extinction curve in Czerny et al. (2004),

$$\frac{A_\lambda}{E_{B-V}} = -1.36 + 13 \log(1/\lambda [\mu\text{m}]), \quad (13)$$

and extrapolate it to the UV/X-ray range ($2500 \text{ \AA} - 2 \text{ keV}$). Here A_λ is an extinction correction at wavelength λ , and E_{B-V} is the color excess measured between the B and V bands, which are customarily used as the extinction measure in the optical/UV band. Subsequently, from the inferred UV/X-ray color excess of $E_{X-UV} = A_X - A_{UV} \sim 0.03 - 0.28$ mag (median and peak values, see Table 3), we can use the relation $E_{X-UV} = 13E_{B-V} \log(\lambda_{UV}/\lambda_X)$ derived from Equation (13) to obtain the color excess of $E_{B-V} \sim 0.001 - 0.01$ mag. This can be interpreted to be predominantly the intrinsic color excess expected for the majority of type I QSOs (Richards et al. 2003). This extinction originates in the circumnuclear medium, e.g., in an obscuring torus, a warped disk-like structure, or an outflowing clumpy wind within ~ 1 pc from the supermassive black hole (Elvis et al. 2002; Gohil & Ballantyne 2017; Gaskell & Harrington 2018; Gaskell et al. 2023), and the host galaxy interstellar medium, also see Stolc et al. (2023) and Czerny et al. (2023c) for discussions. Dust can also be present on the scales of a few thousand gravitational radii, i.e., on subparsec scales, within the BLR clouds (Pandey et al. 2023). Dusty structures can be located close to a supermassive black hole on subparsec scales, especially for lower-luminosity sources. Considering the source at the low-luminosity end, see Table 1, we have the UV luminosity of $\nu_{UV}L_{UV} \sim 1.2 \times 10^{43} \text{ erg s}^{-1}$, which implies the sublimation radius of $r_{\text{sub}} \sim 0.04(T_{\text{sub}}/1500 \text{ K})^{-2.8}(\nu_{UV}L_{UV}/10^{43} \text{ erg s}^{-1})^{1/2}$ pc in the optically thin limit (Barvainis 1987; Zajaček et al. 2014). Actually, in the low-luminosity limit of the Galactic center, compact dusty objects were detected on the scale of ~ 1 milliparsec (Gillissen et al. 2012; Peißker et al. 2021), hence understanding the 3D distribution and geometry of dust in galactic nuclei as a function of their accretion rate is relevant for estimating the intrinsic extinction in different wave bands.

Therefore, the discrepancy between luminosity distances inferred using L_X-L_{UV} and $R-L$ relations is expected for any selection of QSOs. This is consistent with the finding that the application of extinction cuts based on the hard X-ray index and the far-UV slope (Lusso et al. 2020) only slightly mitigates

the extinction problem, as we showed in Section 6.1, by eliminating the outliers forming the tails. However, other qualitative properties of the E_{X-UV} distribution, mainly the peak shifted to positive values, persist even after applying the extinction cuts.

We note that including many lower-luminosity QSOs in the sample likely enhances the extinction effect. Weaver & Horne (2022) in their study of 9242 QSOs, all located in SDSS Stripe 82, derived a median extinction E_{B-V} of 0.1 for redshifts around 2 and higher extinction values for lower and higher redshifts (see their Figure A1).

Getting an estimate of the total reddening in AGN is crucial. The typical method involves hydrogen line ratios along UV, optical, and near-infrared wavelengths such as $\text{Ly}\alpha/\text{H}\beta$, $\text{H}\alpha/\text{H}\beta$, and $\text{Pa}\beta/\text{H}\beta$ (Osterbrock & Ferland 2006; Panda 2022; Gaskell et al. 2023). Other methods require simultaneous measurements in a broad wavelength range (Shuder & MacAlpine 1979; Choloniewski 1981; Cackett et al. 2007). Unfortunately, none of these methods can be implemented for our sample due to the lack of broadband measurements.

7. Conclusions

We find that the extinction (scattering and absorption) of X-ray and UV photons from QSOs contributes to the discrepancy between luminosity distances inferred using L_X-L_{UV} and $R-L$ relations.

For the nonzero luminosity-distance difference, i.e., $\Delta \log D_L = \log D_{L,L_X-L_{UV}} - \log D_{L,R-L}$, the extinction term is equal to $(\Delta \log D_L)_{\text{ext}} = (\tau_X - \tau_{UV}) \log e / [2(1 - \gamma')]$, where τ_X and τ_{UV} are optical depths in the X-ray and UV domains, respectively, and γ' is the slope of the L_X-L_{UV} relation. We found that the distributions of $\Delta \log D_L$ are asymmetric and positively shifted for all the six cosmological models considered. We estimated an average X-ray/UV color index of $\bar{E}_{X-UV} = 0.03 - 0.28$ mag in our sample, based on all six distribution median and peak values. We have shown that this amount of extinction is mild and overall typical for the majority of type I QSOs since it is supposed to originate in the circumnuclear and interstellar media of host galaxies (Czerny et al. 2004). The dust-related systematic problem does not seem to be completely removed by standard hard X-ray and far-UV extinction cuts; hence, some caution is necessary when interpreting the results (Khadka & Ratra 2021, 2022). Therefore, using at least two complementary methods for larger samples in the future is recommended.

Acknowledgments

This research was supported in part by Dr. Richard Jelsma (a Bellarmine University donor), Research Foundation for the SUNY, US DOE grant DE-SC0011840, by the Polish Funding Agency National Science Center, project 2017/26/A/ST9/00756 (Maestro 9), by GAČR EXPRO grant 21-13491X, by Millennium Nucleus NCN19₀₅₈ (TITANs), and by the Conselho Nacional de Desenvolvimento Científico e Tecnológico (CNPq) Fellowships (164753/2020-6 and 313497/2022-2). B.C. and M. Z. acknowledge the Czech-Polish mobility program (MŠMT 8J20PL037 and PPN/BCZ/2019/1/00069). This project has received funding from the European Research Council (ERC) under the European Union's Horizon 2020 research and innovation program (grant agreement No. [951549]). Part of

the computation for this project was performed on the Beocat Research Cluster at Kansas State University.

Appendix A Derivation of $D_{L,R-L}$, $D_{L,L_X-L_{UV}}$, and E_{X-UV} Expressions in the Presence of Extinction

A.1. Derivation of $D_{L,R-L}$

Using the $R-L$ relation in the form of

$$\log\left(\frac{\tau}{\text{days}}\right) = \beta + \gamma \log\left(\frac{L_{3000}}{10^\eta \text{ erg s}^{-1}}\right), \quad (\text{A1})$$

where the monochromatic luminosity L_{3000} can be expressed in the form of the UV flux density at 2500 Å as $L_{3000,\text{int}} = 4\pi D_L^2 F_{3000,\nu} \nu_{3000} = 4\pi D_L^2 F_{UV} (2500/3000)^{\alpha_\nu} \nu_{3000}$, the $R-L$ -based luminosity distance can be evaluated as

$$\begin{aligned} \log D_{L,R-L} &= \frac{1}{2\gamma} (\log \tau - \beta) \\ &\quad - \frac{1}{2} [\log(4\pi) - \eta + 15.036] - \frac{1}{2} \log F_{UV}, \end{aligned} \quad (\text{A2})$$

where we used $\alpha_\nu \sim -0.45$ for the mean QSO continuum slope (Vanden Berk et al. 2020). To extract the extinction term that modifies $\log D_{L,R-L}$, we use the extinction law in the form of $F_{UV} = F_{UV,\text{int}} e^{-\tau_{UV}}$, where $F_{UV,\text{int}}$ is the intrinsic QSO UV flux density. Equation (A2) can then be rewritten as

$$\begin{aligned} \log D_{L,R-L} &= \frac{1}{2\gamma} (\log \tau - \beta) - \frac{1}{2} [\log(4\pi) - \eta + 15.036] \\ &\quad - \frac{1}{2} \log F_{UV,\text{int}} + \frac{\log e}{2} \tau_{UV}, \end{aligned} \quad (\text{A3})$$

where the nonzero UV optical depth clearly increases the $R-L$ luminosity distance with the term $+\frac{\log e}{2} \tau_{UV} \sim +0.2 \tau_{UV}$.

A.2. Derivation of $D_{L,L_X-L_{UV}}$

Analogously, from the L_X-L_{UV} power-law relation parameterized as

$$\log\left(\frac{L_X}{\text{erg s}^{-1} \text{ Hz}^{-1}}\right) = \beta' + \gamma' \log\left(\frac{L_{UV}}{10^{\eta'} \text{ erg s}^{-1} \text{ Hz}^{-1}}\right), \quad (\text{A4})$$

we can derive the L_X-L_{UV} -based luminosity distance $D_{L,L_X-L_{UV}}$ that depends on X-ray and UV monochromatic flux densities at 2 keV and 2500 Å F_X and F_{UV} , respectively. The relation is as follows:

$$\begin{aligned} \log D_{L,L_X-L_{UV}} &= \frac{\beta' - \gamma' \eta'}{2(1 - \gamma')} - \frac{\log(4\pi)}{2} \\ &\quad + \frac{\gamma' \log F_{UV}}{2(1 - \gamma')} - \frac{\log F_X}{2(1 - \gamma')}. \end{aligned} \quad (\text{A5})$$

Using the extinction laws in the UV and the X-ray domains, $F_{UV} = F_{UV,\text{int}} e^{-\tau_{UV}}$ and $F_X = F_{X,\text{int}} e^{-\tau_X}$, respectively, we can

express Equation (A5) as

$$\begin{aligned} \log D_{L,L_X-L_{UV}} &= \frac{\beta' - \gamma' \eta'}{2(1 - \gamma')} - \frac{\log(4\pi)}{2} \\ &\quad + \frac{\gamma' (\log F_{UV,\text{int}} - \tau_{UV} \log e)}{2(1 - \gamma')} \\ &\quad - \frac{\log F_{X,\text{int}} - \tau_X \log e}{2(1 - \gamma')}. \end{aligned} \quad (\text{A6})$$

By separating intrinsic flux density terms from the extinction terms, we obtain

$$\begin{aligned} \log D_{L,L_X-L_{UV}} &= \frac{\beta' - \gamma' \eta'}{2(1 - \gamma')} - \frac{\log(4\pi)}{2} \\ &\quad + \frac{\gamma' \log F_{UV,\text{int}} - \log F_{X,\text{int}}}{2(1 - \gamma')} \\ &\quad + \frac{\tau_X \log e}{2(1 - \gamma')} - \frac{\tau_{UV} \gamma' \log e}{2(1 - \gamma')}. \end{aligned} \quad (\text{A7})$$

Hence, for $\gamma' \sim 0.6$ the extinction modifies $\log D_{L,L_X-L_{UV}}$ by $\sim +0.54 \tau_X - 0.33 \tau_{UV}$, i.e., the L_X-L_{UV} -based luminosity distance depends more strongly on the UV optical depth (it is decreased) than the $R-L$ -based luminosity distance. In addition, it is increased by the nonzero X-ray optical depth, which is not present in the $R-L$ -based luminosity-distance relation. Also, it is essential to note that the extinction effect for the L_X-L_{UV} relation depends on its slope γ' ; hence, this leads to a circularity problem in evaluating the extinction terms.

A.3. Derivation of E_{X-UV}

The color index between the X-ray and UV domains is defined as $E_{X-UV} \equiv A_X - A_{UV} = 1.086(\tau_X - \tau_{UV})$. To obtain E_{X-UV} , we first calculate the difference between $\Delta \log D_L = \log D_{L,L_X-L_{UV}} - \log D_{L,R-L} = \log(D_{L,L_X-L_{UV}}/D_{L,R-L})$ using Equations (A7) and (A3),

$$\begin{aligned} \Delta \log D_L &= \frac{\beta' - \gamma' \eta'}{2(1 - \gamma')} + \frac{\beta - \log \tau - \eta}{2\gamma} - \frac{\eta}{2} + 7.518 + \frac{\log F_{UV,\text{int}} - \log F_{X,\text{int}}}{2(1 - \gamma')} \\ &\quad \underbrace{=0 \text{ for intrinsic quasar emission}} \\ &\quad + \frac{(\tau_X - \tau_{UV}) \log e}{2(1 - \gamma')}, \end{aligned} \quad (\text{A8})$$

where the term $\delta + (\log F_{UV,\text{int}} - \log F_{X,\text{int}})/[2(1 - \gamma')]$ is assumed to sum to zero for the intrinsic quasar emission, and hence the luminosity-distance difference for any source is zero without extinction. The nonzero difference is thus related to the extinction term, from which the difference in the optical depth is $\tau_X - \tau_{UV} = 2(1 - \gamma') \Delta \log D_L / \log e$.

Finally, the color index E_{X-UV} can be expressed just as a function of the luminosity-distance difference and the slope

γ' of the L_X - L_{UV} relation

$$\begin{aligned} E_{X-UV} &= (2.172/\log e)(1 - \gamma')\Delta \log D_L \\ &\simeq 5.001(1 - \gamma')\Delta \log D_L. \end{aligned} \quad (\text{A9})$$

Appendix B

δ versus $(\log F_{UV} - \log F_X)/[2(1 - \gamma')]$ Distributions

To illustrate Equation (A8), i.e., $\Delta \log D_L = \delta + (\log F_{UV} - \log F_X)/[2(1 - \gamma')]$, we compare distributions of δ , $(\log F_{UV} - \log F_X)/[2(1 - \gamma')]$, and their sum $\Delta \log D_L$ in Figure 7 for 58 sources and flat and non-flat Λ CDM models (distributions are similar for the other cosmological models). The mean value of δ is always negative, while the mean value of $(\log F_{UV} - \log F_X)/[2(1 - \gamma')]$ is positive and of a comparable magnitude. However, their sum, which is equivalent to the difference in luminosity-distance logarithms, is characterized by a distribution with positive skewness and a

nonzero mean in all cases (see Figure 7 and Table 2 for the details). This behavior can qualitatively be attributed to the extinction term in Equation (A8) proportional to $\tau_X - \tau_{UV}$, from which the color index E_{X-UV} can be quantified using Equation (A9). If $\tau_X > \tau_{UV}$, then the extinction term is positive and the distribution of $\Delta \log D_L$ is shifted to positive values. The positive skewness is mainly given by the fact that for larger $\log F_{UV} - \log F_X$ the optical depth difference tends to be greater since $\tau_X > \tau_{UV}$ for sources with a more absorbed X-ray emission.

For the sample of 21 sources that pass the reddening criteria of Lusso et al. (2020), the mean value of $\Delta \log D_L = \delta + (\log F_{UV} - \log F_X)/[2(1 - \gamma')]$ decreases for the flat Λ CDM model in comparison with the full sample of 58 sources (0.011 versus 0.017), see Figure 8. This implies that the reddening cuts are beneficial for decreasing the offset; however, the intrinsic extinction contribution seems to still be present.

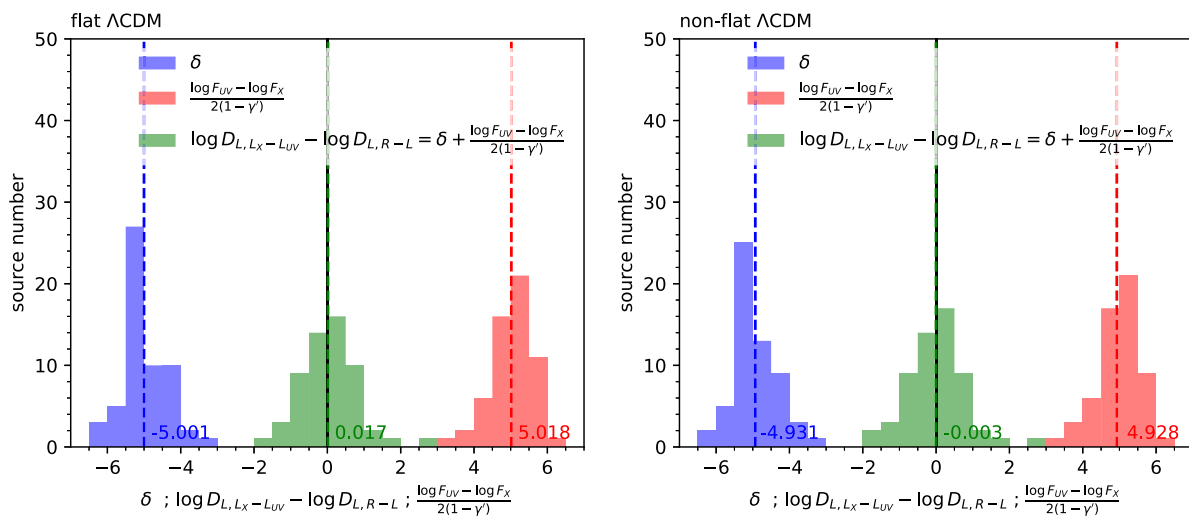


Figure 7. Comparison of distributions of the factor δ (blue histogram; see Equation (A8)), the factor $(\log F_{UV} - \log F_X)/[2(1 - \gamma')]$ (red histogram), and $\log D_{L,L_X-L_{UV}} - \log D_{L,R-L} = \delta + (\log F_{UV} - \log F_X)/[2(1 - \gamma')]$ (green histogram) for 58 sources for the flat and non-flat Λ CDM cosmological models in the left and the right panels, respectively. The black solid vertical line denotes zero, while the colored dashed vertical lines (blue, green, and red) represent the means of the corresponding distributions.

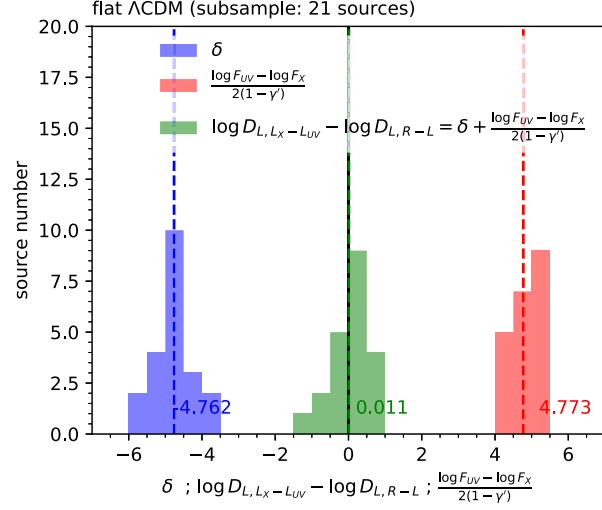


Figure 8. Comparison of distributions of the factor δ (blue histogram; see Equation (A8)), the factor $(\log F_{UV} - \log F_X)/[2(1 - \gamma)']$ (red histogram), and $\log D_{L,L_X-L_{UV}} - \log D_{L,R-L} = \delta + (\log F_{UV} - \log F_X)/[2(1 - \gamma)']$ (green histogram) for the subsample of 21 sources for the flat Λ CDM cosmological model. The black solid vertical line denotes zero, while the colored dashed vertical lines (blue, green, and red) represent the means of the corresponding distributions.

Appendix C E_{X-UV} Distributions

Using Equation (12), i.e., $E_{X-UV} \equiv A_X - A_{UV} \simeq 5.001(1 - \gamma)'\langle(\Delta \log D_L)_{ext}\rangle$, we construct distributions of the color index E_{X-UV} from the luminosity-distance differences for each source. We show histograms of E_{X-UV} for six cosmological models (flat and non-flat Λ CDM, XCDM, and ϕ CDM models from the top to the bottom rows) in Figure 9. All

of the 58 sources have E_{X-UV} in the interval $(-6,6)$ and the histogram bin widths are determined based on Knuth's rule. The red solid vertical line represents the distribution mean, the dashed vertical line denotes the median, and the red-dotted lines represent the 16th and 84th percentiles. We also perform fits of Gaussian and variable Gaussian functions to all the distributions, which are shown by orange-dashed and blue-dotted lines, respectively.

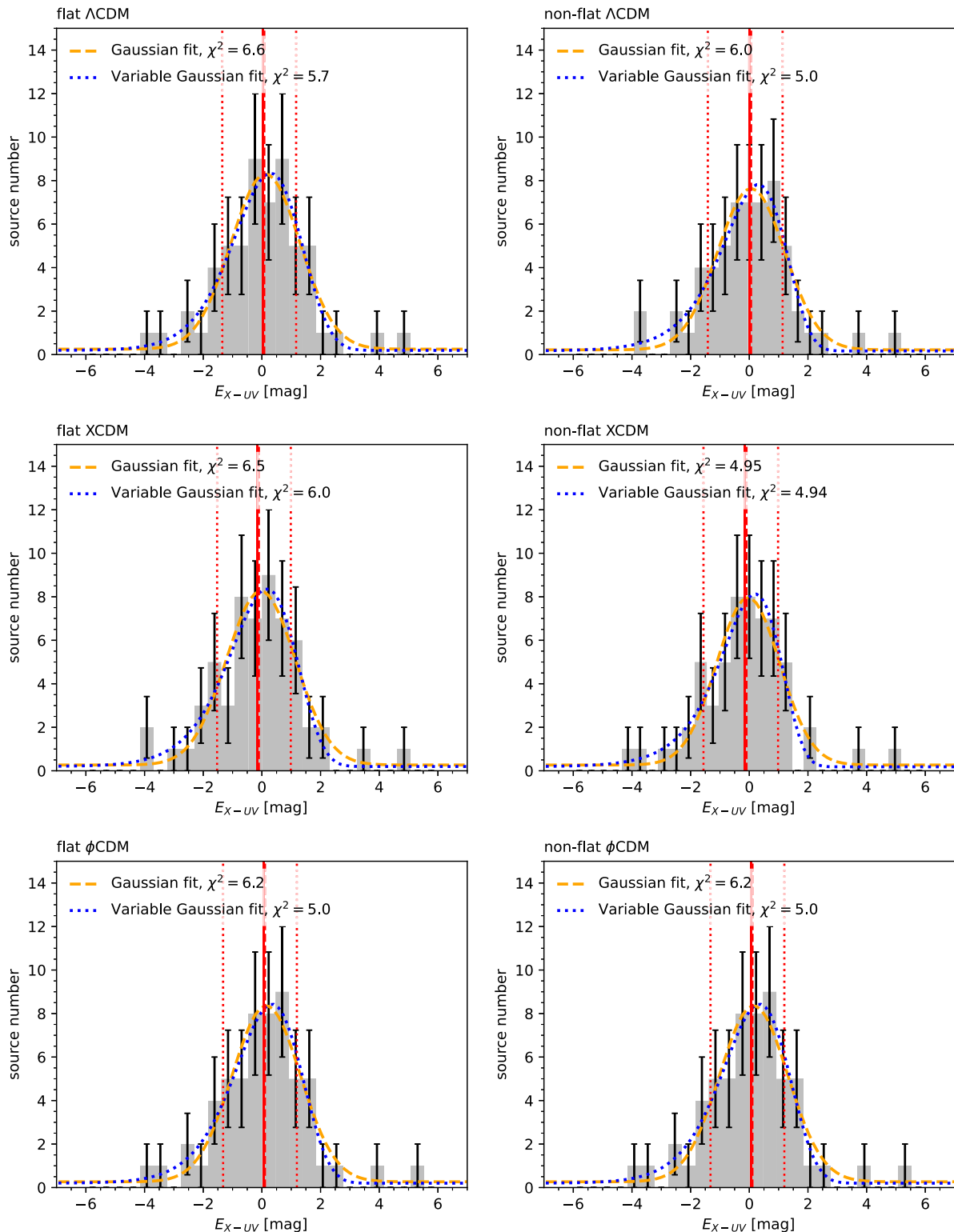


Figure 9. Distributions of the X-ray/UV color indices E_{X-UV} for 58 sources for the flat and non-flat Λ CDM, XCDM, and ϕ CDM cosmological models (from top to bottom row). The X-ray/UV color index $E_{X-UV} = 5.001(1 - \gamma')\Delta \log D_L$ is calculated based on the luminosity distances for each source and the L_X-L_{UV} relation slope for each cosmological model. Solid red vertical lines represent E_{X-UV} means, red-dashed vertical lines represent E_{X-UV} medians, and red-dotted vertical lines represent the corresponding 16th and 84th percentiles. The bin width is set based on the Knuth binning algorithm and the histogram y uncertainties for each bin are $\sigma_{y,i} = \sqrt{N_i}$, where N_i is the number of points in each bin. The best-fit Gaussian function is represented by an orange-dashed line, while the best-fit variable Gaussian function is depicted by a blue-dotted line.

Appendix D Inference of the Reddening Using the SDSS Magnitudes

An alternative possibility to infer the reddening effect in our sample involves using the $ugriz$ magnitudes from the SDSS database. To compare the behavior of our sample, we have adopted the blue and red quasar samples defined by Glikman et al. (2022). They considered red quasars as sources that have $E_{B-V} > 0.25$. We have obtained the u and z magnitudes from the SDSS database, which are not reported by Glikman et al. (2022). The SDSS magnitudes for the Mg II reverberation-mapped sample were taken from Shen et al. (2019). In all cases, the magnitudes were corrected for galactic extinction. Color-color plots are shown in Figure 10, where it is possible to observe the difference between the blue and the red samples. Most of the Mg II reverberation-mapped sources are located at the left, bluer part of the distribution, which indicates that they have $E_{B-V} < 0.25$. This result is consistent with the one found in Section 5. In Figure 10 we also identify the 21 sources that satisfy the selection criteria of Lusso et al. (2020), see Section 2; these exhibit the same behavior as the full 58 source sample. Some of our sources are located in the red quasar zone or show peculiar behavior to the rest of the sample. We have identified three sources (SDSS J141110.95+524815.5, SDSS J142041.78+521701.6, and SDSS J141645.58+534446.8) that are in the red zone or show different behavior in at least two color-color diagrams. The consistent location of SDSS J141110.95+524815.5 and SDSS J142041.78+521701.6 in the red quasar zone suggests that they have a high extinction. SDSS J141645.58+534446.8 shows extreme behavior, but it is

not necessarily located in the red quasar region. However, a visual inspection of the spectrum shows a flat continuum in the optical range, which suggests a high degree of reddening. One of these sources (SDSS J142041.78+521701.6) belongs to the 21 source sample. Thus, the criteria based on the hard X-ray index and far-UV slope criteria of Lusso et al. (2010) seem to be effective in cleaning the sample.

Figure 11 shows the $u-g$ and $g-i$ distributions as a function of redshift. Using the Calzetti et al. (2000) extinction law, we obtained the expected change in relative color as a function of redshift for $E_{B-V} = 0.04, 0.09, 0.15,$ and 0.2 . We assumed a continuum slope of $\alpha = -1.56$ and $\alpha = -0.45$ following the composite spectrum of Vanden Berk et al. (2001) for $u-g$ and $g-i$ colors, respectively. The behavior is the same as the one in Figure 10, red and blue quasar samples occupy different zones in the diagrams, and most of the Mg II reverberation-mapped sources overlap with the blue quasar sample. The E_{B-V} curves indicate that our sample has $E_{B-V} < 0.2$. $E_{B-V} = 0.09$ is in the middle of the distribution, which supports the results found in Section 5. In Figure 11 we also show the limit for red sources at $u-g = 0.8$ according to Richards et al. (2003), which coincides with the $E_{B-V} = 0.2$ curve. Since most of the reverberation-mapped sample is to the left of this curve, this suggests that our sample is more consistent with a blue behavior. The E_{B-V} curves confirm the red color of the three sources identified above. These objects should be excluded from future analyses.

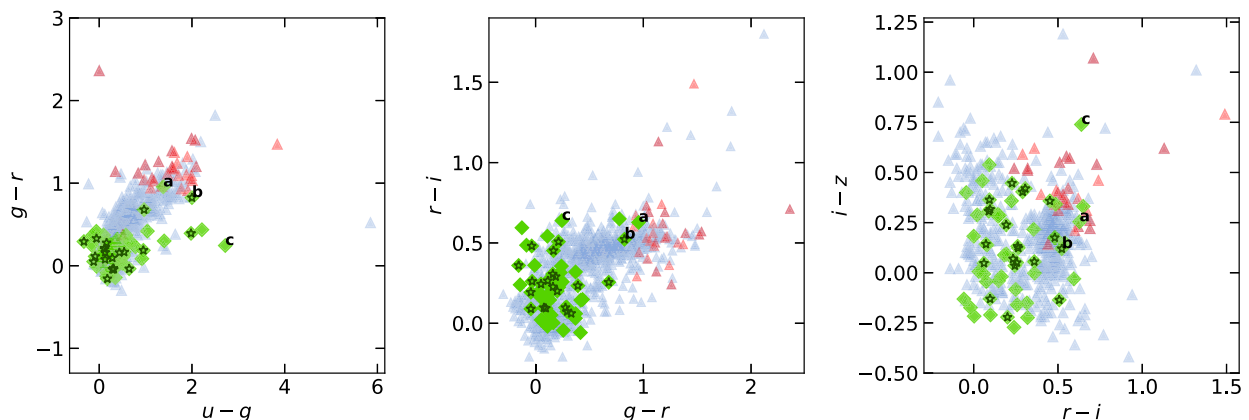


Figure 10. Color-color diagrams for blue and red quasar (triangle symbols) samples defined by Glikman et al. (2022), and the Mg II reverberation-mapped sample (green diamond symbols). Star symbols correspond to the 21 objects described in Section 2. Lowercase letters identify the redder objects of the Mg II reverberation-mapped sample: (a) SDSS J141110.95+524815.5, (b) SDSS J142041.78+521701.6, (c) SDSS J141645.58+534446.8.

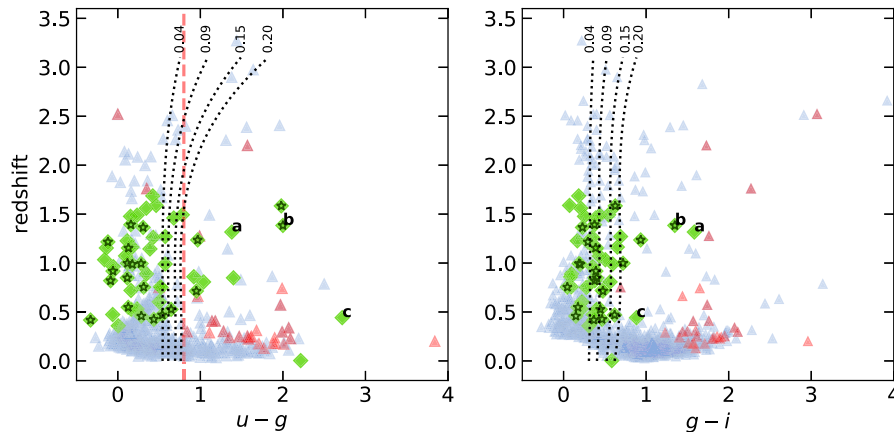


Figure 11. Redshift-color diagrams. The dotted lines represent the expected change in relative color as a function of redshift for $E_{B-v} = 0.04, 0.09, 0.15,$ and 0.20 from left to right, respectively. To estimate the change in E_{B-v} as a function of redshift, we used the Calzetti et al. (2000) extinction law. In the left panel, the vertical red-dashed line indicates the limit for red quasars according to Richards et al. (2003) at $u-g = 0.8$. Symbols have the same meaning as in Figure 10.

ORCID iDs

Michal Zajaček <https://orcid.org/0000-0001-6450-1187>
 Božena Czerny <https://orcid.org/0000-0001-5848-4333>
 Narayan Khadka <https://orcid.org/0000-0001-5512-2716>
 Mary Loli Martínez-Aldama <https://orcid.org/0000-0002-7843-7689>
 Raj Prince <https://orcid.org/0000-0002-1173-7310>
 Swayamrupa Panda <https://orcid.org/0000-0002-5854-7426>
 Bharat Ratra <https://orcid.org/0000-0002-7307-0726>

References

- Abdalla, E., Abellán, G. F., Aboubramah, A., et al. 2022, *JHEAp*, 34, 49
 Adil, A., Albrecht, A., & Knox, L. 2023, *PhRvD*, 107, 063521
 Almeida, A., Anderson, S. F., Argudo-Fernández, M., et al. 2023, *ApJS*, 267, 44
 Banerjee, A., Colgáin, Ó., Sasaki, E., Sheikh-Jabbari, M., & Yang, T. M. M. 2021, *PhLB*, 818, 136366
 Barlow, R. 2004, arXiv:physics/0406120
 Barvainis, R. 1987, *ApJ*, 320, 537
 Birrer, S., Shajib, A. J., Galan, A., et al. 2020, *A&A*, 643, A165
 Brout, D., Scolnic, D., Popovic, B., et al. 2022, *ApJ*, 938, 110
 Brum, C., Diniz, M. R., Riffel, R. A., et al. 2019, *MNRAS*, 486, 691
 Cackett, E. M., Horne, K., & Winkler, H. 2007, *MNRAS*, 380, 669
 Calzetti, D., Armus, L., Bohlin, R. C., et al. 2000, *ApJ*, 533, 682
 Cao, S., Khadka, N., & Ratra, B. 2022a, *MNRAS*, 510, 2928
 Cao, S., & Ratra, B. 2022, *MNRAS*, 513, 5686
 Cao, S., & Ratra, B. 2023a, *PhRvD*, 107, 103521
 Cao, S., & Ratra, B. 2023b, arXiv:2310.15812
 Cao, S., Ryan, J., Khadka, N., & Ratra, B. 2021a, *MNRAS*, 501, 1520
 Cao, S., Ryan, J., & Ratra, B. 2020, *MNRAS*, 497, 3191
 Cao, S., Ryan, J., & Ratra, B. 2021b, *MNRAS*, 504, 300
 Cao, S., Ryan, J., & Ratra, B. 2022b, *MNRAS*, 509, 4745
 Cao, S., Zajaček, M., Czerny, B., Panda, S., & Ratra, B. 2023, arXiv:2309.16516
 Cao, S., Zajaček, M., Panda, S., et al. 2022c, *MNRAS*, 516, 1721
 Cao, S., Zheng, X., Biesiada, M., et al. 2017, *A&A*, 606, A15
 Choloniewski, J. 1981, *AcA*, 31, 293
 Collier, S., Horne, K., Wanders, I., & Peterson, B. M. 1999, *MNRAS Lett.*, 302, L24
 Czerny, B., Cao, S., Jaiswal, V. K., et al. 2023a, *Ap&SS*, 368, 8
 Czerny, B., Li, J., Loska, Z., & Szczerba, R. 2004, *MNRAS Lett.*, 348, L54
 Czerny, B., Martínez-Aldama, M. L., Wojtkowska, G., et al. 2021, *AcPPA*, 139, 389
 Czerny, B., Panda, S., Prince, R., et al. 2023b, *A&A*, 675, A163
 Czerny, B., Zajaček, M., Naddaf, M.-H., et al. 2023c, *EPJD*, 77, 56
 Dahiya, D., & Jain, D. 2023, *RAA*, 23, 095001
 Dainotti, M. G., Bargiacchi, G., Lenart, A. E., et al. 2022, *ApJ*, 931, 106
 de Cruz Pérez, J., Park, C.-G., & Ratra, B. 2023, *PhRvD*, 107, 063522
 de Cruz Perez, J., Sola Peracaula, J., Gomez-Valent, A., & Moreno-Pulido, C. 2021, arXiv:2110.07569
 DES Collaboration, Abdalla, F. B., Avila, S., et al. 2019, *PhRvD*, 99, 123505
 Dhawan, S., Alsing, J., & Vagnozzi, S. 2021, *MNRAS Lett.*, 506, L1
 Di Valentino, E., Melchiorri, A., & Silk, J. 2021, *ApJL*, 908, L9
 Dong, F., Park, C., Hong, S. E., et al. 2023, *ApJ*, 953, 98
 eBOSS Collaboration, Alam, S., Aubert, M., et al. 2021, *PhRvD*, 103, 083533
 Eckart, A., Hüttemann, A., Kiefer, C., et al. 2017, *FoPh*, 47, 553
 Efstathiou, G., & Gratton, S. 2020, *MNRAS Lett.*, 496, L91
 Elvis, M., & Karovska, M. 2002, *ApJL*, 581, L67
 Elvis, M., Marengo, M., & Karovska, M. 2002, *ApJL*, 567, L107
 Favale, A., Gómez-Valent, A., & Migliaccio, M. 2023, *MNRAS*, 523, 3406
 Gaskell, C. M., Anderson, F. C., Birmingham, S. A., & Ghosh, S. 2023, *MNRAS*, 519, 4082
 Gaskell, C. M., & Harrington, P. Z. 2018, *MNRAS*, 478, 1660
 Geng, C.-Q., Hsu, Y.-T., & Lu, J.-R. 2022, *ApJ*, 926, 74
 Gillessen, S., Genzel, R., Fritz, T. K., et al. 2012, *Natur*, 481, 51
 Glanville, A., Howlett, C., & Davis, T. 2022, *MNRAS*, 517, 3087
 Glikman, E., Lacy, M., LaMassa, S., et al. 2022, *ApJ*, 934, 119
 Gohil, R., & Ballantyne, D. R. 2017, *MNRAS*, 468, 4944
 Homayouni, Y., Trump, J. R., Grier, C. J., et al. 2020, *ApJ*, 901, 55
 Hu, J. P., & Wang, F. Y. 2022, *A&A*, 661, A71
 Hu, J.-P., & Wang, F.-Y. 2023, *Univ*, 9, 94
 Jesus, J. F., Valentim, R., Escobal, A. A., Pereira, S. H., & Benndorf, D. 2022, *JCAP*, 2022, 037
 Ivezić, Ž., Kahn, S. M., Tyson, J. A., et al. 2019, *ApJ*, 873, 111
 Karas, V., Svoboda, J., & Zajaček, M. 2021, in RAGtime: Workshops on black holes and neutron stars, 154
 Khadka, N., Luongo, O., Muccino, M., & Ratra, B. 2021a, *JCAP*, 2021, 042
 Khadka, N., Martínez-Aldama, M. L., Zajaček, M., Czerny, B., & Ratra, B. 2022a, *MNRAS*, 513, 1985
 Khadka, N., & Ratra, B. 2020a, *MNRAS*, 492, 4456
 Khadka, N., & Ratra, B. 2020b, *MNRAS*, 497, 263
 Khadka, N., & Ratra, B. 2020c, *MNRAS*, 499, 391
 Khadka, N., & Ratra, B. 2021, *MNRAS*, 502, 6140
 Khadka, N., & Ratra, B. 2022, *MNRAS*, 510, 2753
 Khadka, N., Yu, Z., Zajaček, M., et al. 2021b, *MNRAS*, 508, 4722
 Khadka, N., Zajaček, M., Panda, S., Martínez-Aldama, M. L., & Ratra, B. 2022b, *MNRAS*, 515, 3729
 Khadka, N., Zajaček, M., Prince, R., et al. 2023, *MNRAS*, 522, 1247
 Knuth, K. H. 2006, arXiv:physics/0605197
 Li, X., Keeley, R. E., Shafieloo, A., et al. 2021, *MNRAS*, 507, 919
 Lian, Y., Cao, S., Biesiada, M., et al. 2021, *MNRAS*, 505, 2111
 Lusso, E., Comastri, A., Vignali, C., et al. 2010, *A&A*, 512, A34
 Lusso, E., Risaliti, G., Nardini, E., et al. 2020, *A&A*, 642, A150
 Martínez-Aldama, M. L., Czerny, B., Kawka, D., et al. 2019, *ApJ*, 883, 170
 Metzroth, K. G., Onken, C. A., & Peterson, B. M. 2006, *ApJ*, 647, 901
 Moresco, M., Amati, L., Amendola, L., et al. 2022, *LRR*, 25, 6
 Mukherjee, P., & Banerjee, N. 2022, *PhRvD*, 105, 063516
 Ooba, J., Ratra, B., & Sugiyama, N. 2018a, *ApJ*, 869, 34

- Ooba, J., Ratra, B., & Sugiyama, N. 2018b, *ApJ*, **866**, 68
- Ooba, J., Ratra, B., & Sugiyama, N. 2019, *Ap&SS*, **364**, 176
- Osterbrock, D. E., & Ferland, G. J. 2006, *Astrophysics of gaseous nebulae and active galactic nuclei* (Sausalito, CA: Univ. Science Books)
- Panda, S. 2022, *FrASS*, **9**, 850409
- Panda, S., Martínez-Aldama, M. L., & Zajaček, M. 2019a, *FrASS*, **6**, 75
- Panda, S., & Marziani, P. 2023, *FrASS*, **10**, 31
- Panda, S., Marziani, P., & Czerny, B. 2019b, *ApJ*, **882**, 79
- Panda, S., & Śniegowska, M. 2022, arXiv:2206.10056
- Pandey, A., Czerny, B., Panda, S., et al. 2023, *A&A*, **680**, A102
- Park, C.-G., & Ratra, B. 2018, *ApJ*, **868**, 83
- Park, C.-G., & Ratra, B. 2019a, *Ap&SS*, **364**, 82
- Park, C.-G., & Ratra, B. 2019b, *Ap&SS*, **364**, 134
- Park, C.-G., & Ratra, B. 2020, *PhRvD*, **101**, 083508
- Pavlov, A., Westmoreland, S., Saaidi, K., & Ratra, B. 2013, *PhRvD*, **88**, 123513
- Peebles, P. J. E. 1984, *ApJ*, **284**, 439
- Peebles, P. J. E., & Ratra, B. 1988, *ApJL*, **325**, L17
- Peißker, F., Zajaček, M., Eckart, A., et al. 2021, *ApJ*, **923**, 69
- Perivolaropoulos, L., & Skara, F. 2022, *NewAR*, **95**, 101659
- Petrosian, V., Singal, J., & Mutchnick, S. 2022, *ApJL*, **935**, L19
- Planck Collaboration 2020, *A&A*, **641**, A6
- Prevot, M. L., Lequeux, J., Maurice, E., Prevot, L., & Rocca-Volmerange, B. 1984, *A&A*, **132**, 389
- Rana, A., Jain, D., Mahajan, S., & Mukherjee, A. 2017, *JCAP*, **2017**, 028
- Ratra, B., & Peebles, P. J. E. 1988, *PhRvD*, **37**, 3406
- Renzi, F., Hogg, N. B., & Giarè, W. 2022, *MNRAS*, **513**, 4004
- Rezaei, M., Solà Peracaula, J., & Malekjani, M. 2022, *MNRAS*, **509**, 2593
- Richards, G. T., Hall, P. B., Vanden Berk, D. E., et al. 2003, *AJ*, **126**, 1131
- Risaliti, G., & Lusso, E. 2015, *ApJ*, **815**, 33
- Risaliti, G., & Lusso, E. 2019, *NatAs*, **3**, 272
- Ryan, J., Chen, Y., & Ratra, B. 2019, *MNRAS*, **488**, 3844
- Schlafly, E. F., & Finkbeiner, D. P. 2011, *ApJ*, **737**, 103
- Schlegel, D. J., Finkbeiner, D. P., & Davis, M. 1998, *ApJ*, **500**, 525
- Colgáin, E. Ó., Sheikh-Jabbari, M. M., Solomon, R., et al. 2022, *PhRvD*, **106**, L041301
- Shen, Y., Hall, P. B., Horne, K., et al. 2019, *ApJS*, **241**, 34
- Shen, Y., Horne, K., Grier, C. J., et al. 2016, *ApJ*, **818**, 30
- Shuder, J. M., & MacAlpine, G. M. 1979, *ApJ*, **230**, 348
- Singh, A., Sangwan, A., & Jassal, H. K. 2019, *JCAP*, **2019**, 047
- Sinha, S., & Banerjee, N. 2021, *JCAP*, **2021**, 060
- Solà Peracaula, J., Gómez-Valent, A., & de Cruz Pérez, J. 2019, *PDU*, **25**, 100311
- Stevens, J., Khoramizhad, H., & Saito, S. 2023, *JCAP*, **2023**, 046
- Stolc, M., Zajaček, M., Czerny, B., & Karas, V. 2023, *MNRAS*, **522**, 2869
- Ureña-López, L. A., & Roy, N. 2020, *PhRvD*, **102**, 063510
- Vagnozzi, S., Di Valentino, E., Gariazzo, S., et al. 2021a, *PDU*, **33**, 100851
- Vagnozzi, S., Loeb, A., & Moresco, M. 2021b, *ApJ*, **908**, 84
- Van Raamsdonk, M., & Waddell, C. 2023, arXiv:2305.04946
- Vanden Berk, D. E., Richards, G. T., Bauer, A., et al. 2001, *AJ*, **122**, 549
- Vanden Berk, D. E., Wesolowski, S. C., Yeckley, M. J., et al. 2020, *MNRAS*, **493**, 2745
- Wang, F., Yang, J., Fan, X., et al. 2021, *ApJL*, **907**, L1
- Wang, J.-M., Songsheng, Y.-Y., Li, Y.-R., Du, P., & Zhang, Z.-X. 2020, *NatAs*, **4**, 517
- Weaver, J. R., & Horne, K. 2022, *MNRAS*, **512**, 899
- Wu, P.-J., Qi, J.-Z., & Zhang, X. 2023, *ChPhC*, **47**, 055106
- Xu, T., Chen, Y., Xu, L., & Cao, S. 2022, *PDU*, **36**, 101023
- Yu, H., Ratra, B., & Wang, F.-Y. 2018, *ApJ*, **856**, 3
- Yu, Z., Martini, P., Penton, A., et al. 2021, *MNRAS*, **507**, 3771
- Zajaček, M., Czerny, B., Jaiswal, V. K., et al. 2023, arXiv:2306.15082
- Zajaček, M., Czerny, B., Martínez-Aldama, M. L., et al. 2021, *ApJ*, **912**, 10
- Zajaček, M., Karas, V., & Eckart, A. 2014, *A&A*, **565**, A17
- Zhai, Z., Blanton, M., Slosar, A., & Tinker, J. 2017, *ApJ*, **850**, 183

Paper 7: UV FeII Emission Model and BLR Time Delays








FeII emission has many line transitions, many of which contribute significantly to the UV and the optical spectra of quasars, creating collectively a so-called FeII pseudocontinuum. The UV FeII pseudocontinuum lies in the same wavelength range as the broad emission line of MgII at 280 nm, hence the knowledge of the FeII contribution, or rather a UV FeII model, can affect the inferred properties of the MgII line.

Previously, in Zajaček et al. (2020), we determined the redshift of HE 0413-4031 based on the UV FeII pseudocontinuum, which yielded the value of $z = 1.3764$. In this study, in addition to the 11-year monitoring by the Southern African Large Telescope (SALT), we included a near-IR spectrum obtained by the SOAR telescope. This gave an access to narrow H β (486.1 nm) and [OIII] transitions (495.9 nm and 500.7 nm), which led to a much better determination of the source redshift: $z = 1.39117 \pm 0.00017$. The new and more precise value of the redshift led to a different spectral decomposition into MgII and UV FeII spectral contributions. The properties and the time delay of MgII ($\tau_{\text{MgII}} = 224_{-23}^{+21}$ days) were not significantly influenced. However, the time delay of FeII ($\tau_{\text{FeII}} = 251_{-7}^{+9}$ days) is in agreement with the FeII line full width at half maximum (4200 km s^{-1}), which is slightly smaller than the MgII FWHM. These results are based on the new best-fitting FeII template and the same virial black-hole mass for MgII and FeII lines. Hence, the UV FeII line emitting material is more distant by 27 light days or $\sim 0.023 \text{ pc}$ (4700 AU) than the MgII line emitting material in HE 0413-4031. The new decomposition of the MgII+FeII complex also yields a much smaller blueshift of the MgII line in the range between -270 km s^{-1} and -240 km s^{-1} , which is consistent with the inferred line velocity shifts based on the composite spectra of quasars.

Furthermore, we also collect MgII time-delay measurements for as many as 194 sources, and the best-fit MgII $R_{\text{BLR}} - L$ relation, $\log(\tau/\text{lt. day}) = (0.32 \pm 0.04) \log(L_{3000}/10^{44} \text{ erg s}^{-1}) + (1.74 \pm 0.04)$, remains significantly flatter than $R_{\text{BLR}} - L$ relations for the H β , UV and optical FeII lines whose slopes are consistent with $\gamma \sim 0.5$ within the uncertainties, and hence also with the simple photoionization argument that assumes that the product of the ionization parameter and the electron number density for the broad-line region clouds across all AGN $U_{\text{ion}} n_e = Q(H)/(4\pi R_{\text{BLR}}^2 c)$ is approximately constant, and hence $R_{\text{BLR}} \propto Q(H)^{1/2} \propto L^{1/2}$ since the ionizing photon flux $Q(H) = \int_{\nu_1}^{+\infty} (L_\nu/h\nu) d\nu$ is proportional to the luminosity.

Credit: Zajaček et al. (2024c), A&A 683, A140. Reproduced with permission ©ESO.

UV FeII emission model of HE 0413–4031 and its relation to broad-line time delays★

Michal Zajaček¹, Swayamtrupta Panda²^{***}, Ashwani Pandey³, Raj Prince³, Alberto Rodríguez-Ardila^{2,4}, Vikram Jaiswal³, Bożena Czerny³, Krzysztof Hryniewicz⁵, Maciej Urbanowicz⁶, Piotr Trzcionkowski⁶, Marzena Śniegowska⁷, Zuzanna Fałkowska^{8,3}, Mary Loli Martínez-Aldama⁹, and Norbert Werner¹

¹ Department of Theoretical Physics and Astrophysics, Faculty of Science, Masaryk University, Kotlářská 2, 611 37 Brno, Czech Republic
 e-mail: michal.zajacek31@gmail.com

² Laboratório Nacional de Astrofísica, MCTI, Rua dos Estados Unidos, 154, 37504-364 Itajubá, MG, Brazil

³ Center for Theoretical Physics, Polish Academy of Sciences, Al. Lotników 32/46, 02-668 Warsaw, Poland

⁴ Instituto Nacional de Pesquisas Espaciais, Divisão de Astrofísica, Avenida dos Astronautas 1758, São José dos Campos, 12227-010 SP, Brazil

⁵ National Centre for Nuclear Research, ul. Pasteura 7, 02-093 Warsaw, Poland

⁶ Astronomical Observatory, University of Warsaw, Al. Ujazdowskie 4, 00-478 Warsaw, Poland

⁷ School of Physics and Astronomy, Tel Aviv University, Tel Aviv 69978, Israel

⁸ Faculty of Physics, University of Warsaw, ul. Pasteura 5, 02-093 Warsaw, Poland

⁹ Astronomy Department, Universidad de Concepción, Casilla 160-C, Concepción 4030000, Chile

Received 5 October 2023 / Accepted 20 December 2023

ABSTRACT

Context. FeII emission is a well-known contributor to the UV spectra of active galactic nuclei and the modeling of this part may affect the results obtained for the MgII λ 2800 emission, which is one of the lines used for black hole mass measurements and cosmological applications.

Aims. We tested different FeII emission models when modeling the UV emission of the intermediate-redshift quasar HE 0413–4031 to see how the use of a specific template affects the MgII λ 2800 line properties and the measurement of the MgII λ 2800 and UV FeII time delays with respect to the continuum.

Methods. We used the 11-year monitoring of the selected quasar HE 0413–4031 with the South African Large Telescope (SALT), and we supplemented this monitoring with the near-IR spectrum taken with the SOAR telescope, which gave access to the H β λ 4861 and [OIII] λ 4959, 5007 emission lines at the rest frame and allowed for a precise measurement of the redshift.

Results. A new redshift determination ($z = 1.39117 \pm 0.00017$) using [OIII] λ 4959, 5007 gave a very different value than the previous determination based only on the UV FeII pseudocontinuum ($z = 1.3764$). It favors a different decomposition of the spectrum into MgII and UV FeII emissions. The line characteristics and the time delay of the MgII emission (224^{+21}_{-23} days) are not significantly affected. However, in comparison with the previous analysis, the rest-frame UV FeII time delay (251^{+9}_{-7} days) is consistent with the inferred UV FeII line full width at half maximum (FWHM) of 4200 km s^{-1} that is only slightly smaller than the MgII line FWHM. Hence the FeII-emitting material is more distant than the MgII-emitting gas in HE 0413–4031 by $\sim 0.023 \text{ pc}$ (4700 AU). The inferred velocity shift of both MgII and UV FeII lines with respect to the systemic redshift is now rather low, below 300 km s^{-1} . In addition, we constructed an updated MgII radius-luminosity ($R-L$) relation from 194 sources, which is more than double the previous sample. The MgII $R-L$ relation is flatter than the UV FeII, optical FeII, and H β $R-L$ relations. While the new decomposition of the spectrum is satisfactory, we see a need to create better FeII templates using the newest version of the code CLOUDY.

Key words. accretion, accretion disks – techniques: photometric – techniques: spectroscopic – quasars: emission lines – quasars: individual: HE 0413–4031

1. Introduction

The characteristic property of the bright active galactic nuclei (AGN) is the occurrence of broad and strong emission lines in the optical and UV bands (see Krolik 1999; Karas et al. 2021; Czerny et al. 2023a,b, for reviews). Those emission lines are clearly visible in the individual objects as well as in the quasar composite spectra (e.g., Cristiani & Vio 1990; Francis et al. 1991; Vanden Berk et al. 2001). The strongest emission lines usually listed in the quasar catalogs for individual objects

are H β λ 4861, MgII λ 2800, CIII] λ 1908, CIV λ 1549, and Ly α λ 1215, depending on the object redshift and the coverage in the corresponding rest frame. Many more lines are listed in a single source or smaller sample studies (see, e.g., Martínez-Aldama et al. 2018; Horne et al. 2021; Shen et al. 2023). Apart from the well-specified lines, there is a contribution from the Balmer continuum supplementing the emission of the accretion disk responsible for the continuum emission. The last but very important contributor is the emission from the FeII and FeIII ions (see e.g., Gaskell et al. 2022, for a short review). Numerous transitions present in the optical and UV data lead to the formation of the FeII pseudo-continuum. Particularly, in the vicinity of the MgII line, there is a strong and

* Based on observations made with the Southern African Large Telescope (SALT).

** CNPq Fellow.

overlapping contribution from FeII. The issue has been studied for many years (e.g., Collin-Souffrin et al. 1979; Wills et al. 1980, 1985). The presence of FeII in bright AGN is universal; a similar FeII/MgII line ratio is observed in AGN at all redshifts, from nearby sources to $z \sim 5$ objects (Dietrich et al. 2003).

However, the FeII contribution to the optical band is not well correlated with FeII in the UV domain (Kovačević-Dojčinović & Popović 2015, hereafter also denoted as KDP15; Popović et al. 2019). The optical FeII strongly correlates with the source Eddington ratio, which underlies the concept of the quasar optical main sequence (Boroson & Green 1992; Sulentic et al. 2000; Panda et al. 2018, 2019c). The existence of the corresponding UV quasar plane based on MgII line properties and the UV FeII is not so well established (Śniegowska et al. 2020). The UV and optical FeII emission may be well correlated in a single object but it does not seem to come from the same part of the broad line region (BLR; Panda et al. 2019a; Zhao et al. 2020). In multi-object statistical samples, there is an overall correlation between the quasar luminosity and the UV FeII strength (Clowes et al. 2016). Several works (Marziani et al. 2003; Shen & Ho 2014; Panda et al. 2019c; Zheng 2021; Panda & Marziani 2023) claim that the FeII strength can actually be used as the Eddington ratio indicator.

The strong overlap between the UV FeII and MgII emissions complicates the measurements of the MgII time delay and makes the modeling of the emissivity and the dynamics of UV FeII difficult. The FeII models in this spectral range are either constructed from the data, with objects of extremely narrow emission lines, such as I Zw 1, serving as the best templates (Vestergaard & Wilkes 2001, hereafter also denoted as VW01), or theoretically (Bruhweiler & Verner 2008; Kovačević-Dojčinović & Popović 2015). The analysis is additionally complicated by the fact that the FeII emission can be considerably shifted with respect to the rest frame, which can also make an identification of the individual transitions in the data problematic.

The precision of the spectral decomposition close to the MgII line has several important consequences. First, the measurements of the kinematic width of the FeII and MgII components, and the measurements of the corresponding delays should shed light on the stratification of the BLR. The next issue is the proper determination of the radius-luminosity ($R-L$) relation for the MgII line which is essential for the black hole mass measurements from a single spectrum in large statistical samples (e.g., Wang et al. 2009; Kovačević-Dojčinović et al. 2017; Le et al. 2020). These $R-L$ relations for both MgII and FeII can also reveal stratification of the BLR. Proper determination of the FeII is also important from the point of view of the statistical studies of the AGN properties. The principal component analysis (PCA) approach by Boroson & Green (1992) clearly showed the dominant role of the two parameters: (i) the ratio of the FeII equivalent width in the optical band to the equivalent width of H β line, and (ii) the full width at half maximum (FWHM) of H β line. These two parameters form the optical plane, but in a close analogy, a UV plane can be introduced based on FeII emission in UV and MgII line properties (Panda et al. 2019a; Śniegowska et al. 2020). Finally, the $R-L$ relation can be successfully used in cosmological studies to constrain the expansion rate of the Universe (Khadka et al. 2021).

The spectral decomposition into FeII and MgII can be improved by the wavelength-resolved time delay measurements. Such studies of three intermediate-redshift quasars were performed – for CTS C30-10 (Prince et al. 2022), and for HE 0413–4031 and HE 0435–431 (Prince et al. 2023), each mon-

itored for 11 years with the Southern African Large Telescope (SALT). The results did not imply any outflow but indicated different apparent stratification of the FeII and MgII emissions in the three quasars. The study, when combined with the separate FeII and MgII time delays available from the literature, also enabled us to create the radius-luminosity relation for both spectral features, which suggests more compact emission regions with FeII-emitting clouds being located closer to MgII-emitting material for a lower luminosity, while at higher monochromatic luminosities, both regions are more distant and they radially converge. However, our results were based on the assumption that FeII is at the systemic redshift and this assumption certainly could bias our choice of the FeII template.

The redshift determination for the source HE 0413–4031, which is a bright, intermediate-redshift quasar studied in this paper, was recently obtained based on the high-quality single spectrum in the IR band in the observed frame (Panda et al., in prep.). The spectrum covered well the H β region with accompanying narrow [OIII] $\lambda\lambda 4959, 5007$ lines. The position of the [OIII] line allowed for a precise measurement of the source redshift which was considerably different from the redshift used originally by Zajaček et al. (2020) for the MgII line reverberation mapping and by Prince et al. (2023) for the wavelength-resolved study. The previous value was determined based on the UV FeII pseudocontinuum transitions seen in the observed optical spectrum. Therefore, in this paper, we study several FeII templates with the final aim of fitting better the spectra and checking whether the substantial change in the FeII/MgII decomposition affects the measurement of the MgII and UV FeII time delays. This could have important implications for the use of the quasar emission-line time delays for cosmology (see e.g., Panda et al. 2019b; Czerny et al. 2021, 2023a; Khadka et al. 2021; Zajaček et al. 2021, 2023b; Cao et al. 2022, 2024, for applications).

The paper is organized as follows. We briefly describe the photometric and spectroscopic data in Sect. 2 and present a revised redshift for the source HE 0413–4031. In Sect. 3 we outline the spectral decomposition of our SALT spectra. We present the results (Sect. 4) from the spectral decomposition and the time delay analyses from the spectrophotometric data and highlight the significant effect on the measured parameters due to the change in the redshift for this source. We discuss the implication of the new time delays for the MgII and UV FeII emission lines and show the location of HE 0413–4031 in the updated MgII and FeII $R-L$ relations in Sect. 5. The new $R-L$ relation for MgII is based on the largest sample used for this purpose. We also show a new preliminary FeII spectral model using the updated version of the CLOUDY photoionization code, which exhibits several differences with respect to the older model. Furthermore, within the same section, we discuss the location of this source in the UV quasar main sequence. Finally, we summarize our findings in Sect. 6.

2. Observational data

We use almost the same data for the quasar HE 0413–4031, first identified in the Hamburg-ESO survey by Wisotzki et al. (2000), as was done by Prince et al. (2023). We supplement it with one new spectroscopic long-slit measurement from the Southern African Large Telescope (SALT), obtained in January 2023, so the whole spectroscopic monitoring covers the period from January 2013 till January 2023. The basic raw data reduction is done by the standard SALT pipeline for the Robert Stobbie

Spectrograph (RSS; Burgh et al. 2003; Kobulnicky et al. 2003; Smith et al. 2006; see also Crawford et al. 2010).

We supplement the spectroscopic data with photometric data from several telescopes, as described in Prince et al. (2023). This data is needed for the absolute calibration of the spectra. The basic quasar properties were estimated previously (Zajaček et al. 2020). The black hole mass based on the reverberation mapping and the spectral energy distribution fitting is in the range $\log(M_{\bullet}/M_{\odot}) = 9.0\text{--}9.7$ (Zajaček et al. 2020). The SMBH accretes close to the Eddington limit, $\lambda_{\text{Edd}} = 0.38\text{--}2.18$, which was estimated using the inferred range of SMBH masses and different values of the bolometric correction (see Zajaček et al. 2020, for details). The quasar is bright, with the V magnitude typically about 16.5 as reported by Véron-Cetty & Véron (2010).

The redshift was estimated as $z = 1.3764$ assuming that the UV FeII emission in this source is at the quasar rest frame (Zajaček et al. 2020). Then the best fitting FeII template was d12-m20-20-5.dat (hereafter d12), one of the theoretical templates of Bruhweiler & Verner (2008), corresponding to the cloud number density of 10^{12} cm^{-3} , the turbulent velocity of 20 km s^{-1} , and the hydrogen ionizing photon flux of $10^{20.5}\text{ cm}^{-2}\text{ s}^{-1}$. However, a recent high-quality observation of this source in the near-IR (NIR) using the TripleSpec4 long-slit spectrograph (Schlawin et al. 2014) on the 4.1 m SOAR (see Fig. 1 and Table 1) brought the new determination of the redshift of 1.39117 ± 0.00017 (Panda et al., in prep.). Briefly, we use a custom script that calculates the barycenter of the data points around a selected wavelength range and informs the wavelength with respect to the peak position of the [OIII] λ 5007 emission line. We extract the wavelengths for the doublet [OIII] λ 4959, 5007 lines separately and find that the resulting redshifts are identical up to the 4th decimal place. Henceforth, we consider the value of the redshift derived from the [OIII] λ 5007 line as quoted above. The error on the redshift is estimated from the RMS of the skylines in the spectrum in the 6th order of the cross-dispersed spectrum, that is where the H β region including the [OIII] λ 4959, 5007 are observed.

The observations were made in cross-dispersed mode and the spectral resolution (R) for this spectrum was ~ 3500 across the different dispersion orders. Observations were made nodding in two positions along the slit. Right before the science target, a telluric star (HIP18437), close in airmass to the former, was observed to remove telluric features and to perform the flux calibration. Cu-Hg-Ar arc frames were also observed at the same position as the science target for wavelength calibration. The rms for the calibrated spectrum was found to be 0.201 \AA and the wavelength scale has been realigned to the wavelength of the skylines as recorded on the spectrum of the target. The spectral reduction, extraction, and wavelength calibration procedures were performed using SPECTOOL v4.1, an IDL-based software developed and provided by the SpeX team (Cushing et al. 2004) with some modifications specifically designed for the data format and characteristics of TripleSpec4, written by Katelyn Allers (priv. comm.). Telluric feature removal and flux calibration were done using XTELLCOR (Vacca et al. 2003). The different orders were merged into a single 1D spectrum from 1 to 2.4 microns using the XMERGEORDERS routine.

This new redshift value implies a rough velocity shift by 4400 km s^{-1} . It implies that either the FeII is outflowing with an extreme velocity, higher than typically seen in the UV FeII component (below 3000 km s^{-1} ; Kovačević-Dojčinović & Popović 2015), or the FeII template used in our previous work is not correct. For this reason, we try out different UV FeII templates

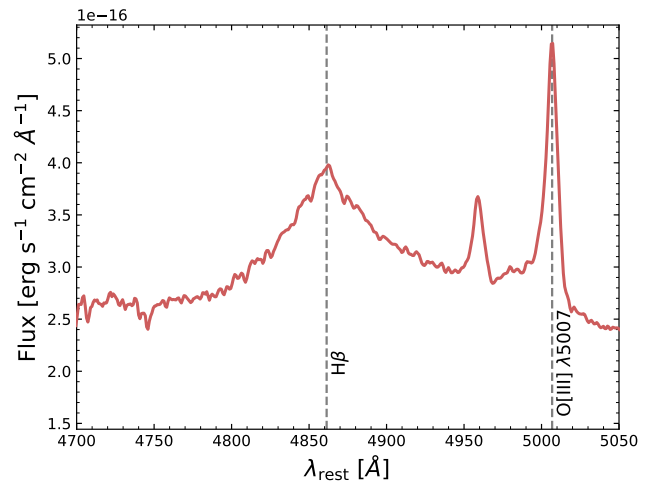


Fig. 1. Rest-frame spectrum for the HE 0413–4031 covering the spectral range around the H β region obtained using the SOAR/TripleSpec4 NIR spectrograph. The redshift ($z = 1.39117 \pm 0.00017$) was estimated using the [O III] λ 5007 emission line. The zero-velocity positions of H β and [O III] λ 5007 emission lines are marked using the dashed vertical lines.

Table 1. SOAR IR fits with redshift $z = 1.39117 \pm 0.00017$ implied by fitting narrow lines.

Component	$FWHM$ [km s^{-1}]	σ [km s^{-1}]	EW [\AA]
Broad H β	5457 ± 238	2820 ± 21	55.1 ± 0.7
Narrow H β	552.3 ± 24.1	229.2 ± 1.7	0.70 ± 0.01
Narrow [O III] λ 4959	552.3 ± 24.1	229.2 ± 1.7	3.60 ± 0.04
Narrow [O III] λ 5007	552.3 ± 24.1	229.2 ± 1.7	9.20 ± 0.11

Notes. The full width at half maximum (FWHM), the line dispersion (σ), and the line equivalent width (EW) are reported for the broad and the narrow components of the H β , and the narrow components for the [O III] λ 4959 and [O III] λ 5007, respectively.

to see if we can obtain a better fit and overall consistency than previously.

3. Spectral decomposition method

The quasar HE 0413–4031 accretes at the high Eddington ratio and it shares the characteristics of type A quasars (Sulentic et al. 2000), analogs of Narrow Line Seyfert 1 class (Osterbrock & Pogge 1985) for lower-mass sources, especially its strong emission lines are well fitted with a single Lorentzian profile. Although the FWHM of the broad H β line is $5457 \pm 238\text{ km s}^{-1}$ (see Table 1), which is above the canonical FWHM division of 4000 km s^{-1} between type A and B quasars (Sulentic et al. 2000), this division shifts toward a larger FWHM for high-luminosity quasars as HE 0413–4031 (see Marziani et al. 2018, for discussion).

Thus, following the previous studies on this source, we assume a single kinematic component for the MgII line shape (Zajaček et al. 2020; Prince et al. 2023). However, we take into account that MgII is a doublet, and this is included in our modeling, assuming the same widths for the two components, fixed separation. The value of the doublet ratio was optimized by Zajaček et al. (2020) using the mean spectrum. We use the same

value of 1.9 in the current paper. The kinematic width, line position, and normalization are free parameters of the model. The underlying continuum is described as a power law with an arbitrary normalization and a slope. We fit the data in a relatively narrow range to avoid issues with broad-band normalization of the SALT spectra. In Prince et al. (2023), we used the rest-frame range of 2700–2900 Å which corresponds to 6416.50–6891.79 Å in the observed frame. Next, we aim to compare fits for the two values of the source redshift. Here we fit the data in the same observed wavelength range, corresponding to fitting the data in the range of 2683.09–2881.84 Å in the rest frame for the new redshift of 1.39117 ± 0.00017 . This is important since there is imperfect subtraction of the sky lines at the longest wavelength tail which might affect the data fitting and proper comparison of the results.

For the FeII pseudocontinuum, we test several templates: theoretical templates of Bruhweiler & Verner (2008), observational VW01 templates, and mixed KDP15 templates. Templates of Bruhweiler & Verner (2008) are just a collection of atomic transitions, so they require two parameters: template broadening and overall normalization. The VW01 template requires also two parameters for additional broadening. KDP15 templates contain six components with independent normalizations (five atomic representative transition groups – Multiplets 60, 61, 62, 63 and 78, plus I Zw 1 component), so overall they require 7 parameters. Optionally, we also consider the presence of the He II line at 2733.28 Å in the quasar spectrum.

4. Results

In this section, we assess the best FeII model template for the precisely determined redshift of HE 0413–4031, and subsequently, we analyze the impact of the selected FeII templates on the MgII and FeII emission full-width at half maximums (FWHMs), equivalent widths (EWs), light-curve properties, and time delays with respect to the continuum emission.

4.1. Spectral decomposition and the best FeII template

In the previous papers (Prince et al. 2023; Zajaček et al. 2020), we used the d12 template of Bruhweiler & Verner (2008). Thus, after the redshift correction, we first fit the data with the same template. However, all the fits with the d12 template for the new redshift are worse. The ratio of the new χ^2 value to the old one is shown in Fig. 2. The previously used FeII template is thus not compatible with the new redshift measurement.

The issue is a suitable representation of the apparent excess which is now seen at ~ 2730 Å, see the spectrum in Fig. 3 close to 6540 Å in the observed frame. With the previous value of the redshift, it was located at ~ 2750 Å and it was fitted by one of the strong FeII transitions seen in all Bruhweiler & Verner (2008) templates. Thus, we supplemented the d12 FeII template with the possibility of the contribution from the He II line $\lambda 2733.28$. This line was observed, for example, in the quasar IRAS P09104+4109 by Tran et al. (2000). We assumed the arbitrary position, the width, and the shift of this additional line. However, this did not improve the fit considerably. We also tested the VW01 template but the fit quality with the new redshift was very low. This could be due to the sharp FeII peaks in this template based on the observed spectrum of I Zw 1 with exceptionally narrow broad emission lines. Thus, we applied additional broadening to this template by convolving it with a Gaussian profile. For a grid of models with the Gaussian width

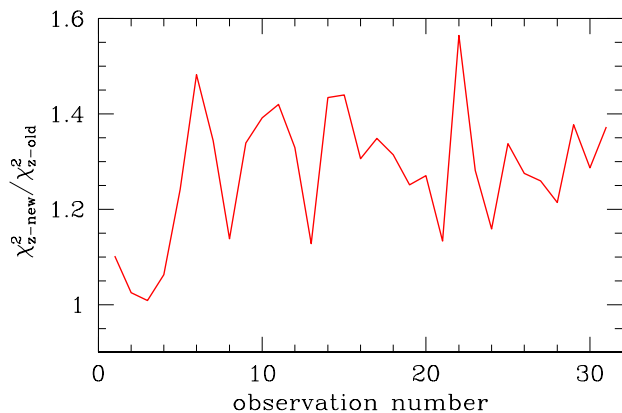


Fig. 2. Ratio of the new to the old value of χ^2 when two redshifts for the FeII template d12 are used.

sampled from 1000 to 1400 km s⁻¹ with the step 100 km s⁻¹, we obtained a χ^2 minimum at 1300 km s⁻¹. We give the value of 2600 km s⁻¹ in Table 2 since this better represents the FWHM. The new fit not only improved in comparison with the previous case but it became much better than the fit of the old template with an extra He II line.

Next, we used the set of UV FeII KDP15 templates. In the previous paper, we did not favor this template (see Zajaček et al. 2020, their Table C1) as it required a two-component shape of the MgII line to give an improved fit with respect to the d12 template. However, we were using smaller values of the redshift there. Now, with the new redshift from the IR data, we can indeed fit the data significantly better with this template.

We compare various spectral fits in detail for Observation 14, which is one of the best from the SALT observing campaign for the studied object (see Table 2). For the KDP15 template, we studied the width range from 3800 km s⁻¹ to 5000 km s⁻¹, and the shift range from +1000 km s⁻¹ to -4000 km s⁻¹. The contour plot is shown in Fig. 4. The best fit was achieved for a zero velocity shift of the FeII contribution and the broadening factor of $FWHM = 4200$ km s⁻¹. The improvement in the χ^2 value is by more than 100, which is significant for the number of new additional parameters of 5 (we now have 6 independent normalization factors of the FeII multiplets instead of 1 free parameter). However, since the number of degrees of freedom in the fits with d12 template and KDP15 template are different, we also determine the Bayesian Information Criterion (BIC) for these fits, which in the case of χ^2 fitting method reduces to $BIC = k \log n + \chi^2$, where k is the number of free parameters in the model and n is the number of data points (in our case, we have 578 points). The strong decrease in the BIC parameter supports the claim that the fit with the KDP15 template and the new redshift is better. The fitted parameters are given in Table 2.

Visually, both fits, d12 and KDP15 with the shift of 0 km s⁻¹ and the broadening of 4200 km s⁻¹ (denoted as KDP15-0-4200), provide a good fit to the data (see Fig. 3, upper panel). However, the decomposition of the spectrum into the MgII component and the FeII pseudo-continuum in both cases is rather different. We plot the FeII component alone in Fig. 3 (middle panel) with the same normalization. The FeII contribution to the spectrum is much lower for the KDP15 template and its shape in the rest frame is very different. We have made a test of fitting another observation (Observation 7) using again a broad range of shifts and widths for the KDP15 template. The best fit was found for slightly different parameters: the best shift of -500 km s⁻¹, and

Table 2. HE 0413–4031 fits of Observation 14 for different decompositions.

Model	$FWHM(\text{MgII})$ [km s^{-1}]	$EW(\text{MgII})$ [Å]	MgII shift [km s^{-1}]	$FWHM(\text{FeII})$	$EW(\text{FeII})$ [Å]	χ^2	k	ΔBIC
$z = 1.37648$, d12	$4601.6^{+105.8}_{-104.6}$	$28.1^{+0.3}_{-0.3}$	1668^{+5}_{-24}	2830	$10.3^{+0.6}_{-0.6}$	1246.04	6	0
$z = 1.37648$, VW01	$5187.5^{+129.4}_{-114.7}$	$29.8^{+0.5}_{-0.5}$	1472^{+37}_{-37}	–	$4.9^{+0.6}_{-0.6}$	1940.00	6	693.96
$z = 1.37648$, VW01	$5218.7^{+110.9}_{-121.6}$	$30.0^{+0.6}_{-0.6}$	1476^{+49}_{-34}	2400 ^(*)	$5.2^{+0.7}_{-0.7}$	1932.50	6	686.46
d12	$4906.3^{+50.3}_{-121.7}$	$28.0^{+0.4}_{-0.4}$	-67^{+19}_{-24}	2830	$5.7^{+0.5}_{-0.6}$	1787.35	6	541.31
d12 + He II $\lambda 2733.28$	$5046.9^{+150.0}_{-119.7}$	$28.9^{+0.3}_{-0.5}$	-108^{+20}_{-34}	2830	$3.8^{+0.7}_{-0.7}$	1485.76	9	258.80
VW01	$5085.9^{+89.0}_{-115.1}$	$33.7^{+0.5}_{-0.6}$	-212^{+12}_{-22}	–	$7.8^{+0.5}_{-0.5}$	1478.00	6	231.96
VW01	$5031.3^{+115.5}_{-109.2}$	$37.2^{+1.0}_{-1.2}$	-237^{+34}_{-9}	2600 ^(*)	$13.8^{+4.0}_{-1.9}$	1189.35	6	-56.69
KDP15-0-4200	$4503.1^{+58.0}_{-58.9}$	$27.1^{+0.2}_{-0.3}$	-270^{+15}_{-15}	4200	$4.0^{+0.43}_{-0.43}$	1130.50	11	-83.74

Notes. When the redshift is not mentioned, $z = 1.39117$ is adopted. Negative velocity implies blueshift and k is the number of free parameters in the model. ^(*)Additional broadening on top of that originally in the template.

$FWHM = 4800 \text{ km s}^{-1}$, although χ^2 at this minimum is not much lower than the χ^2 value for the best shift and FWHM favored for Observation 14.

The properties of the fitted FeII template are also rather surprising since the normalization of the multiplet 62 (see Appendix C in Zajaček et al. 2020, for the descriptions of individual UV FeII transitions), usually dominating at 2750 Å , converged to zero in the fitting process. Instead, most of the FeII flux at the blue wing of MgII (here and in the further text, the “blue wing” of the UV FeII refers to the wavelength range $2683.09\text{--}2800.00 \text{ Å}$ in the source rest frame while the “red wing” refers to the portion at $2800.00\text{--}2881.50 \text{ Å}$) is now provided by the Multiplet 63 as well as by the I Zw 1 component contribution (see Fig. 3, lower panel). It is also surprising to note that the width of the FeII lines in the new fit is only slightly narrower than the FWHM of the MgII line in this observation, which is 4503 km s^{-1} . However, this small FWHM difference is consistent with the inferred MgII and FeII time delays, see Sect. 4.3.

To test the role of the FeII template shape, we fit Observation 14 using the VW01 template. It gave a good fit when an optimized extra broadening was applied but not as good as the KDP15 template. It resulted in a much stronger FeII contribution, comparable to what we obtained for the old redshift and the d12 template. This template also favored the new redshift, as is seen from Table 2.

Since the KDP15-0-4200 template was the most satisfactory for the new redshift, we used it to fit all observations. We allowed all six normalization parameters of the template to vary but the width and the shift were the same. We do not expect drastic variations in the properties of the FeII emission during the campaign.

In Fig. 5, we compare the fit quality for all the observations for the new redshift and the new templates (KDP15 and VW01) to the previously used redshift and the old d12 template. We see that some observations are now fitted better and some are not. Statistically, the new redshift and the new template combination works slightly better since the average ratio of the corresponding χ^2 is 0.99. Specifically, the newly selected template with the new redshift gave the average value of the χ^2 of 1793.77 while the fit to all data with the old redshift and d12 template gave 1797.73. Therefore, on average, we do not see a high improvement, particularly when we keep in mind that the fit has, in principle, five more free parameters related to the FeII template. However, the fit is equally satisfactory as before and it uses the new redshift coming from the IR data.

The new spectral decomposition does not strongly affect the MgII line. The average value of the $EW(\text{MgII})$ is now $28.5 \pm 0.5 \text{ Å}$ with a dispersion of 2.8 Å , while when we use the old redshift and the old template, it is $30.7 \pm 0.6 \text{ Å}$ with the dispersion of 3.2 Å . The small systematic shift is visible in Fig. 5, lower panel and the level of variability dropped slightly. The pattern remains roughly the same as in our old analysis, with the initial strong rise, followed by a decrease up to JD 5000 and smaller variations afterward. Only the roughly systematic shift down by $\sim 2 \text{ Å}$ is visible.

The new fit to MgII also shows an interesting improvement after the change of the redshift. The position of the line during the fitting is a free parameter and the average shift of MgII now is only -234 km s^{-1} (blueshift), so the line is much closer to the systemic redshift than in the previous fitting (1650 km s^{-1} , redshift). The average width of the MgII line remains larger than that of the FeII (4605 km s^{-1} vs. 4200 km s^{-1}). A small systematic shift of the MgII line (from -212 to -270 km s^{-1}) is consistent with the velocity shifts with respect to [OIII] $\lambda 5007$ in the composite spectra of the quasar population (Vanden Berk et al. 2001).

However, the properties of FeII drastically changed. The new decomposition lowered the FeII EW level from the average $12.5 \pm 0.4 \text{ Å}$ down to $3.2 \pm 0.1 \text{ Å}$ in the studied wavelength band. Thus, the fractional variability in $EW(\text{FeII})$ is now higher, 24% while in the previous analysis, it was 17%. We did not subtract the measurement error here, so the quoted value is not the excess variance. In addition, the change does not look like a simple shift pattern but shows considerable randomness in time.

The fitted FeII template in principle has six independent components, corresponding to five Multiplets plus one component named I Zw 1, added for completeness (Kovačević-Dojčinović & Popović 2015). This extra component did not find support in the theoretical analysis of the strongest FeII transitions close to MgII but some strong features contributing at $\sim 2715 \text{ Å}$ and peaking at around $\sim 2840 \text{ Å}$ were present in the spectrum of the object I Zw 1, and such a component seemed to be required to fit the spectra of other objects so it was included in the KDP15 set as a sixth component named UVFeII-I Zw 1 lines. We later refer to this component as I Zw 1 component. However, not all of the six components were actually important for fitting the object studied in this paper. Actually, during the fitting, some of these six components were best fitted with a zero normalization, as in the case of Observation 14.

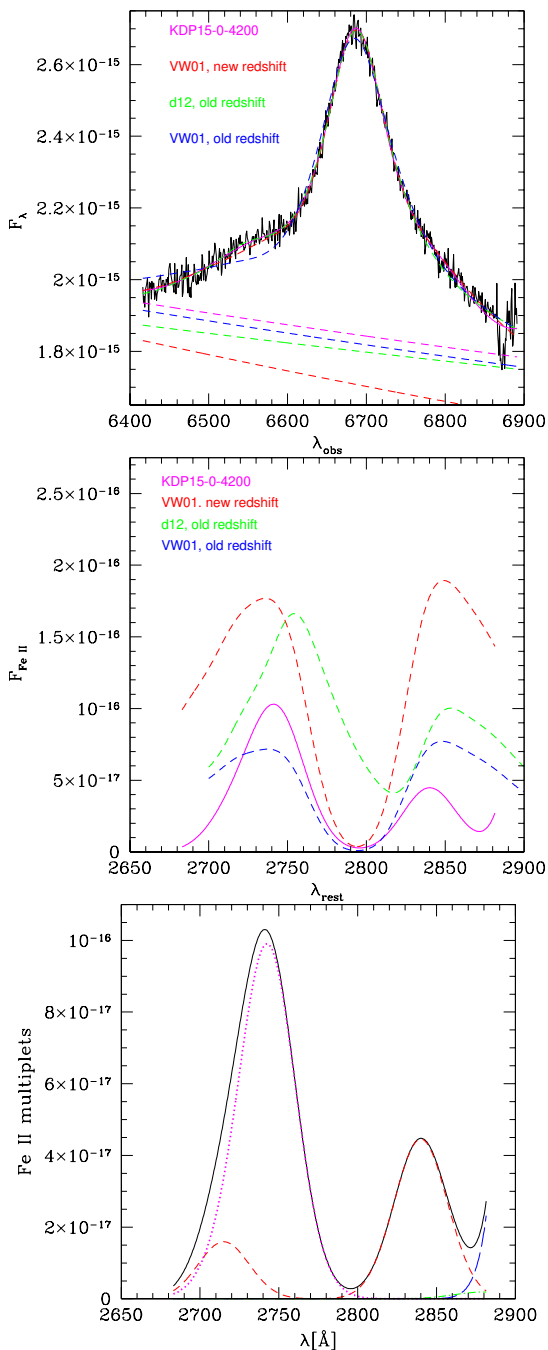


Fig. 3. Modeling spectra with various FeII templates for the old and the new redshift. Upper panel: Four fits of Observation 14 in the observed frame: two models for the old redshift $z = 1.37648$, d12 and VW01 templates with extra broadening, and two for the new redshift $z = 1.39117$, the KDP15 template, shift = 0, $FWHM = 4200 \text{ km s}^{-1}$, and the VW01 template with additional broadening. Dashed lines show the corresponding continua. Middle panel: FeII contribution in the rest frame for all the FeII templates used for the fits in the upper panel (see the legend). Lower panel: Decomposition of the fitted FeII with the KDP15 template into individual multiplets: I Zw 1 (red dashed line), multiplet 60 (blue long dashed), multiplet 61 (green, dash-dot), multiplet 62 (yellow, invisible in the scale), multiplet 63 (magenta, dotted), and multiplet 78 (cyan, almost invisible in the scale), with the black line corresponding to the total FeII emission. The FeII flux density in all three panels is expressed in $\text{erg s}^{-1} \text{cm}^{-2} \text{Å}^{-1}$.

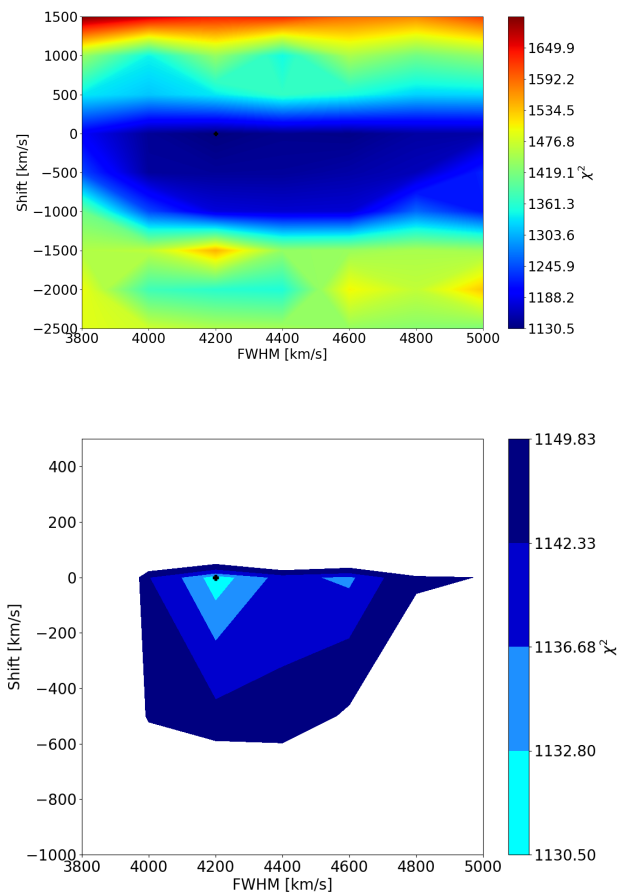


Fig. 4. Contour plot for fitting the KDP15 template to Observation 14. The upper panel shows the results for a broad parameter range, and the lower panel shows the best fit, and 1σ , 2σ , 3σ , and 4σ errors.

The key element that never vanishes is the Multiplet 63. The second component that is important in some of the spectra – but not in all the spectra – is the empirical I Zw 1 component. The largest variation was seen in Multiplet 60 which was occasionally zero, but sometimes present with a relatively large amplitude. This is related to the fact that this transition is usually strong but it peaks around 2950 Å , and below 2900 Å we see only its tail (see Kovačević-Dojčinović & Popović 2015, their Fig. 4). A larger number of the degrees of freedom in the FeII template increased the relative variations of the FeII intensity as a function of time. It happened despite the fact of using the same shift and width in all 32 data sets. We additionally tested the effect of the change of the shift and the FWHM of the FeII on the final FeII strength. As we mentioned above, for Observation 7, the best shift was -500 km s^{-1} , and the best FWHM was 4800 km s^{-1} , which slightly differs from the values adopted here and based on Observation 14. In this nonstandard fit, the EW of FeII was indeed higher, 6.9 Å instead of 3.9 Å for a standard fit illustrated in Fig. 5. However, this value is still below the value obtained with the old redshift (13.8 Å).

To illustrate better the FeII properties in the current fits, we created the average FeII profile by combining FeII contributions from all the observations. In Fig. 6, we show the mean unnormalized FeII as fitted by the model, together with Multiplet 63 (black line). This component peaks at $\sim 2742 \text{ Å}$. The weakness of

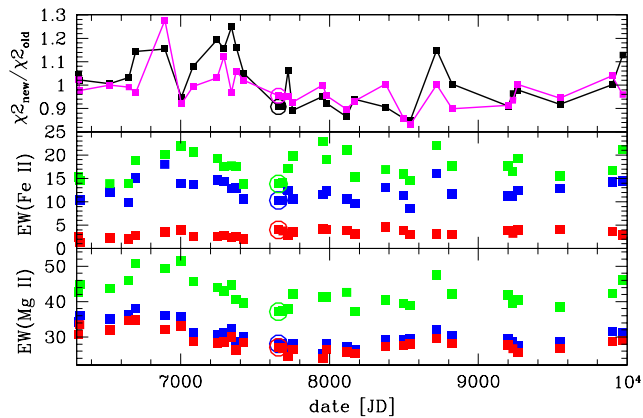


Fig. 5. Comparison of the fit quality using the new UV FeII templates and the previous one. Upper panel: χ^2 ratio between the new redshift fits for the KDP15 template with no shift, 4200 km s⁻¹ broadening (black line), and for the VW01 template (magenta line) with additional broadening and the fit with the d12 template and the old redshift. Middle panel: EW(Fe II). Lower panel: EW(Mg II) in these fits (blue, old redshift and template; red, KDP15; and green, VW01). Observation 14 is highlighted with an open circle.

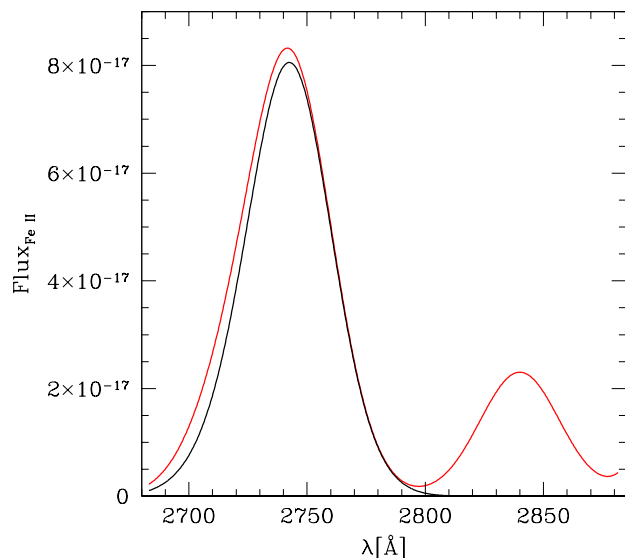


Fig. 6. Mean FeII emission averaged over all 32 observations (red) as fitted by all six components. The black line represents the contribution from the multiplet 63 and the remaining part is almost entirely due to the I Zw 1 component (see KDP15), for FWHM of 4200 km s⁻¹, and no shift with respect to the systemic redshift. FeII flux density is in units of erg s⁻¹ cm⁻² Å⁻¹.

Multiplet 62 is rather surprising since this should be the strongest of the transitions.

4.2. MgII and FeII light curves

To perform time-delay measurements, we created MgII and FeII light curves as we did in Prince et al. (2023) by normalizing each spectrum with the help of photometry and subtracting the underlying power-law component as well as MgII and FeII contributions, accordingly. In comparison to Prince et al. (2023), in this work, we have an additional SALT spectrum taken on January 26, 2023 (MJD 59970) extending the total duration from January

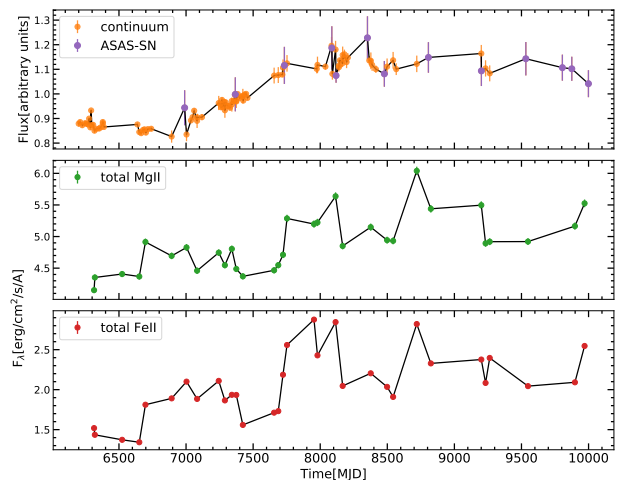


Fig. 7. All photometric light curves including archival data from the ASAS-SN. The middle and lower panels show the total MgII and FeII emission light curves in units of 10⁻¹⁶ erg cm⁻² s⁻¹ derived using the new redshift, $z = 1.39117$, respectively. The FeII pseudocontinuum was modeled using the VW01 template.

2013 to January 2023. The SALT spectrum is reduced following a similar procedure as described in Prince et al. (2023). The total length of the continuum light curve is 3799.30 days with a mean cadence of 37.25 days. The BLR line-emission light curves have a total length of 3655.98 days, with a mean sampling of 117.93 days.

The normalized MgII and FeII light curves, together with the continuum light curve are shown in Fig. 7. For the continuum V band data, the photometric information is collected from various telescopes, namely the 1.5 m telescope at OGLE observatory, 40 cm Bochum Monitoring Telescope (BMT), and SALT measurement with the SALTICAM (all are shown in orange color). In addition, we also include the archival V-band data from ASAS-SN (in purple) to extend the baseline of the continuum emission.

4.3. MgII and FeII time delays

Using the continuum, MgII, and FeII light curves, we performed time-delay analyses to find out if robust time delays can be detected for the new UV FeII templates. In particular, in comparison with the previous time-delay analyses of HE 0413–4031, here we focus on the role of the FeII emission model (template) in affecting the line-emission correlation with the continuum, and thus the time-delay determination.

We used different time-delay methodologies, namely interpolated cross-correlation function (ICCF; Peterson et al. 1998), discrete correlation function (DCF; Edelson & Krolik 1988), z-transferred DCF (zDCF; Alexander 1997), χ^2 method (Czerny et al. 2013), JAVELIN (Zu et al. 2011, 2013, 2016), von Neumann, and Bartels estimators (Chelouche et al. 2017) to infer the best time delay. For completeness, we show the plots and the inferred time-delay estimates for all the methods in Appendix A. For comparison, two comparably good FeII templates were considered to infer the MgII and the FeII emission time delays: the KDP15 template and the VW01 template. The uncertainties were typically inferred using the time-delay peak distributions constructed from several hundred light curves generated using the bootstrap method (see e.g.,

Table 3. Summary of MgII emission time delays inferred using different methodologies.

Method	KDP15	VW01
ICCF – highest r	541 ($r = 0.87$)	606 ($r = 0.73$)
ICCF – peak	552 ⁺⁷⁹ ₋₇₀	605 ⁺³⁰ ₋₂₁₉
ICCF – centroid	491 ⁺⁵⁰ ₋₄₇	517 ⁺⁹⁵ ₋₉₀
DCF	565 ⁺³⁴ ₋₃₄	586 ⁺²⁹ ₋₂₉
zDCF	597 ⁺³⁵ ₋₇₅	638 ⁺⁴⁹ ₋₉₃
χ^2	619 ⁺²⁶ ₋₁₁₆	623 ⁺²⁷ ₋₆₂
Javelin	493 ⁺⁴ ₋₁₅	493 ⁺³ ₋₁₇
Von Neumann	495 ⁺¹² ₋₁₁₃	405 ⁺⁴² ₋₂₇
Bartels	495 ⁺¹⁹ ₋₁₁₃	405 ⁺⁴⁵ ₋₃₄
$\bar{\tau}$ – observer’s frame	538 ⁺⁵¹ ₋₅₆	534 ⁺⁸⁹ ₋₉₄
$\bar{\tau}$ – rest frame	225 ⁺²¹ ₋₂₃	223 ⁺³⁷ ₋₃₉
Final MgII time delay	224 ⁺²¹ ₋₂₃	

Notes. For individual methods, time delays are expressed in days in the observer’s frame, while the last two rows represent the mean time delays expressed in days in the rest frame of the source.

Zajaček et al. 2019, 2020; Prince et al. 2023, where we already applied all the methods used in this paper).

The time delay results for MgII emission are summarized in Table 3, where the values are expressed in the observer’s frame unless stated otherwise. The time delays are generally between ~ 500 and ~ 600 days, except for the Bartels method and the VW01 template, which indicates the best time delay at ~ 405 days. The time-delay calculations for the MgII line with the new redshift give very similar results to what was obtained in Prince et al. (2023) as well as in Zajaček et al. (2020) using the old redshift. This is related to the fact the decomposition in both cases (the older and the new redshift) yielded very similar values of the equivalent width of MgII (see lower panel of Fig. 5).

The MgII light curve is very strongly correlated with the continuum light curve, which implies that the observed continuum is the driving photoionizing emission. In particular, the case of the best-fit FeII template KDP15 exhibits the peak correlation coefficient of $r \sim 0.87$. For the VW01 template, the correlation coefficient only slightly drops to $r \sim 0.73$. This trend is also reflected for other time-delay methods, for which the cases with the VW01 template exhibit lower correlation coefficients (zDCF) or the minima are located at larger values of the corresponding measures (χ^2 , von Neumann, and Bartels estimators, see Appendix A). This can be interpreted as the result of the VW01 FeII emission model, which is older and more approximate than the KDP15 model, which lowers the overall correlation of MgII with the continuum. Despite that the determined best MgII time delays are consistent within the uncertainties among the different time-delay methods and the two templates, see Table 3. By averaging the time delays among different methods and the two templates, we arrive at the final value of $\tau_{\text{MgII}} = 224^{+21}_{-23}$ days in the rest frame of the source. This value is within 2σ uncertainty consistent with the values reported in Prince et al. (2023) and Zajaček et al. (2020), whose mean values are $\sim 26\%$ and $\sim 35\%$ larger than the one found here for the new redshift and KDP15/VW01 templates.

However, the FeII intensity is much different in these two cases. The FeII emission in the new KDP15 decomposition

based on the new redshift is now by a factor of 3 fainter. We performed time-delay computations but we did not obtain a satisfactory solution for the time delay. The situation is best illustrated in the case of the ICCF plot (see Fig. 8, left panel, dashed lines). The maximum value of the correlation coefficient r is close to 0.8 for both KDP15 and VW01 templates which clearly shows that the FeII light curve and the continuum are very well correlated. However, the function peaks close to the zero time delay, see the summary of peak and centroid values for both templates in Table 4 (first three rows). This strongly suggests that the FeII light curve is strongly contaminated by the continuum itself and the decomposition of the spectrum into FeII and continuum is probably not satisfactory.

In the next attempt to search for a FeII time delay, we just consider the blue wing of the FeII emission in the wavelength range $2683.09\text{--}2800.00 \text{ \AA}$, which is dominated by FeII multiplet 63. The blue wing of the FeII emission is more pronounced within the KDP15 model, see Figs. 3 and 6, and thus less contaminated by the continuum. This does not result in a qualitative change of the ICCF and the peak correlation coefficient is again close to zero, see Fig. 8 and Table 4.

Finally, we assess that the large peak close to zero days is due to the continuum long-term trend present in both light curves. For the FeII emission light curve, the trend is present due to significant contamination by continuum. Therefore, to isolate the FeII variability and response, we subtract the long-term (hereafter LT) trend from both light curves using the fitted third-order polynomial in the form $f_{\text{trend}} = f_1(t-t_0)^3 + f_2(t-t_0)^2 + f_3(t-t_0) + f_4$, where f_1 , f_2 , f_3 , and f_4 are the fitted parameters. We show the continuum and the UV FeII emission light curves after the LT trend subtraction in Fig. 9 for the case of the KDP15 template (the FeII emission corresponds to the more prominent blue wing), wherein the top panels we display the original light curves and in the bottom panels we show the corresponding light curves after the LT term subtraction and with the addition of the mean flux densities of the original light curves. This proves efficient in enhancing the correlated and delayed FeII emission (see Fig. 8, solid lines), which is revealed by the asymmetric ICCF that is increasing for positive time delays. When we consider negative and positive time delays in the ranges $(-800, 0)$ days and $(0, +800)$ days, the calculated mean values of correlation coefficients for the templates KDP15, KDP15–blue wing, and VW01 are listed in Table 5, where we see that after the LT trend subtraction (templates denoted by the star), the ICCF gets asymmetric with the mean correlation coefficients for time delays above zero days being greater and positive. For the large time-delay interval of $(-1500, 1500)$ days, the peak and centroid values become larger and mostly positive with respect to the cases without the LT trend subtraction, see Table 4. However, this is at the cost of generally lower correlation with the peak values of only $r \sim 0.3\text{--}0.4$. The well-defined correlation peak at ~ 600 days (in the observer’s frame) for the KDP15 FeII template–blue wing is considered as the best candidate time-delay peak. Thus, when we narrow down the search interval to $(450, 750)$ days for KDP15, KDP15–blue wing, and VW01 templates, all three cases share consistent peak and centroid ICCF values close to ~ 600 days, see Table 4 (last three rows). This is also confirmed visually in Fig. 9 (bottom left panel), where we superpose the rescaled FeII light curve shifted by -600 days. Although these time-delay values correspond to rather low correlation coefficients, we treat the time delay of $\tau_{\text{FeII}} = 251^{+9}_{-7}$ days (average of the peak and the centroid values for the KDP15–blue wing case expressed in the rest frame) as a plausible candidate value of the true FeII emission time delay.

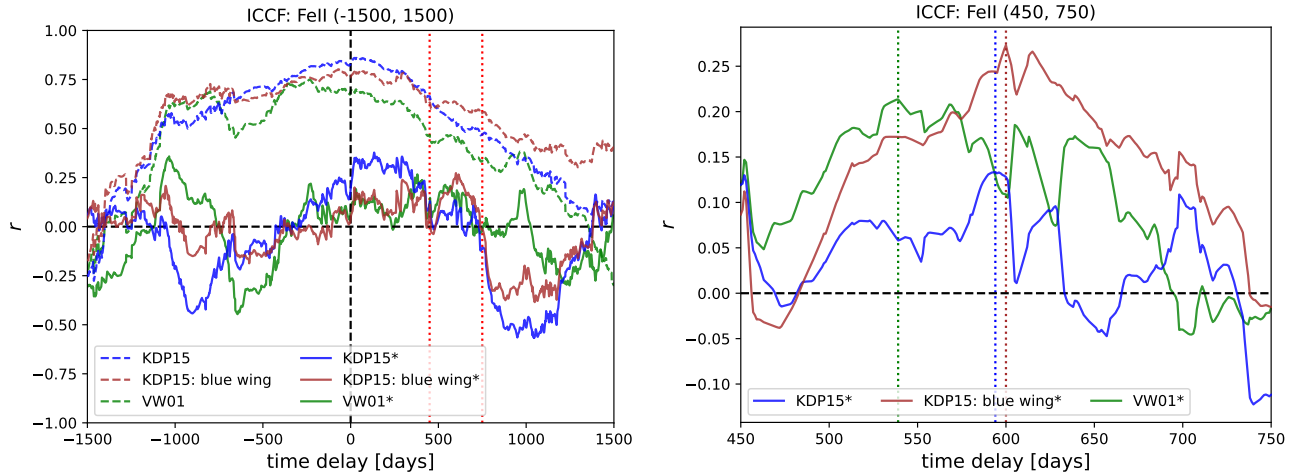


Fig. 8. ICCF for the FeII emission using different FeII templates (KDP15 and VW01). Left panel: The ICCF for the FeII templates KDP15, KDP15–blue wing, and VW01 without the long-term subtraction (dashed lines). By subtracting the long-term trend from the continuum and line-emission light curves, the ICCF becomes asymmetric with respect to zero (solid lines) and the time-delay peak between 450 and 750 days can be identified, especially for the blue-wing part of the KDP15 template. Right panel: The ICCF for all the three considered cases (KDP15, KDP15–blue wing, VW01) in the interval between 450 and 750 days in the observer’s frame. For the best-fitting KDP15 template, the cross-correlation peak is at ~ 600 days. See Table 4 for the summary of the peak and the centroid values (last three rows).

Table 4. Summary of FeII emission time-delay constraints (expressed in days in the observer’s frame) using the ICCF.

Method	KDP15	KDP15 – blue	VW01
ICCF – highest r (–1500,+1500)	50 ($r = 0.86$)	–71 ($r = 0.80$)	–237 ($r = 0.75$)
ICCF – peak (–1500,+1500)	34^{+62}_{-132}	22^{+187}_{-542}	-237^{+270}_{-122}
ICCF – centroid (–1500,+1500)	-38^{+93}_{-109}	-69^{+165}_{-269}	-85^{+92}_{-215}
ICCF (*) – highest r (–1500, +1500)	134 ($r = 0.38$)	600 ($r = 0.27$)	–1034 ($r = 0.36$)
ICCF (*) – peak (–1500, +1500)	134^{+162}_{-234}	128^{+472}_{-1194}	-31^{+569}_{-1016}
ICCF (*) – centroid (–1500, +1500)	127^{+183}_{-219}	114^{+483}_{-1184}	-50^{+580}_{-990}
ICCF (*) – highest r (450, 750)	594 ($r = 0.13$)	600 ($r = 0.27$)	539 ($r = 0.21$)
ICCF (*) – peak (450, 750)	595^{+96}_{-66}	600^{+31}_{-10}	574^{+67}_{-43}
ICCF (*) – centroid (450, 750)	592^{+102}_{-55}	602^{+28}_{-30}	570^{+76}_{-39}
Final FeII time delay (rest frame)		251^{+9}_{-7}	

Notes. The results denoted with the star (ICCF^(*)) represent the cases with the long-term trend subtraction (using the third-order polynomial fit) from both light curves. The time interval in the parentheses denotes the search interval for the best time delay.

In Appendix A.7, we also verify that after the subtraction of the LT trend from the MgII light curve, it is possible to recover the time delay reported previously. Using the ICCF, we can recover a time-delay peak between ~ 400 – 600 days (in the observer’s frame), albeit at a significantly lower correlation coefficient of ~ 0.4 – 0.5 . When the centroid and the peak values are averaged among the two templates, the mean rest-frame time delay 213^{+62}_{-35} days is in agreement with the previously reported time delay without any LT trend subtraction. Hence, in summary, the LT trend subtraction can help recover a time delay between the two light curves, especially for line light curves contaminated by the underlying continuum emission, such as for the FeII emission in this paper, although it is at a cost of lowering the correlation coefficient and increasing the uncertainty in the time-delay determination.

5. Discussion

We analyzed the spectroscopic data collected in the years 2013–2023 with the telescope SALT for the intermediate-

redshift quasar HE 0413–4031, concentrating on the MgII spectral region. These data include one more spectrum than the data analyzed by Prince et al. (2023) but most importantly, in the meantime, we determined the precise redshift to the quasar from the IR observation at the observed frame with the telescope SOAR which is based on the narrow optical [OIII] $\lambda\lambda 4959, 5007$ lines considered as the most reliable indicators of the quasar rest frame. New redshift determination essentially changed the decomposition of the quasar UV spectrum into MgII, FeII, and the underlying continuum. We checked how it affected the time delay measurements.

We showed that the MgII time delay was not affected by the change of the redshift and decomposition. The new decomposition with the UV FeII KDP15 template implies no shift with respect to the systemic redshift while the previous redshift/decomposition indicated the velocity shift between the FeII and MgII. Nevertheless, the time delay remained the same, from 500 to 600 days in the observed frame, independent of the decomposition, redshift, and the time delay measurement

Table 5. Comparison of correlation coefficients for different FeII templates for time delays below and above zero days (up to ∓ 800 days).

Template	(−800, 0)	(0, 800)
KDP15	0.74	0.68
KDP15–blue-wing	0.71	0.68
VW01	0.63	0.53
KDP15 ^(*)	−0.01	0.16
KDP15 ^(*) –blue-wing	−0.04	0.11
VW01 ^(*)	−0.08	0.10

Notes. After the long-term trend subtraction from both continuum and FeII light curves, the ICCF becomes clearly asymmetric, and for time delays larger than zero days, the mean correlation coefficient is greater and positive. The templates denoted by ^(*) represent the light curves with the long-term trend subtraction (last three rows).

method. Thus the maximum systematic error is on the order of 10%. We thus stress that the MgII line time delay can be used reliably for probing the properties of the BLR and for cosmology, and the results are not sensitive to the actual method.

However, the line properties of the FeII emission are very sensitive to the redshift and the best-fitting FeII model. Previously, in Prince et al. (2023) we performed the time-delay analysis of the total FeII emission as well as wavelength-resolved reverberation mapping of the MgII+FeII complex. The recovered MgII and FeII time delays based on different methods, 314.4 and 330.6 days, respectively, are in tension with the MgII and FeII FWHMs, $FWHM(\text{MgII}) = 4380 \text{ km s}^{-1}$ and $FWHM(\text{FeII}) = 2820 \text{ km s}^{-1}$, respectively. Assuming that the MgII and FeII material is fully virialized with the same virial factor, the FeII time delay should be significantly larger than the one reported by Prince et al. (2023), $\tau_{\text{FeII}} = 314.4(4380/2820)^2 \text{ days} \sim 758 \text{ days}$. In the current analysis, with the new redshift and the new KDP15 template, the inferred MgII and FeII time delays and the corresponding FWHMs appear to be fully in agreement since the FeII rest-frame time delay expected from the virialized motion, $\tau_{\text{FeII}} = \tau_{\text{MgII}}(FWHM(\text{MgII})/FWHM(\text{FeII}))^2 \sim 224(4503.1/4200)^2 \text{ days} \sim 257 \text{ days}$, is consistent with the FeII time delay inferred from reverberation, $\tau_{\text{FeII}} = 251_{-7}^{+9} \text{ days}$. This implies that FeII emitting material is more distant than MgII line-emitting material by ~ 27 light days or 0.023 pc ($\sim 4700 \text{ AU}$).

The quasar HE 0413–4031 does not seem to exhibit a separate very broad Gaussian component forming the wings of the MgII line as it is typical for lower Eddington sources (quasar type B population; Sulentic et al. 2000; Kovačević-Dojčinović & Popović 2015), so the line is well modeled by a single Lorentzian shape which helps to disentangle better FeII and MgII emission. This makes the decomposition into MgII and FeII relatively easier than in lower Eddington sources. This property remained true for all our experiments with the two redshifts and various FeII templates. HE 0413–4031 is therefore a good candidate for further FeII studies, complementing the nearby object I Zw 1.

An even more advanced technique is to use the wavelength-resolved time delays which allow us to trace separately the wings of the lines from the core as well as the kinematics of the BLR medium when multiple lines contribute to a given wavelength range. Such studies were done for more than 35 AGNs by various authors (Bentz et al. 2010; Denney et al. 2010;

Grier et al. 2012; Du et al. 2018; De Rosa et al. 2018; Xiao et al. 2018; Zhang et al. 2019; Hu et al. 2020; U et al. 2022) for low-redshift sources. When we analyzed the SALT data for the quasar HE 0413–4031 by subtracting the underlying continuum but without separating the MgII and FeII, we concluded that the FeII emission originates in a region slightly more distant than MgII (Prince et al. 2023). So the issue of the FeII emission region geometry is much more complex due to the pseudo-continuum character of this component than MgII which gives firm and reliable results.

The UV FeII emission template is also relevant for estimating the FeII pseudocontinuum and MgII emission contribution to the AGN UV emission in near-UV photometric bands. This is especially relevant for the future monitoring of nearby AGN using one-band (e.g., the ULTRASAT mission; Shvartzvald et al. 2023) or two-band UV photometry (e.g., the QUVIK mission; Werner et al. 2022, 2023; Krtićka et al. 2023), with the attempt to perform UV continuum reverberation mapping of accretion disks (Zajaček et al. 2023a). The reprocessing of the harder radiation by the BLR clouds dilutes the disk temporal response, which affects the continuum time delay measurements in a distinct way (Netzer 2022). The correct understanding of the UV FeII multiplet emission and its geometric distribution will help to account for and understand the reprocessing contribution by the BLR gas.

5.1. HE0413 and UV MgII and FeII R–L relations

Given the new redshift and best-fit FeII template, which resulted in slightly modified MgII and FeII time delays, we construct an updated UV MgII radius-luminosity relation or R–L relation. We build upon its previous versions presented in Czerny et al. (2019), Zajaček et al. (2020, 2021), Martínez-Aldama et al. (2020), and Prince et al. (2023), where we included a progressively larger number of MgII RM quasars (see also Homayouni et al. 2020; Yu et al. 2023).

Here we combine the sample of RM quasars with significant ($>2\sigma$) detections from the SDSS RM program (163 sources; Shen et al. 2016, 2023; Homayouni et al. 2020), OzDES RM program (25 sources; Yu et al. 2023), and 6 sources from other RM campaigns (Metzroth et al. 2006; Lira et al. 2018; Czerny et al. 2019; Prince et al. 2022, 2023). Altogether we collected 194 measurements, which is one of the largest samples of RM MgII AGN up to today. The sample exhibits a significant positive correlation between the rest-frame time delays and monochromatic luminosities at 3000 \AA with the Pearson correlation coefficient of 0.54 ($p = 2.22 \times 10^{-16}$) and the Spearman rank-order correlation coefficient of 0.50 ($p = 8.56 \times 10^{-14}$). Next we fit the power-law relation $\log(\tau [\text{days}]) = \beta + \gamma \log(L_{3000}/10^{44} \text{ erg s}^{-1})$ to the data. Using the Markov chain Monte Carlo (MCMC) approach implemented in the python package emcee, we infer the best-fit MgII R–L relation,

$$\log\left(\frac{\tau}{\text{day}}\right) = (1.74_{-0.04}^{+0.04}) + (0.32_{-0.04}^{+0.04}) \log\left(\frac{L_{3000}}{10^{44} \text{ erg s}^{-1}}\right). \quad (1)$$

We show the MgII R–L relation including the best-fit relation given by Eq. (2) in Fig. 10, see the top left panel. In the bottom left panel of Fig. 10, we display one-dimensional likelihood distributions and two-dimensional likelihood contours of the searched parameters. We can especially notice a distinct degeneracy (negative correlation) between the intercept and the slope. However, despite this degeneracy, the inferred slope is much flatter than 0.5, which is expected from arguments based

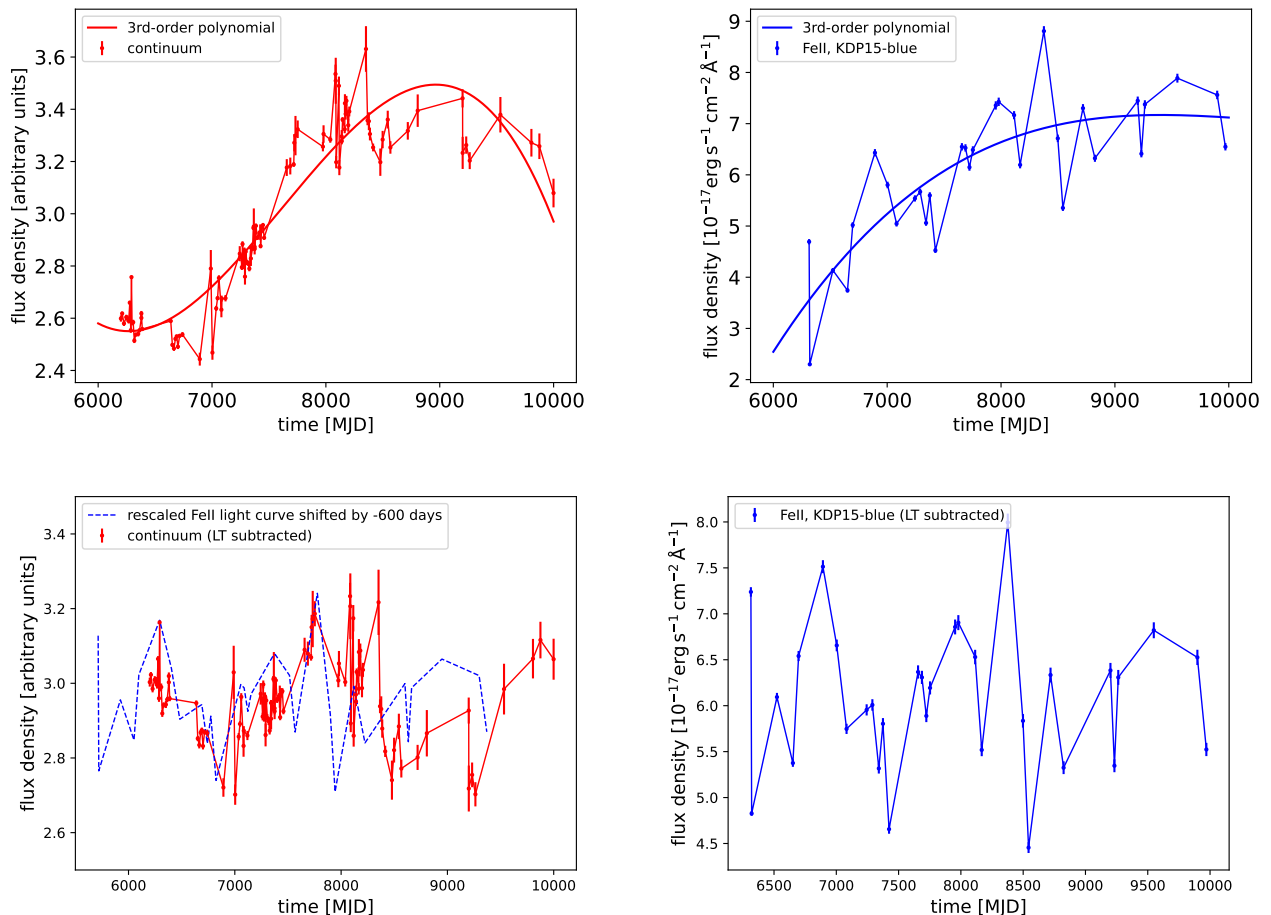


Fig. 9. Time-delay analysis using the long-term (hereafter LT) trend subtraction from continuum and FeII emission light curves. Upper panels: Continuum (left) and FeII emission light curve (right), which was inferred using the KDP15 template considering the more prominent blue wing, with the corresponding 3rd-order polynomial fits. Lower panels: Continuum and FeII emission light curves in the left and the right panels, respectively, after the LT trend was subtracted from both of them. The final light curves were reconstructed by adding the mean flux density value of the corresponding original light curves. In the left panel for the continuum light curve, we also show the rescaled FeII light curve shifted by -600 days, which corresponds to the ICCF maximum for this case.

on the ionization parameter (Davidson & Netzer 1979; see also the discussion in Bentz et al. 2013) or from the dust-based BLR model (Czerny & Hryniewicz 2011). The inferred intrinsic scatter is substantial, $\sigma_{\text{int}} = 0.30^{+0.02}_{-0.02}$, however, it is moderate given a relatively large number of time-delay measurements and comparable to the scatter found previously for a significantly smaller number of sources (Prince et al. 2023; Homayouni et al. 2020).

We also revisit the UV FeII $R-L$ relation, which was first presented in Prince et al. (2022) for 2 measurements only and in Prince et al. (2023) for 4 measurements, given the updated time delay for HE0413-4031 presented in Sect. 4.3. The two best-fit relations (RL1 and RL2) and their corresponding parameters found using the same MCMC approach as for the MgII are shown in Fig. 10 (top and bottom right panels). The two relations stem from the two plausible values for the UV FeII time delay for the quasar CTS C30.10 as found by Prince et al. (2022). This difference is, however, small and the two relations are identical within the uncertainties. The smaller RMS scatter is exhibited by the first UV FeII $R-L$ relation (RL1 in Fig. 10) where we take into account the smaller UV FeII time delay of CTS C30.10 ($\tau_{\text{FeII}} = 180.3^{+26.6}_{-30.0}$ days). The best-fit relation is,

$$\log\left(\frac{\tau}{\text{day}}\right) = (1.18^{+0.21}_{-0.20}) + (0.49^{+0.10}_{-0.09}) \log\left(\frac{L_{3000}}{10^{44} \text{ erg s}^{-1}}\right), \quad (2)$$

with the intrinsic scatter of $\sigma_{\text{int}} = 0.22^{+0.26}_{-0.12}$. For this relation, we show the one-dimensional likelihood distributions and two-dimensional likelihood contours in Fig. 10 (bottom right panel).

Although the number of UV FeII time-delay measurements is limited, we see in Fig. 10 that there is a tendency for UV FeII $R-L$ relation to be positioned below the MgII $R-L$ relation because of the smaller intercept. However, it appears to be steeper than the MgII $R-L$ relation, with the slope $\gamma \sim 0.5$ consistent with the standard photoionization theory of the BLR clouds. This results in larger differences between MgII and UV FeII time delays for lower luminosity sources, for which $\tau_{\text{MgII}} > \tau_{\text{FeII}}$, while at higher luminosities, both relations converge and intersect, which results in $\tau_{\text{MgII}} \lesssim \tau_{\text{FeII}}$. This also appears to be the case of HE 0413-4031 which is effectively at the high luminosity end of both MgII and UV FeII $R-L$ relations. This trend also seems to be in contrast with the $R-L$ relations in the optical domain, where both H β (Bentz et al. 2013) and optical FeII $R-L$ (Prince et al. 2023) relations are nearly identical with each other within the uncertainties when expressed for 3000 Å, see Fig. 10. Their slopes are also

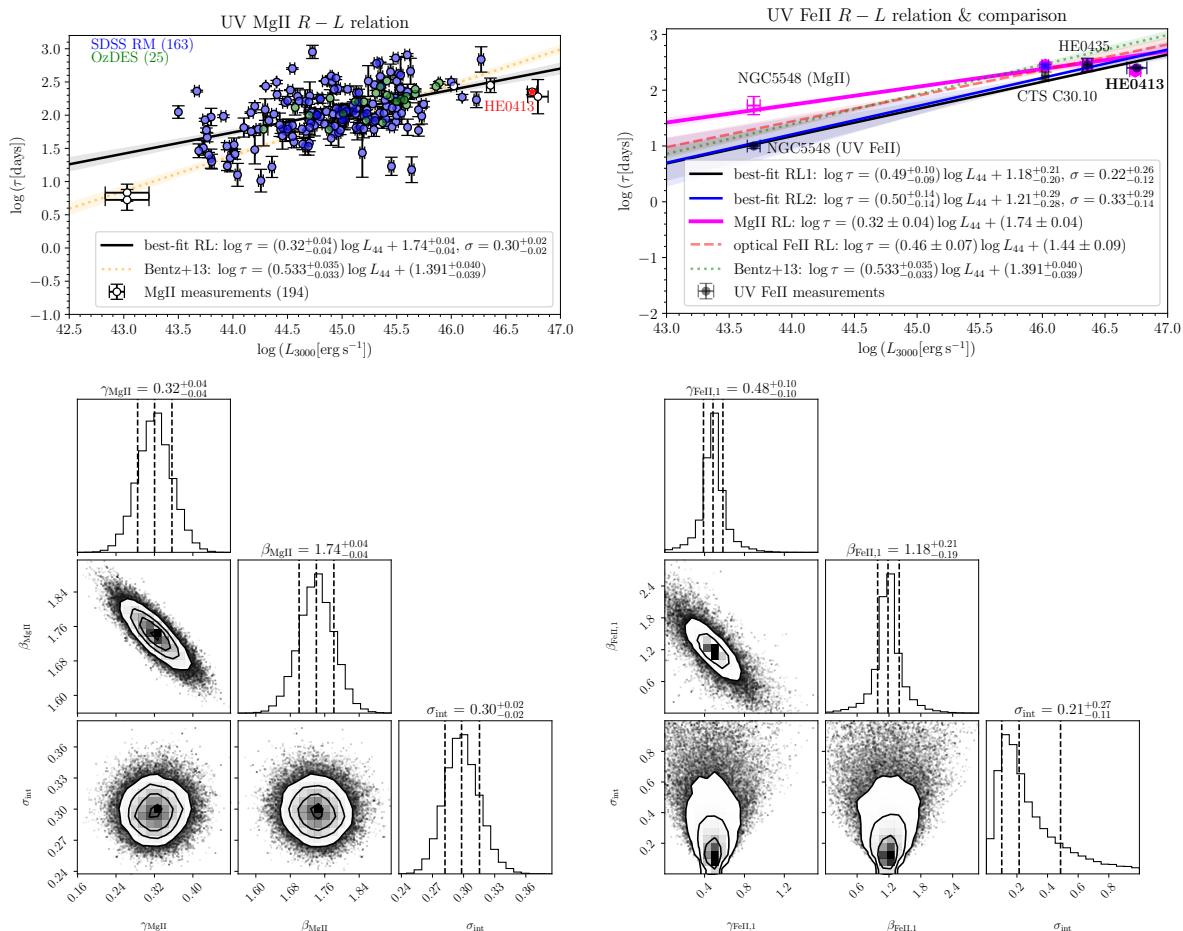


Fig. 10. Position of HE 0413–4031 in the UV MgII and FeII $R-L$ relations. Upper panels: MgII $R-L$ relation (left panel) constructed from 194 measurements (163 SDSS RM, 25 OzDES, and six other sources including HE 0413–4031). The best-fitted relation is in the legend. For comparison, we also include the H β relation (Bentz et al. 2013) recalculated for 3000 Å (dashed orange line). In the right panel, we show the UV FeII $R-L$ relation based on four RM measurements for NGC 5548, CTS C30.10, HE 0435–4312, and HE 0413–4031 (two comparable relations are plotted by solid black and dashed blue lines since there were two plausible FeII time delays for CTS C30.10). The UV FeII relation is steeper and lower than the flatter and higher MgII $R-L$ relation, which results in the convergence and their intersection towards higher luminosity sources. In the right panel, we also show for comparison the optical FeII relation inferred by Prince et al. (2023) from multiple measurements as well as the H β $R-L$ relation by Bentz et al. (2013) that are depicted by dashed red and green lines, respectively. Lower panels: One-dimensional confidence histograms and two-dimensional confidence contours for the searched parameters (slope γ , intercept β , and the intrinsic scatter σ_{int}) of the UV MgII $R-L$ relation (left panel) and of the UV FeII $R-L$ relation (right panel). For the UV FeII $R-L$ relation, we show the case with a smaller scatter, and hence the smaller FeII time delay of CTS C30.10.

in agreement with the simple photoionization arguments unlike MgII $R-L$ relation, which is significantly flatter.

5.2. Simple tests of CLOUDY models of the FeII emission

The three FeII templates we use are almost comparable in the fit quality for Observation 14 (see Fig. 3) but their shapes are considerably different. To have some insight into the physical nature of each template, we use the recent version C22.01 of the code CLOUDY to model the reprocessed continuum (see also Pandey et al. 2023). As in Bruhweiler & Verner (2008), we parameterize the CLOUDY solution with the incident flux, $\log \phi$, the local density of the cloud, $\log n_{\text{H}}$, and the turbulent velocity, v_{turb} . The results are discussed below.

The template d12 used in Prince et al. (2023) was obtained with the CLOUDY several years ago, and in the meantime, the atomic content of the code improved significantly. We

thus compared the available template d12 with the output of the CLOUDY (version 22.01) using the same input parameters: $\log(\phi[\text{cm}^{-2}\text{s}^{-1}]) = 20.5$, $\log(n_{\text{H}}[\text{cm}^{-3}]) = 12$, and the turbulent velocity of 20 km s^{-1} . The column density was assumed to be 10^{24} cm^{-2} . The incident SED was very similar, that is a standard AGN SED in our computation, and the SED from Korista et al. (1997) in Bruhweiler & Verner (2008). We smeared the results with the Gaussian profile corresponding to the FWHM of 4200 km s^{-1} as used in the current paper. The upper panel of Fig. 11 shows the FeII emission over the broadband range (2000–7000 Å). In the middle panel, we show just the enlarged UV part, relevant to the current work. It shows that, compared to the Bruhweiler & Verner (2008) template, there is a marginal shift in the peak of FeII pattern towards a shorter wavelength in the case of the new CLOUDY output; more importantly, though, the bluer portion of the FeII pattern is more asymmetric. Thus, this template is more consistent with the new redshift

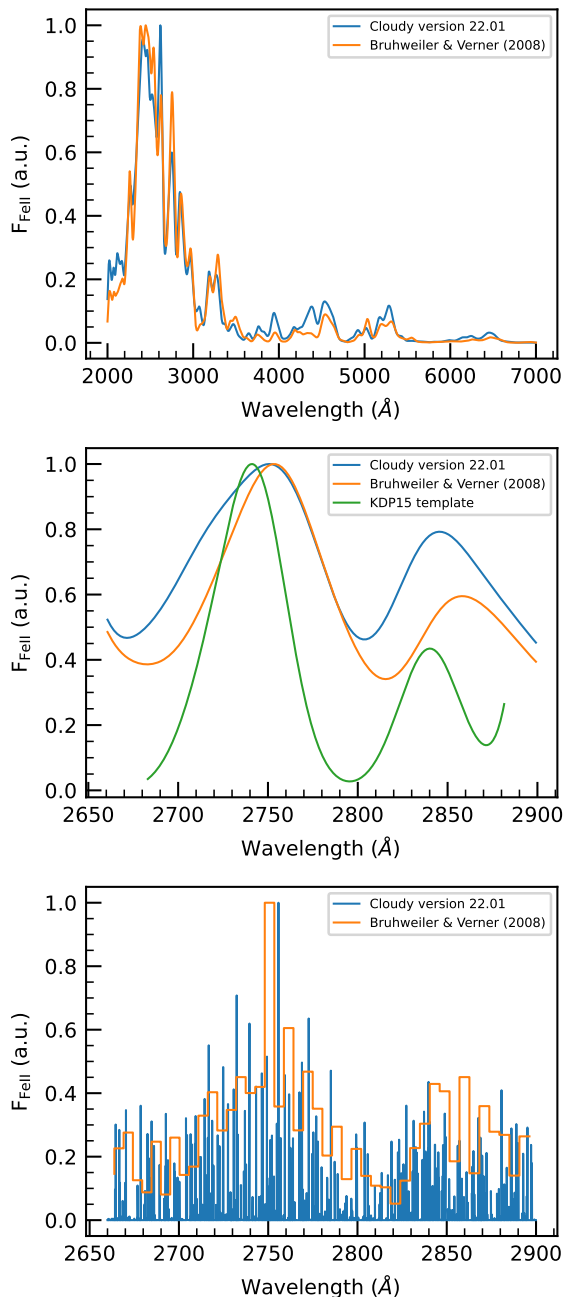


Fig. 11. Comparison of Bruhweiler & Verner (2008) template with the CLOUDY C22.01 output for $\log(\phi[\text{cm}^{-2}\text{s}^{-1}]) = 20.5$, $\log n_{\text{H}}[\text{cm}^{-3}] = 12$, the turbulent velocity of 20 km s^{-1} , and the column density of 10^{24} cm^{-2} . Upper panel: For a wavelength range of $2000\text{--}7000 \text{ \AA}$ with a Gaussian broadening assuming $\text{FWHM} \sim 4200 \text{ km s}^{-1}$. Middle panel: The zoomed-in version of the upper panel in the wavelength range $2650\text{--}2900 \text{ \AA}$. Here we also add the broadened KDP15 template for comparison (green solid line). Lower panel: The nonbroadened version of the middle panel. Here, the templates are renormalized for a better comparison.

when we look at the position of the blue wing of the VW01 and KDP15 templates (see also Fig. 3). Comparing the red-wing peak positions, we see that the red peak of the VW01 template (or d12) is shifted towards the red part and that of KDP15 is shifted slightly towards blue or lower wavelengths. In terms of the intensity, VW01 template is overpredicting the red wing

while the d12 and KDP15 templates show a fainter red-wing (see Fig. 3, middle panel). In addition, the maximum of the KDP15 template is close to 2740 \AA , hence at a slightly smaller wavelength in comparison to the new CLOUDY template. However, the blue peaks of both the old d12 template and the KDP15 template are rather symmetric, while the new CLOUDY template exhibits a prominent blueward asymmetry.

That rather implies that new templates should be constructed for a broader range of parameters and compared to the data which is beyond the scope of the current paper. The KDP15 template has 6 parameters but the setup does not have the required flexibility since finally only two of them were used efficiently, with the other four going frequently to zeros (see Sect. 3 and Fig. 6 for the discussion). Their transitions peak at (maybe) too long wavelengths (2740 \AA – transition 63 and 2747 \AA – transition 62) in the blue wing part to represent well the pattern. The actual number of FeII transitions is very high, as we illustrate in the lower panel of Fig. 11. The strongest transition is close to $\sim 2750 \text{ \AA}$ in both cases. However, in the new computations, some of the transitions at shorter wavelengths, close to 2730 \AA , become stronger, pushing the smeared pattern toward the blue part.

We also checked the CLOUDY output for the ionization parameter $\log(\phi[\text{cm}^{-2}\text{s}^{-1}]) = 20$, local hydrogen density $\log(n[\text{cm}^{-3}]) = 12$, and the turbulent velocity 20 km s^{-1} to see if there are any transitions close to the two peaks visible in the empirical I Zw 1 component: 2715.20 \AA and 2839.88 \AA . Indeed, we see a strong FeII transition at 2715.60 \AA (transition ${}^2G_{9/2}^0 \rightarrow {}^2G_{7/2}^1$), with the intensity $4.0 \times 10^5 \text{ erg s}^{-1} \text{ cm}^{-2}$, and the transition at 2839.80 \AA (transition ${}^6D_{9/2} \rightarrow {}^6P_{7/2}^0$), with the intensity of $1.2 \times 10^6 \text{ erg s}^{-1} \text{ cm}^{-2}$. The ratio of the second to the first one is about 3.08, as in the case of the two peaks in the I Zw 1 component in the KDP15 template (2.80).

In summary, the computations with the use of the latest CLOUDY version give a different shape of the FeII emission than the old d12 template. The shift between the two is seen in the middle panel of Fig. 11 where we plot the broadened version of the templates, but none perfectly represents the peak obtained with the KDP15 template. That shows that there is room for an improvement of the standard one-dimensional FeII templates (not based on several multiplets as in KDP15) as well, but the broad search of the parameter space is beyond the scope of the current paper. It should also be noted that such shifts in the templates can partially be responsible for the large systemic shifts reported in the literature. For example, Rusakov et al. (2023) reports a shift of 4100 km s^{-1} of the broad H β line with respect to the narrow component although the MgII shift is moderate, only by -1200 km s^{-1} , and they propose a shock wave due to the recent supernova as an explanation. But the effect might also be due to the applied FeII template, this time in the optical band.

5.3. Quasar location in the UV plane

The quasar optical plane is a very convenient way to study the statistical properties of quasars (Sulentic et al. 2000; Shen & Ho 2014; Sulentic & Marziani 2015; Fraix-Burnet et al. 2017; Marziani et al. 2018; Panda et al. 2018, 2019c). It is based on a two-dimensional plot using the $\text{FWHM}(\text{H}\beta)$ and the parameter $R_{\text{Fe}} = \text{EW}(\text{FeII}_{\text{opt}})/\text{EW}(\text{H}\beta)$. Here optical FeII

¹ The exact transition was identified using the NIST Spectral Database: https://physics.nist.gov/PhysRefData/ASD/lines_form.html

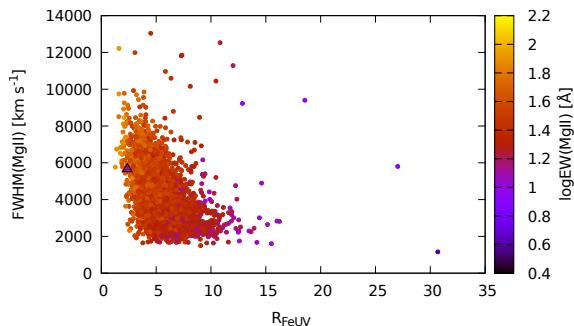


Fig. 12. Quasar UV plane with sources from Śniegowska et al. (2020). The location of the quasar HE 0413–4031 is marked with a triangle.

is usually measured close to $H\beta$, in the spectral range of 4434–4684 Å (Boroson & Green 1992; Marziani et al. 2018; Panda et al. 2018). The study of the quasar main sequence allows us to understand the diversity of Type-1 AGNs and how their spectral properties are tied to the fundamental black hole parameters, such as their mass and accretion rate (Marziani et al. 2018; Panda et al. 2018, 2019c,a; Panda 2021) and the physical conditions of the broad line-emitting region (Panda et al. 2018, 2019c; Śniegowska et al. 2021; Panda 2022; Mengistue et al. 2023).

When the near-UV spectra are studied, a similar concept of the UV plane can be introduced (Śniegowska et al. 2020). A large sample of objects was located on this plane using the QSFIT package (Calderone et al. 2017) for data analysis. This package is based on the VW01 FeII template. For the quasar studies in this paper, we also have the results of fitting the VW01 template for Observation 14. The difference between the QSFIT and our fitting is in the wavelength range which covers 1250–3090 Å while we fit only the range 2683.09448–2881.49854. To make the values of EW comparable, we integrated the VW01 template in the two ranges and determined the scaling parameter 6.39345. We adopted the second solution for this template from Table 2 since the broadened version works better. After rescaling, the parameters of UV FeII are the following: $EW(\text{FeII}) = 88.23$ Å, and $R_{\text{Fe}} = 2.37$.

The location of the quasar HE 0413–4031 in the UV plane together with the sample from Śniegowska et al. (2020) is shown in Fig. 12 with a triangle colored with $EW(\text{MgII})$ as the rest of the sample. The UV FeII emission seems rather weak in the studied object. In the whole sample of Śniegowska et al. (2020), there are only 14 quasars with $R_{\text{Fe}} < 2.0$, and two with $R_{\text{Fe}} < 1.5$. The number of sources with $R_{\text{Fe}} < 2.37$ is 47 (out of 2962 total). The smallest value in this sample is 1.28 ± 0.15 , for the object SDSS 100352.65+212851.5 with the $FWHM(\text{MgII}) = 5760$ km s⁻¹.

6. Conclusions

Our detailed study of the bright, intermediate-redshift quasar HE 0413–4031 based on 10-year monitoring with SALT combined with a single IR exposure with the telescope SOAR showed that

- determination of the redshift from a narrow emission line is important for the spectral decomposition of the entire IR/optical/UV band. The precise redshift determination of $z = 1.39117 \pm 0.00017$ is significantly larger with respect to the previous value ($z = 1.3764$),
- the decomposition of the MgII+FeII complex based on the precise redshift results only in the small blueshifted offset of the MgII line in the range between -240 and -270 km s⁻¹,

which is consistent with the quasar composite spectra of the UV region,

- the velocity of the MgII line with respect to the systemic redshift is therefore significantly affected by the new redshift and the corresponding template since previously the velocity shift was in excess of 1000 km s⁻¹,
- some properties of the strong UV line, in particular MgII, such as its FWHM, EW, and the time delay with respect to the continuum are determined robustly, even without precise redshift determination, so applications of MgII line for cosmology are justified,
- the MgII emission based on the best-fitting KDP15 template with $FWHM(\text{MgII}) = 4503.1$ km s⁻¹ is significantly correlated with the continuum. The final MgII time delay in the rest frame of the source, which is based on 7 different time-delay methods, is $\tau_{\text{MgII}} = 224^{+21}_{-23}$ days,
- determination of the FeII properties, including its time delay with respect to the continuum, is very sensitive to the proper redshift determination and the use of the proper FeII template. The FeII emission is also strongly correlated with the continuum (the peak correlation coefficient is $r = 0.86$), but the peak time delay is consistent with zero, which suggests that the FeII light curve is strongly contaminated with the continuum long-term trend,
- after subtracting the long-term trend from both continuum and FeII light curves, we detect the candidate FeII time delay at $\tau = 251^{+9}_{-7}$ days in the rest frame, albeit the correlation coefficient is relatively low ($r = 0.27$),
- the rest-frame time delay of UV FeII is consistent with the MgII/FeII FWHMs inferred using the FeII best-fit template KDP15. Assuming that the MgII/FeII-line emitting material is fully virialized, the FeII time delay should be $\tau_{\text{FeII}} = \tau_{\text{MgII}}(FWHM_{\text{MgII}}/FWHM_{\text{FeII}})^2 \sim 257$ days, which is consistent with the reverberation result. Hence, for HE 0413–4031, the UV FeII material is more distant than the MgII line-emitting material by ~ 27 light days,
- we update the MgII radius-luminosity relation with new measurements, which results in 194 sources, that is more than twice as much as used previously. The MgII R – L relation is significantly flatter than the UV FeII, optical FeII, and $H\beta$ R – L relations,
- we suggest to build new FeII emission templates based on the newest version of the photoionization code CLOUDY since there are new FeII transitions included that indicate extension of the emission towards shorter wavelengths with respect to the older FeII templates currently in usage.

Acknowledgements. We thank the anonymous referee for constructive comments, which helped to improve the manuscript. All spectroscopic observations reported in this paper were obtained with the Southern African Large Telescope (SALT). The project is based on observations made with the SALT under programs 2012-2-POL-003, 2013-1-POL-RSA-002, 2013-2-POL-RSA-001, 2014-1-POL-RSA-001, 2014-2-SCI-004, 2015-1-SCI-006, 2015-2-SCI-017, 2016-1-SCI-011, 2016-2-SCI-024, 2017-1-SCI-009, 2017-2-SCI-033, 2018-1-MLT-004 (PI: B. Czerny). Polish participation in SALT is funded by grant No. MEiN nr 2021/WK/01. Based in part on observations obtained at the Southern Astrophysical Research (SOAR) telescope, which is a joint project of the Ministério da Ciência, Tecnologia e Inovações (MCTI/LNA) do Brasil, the US National Science Foundation’s NOIRLab, the University of North Carolina at Chapel Hill (UNC), and Michigan State University (MSU). The project was partially supported by the Polish Funding Agency National Science Centre, project 2017/26/A/ST9/00756 (MAESTRO 9). BC and MZ acknowledge the OPUS-LAP/GAČR-LA bilateral project (2021/43/1/ST9/01352/OPUS 22 and GF23-04053L). This project has received funding from the European Research Council (ERC) under the European Union’s Horizon 2020 research and innovation program (grant agreement No. [951549]). SP acknowledges the financial support from the Conselho Nacional de Desenvolvimento Científico

e Tecnológico (CNPq) Fellowships (164753/2020-6 and 313497/2022-2). MS acknowledges support from the Polish Funding Agency National Science Centre, project 2021/41/N/ST9/02280 (PRELUDIUM 20), the European Research Council (ERC) under the European Union's Horizon 2020 research and innovation program (grant agreement 950533), and the Israel Science Foundation, (grant 1849/19). M.L.M.-A. acknowledges financial support from Millennium Nucleus NCN19-058 (TITANs). NW acknowledges the financial support from the GAČR EXPRO grant no GX21-13491X. We are grateful to Marianne Vestergaard for allowing us to use their FeII template.

References

- Alexander, T. 1997, in *Astronomical Time Series*, eds. D. Maoz, A. Sternberg, & E. M. Leibowitz, *Astrophys. Space Sci. Libr.*, 218, 163
- Bentz, M. C., Horne, K., Barth, A. J., et al. 2010, *ApJ*, 720, L46
- Bentz, M. C., Denney, K. D., Grier, C. J., et al. 2013, *ApJ*, 767, 149
- Boroson, T. A., & Green, R. F. 1992, *ApJS*, 80, 109
- Bruhweiler, F., & Verner, E. 2008, *ApJ*, 675, 83
- Burgh, E. B., Nordsieck, K. H., Kobulnicky, H. A., et al. 2003, in *Instrument Design and Performance for Optical/Infrared Ground-based Telescopes*, eds. M. Iye, & A. F. M. Moorwood, *SPIE Conf. Ser.*, 4841, 1471
- Calderone, G., Nicastro, L., Ghisellini, G., et al. 2017, *MNRAS*, 472, 4051
- Cao, S., Zajaček, M., Panda, S., et al. 2022, *MNRAS*, 516, 1721
- Cao, S., Zajaček, M., Czerny, B., Panda, S., & Ratra, B. 2024, *MNRAS*, 528, 6444
- Chelouche, D., Pozo-Nuñez, F., & Zucker, S. 2017, *ApJ*, 844, 146
- Clowes, R. G., Habertzell, L., Raghunathan, S., et al. 2016, *MNRAS*, 460, 1428
- Collin-Souffrin, S., Joly, M., Heidmann, N., & Dumont, S. 1979, *A&A*, 72, 293
- Crawford, S. M., Still, M., Schellart, P., et al. 2010, in *Observatory Operations: Strategies, Processes, and Systems III*, eds. D. R. Silva, A. B. Peck, & B. T. Soifer, *SPIE Conf. Ser.*, 7737, 773725
- Cristiani, S., & Vio, R. 1990, *A&A*, 227, 385
- Cushing, M. C., Vacca, W. D., & Rayner, J. T. 2004, *PASP*, 116, 362
- Czerny, B., & Hryniewicz, K. 2011, *A&A*, 525, L8
- Czerny, B., Hryniewicz, K., Maity, I., et al. 2013, *A&A*, 556, A97
- Czerny, B., Olejak, A., Rałowski, M., et al. 2019, *ApJ*, 880, 46
- Czerny, B., Martínez-Aldama, M. L., Wojtkowska, G., et al. 2021, *Acta Phys. Pol. A*, 139, 389
- Czerny, B., Cao, S., Jaiswal, V. K., et al. 2023a, *Ap&SS*, 368, 8
- Czerny, B., Zajaček, M., Naddaf, M.-H., et al. 2023b, *Eur. Phys. J. D*, 77, 56
- Davidson, K., & Netzer, H. 1979, *Rev. Mod. Phys.*, 51, 715
- Denney, K. D., Peterson, B. M., Pogge, R. W., et al. 2010, *ApJ*, 721, 715
- De Rosa, G., Fausnaugh, M. M., Grier, C. J., et al. 2018, *ApJ*, 866, 133
- Dietrich, M., Hamann, F., Appenzeller, I., & Vestergaard, M. 2003, *ApJ*, 596, 817
- Du, P., Brotherton, M. S., Wang, K., et al. 2018, *ApJ*, 869, 142
- Edelson, R. A., & Krolik, J. H. 1988, *ApJ*, 333, 646
- Fraix-Burnet, D., Marziani, P., D'Onofrio, M., & Dultzin, D. 2017, *Front. Astron. Space Sci.*, 4, 1
- Francis, P. J., Hewett, P. C., Foltz, C. B., et al. 1991, *ApJ*, 373, 465
- Gaskell, M., Thakur, N., Tian, B., & Saravanan, A. 2022, *Astron. Nachr.*, 343, e210112
- Grier, C. J., Peterson, B. M., Pogge, R. W., et al. 2012, *ApJ*, 755, 60
- Homayouni, Y., Trump, J. R., Grier, C. J., et al. 2020, *ApJ*, 901, 55
- Horne, K., De Rosa, G., Peterson, B. M., et al. 2021, *ApJ*, 907, 76
- Hu, C., Li, S.-S., Guo, W.-J., et al. 2020, *ApJ*, 905, 75
- Karas, V., Svoboda, J., & Zajaček, M. 2021, in *RAGtime Workshops on Black Holes and Neutron Stars*, E1
- Kelly, B. C., Bechtold, J., & Siemiginowska, A. 2009, *ApJ*, 698, 895
- Khadka, N., Yu, Z., Zajaček, M., et al. 2021, *MNRAS*, 508, 4722
- Kobulnicky, H. A., Nordsieck, K. H., Burgh, E. B., et al. 2003, in *Instrument Design and Performance for Optical/Infrared Ground-based Telescopes*, eds. M. Iye, & A. F. M. Moorwood, *SPIE Conf. Ser.*, 4841, 1634
- Korista, K., Baldwin, J., Ferland, G., & Verner, D. 1997, *ApJS*, 108, 401
- Kovačević-Dojčinović, J., & Popović, L. Č. 2015, *ApJS*, 221, 35
- Kovačević-Dojčinović, J., Marčeta-Mandić, S., & Popović, L. Č. 2017, *Front. Astron. Space Sci.*, 4, 7
- Kozłowski, S. 2016, *ApJ*, 826, 118
- Kozłowski, S., Kochanek, C. S., Udalski, A., et al. 2010, *ApJ*, 708, 927
- Krolik, J. H. 1999, *Active Galactic Nuclei : from the Central Black Hole to the Galactic Environment*
- Krtićka, J., Benáček, J., Budaj, J., et al. 2023, *Space Sci. Rev.*, accepted [arXiv:2306.15081]
- Le, H. A. N., Woo, J.-H., & Xue, Y. 2020, *ApJ*, 901, 35
- Lira, P., Kaspi, S., Netzer, H., et al. 2018, *ApJ*, 865, 56
- MacLeod, C. L., Ivezić, Z., Kochanek, C. S., et al. 2010, *ApJ*, 721, 1014
- Martínez-Aldama, M. L., del Olmo, A., Marziani, P., et al. 2018, *A&A*, 618, A179
- Martínez-Aldama, M. L., Zajaček, M., Czerny, B., & Panda, S. 2020, *ApJ*, 903, 86
- Marziani, P., Zamanov, R. K., Sulentic, J. W., & Calvani, M. 2003, *MNRAS*, 345, 1133
- Marziani, P., Dultzin, D., Sulentic, J. W., et al. 2018, *Front. Astron. Space Sci.*, 5, 6
- Mengistue, S. T., Del Olmo, A., Marziani, P., et al. 2023, *MNRAS*, 525, 4474
- Metzroth, K. G., Onken, C. A., & Peterson, B. M. 2006, *ApJ*, 647, 901
- Netzer, H. 2022, *MNRAS*, 509, 2637
- Osterbrock, D. E., & Pogge, R. W. 1985, *ApJ*, 297, 166
- Panda, S. 2021, *Ph.D. Thesis, Polish Academy of Sciences, Institute of Physics, Poland*
- Panda, S. 2022, *Front. Astron. Space Sci.*, 9, 850409
- Panda, S., & Marziani, P. 2023, *Front. Astron. Space Sci.*, 10, 1130103
- Panda, S., Czerny, B., Adhikari, T. P., et al. 2018, *ApJ*, 866, 115
- Panda, S., Czerny, B., Done, C., & Kubota, A. 2019a, *ApJ*, 875, 133
- Panda, S., Martínez-Aldama, M. L., & Zajaček, M. 2019b, *Front. Astron. Space Sci.*, 6, 75
- Panda, S., Marziani, P., & Czerny, B. 2019c, *ApJ*, 882, 79
- Pandey, A., Czerny, B., Panda, S., et al. 2023, *A&A*, 680, A102
- Peterson, B. M., Wanders, I., Horne, K., et al. 1998, *PASP*, 110, 660
- Popović, L. Č., Kovačević-Dojčinović, J., & Marčeta-Mandić, S. 2019, *MNRAS*, 484, 3180
- Prince, R., Zajaček, M., Czerny, B., et al. 2022, *A&A*, 667, A42
- Prince, R., Zajaček, M., Panda, S., et al. 2023, *A&A*, 678, A189
- Robertson, D. R. S., Gallo, L. C., Zoghbi, A., & Fabian, A. C. 2015, *MNRAS*, 453, 3455
- Rusakov, V., Steinhart, C. L., Schramm, M., et al. 2023, *ApJ*, 944, 217
- Schlawin, E., Herter, T. L., Henderson, C., et al. 2014, in *Ground-based and Airborne Instrumentation for Astronomy V*, eds. S. K. Ramsay, I. S. McLean, & H. Takami, *SPIE Conf. Ser.*, 9147, 91472H
- Shen, Y., & Ho, L. C. 2014, *Nature*, 513, 210
- Shen, Y., Horne, K., Grier, C. J., et al. 2016, *ApJ*, 818, 30
- Shen, Y., Grier, C. J., Horne, K., et al. 2023, *ArXiv eprints [arXiv:2305.01014]*
- Shvartzvald, Y., Waxman, E., Gal-Yam, A., et al. 2023, *AAS*, submitted [arXiv:2304.14482]
- Smith, M. P., Nordsieck, K. H., Burgh, E. B., et al. 2006, *SPIE Conf. Ser.*, 6269, 62692A
- Śniegowska, M., Kozłowski, S., Czerny, B., Panda, S., & Hryniewicz, K. 2020, *ApJ*, 900, 64
- Śniegowska, M., Marziani, P., Czerny, B., et al. 2021, *ApJ*, 910, 115
- Sulentic, J., & Marziani, P. 2015, *Front. Astron. Space Sci.*, 2, 6
- Sulentic, J. W., Marziani, P., & Dultzin-Hacyan, D. 2000, *ARA&A*, 38, 521
- Tran, H. D., Cohen, M. H., & Villar-Martin, M. 2000, *AJ*, 120, 562
- U, V., Barth, A. J., Vogler, H. A., et al. 2022, *ApJ*, 925, 52
- Vacca, W. D., Cushing, M. C., & Rayner, J. T. 2003, *PASP*, 115, 389
- Vanden Berk, D. E., Richards, G. T., Bauer, A., et al. 2001, *AJ*, 122, 549
- Véron-Cetty, M. P., & Véron, P. 2010, *A&A*, 518, A10
- Vestergaard, M., & Wilkes, B. J. 2001, *ApJS*, 134, 1
- Wang, J.-G., Dong, X.-B., Wang, T.-G., et al. 2009, *ApJ*, 707, 1334
- Werner, N., Řípa, J., Münz, F., et al. 2022, in *Space Telescopes and Instrumentation 2022: Ultraviolet to Gamma Ray*, eds. J. W. A. den Herder, S. Nikzad, & K. Nakazawa, *SPIE Conf. Ser.*, 12181, 121810B
- Werner, N., Řípa, J., Thöne, C., et al. 2023, *Space Sci. Rev.*, accepted [arXiv:2306.15080]
- Wills, B. J., Netzer, H., Uomoto, A. K., & Wills, D. 1980, *ApJ*, 237, 319
- Wills, B. J., Netzer, H., & Wills, D. 1985, *ApJ*, 288, 94
- Wisotzki, L., Christlieb, N., Bade, N., et al. 2000, *A&A*, 358, 77
- Xiao, M., Du, P., Lu, K.-K., et al. 2018, *ApJ*, 865, L8
- Yu, Z., Martini, P., Penton, A., et al. 2023, *MNRAS*, 522, 4132
- Zajaček, M., Czerny, B., Martínez-Aldama, M. L., & Karas, V. 2019, *Astron. Nachr.*, 340, 577
- Zajaček, M., Czerny, B., Martínez-Aldama, M. L., et al. 2020, *ApJ*, 896, 146
- Zajaček, M., Czerny, B., Martínez-Aldama, M. L., et al. 2021, *ApJ*, 912, 10
- Zajaček, M., Czerny, B., Jaiswal, V. K., et al. 2023a, *Space Sci. Rev.*, submitted [arXiv:2306.15082]
- Zajaček, M., Czerny, B., Khadka, N., et al. 2023b, *AAS*, submitted [arXiv:2305.08179]
- Zhang, Z.-X., Du, P., Smith, P. S., et al. 2019, *ApJ*, 876, 49
- Zhao, B.-X., Bian, W.-H., Yu, L.-M., & Wang, C. 2020, *Ap&SS*, 365, 22
- Zheng, W. 2021, *MNRAS*, 506, 3797
- Zu, Y., Kochanek, C. S., & Peterson, B. M. 2011, *ApJ*, 735, 80
- Zu, Y., Kochanek, C. S., Kozłowski, S., & Udalski, A. 2013, *ApJ*, 765, 106
- Zu, Y., Kochanek, C. S., Kozłowski, S., & Peterson, B. M. 2016, *ApJ*, 819, 122

Appendix A: MgII time-delay determinations

A.1. Interpolated cross-correlation function

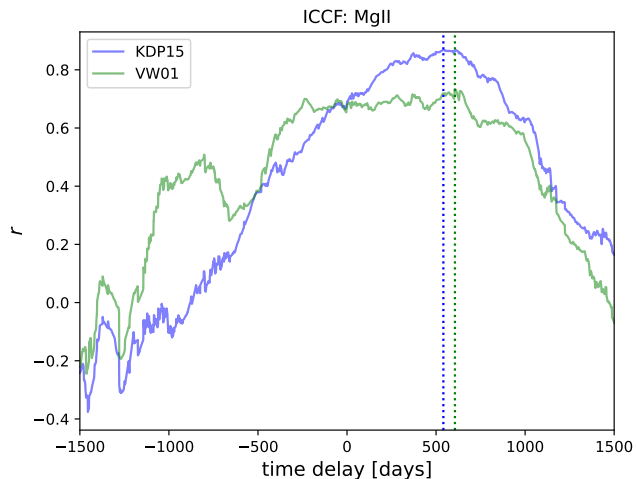


Fig. A.1. ICCF for the MgII emission using the KDP15 and the VW01 templates depicted by blue and green lines, respectively. The dotted vertical lines show the time-delay peaks at 541 and 606 days (highest cross-correlation coefficient).

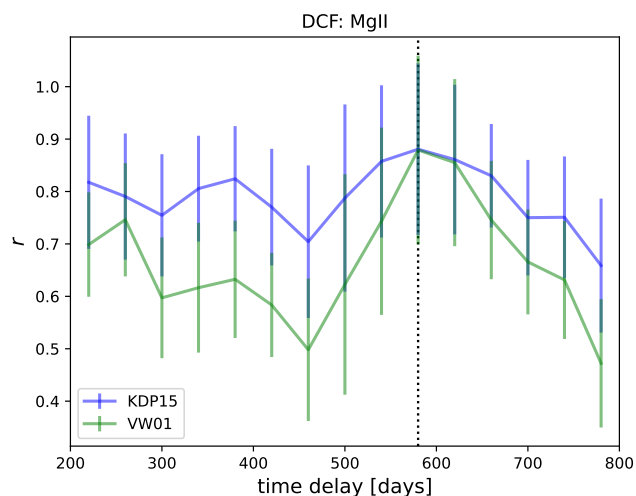


Fig. A.2. DCF for the MgII emission using the KDP15 and the VW01 templates depicted by blue and green lines, respectively. The dotted vertical line shows the time-delay peak at 580 days (highest correlation coefficient).

We calculate the Interpolated cross-correlation function (ICCF) using the basic definition of the cross-correlation coefficient between two light-curve points separated by the time delay $\tau_k = k\Delta t$,

$$CCF(\tau_k) = \frac{(1/N) \sum_{i=1}^{N-k} (x_i - \bar{x})(y_{i+k} - \bar{y})}{[(1/N) \sum_{i=1}^N (x_i - \bar{x})^2]^{1/2} [(1/N) \sum_{i=1}^N (y_i - \bar{y})^2]^{1/2}}, \quad (\text{A.1})$$

where $\Delta t = t_{i+1} - t_i$ is the regular time step, and \bar{x} and \bar{y} denote light curve means. Both continuum and line-emission light curves are interpolated with the time step of $\Delta t = 1$ day

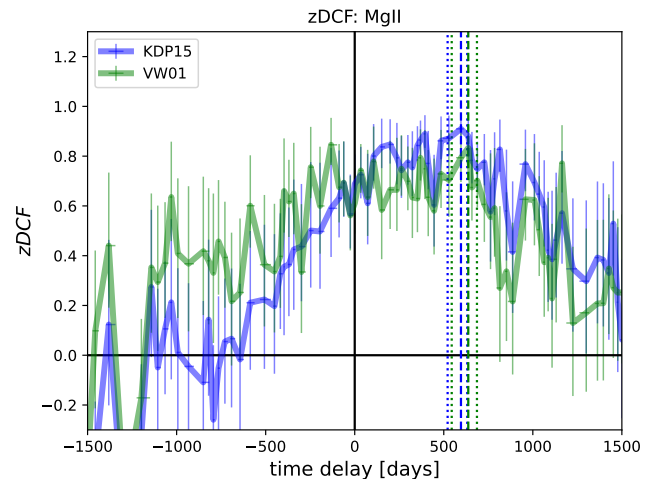


Fig. A.3. zDCF for the MgII emission using the KDP15 and the VW01 templates depicted by blue and green lines, respectively, with the corresponding error bars. The dashed vertical lines show the time-delay peaks at 597 days (KDP15) and 638 days (VW01) while the dotted lines mark the corresponding 1σ uncertainties.

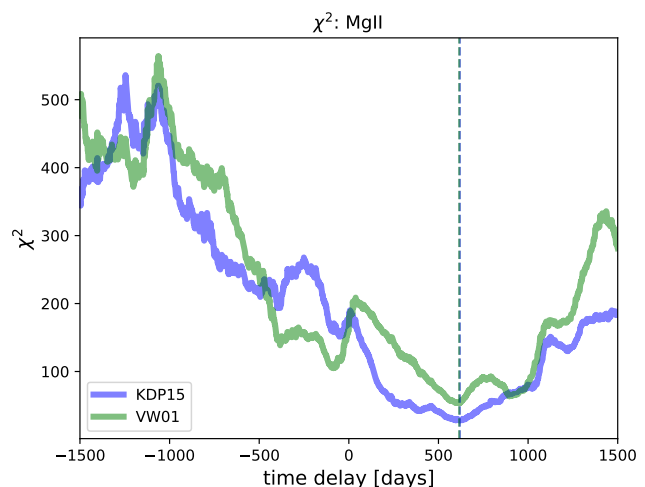


Fig. A.4. χ^2 as a function of a time delay (in the observer's frame) for the MgII emission using the KDP15 and the VW01 templates depicted by blue and green lines, respectively. The dashed vertical lines depict the time-delay peaks at 619 days (KDP15) and 616 days (VW01).

(symmetric interpolation). In Figure A.1, we show the ICCF for the MgII line emission inferred using the KDP15 template and the VW01 template.

A.2. Discrete correlation function (DCF)

We employ the discrete correlation function (DCF) that is suited for irregular and unevenly sampled light curves (Edelson & Krolik 1988). We utilize the python implementation of the DCF by Robertson et al. (2015). For both KDP15 and VW01 FeII templates, we show the DCF results in Figure A.2.

A.3. z-transfered DCF (zDCF)

The z-transfered DCF replaces equidistant time bins with equipopulation time bins. The minimum number of overlapping

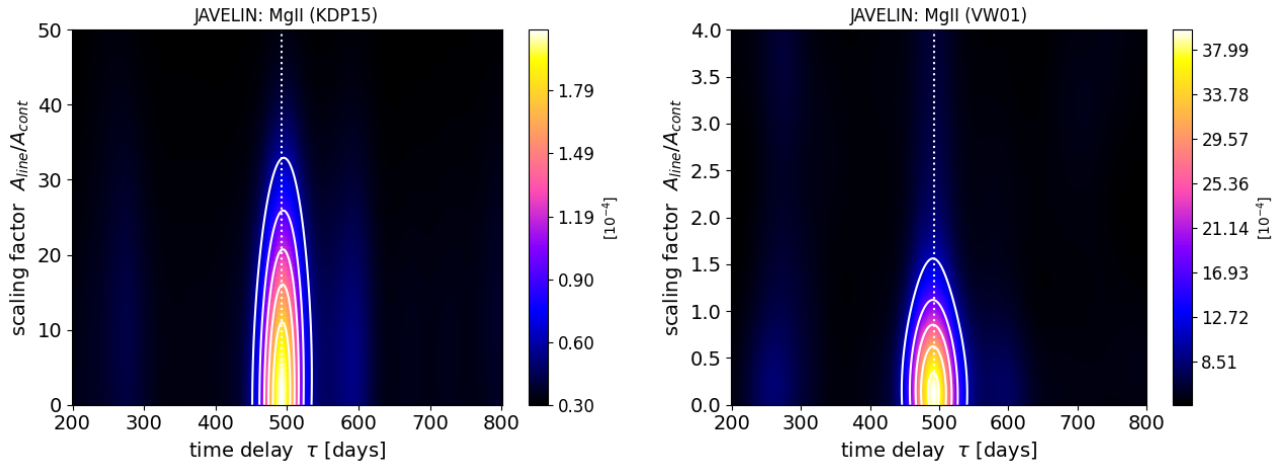


Fig. A.5. Heat map with contours for the posterior distributions of the scaling factor vs. the time delay (in the observer’s frame) as determined by the JAVELIN method for the MgII emission light curve. We performed the analysis using the KDP15 FeII template (left panel) and the VW01 FeII template (right panel). The dashed vertical line depicts the time-delay peak at 492.5 days, which is the same for both FeII templates. The color scale depicts the Gaussian kernel density of MCMC realizations (altogether 40 000) in the scaling factor–time delay plane with the grid of 400×400 bins.

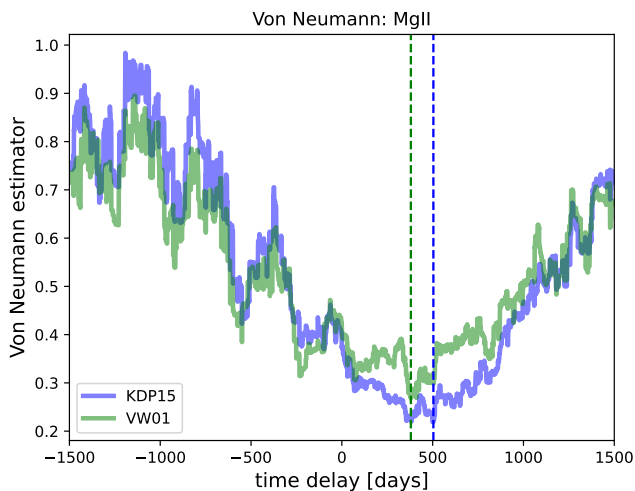


Fig. A.6. Von Neumann estimator as a function of a time delay (in the observer’s frame) for the MgII emission using the KDP15 and the VW01 templates depicted by blue and green lines, respectively. The dashed vertical lines depict the time delays corresponding to the estimator minima at 504 days (KDP15) and 380 days (VW01), respectively.

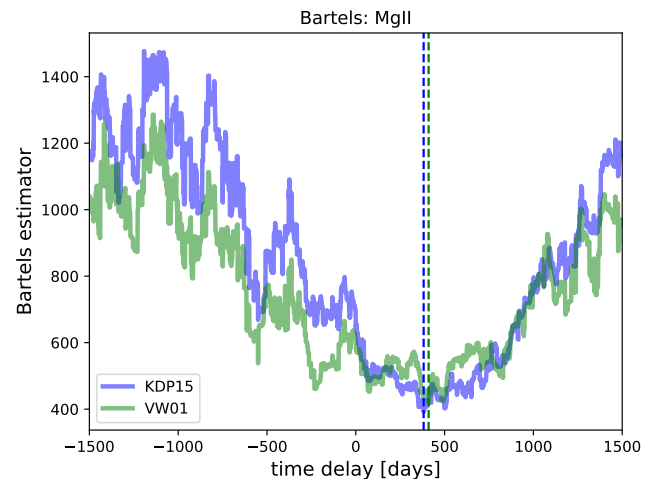


Fig. A.7. Bartels estimator as a function of a time delay (in the observer’s frame) for the MgII emission using the KDP15 and the VW01 templates depicted by blue and the green lines, respectively. The dashed vertical lines depict the time delays corresponding to the estimator minima at 382 days (KDP15) and 410 days (VW01), respectively.

light-curve pairs is 12. The method was developed by Alexander (1997), who also implemented it within a fortran code. The zDCF is suitable for sparse and irregular light curves. In Figure A.3, we show zDCF as a function of the observed time delay for both KDP15 and VW01 FeII templates that are depicted by blue and green lines, respectively.

A.4. χ^2 method

We also apply the χ^2 method frequently used in lensing studies. Czerny et al. (2013) showed that this method performs better than the ICCF for red-noise AGN variability. In Figure A.4, we show χ^2 as a function of the time delay of the MgII line emission with respect to the photoionizing continuum. The solid blue line

stands for the KDP15 FeII template, while the solid green line represents the VW01 template.

A.5. JAVELIN

Another method to estimate the time delay in galactic nuclei is to model the continuum emission as a stochastic process, for example by using a damped random walk (Kelly et al. 2009; Kozłowski et al. 2010; MacLeod et al. 2010; Kozłowski 2016), and to assume that the line emission is a time-delayed, scaled, and smoothed version of the continuum emission. Based on this approach the JAVELIN package (Just Another Vehicle for Estimating Lags In Nuclei) was developed and tested (Zu et al. 2011, 2013, 2016). We applied JAVELIN to infer independently the time delay of the MgII emission with respect to the continuum.

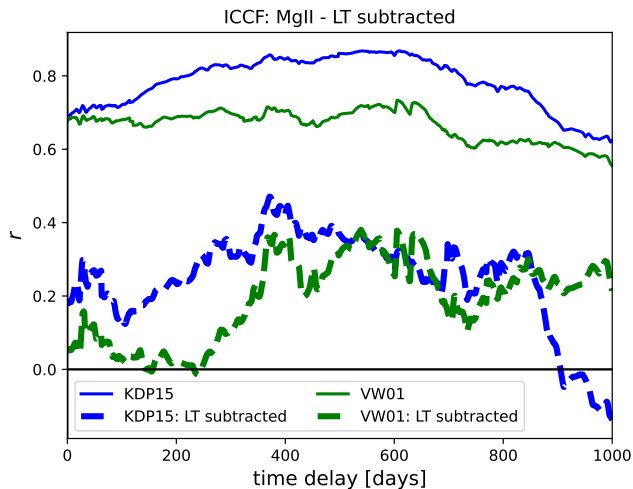


Fig. A.8. ICCF as a function of the time delay in the observer’s frame for the MgII light curve with the LT trend subtraction. Solid lines correspond to the original light curves (blue for the KDP15 template and green for the VW01 template). Dashed lines correspond to the continuum and the MgII light curves with the LT trend subtracted using the third-order polynomial to represent the LT trend (a blue dashed line stands for the KDP15 template, while the green dashed line corresponds to the VW01 template). Although a significant drop in the correlation coefficient is noticeable, the main time-delay peak around $\sim 400 - 600$ days can be recovered.

In Figure A.5, we plot the heatmaps of the scaling factor vs. time delay. In the left panel, we present the case with the KDP15 FeII template, while in the right panel, we show the case with the VW01 FeII template.

A.6. Measures of regularity and randomness

Recently, the estimators of time-series regularity or randomness were proposed as a way to estimate the true time delay between the two light curves (Chelouche et al. 2017).

In Figure A.6, we present the von Neumann estimator as a function of the time delay in the observer’s frame of reference. As was done previously for the other methods, two FeII templates are compared: KDP15 (blue line) and VW01 (green line). Furthermore, we also calculate the Bartels estimator, which is

Table A.1. Summary of MgII emission time delays inferred using the ICCF for the light curves with the LT trend subtracted. Time delays are expressed in days in the observer’s frame, while the last two rows represent the mean time delays expressed in days in the rest frame of the source.

Method	KDP15	VW01
ICCF* - highest r	372 ($r = 0.47$)	539 ($r = 0.38$)
ICCF* - peak	410^{+345}_{-50}	605^{+242}_{-238}
ICCF* - centroid	446^{+317}_{-103}	571^{+275}_{-203}
$\bar{\tau}$ - observer’s frame	428^{+234}_{-57}	588^{+183}_{-156}
$\bar{\tau}$ - rest frame	179^{+98}_{-24}	246^{+77}_{-65}
Final MgII time delay	213^{+62}_{-35}	

similar to the von Neumann estimator but rather operates on the ranked combined light curve. In Figure A.7, we show the Bartels estimator values as a function of the time delay for both templates. Overall, the minima values and their uncertainties as inferred from the best time-delay distributions are quite similar to the values determined using the von Neumann estimator.

A.7. Subtraction of long-term trend

In a similar way as for the UV FeII line (see Subsection 4.3), we verify that for the MgII light curve the long-term (LT) trend subtraction does not obliterate the main time-delay peak.

We fit the third-order polynomial to both continuum and MgII light curves. Subsequently, we subtract the best-fit trend from both light curves. Then we apply the ICCF, for which we find the time delays corresponding to the peak r value, the centroid, and the peak distributions. Both KDP15 and VW01 templates are considered. The results are summarized in Table A.1.

It is possible to recover the time delay at $\sim 400 - 600$ days in the observer’s frame, although with a significantly lower correlation of $r \sim 0.38 - 0.47$. For the KDP15 template, the peak and centroid time delays are smaller than the previously determined values, though within the uncertainties they are consistent with the time delays reported without any subtraction. When we average the peak and the centroid values for both templates, the rest-frame time delay is 213^{+62}_{-35} days, which is in agreement with the previously reported value.

Discussion and Conclusions

*"The history of astronomy is a
history of receding horizons."*

— Edwin Powell Hubble
(1889-1953)

The common theme of the seven papers presented in this *Habilitation Thesis* (see Chapters 2 through 8) is the astrophysics of galactic nuclei. Five papers that are included in Chapters 2, 3, 5, 7, and 8 deal with the nuclei of other galaxies, while two papers (Paper 3 in Chapter 4 and Paper 5 in Chapter 7) focus on the Galactic center, i.e. the nucleus of our own Milky Way galaxy.

Although the topics of the papers may seem quite heterogeneous and just loosely related, it is just an illusion since the activity of a galactic nucleus appears to be crucial for understanding the evolution of not only our own Galaxy but galaxies in general. In analogy to stars, galaxies undergo an evolution with different phases since their formation, which took place just during the first 200 - 400 million years after the Big Bang (corresponding to the redshift range $z \sim 20 - 11$). This evolution involved accumulation of gas, from which stars formed, as well as simultaneously different feedback processes operated – supernovae and the activity of the central SMBH. The energy and the momentum feedback from supernovae and the SMBH led to the expulsion and heating of the cold gas, which would otherwise be available for star formation and the accretion onto the SMBH. In this way, the central SMBHs can play a central role in shaping galaxies by regulating star-formation across the whole galaxy as well as its own activity.

Studying the galaxy evolution is even more complicated when one considers that the expansion of the Universe should be properly included. It is represented by the Hubble parameter that depends on the redshift (scaling parameter and thus cosmic time) as well as the cosmological parameters, $H(z, \mathbf{p})$. The expansion of the Universe and structure formation during its evolution implies that the mergers of galaxies of different sizes can occur and are indeed observed across the cosmic history. When two galaxies merge, star formation and the accretion onto the SMBH tend to be enhanced due to the refuelling of gas reservoir. To get the grasp of the main ingredients of galaxy evolution, we illustrate the sources of cold

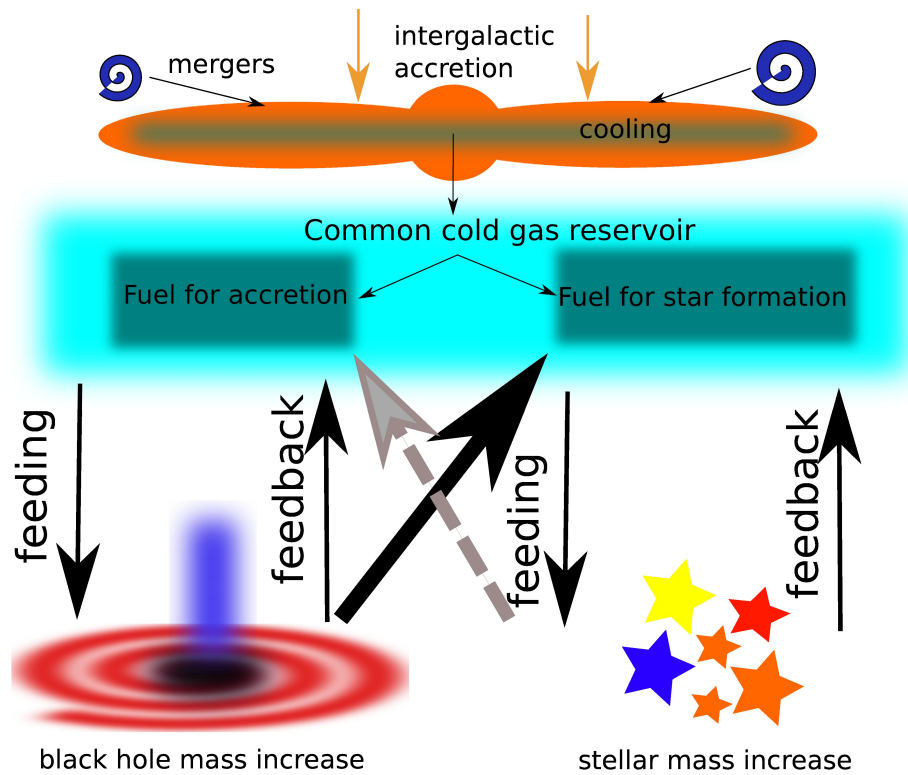


Figure 9.1: Illustration of the main processes affecting the galaxy evolution across the cosmic history. The basic ingredient is the reservoir of cold gas, from which stars can form and which also feeds the central SMBH(s). This reservoir can be supplied by the intergalactic accretion and mergers (top). In contrast, it is depleted by negative feedback processes, such as the active galactic nucleus and supernova explosions of massive stars (bottom). The figure is adopted from [Karas et al. \(2021\)](#). Courtesy of Michal Zajaček.

gas (intergalactic accretion and mergers) and the feedback processes (SMBHs and stars) in Fig. 9.1.

By studying the Galactic center and low- to intermediate-redshift galaxies, we can study in detail star-formation and accretion processes that are common for the galaxy evolution throughout the cosmic history. In particular, the compact nuclear star cluster (NSC) at the center of the Milky Way is a unique laboratory for studying the mutual dynamical interaction among stars, compact remnants, infalling gas, and the activity of the SMBH ([Schödel et al. 2014b](#)). Specifically, in Paper 3 (Chapter 4), we proposed a new feedback process of how the active nuclear jet can affect the evolved, late-type stars that are expected to dominate the composition of the nuclear star cluster. An estimated mass removal caused by the red-giant collision with the nuclear jet can both make old stars appear younger and the colliding star can also affect the velocity field and the composition of the jet flow. We suggest that the red giant-jet collisions can partially address the missing bright red giants in the inner nuclear star cluster of the Milky Way. It complements other processes that operate closer to the SMBH (tidal disruption of red-giant envelopes) and further away (collisions of red giants with the dense, star-forming clumps within a large-scale gaseous disc), see also Fig. 9.2 for the illustration and [Zajaček et al. \(2020\)](#) for more details. In the dense environment of the nuclear star cluster, star-star and star-compact remnant collisions can also contribute to the overall dearth of evolved stars within the inner half parsec, as was first detected by [Sellgren](#)

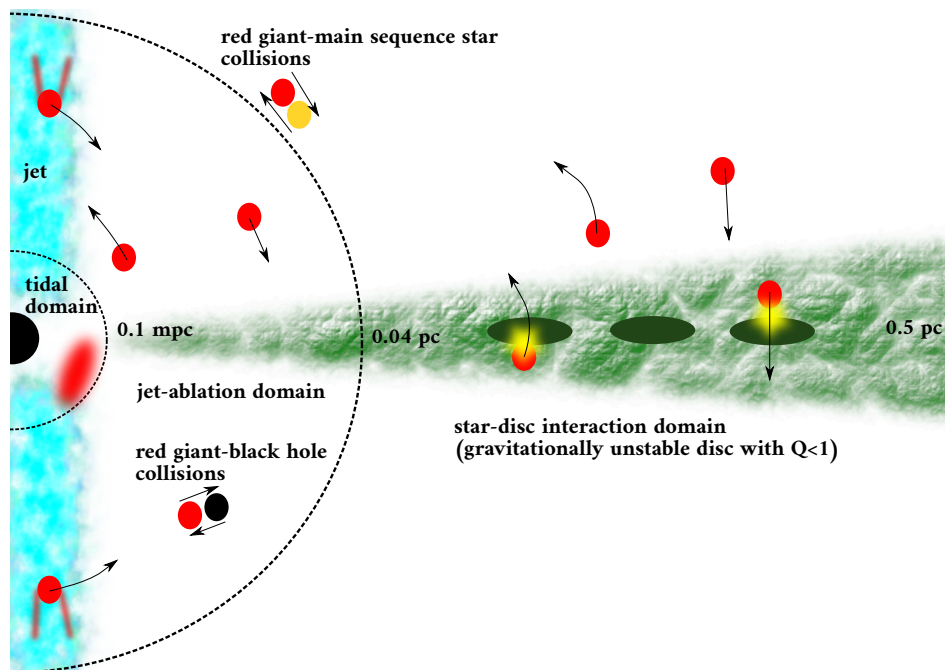


Figure 9.2: Illustration of the processes that likely contributed to the depletion of late-type stars (red giants/supergiants, asymptotic giant-branch stars) in the inner 0.5 pc of the Galactic center. It seems that the depletion of red giants is linked to the enhanced accretion activity of Sgr A* a few million years ago, which could have been accompanied by an active nuclear jet. In the vicinity of the SMBH, tidal forces perturb large envelopes of red giants, while at larger distances, a gravitationally unstable disc hosts denser cores, with which orbiting red giants can collide and lose mass through increased ram pressure. At the intermediate scales ($\gtrsim 0.1$ mpc and $\lesssim 0.04$ pc), red giant collisions with the jet can ablate their outer layers. Throughout the dense nuclear star cluster, red giant–main-sequence star and red giant – compact remnant collisions take place occasionally and hence can contribute to the depletion of red giants.

et al. (1990) via the decrease in the CO bandhead absorption strength.

Moreover, by studying the orbits and the light curves of orbiting stars around the SMBH, one can in principle constrain their nature by the level of brightening due to the Doppler effect (see Paper 5 in Chapter 6). Objects with colder atmospheres, e.g. dust-enshrouded stars or brown dwarfs, as well as non-thermal spectra, e.g. pulsars, generally exhibit an enhanced Doppler (de)boosting with respect to main-sequence stars by a factor of four to ten. With high enough near- and mid-infrared photometric sensitivity in the near future, this effect could help constrain the low-mass end of the Galactic center stellar population, and thus its initial mass function in the vicinity of the SMBH. One exciting possibility is the discovery of a brown-dwarf population in the Galactic center, which would constrain the star-formation process not only in the center of the Milky Way but also in other galactic nuclei.

Potential cycles of AGN feedback associated with the activity of the SMBH can be revealed by studying optical-radio properties of a sample of radio galaxies. In particular, in Paper 1 (Chapter 2) we studied the distribution of a radio spectral index (4.85 GHz–10.45 GHz) in the narrow-line optical diagnostic diagrams. Seyfert galaxies tend to have high ionization potential and a large radio loudness and they also have rather steep spectral indices

($\alpha < -0.7$), which can be associated with older radio structures (radio lobes). On the other hand, low-ionization nuclear emission-line region (LINER) galaxies are characterized by a rather low radio loudness, but they have flatter to inverted radio spectral indices. This indicates that a substantial fraction of LINER galaxies are undergoing a renewed nuclear activity with compact, optically thick radio cores and jets. Hence, in some sense, the standard optical diagnostic diagram (Baldwin-Phillips-Terlevich/BPT diagram) seems to trace galaxy-evolutionary cycles in the nearby Universe, i.e. in the recent cosmic history. However, the described cycles of nuclear (accretion disc-jet) activity are expected to have occurred since the formation of the first SMBH seeds. Linking this back to the studies of the Galactic center nuclear star cluster (Papers 3 and 5), a question arises if and how a dense collection of stars with their stellar winds, sometimes really powerful (Wolf-Rayet stars and supernovae), can influence the cycles of the nuclear activity and the associated radiative and radio-mechanical feedback. In Zajaček et al. (2022), we studied the change in the size of the stagnation radius, which is the length-scale from the SMBH where the radial flow velocity goes through zero, i.e. it divides the inflow from the outflow region. The basic effect is that for a missing NSC or a core-like number-density distribution the stagnation radius is larger than for a cusp-like distribution of the NSC, see Fig. 9.3. This can influence the amount of the gas inflow towards the SMBH and hence the nuclear feedback, though a more detailed numerical model analysis in combination with optical/X-ray data is necessary to draw more robust conclusions.

To understand the distribution and the kinematics of the ionized gas in the vicinity of an active galactic nucleus, which is the source of characteristic broad lines in the UV/optical portion of a typical AGN spectrum (e.g., MgII and FeII), we performed the reverberation mapping of two intermediate-redshift quasars: HE 0413-4031 (Paper 2 in Chapter 3) and HE 0435-4312 (Paper 4 in Chapter 5). For both of the studied quasars, the rest-frame time delay of the MgII broad-line emission is about 200-300 days. Because of their high UV luminosities ($L_{3000} \sim 10^{46} - 10^{47} \text{ erg s}^{-1}$), both quasars have been essential for constraining the MgII broad-line region radius-luminosity relation ($R_{\text{BLR}} - L$ relation or correlation). Hence, in analogy to $\text{H}\beta$ $R_{\text{BLR}} - L$ relation, which has been constructed from reverberation mapping of nearby, low-redshift quasars (see e.g. Bentz et al. 2013; Martínez-Aldama et al. 2019), MgII $R_{\text{BLR}} - L$ relation can be used to determine SMBH masses for higher, intermediate-redshift AGN just from one obtained spectrum. This way the growth of SMBHs close to the peak of the SMBH/star formation activity can be better understood. At the moment, the MgII $R_{\text{BLR}} - L$ is well constrained using the reverberation mapping of nearly 200 sources, see Fig. 9.4. However, it has a substantial scatter around the best-fit relation. The slope of the best-fit MgII $R_{\text{BLR}} - L$ relation is also significantly flatter than the $\text{H}\beta$ $R_{\text{BLR}} - L$ relation as well as the optical and UV FeII relations ($\gamma \sim 0.3$ vs. 0.5), and hence it also deviates from the simple photoionization arguments inferred using the definition of the ionization parameter. Both the reason behind a considerable scatter and the MgII $R_{\text{BLR}} - L$ relation flatness will need to be addressed using advanced photoionization and dynamical models of the MgII line-emitting material, including a proper treatment of radiation pressure acting on the gaseous-dusty material at the BLR length-scales in addition to the dominant gravitational field of the SMBH.

A difficulty with the spectral decomposition of the quasar continuum emission and the MgII broad-line emission is that the MgII line emission overlaps spectrally with the UV FeII pseudocontinuum. For the MgII line flux determination, a precise FeII model is desired. In Paper 7 (Chapter 8), utilizing the precise redshift determination for HE 0413-4031, we analyze how different FeII templates affect MgII and FeII properties and their correspond-

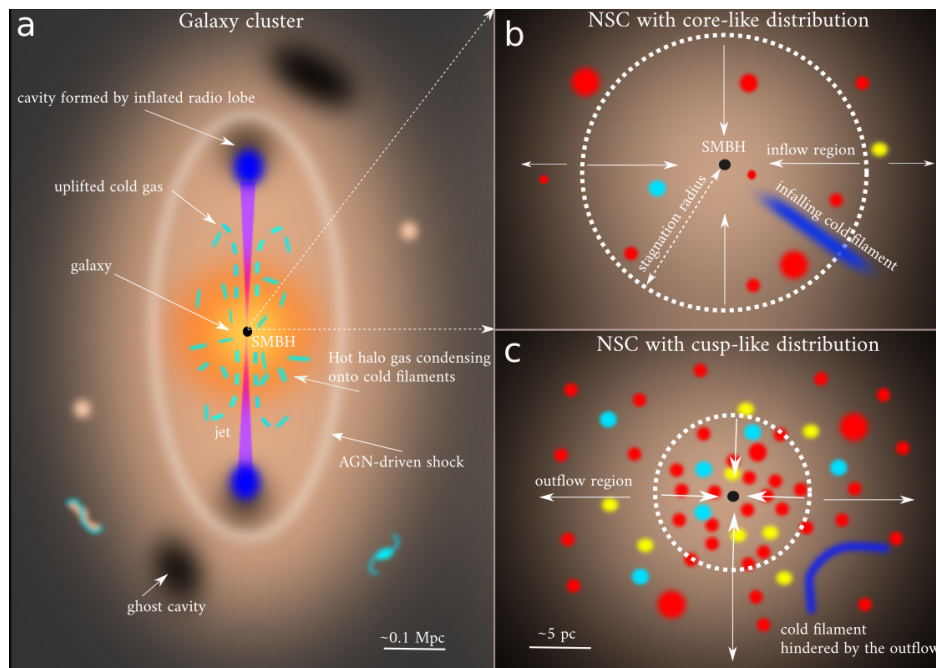


Figure 9.3: Potential relation between the Nuclear Star Cluster (NSC) surface brightness (number-density distribution) and the nuclear feedback. Panel (a) on the left shows a large-scale AGN feedback (on the scale of megaparsecs), in particular radio-mechanical feedback in the circumgalactic medium, which heats up the gas and prevents it from cooling and forming stars. Since the nuclear feedback on large scales has the origin at the very center of galaxies, within the Bondi radius of the SMBH, the way how wind-blowing stars are distributed around the SMBH may affect the size of the inflow/outflow regions (see Panels b and c on the right). Specifically, for a cusp-like distribution (panel c) we expect a smaller stagnation radius than for a core-like distribution of the NSC.

ing time delays with respect to the driving photoionizing continuum. The precise redshift determination based on the narrow [OIII] lines (1.39117 ± 0.00017) leads to a different spectral decomposition than the previous one based on the approximate redshift inferred from the FeII pseudocontinuum. In particular, the systematic blueshift of the MgII line is only 300 km s^{-1} and the FeII FWHM of 4200 km s^{-1} is consistent with its slightly larger time delay with respect to the MgII line (251 days vs. 224 days in the rest frame). Based on this specific analysis, we recognize that a more precise model of the FeII pseudocontinuum, which consists of plenty FeII transitions, is required to yield a satisfactory MgII/FeII decomposition. Older FeII templates currently in use are empirical, theoretical or the combination of both approaches but generally based on just specific sources and incomplete line transitions.

However, despite different FeII templates, the MgII line properties and its time delay in HE 0413-4031 were not affected significantly by the spectral decomposition. The MgII broad-line emission can therefore be reliably used for the SMBH mass determination as well as applied to standardize quasars and use them as alternative cosmological probes (see e.g. Czerny et al. 2023, and references therein). In comparison with standard cosmological probes, such as type Ia supernovae, AGN with their broad redshift range from $z \approx 0$ to $z \sim 7$ and potentially more bridge local, cosmic-ladder measurements in the late Universe with the distant cosmic microwave background (CMB) in the early Universe. In this way,

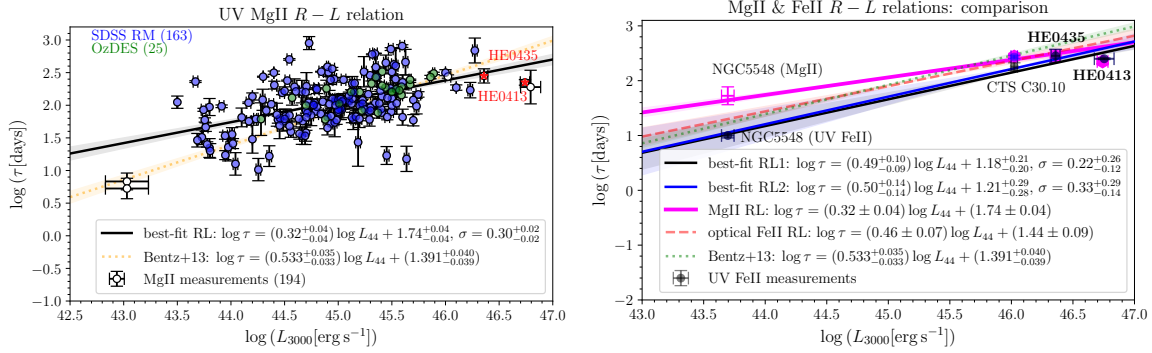


Figure 9.4: UV MgII and FeII radius-luminosity relations. *Left panel:* MgII radius-luminosity relation for 194 quasars, including 163 SDSS RM sources, 25 OzDES sources, and 6 sources from other programs. In particular, we highlight two measurements of the MgII time delay for HE 0413-4031 (Paper 2) and HE 0435-4312 (Paper 4) denoted by red stars, which are among few high-luminosity sources that are crucial for constraining the MgII $R_{\text{BLR}} - L$ relation. *Right panel:* MgII and FeII $R_{\text{BLR}} - L$ relations in the UV domain and their comparison with optical $H\beta$ and FeII relations. Optical $H\beta$ and FeII relations are shifted towards larger time delays (radii) in comparison with the UV FeII $R_{\text{BLR}} - L$ relation. MgII $R_{\text{BLR}} - L$ relation is clearly flatter than the other relations, which leads to the large separation of the MgII line-emitting material at smaller luminosities and a comparable time delay (radius) at high luminosities.



Figure 9.5: Turning quasars into standardizable candles. Using non-linear power-law relations, such as the broad-line region $R_{\text{BLR}} - L$ relation and the X-ray/UV luminosity relation $L_X - L_{\text{UV}}$, one can test whether quasars can be standardized and used as cosmological probes. The illustration depicts the UV emission of an accretion disc (blue) and a relatively fainter X-ray emission of the hot corona (yellow, above the disc). Since the $L_X - L_{\text{UV}}$ relation is non-linear, the luminosity distance can be determined to a given quasar. Copyright: NASA / CXC / M. Weiss

cosmological constraints based on quasars can help solve current cosmological tensions, such as the Hubble tension (see e.g. Abdalla et al. 2022). Currently, two non-linear power-law relations can be used to standardize quasars: (i) correlation between UV and X-ray luminosities or the $L_X - L_{UV}$ relation (Risaliti & Lusso 2019) and (ii) broad-line region radius-luminosity relation or $R_{BLR} - L$ relation (Khadka et al. 2021). The quasar standardization procedure using relations (i) and (ii) thus nicely connects, in principle, AGN “microphysics” with the large-scale structure of the Universe, see Fig. 9.5 for illustration. The question arises if the two standardization relations are mutually consistent, i.e. if they yield consistent cosmological constraints for the same sample of sources. In Khadka et al. (2023), we identified the sample of 58 sources (59 measurements) that have a significant X-ray emission and were also reverberation-mapped, hence both relations can be applied to them. For these sources, the $L_X - L_{UV}$ relation prefers a larger value of the current relative matter density parameter Ω_{m0} in comparison with the value inferred using the $R_{BLR} - L$ relation as well as the value derived using standard cosmological probes. In Paper 6 (Chapter 7) we analyze the distributions of the differences of luminosity distances ($\Delta \log D_L \equiv \log D_{L,L_X-L_{UV}} - \log D_{L,R-L}$) in different cosmological models. We find that the distributions are generally asymmetric and the peak is shifted to positive values, which implies that one method is more affected by a certain systematic effect. We find that the differential extinction of UV and X-ray photons always contributes to the non-zero luminosity-distance difference and that the X-ray/UV luminosity relation is more affected by extinction than the $R_{BLR} - L$ relation. This opens a way for the further application of the broad-line region $R_{BLR} - L$ relation in cosmological studies.

In conclusion, based on Papers 1-7 presented in this *Habilitation Thesis* (and references therein), the existence of SMBH(s) is currently firmly established. The main evidence is the following. First, we can detect its gravitational influence via the motion of S stars and other objects (e.g. “G” objects) in the Galactic center. Second, in other galactic nuclei, their gravitational influence is revealed via broad emission lines, which is the manifestation of the fast motion of an ionized, clumpy material around SMBHs. SMBHs also clearly affect the evolution of their host galaxies, which is hinted by several correlations between their masses and large-scale properties of their hosts (velocity dispersion, bulge mass). One of the main driving mechanisms behind these correlations is the AGN feedback, whose strength and nature (radiative or radio-mechanical) traced by the ionization potential and the radio loudness varies across different optical spectral classes of galaxies. This shows that the SMBH activity can generally be variable and recurrent in the nearby Universe (low to intermediate redshifts). The imprints of the AGN feedback can be traced on the large scales of galaxy groups and clusters (e.g. it prevents the warm/hot intergalactic medium from cooling; X-ray cavities), but the epochs of an enhanced nuclear activity could have plausibly left fingerprints at the small scale as well. In particular, there may be distinct traces revealed via the properties of nuclear star clusters due to repetitive star-disc and star-jet collisions.

Since antiquity, the center of the Universe has been shifting – once it was the Earth, then the Sun, and later the Galactic center. Now we know that there is no particular center of the Universe, which is also known as the Copernican principle. However, for our Universe “island”, the Milky Way, to which we are gravitationally bound, the supermassive black hole Sgr A* is the true center, both dynamical and geometric, which has also been influencing the Milky Way on larger scales via its variable activity during the past billions of years. Therefore, in any modern orrery demonstration (see Fig. 9.6), the supermassive black hole should be present at its center to mark its significance, not only for the Milky Way, but also for other galaxies, and thus the Universe as a whole.

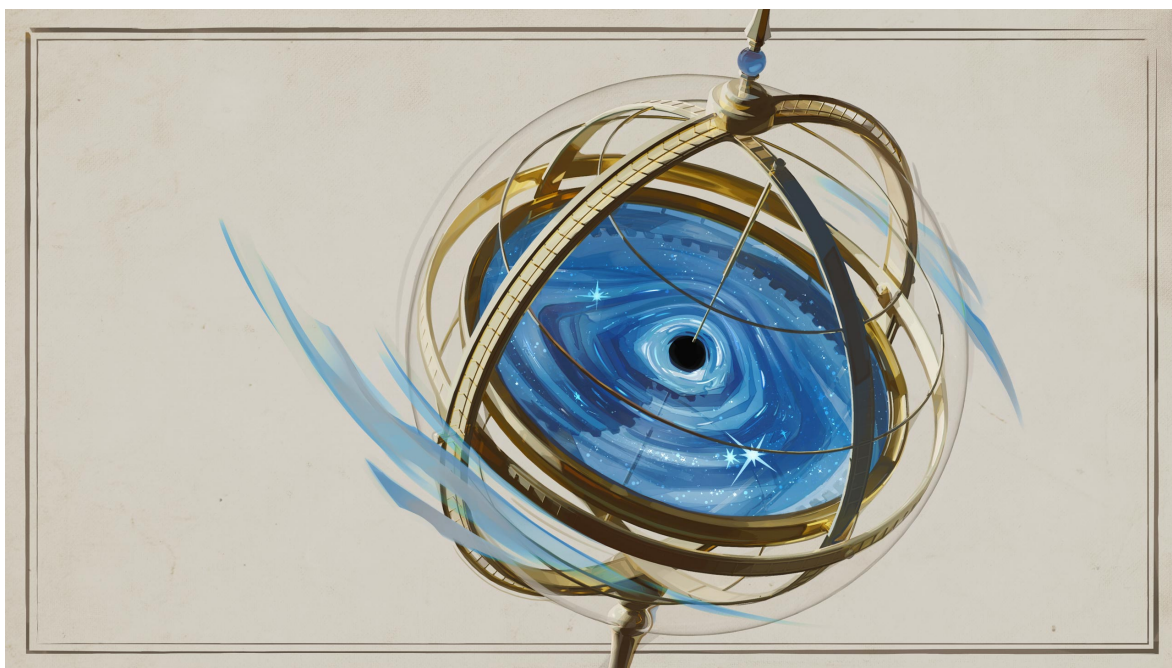


Figure 9.6: Orrery with the black hole at its center. Author: Olena Shmahalo (for *Quanta magazine*).



Bibliography

- Abbott, B. P., Abbott, R., Abbott, T. D., et al. 2016, *Phys. Rev. Lett.*, 116, 061102
- Abdalla, E., Abellán, G. F., Aboubrahim, A., et al. 2022, *Journal of High Energy Astrophysics*, 34, 49
- Abramowicz, M. A., Chen, X., Kato, S., Lasota, J.-P., & Regev, O. 1995, *ApJ*, 438, L37
- Abramowicz, M. A., Czerny, B., Lasota, J. P., & Szuszkiewicz, E. 1988, *ApJ*, 332, 646
- Abramowicz, M. A., Igumenshchev, I. V., Quataert, E., & Narayan, R. 2002, *ApJ*, 565, 1101
- Alexander, D. M. & Hickox, R. C. 2012, *NewAR*, 56, 93
- Alexander, T. 2017, *ARA&A*, 55, 17
- Ali, B., Paul, D., Eckart, A., et al. 2020, *ApJ*, 896, 100
- Amaro-Seoane, P., Andrews, J., Arca Sedda, M., et al. 2023, *Living Reviews in Relativity*, 26, 2
- Amaro-Seoane, P. & Chen, X. 2014, *ApJ*, 781, L18
- Amaro-Seoane, P., Chen, X., Schödel, R., & Casanellas, J. 2020, *MNRAS*, 492, 250
- Antonucci, R. 1993, *ARA&A*, 31, 473
- Arcodia, R., Merloni, A., Nandra, K., et al. 2021, *Nature*, 592, 704
- Baganoff, F. K., Maeda, Y., Morris, M., et al. 2003, *ApJ*, 591, 891
- Bahcall, J. N. & Wolf, R. A. 1976, *ApJ*, 209, 214
- Bahcall, J. N. & Wolf, R. A. 1977, *ApJ*, 216, 883
- Balbus, S. A. & Hawley, J. F. 1992, *ApJ*, 400, 610
- Balick, B. & Brown, R. L. 1974, *ApJ*, 194, 265

- Bally, J. & Hi-GAL Team. 2014, in IAU Symposium, Vol. 303, The Galactic Center: Feeding and Feedback in a Normal Galactic Nucleus, ed. L. O. Sjouwerman, C. C. Lang, & J. Ott, 1–14
- Bally, J., Stark, A. A., Wilson, R. W., & Henkel, C. 1987, *ApJS*, 65, 13
- Bally, J., Stark, A. A., Wilson, R. W., & Henkel, C. 1988, *ApJ*, 324, 223
- Becker, R. H., White, R. L., & Helfand, D. J. 1995, *ApJ*, 450, 559
- Becklin, E. E. & Neugebauer, G. 1968, *ApJ*, 151, 145
- Bentz, M. C., Denney, K. D., Grier, C. J., et al. 2013, *ApJ*, 767, 149
- Bentz, M. C., Peterson, B. M., Netzer, H., Pogge, R. W., & Vestergaard, M. 2009, *ApJ*, 697, 160
- Bentz, M. C., Peterson, B. M., Pogge, R. W., Vestergaard, M., & Onken, C. A. 2006, *ApJ*, 644, 133
- Bisnovatyi-Kogan, G. S. & Ruzmaikin, A. A. 1974, *Ap&SS*, 28, 45
- Bisnovatyi-Kogan, G. S. & Ruzmaikin, A. A. 1976, *Ap&SS*, 42, 401
- Blaauw, A., Gum, C. S., Pawsey, J. L., & Westerhout, G. 1960, *MNRAS*, 121, 123
- Bland-Hawthorn, J., Maloney, P. R., Sutherland, R., et al. 2019, *ApJ*, 886, 45
- Blandford, R. D. & McKee, C. F. 1982, *ApJ*, 255, 419
- Blank, M., Morris, M. R., Frank, A., Carroll-Nellenback, J. J., & Duschl, W. J. 2016, *MNRAS*, 459, 1721
- Broderick, A. E. & Loeb, A. 2006, *MNRAS*, 367, 905
- Brown, R. L. 1982, *ApJ*, 262, 110
- Bryant, A. & Krabbe, A. 2021, *NewAR*, 93, 101630
- Buchholz, R. M., Schödel, R., & Eckart, A. 2009, *A&A*, 499, 483
- Burbidge, G. R. 1958, *ApJ*, 128, 1
- Cackett, E. M., Bentz, M. C., & Kara, E. 2021, *iScience*, 24, 102557
- Cackett, E. M., Chiang, C.-Y., McHardy, I., et al. 2018, *ApJ*, 857, 53
- Cao, S., Zajaček, M., Czerny, B., Panda, S., & Ratra, B. 2024, *MNRAS*, 528, 6444
- Cao, S., Zajaček, M., Panda, S., et al. 2022, *MNRAS*, 516, 1721
- Chelouche, D., Pozo Nuñez, F., & Kaspi, S. 2019, *Nature Astronomy*, 3, 251
- Chen, X. & Amaro-Seoane, P. 2014, *ApJ*, 786, L14

- Chiaberge, M., Gilli, R., Lotz, J. M., & Norman, C. 2015, *ApJ*, 806, 147
- Christopher, M. H., Scoville, N. Z., Stolovy, S. R., & Yun, M. S. 2005, *ApJ*, 622, 346
- Churchwell, E., Babler, B. L., Meade, M. R., et al. 2009, *PASP*, 121, 213
- Ciurlo, A., Campbell, R. D., Morris, M. R., et al. 2020, *Nature*, 577, 337
- Collin, S., Kawaguchi, T., Peterson, B. M., & Vestergaard, M. 2006, *A&A*, 456, 75
- Collin-Souffrin, S. & Dumont, A. M. 1990, *A&A*, 229, 292
- Collin-Souffrin, S., Dyson, J. E., McDowell, J. C., & Perry, J. J. 1988, *MNRAS*, 232, 539
- Contopoulos, G. & Mertzaniades, C. 1977, *A&A*, 61, 477
- Cuadra, J., Nayakshin, S., & Martins, F. 2008, *MNRAS*, 383, 458
- Czerny, B. 2019, *Open Astronomy*, 28, 200
- Czerny, B., Cao, S., Jaiswal, V. K., et al. 2023, *Ap&SS*, 368, 8
- Czerny, B. & Elvis, M. 1987, *ApJ*, 321, 305
- Czerny, B. & Hryniewicz, K. 2011, *A&A*, 525, L8
- Czerny, B., Kunneriath, D., Karas, V., & Das, T. K. 2013, *A&A*, 555, A97
- Czerny, B., Li, Y.-R., Hryniewicz, K., et al. 2017, *ApJ*, 846, 154
- Czerny, B., Olejak, A., Rałowski, M., et al. 2019, *ApJ*, 880, 46
- Czerny, B., Różańska, A., & Kuraszkiewicz, J. 2004, *A&A*, 428, 39
- Dewangan, G. C., Tripathi, P., Papadakis, I. E., & Singh, K. P. 2021, *MNRAS*, 504, 4015
- Dexter, J., Agol, E., Fragile, P. C., & McKinney, J. C. 2010, *ApJ*, 717, 1092
- Dibai, E. A. 1977, *Soviet Astronomy Letters*, 3, 1
- Doeleman, S. S., Weintroub, J., Rogers, A. E. E., et al. 2008, *Nature*, 455, 78
- Done, C. & Gierliński, M. 2005, *MNRAS*, 364, 208
- Dyson, F. W., Eddington, A. S., & Davidson, C. 1920, *Philosophical Transactions of the Royal Society of London Series A*, 220, 291
- Eatough, R. P., Falcke, H., Karuppusamy, R., et al. 2013, *Nature*, 501, 391
- Eckart, A., Baganoff, F. K., Zamaninasab, M., et al. 2008, *A&A*, 479, 625
- Eckart, A., García-Marín, M., Vogel, S. N., et al. 2012, *A&A*, 537, A52
- Eckart, A. & Genzel, R. 1996, *Nature*, 383, 415
- Eckart, A. & Genzel, R. 1997, *MNRAS*, 284, 576

- Eckart, A., Genzel, R., Ott, T., & Schödel, R. 2002, MNRAS, 331, 917
- Eckart, A. & Idriz, M. 2023, Australian Journal of Islamic Studies, 8, 1–15
- Eckart, A., Mužić, K., Yazici, S., et al. 2013, A&A, 551, A18
- Eckart, A., Schödel, R., Meyer, L., et al. 2006, A&A, 455, 1
- Eckart, A., Zajacek, M., Valencia-S, M., et al. 2019, in Journal of Physics Conference Series, Vol. 1258, Journal of Physics Conference Series (IOP), 012019
- Edelson, R., Gelbord, J. M., Horne, K., et al. 2015, ApJ, 806, 129
- Edge, D. O., Shakeshaft, J. R., McAdam, W. B., Baldwin, J. E., & Archer, S. 1959, MmRAS, 68, 37
- Einstein, A. 1939, Annals of Mathematics, 40, 922
- Evans, P. A., Nixon, C. J., Campana, S., et al. 2023, Nature Astronomy, 7, 1368
- Event Horizon Telescope Collaboration, Akiyama, K., Alberdi, A., et al. 2024, ApJ, 964, L25
- Event Horizon Telescope Collaboration, Akiyama, K., Alberdi, A., et al. 2022, ApJ, 930, L12
- Event Horizon Telescope Collaboration, Akiyama, K., Alberdi, A., et al. 2019, ApJ, 875, L1
- Ewing, A. 1964, Science News Letter, 85, 39
- Faber, S. M., Dressler, A., Davies, R. L., et al. 1987, in Nearly Normal Galaxies. From the Planck Time to the Present, ed. S. M. Faber, 175
- Faber, S. M. & Jackson, R. E. 1976, ApJ, 204, 668
- Falcke, H. & Markoff, S. 2000, A&A, 362, 113
- Falcke, H., Melia, F., & Agol, E. 2000, ApJ, 528, L13
- Fausnaugh, M. M., Denney, K. D., Barth, A. J., et al. 2016, ApJ, 821, 56
- Ferrarese, L. & Merritt, D. 2000, ApJ, 539, L9
- Ferrière, K., Gillard, W., & Jean, P. 2007, A&A, 467, 611
- Franchini, A., Bonetti, M., Lupi, A., et al. 2023, A&A, 675, A100
- Frank, J., King, A., & Raine, D. J. 2002, Accretion Power in Astrophysics: Third Edition (Cambridge, UK: Cambridge University Press)
- Garland, I. L., Walmsley, M., Silcock, M. S., et al. 2024, MNRAS, 532, 2320
- Gaskell, C. M. 2009, NewAR, 53, 140
- Gebhardt, K., Kormendy, J., Ho, L. C., et al. 2000, ApJ, 543, L5
- Generozov, A., Stone, N. C., & Metzger, B. D. 2015, MNRAS, 453, 775

- Genzel, R. 2022, *Reviews of Modern Physics*, 94, 020501
- Genzel, R., Eisenhauer, F., & Gillessen, S. 2010, *Reviews of Modern Physics*, 82, 3121
- Genzel, R., Thatte, N., Krabbe, A., Kroker, H., & Tacconi-Garman, L. E. 1996, *ApJ*, 472, 153
- Genzel, R., Watson, D. M., Crawford, M. K., & Townes, C. H. 1985, *ApJ*, 297, 766
- Gezari, S. 2021, *ARA&A*, 59, 21
- Ghez, A. M., Duchêne, G., Matthews, K., et al. 2003, *ApJ*, 586, L127
- Ghez, A. M., Klein, B. L., Morris, M., & Becklin, E. E. 1998, *ApJ*, 509, 678
- Ghez, A. M., Morris, M., Becklin, E. E., Tanner, A., & Kremenek, T. 2000, *Nature*, 407, 349
- Giacconi, R., Murray, S., Gursky, H., et al. 1972, *ApJ*, 178, 281
- Gillessen, S., Eisenhauer, F., Trippe, S., et al. 2009, *ApJ*, 692, 1075
- Gillessen, S., Genzel, R., Fritz, T. K., et al. 2013, *ApJ*, 774, 44
- Gillessen, S., Genzel, R., Fritz, T. K., et al. 2012, *Nature*, 481, 51
- Gillessen, S., Plewa, P. M., Eisenhauer, F., et al. 2017, *ApJ*, 837, 30
- GRAVITY Collaboration, Abuter, R., Accardo, M., et al. 2017, *A&A*, 602, A94
- GRAVITY Collaboration, Abuter, R., Amorim, A., et al. 2018, *A&A*, 618, L10
- GRAVITY Collaboration, Amorim, A., Bauböck, M., et al. 2021, *A&A*, 648, A117
- GRAVITY Collaboration, Amorim, A., Bauböck, M., et al. 2020a, *A&A*, 643, A154
- GRAVITY Collaboration, Amorim, A., Bourdarot, G., et al. 2024, *A&A*, 684, A167
- GRAVITY Collaboration, Bauböck, M., Dexter, J., et al. 2020b, *A&A*, 635, A143
- Gravity Collaboration, Sturm, E., Dexter, J., et al. 2018, *Nature*, 563, 657
- Greene, J. E., Strader, J., & Ho, L. C. 2020, *ARA&A*, 58, 257
- Greenhill, L. 2002, in *IAU Symposium*, Vol. 206, *Cosmic Masers: From Proto-Stars to Black Holes*, ed. V. Migenes & M. J. Reid, 381
- Guesten, R., Genzel, R., Wright, M. C. H., et al. 1987, *ApJ*, 318, 124
- Guesten, R. & Henkel, C. 1983, *A&A*, 125, 136
- Gültekin, K., Richstone, D. O., Gebhardt, K., et al. 2009, *ApJ*, 698, 198
- Guolo, M., Pasham, D. R., Zajaček, M., et al. 2024, *Nature Astronomy*, 8, 347
- Habibi, M., Gillessen, S., Martins, F., et al. 2017, *ApJ*, 847, 120
- Habibi, M., Gillessen, S., Pfuhl, O., et al. 2019, *ApJ*, 872, L15

- Hailey, C. J., Mori, K., Bauer, F. E., et al. 2018, *Nature*, 556, 70
- Hazard, C., Mackey, M. B., & Shimmins, A. J. 1963, *Nature*, 197, 1037
- Henshaw, J. D., Barnes, A. T., Battersby, C., et al. 2023, in *Astronomical Society of the Pacific Conference Series*, Vol. 534, *Protostars and Planets VII*, ed. S. Inutsuka, Y. Aikawa, T. Muto, K. Tomida, & M. Tamura, 83
- Hernquist, L. & Mihos, J. C. 1995, *ApJ*, 448, 41
- Herschel, W. 1785, *Philosophical Transactions of the Royal Society of London*, 75, 213
- Hills, J. G. 1975, *Nature*, 254, 295
- Hills, J. G. 1988, *Nature*, 331, 687
- Hobbs, A. & Nayakshin, S. 2009, *MNRAS*, 394, 191
- Homayouni, Y., Trump, J. R., Grier, C. J., et al. 2020, *ApJ*, 901, 55
- Honma, F. 1996, *PASJ*, 48, 77
- Hopman, C. & Alexander, T. 2006, *ApJ*, 645, 1152
- Hsieh, P.-Y., Koch, P. M., Kim, W.-T., et al. 2021, *ApJ*, 913, 94
- Inui, T., Koyama, K., Matsumoto, H., & Tsuru, T. G. 2009, *PASJ*, 61, S241
- Jahnke, K. & Macciò, A. V. 2011, *ApJ*, 734, 92
- Jaiswal, V. K., Prince, R., Panda, S., & Czerny, B. 2023, *A&A*, 670, A147
- Jalali, B., Pelupessy, F. I., Eckart, A., et al. 2014, *MNRAS*, 444, 1205
- Jansky, K. G. 1933, *Nature*, 132, 66
- J Jeans, J. H. 1919, *MNRAS*, 79, 408
- Karas, V. & Bao, G. 1992, *A&A*, 257, 531
- Karas, V., Svoboda, J., & Zajaček, M. 2021, *Selected Chapters on Active Galactic Nuclei as Relativistic Systems (Silesian University in Opava)*, 154
- Kaspi, S., Brandt, W. N., Maoz, D., et al. 2021, *ApJ*, 915, 129
- Kaspi, S., Maoz, D., Netzer, H., et al. 2005, *ApJ*, 629, 61
- Kaspi, S., Smith, P. S., Netzer, H., et al. 2000, *ApJ*, 533, 631
- Kato, S., Fukue, J., & Mineshige, S. 2008, *Black-Hole Accretion Disks — Towards a New Paradigm (Kyoto, Japan: Kyoto University Press)*
- Kato, S. & Nakamura, K. E. 1998, *PASJ*, 50, 559
- Kejriwal, S., Witzany, V., Zajaček, M., Pasham, D. R., & Chua, A. J. K. 2024, *MNRAS*, 532, 2143

- Kerr, R. P. 1963, *Phys. Rev. Lett.*, 11, 237
- Khadka, N., Martínez-Aldama, M. L., Zajaček, M., Czerny, B., & Ratra, B. 2022a, *MNRAS*, 513, 1985
- Khadka, N. & Ratra, B. 2022, *MNRAS*, 510, 2753
- Khadka, N., Yu, Z., Zajaček, M., et al. 2021, *MNRAS*, 508, 4722
- Khadka, N., Zajaček, M., Panda, S., Martínez-Aldama, M. L., & Ratra, B. 2022b, *MNRAS*, 515, 3729
- Khadka, N., Zajaček, M., Prince, R., et al. 2023, *MNRAS*, 522, 1247
- Kim, S. S., Figer, D. F., & Morris, M. 2004, *ApJ*, 607, L123
- Kormendy, J. & Bender, R. 1999, *ApJ*, 522, 772
- Koyama, K., Awaki, H., Kunieda, H., Takano, S., & Tawara, Y. 1989, *Nature*, 339, 603
- Krabbe, A., Genzel, R., Eckart, A., et al. 1995, *ApJ*, 447, L95
- Krolik, J. H. & Linial, I. 2022, *ApJ*, 941, 24
- Kruijssen, J. M. D., Longmore, S. N., Elmegreen, B. G., et al. 2014, *MNRAS*, 440, 3370
- Kumar, S., Dewangan, G. C., Singh, K. P., et al. 2023, *ApJ*, 950, 90
- Kurfürst, P., Zajaček, M., Werner, N., & Krtićka, J. 2024, arXiv e-prints, arXiv:2409.17773
- Lauer, T. R., Faber, S. M., Groth, E. J., et al. 1993, *AJ*, 106, 1436
- Launhardt, R., Zylka, R., & Mezger, P. G. 2002, *A&A*, 384, 112
- Leavitt, H. S. 1908, *Annals of Harvard College Observatory*, 60, 87
- Leavitt, H. S. & Pickering, E. C. 1912, *Harvard College Observatory Circular*, 173, 1
- Levin, Y. & Beloborodov, A. M. 2003, *ApJ*, 590, L33
- Li, Y.-P., Yuan, F., Yuan, Q., et al. 2015, *ApJ*, 810, 19
- Linial, I. & Metzger, B. D. 2023, *ApJ*, 957, 34
- Liu, Z., Malyali, A., Krumpe, M., et al. 2023, *A&A*, 669, A75
- Lobban, A. & King, A. 2022, *MNRAS*, 511, 1992
- Longmore, S. N., Kruijssen, J. M. D., Bally, J., et al. 2013, *MNRAS*, 433, L15
- Lynden-Bell, D. 1969, *Nature*, 223, 690
- Lynden-Bell, D. & Rees, M. J. 1971, *MNRAS*, 152, 461
- Macchetto, F., Marconi, A., Axon, D. J., et al. 1997, *ApJ*, 489, 579

- Madau, P. & Dickinson, M. 2014, *ARA&A*, 52, 415
- Magorrian, J., Tremaine, S., Richstone, D., et al. 1998, *AJ*, 115, 2285
- Mahadevan, R. 1997, *ApJ*, 477, 585
- Mapelli, M. & Gualandris, A. 2016, in *Lecture Notes in Physics*, Berlin Springer Verlag, ed. F. Haardt, V. Gorini, U. Moschella, A. Treves, & M. Colpi, Vol. 905, 205
- Marconi, A. & Hunt, L. K. 2003, *ApJ*, 589, L21
- Marin, F., Churazov, E., Khabibullin, I., et al. 2023, *Nature*, 619, 41
- Marrone, D. P., Moran, J. M., Zhao, J.-H., & Rao, R. 2007, *ApJ*, 654, L57
- Martin, G., Kaviraj, S., Volonteri, M., et al. 2018, *MNRAS*, 476, 2801
- Martínez-Aldama, M. L., Czerny, B., Kawka, D., et al. 2019, *ApJ*, 883, 170
- Matthee, J., Naidu, R. P., Brammer, G., et al. 2024, *ApJ*, 963, 129
- Matthews, T. A. & Sandage, A. R. 1963, *ApJ*, 138, 30
- McAlpine, S., Harrison, C. M., Rosario, D. J., et al. 2020, *MNRAS*, 494, 5713
- McGee, R. X. & Bolton, J. G. 1954, *Nature*, 173, 985
- Mejía-Restrepo, J. E., Lira, P., Netzer, H., Trakhtenbrot, B., & Capellupo, D. M. 2018, *Nature Astronomy*, 2, 63
- Menten, K. M., Reid, M. J., Eckart, A., & Genzel, R. 1997, *ApJ*, 475, L111
- Merritt, D. 2013, *Dynamics and Evolution of Galactic Nuclei* (Princeton: Princeton University Press)
- Merritt, D. & Wang, J. 2005, *ApJ*, 621, L101
- Meyer, L., Eckart, A., Schödel, R., et al. 2006, *A&A*, 460, 15
- Mezger, P. G., Zylka, R., Salter, C. J., et al. 1989, *A&A*, 209, 337
- Mills, E. A. C., Togi, A., & Kaufman, M. 2017, *ApJ*, 850, 192
- Miniutti, G. & Fabian, A. C. 2004, *MNRAS*, 349, 1435
- Miniutti, G., Saxton, R. D., Giustini, M., et al. 2019, *Nature*, 573, 381
- Miyoshi, M., Moran, J., Herrnstein, J., et al. 1995, *Nature*, 373, 127
- Molinari, S., Bally, J., Noriega-Crespo, A., et al. 2011, *ApJ*, 735, L33
- Morris, M. 1993, *ApJ*, 408, 496
- Morris, M. & Serabyn, E. 1996, *ARA&A*, 34, 645

- Morris, M. R. 2015, in *Lessons from the Local Group: A Conference in honor of David Block and Bruce Elmegreen*, ed. K. Freeman, B. Elmegreen, D. Block, & M. Woolway, 391
- Moser, L., Sánchez-Monge, Á., Eckart, A., et al. 2017, *A&A*, 603, A68
- Mossoux, E. & Eckart, A. 2018, *MNRAS*, 474, 3787
- Muno, M. P., Pfahl, E., Baganoff, F. K., et al. 2005, *ApJ*, 622, L113
- Murchikova, E. M., Phinney, E. S., Pancoast, A., & Blandford, R. D. 2019, *Nature*, 570, 83
- Mužić, K., Eckart, A., Schödel, R., et al. 2010, *A&A*, 521, A13
- Naddaf, M. H. & Czerny, B. 2022, *A&A*, 663, A77
- Naddaf, M.-H., Czerny, B., & Szczerba, R. 2021, *ApJ*, 920, 30
- Najarro, F., Krabbe, A., Genzel, R., et al. 1997, *A&A*, 325, 700
- Narayan, R., Igumenshchev, I. V., & Abramowicz, M. A. 2003, *PASJ*, 55, L69
- Natarajan, P., Pacucci, F., Ricarte, A., et al. 2024, *ApJ*, 960, L1
- Netzer, H. 2022, *MNRAS*, 509, 2637
- Netzer, H. & Peterson, B. M. 1997, in *Astrophysics and Space Science Library*, Vol. 218, *Astronomical Time Series*, ed. D. Maoz, A. Sternberg, & E. M. Leibowitz, 85
- Neumayer, N., Seth, A., & Böker, T. 2020, *A&A Rev.*, 28, 4
- Newman, E. T., Couch, E., Chinnapared, K., et al. 1965, *Journal of Mathematical Physics*, 6, 918
- Nicholl, M., Pasham, D. R., Mummery, A., et al. 2024, *Nature*, 634, 804
- Nishiyama, S. & Schödel, R. 2013, *A&A*, 549, A57
- Nogueras-Lara, F., Schödel, R., Gallego-Calvente, A. T., et al. 2020, *Nature Astronomy*, 4, 377
- Nordström, G. 1918, *Koninklijke Nederlandse Akademie van Wetenschappen Proceedings Series B Physical Sciences*, 20, 1238
- Novikov, I. D. & Thorne, K. S. 1973, in *Black Holes (Les Astres Occlus)*, ed. C. Dewitt & B. S. Dewitt, 343–450
- Oppenheimer, J. R. & Snyder, H. 1939, *Physical Review*, 56, 455
- Panda, S., Marziani, P., & Czerny, B. 2019, *ApJ*, 882, 79
- Parsa, M., Eckart, A., Shahzamanian, B., et al. 2017, *ApJ*, 845, 22
- Pasham, D., Coughlin, E., Nixon, C., et al. 2024a, arXiv e-prints, arXiv:2411.05948
- Pasham, D. R., Coughlin, E. R., Zajaček, M., et al. 2024b, *ApJ*, 963, L47

- Pasham, D. R., Tombesi, F., Suková, P., et al. 2024c, *Science Advances*, 10, eadj8898
- Pasham, D. R., Zajaček, M., Nixon, C. J., et al. 2024d, *Nature*, 630, 325
- Payne, A. V., Shappee, B. J., Hinkle, J. T., et al. 2022, *ApJ*, 926, 142
- Peebles, P. J. E. 1972, *ApJ*, 178, 371
- Peißker, F., Ali, B., Zajaček, M., et al. 2021a, *ApJ*, 909, 62
- Peißker, F., Eckart, A., Zajaček, M., Ali, B., & Parsa, M. 2020a, *ApJ*, 899, 50
- Peißker, F., Eckart, A., Zajaček, M., & Britzen, S. 2022, *ApJ*, 933, 49
- Peißker, F., Hosseini, S. E., Zajaček, M., et al. 2020b, *A&A*, 634, A35
- Peißker, F., Zajaček, M., Eckart, A., et al. 2021b, *ApJ*, 923, 69
- Peißker, F., Zajaček, M., Eckart, A., et al. 2019, *A&A*, 624, A97
- Peissker, F., Zajaček, M., Labadie, L., et al. 2024, *Nature Communications*, 15, 1
- Peißker, F., Zajaček, M., Labaj, M., et al. 2024a, *ApJ*, 970, 74
- Peißker, F., Zajaček, M., Melamed, M., et al. 2024b, *A&A*, 686, A235
- Peißker, F., Zajaček, M., Sabha, N. B., et al. 2023, *ApJ*, 944, 231
- Pen, U.-L., Matzner, C. D., & Wong, S. 2003, *ApJ*, 596, L207
- Penrose, R. 1963, *Phys. Rev. Lett.*, 10, 66
- Penrose, R. 1965, *Phys. Rev. Lett.*, 14, 57
- Perivolaropoulos, L. & Skara, F. 2022, *NewAR*, 95, 101659
- Pesce, D. W., Palumbo, D. C. M., Narayan, R., et al. 2021, *ApJ*, 923, 260
- Peters, P. C. 1964, *Physical Review*, 136, 1224
- Peterson, B. M., Ferrarese, L., Gilbert, K. M., et al. 2004, *ApJ*, 613, 682
- Pfuhl, O., Fritz, T. K., Zilka, M., et al. 2011, *ApJ*, 741, 108
- Piddington, J. H. & Minnett, H. C. 1951, *Australian Journal of Scientific Research A Physical Sciences*, 4, 459
- Planck Collaboration, Aghanim, N., Akrami, Y., et al. 2020, *A&A*, 641, A6
- Pounds, K. A., Reeves, J. N., King, A. R., et al. 2003, *MNRAS*, 345, 705
- Predehl, P., Sunyaev, R. A., Becker, W., et al. 2020, *Nature*, 588, 227
- Quataert, E. 2004, *ApJ*, 613, 322
- Rafikov, R. R. 2020, *ApJ*, 905, L35

- Rees, M. J. 1988, *Nature*, 333, 523
- Reissner, H. 1916, *Annalen der Physik*, 355, 106
- Remillard, R. A. & McClintock, J. E. 2006, *ARA&A*, 44, 49
- Requena-Torres, M. A., Güsten, R., Weiß, A., et al. 2012, *A&A*, 542, L21
- Ressler, S. M., Quataert, E., & Stone, J. M. 2019, *MNRAS*, 482, L123
- Ressler, S. M., White, C. J., Quataert, E., & Stone, J. M. 2020, *ApJ*, 896, L6
- Richards, G. T., Croom, S. M., Anderson, S. F., et al. 2005, *MNRAS*, 360, 839
- Riess, A. G., Fliri, J., & Valls-Gabaud, D. 2012, *ApJ*, 745, 156
- Riess, A. G., Yuan, W., Macri, L. M., et al. 2022, *ApJ*, 934, L7
- Risaliti, G. & Lusso, E. 2019, *Nature Astronomy*, 3, 272
- Roupas, Z., Kocsis, B., & Tremaine, S. 2017, *ApJ*, 842, 90
- Royster, M. J., Yusef-Zadeh, F., Wardle, M., et al. 2019, *ApJ*, 872, 2
- Ryu, T., Krolik, J., Piran, T., & Noble, S. C. 2020, *ApJ*, 904, 99
- Sabha, N., Eckart, A., Merritt, D., et al. 2012, *A&A*, 545, A70
- Salpeter, E. E. 1964, *ApJ*, 140, 796
- Sanchez-Bermudez, J., Schödel, R., Alberdi, A., et al. 2014, *A&A*, 567, A21
- Schaffer, S. 1979, *Journal for the History of Astronomy*, 10, 42
- Schawinski, K., Koss, M., Berney, S., & Sartori, L. F. 2015, *MNRAS*, 451, 2517
- Schlegel, D. J., Finkbeiner, D. P., & Davis, M. 1998, *ApJ*, 500, 525
- Schmidt, M. 1963, *Nature*, 197, 1040
- Schödel, R., Feldmeier, A., Kunneriath, D., et al. 2014a, *A&A*, 566, A47
- Schödel, R., Feldmeier, A., Neumayer, N., Meyer, L., & Yelda, S. 2014b, *Classical and Quantum Gravity*, 31, 244007
- Schödel, R., Merritt, D., & Eckart, A. 2009, *A&A*, 502, 91
- Schödel, R., Nogueras-Lara, F., Gallego-Cano, E., et al. 2020, *A&A*, 641, A102
- Schödel, R., Ott, T., Genzel, R., et al. 2002, *Nature*, 419, 694
- Schödel, R., Yelda, S., Ghez, A., et al. 2013, *MNRAS*, 429, 1367
- Schoedel, R., Alberdi, A., Jimenez-Serra, I., et al. 2024, arXiv e-prints, arXiv:2406.04022
- Schönrich, R., Aumer, M., & Sale, S. E. 2015, *ApJ*, 812, L21

- Schucking, E. L. 1989, *Physics Today*, 42, 46
- Schwarzschild, K. 1916, *Abh. Konigl. Preuss. Akad. Wissenschaften Jahre 1906,92*, Berlin,1907, 1916, 189
- Scoville, N. & Burkert, A. 2013, *ApJ*, 768, 108
- Sellgren, K., McGinn, M. T., Becklin, E. E., & Hall, D. N. 1990, *ApJ*, 359, 112
- Seyfert, C. K. 1943, *ApJ*, 97, 28
- Shakura, N. I. & Sunyaev, R. A. 1973, *A&A*, 24, 337
- Shapley, H. 1918, *PASP*, 30, 42
- Shcherbakov, R. V. & Baganoff, F. K. 2010, *ApJ*, 716, 504
- Smethurst, R. J., Beckmann, R. S., Simmons, B. D., et al. 2024, *MNRAS*, 527, 10855
- Sniegowska, M., Czerny, B., Bon, E., & Bon, N. 2020, *A&A*, 641, A167
- Śniegowska, M., Grzędzielski, M., Czerny, B., & Janiuk, A. 2023, *A&A*, 672, A19
- Soltan, A. 1982, *MNRAS*, 200, 115
- Stephan, A. P., Naoz, S., Ghez, A. M., et al. 2019, *ApJ*, 878, 58
- Stephan, A. P., Naoz, S., Ghez, A. M., et al. 2016, *MNRAS*, 460, 3494
- Stoughton, C., Lupton, R. H., Bernardi, M., et al. 2002, *AJ*, 123, 485
- Stuchlík, Z. & Bao, G. 1992, *General Relativity and Gravitation*, 24, 945
- Su, M., Slatyer, T. R., & Finkbeiner, D. P. 2010, *ApJ*, 724, 1044
- Suková, P., Tombesi, F., Pasham, D. R., et al. 2024, arXiv e-prints, arXiv:2411.04592
- Suková, P., Zajaček, M., Witzany, V., & Karas, V. 2021, *ApJ*, 917, 43
- Sunyaev, R. & Churazov, E. 1998, *MNRAS*, 297, 1279
- Svoboda, J., Guainazzi, M., & Merloni, A. 2017, *A&A*, 603, A127
- Takekawa, S., Oka, T., & Tanaka, K. 2017, *ApJ*, 834, 121
- Thim, F., Hoessel, J. G., Saha, A., et al. 2004, *AJ*, 127, 2322
- Tombesi, F., Cappi, M., Reeves, J. N., et al. 2010, *A&A*, 521, A57
- Tremaine, S. 1995, *AJ*, 110, 628
- Trumpler, R. J. 1930, *Lick Observatory Bulletin*, 420, 154
- Tully, R. B. & Fisher, J. R. 1977, *A&A*, 54, 661
- Urry, C. M. & Padovani, P. 1995, *PASP*, 107, 803

- Valencia-S., M., Eckart, A., Zajaček, M., et al. 2015, *ApJ*, 800, 125
- van der Laan, H. 1966, *Nature*, 211, 1131
- von Fellenberg, S. D., Gillessen, S., Stadler, J., et al. 2022, *ApJ*, 932, L6
- von Fellenberg, S. D., Janssen, M., Davelaar, J., et al. 2023, *A&A*, 672, L5
- Štolc, M., Zajaček, M., Czerny, B., & Karas, V. 2023, *MNRAS*, 522, 2869
- Wang, J.-M. & Zhou, Y.-Y. 1999, *ApJ*, 516, 420
- Wang, Q. D., Gotthelf, E. V., & Lang, C. C. 2002, *Nature*, 415, 148
- Wang, Q. D., Nowak, M. A., Markoff, S. B., et al. 2013, *Science*, 341, 981
- Wardle, M. & Yusef-Zadeh, F. 2008, *ApJ*, 683, L37
- Wevers, T. 2020, *MNRAS*, 497, L1
- Wevers, T., Coughlin, E. R., Pasham, D. R., et al. 2023, *ApJ*, 942, L33
- Wevers, T., Pasham, D. R., van Velzen, S., et al. 2021, *ApJ*, 912, 151
- Wheeler, J. A. 1968, *American Scientist*, 56, 1
- Wielgus, M., Moscibrodzka, M., Vos, J., et al. 2022, *A&A*, 665, L6
- Wilkin, F. P. 1996, *ApJ*, 459, L31
- Witzel, G., Ghez, A. M., Morris, M. R., et al. 2014, *ApJ*, 796, L8
- Witzel, G., Martinez, G., Willner, S. P., et al. 2021, *ApJ*, 917, 73
- Woltjer, L. 1959, *ApJ*, 130, 38
- Woo, J.-H., Yoon, Y., Park, S., Park, D., & Kim, S. C. 2015, *ApJ*, 801, 38
- Yalinewich, A., Sari, R., Generozov, A., Stone, N. C., & Metzger, B. D. 2018, *MNRAS*, 479, 4778
- Yu, Z., Martini, P., Penton, A., et al. 2023, *MNRAS*, 522, 4132
- Yuan, F., Bu, D., & Wu, M. 2012, *ApJ*, 761, 130
- Yuan, F., Lin, J., Wu, K., & Ho, L. C. 2009, *MNRAS*, 395, 2183
- Yuan, F. & Narayan, R. 2014, *ARA&A*, 52, 529
- Yuan, F., Quataert, E., & Narayan, R. 2003, *ApJ*, 598, 301
- Yusef-Zadeh, F., Bushouse, H., Wardle, M., et al. 2009a, *ApJ*, 706, 348
- Yusef-Zadeh, F., Hewitt, J. W., Arendt, R. G., et al. 2009b, *ApJ*, 702, 178
- Yusef-Zadeh, F., Roberts, D., Wardle, M., Heinke, C. O., & Bower, G. C. 2006, *ApJ*, 650, 189

- Yusef-Zadeh, F., Royster, M., Wardle, M., et al. 2020, *MNRAS*, 499, 3909
- Yusef-Zadeh, F., Wardle, M., Heinke, C., et al. 2008, *ApJ*, 682, 361
- Yusef-Zadeh, F., Wardle, M., Schödel, R., et al. 2016, *ApJ*, 819, 60
- Zajacek, M. 2017, *The Observatory*, 137, 267
- Zajacek, M., Eckart, A., & Hosseini, S. E. 2018, in *Accretion Processes in Cosmic Sources - II*, 49
- Zajacek, M., Karas, V., & Kunneriath, D. 2015, *Acta Polytechnica*, 55, 203
- Zajacek, M. & Tursunov, A. 2019, *The Observatory*, 139, 231
- Zajaček, M. 2021, *ApJ*, 915, 111
- Zajaček, M., Araudo, A., Karas, V., Czerny, B., & Eckart, A. 2020, *ApJ*, 903, 140
- Zajaček, M., Araudo, A., Karas, V., et al. 2020, in *RAGtime 20-22: Workshops on Black Holes and Neutron Stars. Proceedings of RAGtime 20-22*. Edited by Z. Stuchlík, ed. Z. Stuchlík, G. Török, & V. Karas, 357–374
- Zajaček, M., Britzen, S., Eckart, A., et al. 2017, *A&A*, 602, A121
- Zajaček, M., Busch, G., Valencia-S., M., et al. 2019a, *A&A*, 630, A83
- Zajaček, M., Czerny, B., Jaiswal, V. K., et al. 2024a, *Space Sci. Rev.*, 220, 29
- Zajaček, M., Czerny, B., Khadka, N., et al. 2024b, *ApJ*, 961, 229
- Zajaček, M., Czerny, B., Martínez-Aldama, M. L., & Karas, V. 2019b, *Astronomische Nachrichten*, 340, 577
- Zajaček, M., Czerny, B., Martínez-Aldama, M. L., et al. 2020, *ApJ*, 896, 146
- Zajaček, M., Czerny, B., Martínez-Aldama, M. L., et al. 2021, *ApJ*, 912, 10
- Zajaček, M., Czerny, B., Schödel, R., Werner, N., & Karas, V. 2022, *Nature Astronomy*, 6, 1008
- Zajaček, M., Eckart, A., Karas, V., et al. 2016, *MNRAS*, 455, 1257
- Zajaček, M., Karas, V., & Eckart, A. 2014, *A&A*, 565, A17
- Zajaček, M., Panda, S., Pandey, A., et al. 2024c, *A&A*, 683, A140
- Zajaček, M., Pikhartová, M., & Peissker, F. 2024d, arXiv e-prints, arXiv:2410.00304
- Zajaček, M., Suková, P., Karas, V., et al. 2024e, arXiv e-prints, arXiv:2410.12090
- Zajaček, M., Tursunov, A., Eckart, A., & Britzen, S. 2018, *MNRAS*, 480, 4408
- Zajaček, M. & Tursunov, A. A. 2018, *Astronomische Nachrichten*, 339, 324

Zamaninasab, M., Eckart, A., Dovčiak, M., et al. 2011, MNRAS, 413, 322

Zel'dovich, Y. B. & Novikov, I. D. 1965, Soviet Physics Doklady, 9, 834

Zhao, J.-H., Blundell, R., Moran, J. M., et al. 2010, ApJ, 723, 1097

Zhao, J.-H., Morris, M. R., Goss, W. M., & An, T. 2009, ApJ, 699, 186



Curriculum Vitae

Name and surname, including degrees: RNDr. Michal Zajaček, Dr. rer. nat.

Date and place of birth: December 31st 1988, Malacky, Slovakia

Citizenship: Slovak

Permanent residence: L. Novomeského 4, 901 01 Malacky, Slovakia

Current position, unit, institution: astrophysics researcher, Department of Theoretical Physics and Astrophysics, Faculty of Science, Masaryk University

Education:

- September 17, 2014 - October 12, 2017: University of Cologne / Max Planck Institute for Radioastronomy (Cologne / Bonn, Germany) - Dr. rer. nat. in Experimental Physics, graduated as very good with the grade 1.00; Thesis title: *Interaction between interstellar medium and black hole environment* (Supervisor: Prof. Dr. Andreas Eckart)
- December 15, 2014: Charles University in Prague (Prague, Czechia) - Rigorosum examination – RNDr. degree; Thesis title: *Neutron stars near a galactic centre*
- 2012–2014: Charles University in Prague (Prague, Czechia) - Master of Science in Astronomy & Astrophysics, graduated with honours; Thesis title: *Neutron stars near a galactic centre* (Supervisor: Prof. Dr. Vladimír Karas)
- 2009–2012: Charles University in Prague (Prague, Czechia) - Bachelor of Science in General Physics, graduated with honours; Thesis title: *The Late Heavy Bombardment at various places of the Solar System* (Supervisor: Prof. Dr. Miroslav Brož)

Work experience:

- July 2021 - present: Masaryk University, Faculty of Science, Department of Theoretical Physics and Astrophysics (Brno, Czechia); position: postdoctoral researcher & lecturer, principal investigator of the Czech Science Foundation Junior Star grant “Stars in galactic nuclei: interrelation with massive black holes”
- January 2019 - June 2021: Center for Theoretical Physics, Polish Academy of Sciences (Warsaw, Poland); position: postdoctoral researcher (PI: Prof. Bożena Czerny)

- October 2017 - January 2019: Max Planck Institute for Radioastronomy (Bonn, Germany); position: junior postdoctoral researcher (PIs: Dr. Silke Britzen, Prof. J. Anton Zensus)



Significant Research Results

Significant research outcomes of the associate professor candidate are listed in this section. In the first subsection, first-author papers published in international, peer-reviewed journals are included while in the following subsection we list manuscripts co-authored by the candidate that were published in *Nature* and *Science* journals or papers published in a *Letter* format.

First-author refereed publications

- **ZAJAČEK, M.***(corresponding author)*, B. CZERNY, N. KHADKA, M. L. MARTINEZ-ALDAMA, R. PRINCE, S. PANDA and B. RATRA. *Effect of Extinction on Quasar Luminosity Distances Determined from UV and X-Ray Flux Measurements*. *Astrophysical Journal*. 2024, 961(2, Article 229). ISSN 1538-4357. Available at: doi:10.3847/1538-4357/ad11dc; citation: [Zajaček et al. \(2024b\)](#)
- **ZAJAČEK, M.***(corresponding author)*, B. CZERNY, V. K. JAISWAL, M. ŠTOLC, V. KARAS, A. PANDEY, D. R. PASHAM, M. ŚNIEGOWSKA, V. WITZANY, P. SUKOVA, F. MUNZ, N. WERNER, J. ŘÍPA, J. MERC, M. LABAJ, P. KURFÜRST and J. KRTIČKA. *Science with a Small Two-Band UV-Photometry Mission III: Active Galactic Nuclei and Nuclear Transients*. *Space Science Reviews*. 2024, 220(3, Article 29). ISSN 1572-9672. Available at: doi:10.1007/s11214-024-01062-5; citation: [Zajaček et al. \(2024a\)](#)
- **ZAJAČEK, M.***(corresponding author)*, S. PANDA, A. PANDEY, R. PRINCE, A. RODRIGUEZ-ARDILA, V. JAISWAL, B. CZERNY, K. HRYNIEWICZ, M. URBANOWICZ, P. TRZCIONKOWSKI, M. ŚNIEGOWSKA, Z. FALKOWSKA, M. L. MARTINEZ-ALDAMA and N. WERNER. *UV FeII emission model of HE 0413-4031 and its relation to broad-line time delays*. *Astronomy & Astrophysics*. 2024, 683(A140, Article A140). ISSN 1432-0746. Available at: doi:10.1051/0004-6361/202348172; citation: [Zajaček et al. \(2024c\)](#)
- **ZAJAČEK, M.***(corresponding author)*. *Enhanced Doppler Beaming for Dust-enshrouded Objects and Pulsars in the Galactic Center*. *Astrophysical Journal*. 2021, 915(2, Article 111). ISSN 1538-4357. Available at: doi:10.3847/1538-4357/ac043a; citation: [Zajaček \(2021\)](#)

- **ZAJAČEK, M.***(corresponding author)*, B. CZERNY, M. L. MARTINEZ-ALDAMA, M. RALOWSKI, A. OLEJAK, R. PRZYLUSKI, S. PANDA, K. HRYNIEWICZ, M. ŚNIEGOWSKA, M.-H. NADDAF, R. PRINCE, W. PYCH, G. PIETRZYNSKI, C. Sobrino FIGAREDO, M. HAAS, J. ŚREDZINSKA, M. KRUPA, A. KURCZ, A. UDALSKI, V. KARAS, M. SARNA, H. L. WORTERS, R. R. SEFAKO and A. GENADE. *Time Delay of Mg II Emission Response for the Luminous Quasar HE 0435-4312: toward Application of the High-accretor Radius–Luminosity Relation in Cosmology*. *Astrophysical Journal*. 2021, 912(1, Article 10). ISSN 1538-4357. Available at: doi:10.3847/1538-4357/abe9b2; citation: [Zajaček et al. \(2021\)](#)
- **ZAJAČEK, M.***(corresponding author)*, A. ARAUDO, V. KARAS, B. CZERNY and A. ECKART. *Depletion of Bright Red Giants in the Galactic Center during Its Active Phases*. *Astrophysical Journal*. 2020, 903(2, Article 140). ISSN 1538-4357. Available at: doi:10.3847/1538-4357/abbd94; citation: [Zajaček et al. \(2020\)](#)
- **ZAJAČEK, M.***(corresponding author)*, B. CZERNY, M. L. MARTINEZ-ALDAMA, M. RALOWSKI, A. OLEJAK, S. PANDA, K. HRYNIEWICZ, M. ŚNIEGOWSKA, M.-H. NADDAF, W. PYCH, G. PIETRZYNSKI, C. Sobrino FIGAREDO, M. HAAS, J. ŚREDZINSKA, M. KRUPA, A. KURCZ, A. UDALSKI, M. GORSKI and M. SARNA. *Time-delay Measurement of Mg II Broad-line Response for the Highly Accreting Quasar HE 0413-4031: Implications for the Mg II-based Radius-Luminosity Relation*. *Astrophysical Journal*. 2020, 896(2, Article 146). ISSN 1538-4357. Available at: doi:10.3847/1538-4357/ab94ae; citation: [Zajaček et al. \(2020\)](#)
- **ZAJAČEK, M.***(corresponding author)*, G. BUSCH, M. VALENCIA-S, A. ECKART, S. BRITZEN, L. FUHRMANN, J. SCHNEELOCH, N. FAZELI, K. C. HARRINGTON and J. A. ZENSUS. *Radio spectral index distribution of SDSS-FIRST sources across optical diagnostic diagrams*. *Astronomy & Astrophysics*. 2019, 630(A83, Article A83). ISSN 1432-0746. Available at: doi:10.1051/0004-6361/201833388; citation: [Zajaček et al. \(2019a\)](#)
- **ZAJAČEK, M.***(corresponding author)*, B. CZERNY, M. L. MARTINEZ-ALDAMA and V. KARAS. *Reverberation mapping of distant quasars: Time lag determination using different methods*. *Astronomische Nachrichten*. 2019, 340(7), 577–585. ISSN 1521-3994. Available at: doi:10.1002/asna.201913659; citation: [Zajaček et al. \(2019b\)](#)
- **ZAJAČEK, M.***(corresponding author)* and A. TURSUNOV. *The Electric Charge Of Black Holes: Is It Really Always Negligible?*. *Observatory*. 2019, 139(1273), 231–236. ISSN 0029-7704; citation: [Zajacek & Tursunov \(2019\)](#)
- **ZAJAČEK, M.***(corresponding author)* and A. A. TURSUNOV. *A stellar fly-by close to the Galactic center: Can we detect stars on highly relativistic orbits?*. *Astronomische Nachrichten*. 2018, 339(5), 324–330. ISSN 1521-3994. Available at: doi:10.1002/asna.201813499; citation: [Zajaček & Tursunov \(2018\)](#)
- **ZAJAČEK, M.***(corresponding author)*, A. TURSUNOV, A. ECKART and S. BRITZEN. *On the charge of the Galactic centre black hole*. *Monthly Notices of the Royal Astronomical Society*. 2018, 480(4), 4408–4423. ISSN 1365-2966. Available at: doi:10.1093/mnras/sty2182; citation: [Zajaček et al. \(2018\)](#)

- **ZAJAČEK, M.***(corresponding author)*. *Cologne-Prague-Kiel Meetings 2013-2017: From Accretion To Star Formation In Galactic Nuclei*. Observatory. 2017, 137(1261), 267–272. ISSN 0029-7704; citation: [Zajacek \(2017\)](#)
- **ZAJAČEK, M.***(corresponding author)*, S. BRITZEN, A. ECKART, B. SHAHZAMANIAN, G. BUSCH, V. KARAS, M. PARSA, F. PEISSKER, M. DOVČIAK, M. SUBROWEIT, F. DINNBIER and J. A. ZENSUS. *Nature of the Galactic centre NIR-excess sources: I. What can we learn from the continuum observations of the DSO/G2 source?*. *Astronomy & Astrophysics*. 2017, 602(A121, Article A121). ISSN 1432-0746. Available at: doi:10.1051/0004-6361/201730532; citation: [Zajaček et al. \(2017\)](#)
- **ZAJAČEK, M.***(corresponding author)*, A. ECKART, V. KARAS, D. KUNNERIATH, B. SHAHZAMANIAN, N. SABHA, K. MUZIC and M. VALENCIA-S. *Effect of an isotropic outflow from the Galactic Centre on the bow-shock evolution along the orbit*. *Monthly Notices of the Royal Astronomical Society*. 2016, 455(2), 1257–1274. ISSN 1365-2966. Available at: doi:10.1093/mnras/stv2357; citation: [Zajaček et al. \(2016\)](#)
- **ZAJAČEK, M.***(corresponding author)*, V. KARAS and D. KUNNERIATH. *Galactic Center Minispiral: Interaction Modes Of Neutron Stars*. *Acta Polytechnica*. 2015, 55(3), 203–214. ISSN 1805-2363. Available at: doi:10.14311/Ap.2015.55.0203; citation: [Zajacek et al. \(2015\)](#)
- **ZAJAČEK, Michal***(corresponding author)*, V. KARAS and A. ECKART. *Dust-enshrouded star near supermassive black hole: predictions for high-eccentricity passages near low-luminosity galactic nuclei*. *Astronomy & Astrophysics*. 2014, 565(A17, Article A17). ISSN 1432-0746. Available at: doi:10.1051/0004-6361/201322713; citation: [Zajaček et al. \(2014\)](#)

Publications in *Nature*, *Science*, and *Letter* format

- PEISSKER, F., **M. ZAJAČEK**, L. LABADIE, E. BORDIER, A. ECKART, M. MELAMED and V. KARAS. *A binary system in the S cluster close to the supermassive black hole Sagittarius A**. *Nature Communications*. 2024, 15(10608). ISSN 2041-1723. Available at: doi: 10.1038/s41467-024-54748-3; citation: [Peissker et al. \(2024\)](#)
- PASHAM, D. R., F. TOMBESI, P. SUKOVÁ, **M. ZAJAČEK**, S. RAKSHIT, E. COUGHLIN, P. KOSEC, V. KARAS, M. MASTERSON, A. MUMMERY, T. W. - S. HOLOIEN, M. GUOLO, J. HINKLE, B. RIPPERDA, V. WITZANY, B. SHAPPEE, E. KARA, A. HORESH, S. VAN VELZEN, I. SFARADI, D. KAPLAN, N. BURGER, T. MURPHY, R. REMILLARD, J. F. STEINER, T. WEVERS, R. ARCODIA, J. BUCHNER, A. MERLONI, A. MALYALI, A. FABIAN, M. FAUSNAUGH, T. DAYLAN, D. ALTAMIRANO, A. PAYNE and E. C. FERRARA. *A case for a binary black hole system revealed via quasi-periodic outflows*. *Science Advances*. 2024, 10(13, Article eadj8898). ISSN 2375-2548. Available at: doi:10.1126/sciadv.adj8898; citation: [Pasham et al. \(2024c\)](#)
- PASHAM, D. R., E. R. COUGHLIN, **M. ZAJAČEK**, I. LINIAL, P. SUKOVÁ, C. J. NIXON, A. JANIUK, M. ŚNIEGOWSKA, V. WITZANY, V. KARAS, M. KRUMPE, D. ALTAMIRANO, T. WEVERS and R. ARCODIA. *Alive but Barely Kicking: News from*

3+ yr of Swift and XMM-Newton X-Ray Monitoring of Quasiperiodic Eruptions from eRO-QPE1. *Astrophysical Journal Letters*. 2024, 963(2, Article L47). ISSN 2041-8213. Available at: doi:10.3847/2041-8213/ad2a5c; citation: [Pasham et al. \(2024b\)](#)

- PASHAM, D. R., **M. ZAJAČEK**, C. J. NIXON, E. R. COUGHLIN, M. ŚNIEGOWSKA, A. JANIUK, B. CZERNY, T. WEVERS, M. GUOLO, Y. AJAY and M. LOEWENSTEIN. *Lense–Thirring precession after a supermassive black hole disrupts a star*. *Nature*. 2024. 630(8016), 325–328. ISSN 1476-4687. Available at: doi:10.1038/s41586-024-07433-w; citation: [Pasham et al. \(2024d\)](#)
- GUOLO, M., D. R. PASHAM, **M. ZAJAČEK**, E. R. COUGHLIN, S. GEZARI, P. SUKOVÁ, T. WEVERS, V. WITZANY, F. TOMBESI, S. VAN VELZEN, K. D. ALEXANDER, Y. YAO, R. ARCODIA, V. KARAS, J. C. A. MILLER-JONES, R. REMILLARD, K. GENDREAU and E. C. FERRARA. *X-ray eruptions every 22 days from the nucleus of a nearby galaxy*. *Nature Astronomy*. 2024, 8(3). ISSN 2397-3366. Available at: doi:10.1038/s41550-023-02178-4; citation: [Guolo et al. \(2024\)](#)



Acknowledgements

*“If I have seen further it is by
standing on the shoulders of
Giants.”*

— Isaac Newton
(1642/1643-1726/1727), in a letter
to Robert Hooke,
February 5th, 1675

Since this is my fourth thesis already, I confirm that all of my previous acknowledgements are still fully valid :) At this point I would like to express my sincere acknowledgements to the people who have enabled me to do research, motivated me, and from whom I have learned a lot for the subsequent research work. To start with my Bachelor Thesis, I am grateful to Prof. Dr. Miroslav Brož, who supervised me during my bachelor studies at the Charles University in Prague. From Prof. Brož, and also Prof. David Vokrouhlický, Prof. Ladislav Šubr, and other researchers and lecturers at the Astronomical Institute of the Charles University, I got very important basics of the analysis techniques in celestial mechanics, which I have been using in various problems. Later I continued with my master thesis focused on the Galactic center. At this stage my master-thesis supervisor Prof. Dr. Vladimír Karas played a big role. He suggested the topic “Neutron stars near a galactic center”, which sounded as very exotic to me but at the same time thrilling. I invested a lot of time into trying to find a way to detect the “hidden” population of neutron stars close to the Galactic center. I think we succeeded partially and the results got published to a certain extent, though we should still finalize it now after 10 years! In general, I learned a lot about the center of the Milky Way during this period. Especially the twist towards the mysterious G2 “cloud”, which is likely not a pure cloud anymore, has been highly influential and probably affected my whole career afterwards.

I really enjoyed my PhD studies at the University of Cologne/Max Planck Institute for Radioastronomy, especially many discussions with my supervisor Prof. Dr. Andreas Eckart and a lot of advice from him. Andreas has always been very kind, patient, and supportive, which is quite rare in current busy times. I would also like to express big thanks to the whole Cologne and Bonn groups, in particular our *aegroup*, especially to Dr. Florian Peissker, with whom we intensively collaborate till now on many problems and puzzling objects in the

Galactic Center region. In addition, we discussed a lot with Mónica Valencia-Schneider, Gerold Busch, Nastaran Fazeli, Matthias Subroweit, and many others.

In the following stage of my career, I continued as a junior postdoctoral fellow at the Max Planck Institute for Radioastronomy in Bonn. I was supported by a large collaborative research grant SFB 956. During this time I really appreciated the collaboration with Dr. Silke Britzen and colleagues concerning the investigation of jet kinematics and precession in blazars and other radio galaxies. One of our favourite sources has been OJ287, the “Rosetta stone” of blazars, which exhibits an exemplary jet precession/nutation pattern, and we actually managed to prove it. This collaboration continues till now and has been bringing very interesting results, also concerning the connection between the jet precession and SED changes and a potential origin of high-energy neutrinos in blazars.

I would also like to highlight the contribution of Dr. Arman Tursunov from the Silesian University in Opava (now a Humboldt fellow at MPIfR), who has not only been an exemplary collaborator but also one of my best friends among friends-scientists. The work on the black-hole charge and the related spin-offs has gained a lot of world-wide visibility and impact, which I didn’t expect at the time when we started to discuss the problem of the black-hole charge “over some Kölsch beer” back in Bad Honnef close to Bonn.

Later, during the years 2019-2021, I spent my second postdoc in Warsaw, at the Center for Theoretical Physics of the Polish Academic of Sciences, in the group of Prof. Bożena Czerny. Bożena is probably one of the most clever and “universal”, or as one would call it in music – multi-instrumental, astrophysicists I have ever met. During this time I partially switched from the extremely underluminous Galactic center to (mostly, but not only) intermediate-redshift quasars, some of which accrete close to the Eddington limit. This experience complemented my previous expertise and I started to understand more connections among systems accreting at different rates. Some of these aspects I tried to stress in this thesis. I have also enjoyed many discussions and collaborative projects with the whole Warsaw group – to name the most influential people – Swayam Panda, Marzenka Śniegowska, Mary Loli Martinez Aldama, Mohammad Naddaf, Raj Prince, Vikram Kumar Jaiswal, Ashwani Pandey, Amit Kumar, and many other people at the CFT PAN and CAMK. I also have to stress that now, in retrospect, I really appreciate that we remained well focused and organized during the COVID pandemic lock-downs and we managed to discuss and solve many problems via numerous zooms.

After my Warsaw stay, in 2021 I got a position at the Masaryk Universe in Brno, the Czech Republic, in the High-energy Astrophysics group led by Prof. Norbert Werner. I would really like to express my gratitude to Norbert, the leader of the High-Energy Astrophysics group, and Prof. Rikard von Unge, the director of the Department of Theoretical Physics and Astrophysics, for this opportunity to continue with my research in Brno, which is only ~ 100 km from my home-town Malacky. I especially thank Norbi for his support, many discussions about interesting projects on the Earth and in space, and also interviews about other, sometimes even personal matters. The workplace that I found in Brno is generally very positively oriented and constructive. I also got an opportunity to supervise students and to contribute to the course on the Structure and the Evolution of the Universe. I would like to thank all the current and past members of the HEA group for a stimulating environment and a lot of scientific and other fun. These people are mainly the following ones (the order is quite random): Petr Kurfürst, Jean-Paul Breuer, Tomáš Plšek, Matej Kosiba, Dan Hu, Orsi Kovács, Jakub Řípa, Filip Münz, Filip Hroch, Henry Best, Izzy Garland, Congyao Zhang, Matúš Labaj, Martin Mondek, Martin Kolář, Monika Pikhartová, Lýdia Štofánová, Marianna Dafčíková, Jolie L’Heureux, Ania Wójtowicz, Kristýna Voroboková, Kristína Kallová, Klaudia Protušová,

Ramona Valková, Lea Szakszonová, Romana Grossová, Samuel Kováčik, Artem Gorodilov, Wladimiro Leone, Edoardo Borciani, Jakub Vyskočil, and many students (I apologize if I forgot someone, I tried not to :)). I also thank Terka Jeřábková, my new/old colleague and friend, for a lot of stimulating discussions and advice during the past 10 years since our studies in Prague. In addition, I am proud of Lýdia Štofánová, another new/old colleague, who was also my first student that I mentored, for the successful defence of her PhD thesis and a continuing career in astrophysics and space-related activities. I hope that I learned from my mistakes that I did during the counselling of Lýdia's thesis and I apologize to her and Vladimír (Karas) if it caused trouble and extra work since I was mostly out of Prague in Cologne at that time.

I would also like to thank for a lot of support and advice to Prof. Zdeněk Mikulášek, Prof. Rikard von Unge, Prof. Miloš Zejda, Prof. Jiří Krtička, Dr. Honza Janík, Vašek Glos, Mrs. Santarová, and all the other colleagues at the Department of Theoretical Physics. I have to admit that I enjoy our common morning coffees on Friday before the institute seminar – and for this reason I am willing to always sacrifice some money to buy typical Czech pastries and cakes – it is always fun to discuss with people with a different expertise and views.

I would also like to express my gratitude for many stimulating discussions and input to my close scientific collaborators during the last 5 years (some of whom were not explicitly mentioned earlier), these are mainly Florian Peissker, Silke Britzen, Petra Suková, Vojta Witzany, Arman Tursunov, DJ Pasham, Muryel Guolo, Francesco Tombesi, Eric Coughlin, Ali Kurmus, Louis Deslauriers, Bharat Ratra, Narayan Khadka, Shulei Cao, Bart Ripperda, Sean Ressler, Shubham Kejriwal, Alvin Chua, Ana Laura Müller, Anabella Araudo, Jirka Horák, Ladislav Šubr, Myank Singhal, Maria Melamed, Emma Bordier, Marcel Štolc, Sebastiano von Fellenberg, Christian Fendt, and many, many others.

During the years after my PhD studies, I have appreciated the support of several research grants that largely enabled to do research presented in this thesis. During my stay at the MPIfR in Bonn and at the University of Cologne (2017-2019), I was supported by SFB 956 (“Conditions and Impact of Star Formation – Astrophysics, Instrumentation and Laboratory Research”). Subsequently, during my postdoctoral fellowship at the Center for Theoretical Physics, Polish Academy of Sciences in Warsaw (2019-2021) I received the support from the National Science Center, Poland, grant No. 2017/26/A/ST9/00756 (Maestro 9). During my current research stay at the Masaryk University in Brno, I have been supported by several research grants, specifically the Czech Science Foundation EXPRO grant no. GX21-13491X (“Exploring the Hot Universe and Understanding Comic Feedback”), MUNI Award in Science and Humanities 3 (Space-Based High-Energy Astrophysics, MUNI/I/0003/2020), the Czech Science Foundation Lead Agency grant no. GF23-04053L (Czech-Polish bilateral grant “Weather effects in using disk continuum time delays in active galactic nuclei to measure the expansion rate of the Universe”), and the Czech Science Foundation Junior Star grant no. GM24-10599M (“Stars in galactic nuclei: interrelation with massive black holes”).

I would also like to highlight the work of the Slovak Association for Youth, Science, and Technology (AMAVET), who helped me to present my project about the measurement of the Solar “constant” at the nationwide Science and Technology Fair in 2008. Meeting many talented and motivated peers certainly boosted my motivation further. Subsequently, I became involved in the science popularization projects of AMAVET. I was also a member of the Local Organization Committee of the MILSET Expo Sciences International in Bratislava in 2011 as well as in 2013 in Abu Dhabi. Every year I do my best to serve as a judge at the Science and Technology fair in Bratislava, which always boosts my motivation to continue

doing science while talking to many young motivated people. On an international level, I also served as an adult-in-charge at the Intel International Science and Engineering Fair (ISEF) in Phoenix, Arizona in 2019 and at the Genius Olympiad 2023 and 2024 in Rochester, New York. At the Genius Olympiad, I also served as a judge of the selected projects twice.

Concerning the preparation of this Habilitation Thesis and the whole procedure, I owe many thanks to Mgr. Michaela Švestková and Mgr. Jana Procházková for all of their guidance and for checking details in my documents. In addition, I really appreciate the help of Mgr. Jana Nguyen Baluchová and Mgr. Marie Novosadová Šípková with collecting all of my published papers in the right format and listing their corresponding citations. Without their help, the whole preparation process would be much slower. I would also like to thank Prof. Božena Czerny for reading and checking the parts of this thesis, mainly the Introduction. I am also grateful to Vladimír Karas for his comments and recommendations during the writing process.

Last but not the most important, I would like to thank my closest family, especially my parents, Viera and Marián, my sister Barbora, and her children Nina, Sebastian, and Kristian, for a lot of support, love, and encouragement, without which this work would not be possible. I would like to thank all the other (non-astronomy) family members and friends in Slovakia, the Czech Republic, and elsewhere for all the support, inquiring questions, comments, and encouragement that helped me to push forward all the scientific, popularization as well as non-scientific efforts in my life :)

Photogallery

This small photogallery illustrates my research and educational activities both at home and abroad. Figure 1 captures a moment after my successful PhD Thesis defence in Cologne, Germany. Figures 2, 4, 5 were taken during my participation at talks, seminars, and conferences in the Czech Republic, while Figures 3, 6, 7 capture such events abroad. Figure 8 represents a pie chart from the NASA Astrophysics Data System showing my overall co-author connections at the end of 2024.



Figure 1: A moment after the PhD defence on October 12, 2017 at the University of Cologne. Photography author: V. Karas



Figure 2: Enjoying a canteen lunch with Prof. Jiří Bičák (1942-2024) at the Faculty of Mathematics and Physics of the Charles University in Prague. The photo was taken after my talk about the James Webb Space Telescope (“James Webb Space Telescope and Intricate Physics of Star Formation in the Galactic Center and Beyond”) presented at the Department of Theoretical Physics colloquium on February 22nd, 2022.



Figure 3: A conference group photo at the Eighth Giant Magellan Telescope Community Science Meeting focused on *Black holes at all scales*. The photo was taken at the beginning of September 2022 in the Village of Oak Creek, Sedona, Arizona.



Figure 4: Lecturers of the Autumn school of astronomy, physics and mathematics at the Cheb High School. The photo was taken at the end of the school on Friday, November 11, 2022. The lecturers in the photography are (from the left to the right): Prof. Zdeněk Mikulášek, Prof. Petr Chvosta, Mgr. Jaroslava Dirlbecková, Mgr. Jan Dirlbeck, Dr. Jiří Grygar, and me.



Figure 5: A conference group photo taken at the Cologne-Prague-Brno meeting, June 1st-3rd, 2022, at the Brno Observatory and Planetarium.



Figure 6: A photo with the members of the Center for Computational Relativity and Gravitation led by Prof. Manuella Campanelli at the Rochester Institute of Technology. Prof. Campanelli is the third person from the right. I gave a presentation at the RIT on the Lense-Thirring precession of the accretion disc-jet system in galactic nuclei on June 14th, 2024.



Figure 7: Among Czecho-slovak young participants at the 73rd Lindau Nobel Laureate Meeting, June 30th - July 5th 2024, Lindau, Germany. In the photo, there is David Wineland (Nobel prize in physics, 2012; fourth from the right) and Countess Bettina Bernadotte af Wisborg, the president of the Council of the Lindau Nobel Laureatte Meeting (fourth from the left).

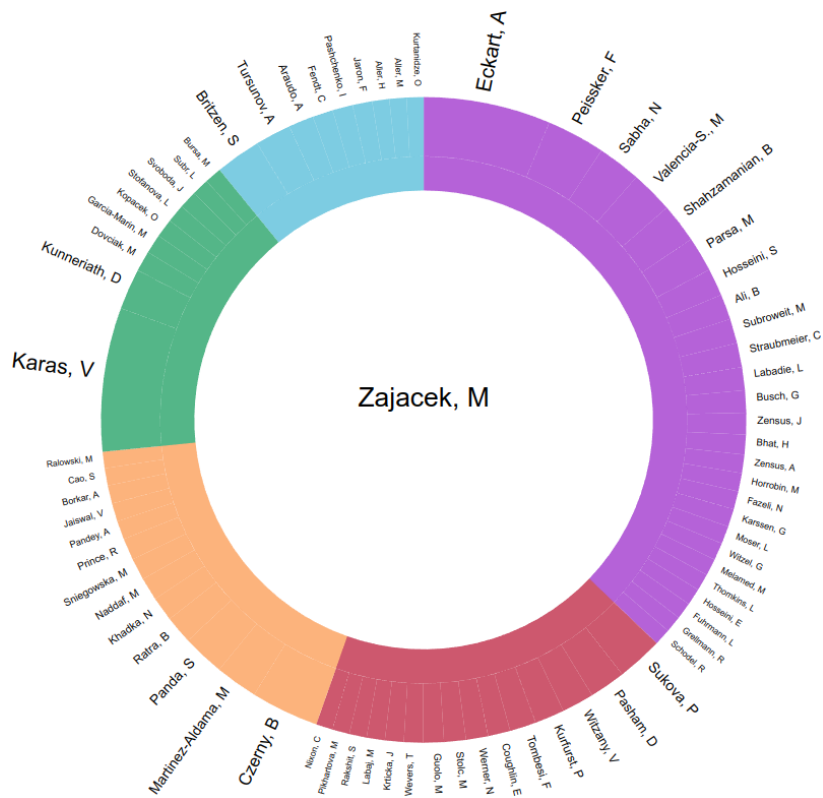


Figure 8: A pie chart of the author network as of December 2024 according to NASA Astrophysics Data System.